NUCLEAR CHEMISTRY
Annual Report
1971

Lawrence Berkeley Laboratory
University of California
Berkeley, California

DISCLAIMER

LBL - 666
UC - 4 Chemistry
TID - 4500 (59th Ed.)

NUCLEAR CHEMISTRY
Annual Report
1971

Lawrence Berkeley Laboratory
University of California
Berkeley, California

Work done under
U.S. Atomic Energy Commission
Contract No. W-7405-eng-48

May 1972

Printed in the United States of America
Available from
National Technical Information Service
U.S. Department of Commerce
5285 Port Royal Road
Springfield, Virginia 22151
Price: Printed Copy $6.00; Microfiche $0.95

Contents

I. Nuclear Structure and Nuclear Properties

Nuclear Spectroscopy and Radioactivity

Nuclear Reactions and Scattering

Nuclear Theory

Fission

E4 MOMENTS IN ^{152}Sm AND ^{154}Sm†

F. S. Stephens, R. M. Diamond, and J. de Boer*

We have previously[1] reported results on the E4 transition moment of ^{152}Sm determined by comparing the experimental and calculated yields of the 4^+ rotational state following Coulomb excitation with ^{4}He projectiles. This moment is of particular interest since it is likely to result from the intrinsic shape of ^{152}Sm; and, if so, can give rather detailed information about that shape. Although data were taken on ^{154}Sm during the original experiments, these could not be interpreted due to the lack of a sufficiently accurate value for B(E2; $4 \rightarrow 2$). This B(E2) value now has been measured with sufficient accuracy and, in addition, the best value for the B(E2; $2 \rightarrow 0$) of ^{152}Sm has been reviewed and adjusted slightly from the previously used value. Finally, the quantum-mechanical corrections to the cross sections have recently been calculated by Alder et al. for both ^{152}Sm and ^{154}Sm. Thus, the intent here is to present and discuss the current best values for the E4 moments of these two Sm nuclei.

The experiments consisted of an accurate comparison of the cross sections of the $4 \rightarrow 2$ transitions in ^{152}Sm and ^{154}Sm with those of the $2 \rightarrow 0$ transitions in ^{150}Sm and ^{152}Sm using both the same (natural samarium) target and different (enriched Sm) targets following Coulomb excitation with ^{4}He projectiles. The cross sections of the $2 \rightarrow 0$ transitions could be calculated from the known B(E2;$2 \rightarrow 0$) values, and these transitions thus served as two independent internal standards, against which the cross sections for production of the 4^+ states in ^{152}Sm and ^{154}Sm could be evaluated. Separate results were obtained from the singles gamma-ray spectra and from those in coincidence with backscattered ^{4}He projectiles. Figure 1 shows the measured 4^+ total (differential) cross sections for ^{154}Sm, σ ($d\sigma$), divided by those calculated using the semiclassical Coulomb-excitation program,[4] σ_0 ($d\sigma_0$), versus the bombarding energy. The cross sections include the feeding from higher-lying levels. The data do not vary significantly with type of target, type of measurement, or bombarding energy in the range from 10-12.5 MeV. If we ignore the very small variation with bombarding energy which is expected in the ratio σ/σ_0 ($d\sigma/d\sigma_0$), then we can form average results which are given in Table I. The error limits quoted for these ratios are the rms deviation of the results from the mean value, and therefore do not contain any of the systematic uncertainties.

For the interpretation of these results in terms of an E4 moment, the semiclassical calculated cross sections must be corrected for quantal effects. These have recently been calculated,[3] and amount to a reduction of the calculated 4^+ cross sections by about 7% in both ^{152}Sm and ^{154}Sm. The quantal corrections to the calculated 2^+ cross sections, which serve as the normalization, are less than 1%. Thus the ratios of the measured cross sections to the quantal cross sections are about 6% larger than the values in Table I. The quantum-mechanical calculations show that the fractional change of the

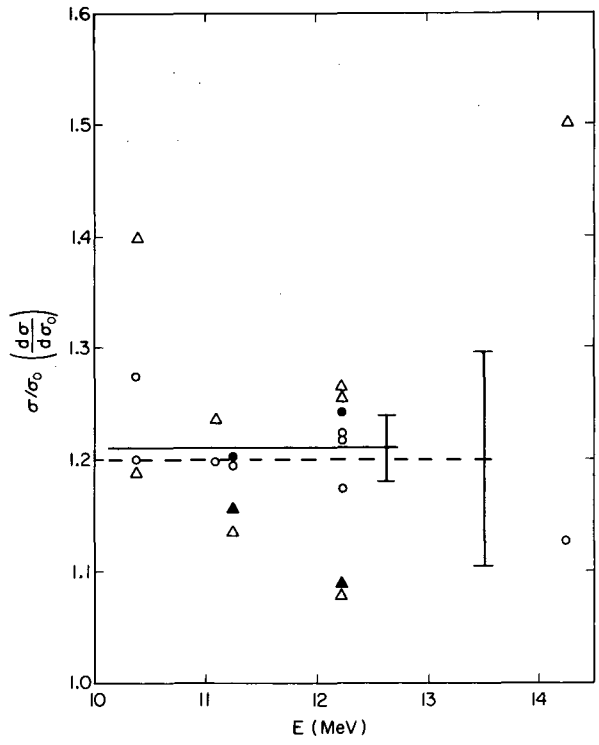

Fig. 1. Ratio of experimental to calculated (semiclassical) cross sections for ^{154}Sm versus the bombarding energy. The triangles are backscatter coincidence measurements and the circles are singles measurements. The open and closed points correspond to natural and enriched Sm targets, respectively. The solid and dashed lines are the average of the singles and coincidence points, respectively, for energies below 12.5 MeV. The error bars indicate the rms deviation of the points from the lines. (XBL 714-3332)

Table I. Averaged results and extracted values.

	^{152}Sm	^{154}Sm
Total cross-section ratio for 4^+ state, σ/σ_0	1.11 ± 0.02	1.21 ± 0.03
Diff. cross section ratio for 4^+ state, $d\sigma/d\sigma_0$	1.11 ± 0.04	1.20 ± 0.09
$\langle 0^+ \| \mathcal{M}(E4) \| 4^+ \rangle$ [eb^2]	+0.45 ± 0.09	+0.67 ± 0.08
β_2	+0.248	+0.261
β_4	+0.09 ± 0.03	+0.13 ± 0.03

cross section due to E4 moments is adequately represented by the semiclassical calculation.[4] For the analysis of the present data, the ratios of cross sections given in Table I were therefore increased by 6% and then evaluated in terms of $\langle 0^+ \| \mathcal{M}(E4) \| 4^+ \rangle$ by the semiclassical calculations as was done previously.[1] The results for ^{152}Sm and ^{154}Sm are given in Table I. The error limits correspond to about 5% uncertainty in the combined ratios σ/σ_0 and $d\sigma/d\sigma_0$, which is our best estimate of the experimental uncertainties and those coming from the parameters entering the analysis. The ^{152}Sm value is about 30% higher than our previous number, due almost entirely to the quantal corrections. A more detailed account of the important sources of uncertainty was given in Ref. 1.

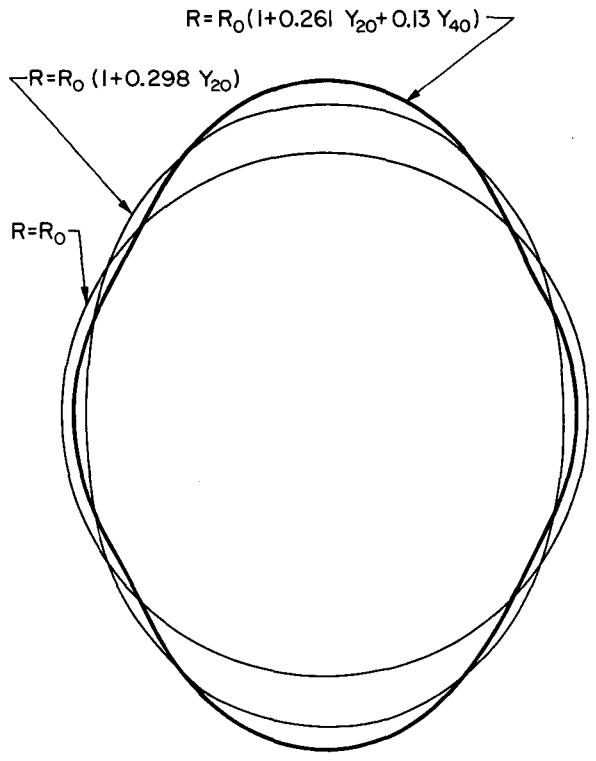

Fig. 2. The shape of ^{154}Sm indicated by the present measurements (heavy line) together with the shape having no Y_{40} term but the same B(E2; $0 \rightarrow 2$), and a sphere with the same R_0. (XBL 714-3333)

If, as previously, the nucleus is assumed to be a rigid uniformly charged rotor with a sharp surface defined by

$$R = R_0(1 + \beta_2 Y_{20} + \beta_4 Y_{40}),$$

then β_2 and β_4 can be evaluated from the measured E2 and E4 transition moments. Using $R_0 = 1.2\ A^{1/3}$ F, we find the values for β_2 and β_4 given in Table I. In Fig. 2 this shape for ^{154}Sm is shown together with (a) the shape that has $\beta_4 = 0$ and the same E2 moment and (b) the sphere having the same R_0. These β_4 values for the nuclear charge distribution are about twice those obtained for the nuclear field from (α, α') measurements above the Coulomb barrier.[5-7] They are also somewhat larger than expected on the basis of present calculations of nuclear shapes.[8] This conclusion differs from that in our previous paper,[1] since (a) the value for ^{154}Sm is considerably larger than that for ^{152}Sm and (b) the quantal corrections for ^{152}Sm cause a 50% increase in β_4 for that nucleus.

It is possible that the difference in the β_4 values given by the two methods is due to an error in one of them. The analysis of the Coulomb-excitation data is rather unambiguous, but the experiment is difficult since a difference of only 5—10% in the ratio σ/σ_0 ($d\sigma/d\sigma_0$) could remove the discrepancy. In this re-

gard, some independent experimental results would be valuable, both on the 4^+ cross sections and on the input B(E2) values. The (α,α') experimental results are known with sufficient accuracy, but the analysis of these data is much more complex than that for pure Coulomb excitation. However, the most straightforward explanation is that the different β_4 values represent a slightly different shape for the charge distribution and the nuclear field in these nuclei. Figure 2 shows the difference between $\beta_4 = 0$ and $\beta_4 = +0.13$; and the difference between β_4 from (α,α') data and ours is only about half this large (variations of about ± 0.2 F in the nuclear surface) if R_0 and β_2 are similar to those in Fig. 2. It does not seem implausible to us that such differences could exist. Thus, the exact meaning of these β_4 values seems to us to be an open and very interesting problem.

Footnotes and References

†Condensed from Phys. Rev. Letters 27, 1151 (1971).

*Present address: University of Munich, Munich, Germany.

1. F. S. Stephens, R. M. Diamond, N. K. Glendenning, and J. de Boer, Phys. Rev. Letters 24, 1137 (1970).

2. R. M. Diamond, G. D. Symons, J. Quebert, K. Nakai, H. Maier, J. Leigh, and F. S. Stephens, to be published.

3. K. Alder, R. Morf, and F. Roesel, Phys. Letters 32B, 645 (1970); and private communication (1970-71).

4. A. Winther and J. de Boer, California Institute of Technology Technical Report, 1965 (unpublished), and in Coulomb Excitation, edited by K. Alder and A. Winther (Academic Press, New York, 1966), p. 303; A. Halm et al., private communication.

5. D. L. Hendrie, N. K. Glendenning, B. G. Harvey, O. N. Jarvis, H. H. Duhm, J. Saudinos, and J. Mahoney, Phys. Letters 26B, 127 (1968).

6. N. K. Glendenning and R. S. Mackintosh, Phys. Letters 29B, 626 (1969).

7. A. A. Aponick, Jr., C. M. Chesterfield, D. A. Bromley, and N. K. Glendenning, Nucl. Phys. A159, 367 (1970).

8. S. G Nilsson, C. F. Tsang, A. Sobiczewski, Z. Szymanski, S. Wycech, C. Gustafson, I.-L. Lamm, P. Möller, and B. Nilsson, Nucl. Phys. A131, 1 (1969).

MEASUREMENT OF THE MAGNETIC MOMENT AND LIFETIME OF THE $13/2^+$ LEVEL IN ^{205}Pb†

K. H. Maier,* J. R. Leigh,‡ and R. M. Diamond

Magnetic moments in the region around ^{208}Pb are of great interest since they show large deviations from the shell-model predictions even though this model is otherwise particularly successful for these nuclei. So far only the g factors for protons in $h_{9/2}$ (Ref. 1) and $i_{13/2}$ (Ref. 2) orbits around the ^{208}Pb core and the $p_{1/2}$ (Ref. 1) and $f_{5/2}$ (Ref. 3) neutron hole in this core have been measured.

The present work, and a following study, aims to determine the magnetic moment of the $i_{13/2}$ neutron hole. Clearly the most desirable measurement would be the moment of the $13/2^+$ level in ^{207}Pb which is just an $i_{13/2}$ neutron hole in ^{208}Pb. However the half-life of this level ($T_{1/2} = 0.743 \pm 0.022$ sec)[4] makes this very difficult in general, and impossible for us.

The decay scheme of the $13/2^+$ isomer in ^{205}Pb is shown in Fig. 1. Its qualitative features, energies, spins, and multipolarities had been established already, and are taken from Ref. 1, while the half-life and intensities given are the results of this work. The isomer was produced through the reaction ^{204}Hg$(\alpha, 3n)$ ^{205}Pb with 41-MeV α particles on a thick liquid ^{204}Hg target (enriched to 80%). The γ rays were detected with a 35 cm^3 coaxial Ge(Li) detector. Electronics that recover rapidly from heavy overloading during the beam pulses were necessary to make the experiments possible.

The g factor was measured by the method of differential perturbed angular distributions following reactions (DPAD). In this, the isomer is produced and aligned by means of a nuclear reaction induced by a pulsed beam. A magnetic field H is applied to the target perpendicular to the beam axis, and causes a Larmor precession of the nuclei ($\omega_L = -g \cdot H \cdot \mu_N/\hbar$). The angular distribution of the de-exciting γ

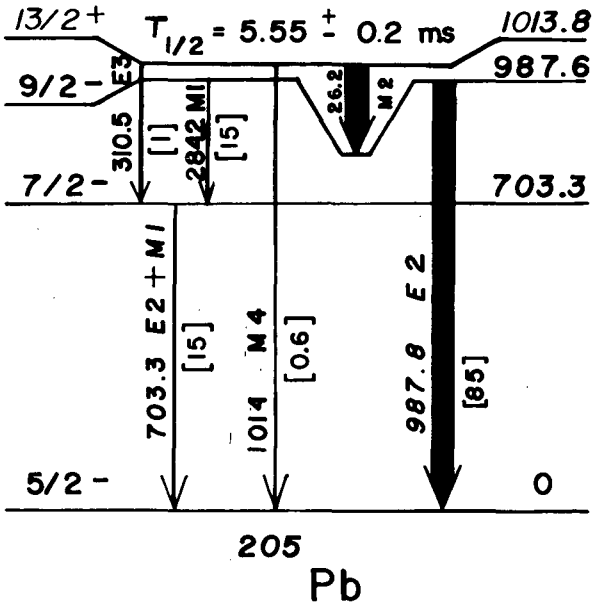

Fig. 1. Decay scheme of the $13/2^+$ isomer in ^{205}Pb. Spins, multipolarities, and energies are from Ref. 1. (XBL 712-218)

rays rotates likewise. Therefore a detector positioned in the plane perpendicular to the magnetic field direction shows a sinusoidal modulation of the count rate superimposed on the exponential decay:

$$I(t,\theta) = \exp(-\lambda t)\{1+\exp(-\rho t)A_2P_2[\cos(\theta-\omega_L t)]\}. \quad (1)$$

Here t is the time elapsed from the centroid of the beam pulse, θ is the angle between the detector and the beam direction, λ is the decay constant, and A_2 is the angular distribution coefficient of the observed transition. Higher terms than P_2 in the angular distribution are neglected since they are small. The following conditions have to be fulfilled for the present measurement: Δt (width of beam pulse) $\ll T = \pi/\omega_L$ (period of rotation of the angular distribution) $\ll T_R$ (relaxation time), and T_{rep} (repetition time of the beam) $\gg T_{1/2}$. For an estimated g factor of -0.1 and a field of 50 G, the time for one revolution of the angular distribution would be T = 130 μsec, so beam pulses of width Δt = 20 μsec were used. The beam repetition time was T_{rep} = 1/36 sec.

The time distribution of the 988-keV line as accumulated in 8 hours of running is shown in Fig. 2. The measuring interval started about 50 μsec after the beam pulse and was 1.1 msec wide. The 50-μsec delay was necessary mainly because of the strong excitation of the 7^- isomer in ^{206}Pb ($T_{1/2}$ = 120 μsec) through the ^{204}Hg

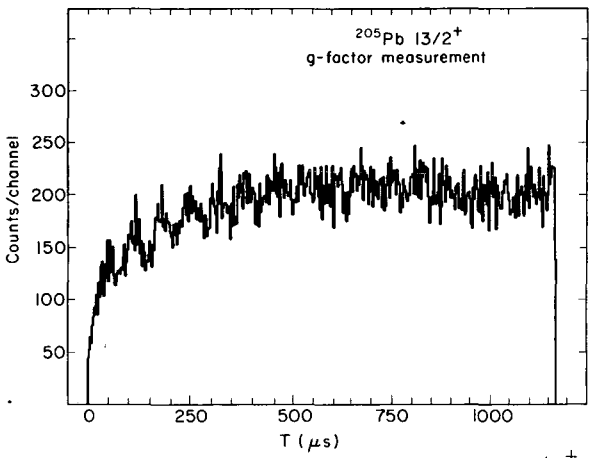

Fig. 2. g-Factor measurement of the $13/2^+$ level in ^{205}Pb. Time distribution of the 988-keV line. The interval shown starts about 50 μsec after the beam pulse. (XBL 712-2879)

$(\alpha, 2n)$-reaction in the thick target. The initial rise seen in the time distribution is due to the dead time introduced in the pile-up rejector by this isomer. The background under the 988-keV line was less than 5%. Though the oscillations due to the Larmor precession are clearly visible in Fig. 2, an evaluation according to Eq. (1) is difficult due to the dead time distortion of the spectrum. Therefore the standard procedure of positioning the detector at 45° and measuring with the field both up and down while everything else is kept constant was used. One then can evaluate the ratio:

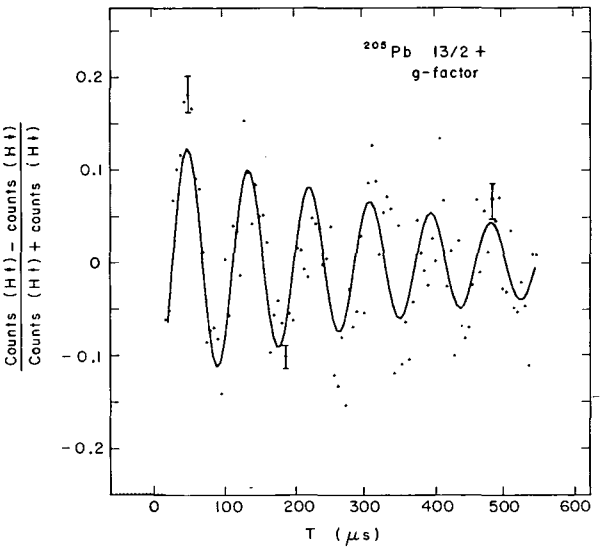

Fig. 3. The ratio $[I(H\uparrow) - I(H\downarrow)]/[I(H\uparrow)+I(H\downarrow)]$ together with the least-square fit. (XBL 713-3035)

$$\frac{I(H\uparrow) - I(H\downarrow)}{I(H\uparrow) + I(H\downarrow)} = \frac{3A_2 \exp(-\rho t)\sin(2\omega_L t)}{4 + A_2 \exp(-\rho t)} . \quad (2)$$

Actually at $\theta = 45°$ only the sign of the product of A_2 and g is determined. However, we checked in a separate experiment that the sign of A_2 is positive, as expected for a stretched E2 transition. The results are: $g = -0.150 \pm 0.004$, $A_2 = +0.3$, $T_R = 0.4 \pm 0.2$ msec. The apparent g factor has to be corrected for a diamagnetic and Knight shift of the field at the nucleus. The Knight shift for lead in liquid mercury can only be estimated from the known shifts for mercury in mercury (2.4%)[5] and lead in lead (1.5%).[5] It turns out that it just cancels the diamagnetic shift (- 1.7%).[6] However, an additional error of 1% has been allowed for these corrections. Thus the final result is:

$$g(13/2^+ {}^{205}\mathrm{Pb}) = (-0.150 \pm 0.006) \text{ (corrected)},$$

which corresponds to a magnetic moment, $\mu = (-0.975 \pm 0.040)$ nm.

Footnotes and References

†Condensed from LBL-202; to be published in Nuclear Physics.

*Present address: Hahn-Meitner-Institut, Berlin.

‡Present address: Department of Physics, Australian National University, Canberra.

1. C. M. Lederer, J. M. Hollander, and I. Perlman, Table of Isotopes (Wiley & Sons, New York, 1967.

2. T. Yamazaki, T. Nomura, S. Nagamiya, and T. Katou, Phys. Rev. Letters 25, 547 (1970).

3. H. J. Körner, K. Auerbach, J. Braunsfurth, and E. Gerdau, Nucl. Phys. 86, 395 (1966).

4. H. P. Yule, Nucl. Phys. A94, 442 (1966).

5. L. E. Drain, Met. Rev. 12, 195 (1967).

6. F. D. Feiock and W. R. Johnson, Phys. Rev. Letters 21, 785 (1968).

STROBOSCOPIC MEASUREMENT OF THE g FACTORS OF THE $21/2^+$ Isomer in ^{207}Bi†

K. H. Maier,* K. Nakai,‡ J. R. Leigh,§ R. M. Diamond, and F. S. Stephens

This is one of three related papers on magnetic moments near ^{208}Pb. Although in general the shell model works especially well in this region, its predictions of magnetic moments even for very pure single-particle states deviate appreciably from the experimental results. A study of these deviations was the main interest of this series; the present paper reports on the g-factor measurement of the $21/2^+$ level ($T_{1/2} = 182\mu$sec) in ^{207}Bi. This level is proposed by Bergström et al.[1] to result from coupling an $h_{9/2}$ proton to the ^{206}Pb 7^- level, whose dominant configuration is $|p^{-1}_{1/2}\, i_{13/2}\rangle_{7^-}$. Since the moment of the $h_{9/2}$ proton is known from the ^{209}Bi ground state, we can find out how compatible these moments are, and check on the purity of the wave functions or on the validity of calculating the moment of a complex state from those of its constituents.

The SOPAD method (stroboscopic observation of perturbed angular distributions) following nuclear reactions was used. It can be summarized as follows. (i) A pulsed beam produces an aligned isomeric level through a nuclear reaction. (ii) The conditions for the production are such that the isomer is left in an environment in which the alignment is preserved for a time comparable to the lifetime of the level or longer. (iii) An applied magnetic field causes a Larmor precession of the nuclei which is observed through the corresponding rotation of the angular distribution of the de-exciting γ rays. At a particular angle this shows up as a modulation of the time distribution of the γ-ray transitions.

The (HI, xnγ) reactions, such as ^{204}Hg(^{7}Li, 4n)^{207}Bi used here, preferentially populate low-lying high-spin levels due to the large amount of angular momentum brought into the compound nucleus. Since this angular momentum comes almost exclusively from the orbital angular momentum in the entrance channel and so is perpendicular to the beam direction, the isomer will be well aligned.

To achieve a relaxation time of the order of 100μsec, liquid metal targets seem to be

the best choice. Disturbances of the electron shell of the recoiling nucleus and of the surroundings heal very quickly, and the short correlation time of the fluctuating environment tends to average out to zero the fields from neighboring atoms.

The count rate $I(\theta, t)$ of a γ ray de-exciting the isomer at an angle θ with respect to the beam and at a time t after the centroid of the last beam pulse and with a magnetic field H applied perpendicular to the plane containing the beam and detector is:

$$I(\theta, t) = \sum_{n=0}^{\infty} \exp\left[-\lambda(t+nT)\right] \times \left\{1 + A_2 \exp\left[-\rho(t+nT)\right] P_2\left[\cos(\theta - \omega_L(t+nT)\right]\right\}. \quad (1)$$

Here $\lambda = 1/\tau$ is the decay constant; T the repetition time of the beam pulses; A_2 the usual coefficient of the angular distribution; $1/\rho = T_r$, the relaxation time; and $\omega_L = -g \cdot H \cdot \mu_N/\hbar$, the Larmor frequency.

If $T << \tau$, the stroboscopic method may be used. This has been developed by the group at the Hahn-Meitner-Institut, Berlin,[2] and has been discussed in detail in Ref. 3 and by Nagamiya and Sugimoto.[4] In this method one counts at an appropriate angle and time window, for instance, $\theta = 45°$ and $t = 1/4T$, and varies the magnetic field; the count rate will then show a resonance for $\pi/\omega_L = T$, with the area under the resonance determined by A_2 and the width about proportional to $(1/\tau + 1/T_R)$. To fit the measured data, the sum in Eq. (1) has been performed in closed form and so have the integrations over the rectangular beam pulse, the width of the counting window, and the angle covered by the detector. A considerable improvement in the experiment is achieved with a two-detector, two-time-window setup. The double ratio of count rates

$$\frac{I(45°,\ 1/4T)/I(45°,\ 3/4T)}{I(-45°,\ 1/4T)/I(-45°,\ 3/4T)} \quad (2)$$

shows the resonance about 4 times stronger, and nearly all errors due to misalignment cancel to first order.

The decay scheme of the isomer, as investigated by Bergström et al.,[1] is shown in Fig. 1. The energy spectrum as seen in the stroboscopic experiment is shown in Fig. 2. Unlabeled lines exhibit different half-lives; no attempt was made to assign them. Figure 3 shows the resonance for the 669-keV transition. The five strongest lines have been

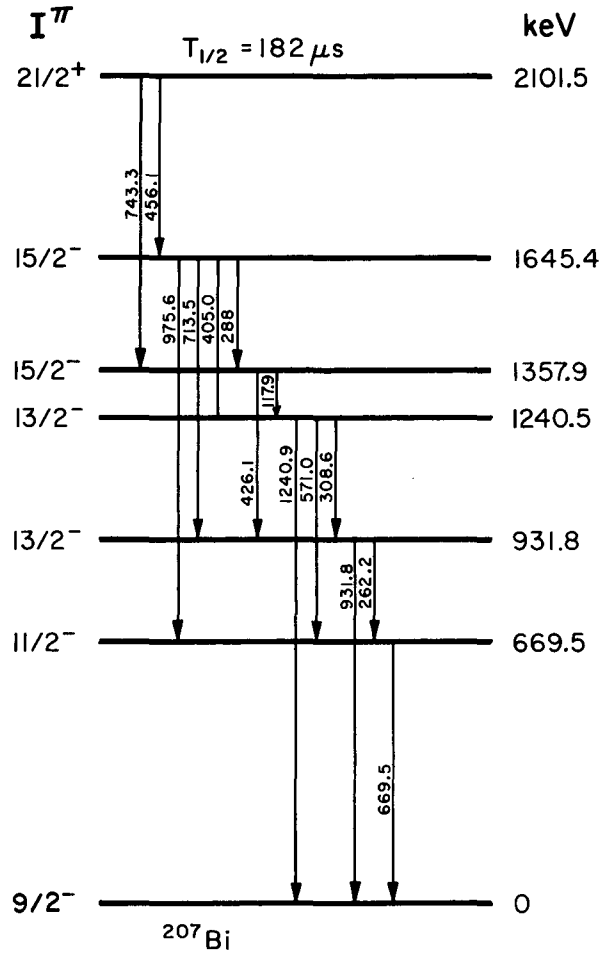

Fig. 1. Decay scheme of the $21/2^+$ isomer in ^{207}Bi. (Derived from Ref. 1.)

(XBL 705-2808)

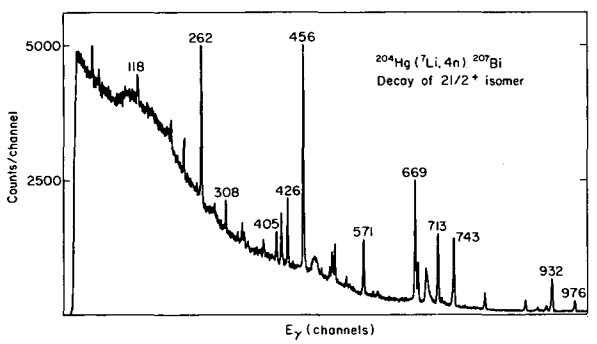

Fig. 2. Energy distribution of the γ rays from the decay of the $21/2^+$ isomer in ^{207}Bi as recorded in the stroboscopic experiment.

(XBL 705-2874)

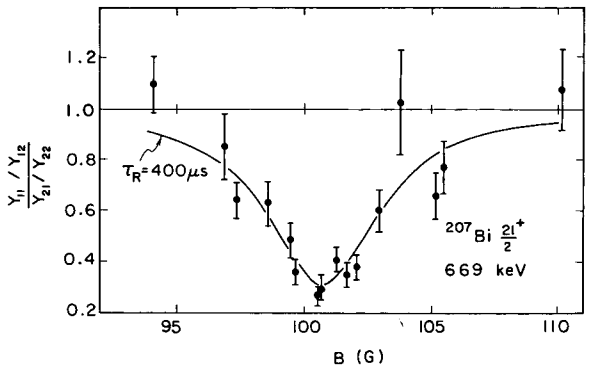

Fig. 3. Stroboscopic resonance (double ratio of count rates) for the 669-keV (M1-E2)-transition in the decay of the $21/2^+$ isomer in ^{207}Bi. The curve is a best fit for g and A_2, assuming a relaxation time of 400μsec.

(XBL 705-2870)

evaluated, and the results are summarized in Table I. The error in the g factor is determined by the accuracy of the field measurement, yielding:

$$g(^{207}\text{Bi } 21/2^+) = (+0.325 \pm 0.0003)\text{nm} \quad \text{(uncorrected)}.$$

The actual field at the nucleus can deviate from the applied external magnetic field because of the Knight shift and the diamagnetic correction. These appear to have a magnitude of the order of 2%, but to cancel each other. Therefore:

$$g(^{207}\text{Bi } 21/2^+) = (+0.325 \pm 0.006)\text{nm(corrected)}.$$

The situation for the $21/2^+$ level in ^{207}Bi is clear. Calculating its moment from those measured for the ^{206}Pb 7^- level and the $(\pi h_{9/2})$ ^{209}Bi ground state gives $\mu = 3.39$ nm, in perfect agreement with the measured $\mu = (3.41 \pm 0.06)$nm. So the proposed wave function[1] (^{206}Pb 7^-, $\pi h_{9/2})21/2^+$ is verified. Simultaneously, this is a remarkable example of the validity of combining the measured moments according to the rules for the single-particle operator[5] even though the individual moments deviate appreciably from the Schmidt values. This, and similar examples confirming the additivity of magnetic moments near ^{208}Pb, are described in Ref. 6.

Table I. Results of the stroboscopic experiment on the ^{207}Bi $21/2^+$ isomer. The values given for A_2, T_R, and g are the results of best fits to the measured resonance as described in the text.

E_γ (keV)	Multipolarity	A_2	T_R (μsec)	g (nm)
262	M1 + E2	-0.34	220	0.3258
456	E3	0.43	410	0.3248
669	M1 + E2	-0.62	620	0.3256
713	M1 + E2	-0.44	660	0.3250
743	E3	0.54	390	0.3254

Footnotes and References

†Condensed from LBL-243; to be published in Nuclear Physics.

*Present address: Hahn-Neitner-Institut, Berlin, Germany.

‡Present address: Department of Physics, University of Tokyo, Japan.

§Present address: Department of Physics, Australian National University, Canberra, Australia.

1. I. Bergström, C. J. Herrlander, O. Thieberger, and J. Blomqvist, Phys. Rev. 181, 1642 (1969).

2. J. Christiansen, H. -E. Mahnke, E. Recknagel, D. Riegel, G. Weyer, and W. Witthuhn, Phys. Rev. Letters 21, 554 (1968).

3. J. Christiansen, H. -E. Mahnke, E. Recknagel, D. Riegel, G. Schatz, G. Weyer, and W. Witthuhn, Phys. Rev. C1, 613 (1970).

4. S. Nagamiya and K. Sugimoto, Osaka University Report OULNS 69-3, 1969.

5. A. de Shalit and I. Talmi, Nuclear Shell Theory (1963), pp. 56 and 449.

6. K. H. Maier, K. Nakai, J. R. Leigh, R. Diamond, and F. S. Stephens, Nucl. Phys., to be published.

EFFECTIVE SINGLE-PARTICLE MAGNETIC MOMENTS AROUND ^{208}Pb†

K. H. Maier,* K. Nakai,‡ J. R. Leigh,§ R. M. Diamond, and F. S. Stephens

The well-known failure of the shell model to predict the experimental magnetic moments around ^{208}Pb, a region where it is particularly successful otherwise, has stimulated much theoretical work to explain the deviations.[1-8] The main point common to all this work is to consider core excitations caused by the residual interaction in which a nucleon is excited from a filled level in the core to its empty spin-orbit partner orbital. Taking these core excitations into account, and also the anomalous orbital g factor, δg_ℓ, one can express the magnetic moment for a single particle in the orbital $j = \ell \pm 1/2$:

$$\text{protons: } \mu = j\left[(g_{\ell p} + \delta g_{\ell p}) \pm \frac{(g_{sp} - \delta g_s) - (g_{\ell p} + \delta g_{\ell p})}{2\ell + 1}\right] - g_p \langle (i^2 Y_2 s)_1 \rangle + X, \quad (1a)$$

$$\text{neutrons: } \mu = j\left[(g_{\ell n} + \delta g_{\ell n}) \pm \frac{(g_{sn} + \delta g_s) - (g_{\ell n} + \delta g_{\ell n})}{2\ell + 1}\right] + g_p \langle (i^2 Y_2 s)_1 \rangle + X, \quad (1b)$$

$$\text{with } \langle (i^2 Y_2 s)_1 \rangle = \frac{1 \mp (j + \frac{1}{2})}{4\sqrt{2\pi}\,(j+1)}. \quad (2)$$

Here X stands for complicated contributions from exchange intervals, while the other terms constitute the direct part. The quantity g_s has the usual value 5.58 or -3.82 for proton or neutron, respectively, and the parameters δg_s and g_p represent the core-polarization terms.

Recently, a number of new experiments have been performed. Yamazaki and co-workers measured the moments of the 8^+ (Ref. 10) and 11^- (Ref. 11) levels in ^{210}Po, of the 8^+ level in ^{208}Po (Ref. 12) and of the $17/2^-$ isomer in ^{209}Po (Ref. 13). We determined the g factors of the $13/2^+$ isomer in ^{205}Pb (Ref. 14), of the 7^- level in ^{206}Pb, the $21/2^+$ level in ^{207}Bi, and the 8^+ level in ^{212}Rn (Ref. 15). The 15^- state in ^{210}At has been measured by Bergström et al.[16] and very recently the g factor of the 12^+ level in ^{206}Pb has been measured by Nakai et al.[17] These are all quite pure shell-model states. By combining the new results with the earlier work, enough data are now available so that we can try to check the validity of this expression and the importance of the terms in it.

Table I (upper part) summarizes the measured magnetic moments of good shell-model levels around ^{208}Pb. The dominant configurations are given in column 3, and for the sake of definiteness we will consider only these configurations, as any admixtures should be small and are not known well enough to allow reliable corrections. The lower part of the table contains the other four measured moments that lend themselves to this treatment only with limitations, as serious doubts exist as to the purity of their wave functions.

The four parameters δg_s, g_p, $\delta g_{\ell p}$, and $\delta g_{\ell n}$ in Eqs. (1) and (2) have been determined from a least-square fit to the five single-particle moments given first in Table I. The result is: $\delta g_s = 3.43$, $g_p = 4.55$, $\delta g_{\ell p} = 0.09$, and $\delta g_{\ell n} = 0.06$ (all in nm). The moments calculated with these parameters are given in column 7 of the table, and the contributions from δg_s, g_p, δg_ℓ separately are listed in columns 8-10. The agreement with experiment is good, particularly if one compares with the corresponding values.

Thus, it is possible to account for all the measured magnetic moments of good shell-model levels around ^{208}Pb, using a surprisingly simple and effective operator with a few reasonable parameters. This in turn means that the assumptions involved are likely to be valid. They are: (i) The wave functions of the levels considered are quite pure, (ii) the exchange terms are unimportant, (iii) the interaction causing the polarization of the core is predominantly of the type $(\sigma_i \cdot \sigma_j)(\tau_i \cdot \tau_j)$ and of long range. In addition, the measured g factors around ^{208}Pb firmly establish the additivity of the magnetic moments in this region.

It is also of interest to consider allowed M1 transitions. For a transition between single-particle levels from $j_1 = \ell + 1/2$ to $j_2 = \ell - 1/2$ the B(M1) value calculated with the effective operator becomes (in units of $\frac{3}{4\pi}\left(\frac{e\hbar}{2Mc}\right)^2$):

$$B(M1,\ \ell + \tfrac{1}{2} \to \ell - \tfrac{1}{2}) = \frac{\ell}{(2\ell+1)} \times \left[(g_s + \delta g_s) - (g_\ell + \delta g_\ell) + \frac{1}{4\sqrt{2\pi}}\, g_p\right]^2. \quad (3)$$

The sign in front of δg_s and g_p has been chosen

Table I. Magnetic moments of shell-model states around ^{208}Pb.†

Level		E_x (MeV)	Dominant configuration	μ experiment	μ Schmidt	μ added	μ calculated	Contributions from δg_s	g_p	δg_e
$9/2^-$	^{209}Bi	g.s.	$\pi h_{9/2}$	4.08[a]	2.62		3.98	1.40	-0.50	+0.44
$1/2^-$	^{207}Pb	g.2.	$\nu p_{1/2}$	0.59[a]	0.64		0.63	-0.57	+0.60	-0.04
$5/2^-$	^{207}Pb	0.579	$\nu f_{5/2}$	0.65(5)[b]	1.37		0.49	-0.23	+0.52	-0.17
$13/2^+$	^{205}Pb	1.014	$\nu i_{13/2}^{-1}$, $(\nu p_{1/2}^{-2})_0$	-0.98[c]	-1.91		-0.91	+1.72	-0.36	-0.35
	d		$\pi i_{13/2}$	7.9[d]	8.79		+7.98	-1.72	+0.36	+0.54
11^-	^{210}Po	~2.80	$\pi i_{13/2}$, $\pi h_{9/2}$	12.0[e]	10.66		11.96			
8^+	^{210}Po	~1.50	$\pi h_{9/2}^2$	7.30[f]	4.66	7.26	7.07			
12^+	^{206}Pb	4.027	$\nu i_{13/2}^{-9}$	-1.82[g]	3.53	-1.80	-1.67			
$17/2^-$	^{209}Po	~1.50	$(\pi h_{9/2}^2)_{8^+}$, $\nu p_{1/2}^{-1}$	7.48(43)[h]	4.9	7.89	7.70			
7^-	^{206}Pb	2.200	$\nu p_{1/2}^{-1}$, $\nu i_{13/2}^{-1}$	-0.15[i]	-1.26	-0.39	-0.27			
$21/2^+$	^{207}Bi	2.102	$(\nu i_{13/2}^{-1}, \nu p_{1/2}^{-1})_{7^-}, \pi h_{9/2}$	3.41[i]	1.15	3.39	3.18			
8^+	^{208}Po	1.532	$(\nu p_{1/2}^{-2})_{0^+}, (\pi h_{9/2}^2)_{8^+}$	7.88[j]	4.66	7.26	7.07			
8^+	^{212}Rn	~1.690	$\pi h_{9/2}$	7.12[i]	4.66	7.26	7.07			
15^-	^{210}At	2.549	$(\pi h_{9/2}^2, \pi i_{13/2})_{29/2^+}$, $\nu p_{1/2}^{-1}$	15.7[k]	14.1	16.1	15.68			
$1/2^+$	^{205}Tl	g.s.	$(\nu p_{1/2}^{-2})_{0^+}, \pi s_{1/2}^{-1}$	1.63[a]	2.79		1.08			
1^-	^{210}Si	g.s.	$\pi h_{9/2}$, $\nu g_{9/2}$	±0.04[a]	0.08		0.36			
6^-	^{206}Pb	2.385	$\nu p_{1/2}^{-1}$, $\nu i_{13/2}^{-1}$	0.78(42)[l]	-2.44	-1.50	-1.44			
$7/2^-$	^{211}Bi	0.405	$(\nu g_{9/2}^2)_0 \pi f_{7/2}^2$	4.41(65)[a]	5.79		4.65			

Table I (continued).

†All moments are given in nuclear magnetons. Column 4 gives the experimental values and the errors exceeding 3%. Column 5 shows the predictions of the shell model for the configuration of column 3, using the free nucleon moments. The values of column 6 are obtained by using the formalism of the single-particle operator from the measured values of the configurations constituting these levels. Column 7 shows the predictions for the effective operator [Eqs. (2-4)] with the contributions from the terms in δg_s, g_p, and $\delta g_{\ell p}$ given in columns 8-10.

---

[a] Table of Nuclear Moments, compiled by V. Shirley, in Hyperfine Structure and Nuclear Radiations, edited by E. Matthias and D. A. Shirley (North-Holland, Amsterdam, 1968).

[b] H. J. Körner, K. Auerbach, J. Braunsfurth, and E. Gerdau, Nucl. Phys. 86, 395 (1966).

[c] Ref. 14.

[d] Derived from the measured values of the $9/2^-$ ^{209}Bi g.s. and the 11^- ^{210}Po level, assuming a pure configuration.

[e] Ref. 11.

[f] Ref. 10.

[g] Ref. 17.

[h] Ref. 13.

[i] Ref. 15.

[j] Ref. 12.

[k] Ref. 16.

[l] Ref. 23.

for neutrons; for protons it has to be reversed. Contrary to the static case in which δg_s and g_p give contributions of opposite sign, here they both decrease B(M1), in agreement with the calculations of Ref. 7. Using the parameters determined from the static moments, the B(M1) values for the $f_{7/2} \rightarrow f_{5/2}$ and $p_{3/2} \rightarrow p_{1/2}$ transitions in ^{207}Pb are reduced by a factor of more than 100 relative to the s.p. values, while experimentally these factors are only 4 (Ref. 17) and 3 (Ref. 18), respectively. Mottelson[4] has pointed out already that the measured lifetime[19] of the $4^+ \rightarrow 5^+$ M1 transition ($s_{1/2}$ spin flip of the $\pi s_{1/2}^{-1}$, $\nu g_{1/2}$ configuration) in ^{208}Tl which shows no hindrance at all, poses a severe problem to the core-polarization picture. This difficulty now seems to be more general and so in spite of the excellent agreement for the static moments, the difficulties with M1 transition moments suggest that additional features may be involved.

Footnotes and References

†Condensed from UCRL-19593, to be published in Nuclear Physics.

*Present address: Hahn-Meitner-Institut, Berlin, Germany.

‡Present address: Department of Physics, University of Tokyo, Japan.

§Present address: Department of Physics, Australian National University, Canberra, Australia.

1. Arima and H. Horie, Progr. Theor. Phys. 11, 509 (1954).

2. R. J. Blin-Stoyle and M. A. Perks, Proc. Phys. Soc. (London) A67, 885 (1954).

3. E. Bodenstedt and J. D. Rogers, in Perturbed Angular Correlations, edited by E. Karlsson, E. Matthias, and K. Siegbahn (North-Holland, Amsterdam, 1964), p. 93.

4. B. R. Mottelson, Nordita publications, No. 288, p. 54.

5. J. Blomqvist, N. Freed, and H. O. Zetterström, Phys. Letters 18, 47 (1965).

6. A. Bohr and B. R. Mottelson, Nuclear Structure, Vol. I (Benjamin, New York and Amsterdam, 1969), p. 336.

7. K. Harada and S. Pittel, Nucl. Phys. A159, 209 (1970).

8. Further references given in 1-7.

9. T. Yamazaki, T. Nomura, T. Katou, T. Inamura, A. Hashizume, and Y. Tendou, Phys. Rev. Letters 24, 317 (1970).

10. T. Yamazaki, T. Nomura, S. Nagamiya, and T. Katou, Phys. Rev. Letters 25, 547 (1970).

11. S. Nagamiya, T. Nomura, and T. Yamazaki, Nucl. Phys. A159, 543 (1970).

12. T. Yamazaki and E. Matthias, Phys. Rev. 175, 1476 (1968).

13. K. H. Maier, K. Nakai, F. S. Stephens, and R. M. Diamond, to be published.

14. K. H. Maier, K. Nakai, J. R. Leigh, F. S. Stephens, and R. M. Diamond, to be published.

15. I. Bergström, A. Filevich, K. G. Rensfelt, J. Sztakier, and K. Nakai, to be published.

16. K. Nakai, B. Herskind, S. Blomqvist, A. Filevich, K. G. Rensfelt, and J. Sztakier, to be published.

17. Actually only the M1-E2 mixing ratio has been measured. See Ref. 6, p. 344.

18. H. V. Klapdor, P. von Brentano, E. Grosse, and K. Haberkant, Nucl. Phys. A152, 263 (1970).

19. K. D. Sevier, Nucl. Phys. 61, 601 (1965).

A HIGH-SPIN ISOMER IN ^{211}At†

K. H. Maier,* J. R. Leigh,‡ F. Pühlhofer,§ and R. M. Diamond

In a recent study of several N = 126 isotones[1] an isomer of half-life 4.2±0.4 μsec was observed in ^{211}At; it has the following very interesting properties: 1) the isomer lies at an excitation energy of 4.816 MeV, 2) it has very high angular momentum, $I \approx 39/2$, 3) it decays essentially by a single cascade sequence of 9 γ rays, only one branching being observed, and 4) the isomeric transition has E3 multipolarity and shows considerable en-

Table I. Electron conversion and angular distribution coefficients for transitions in ^{211}At.

E_γ	I_γ	α_K		α_L		α_M		A_2		Multipolarity	I_γ total/I_γ isomer[a]	
		Exp	Theory	Exp	Theory	Exp	Theory	Exp	Theory		34-MeV α	41-MeV ^{7}Li
1067.1±0.5	109 ±11	0.004 ±0.002	E1 0.002 E2 0.005					+0.22 ±0.04	E2 +0.44 M1 -0.31	E2	7.6±0.6	7.5±0.8
253.5±0.5	82[b]	0.08 ±0.02	E2 0.10 M1 0.74	0.092[c]	E2 0.092	0.026 ±0.005	E2 0.03 M1 0.03	+0.24 ±0.02	E2 +0.42 M1 -0.29	E2	6.5±0.2	7.5±0.3
96.0±0.5	7±2			6.5 ±2.0	E2 6.8 M1 2.1	1.5 ±0.5	E2 1.9 M1 0.5			E2	5.0±1	
511.2±0.5	105 ±15	0.12 ±0.03	M1 0.11 E2 0.022	0.02 ±0.005	M1 0.02 E2 0.007			-0.20 ±0.03	M1 -0.28 E2 +0.40	M1	5.3±0.6	5.7±0.6
689.4±0.5	79 ±10	0.013 ±0.01	E1 0.005 E2 0.012 E3 0.03							E1, E2	3.5±1	4.2±1
713.6±0.5	23 ±5	0.05 ±0.04	E3 0.03 M1 0.05 M2 0.10							M1, E3	3.5±1	3.5±1.5
1536±1	97 ±10										1.2±0.2	1.60±0.15
203.7±0.5	40 ±4	0.9 ±0.3	M1 1.35 E3 0.42	0.3 ±0.06	M1 0.25 E3 3.2	0.06 ±0.02	M1 0.06 E3 0.95	+0.3 ±0.1		M1	1.1±0.3	1.5±0.3
435.1±0.5	89 ±10	0.09 ±0.02	E3 0.08 M1 0.17	0.07 ±0.02	E3 0.08 M1 0.03	0.02 ±0.006	E3 0.02 M1 0.007		E3 0.7 E2 0.4 M1-0.3	E3	1	1

[a]Normalized to unity for 435-keV transition.

[b]Normalized to total transition intensity of 100.

[c]Electron intensities have been normalized to yield the theoretical L conversion coefficient for the 253-keV transition.

hancement over the single-particle estimate.

^{211}At has been populated following (heavy ion, xn) reactions using beams of ^{4}He, ^{7}Li, and ^{11}B from the Berkeley Hilac incident on targets of ^{209}Bi, ^{208}Pb, and ^{204}Hg, respectively. The 5-msec Hilac beam pulse (repeated 36 times per sec) was chopped with an electrostatic deflector system to give microsecond beam pulses with variable repeat intervals. Ge(Li) γ-ray spectra have been recorded both in-beam and in the intervals between the microsecond pulses. Excitation functions, both delayed and in-beam, were obtained with the ^{4}He and ^{7}Li beams. In both cases the isomer yield peaked 8 to 10 MeV higher than the prompt component, indicating the high angular momentum of the state. A solenoidal spectrometer with a cooled Si detector was used to record conversion-electron spectra both delayed and in-beam. The half-life of the isomer has been determined by recording Ge(Li) γ-ray spectra obtained in four successive time intervals of 4 μsec each. In-beam angular distributions were performed to obtain A_2's for the transitions with a strong prompt component. The g factor of the 4 μsec state was measured using a pulsed-beam time-differential method, the nuclear alignment being preserved by use of a liquid ^{204}Hg target. The data are summarized in Table I.

A PDP-7 on-line computer system was used to record all γ-γ coincidence events associated with the isomeric decay. The coincidences establish that the transitions form essentially a single cascade, and reveal two other isomeric states in the decay chain with half-lives of the order of 50 nsec. These delays, along with measurements of the prompt-to-delayed intensity ratios of the γ rays, establish the time ordering of the transitions. The level scheme shown in Fig. 1 is thus established. Our data do not determine the 25-to 689-keV sequence, but a recently published study on this same nucleus has done so.[2]

The spins of states up to the $23/2^-$ level at 1928 keV can be assigned with confidence. In making the spin assignments we have assumed that the angular momenta of the observed states increase monotonically with energy. This assumption is supported by the excitation function data and the single-cascade decay mode of the isomer. The delay associated with the 713-keV transition favors the E3 rather than M1 assignment. The only transition whose multipolarity cannot be assigned is the 1536-keV γ ray. The γ-γ coincidence work indicates that the half-life of the 4177-keV state is $\leq$10 nsec. This implies a dipole or quadrupole transition (magnetic or electric), but an enhanced E3 transition cannot be ruled out.

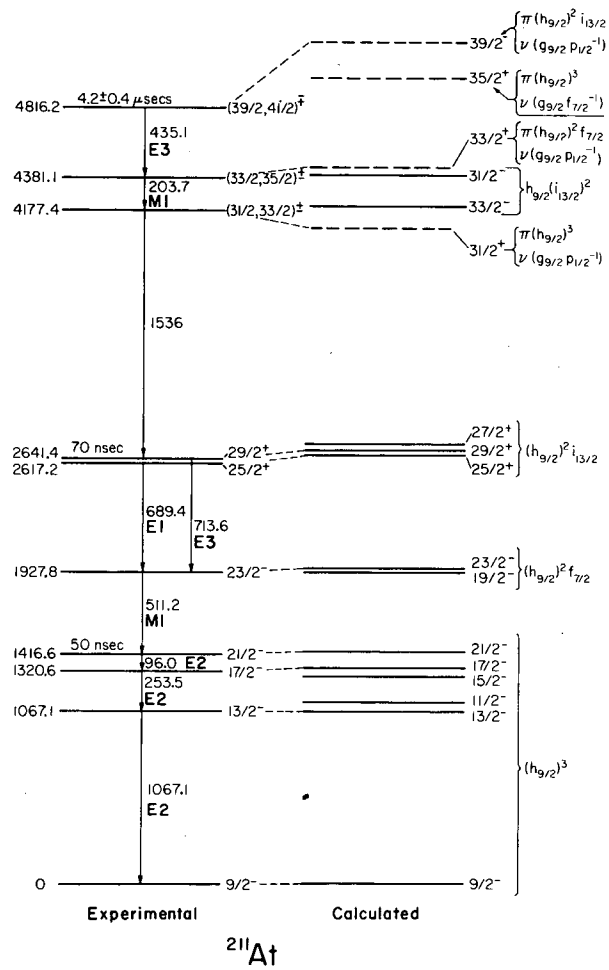

Fig. 1. Experimental and calculated partial level schemes for ^{211}At. Only the lowest level of each spin ($I \geq 9/2$) is shown in the calculated scheme; the solid lines are the 3-proton states, and the dashed lines are 4p-1h states. The dominant configuration of each state is indicated. (XBL 714-3252)

Results of a shell-model calculation described in the following paper[3] are also shown in Fig. 1 in comparison with the experimental level scheme. Three-proton configurations can be assigned to the experimental levels observed up to the $29/2^+$ state. For the three highest levels, 4p-1h configurations are suggested by the model, in particular a

$$(\pi h_{9/2}^{2}\, \pi i_{13/2})_{29/2^+} \cdot (\nu g_{9/2}\, \nu p_{1/2}^{-1})_{5^-}$$

configuration with $J = 39/2^-$ for the isomeric state at 4816 keV.

Bergström, et al.[2] have observed the $29/2^+$ state as a 70-nsec isomer following the ^{209}Bi $(\alpha, 2n)^{211}$At reaction. The deduced level

schemes are identical below the $29/2^+$ level and the more accurate half-lives measured in Ref. 2 are indicated in Fig. 1 for the $21/2^-$ and $29/2^+$ states. Our measured branching ratio for the $29/2^+$ state gives the reduced transition probability for the 713-keV transition [$T_{1/2}(\gamma) = 325$ nsec], B(E3, 713 keV) = $40\,000 \pm 10\,000$ e^2 fm^6, which is in rough agreement with the value $51\,000 \pm 7000$ e^2 fm^6 found in Ref. 2. The order-of-magnitude enhancement over the expected single-particle value has been described there in terms of admixtures of the 3^- octupole state of the ^{208}Pb core to these three-particle states.

From the measured half-life of the 4816-keV state we obtain B(E3, 435 keV) = $83\,000 \pm 9000$ e^2 fm^6, and this is comparable to the transition rate for the 3^- state of ^{208}Pb (Ref. 4). Admixtures of the 3^- core-excited state to the proposed configurations, similar to those of the $29/2^+$ and $23/2^-$ levels[2] may be expected, and it has been suggested that the still larger B(E3) value observed in this case is due to a small admixture of a higher-lying configuration,

$$(\pi h_{9/2}^2 \pi f_{7/2})_{23/2^-} \cdot (\nu j_{15/2} \nu p_{1/2}^{-1})_{8^+}$$

which also has a large E3 moment to the $33/2^-$ configuration.[5]

The g factor of the isomeric state was measured as 0.72 ± 0.07. This is in reasonable agreement with the value 0.77 obtained for the suggested configuration, including the core coupling effects. Thus, the measured properties of the states above 4 MeV may be described by the assigned configurations indicated in Fig. 1, with the inclusion of admixtures of the 3^- core excited state (and an additional few % of another $39/2^-$ configuration).

Footnotes and References

†Condensed from Phys. Letters 35B, 401 (1971).

*Present address: Hahn-Meitner-Institut, Berlin, Germany.

‡Present address: Department of Nuclear Physics, Australian National University, Canberra, Australia.

§On leave from Physikalisches Institut der Universität, Marburg, Germany.

1. K. H. Maier, J. R. Leigh, R. M. Diamond, to be published.

2. I. Bergström, B. Fant, C. J. Herrlander, K. Wikström and J. Blomqvist, Physica Scripta 1, 243 (1970).

3. F. Pühlhofer, following report.

4. A. R. Barnett and W. R. Phillips, Phys. Rev. 186, 1205 (1969); value adopted in Nuclear Data Sheets, Vol. 5, No. 5 (1971).

5. J. Blomqvist, private communication (1971).

THREE-PARTICLE AND FOUR-PARTICLE ONE-HOLE STATES IN ^{211}At

F. Pühlhofer*

The experimental results[1] obtained for the level scheme of ^{211}At stimulated the interest in a shell-model calculation for this nucleus. The theory was intended to identify the structure of the states observed up to 4.8 MeV excitation. Some of the results were shown in the preceding paper. The calculations are described here in more detail and compared with all experimental data available.

The low-lying states of ^{211}At are expected to be described by the degrees of freedom of three protons outside an inert ^{208}Pb core. In the calculation, the $h_{9/2}$, $f_{7/2}$, and $i_{13/2}$ orbitals were included, with single-particle energies taken from the spectrum of ^{209}Bi. This yields a basis set of about 330 states with spins from 1/2 to 33/2 and excitation energies up to 4.8 MeV. For the proton-proton interaction a semiempirical force was used, determined in the following way. A central force, with parameters obtained by Glendenning and Harada,[2] was used to calculate the two-particle states of ^{210}Po. This relatively simple interaction gives an approximate description of the spectrum of ^{210}Po. The deviations between experimental[3] and calculated level energies are of the order of 50 keV at low excitation energy and about 100 keV at 3-MeV excitation energy. A few levels, however, are badly predicted, e.g., the $(h_{9/2} i_{13/2})_{11^-}$ state, which is about 450 keV higher than calculated. Since, at least according to the model, the states in ^{210}Po generally do not have large configuration admixtures—the dominant configuration usually contributes 98% or more, except in 0^+ states—such discrepancies can be blamed to a large

extent on the diagonal matrix elements. Accordingly, we modified the diagonal elements of the Glendenning-Harada interaction, leaving the non-diagonal ones unchanged. Most of the matrix elements of the $f_{7/2}^2$, $f_{7/2}i_{13/2}$, and $i_{13/2}^2$ configuration could not be adjusted, since practically no experimental data are available for these levels.

In Fig. 1, the calculated three-particle spectrum of ^{211}At is compared with the levels known experimentally (from Bergström et al.[4] and Maier et al.[1]) Above 1.6 MeV, only levels near the yrast line are given. These levels are most likely to be observed when the nucleus is produced in (α, xn) or (heavy ion, xn) reactions. The agreement between theory and experiment is very good. The maximum discrepancy in excitation energy is about 60 keV. The procedure of adjusting the two-particle matrix elements according to the experimental spectrum of ^{210}Po had an essential influence on the accuracy of the calculation.

The wave functions obtained for the three-particle states of ^{211}At show that the configuration mixing is in general small. (This does not hold for the mixing between the substates of a configuration.) The dominant configuration usually accounts for more than 97% of the wave function. Stronger configuration mixing occurs only between states with seniority 1; that means with configurations like $(j'^2)_{0^+} \cdot j$ or j^3 and $J=j=9/2^-$, $7/2^-$, or $13/2^+$. This is a direct consequence of the stronger mixing of the 0^+ states in ^{210}Po (pairing interaction). In ^{211}At, the levels of a certain configuration do not split up more than 500 keV, except for the states mentioned.

As discussed in Ref. 1, the isomeric state observed at 4.816 MeV in ^{211}At has a spin which is certainly greater than 33/2, the maximum spin obtainable for a three-particle configuration in the whole proton shell between Z = 82 and 126. It can be shown that excitations of a neutron in the ^{208}Pb core are the most likely explanation for this state as well as for the yrast levels above it. We therefore calculated the energies of the yrast states of the 4p-1h configuration, assuming that they consist of

a) three protons with the dominant configuration and energy of the lower yrast levels of ^{211}At;

b) one neutron in the four lowest single-particle states of ^{209}Pb;

c) one neutron hole in the four lowest hole states of ^{207}Pb.

The proton-neutron, proton-neutron hole and neutron-neutron hole interactions were taken from the experimental level schemes of ^{210}Bi, ^{208}Bi, and ^{208}Pb. Any mixing with the three-particle states and between the 4p-1h states

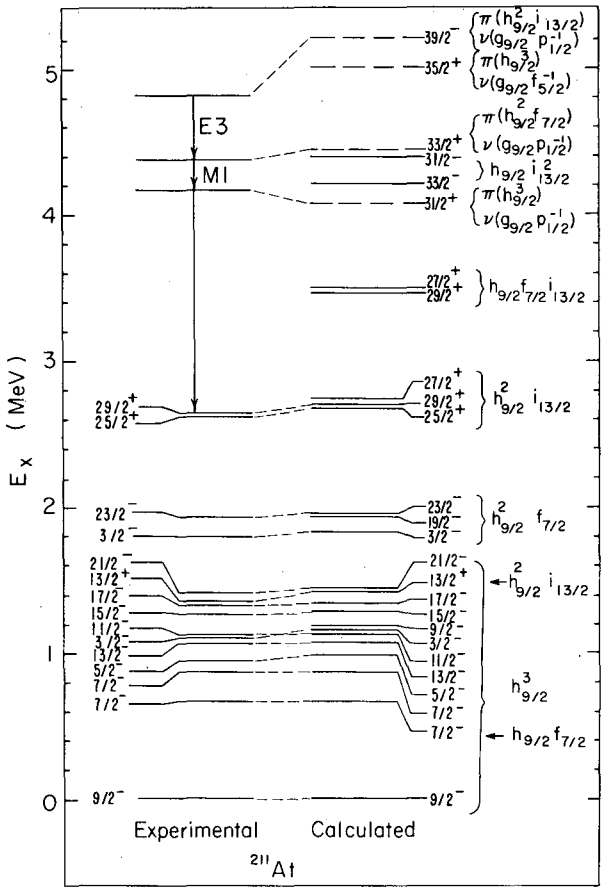

Fig. 1. Comparison between the experimental[1,4] and calculated level scheme of ^{211}At. Above 1.6 MeV, only levels near the yrast line are shown (except for a $3/2^-$ state). Solid lines in the theoretical spectrum are for three-proton states, dashed lines for 4p-1h states. The dominant configurations are indicated. (XBL 721-2071)

themselves was neglected. This implies that we cannot expect the energies of states with collective core excitations to be reproduced. However, it can be easily shown by means of a weak-coupling model that states built on the 3^- excitation of the ^{208}Pb core do not belong to the yrast states.

As a consequence of the approximations made here, the theory is expected to be less accurate than for the three-proton states. Results are shown in Fig. 1. It is suggested that the isomer at 4.816 MeV in ^{211}At is a 4p-1h state with $J = 39/2^-$ with three protons in the configuration of the $29/2^+$ state at 2.641 MeV coupled to a $(g_{9/2}p_{1/2}^{-1})_{5^-}$ neutron configuration. The two levels at 4.381 and 4.177 MeV are probably also 4p-1h states involving the $23/2^-$ and $21/2^-$ three-proton states coupled

to the same neutron configuration. The only other candidate for a 4p-1h state is a $1/2^+$ state observed[4] at E_x = 2.479 MeV, which is strongly populated in the β decay of ^{211}Rn. The calculated excitation energy of the lowest $1/2^+$ state is 2.40 MeV, its dominant configuration $(\pi h_{9/2}^3)_{9/2^-} \cdot (\nu g_{9/2} \cdot \nu p_{1/2}^{-1})$. The first three-particle state with $J = 1/2^+$ is calculated to be at 2.78 MeV.

Summarizing, one may say that the theory accounts for all the states observed in ^{211}At and is therefore a valuable means to understand their structure.

Footnote and References

*On leave from Physikalisches Institut der Universität, Marburg, Germany.

1. K. H. Maier, J. R. Leigh, F. Pühlhofer, and R. M. Diamond, Phys. Letters 35B, 401 (1971), and preceding paper in this Annual Report.

2. N. K. Glendenning and K. Harada, Nucl. Phys. 72, 481 (1965).

3. S. G. Prussin and J. M Hollander, Nucl. Phys. A110, 176 (1968); L. Jardine, thesis, LBL-246 (1971); I. Bergström, J. Blomquist, B. Fant, and K. Wikström, Research Institute for Physics, Stockholm, Annual Report 1970; R. Tickle and J. Bardwick, Phys. Letters 36B, 32 (1971); W. A Lanford, W. P. Alford, and H. W. Fulbright, Bull. Am. Phys. Soc. 16, 493 (1971).

4. I. Bergström, B. Fant, C. J. Herrlander, B. Thieberger, K. Wikström, and G. Astner, Phys. Letters 32B, 476 (1970); G. Astner, Research Institute for Physics, Stockholm, Annual Report 1969; I. Bergström, B. Fant, C. J. Herrlander, K. Wikström, and J. Blomquist, Physica Scripta 1, 243 (1970).

ON-LINE STUDY OF α-EMITTING PRODUCTS OF INTERACTION OF HEAVY NUCLEI WITH 5-GeV PROTONS

R. E. Eppley, J. D. Bowman, and E. K. Hyde

During the past several years a nuclear chemical program has been conducted at the Bevatron for the purpose of studying the nature of the interaction of complex nuclei with 5-GeV protons. Major emphasis has been on the investigation of light fragments (isotopes of He, Li, Be, B, C, etc.) ejected from U and Ag targets.[1,2] The identity, energy spectra, and angular distributions of these fragments were measured with telescopes of semiconductor detectors. In order to investigate products of higher mass, different experimental techniques are required. Traditionally, radiochemical or mass-spectrometric methods have been used to study products of medium or heavy mass. In the past year we decided to test the helium-jet transfer technique as a means of investigating short-lived alpha emitters produced in nuclear reactions induced by GeV protons. In the design of this test experiment we were guided by our experience at the Hilac in the investigation of short-lived α emitters in the Po to Pa region carried out by on-line experiments in the heavy-ion beam.[3,4]

The equipment used in the experiment is discussed in another contribution to this annual report.[5] A cylindrically shaped reaction cell with 2.5-in. entrance and exit windows of 0.027-in. aluminum was placed in one of the external beam lines of the Bevatron. The target foil was affixed to the inside surface of the entrance window. Reaction products recoiled out of the target into 2 atmospheres of helium gas. This helium was pumped out of the reaction cell through a controlled leak, carrying with it the radioactive reaction products through 20 feet of small-diameter plastic tubing to an evacuated counting chamber outside the accelerator shielding. The products were deposited on an aluminum foil and the alpha radiations subsequently emitted by them were measured with surface-barrier semiconductor detectors.

Representative spectra of α particles emitted by products from the interaction of 5-GeV protons with U, Th, Au, and Ta targets are shown in Fig. 1. To obtain these spectra, reaction products were deposited on a catcher plate for 30 sec, then the plate was flipped to a position in front of a semiconductor detector for a 30-sec counting period, following which it was moved back to its original position for collection of more activity. This cycle was repeated over a several-hour period. The proton pulses occurred at 6-sec intervals and contained from 3 to 7×10^{11} protons. The elapsed time from the moment of flipping of the sample

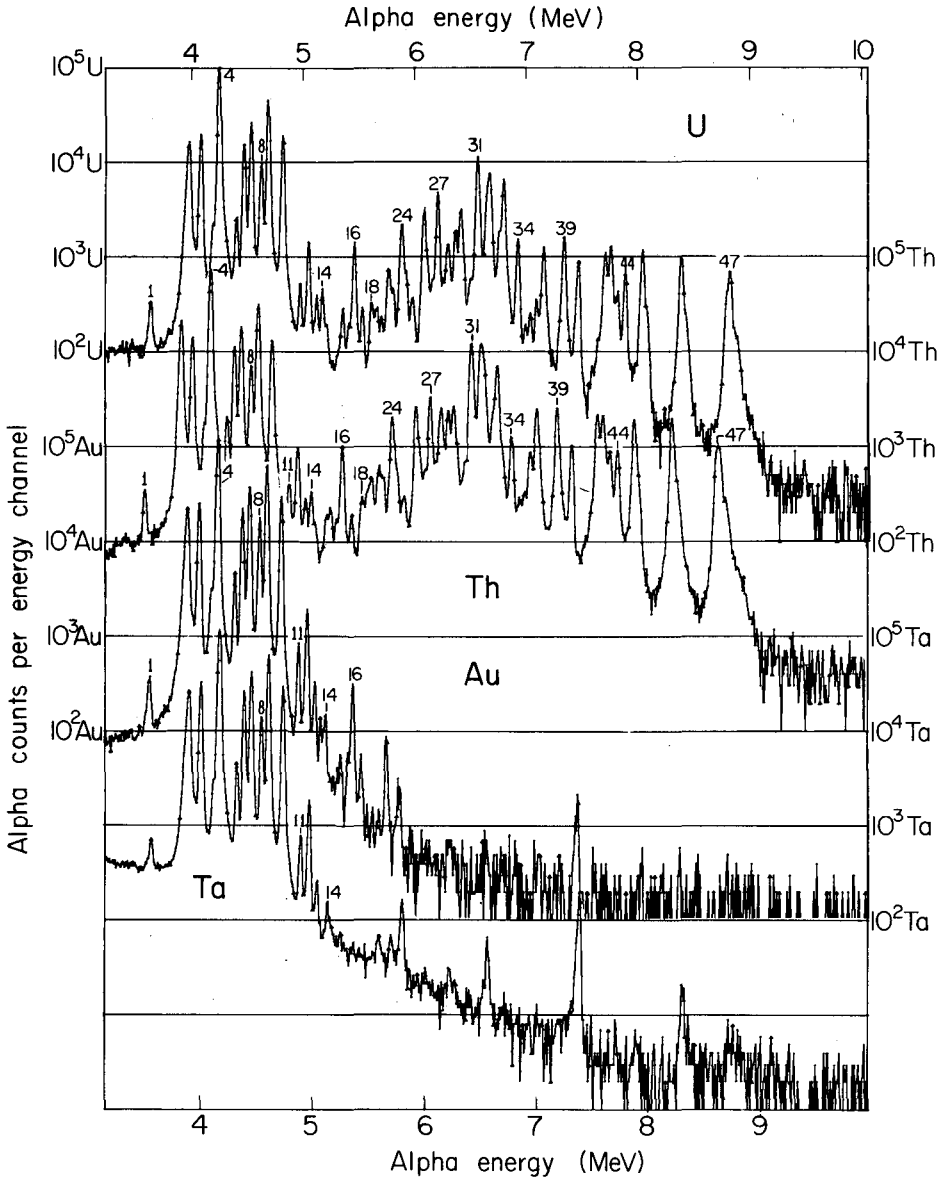

Fig. 1. Alpha spectra associated with products of interaction of 5-GeV protons with U, Th, Au and Ta. Sample collection for 3 min, followed by alpha counting for 3 min.
(XBL 721-2146)

to its position in front of the detector was recorded together with the α pulse height for each event. After the experiment it was possible to make time sortings of the data to determine the decay profile of individual α peaks. A 30-sec time interval was suitable for investigation of half-lives in the 1- to 10-sec range. Cycle times of 2 and 10 min were also used. Figure 2 is an example of the changing nature of the spectra when the data were time-sorted. Figure 3 is an example of a half-life determination by time-sorting the data for an individual peak.

Comparison of the E_α and $T_{1/2}$ values with literature values gave unambiguous identification of all but a few of the peaks in Fig. 1. Once identity was established, several peaks whose energy values were well known from the literature were used as internal standards

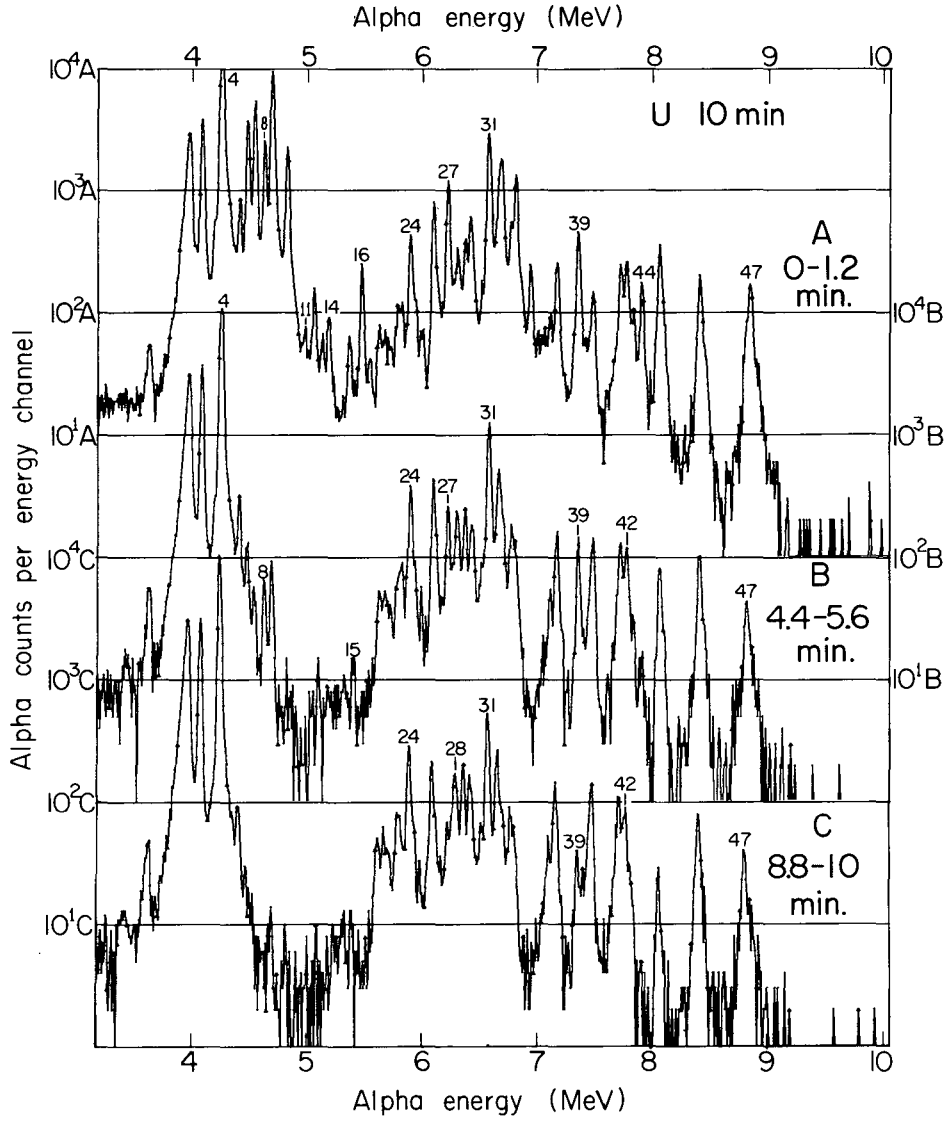

Fig. 2. Alpha spectra associated with products of interaction of 5-GeV protons with U. Sample collection for 10 min, followed by alpha counting for 10 min. The events recorded during three intervals in the 10-min counting period are shown.

(XBL 718-2147)

to calibrate the energy scale precisely and to determine the energy of many other peaks with an accuracy higher than were previously known.

Prominent among the products from all four targets was a group of rare earth α emitters from the known island of α radioactivity lying just above the 82-neutron shell. The identity of these peaks is given in Table I.

In the experiments with Au targets a number of higher-Z alpha emitters like ^{177}Pt, ^{178}Pt, and ^{175}Ir were observed. In the runs with Th or U targets a large number of α emitters in the Bi to Ra region were identified.

The data are now being reduced and a report is being written. The results are of interest for the following four reasons.

(1) They show that the He jet transfer

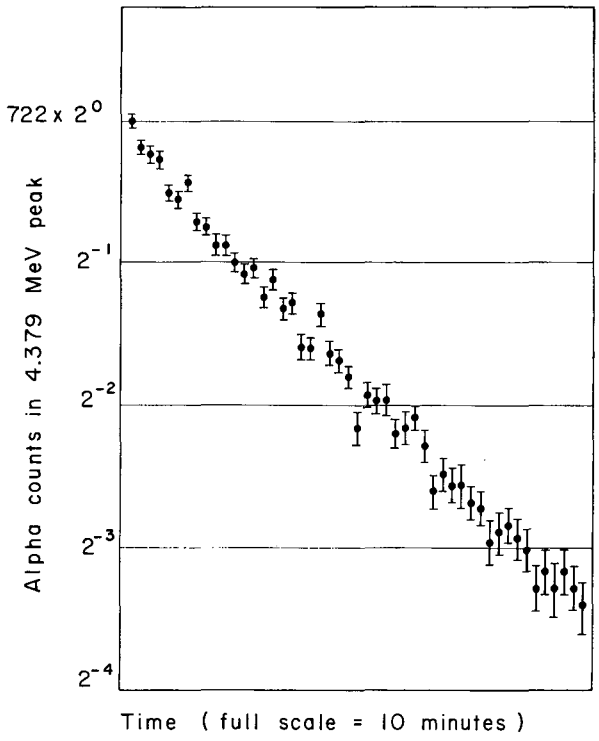

Fig. 3. Representative decay curve for time-sorted data for alpha particles of 4.379 MeV (^{152}Ho). (XBL 717-3920)

method can be applied to reaction studies in beams of GeV protons and that efficient transport of products through many meters of small-diameter capillary is feasible.

(2) They provide improved α-particle energies and half-lives for a large number of the rare earth α emitters. The fact that so many of these nuclides can be prepared as a single sample is a distinct aid in obtaining this spectrographic information.

(3) They provide relative (and ultimately) absolute cross-section data on a selection of products and these data will be of use in describing the nature of the break-up of complex nuclei under bombardment with GeV particles. Perhaps the most important feature will be the sampling of the charge distribution curve far from stability in the rare earth region. Such information may be important for evaluation of the limitations of high-energy nuclear reactions as a means of production of exotic nuclei far from stability.

(4) They suggest other interesting experiments to be performed with lower-Z targets than those used so far. Experiments are in progress to investigate these.

Table I.

Peak No.	Identified nuclide	
1	2.3h	^{152}Dy
2	16m	^{155}Ho
2	4.1h	^{149}Tb
3	17.7m	^{151}Dy
4	4.5m	^{154}Er
4	7.2m	^{150}Dy
5	142s	^{152}Ho
6	52s	^{152m}Ho
7	36s	^{151}Ho
8	42s	^{151m}Ho
9	36s	^{153}Er
10	10.7s	^{152}Er
11	5s	^{154}Tm
12	3s	^{154m}Tm
13	1.6s	^{153}Tm
14	1.6s	^{155}Yb

References

1. A. M. Poskanzer, G. W. Butler, and E. K. Hyde, Phys. Rev. C3, 1 (1971).

2. E. K. Hyde, G. W. Butler, and A. M. Poskanzer, Phys. Rev. C4, 1759 (1971).

3. K. Valli and E. K. Hyde, Phys. Rev. 176, 1377 (1968).

4. J. Borggreen, K. Valli, and E. K. Hyde, Phys. Rev. C2, 1841 (1970).

5. See Section IV, Equipment Used in the Helium-Jet Experiments at the Bevatron.

CALORIMETRIC DETERMINATION OF DECAY ENERGY OF URANIUM-235m, AND THE IMPLICATIONS FOR COSMOLOGY*

B. E. Culler

The isomeric state of uranium-235 decays by internal conversion with a half-life of 26.5 min, emitting electrons of extremely low energy. Hence, the transition energy is very difficult to measure by the conventional means of electron spectroscopy, although several attempts have been made.[1-4] The energies obtained in these measurements ranged from 23 eV to 75 eV, the higher energy measurements having been obtained from the more active sources.

As a totally new approach to the problem, a Wheatstone bridge calorimeter capable of measuring 10^{-9} thermal watt was designed and constructed. Because the heat capacity of the system must be kept as low as possible, one of the two heat-sensitive devices (thermistors) used as arms of the bridge is also used as the sample holder. When a sample of uranium-235m is placed on one of the thermistors, the self-absorption of the soft electrons within the sample and thermistor changes its temperature and therefore the resistance of that arm of the bridge. The bridge is then rebalanced by means of a variable precision resistor. As the uranium-235m activity dies away with its 26.5-min half-life, the resistance of the sample-holding thermistor changes accordingly, and the resulting imbalance of the bridge is measured as a function of time. The circuit diagram for the calorimeter is shown in Fig. 1. The calorimeter is calibrated by rf heating. Any possibility of a systematic error in either the measurement or calibration was eliminated by measuring the α-decay energy of bismuth-212. Excellent agreement with the known energy was obtained.

Uranium-235m is formed by the α decay of

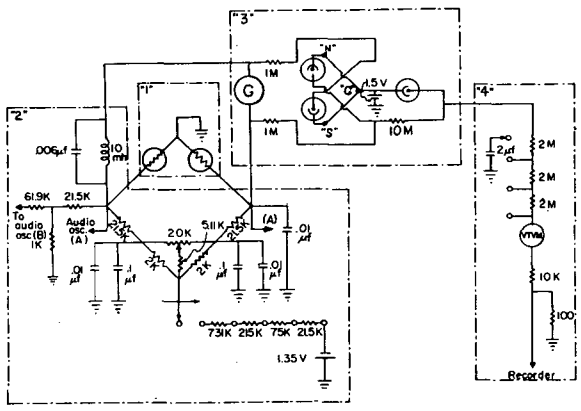

Fig. 1. (XBL 718-4077)

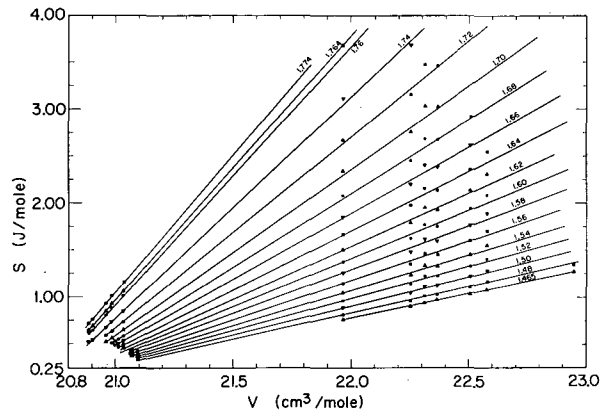

Fig. 2. (XBL 718-4181)

plutonium-239, so the sample of uranium-235m was obtained by a diethyl ether extraction from a plutonium-239 stock solution which was maintained in the Pu(III) oxidation state by ferrous sulfamate. Zinc nitrate was the salting-out agent. The sample was reduced in volume, taken up in 8N nitric acid and placed on an anion exchange column. Elution was done with 0.1N hydrochloric acid. The sample, now free of inorganic mass and approximately 2-3λ in volume, was placed on the sample-holding thermistor.

The data obtained from the calorimeter was in the form of a trace of power versus time, recorded by a Speedomax recorder as the experiment was in progress. Each set of matched thermistors used as the heat-sensitive arms of the bridge produced a characteristic short-lived exponential curve of its own, which had to be used along with the exponential decay curve of the sample (half-life, 26.5 min) in analyzing the data from the runs. The method used is identical to that used in resolving compound radioactive decay curves. Figure 2 is the data curve from one run. The 4.0-min line describes the exponential behavior of the thermistor set. The 26.5-min line results from the dissipation of the decay energy of uranium-235m within the thermistor.

The total decay energy of uranium-235m was found to be 572 ± 33 eV.

The nuclear properties of the isomeric state are of particular interest since the isomer serves as a possible loss mechanism of uranium-235 in space. If this occurs, it

would affect the calculation of the age of the galaxy by Fowler, Hoyle and others using the ratio uranium-235/uranium-238.[5] To estimate the fraction of uranium-235 existing as the isomer in interstellar space, the expression for the probability of Coulomb excitation derived by Alder, et al. was used.[6] In regions of space typified by our solar system the fraction of isomer is negligible.

To substantiate the conclusion that there is no loss of uranium-235 through the isomer, the half-life for α decay of the isomeric state was calculated. The unhindered half-lives of the uranium isotopes were used to obtain an unhindered half-life for the isomer. This value was then corrected by applying the hindrance factors for the α decay of plutonium-239, which has the same intrinsic spin state as uranium-235m. The half-life for α decay of the isomeric state was calculated to be 5.9×10^8 years, nearly equal to that of the ground state.

It was therefore concluded that the existence of the isomeric state poses no problem in the determination of the age of the galaxy.

Footnote and References

*Condensed from LBL-221.

1. M. C. Michel, F. Asaro, and I. Perlman, Am. Phys. Soc. Bull. II 2, 394 (1957).

2. M. S. Freedman, F. T. Porter, F. Wagner, and P. P. Day, Phys. Rev. 108, 836 (1957).

3. H. Mazaki and S. Shimizu, Phys. Letters 23, 137 (1966).

4. N. de Mevergnies, to be published.

5. W. A. Fowler, Proc. Nat. Acad. Sci. 52, 524 (1964).

6. R. Alder, A. Bohr, T. Huus, B. Mottelson, and A. Winther, Rev. Mod. Phys. 28, 432 (1956).

PLUTONIUM-244: CONFIRMATION AS AN EXTINCT RADIOACTIVITY*

E. C. Alexander, Jr.,† R. S. Lewis,† J. H. Reynolds,† and M. C. Michel

Kuroda's 1960 hypothesis[1] that 82 m. y. ^{244}Pu was extant in the early solar system and contributed importantly to isotopic anomalies in xenon has received much support from xenon studies in meteorites. Starting with the observation[2] in Kuroda's laboratory that xenon from the calcium-rich achondrite Pasamonte is enriched in the fissiogenic isotopes $^{131,132,134,136}Xe$, an impressive body of indirect evidence for the hypothesis has been assembled by various meteoriticists: (a) observation of a reproducible spectrum of fission-like xenon in the achondrites[3-7] where low concentrations of other xenon components and high concentrations of uranium and the rare earths are favorable for the detection of an extinct plutonium ratioactivity which fissions; (b) observation of exceptionally pure samples of xenon of this composition in the uniquely uranium-rich achondrite Angra dos Reis;[8] (c) observation of exceptionally high concentrations of this same xenon[9] in a uranium-rich mineral (whitlockite) from the chondrite St. Séverin, a mineral where an excess of fission tracks had previously been noted;[10] (d) demonstration that the "achondritic fission xenon" in the chondrite St. Séverin is released in correlation with a fission component implanted at uranium sites in the meteorite by neutron irradiation.[11] The implications of this extinct radioactivity for chronologies of the solar system[12] and of galactic nucleosynthesis[13-15] have been noted. But throughout this history the identification of the nuclide responsible for the fissiogenic component as ^{244}Pu has been inferential. That is, any actinide with a long half-life and a partial decay by spontaneous fission would have met the specifications. It clearly was important to measure the mass spectrum of fission xenon from a laboratory sample of ^{244}Pu.

Our sample was 13.0 mg of ^{244}Pu as PuO_2 which had been electromagnetically separated at Oak Ridge from large quantities of neutron-irradiated Pu. An assay, provided with the sample, of the isotopic composition of the plutonium is set out in Table I, together with the α and spontaneous-fission half-lives needed for computing the expected accumulations of fission xenon in such a sample. The sample was precipitated in April 1969 and outgassed for xenon analysis 23 months later. The calculated yields of ^{136}Xe from 23-month decay of each isotope are included in the table, assuming 6% fission yields in all cases. The total contamination of the fission ^{136}Xe from ^{244}Pu decay by fission of all the other nuclides was thus found to be only 0.8%.

Table I. Composition of Pu sample.

Isotope	Atom % of Sample [a]	Decay constants [b]	Calculated ^{136}Xe [f] from 23-month decay of 14.7 mg of PuO_2 (cc STP)
^{244}Pu	99.06	$t_{1/2}(\alpha) = 8.18\times10^{7}$ yr	1.44×10^{-12}
		$t_{1/2}(S.F.) = 6.55\times10^{10}$ yr	
^{242}Pu	0.904	$t_{1/2}(\alpha) = 3.76\times10^{5}$ yr	1.23×10^{-14}
		$t_{1/2}(S.F.) = 7.0\times10^{10}$ yr	
^{241}Pu	0.002	$t_{1/2}(\beta^-) = 13.2$ yr	$(\sim 3.5\times10^{-21})$ [c]
^{240}Pu	0.007	$t_{1/2}(\alpha) = 6580$ yr	4.9×10^{-17}
		$t_{1/2}(S.F.) = 1.4\times10^{11}$ yr	
^{239}Pu	0.180	$t_{1/2}(\alpha) = 24300$ yr	3.18×10^{-20}
		$t_{1/2}(S.F.) = 5.5\times10^{15}$ yr	
^{238}Pu	<0.006	$t_{1/2}(\alpha) = 86.4$ yr	$<1.2\times10^{-16}$
		$t_{1/2}(S.F.) = 4.9\times10^{10}$ yr	

[a] Isotope analysis supplied by Electromagnetic Isotope Separator Group at Oak Ridge National Laboratory.

[b] ^{244}Pu decay constants from Ref. 28. All other constants are the average of the values listed in Ref. 29.

[c] Calculated with $t_{1/2}(S.F.)$ for ^{239}Pu; $t_{1/2}(S.F.)$ for ^{241}Pu is unknown.

Xenon was outgassed from the sample in a tungsten crucible heated by electromagnetic induction to temperatures above 2000°C, purified in a glass vacuum system with a titanium-zirconium getter, and collected on a cooled charcoal trap. The krypton and xenon fractions were analyzed separately in a mass spectrometer in the static mode—i.e., without pumping during the analysis. Calibration and blank runs were performed by standardized techniques.

No useful data were obtained for krypton because of the small sample size relative to the contaminant gases, but the xenon results are given in Table II. No significant impurity gases were observed, and a typical sweep of the spectrum is shown in Fig. 1.

The fissiogenic xenon spectrum from ^{244}Pu is interestingly different from the spectrum for ^{244}Cm (Ref. 16; see Fig. 2), but we focus attention here upon the cosmological implications of the ^{244}Pu spectrum. Rowe[7] has recently compiled various measurements of the meteoritic spectrum of fission xenon attributed

Table II. Xenon extracted from 14.7 mg of $^{244}PuO_2$.

Temp. (°C)	$[^{129}Xe]$ $\times 10^{-12}$ cc	128	129	130	131	132	134	136	$[^{136}Xe^f]$ [a] $\times 10^{-12}$ cc
350	0.73	0.072 ±0.002	≡ 1.000	0.163 ±0.005	0.802 ±0.012	1.003 ±0.012	0.397 ±0.006	0.338 ±0.002	< 0.003
700	1.73	0.075 ±0.002	≡ 1.000	0.165 ±0.003	0.861 ±0.009	1.191 ±0.013	0.604 ±0.011	0.548 ±0.014	
		Fission yields:[a]			0.284 ±0.044	0.819 0.081	0.982 0.082	≡ 1.000	0.37
1550	1.72	0.076 ±0.002	≡ 1.000	0.155 ±0.003	0.933 ±0.014	1.513 ±0.017	0.910 ±0.015	0.900 ±0.008	
		Fission yields:[a]			0.234 ±0.025	0.878 ±0.033	0.913 ±0.029	≡ 1.000	0.97
2150[b]	0.06	0.08 ±0.01	≡ 1.000	0.17 ±0.01	0.77 ±0.03	0.96 ±0.03	0.41 ±0.01	0.34 ±0.01	< 0.0006
Atmospheric xenon[30]		0.073	≡ 1.000	0.154	0.801	1.017	0.395	0.336	
Adopted fission yields for ^{244}Pu					0.246 ±0.022	0.870 ±0.031	0.921 ±0.027	≡ 1.00	

[a] The amounts of fission xenon were calculated from the formula $\delta^i = (^iXe/^{129}Xe)$ sample - $(^iXe/^{129}Xe)$ atmosphere. The relative yields shown are $\delta i/\delta^{136}$.

[b] The 2150° fraction is typical of the lower temperature blanks and provides a good measure of size and isotopic composition of the blanks.

Table III. Comparison of meteoritic fission yields with ^{244}Pu fission yields.

	Reference	Fission yield 131	132	134	136
Pasamonte	5 from data	33	93	91	≡ 100
	of 3	± 3	± 8	± 2.5	
Pasamonte	6	25	88.5	94	≡ 100
		± 3	± 3	± 5	
Whitlockite from	9	31	97	93	100
St. Séverin		± 8	± 8	± 1	
Kapoeta	7	26	88	91	100
		± 3	± 4	± 5	
^{244}Pu	This work	24.6	87.0	92.1	100
		±2.2	±3.1	±2.7	

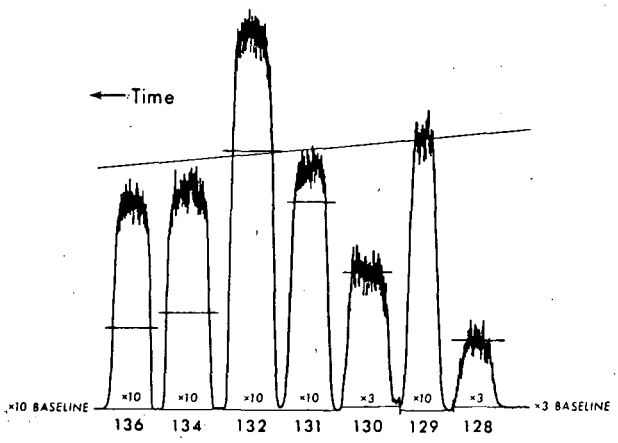

Fig. 1. Mass spectrum of xenon extracted at 1550°C from PuO_2 and sealed off in the mass spectrometer. The slanted line through the peak at a mass of 129 shows the extent of spectrometer pumping. The horizontal lines show the amount of atmospheric xenon relative to mass 129. Excesses at masses 136, 134, 132, and 131 represent the ^{244}Pu spontaneous fission component. The magnetic sweep rate was increased between peaks.

(XBL 722-338)

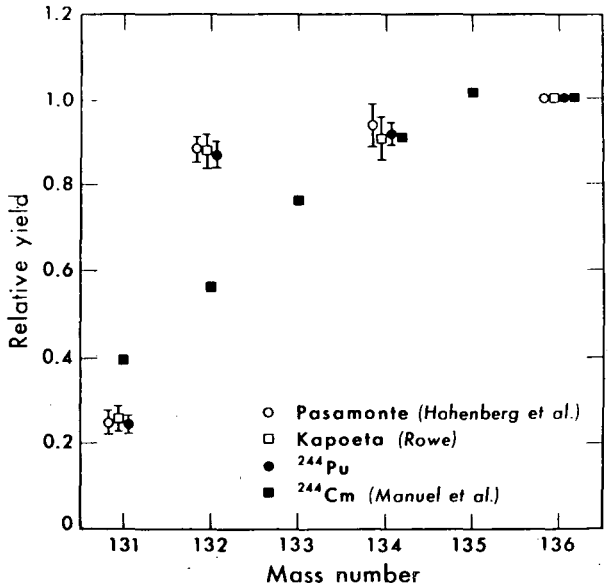

Fig. 2. A comparison of the fissiogenic xenon spectra from the achondritic meteorites Pasamonte[6] and Kapoeta[7] and the spontaneous fission spectrum from a laboratory sample of ^{244}Pu. The xenon spectrum from the spontaneous fission of ^{244}Cm[16] is also shown. The pattern of xenon isotopes from the spontaneous fission of ^{244}Pu agrees perfectly with the achondritic spectra.

(XBL 722-339)

to ^{244}Pu (so-called achondritic or "Pasamonte type" fission xenon); we reproduce a similar compilation in Table III. Agreement between the meteoritic spectra and the ^{244}Pu spectrum is excellent, especially for the two meteoritic spectra based on Berkeley data, which we have plotted in Fig. 2. In particular the unusual "signature" of the achondritic fission xenon, with approximately equal yields at masses 132, 134, and 136, is faithfully reproduced in the laboratory fission sample. There no longer can be any reasonable doubt that achondritic fission xenon was correctly assigned to the spontaneous fission of ^{244}Pu.

The main effect of this observation is to place on a firm footing a number of conclusions which were previously stated in the literature. But it is useful to collect here briefly what we consider to be the chief implications of confirmation of the ^{244}Pu hypothesis:

(1) We now have observed in the solar system two completely authenticated extinct radioactivities, ^{129}I and ^{244}Pu.

(2) Previous measurements of the ratio $^{244}Pu/^{238}U$ in meteorites are now on a firm basis with respect to the extinct nuclide and its decay constants. We attribute special importance to Podosek's[11] measurements of this ratio, since his method infers it from retentively sited xenon, and combines the plutonium and uranium measurements in a single experiment on one sample. All four meteorites for which he has thus far been able to make the measurement (one chondrite and three achondrites) gave approximately the same result: $^{244}Pu/^{238}U \approx 0.013$ at the time of meteorite formation. These substantial plutonium concentrations in the early solar system require that r-process nucleosynthesis was ongoing in the galaxy at the time of the birth of the Sun.

(3) Three separate decay schemes now point to a compact interval of time ($\sim 10^7$ years) for meteorite formation: $^{87}Rb \rightarrow {}^{87}Sr$ (Ref. 17), $^{129}I \rightarrow {}^{129}Xe$ (Ref. 18), and $^{244}Pu \rightarrow {}^{131\text{-}136}Xe$ (Ref. 19).

(4) Since late r-process nucleosynthesis has to be invoked to produce ^{244}Pu in the early solar system it seems unnecessary to invoke other sources for ^{129}I, which is also an r-process nuclide; and no evidence for other important sources of ^{129}I has as yet been found.[19]

(5) With ^{129}I so ascribed to galactic sources, the time interval between cessation of nucleosynthesis for the solar system and meteorite formation cannot exceed several hundred million years.[20]

(6) Models for the chronology of nucleosynthesis now have to be consistent with known ratios for early solar system abundances of ^{232}Th, ^{235}U, ^{238}U, and ^{244}Pu. Constraints imposed by these nuclides have received attention in the literature,[13] but calculations emphasize ratios of $^{244}Pu/^{238}U$ that are probably too high. We believe that the more relevant calculations are those with Podosek's plutonium-uranium ratio.[11] Calculations of this type[14,15,21] indicate that the need for a "late spike" of ^{244}Pu synthesis just before solar system formation is less clear.

(7) Attention can now be more clearly focused on the question of the origin of the fission-like xenon in carbonaceous chondrites, which has an isotopic composition different from ^{244}Pu fission.[22] It is important in this connection to have better knowledge, from ^{129}I-^{129}Xe dating, of the formation times for the carbonaceous chondrites. Existing evidence is somewhat weak but indicates that these meteorities formed at the same time as the others.[18,23] If this is true and if the anomalous xenon there is genuinely fissiogenic, its unique occurrence in the carbonaceous chondrites cannot be explained on the basis of an exceptionally short half-life for the fissioning nuclide. One must argue from its absence in achondrites and its presence in carbonaceous chondrites that the nuclide is chemically different from the actinides and is probably more volatile. As a result, serious consideration must be given to the suggestion by Anders and Heymann,[24] that a super-heavy element, which could be both volatile and fissioning, may have been present in the carbonaceous chondrites. The possible existence of super-heavy elements is now generally accepted.[25]

(8) Searches for ^{244}Pu in lunar rocks should continue. The oldest lunar rocks encountered to date are essentially threshold objects for the observation of lunar plutonium.[26] Slightly older rocks can be expected to give positive results.

(9) Detailed predictions based on theories of both r-process and s-process nucleosynthesis have recently met rather stringent experimental tests. The presence of ^{244}Pu in the early solar system confirms the r-process as ongoing in the galaxy, and predictions from s-process theory of the relative values of cross sections of certain fast neutrons in samarium and tellurium have been strikingly confirmed.[27] Scientists, at Oak Ridge played a major role in both tests. The success of the present work depended greatly upon the superb sample of ^{244}Pu which was prepared by the Electromagnetic Isotope Separator Group at the Oak Ridge National Laboratory.

Footnotes and References

*Condensed from Science, 172, 837 (1971) May.

†Department of Physics, University of California, Berkeley.

1. P. K. Kuroda, Nature 187, 36 (1960).

2. M. W. Rowe and P. K. Kuroda, J. Geophys. Res. 70, 709 (1965).

3. M. W. Rowe and D. D. Bogard, J. Geophys. Rev. 71, 4182 (1966).

4. P. K. Kuroda, M. W. Rowe, R. S. Clark, and R. Ganapathy, Nature 212, 241 (1966); R. O. Pepin, J. Geophys. Res. 71, 2815 (1966).

5. K. Marti, P. Eberhardt, and J. Geiss, Z. Naturforsch. 21a, 398 (1966).

6. C. M. Hohenberg, M. N. Munk, and J. H. Reynolds, J. Geophys. Res. 72, 3139 (1967).

7. M. W. Rowe, Geochim. Cosmochim. Acta 34, 1019 (1970).

8. C. M. Hohenberg, Geochim. Cosmochim. Acta 34, 185 (1970).

9. G. J. Wasserburg, J. G. Huneke, and D. S. Burnett, Phys. Rev. Letters 22, 1198 (1969) and J. Geophys. Res. 74, 4221 (1969).

10. Y. Cantalaube, M. Maurette, and P. Pellas, in Radioactive Dating and Methods of Low Level Counting (Atomic Energy Agency, Vienna, 1967), p. 213.

11. F. A. Podosek, Earth Planet. Sci. Letters 8, 183 (1970).

12. D. D. Sabu and P. K. Kuroda, Nature 216, 442 (1967); J. H. Reynolds, Nature 218, 1024 (1968).

13. C. M. Hohenberg, Science 166, 212 (1969); G. J. Wasserburg, D. N. Schramm, and J. C. Huneke, Astrophys. J. 157, L91 (1969).

14. G. J. Wasserburg, D. N. Schramm, and J. C. Huneke, Astrophys. J. 157, L91 (1969).

15. W. A. Fowler, in Cosmology, Fusion, and Other Matter: A Memorial to George Gamow, edited by F. Reines (Colorado Associated University Press, Boulder, in press).

16. O. K. Manuel, V. J. Becker, M. S. Boulos, and B. Srinivasan, Radiochemical Determinations of Heavy Elements and Contribution to Noble Gas Anomalies, Progress Report to National Science Foundation, June 15, 1970, p. 12.

17. D. A. Papanastassiou and G. J. Wasserburg, Earth Planet. Sci. Letters 5, 361 (1969).

18. C. M. Hohenberg, F. A. Podosek, and J. H. Reynolds, Science 156, 202 (1967); F. A. Podosek, Geochim. Cosmochim Acta 34, 341 (1970).

19. J. H. Reynolds, Ann. Rev. Nucl. Sci. 17, 253 (1967).

20. J. H. Reynolds, Phys. Rev. Letters 4, 8 (1960).

21. P. K. Davis and C. M. Hohenberg, private communication (1970).

22. R. O. Pepin in Origin and Distribution of the Elements, edited by L. H. Ahrens (Pergamon, Oxford, 1968), p. 379.

23. F. A. Podosek and C. M. Hohenberg, Earth Planet. Sci. Letters 8, 443 (1970).

24. E. Anders and D. Heymann, Science 164, 821 (1969).

25. G. T. Seaborg, Ann. Rev. Nucl. Sci. 18, 53 (1968).

26. A. L. Albee, D. S. Burnett, A. A. Chudos, E. L. Haines, J. C. Huneke, D. A. Papanastassiou, F. A. Podosek, G. P. Russ III, and G. J. Wasserburg, Earth Planet. Sci. Letters 9, 137 (1970); E. C. Alexander, Jr., Earth Planet. Sci. Letters 9, 201 (1970); W. A. Kaiser, in Proceedings of the Apollo 12 Conference (in press).

27. R. L. Macklin, J. H. Gibbons, and T. Inada, Nature 197, 369 (1963); R. L. Macklin and J. H. Gibbons, Ap. J. 149, 577 (1967).

28. P. R. Fields, A. M. Friedman, J. Milsted, J. Lerner, C. M. Stevens, D. Metta, and W. K. Sabine, Nature 212, 131 (1966).

29. C. M. Lederer, J. M. Hollander, and I. Perlman, Table of Isotopes, 6th ed. (John Wiley, New York, 1967), pp. 144 and 145.

30. A. D. Nier, Phys. Rev. 79, 450 (1959).

31. We thank G. A. McCrory and R. H. Escoboles for assistance in design and construction of the extraction system and its many prototypes and P. K. Davis for writing the computer programs used for data reduction. The Pu sample was obtained through the Transplutonium Program of the Atomic Energy Commission Division of Research. This work was supported in large part by the U. S. Atomic Energy Commission and bears Code Number UCB-34P32-79.

DECAY OF ^{210}At TO LEVELS IN ^{210}Po†

L. J. Jardine, S. G. Prussin, and J. M. Hollander

The electron-capture decay of $^{210}_{85}$At has been studied with Ge(Li) γ-ray spectrometers and a Si(Li) electron spectrometer. Present data have been used to define 23 levels in $^{210}_{84}$Po. The multipolarity of 36 transitions have been determined and combined with data

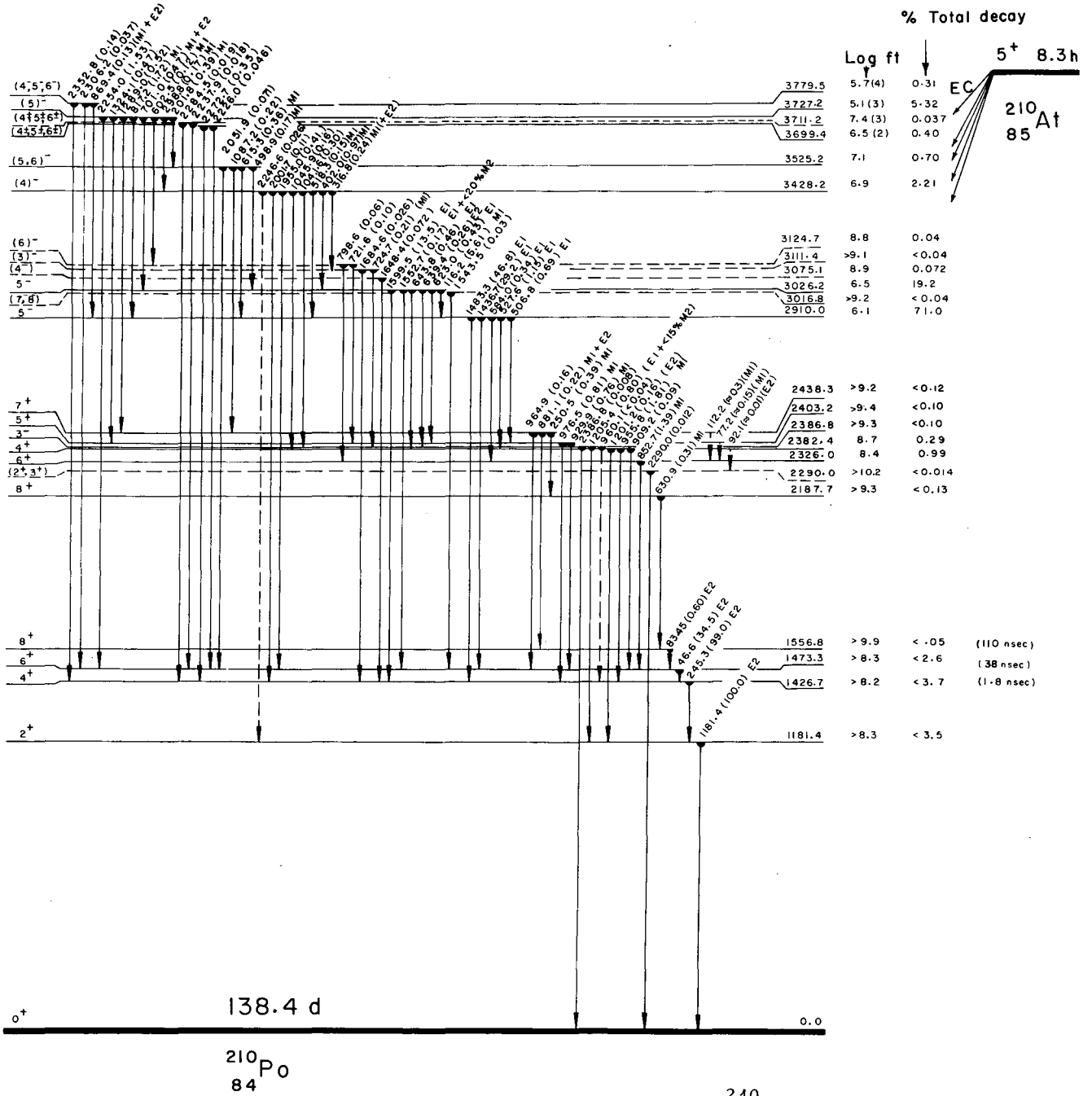

Fig. 1. Experimental decay scheme of ^{210}At. (Absolute transition intensities are shown on the level scheme.) (XBL 719-4407 A)

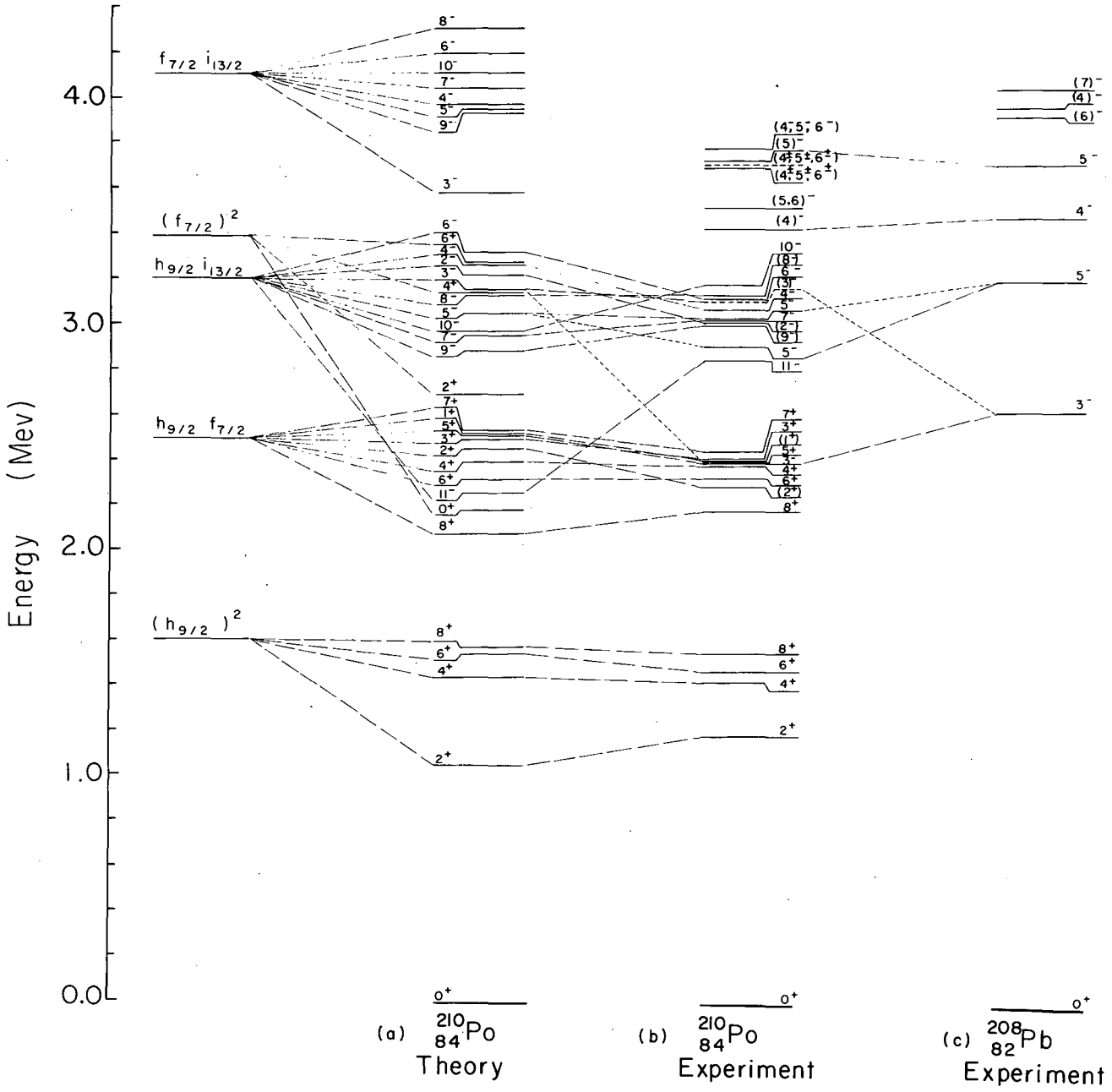

Fig. 2. Comparison of the experimental level scheme of ^{210}Po (b) with a shell-model calculation[4] (a) and with the experimental level scheme of ^{208}Pb (c).[5] The dotted lines connect levels believed to have components due to the same configuration. The zero-order energies of the two-proton configurations in ^{210}Po are shown to the left. (XBL 7111-4675A)

from recent reaction studies[1-3] to assign spins and parities to these levels. Figure 1 shows the decay scheme.

The lower-lying level structure is expected to arise from configurations of the two protons beyond the ^{208}Pb core. All levels arising from the configuration $\pi(h_{9/2})^2$ have been identified and except for the lowest spin members, all levels due to the configurations $\pi(h_{9/2}\ f_{7/2})$ and $\pi(h_{9/2}\ i_{13/2})$ have also been identified. We show in Fig. 2 a comparison of known states [1-3] in ^{210}Po with a two-proton shell-model calculation[4] and the experimental[4,5] level spectrum of ^{208}Pb.

Evidence is presented which locates the 3^- collective state in ^{210}Po at 2400 keV above the ground state. The 200-keV depression in energy from that observed in ^{208}Pb is believed due in part to configuration mixing with the 3^- member of the $\pi(h_{9/2}\ i_{13/2})$ multiplet.

The EC decay of ^{210}At to pure two-proton configurations is highly hindered, whereas the decays of the first-forbidden type to the two 5^- levels at ~3 MeV are unhindered. The unhindered transitions to odd-parity states are believed due to neutron and proton excitations of the ^{208}Pb core. In ^{208}Pb the 5^- member of the $\nu(g_{9/2}\ p_{1/2}^{-1})$ multiplet has been established[5] at the excitation energy of 3.2 MeV. The energy of this core state is close to the 5^- member from the $\pi(h_{9/2}\ i_{13/2})$ multiplet in ^{210}Po, and it is reasonable to assume that the same configuration also contributes to the 5^- two-proton state in ^{210}Po. A first-forbidden transition proceeding via this core admixed component would be unhindered as the transition would be from a $h_{9/2}$ proton to a $g_{9/2}$ neutron. An analysis of the relative log ft values of the two 5^- states near 3 MeV allowed the following experimental wave functions to be constructed:

$$\psi_{5^-}(2910.0) = 0.534\ |\pi(h_{9/2}\ i_{13/2})\rangle_{5^-} + 0.846\ |\nu(g_{9/2}\ p_{1/2}^{-1})\rangle_{5^-}$$

$$\psi_{5^-}(3026.2) = 0.846\ |\pi(h_{9/2}\ i_{13/2})\rangle_{5^-} \mp 0.534\ |\nu(g_{9/2}\ p_{1/2}^{-1})\rangle_{5^-}.$$

Thus, the lower 5^- state at 2910.0 keV contains approximately 70% of the strength of the core excitation $\nu(g_{9/2}\ p_{1/2}^{-1})$. Electron-capture transition rates to other odd-parity states above 3 MeV are discussed in terms of additional neutron and proton-proton particle-hole excitations of the ^{208}Pb core.

Transition probabilities for the gamma decay of the $\pi(h_{9/2})^2$ and $\pi(h_{9/2}\ f_{7/2})$ even parity multiplets have been calculated by using several sets of shell-model wave functions.[4,6]

Footnote and References

†Condensed from LBL-278, November 1971; to be published in Nucl. Phys. (1972).

1. R. Tickle, Phys. Letters 36B, 32 (1971); private communication, September 1971.

2. W. F. Lanford, private communication, March and September 1971.

3. I. Bergström, J. Blomqvist, B. Faut, and K. Wikström, Research Institute for Physics, Stockholm, Annual Report (1970), 80.

4. C. W. Ma and W. W. True, private communication, September 1971.

5. M. B. Lewis, Nucl. Data Sheets B5, 264 (1971).

6. Y. E. Kim and J. O. Rasmussen, Nucl. Phys. 47, 184 (1963); 61, 173 (1965).

TABLE OF ISOTOPES

C. M. Lederer and J. M. Hollander

Compilation of the seventh edition began in early 1971. Due to the size of the effort required, methods for compilation and production of the seventh edition are different from those used to produce previous editions in a number of respects:

1. Compilation of the data is a group project. Four full-time and two part-time chemists are currently compiling the table: Egardo Browne, Janis Dairiki, Ray Doebler, Leslie Jardine, Adnan Shihab-Eldin, and Virginia Shirley. (Dr. Jardine replaces Audrey Buyrn,

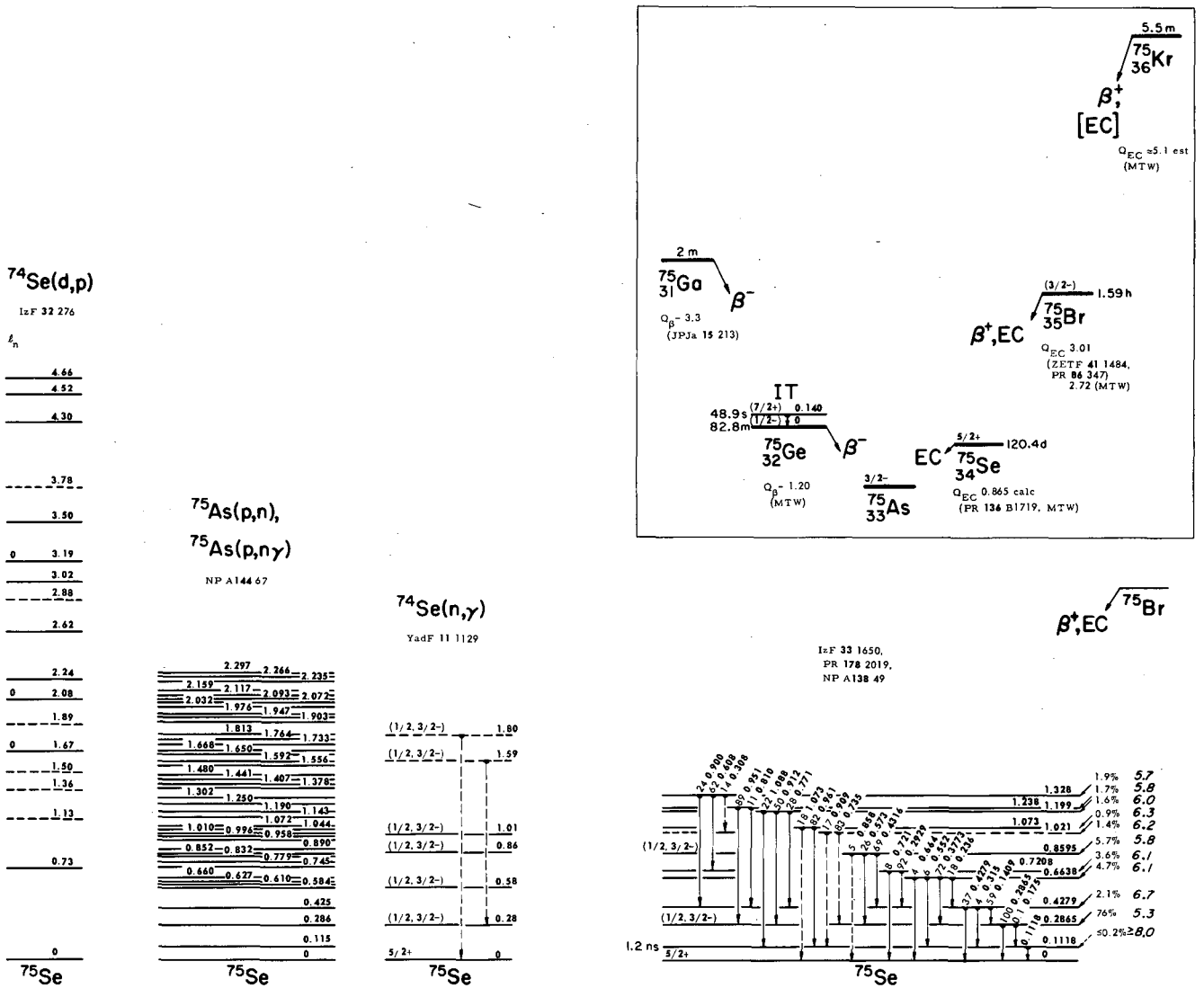

Fig. 1. Sample format for a level scheme (^{75}Se) and a skeleton mass chain. (Material not proofread.) (XBL 716-3664)

who left in August and is currently an NIRA Compiling Fellow at MIT). The group is assisted by a full-time secretary-librarian-typist, Maureen Whalley.

2. A large effort at computerization is under way, under the supervision of Carl Quong (Math and Computing).

a. A multifont text input-editor, consisting of a keyboard and scope display driven by a small computer system is being programmed for input of tabular data. (A prototype of this device was described in UCRL-18530 and UCRL-18667, p. 9 (1968) Annual Report). This programming, nearing completion, is being done by Manny Clinnick (Math and Computing), and Ed Romascan (Physics, Group A). A system is expected to be operative in February 1972.

b. Data file programs, which perform exhaustive checks on the input data, store them in a random-accessible file, and produce proof or final copy, are being developed by Ardith Kenney and Leo Vardas. A program to handle level-scheme data and produce proof and final level diagrams is being written by M. Lederer. These programs are expected to be working early in 1972 and to be essentially complete by the end of the year.

c. An index file of "keywords" for every reference, ordered by isotope, is in routine use as the compiler's index to the literature. The file is updated three times a year with "recent references" issues of Nuclear Data B, supplied to us on magnetic tape by the Nuclear Group at ORNL. Our programs check and edit the new tapes, merge them into a random-accessible master file, and provide prints of the new references or the entire file for use by the compilers. The automatic checking by the program and some spot-checking by the compilers has provided useful feedback to the Nuclear Data Group.

3. Content and Format of the Seventh Edition. The content of the seventh edition will be expanded from earlier editions to include more data from nuclear reactions. Level schemes will include one illustration for each isotope, consisting of a decay scheme, with feeding from all radioactive parents, alongside a set of level diagrams, one for each reaction populating that nucleus. The form of the decay schemes will be similar to that of the sixth edition. Reaction level schemes will include levels and their properties (energies, spins, and parities, ℓ-transfer values, etc.). Where gamma rays have been measured in a reaction, the gamma-transitions will be indicated, unless the gamma rays only define the level (e.g., direct gamma rays from the capture state in thermal neutron capture will be omitted).

There will not be an arbitrary energy cutoff for levels; rather, where the levels are so numerous that all cannot be included, the schemes will be abridged [e.g., by indicating "27 more (d, p) levels between 4 and 5 MeV"]. This policy applies to levels from decay as well as reaction experiments.

A sample level scheme for the nucleus ^{75}Se is given in the accompanying figure. In addition to the drawing for each isotope, there will be a "skeleton" A-chain drawing, showing the decay relationships and Q values for each mass chain (see Fig. 1).

Tabular data will include only ground-state, radioactive decay, and level data. The scope of data categories covered and policies on selection of data will be similar to that of the sixth edition. All information, including categories of data covered in "Table I" of the sixth edition, will be given in a single table, similar in layout to "Table II" of the sixth edition.

As of December 1971, 90 mass numbers have been compiled. We are aiming to produce the seventh edition in about three years.

A STUDY OF 66-SEC ISOMERIC STATE OF ^{222}Ac†

K. A. Eskola*

Results of an extensive survey of α-active isotopes between lead and uranium have been reported by Valli and Hyde et al., in a series of articles.[1-8] The 66-sec α-emitting isomeric state, ^{222m}Ac, reported here, was discovered as a byproduct of a study of ^{261}Rf.[9]

Earlier studies[10-12] of ^{222}Ac have been carried out by producing the 1.8-min ^{226}Pa in bombardments of thorium with high-energy deuterons and following its α-decay through the chain ^{226}Pa- ^{222}Ac- ^{218}Fr- ^{214}At- ^{210}Bi. By use of the recoil collection method, Meinke et al.[12] were able to separate ^{222}Ac from its parent, ^{226}Pa, and obtained a value of 5.5 ± 0.5 sec for its half-life.

With similar techniques, but using Au-Si

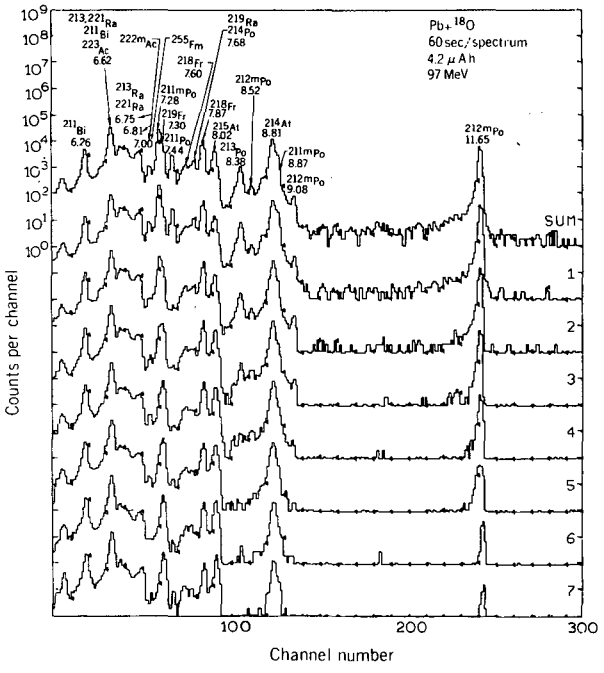

Fig. 1. A series of α-particle spectra produced by bombardments of Pb with ^{18}O ions. The individual spectra show the total of counts recorded at each of the seven stations by the two movable detectors when facing the wheel. The sum of the seven spectra is plotted topmost. The wheel-stepping interval, the integrated beam reading and the bombardment energy are indicated. (XBL 718-6367)

surface-barrier detectors, McCoy[13] associated two α-particle groups, one at 6.998 MeV (94%) and the other at 6.952 MeV (6%), with the decay of the 5.5-sec ^{222}Ac. We have assigned the 66-sec α-activity with a complex α-particle spectrum to ^{222m}Ac by showing that the α particles are promptly followed by 7.87-MeV and 8.81-MeV α particles of short-lived ^{218}Fr and ^{214}At.

The experimental techniques and apparatus used have been described in some detail in References 14 and 15. The 66-sec α activity was observed in bombardments of ≈ 100 $\mu g/cm^2$ natural Pb targets with both ^{16}O and ^{18}O ions and a Bi target with ^{15}N and ^{18}O. (Recently the activity has also been observed by Eppley et al.[16] when bombarding Th and U targets by 5-GeV protons from the Bevatron.) The series of α-particle spectra displayed in Fig. 1 resulted from bombardment of the Pb target with 97-MeV ^{18}O ions. Most of the activities belong to members of α-decay chains originating from Ac and Ra isotopes. However, it is readily seen that the 7.87-MeV and 8.81-MeV peaks assigned to ^{218}Fr and ^{214}At, respectively, decay with a half-life of about a minute instead of the 5.5-sec half-life of ^{222}Ac. A half-life of 66±3 sec is derived for the 7.87-MeV α-particle group by a least-squares analysis.

A search for a possible precursor to the 7.87-MeV α-particle activity naturally leads to a closer study of the complex cluster of peaks in the 6.5- to 7.0-MeV energy region, where one would expect to find an Ac α emitter with a half-life of a minute. As shown in Fig. 1 the 2.3-min ^{211}Bi, 2.7 min ^{213}Ra and its electron-capture (EC) daughter 35-sec ^{213}Fr, 30-sec ^{221}Ra, 2.2-min ^{223}Ac and 20-h ^{255}Fm also contribute to the α-particle spectrum in this energy region. The ^{255}Fm also was produced in unrelated bombardments preceding the one resulting in the spectrum shown in Fig. 1. To single out the contribution of the possible ^{222}Ac α activity from a host of interfering activities, we looked for time-correlated α-decay events where an α particle was followed within 50 msec by an α particle in either the 7.87-MeV or 8.81-MeV peak. The α-particle spectra resulting from the search are plotted in Fig. 2. Accidental correlations due to a high counting rate have been accounted for by subtracting from the above correlations the ones where a 7.87-MeV or 8.81-MeV α particle preceded an α particle in the 6.5- to 7.1-MeV range. On the left side in Fig. 2 the correlations detected at the first station, or within the first 60 sec after the irradiation, are plotted in four 15-sec time subgroups. To the right these same counts are summed up in the first spectrum and the three spectra underneath arise from correlated events found at the three succeeding stations. The fast decaying component in the prominent 7.01-MeV peak is associated with the previously known 5.5-sec α activity of ^{222}Ac. The energies, intensities and hindrance factors for α-particle groups contributing to the composite spectrum are presented in Table I. The shape of the 7.87-MeV ^{218}Fr peak was used as a standard when resolving the spectrum into its components. The hindrance factors were calculated using the spin-independent ($\ell = 0$) equations of Preston.[17] A value of 9.29 fm was chosen for the radius parameter R.

A study of the α-particle spectra recorded by the movable detectors when in the off-wheel position, combined with the spectra recorded by the stationary detectors facing them, indicated that the 66-sec metastable state also decays by γ-ray emission and feeds the 5.5-sec state, which probably is the ground state. The recoil energy imparted to the residual atoms by the decay transfers a part of the atoms onto the detectors facing the wheel and their subsequent decay by α-particle emission is observed in the off-wheel position.

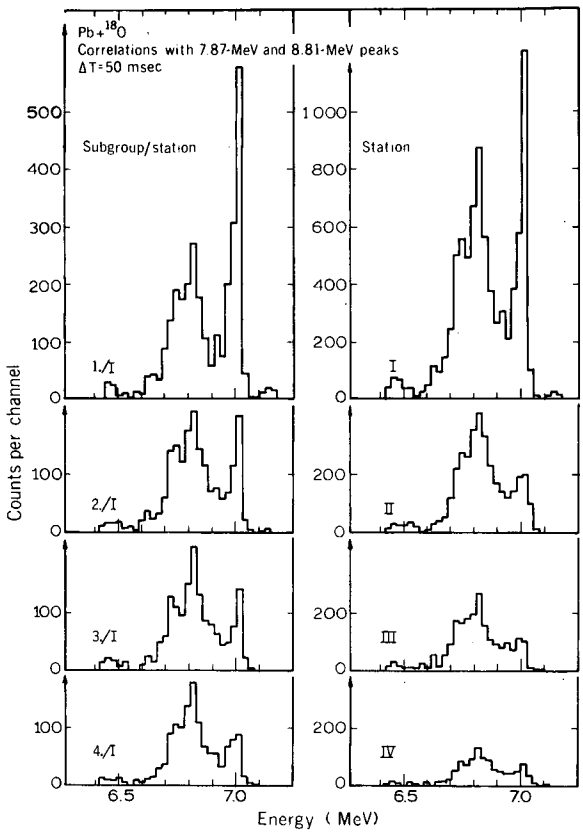

Fig. 2. The spectrum of α-decay events were followed within 50 msec by another event recorded at either the 7.87-MeV or 8.81-MeV peak. The events observed at the first detector station are displayed in four consecutive 15-sec subgroups on the left side. To the right the correlated events from the first four stations are plotted. (XBL 718-6366)

On the basis of the calculated and observed intensity ratios in the various spectra we obtain a lower limit of $3 \pm 1\%$ and an upper limit of 10% for the decay of the 66-sec metastable state by isomeric transition.

^{222m}Ac also seems to decay by EC to the levels of 38-sec ^{222}Ra. Approximate values of 0.7% and 2% of the lower and upper limits for the EC branching were obtained by comparing the observed number of counts in the 7.13-MeV peak of ^{218}Rn both in on- and off-wheel positions with the observed number of counts atrributable to ^{222m}Ac.

Because the event times were measured with an accuracy of only 50 msec, an accurate half-life measurement for the daughter, ^{218}Fr, was not possible. However, a value of 0.7 ± 0.6 msec was deduced on the basis of the observed ratio, 0.019 ± 0.017, between

Table I. Alpha-particle groups associated with the decay of the 66-sec ^{222m}Ac.

Alpha-particle energy (MeV)	Intensity (%)	Hindrance factor
6.46 ± 0.02	2 ± 1	13
6.71 ± 0.02	8 ± 4	33
6.75 ± 0.02	15 ± 5	25
6.81 ± 0.01	27 ± 10	24
6.84 ± 0.02	10 ± 5	85
6.89 ± 0.02	15 ± 5	85
6.97 ± 0.02	8 ± 3	310
7.00 ± 0.02	15 ± 5	220

those pairs of events where ^{222}Ac and ^{218}Fr α decays followed each other within the same 50-msec interval and those where the two events were recorded in two consecutive 50-msec intervals.

There seems to be a discrepancy of some 10-40 keV between the α-particle-energy values reported in this work and those given by McCoy.[13] Thus we have found the energies 7.01, 7.87, and 8.81 MeV for the 5.5-sec ^{222}Ac, 0.7-msec ^{218}Fr and 2-μsec ^{214}At, respectively, while the corresponding energies of McCoy are 6.998, 7.845, and 8.777 MeV. Our values are based on the analysis of the spectra by the SAMPO computer program[18] using the 7.136-MeV ^{214}Ra and 8.675-MeV ^{215}Rn as internal energy standards.[4,7]

The relative cross sections for some of the more prominent reaction products in bombardments of the lead target by ^{18}O ions are shown in Fig. 3. Because of the natural isotopic composition of the lead target, several reactions may substantially contribute to the production of an isotope. The predominant component in each case seems to come from the most abundant isotope, ^{208}Pb, in the target, i.e., from the reactions ^{208}Pb(^{18}O, 3n)^{223}Th, ^{208}Pb(^{18}O, p2n)^{223}Ac, ^{208}Pb(^{18}O, p3n)^{222m}Ac, ^{208}Pb(^{18}O, αn)^{221}Ra, and ^{208}Pb(^{18}O, ^{14}C)^{212m}Po.

The cross-section ratio of the 66-sec state to the 5.5-sec state of ^{222}Ac was measured to be 3.9 ± 0.5 for the 97-MeV ^{18}O ions. The isomeric ratio was found to be relatively constant near the peak of the cross-section curve. It was not studied more closely at lower bombarding energies because of the low yields.

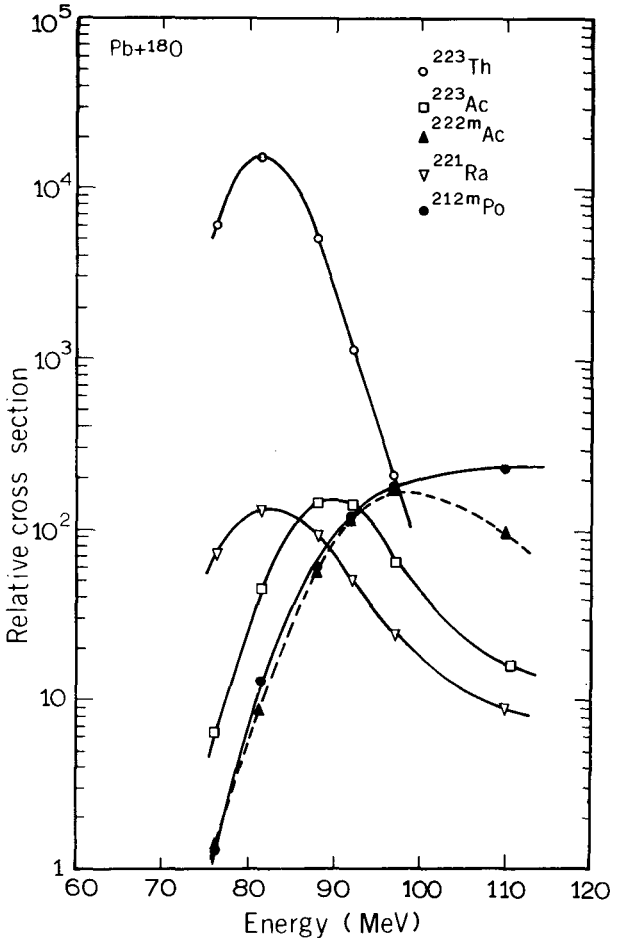

Fig. 3. Excitation curves for some of the activities produced in the bombardments of Pb by ^{18}O ions. (XBL 718-6369)

Of the earlier studied isotopes of actinium, only ^{216}Ac has been found to have an α-emitting metastable state.[6,19] The isomerism is caused by the close proximity of 9^- and 1^- states, which are members of a multiplet arising from the $(2g\ 9/2)_n\ (1h\ 9/2)_p$ single-particle configuration. No evidence of the existence of a similar high-spin isomer in ^{218}Ac was seen by Torgerson and Macfarlane[19] in their recent study of the odd proton, N = 127 isotopes. Borggreen et.al., also did not find any direct indication of the existence of isomers in ^{218}Ac or ^{220}Ac in connection with their studies of protactinium isotopes with mass numbers 222-225.[8] It thus seems that this particular type of isomerism is confined to N = 127 isotones.

A possible explanation for the presence of a long-lived α-emitting isomer in ^{222}Ac is derived from the Nilsson model level scheme. Borggreen and his co-workers[8] observed that the α-particle energies of N = 133 isotones were systematically lower than expected on the basis of the regular behavior in neighboring isotones. They suggested that this anomalous trend might be caused by the occurrence of some individual particle level of high spin. Such a level could well be the $13/2^+$ [606 ↑] level predicted to be favored by the 131st and 132nd neutron in the recent level scheme calculation by S. G. Nilsson et al.[20] However, for the scheme to be applicable one has to postulate the onset of stable ground-state deformation for the nuclei in the region of A near 225 with deformation parameters $\epsilon \sim 0.2$ and $\epsilon_4 = -0.04$. The coupling of $13/2^+$[651 ↑] level, would provide a high-spin multiplet that could be the source of the 66-sec metastable state. An application of the Gallagher-Moszkowski coupling rule gives a spin of 5^+ for the lowest state of the spin multiplet.

On the basis of the measured isomeric ratio it seems likely that the 66-sec level has a higher spin than the 5.5-sec level. Although the cross sections for the production of the two isomeric states are relatively small, a more detailed study of their properties by use of α - γ and α-conversion electron coincidence measurements is feasible and could provide valuable information on the applicability of the Nilsson model level scheme in this transition region. A careful search might also result in discovery of similar isomerism in nearby odd-odd isotopes.

I would like to express my thanks to Dr. Albert Ghiorso and Dr. Matti Nurmia for help in the experiments. The skills and helpfulness of the Hilac crew are also deeply appreciated.

Footnotes and References

†Condensed from Phys. Rev. C5, 942 (1972).

*On leave of absence from Department of Physics, University of Helsinki, Helsinki, Finland.

1. W. Treytl and K. Valli, Nucl. Phys. A97, 405 (1967).

2. K. Valli, M. J. Nurmia, and E. K. Hyde, Phys. Rev. 159, 1013 (1967).

3. K. Valli, E. K. Hyde, and W. Treytl, J. Inorg. Nucl. Chem. 29, 2503 (1967).

4. K. Valli, W. J. Treytl, and E. K. Hyde, Phys. Rev. 161, 1284 (1967).

5. K. Valli, W. J. Treytl, and E. K. Hyde, Phys. Rev. 167, 1094 (1968).

6. K. Valli and E. K. Hyde, Phys. Rev. 176, 1377 (1968).

7. K. Valli, E. K. Hyde, and J. Borggreen, Phys. Rev. C1, 2115 (1970).

8. J. Borggreen, K. Valli, and E. K. Hyde, Phys. Rev. C2, 1841 (1970).

9. A. Ghiorso, M. Nurmia, K. Eskola, and P. Eskola, Phys. Letters 32B, 95 (1970).

10. W. W. Meinke, A. Ghiorso, and G. T. Seaborg, Phys. Rev. 75, 314 (1949).

11. W. W. Meinke, A. Ghiorso, and G. T. Seaborg, Phys. Rev. 81, 782 (1951).

12. W. W. Meinke, A. Ghiorso, and G. T. Seaborg, Phys. Rev. 85, 429 (1952).

13. J. L. McCoy, Soc. Sci. Fennica, Commentationes Phys.-Math., 30, 1 (1964).

14. A. Ghiorso, Proceedings of the Robert A. Welch Foundation Conference on Chemical Research XIII. The Transuranium Elements-The Mendeleev Centennial, Houston, 1969 (Robert A. Welch Foundation, Houston, Texas, 1970), p. 107.

15. K. Eskola, P. Eskola, M. Nurmia, and A. Ghiorso, Phys. Rev. C4, 632 (1971).

16. R. E. Eppley, E. K. Hyde, and J. D. Bowman, private communication (1971).

17. M. A. Preston, Phys. Rev. 71, 865 (1946).

18. J. T. Routti and S. G. Prussin, Nucl. Instr. Methods 72, 125 (1969).

19. D. F. Torgerson and R. D. Macfarlane, Phys. Rev. C2, 2309 (1970).

20. S. G. Nilsson, C. F. Tsang, A. Sobiczewski, Z. Szymanski, S. Wycech, C. Gustafson, I. L. Lamm, P. Moller, and B. Nilsson, Nucl. Phys. A131, 1 (1969).

TWO NEW ALPHA-PARTICLE EMITTING ISOTOPES OF ELEMENT 105: ^{261}Ha AND ^{262}Ha†

A. Ghiorso, M. J. Nurmia, K. A. Eskola,* and P. L. Eskola

By bombardment of a ^{250}Cf target with ^{15}N ions and ^{249}Bk targets with both ^{16}O and ^{18}O ions we have produced two new α-particle emitters, one an 8.93-MeV, 1.8-sec activity assigned to ^{261}Ha, the other an 8.45-MeV, 40-sec activity assigned to ^{262}Ha. Genetic relationships between the new activities and the known nuclides ^{257}Lr and ^{258}Lr have been established by both α-recoil milking and time-correlation measurements.

Both the ^{250}Cf and ^{249}Bk targets were prepared by the molecular plating method and deposited on an area of 0.18 cm^2. The isotopic composition of the 350 μg/cm^2 ^{250}Cf target was 6.1% ^{249}Cf, 86.5% ^{250}Cf, 6.8% ^{251}Cf, and 0.6% ^{252}Cf. Several berkelium targets of 300-400 μg/cm^2 thickness were used; the amount of ^{249}Cf in them due to decay of 314-day ^{249}Bk after chemical separation did not exceed 10%. The targets were bombarded by ^{15}N, ^{16}O, and ^{18}O ions accelerated by the Berkeley Hilac.

The experiments were carried out with apparatus similar to that described in Refs. 1-3. The product atoms were swept out of the target region through a 0.4-mm diameter orifice into a rough vacuum where the He jet deposited them onto the periphery of a vertically mounted wheel. The wheel was periodically rotated to place the collected recoil atoms next to a series of peripherally mounted Si-Au surface-barrier detectors. There were seven detector stations arranged equidistantly at 45° intervals around the wheel. Two movable and two stationary detectors were used at each of the seven locations. While one set of movable detectors was recording α-decay events from atoms on the wheel, the other set and its stationary complement were analyzing the daughter α-particle activities which had recoiled off the wheel into the crystals.

The α-particle spectra displayed in Fig. 1 resulted from bombardments of the ^{250}Cf target with 83-MeV ^{15}N ions. The complex group of peaks at about 8.9 MeV has been assigned to ^{261}Ha and its α-decay daughter, 8.87-MeV, 0.6-sec ^{257}Lr.[3] Excluding the contribution of ^{257}Lr produced directly in the bombardment, the whole complex decays with a half-life of 1.8±0.6 sec, or with the same half-life as the 8.93-MeV group. The 6.54 , 6.65 , and 6.77-MeV francium peaks are due to a small lead impurity in the target. The

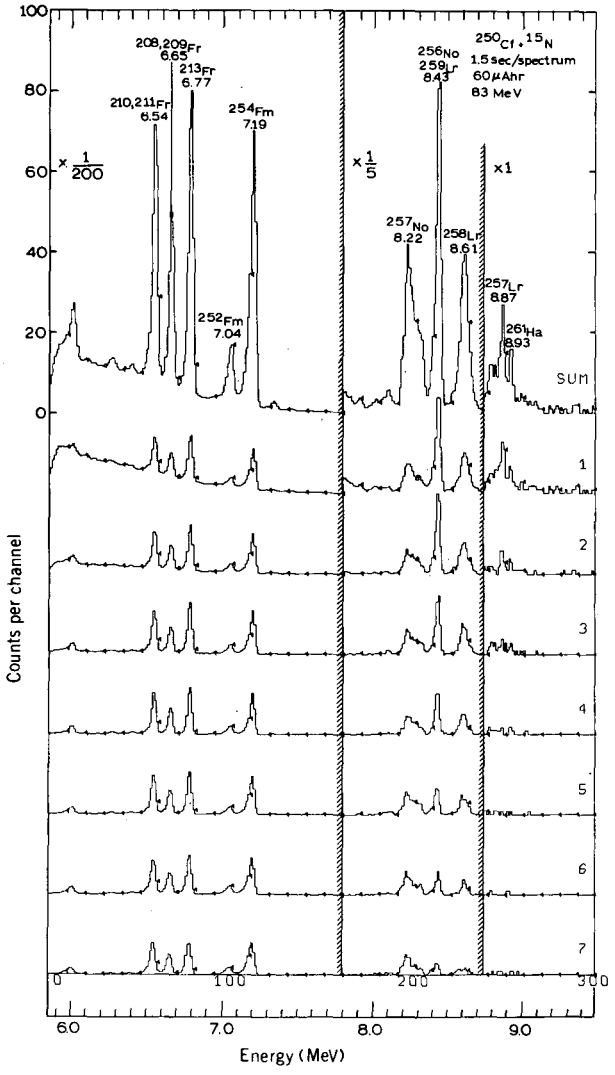

Fig. 1. A series of α-particle spectra produced by bombardments of ^{250}Cf with ^{15}N ions. The wheel-cycle rate, the integrated beam current reading, and the bombardment energy are indicated in the figure. The individual spectra are composed of counts recorded at each of the seven stations by the two movable detectors when facing the wheel. The sum of the seven spectra is plotted topmost. (XBL 714-6323)

activities left in the detecting crystals as shown by the α-particle spectra recorded by the detectors in the off-wheel position had 10 counts in the 8.75- to 8.90-MeV region for a 37-μAh experiment with a distribution of 5, 1, 1, and 3 counts recorded in the first four stations. Within the 2-sec shuttle period, the quadrants had 4, 5, 0, and 1 of these counts, respectively. The above distribution is compatible with the α-recoil daughter activity being 8.87-MeV, 0.6-sec ^{257}Lr,[3] and hence its precursor being 1.8 sec ^{261}Ha. The ratio of detected mother atoms to detected daughter atoms is 4.0 ± 1.4, which agrees with the value $5.0 \pm {}^{1.6}_{0.8}$ calculated by taking into account geometry and time factors. Calculation based on spin-independent ($\ell = 0$) equations of Preston[4] and a radius parameter of 9.45 fm give a hindrance factor of 2 for the 8.93-MeV α transition.

The 8.93-MeV, 1.8-sec activity was also produced by bombardments of ^{249}Bk with 92-MeV ^{16}O ions. In a 127-μAh bombardment, 25 counts were recorded in the 8.93-MeV peak and 7 α-recoil events in the 8.75- to 8.9-MeV range by the detectors in the off-wheel position.

Additional evidence for the isotopic assignment of the new α-particle activity was provided by mother-daughter time-correlation measurements. The distribution of counts recorded in the energy interval of 8.7 to 9.1 MeV for both the mother and the daughter, and following one another within 6 sec, is displayed on the left-hand side of Fig. 2 in several ways. The solid and open circles mark data obtained from bombardments of ^{249}Bk with ^{16}O ions and ^{250}Cf with ^{15}N ions, respectively. In both bombardments the wheel-cycle rate was 1.5 sec. The α-particle energy for the mother group is 8.93 MeV, while the daughter has a more complex structure with groups at about

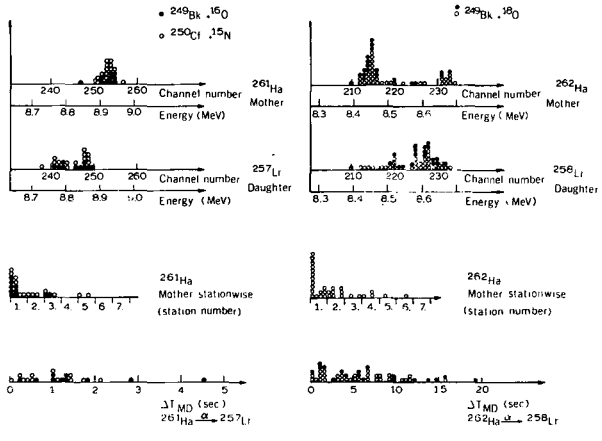

Fig. 2. The distribution of time-correlated events in bombardments of ^{249}Bk with ^{16}O ions and ^{250}Cf with ^{15}N ions (to the left), and in the bombardments of ^{249}Bk with ^{18}O ions (to the right). Energy spectra of mother and daughter events are shown above, the distribution of mother events by station number and quadrant of the wheel cycle is given in the middle, and the difference in time of occurrence between mother and daughter events is displayed in the bottom. (XBL 714-6325)

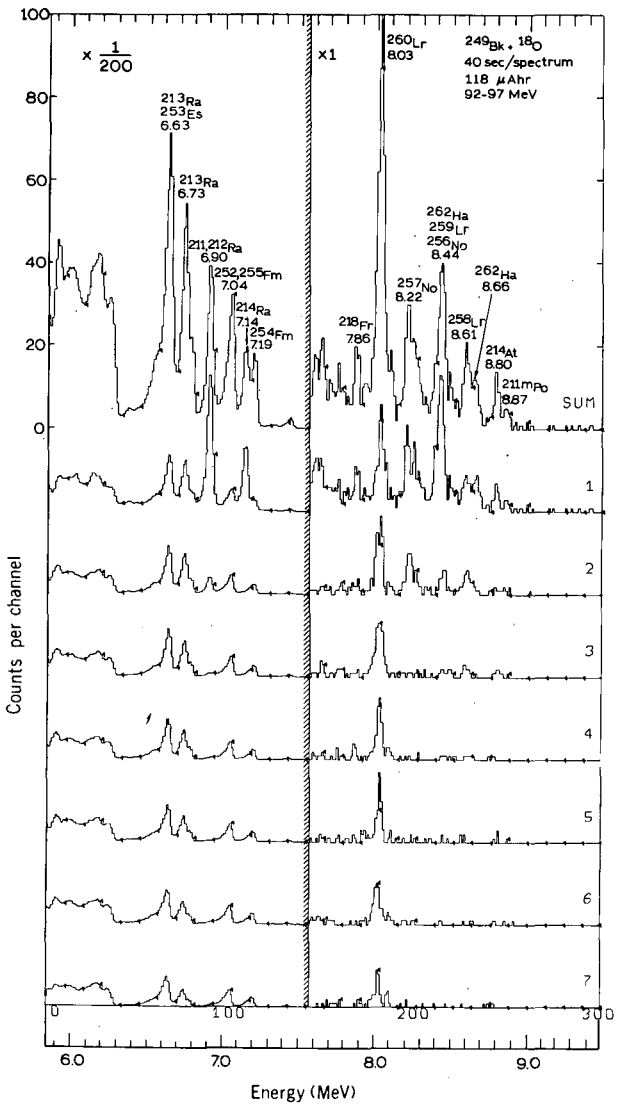

Fig. 3. A series of α-particle spectra resulting from bombarding a ^{249}Bk target with ^{18}O ions. The arrangement of the spectra and the data pertinent to the bombardment correspond to those in Fig. 1. (XBL 714-6321)

8.79 and 8.86 MeV. The half-life of the mother activity is 2 ± 1 sec and that of the daughter $0.8 \pm {}^{0.5}_{0.3}$ sec on the basis of the two lower distributions. The properties of the daughter activity are consistent with those of 8.87-MeV, 0.6-sec ^{257}Lr (Ref. 3) and, consequently, the mother is assigned to ^{261}Ha. Thirteen correlated pairs were recorded in the ^{250}Cf bombardment; the expected number of random correlations is about 0.5 in the whole energy interval of 8.7 to 9.1 MeV.

^{262}Ha

The α-particle spectra displayed in Fig. 3 resulted from a 118-μAh bombardment of a ^{249}Bk target with ^{18}O ions. The new (40±10)-sec activity which is assigned to ^{262}Ha has a complex α-particle spectrum with most prominent peaks at 8.45 and 8.66 MeV. The latter peak is masked by the 8.6-MeV cluster of peaks that belongs to the α-decay daughter, ^{258}Lr. The intensity values for the 8.45- and 8.66-MeV α transitions are roughly 80% and 20%; a value of 9.50 fm for the radius parameter yields hindrance factors 2 and 40 for these transitions. The amount of lead impurity in this particular ^{249}Bk target was very low and therefore the interference from lead-induced activities such as ^{214}At and ^{211m}Po is not serious. The ^{249}Cf present in the target is the source of the ^{256}No and ^{257}No activities in the spectra. The lawrencium activities either are a result of (^{15}N, αxn)-type reactions (^{260}Lr and ^{259}Lr partly, at least) or are genetically related to the activities produced in the bombardment (^{258}Lr). The 8.03-MeV, 3.0-min ^{260}Lr was first produced in this bombardment.[3]

The α-particle spectra shown in Fig. 4 represent the total of counts recorded by the detectors in the off-wheel position at each of the seven stations. The half-life value for the counts in 8.5 to 8.7-MeV range is 65 ± 25 sec. An examination of the decay of the 8.5- to 8.7-MeV activity within the 8-sec shuttle period gives a half-life of 4.5 ± 2 sec. The ratio of observed mother atoms to recoil daughter atoms is 5.0 ± 1.2 (100:20) for the 118-μAh bombardment, while the calculated value is 3.1 ± 0.2. Altogether the data are consistent with the parent activity being (40 ± 10)-sec ^{262}Ha and the daughter activity 8.6-MeV, 4.2-sec ^{258}Lr.

A two-dimensional array of time-correlated events observed in the 118-μAh bombardment of ^{249}Bk with ^{18}O ions is shown in Fig. 5. A maximum of 20 sec was allowed between the occurrence of mother and daughter events. The events in the region enclosed by the broken line stand out from the background due to random correlations. In the region including the 8.45-MeV peak for the mother and the complex 8.6-MeV peak for the daughter, less than two random correlations are expected on the average. The four distributions in the right half of Fig. 2 provide further information about the time-correlated events in ^{249}Bk bombardment with ^{18}O ions. The open circles are the events enclosed by the broken line in Fig. 5 and the closed circles mark events recorded in experiments where other ^{249}Bk targets and 60-sec wheel-cycle rate were used. The α-particle spectrum of the parent activity is complex with the most prominent peak at 8.45-MeV. Both the time-correlated mother events and

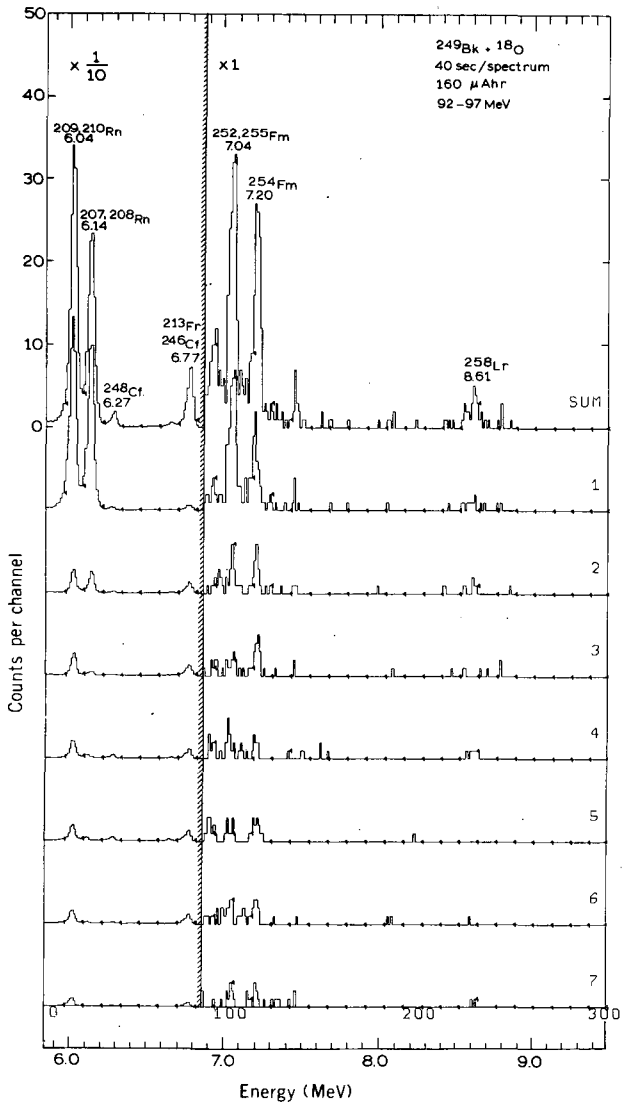

Fig. 4. The α-particle spectra recorded by the detectors in the off-wheel position and resulting from bombardments of ^{249}Bk with ^{18}O ions. The arrangement of the spectra and the data pertinent to the bombardment correspond to those in Fig. 1.
(XBL 714-6322)

the spectra in Fig. 3 indicate that there is an α-particle group at 8.66 MeV. However, as can be seen in Fig. 5, some of the events in this peak seem to be correlated with an 8.50-MeV daughter. The half-life of the mother activity is 43 ± 15 sec, which value is derived from the stationwise distribution of parent events. The daughter activity with a half-life of 5 ± 2 sec and a cluster of α-particle groups centered at 8.6 MeV has the characteristics of 8.6-MeV, 4.2-sec ^{258}Lr. The mother is therefore assigned to ^{262}Ha.

No evidence for an activity decaying by spontaneous fission and having a half-life of 2 sec was observed in bombardments of ^{249}Bk with ^{18}O ions, and ^{250}Cf with ^{15}N ions. However, because of a background of fission events caused by decay of 2.6-h ^{256}Fm, we can only set an upper limit of 50% to branching by spontaneous fission of ^{261}Ha. In bombardments of ^{249}Bk with ^{18}O ions, a (25 ± 10)-sec spontaneous-fission activity was extracted from the ^{256}Fm-induced background. If this activity is associated with the 8.45-MeV, 40-sec α-particle activity assigned to ^{262}Ha, it could arise from branching by spontaneous fission of ^{262}Ha or from its electron-capture decay to ^{262}Rf, which is probably a very short-lived SF emitter. We cannot rule out other alternatives such as ^{263}Ha and ^{263}Rf as possible sources of the 25-sec activity, but if the fissions are related to ^{262}Ha, the branching by spontaneous fission or electron capture is about 60%.

Early attempts to identify α-particle emitting isotopes of element 105 were reported by Flerov et al., in 1968.[6,7] Their preliminary conclusion was that they observed the isotopes ^{261}105 with $E_\alpha = 9.4 \pm 0.1$ MeV, $0.1 < T_{1/2} < 3$ sec, and ^{260}105 with $E_\alpha = 9.7 \pm 0.1$ MeV, $T_{1/2} > 0.01$ sec. In our paper[1] on ^{260}Ha we have discussed these findings in some detail and indicated that they were not compatible with our results. More recently, new work on

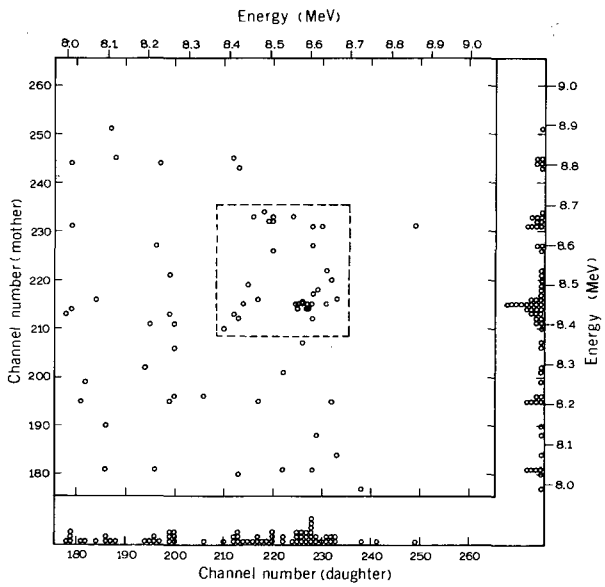

Fig. 5. A two-dimensional presentation of time-correlated events observed in the bombardment of ^{249}Bk with ^{18}O ions. The region enclosed by the broken line was included in the distribution shown in Fig. 2. The histograms on the side are spectra composed of daughter events (horizontal) or mother events (vertical) only. (XBL 714-6324)

both spontaneous-fission[8, 9] as well as α-activities[10] assigned to element 105 have been reported by the Dubna group.

In their study of α-particle activities produced by bombarding ^{243}Am with ^{22}Ne ions, Druin et al.[10] found evidence for an activity with a half-life of 1.4 ± 0.6 sec and with α-particle groups at 8.9 and 9.1 MeV. The assignment of this activity to either ^{260}105 or ^{261}105 was based on 7 time-correlated pairs of events with the mother in the region of 8.8 to 9.2 MeV and the daughter in the region of 8.3 to 8.6 MeV. It was assumed that both ^{256}Lr and ^{257}Lr have the same decay properties. Our earlier studies[1] on ^{260}Ha and pertinent Lr isotopes[3] show, however, that this assumption is false and that such correlated events could arise only from the sequence

$$^{260}\text{Ha} \xrightarrow[9.1\ \text{MeV}]{1.6\ \text{sec}} {}^{256}\text{Lr} \xrightarrow[8.3\text{-}8.6\ \text{MeV}]{31\ \text{sec}},$$

but not from the sequence

$$^{261}\text{Ha} \xrightarrow[8.93\ \text{MeV}]{1.8\ \text{sec}} {}^{257}\text{Lr} \xrightarrow[8.87\ \text{MeV}]{0.6\ \text{sec}}.$$

Because more detailed information of the energy and time distributions of the correlated events was not given in the paper by Druin et al.[10] it is not possible to determine how many of the pairs might actually belong to the former genetic sequence. Moreover, a detailed evaluation of the presented α-particle spectrum is difficult because only a few of the peaks have been assigned to known activities and because the contributions from lead-induced reactions—those producing Th and Pa isotopes in particular—are not discussed.

The upper limits obtained by us for branching by spontaneous fission for ^{260}Ha,[1] or ^{261}Ha are so far compatible with the possibility that the 1.8-sec spontaneous-fission activity reported by Flerov et al.[8, 9] could be due to one of these isotopes.

We wish to express our thanks to the personnel at the Hilac for their contributions in the many phases of this work and to our colleague, James Harris, who was instrumental in the preparation of the targets.

Footnotes and References

†Condensed from Phys. Rev. C4, 1850 (1971).

*On leave of absence from the University of Helsinki, Helsinki, Finland.

1. A. Ghiorso, M. Nurmia, K. Eskola, J. Harris, and P. Eskola, Phys. Rev. Letters 24, 1498 (1970).

2. A. Ghiorso, in Proceedings of the Robert A. Welch Foundation Conferences on Chemical Research, XIII. The Transruanium Elements—The Mendeleev Centennial, November 1969, Houston, Texas (Robert A. Welch Foundation, Houston, Texas, 1970) p. 107.

3. K. Eskola, P. Eskola, M. Nurmia, and A. Ghiorso, Phys. Rev. C4, 632 (1971).

4. M. A. Preston, Phys. Rev. 71, 865 (1947).

5. E. K. Hulet, J. F. Wild, R. W. Lougheed, J. E. Evans, B. J. Qualheim, M. J. Nurmia, and A. Ghiorso, Phys. Rev. Letters 26, 523 (1971).

6. G. N. Flerov, in Proc. Intern. Conf. Nucl. Struct., Tokyo (1967), edited by J. Sanada, Suppl. J. Phys. Soc. Japan 24, 237 (1968).

7. G. N. Flerov, V. A. Druin, A. G. Demin, Yu. V. Lobanov, N. K. Kharitonov, and L. P. Chelnokov, Joint Institute for Nuclear Research Preprint JINR-P7-3808, 1968 (unpublished).

8. G. N. Flerov, Yu. Ts. Oganesian, Yu. V. Lobanov, Yu. A. Lasarev, and S. P. Tretiskova, Joint Institute for Nuclear Research Report No. JINR-P7-4932, 1970 (unpublished).

9. G. N. Flerov, Yu. Ts. Oganesian, Yu. V. Lobanov, Yu. A. Lasarev, S. P. Tretiakova, J. V. Kolesov, and V. M. Plotko, Nucl. Phys. A160, 181 (1971).

10. V. A. Druin, A. G. Demin, Yu. P. Kharitonov, G. N. Akapiev, V. I. Rud, G. Ya. Sun-Tsin-Yan, L. P. Chelnokov, K. A. Gabrilov, Joint Institute for Nuclear Research Report No. JINR-P7-5161, 1970 (unpublished).

HEAVY-ELEMENT RESEARCH AT THE BERKELEY HILAC*

M. J. Nurmia

As an introduction I believe that I should say a few words about our machine, the Berkeley Hilac, that ended its glorious career recently. Under the leadership of the veteran element hunter, Albert Ghiorso, the Hilac has made a substantial contribution to our knowledge of the nuclear and chemical properties of the heaviest elements. As a result of only one of the lines of research pursued at the Hilac, over a hundred new isotopes, mostly of elements ranging from iridium to hahnium, were discovered by several research groups. Four new elements, nobelium, lawrencium, rutherfordium, and hahnium, were discovered and some chemical properties of the first three were established with the help of the Hilac, although I should mention that these new-element discoveries have been contested to varying degrees by our dear competitors at Dubna in the Soviet Union.

The basic method producing the heaviest known elements is to take a relatively long-lived isotope of a heavy element and bombard it with suitable particles, such as carbon, nitrogen or oxygen ions. At Berkeley we tend to use the heaviest possible targets, such as californium or einsteinium, whereas the Dubna group prefers somewhat lighter and less radioactive targets, such as plutonium and americium, and correspondingly heavier projectiles, to attain the same atomic numbers.

A very serious problem is that heavy-metal impurities, especially lead, in the targets cause serious interference by giving rise to short-lived α-decay chains that include members with high α energies (8 to 9 MeV and beyond) right in the region where we look for α emission from the new elements. Lead has a tendency of finding its way to the targets especially in the molecular plating process, and it is quite difficult to reduce the lead content of these targets below a few nanograms.

In some cases it is possible to look for other kinds of radiation beside α particles. A seemingly attractive possibility is fission: fission fragments can be recorded with mica, glass, or plastic detectors, and the problem of impurities in the target becomes less severe. However, as Al Ghiorso put it at the Houston conference a year and half ago, one α particle is worth maybe 100, maybe 10 000 fissions. When it is a question of identifying a new activity, an α-decay event has two basic advantages: first, the α particle has a definite energy that can be measured very accurately, and second, it leaves a daughter nucleus that will serve as a positive identification of the parent. On the contrary, fission events all look alike and destroy the nucleus without leaving a daughter that could be used to identify the mother. This is why we at Berkeley have always been somewhat unhappy about fission activities - we have cases where we have recorded thousands of fission counts from a given activity but we have still been unable to assign them with the same degree of confidence as in the case of an α activity.

On the other hand, the Dubna group has specialized in fission work and has performed several very interesting experiments with fission activities.

An important refinement was introduced over two years ago when each detector in our vertical-wheel α-spectroscopy system was replaced by a shuttle carrying two detectors. These movable detectors are now called mother detectors; when facing the wheel they, of course, record α particles emitted by the atoms caught on the wheel. However, in about one-half of the cases the α particle is emitted into the wheel, escaping detection. But in those cases the daughter atom is ejected from the wheel by the recoil of the α emission and it usually is caught by the mother crystal.

After a suitable collection period the shuttle is actuated and the mother crystal is moved away from the wheel to face a stationary "daughter" crystal. Now the decay of the daughter atoms can be examined at a good geometry free from interference, while another mother crystal records the α particles from the wheel and collects more daughter atoms.

We now use seven stations, each with two mother and two daughter crystals, making a total of 28 crystals. All these signals are separately amplified and then equipped with identification and timing signals, which are all stored on magnetic tape. After an experiment, which can last for a day or more, the data on the tape are sorted with a computer to recover the spectra as seen at the various detector stations during given time intervals after each rotation of the wheel, and to look for time correlations between mother and daughter events.

I would like now to discuss some recent developments.

First of all we have found four new isotopes

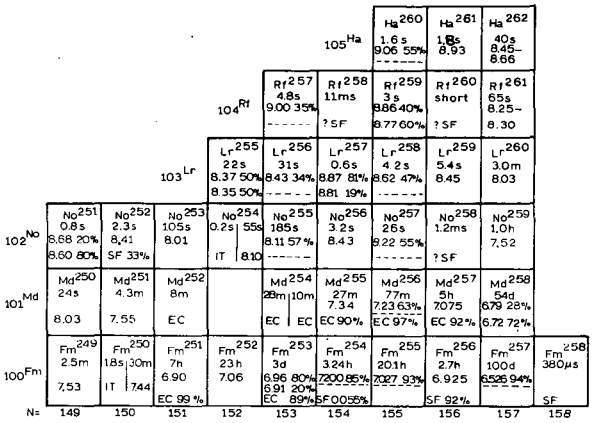

Fig. 1. Portion of the nuclide chart showing the energies and abundances of prominent alpha-particle emissions, and other decay modes observed. (XBL 714-6326)

of mendelevium and two of einsteinium.

Most of other new results are summarized in the portion of the nuclide chart shown in Fig. 1.

Proceeding from the bottom up, the first new nuclide is ^{258}Fm. After a long search this isotope was finally found by Ken Hulet's group in cooperation with us at the Hilac. We bombarded about 10^9 atoms in ^{257}Fm, recovered from the Hutch experiment, with 12.5-MeV deuterons and found that ^{258}Fm has a very short half-life: 380 μsec.

This is one instance where the assignment of a fission activity can be made with a great deal of confidence. The cross section for the reaction forming the fission activity was measured to be 35 mb, which is consistent with the expected (d,p) reaction, but 10 to 30 times larger than the cross sections expected for compound-nucleus reactions with deuterons. Repeated chemical purifications and bombardments of targets containing possible impurities showed that the activity was indeed produced from ^{257}Fm.

A very interesting recent discovery is an isotope of nobelium with the long half-life of one hour. This nuclide, ^{259}No, was found at Oak Ridge and subsequently confirmed by us at Berkeley.

Over two years ago we noticed that two nuclides, ^{254}No and ^{250}Fm, were being mysteriously transferred from the wheel to the mother crystals. After eliminating other possible causes we have concluded that it is due to an isomeric transition in these isotopes. The half-lives of the isomers are shown in the figure. We have not detected any other decay modes, such as fission or alpha decay.

We have recently completed a survey of all lawrencium isotopes with mass numbers from 255 to 260.

^{258}Lr was the one seen at Berkeley in the discovery experiment ten years ago, although it was then tentatively assumed to be ^{257}Lr. Later on the Dubna group reported that they had found ^{257}Lr and that its half-life was much longer, about 35 sec. This was not the end of the story, for we finally found the real ^{257}Lr, identified it by numerous cross-bombardments, and determined its half-life to be much shorter, 0.6 sec.

We have found two new isotopes of hahnium, ^{261}Ha and ^{262}Ha. The former was observed both by bombarding ^{250}Cf with ^{15}N and ^{249}Bk with ^{16}O. The latter was made by bombarding ^{249}Bk with ^{18}O.

In Fig. 2 there is a spectrum from the latter experiment showing the peaks of ^{262}Ha nicely mixed with other activities. However, the mother-daughter system solves the problem: Fig. 3 shows the daughter spectrum, i.e., α counts recorded in the mother-daughter crystal "sandwich" while the mother crystal was shuttled off the wheel. This spectrum is clearly recognizable as that of ^{258}Lr and exhibits the right half-life so that the mother must be ^{262}Ha. One can now separate the mother α spectrum from the mixture shown in the previous figure by looking for α counts that preceded these daughter counts. The result is shown in Fig. 4. The mother clearly has two major α peaks at 8.45 and 8.66 MeV.

Let us now take a last look at good old Fig. 1. What is nature trying to tell us with those numbers? The most interesting area, of course, is the upper end and the upper right corner—the direction towards the new elements and, hopefully, the super-elements. As far as α activities are concerned, two trends are evident. First, the alpha half-lives show a beautiful increasing trend as one proceeds to the right among the isotopes of a given element. The new isotopes, ^{259}No, ^{260}Lr and ^{262}Ha all confirm this. Second, the α half-lives do not decrease very drastically as one proceeds upwards along a given neutron number. All hahnium isotopes are much longer-lived than we dared hope a few years ago.

I think that we are beginning to see a change in the systematics of the α energies as compared to the situation a little further down. Let us look at Fig. 5. It shows the Q α's as

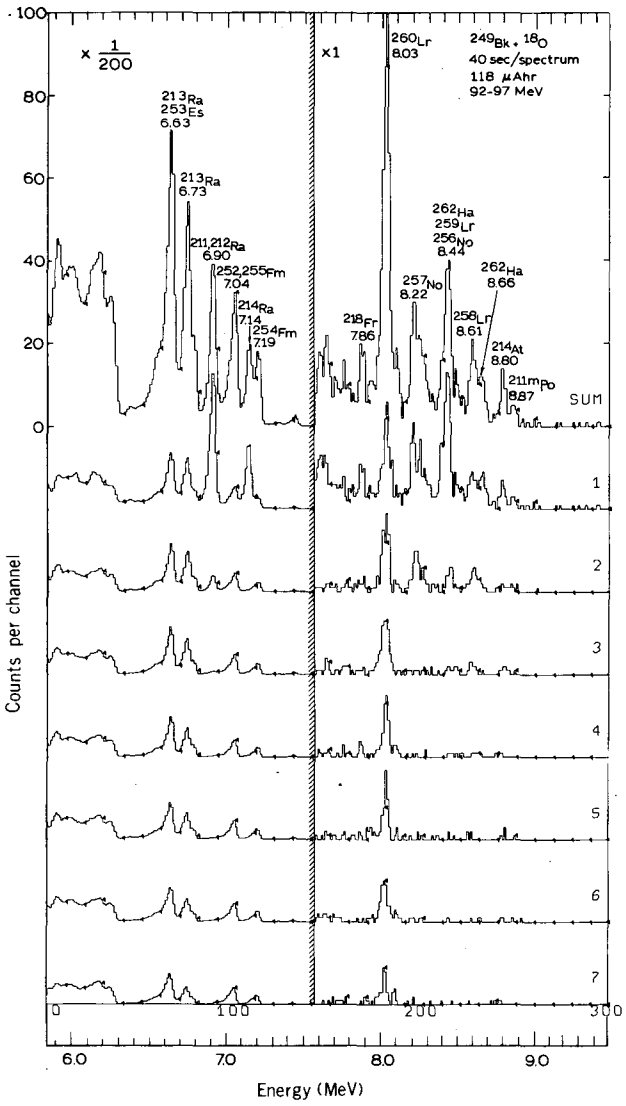

Fig. 2. A series of alpha-particle spectra from a bombardment of ^{249}Bk with ^{18}O. The wheel-cycle rate, the integrated beam current and the bombarding energy are indicated in the figure. The individual spectra are composed of counts recorded at each of the seven detector stations by the two movable detectors when facing the wheel. The sum of the seven spectra is plotted topmost. (XBL 714-6321)

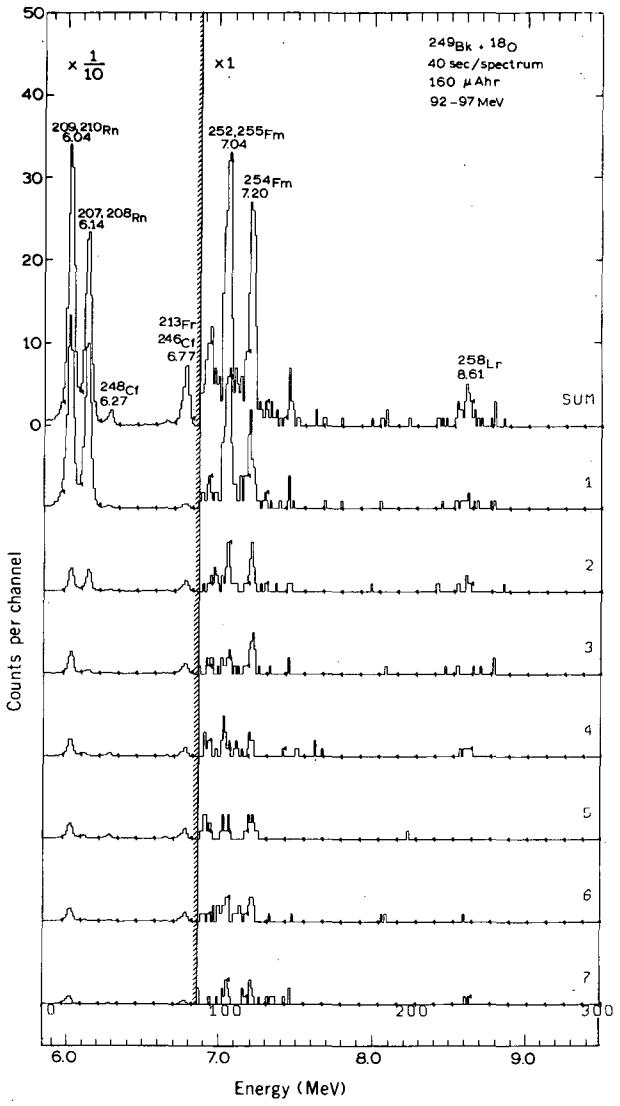

Fig. 3. A series of "daughter" spectra corresponding to the "mother" spectra shown in the previous figure. These counts were recorded by the movable detectors when not facing the wheel, and by the stationary detectors facing the "mother" detectors.
(XBL 714-6322)

a function of Z and N. The curves below Es and Fm look pretty much like those two. But notice how steeply the α-energy curves come down at No and above! That was the first trend—longer half-lives going to the right. Now take a value of N, say 157 and go up. First the points are rather far apart showing that the alpha energy increases rapidly going from one element to the next, but then the jumps become shorter. Trend two! Note that our points for hahnium are all pretty close to the rutherfordium points in accordance with this trend. I have also shown on this figure the values observed at Dubna for ^{260}Ha and ^{261}Ha, 9.7 and 9.4 MeV respectively. Our results do not confirm the Soviet observations, but should they be correct, the trend of α energies with Z will not be like I said.

I do not dare to go back to Fig. 1 any more,

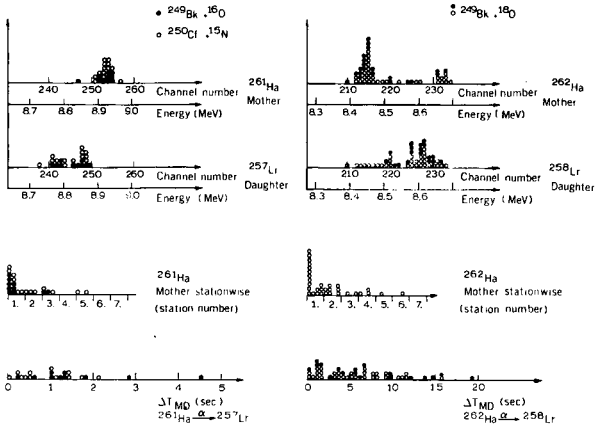

Fig. 4. Right side: Time-correlated "mother" and "daughter" events from bombardment of ^{249}Bk with ^{18}O. The mother and daughter events from all detector stations are shown summed in the two spectra on top. Below, the distribution of the mother counts among the seven stations is shown together with the time interval distribution between the two correlated events. These two distributions are used to obtain the half-lives of the mother and the daughter.

Left side: Similar data from two different bombardments used to synthesize ^{261}Ha.

(XBL 714-6325)

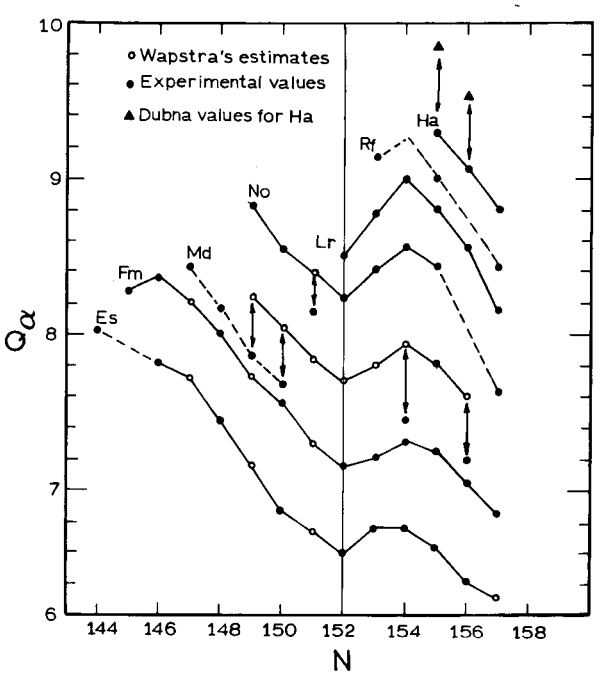

Fig. 5. Alpha decay energies of the isotopes of the heaviest elements as a function of their neutron number. (XBL 714-6356)

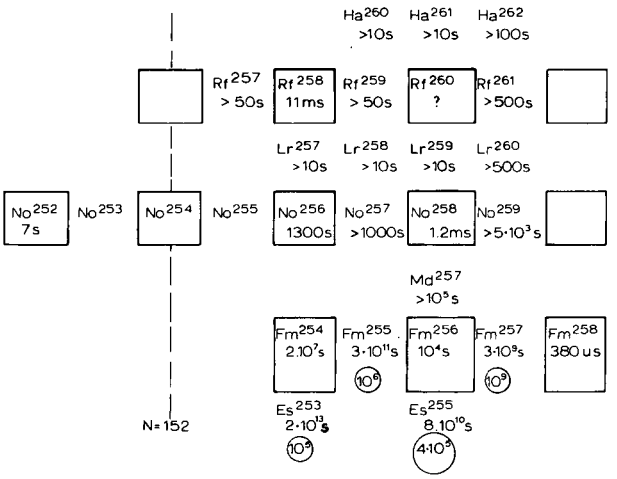

Fig. 6. Measured spontaneous-fission half-lives and their estimated upper limits for isotopes of the heaviest elements. Even-even nuclides are shown as squares; for odd-A nuclides an appproximate SF "hindrance factor" is shown circled below the SF half-life.

(XBL 714-6341)

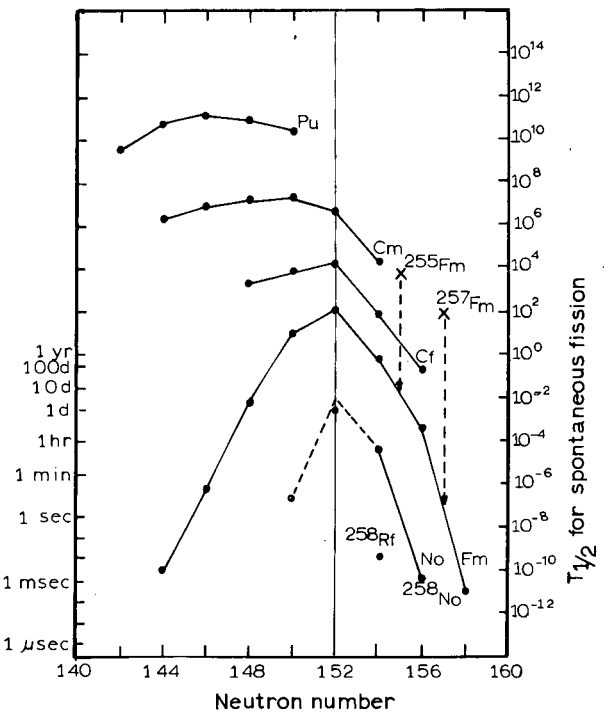

Fig. 7. SF half-lives of isotopes of the heaviest elements as a function of their neutron numbers. (XBL 714-6357)

so let us look at Fig. 6. This is about spontaneous fission and the half-lives shown are fission half-lives. The even-even nuclides are shown as squares; you will note that in the isobar of 256 the half-lives are of the order of 10^3 to 10^4 sec—based on the grand statistics of two cases—and that in the isobar of 258 they are about one msec. This is almost all the material we have!

If we believe that these five points are sufficient to indicate a trend, then it will be that the contours of constant fission half-lives are more or less parallel to the isobar lines and that the rate of decrease is extremely rapid - a factor of 10^6 or so per two units of mass: either two protons or two neutrons.

It is well known that odd-mass nuclides have much longer fission half-lives than those obtained from an interpolation from their even-even neighbors. These hindrance factors can be large—some cases are shown circled in the figure.

Now, we have not seen fissions in ^{261}Rf and that places the lower limit of its fission half-life to about 500 sec. If we were to extrapolate the trend of the half-lives of the even-even isotopes - 10^6 per two mass units - we would get a half-life in the nanosec region for ^{260}Rf and some femtosec for ^{262}Rf. This does not sound right, and moreover it would imply a tremendous hindrance factor, in the region of 10^{14} or more, for ^{261}Rf. The same argument is valid in other cases, so that it seems reasonable to assume that the very drastic shortening of fission half-lives is going to level off as we obtain further data.

This same situation is illustrated in Fig. 7. You will note that the fission half-life or even-even isotopes of a given element tends to attain a maximum near-beta stability and to decrease almost symmetrically on both sides of it. The 152-neutron subshell seems to introduce a disturbance, but anyway there is no evidence as yet of any leveling off of the lines for fission half-lives—they just seem to go down steeper and steeper as N or Z increases. But, somewhere there waits the magic island, and, with the help of the SuperHilac and other projects, we hope to be able to chart our way across this chasm that now looks so menacing.

Footnote

*Condensed from an invited talk given at the APS meeting in Washington, D. C., April 1971; UCRL-20497.

COMMENTS ON "CHEMICAL SEPARATION OF KURCHATOVIUM"*†

A. Ghiorso, M. J. Nurmia, K. A. Eskola,‡ and P. L. Eskola

The Editor has asked for our comments on the paper of Zvara et al.,† inasmuch as the work reported seems to bear upon the discovery of element 104.

In the present paper this Dubna group now interprets the ephemeral "kurchatovium" activity (which, it should be remembered, originally was characterized with a half-life of 0.3 sec) in terms of an assumed spontaneous-fission (SF) branching decay of the nuclide, ^{259}Rf. This isotope of rutherfordium was discovered by our group[1] and characterized as a 3-sec α emitter with main α-particle groups at 8.86 and 8.77 MeV. For the following reasons we cannot agree that the new experiment which they report upon does support their claim to prior discovery of element 104.

1. At present we have only set an upper limit of 20% for the SF branching of ^{259}Rf and such a limit does not by itself rule out the possibility that they have observed such a branching. It seems to us, however, that it would be very surprising if the branching is high enough ($\approx 10\%$) to account for the fissions observed in the Dubna experiments. Recall that ^{261}Rf, a 65-sec α emitter discovered by our group,[2] has already been shown to have an SF $T_{1/2}$ greater than 500 sec and this isotope has two more neutrons than ^{259}Rf. From the precipitous slope[3,4] of SF $T_{1/2}$ vs N for nuclides with more than 152 neutrons one would expect the half-life of ^{259}Rf to be orders of magnitude longer than that of ^{261}Rf.

2. It should be noted that the new Dubna experiment gives no information about the half-life to the activity responsible for the fissions observed in section III of their apparatus. They assume that the half-life must be the same as that observed in recent, purely physical experiments in which a 4.5-sec SF activity was observed.[5] In a paper[6] published in 1966 it was pointed out that as much as 2% of the gross activity produced in a given experiment was able somehow to pass through a hot filter interposed in the chromatographic

column line. It would seem logical to us to expect a much greater fraction to pass downstream through a straight tube which did not have any filter at all and consequently we wonder whether the ^{256}Md-^{256}Fm SF-emitting duo could conceivably be responsible for the 16 events observed.

3. A rather puzzling result of the new experiment is the apparent absence of the 0.1-sec (née 0.3-sec) "kurchatovium" atoms which should have decayed "in flight" in section II of their chromatographic column. From their previous work this "^{260}Ku" activity should be almost as abundant as the "4.5-sec" activity. Does this prove chemically that the 0.1-sec spontaneous fission activity is not due to element 104? If so, then it is worth noting that the non-chemical angular-collimation and excitation-function evidence that "proved" that it was due to element 104 is of the same character as that which purportedly showed that the 4.5-sec activity was due to that element.

We believe that these comments raise some valid questions as to whether or not "element 104 (kurchatovium-Ku) was chemically isolated and identified." We hope to provide satisfactory answers in some new experiments which we will undertake in the near future.

Footnotes and References

*Published in Inorg. Nucl. Chem. Letters 7, 1117 (1971).

†I. Zvara, V. Z. Belov, L. P. Chelnokov, V. P. Domanov, M. Hussonois, Yu. S. Kortkin, V. A. Schegolev, and M. R. Shalayevsky, "Chemical Separation of Kurchatovium," published in Inorg. Nucl. Chem. Letters 7, 1109 (1971).

‡On leave of absence from Department of Physics, University of Helsinki, Helsinki, Finland.

1. A. Ghiorso, M. Nurmia, J. Harris, K. Eskola, and P. Eskola, Phys. Rev. Letters 22, 1317 (1969).

2. A. Ghiorso, M. Nurmia, K. Eskola, and P. Eskola, Phys. Letters 32B, 95 (1970).

3. A. Ghiorso and T. Sikkeland, Phys. Today 20, 25 (1967).

4. E. K. Hulet, J. F. Wild, R. W. Lougheed, J. E. Evans, B J. Qualheim, M. Nurmia, and A. Ghiorso, Phys. Rev. Letters 26, 523 (1971).

5. G. N. Flerov, Yu. A. Lazarev, Yu. V. Lobanov, Yu. Ts. Oganesyan, and S. P. Tretiakova, Internat. Conf. Heavy Ion Phys., Dubna, 1971.

6. I. Zvara, Yu. T. Chuburkov, R. Tsaletka, T. S. Zvarova, M. R. Shalaevskii, and B. V. Shilov, At. Energ. (USSR) 21, 83 (1966) [transl.: Soviet J. At. Energy 21, 709 (1966)].

EXPERIMENTAL INVESTIGATION OF THE ELECTRON CAPTURE DECAY OF ^{210}At AND ^{209}At: THE LEVEL SCHEMES OF ^{210}Po AND ^{209}Po

L. J. Jardine

The nuclear levels of ^{210}Po and ^{209}Po populated by the electron-capture decay of ^{210}At and ^{209}At have been studied. Experimental level schemes have been constructed by using data obtained from γ-ray singles, internal conversion electron, and γ-γ coincidence measurements with high-resolution Ge(Li) and Si(Li) spectrometers.

For the case of ^{210}Po, present data have been used to define 23 levels. The multipolarity of 36 transitions in ^{210}Po have been determined and combined with data from recent reaction studies to assign spins and parities to the levels. All levels arising from the two-proton configuration $(h_{9/2})^2$ and from the multiplets due to the configurations $(h_{9/2}\ f_{7/2})$ and $(h_{9/2}\ i_{13/2})$, except for the lowest spin members, have been identified. The level structure is compared with two-proton shell-model calculations, and experimental transition probabilities for γ decay of the $(h_{9/2}\ f_{7/2})$ and $(h_{9/2})^2$ proton multiplets are compared with predictions using several sets of shell-model wave functions. Evidence is presented which locates the 3^- collective level in ^{210}Po at 2400 keV above the ground state. The electron-capture transition rates to odd parity levels above 2.9 MeV are discussed in terms of neutron-neutron and proton-proton particle-hole excitations of the ^{208}Pb core. A weak-coupling calculation using experimental

data of neighboring isotopes in the lead region was made for the energies of the 3^- and 5^- core states of ^{210}Po.

For the case of ^{209}Po, 20 levels have been defined by the present data. Multipolarities of 31 transitions in ^{209}Po have been determined and used to assign spins and parities to the levels. Five states arising from the odd neutron in ^{209}Po have been assigned by a comparison of the experimental level spectrum and the decay characteristics of levels with a shell-model calculation and the levels in ^{207}Pb. A weak-coupling calculation using experimental data from isotopes in the lead region to approximate residual interactions was found to explain the level structure of ^{209}Po below 2 MeV.

INVESTIGATION OF BROAD RESONANCES IN THE THREE-NEUTRON SYSTEM VIA THE $^3He(^3He,t)^3p$ REACTION FROM 45 TO 60 MeV

J. P. Meulders,* H. E. Conzett, and Ch. Leemann

During the past several years, many experiments have been performed to search for excited states of the three-nucleon system.[1] Recent evidence for a T = 1/2 resonance in ^3He has been reported in the excitation function for the radiative capture of protons by deuterons.[2] The suggested resonance was at an excitation energy of 19.5 MeV with a width of about 2 MeV. No other reactions that involve only three strongly interacting particles, such as nucleon-deuteron scattering or inelastic electron-^3He scattering, have shown any evidence for a resonance.

Evidence for broad T = 3/2 three-nucleon resonances has been presented from reactions involving four strongly interacting particles, namely the reactions[3] $^3He(p,n)3p$ and $^3H(p,n)$ and the reaction[4] $^3He(\pi^-,\pi^+)3n$. In these investigations, broad peaks were seen near the high-energy ends of the neutron and π^+ spectra at forward angles, and were interpreted as evidence for broad resonances in the 3p, $^3He^*$, and 3n systems near 10-MeV excitation with respect to the three-nucleon mass. However, Phillips[5] subsequently showed that the broad peak in the π^+ spectrum could be explained as resulting from the reaction mechanism itself and from the known strong final-state interaction between two neutrons at low relative energy.[6] Thus, there was no need to postulate an additional three-neutron resonance to explain the experimental results.

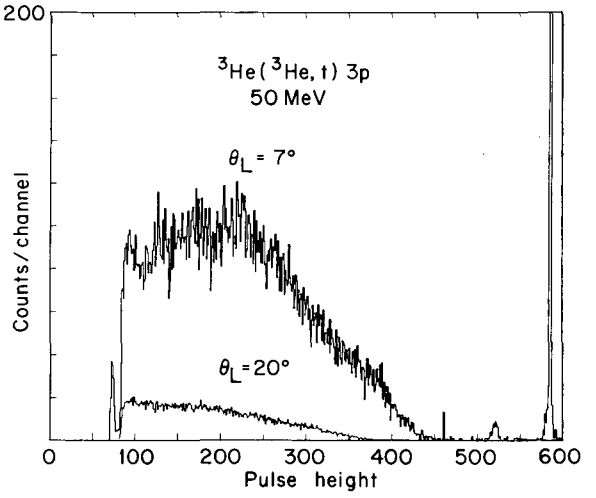

Fig. 1. Triton spectra at 50 MeV.

(XBL 723-2521)

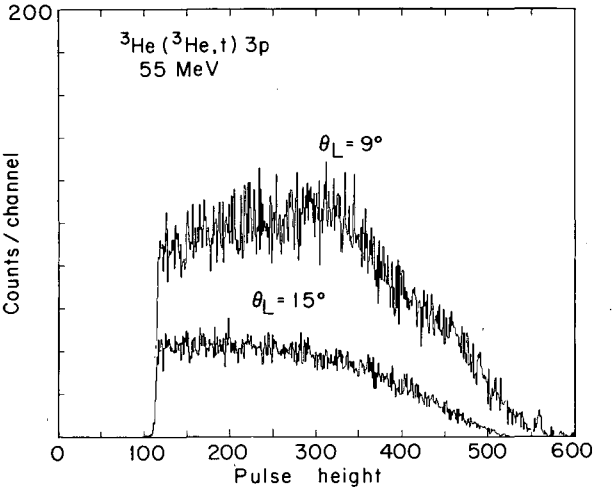

Fig. 2. Triton spectra at 55 MeV.

(XBL 723-2522)

Since similar arguments apply to the $^3He(p,n)3p$ result, we have undertaken investigation of $^3He(^3He,t)3p$ reaction, which also gives the 3p system in the final state. If a 3p resonance exists, it should be seen with the same excitation energy and width, independent of the reaction, the production

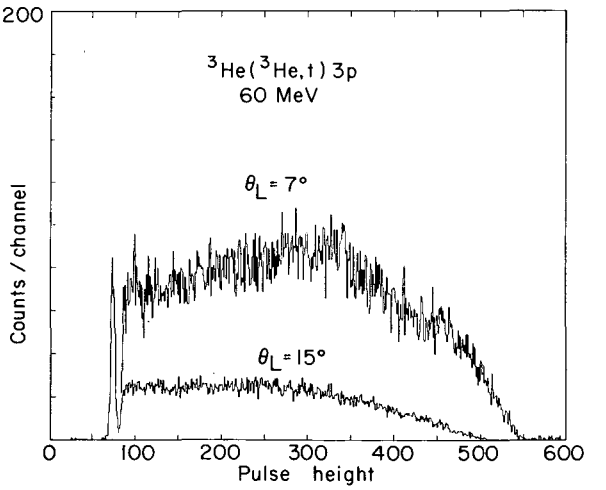

Fig. 3. Triton spectra at 60 MeV.

(XBL 723-2523)

angle, and of the beam energy used to produce it. Thus, our experiment provides another reaction as well as variations in production angle from 15 to 100°c. m. and in energy from 45 to 60 MeV.

In a previous study of this reaction at 44 MeV,[7] a broad peak was seen corresponding to a 3p excitation energy near 12 MeV. It was attributed to Coulomb distortion of a four-body phase-space distribution, and no attempt was made to establish the Q value for the peak as a function of angle of the observed triton.

Figures 1-3 show spectra taken at 50, 55, and 60 MeV, respectively. The broad peaking at the forward angles is clearly seen. After transformation of these data to the c. m. system, determinations of the Q value and width of the peak as functions of angle and incident beam energy should enable us to deduce that it either corresponds to a 3p resonance or is, in fact, a kinematical effect arising from the direct-reaction mechanism coupled with the known strong final-state interaction between two protons at low relative energy.

Footnotes and References

*Present address: Centre de Physique Nucléaire, Université de Louvain, Belgium.

1. Reviewed by I. Slaus, in Three Body Problem in Nuclear and Particle Physics, edited by J. S. C. McKee and P. M. Ralph (North Holland, Amsterdam, 1970), p. 355ff.

2. A. Van der Woude, M. L. Halbert, C. R. Bingham, and B. D. Belt, Phys. Rev. Letters 26, 909 (1971).

3. L. E. Williams, C. J. Batty, B. E. Bonner, C. Tschalär, H. C. Benöhr, and A. S. Clough, Phys. Rev. Letters 23, 1181 (1969).

4. J. Sperinde, D. Fredrickson, R. Hinkins, V. Perez-Mendez, and B. Smith, Phys. Letters 32B, 125 (1970).

5. A. C. Phillips, Phys. Letters 33B, 260 (1970).

6. See, e. g., E. Baumgartner, H. E. Conzett, E. Shield, and R. J. Slobodrian, Phys. Rev. Letters 16, 105 (1966).

7. T. A. Tombrello and R. J. Slobodrian, Nucl. Phys. A111, 236 (1968).

POLARIZATION AND CROSS-SECTION MEASUREMENTS FOR p-^{4}He ELASTIC SCATTERING BETWEEN 20 AND 45 MeV*

A. D. Bacher,† G. R. Plattner,‡ H. E. Conzett, D. J. Clark, H. Grunder, and W. F. Tivol§

The low-lying T = 1/2 states of the five-nucleon system have been studied extensively and a quantitative understanding of their properties has been achieved.[1] Most recent work has centered around the existence and structure of highly excited T = 1/2 states, particularly in ^{5}Li. A natural way of reaching the excitation energies of interest is to use the d+^{3}He channel which at threshold has an excitation energy of 16.38 MeV. This approach has been widely taken, despite the difficulties which result from the complicated spin structure of the spin 1-spin 1/2 channel. A variety of experimental evidence for excited states in ^{5}Li has been accumulated, but no quantitative explanations have yet been put forth for the anomalies seen in d-^{3}He elastic scattering[2,3] and in the ^{3}He(d, p)^{4}He reaction.[4,5]

The analysis of resonance effects corresponding to states in ^{5}Li will be simplified if they can be observed in the p+^{4}He channel with its single channel spin. States with a structure other than p+^{4}He (i. e., unlike the ground and first excited states of ^{5}Li) will, however, be only weakly excited via the proton channel. If in addition such states are situated well above the threshold of their main decay channel, they will be very broad and difficult to detect. Indeed, measurements of p-^{4}He cross-section excitation functions[6] do not show any effects corresponding to the structure observed in the d+^{3}He channel.

Since polarization data provide independent information about the scattering amplitudes, a detailed experimental study of p+^{4}He elastic scattering between 20 and 45 MeV was undertaken with particular emphasis on an accurate set of polarization measurements. Cross-section data were also obtained but the experimental configuration did not allow comparable precision.

Both polarization and cross-section measurements were performed simultaneously with the polarized beam from the Berkeley 88-inch cyclotron. The extracted external beam of 80-120 nA was transported to a 36-in. -diameter scattering chamber and focused onto a target cell containing commercially available high-purity helium. After passage through the main target, the beam could be slowed down by a set of removable aluminum absorbers. It then passed through a second helium-filled gas cell used as a polarimeter. A circular collimator was placed just in front of the polarimeter target to produce a well-defined beam spot. As a result of the additional beam collimation after the primary target, a meaningful beam current integration was not possible. For this reason, only relative angular distributions of the cross section could be obtained. The protons scattered from the primary target were detected in four pairs of Li-drifted silicon detectors. The two detectors in each pair were placed at equal angles on opposite sides of the beam. The angular acceptance of the detectors was approximately $\pm 0.5°$ in both θ and azimuthal angle Φ. The angle settings were accurate to better than 0.1°. In the polarimeter a pair of ΔE-E counter telescopes at equal angles on opposite sides of the beam detected the protons scattered from the second helium target. The scattering angle could be varied to correspond to the maximum analyzing efficiency.

For each angle setting of the main detector assembly, alternate runs of equal length were taken with the spin vector of the incident beam oriented up and down with respect to the scattering plane. This change of sign of the incident beam polarization was obtained by reversing the magnetic field of the ionizer at the ion source. A test showed that within statistical errors no artificial asymmetry larger than 0.003 was produced by a possible displacement or angular shift of the beam in correlation with the reversal of spin direction. The polarization $p(\theta)$ was calculated from the ratios of left and right detector yields as described in Ref. 7. The beam polarization was determined from the data taken simultaneously in the polarimeter. Cross-section values were obtained from the polarized beam runs by averaging over the spin-up and spin-down runs. As stated before, an absolute determination of the beam intensity was not feasible. In order to extract absolute cross sections from our relative measurements, it was necessary to normalize to existing data.[6,8] In a first set of runs, polarization and cross-section angular distributions were measured in approximately 2-MeV intervals from 20 to 40 MeV. A second set of measurements was performed between 22.5 and 24.5 MeV in steps of approximately 150 keV to determine the effects of the p-^{4}He resonance corresponding to the 16.7-MeV $3/2^+$ level in ^{5}Li. In order to investigate the existence of a weak anomaly discovered near 30 MeV, an excitation function at one angle was then taken from 24 to 30.5 MeV in 0.5-MeV steps. Finally, an absolute normalization of all the measured polarization angular distributions was determined.

It was decided that the polarization in p-^{4}He elastic scattering near 14.5 MeV was sufficiently well known[9,10] and varying slowly enough as a function of energy to constitute an excellent reference on which to base our normalization. A value of $p = -0.771 \pm 0.008$ at $\theta_{c.m.} = 80°$ and $E_p = 14.5$ MeV was subsequently used as a reference. This value was deduced from the energy-dependent set of phase shifts of Ref. 10, which in that energy region are based primarily on the data of Ref. 9. The influence of the finite geometry of our polarimeter setup was taken into account. This resulted in a slightly reduced reference value for the polarimeter analyzing power at 14.5 MeV and $\theta_{c.m.} = 80°$ of $A = -0.759 \pm 0.011$. Since it was necessary to reduce the beam energy considerably between the main target and the polarimeter in order to compare our highest energies with 14.5 MeV without too many intermediate steps, a test was performed to check that a large energy degradation would not influence the beam polarization measurements.

For this test, two runs were made at a proton energy of 45 MeV in the primary target. While monitoring the beam polarization with the main detection system at back angles, the polarimeter was run at a fixed angle θ, first at 37 MeV and then at 30 MeV. Thus, for these two energies the ratio of effective polarimeter analyzing power at the angle θ could be determined. A similar set of two runs, both with the beam polarization monitored with the main detection system at 37 MeV, and with the polarimeter run again at the same angle θ, first at 37 MeV and then at 30 MeV, yielded another independent measurement of the same quantity under very different circumstances (zero absorber thickness at 37 MeV, and roughly half the absorber thickness at 30 MeV). The two numbers thus obtained agreed within the combined statistical uncertainties of 0.4%. From this we concluded that in our setup no undesirable effects would be introduced by the energy degraders. We then proceeded to the actual normalization of our polarization data relative to the 14.5-MeV reference. A first measurement linked our 20-MeV data to the reference point. The beam polarization was monitored with the main detection system at 20 MeV, while the polari-

meter was run first at 20 MeV and then at 14.5 MeV, thus yielding the ratio of the analyzing powers at the angle used ($\theta_{c.m.} = 80°$) at these two energies. A second similar measurement was performed with the beam polarization monitored at 30 MeV and the polarimeter run successively at 14.5, 20, 22, 24, 26, 28, and 30 MeV. This yielded another calibration for the 20-MeV data plus one calibration for all the other energies. A third run with the beam polarization monitored at 40 MeV and the polarimeter run at 26, 28, 30, 32, 34, 37, and 40 MeV finally linked the remaining energies to our reference point, yielding in addition a second independent calibration for the 26-, 28-, and 30-MeV data.

Figure 1 shows two typical angular distributions of the polarization $p(\theta)$ and the differential cross section $\sigma(\theta)$. In Fig. 2, excitation functions of the polarization across the narrow resonance near 23 MeV are shown for 3 of the 15 angles investigated. The dashed lines are intended as a guide to the eye. A contour plot of the experimental polarization between 16 and 45 MeV is shown in Fig. 3. The data below 20 MeV are taken from Refs. 9 and 10. The match between our polarization data and the existing data below 20 MeV is excellent. The same comment also applies at the higher energies. Both double-scattering measurements[11,12] as well as older data obtained with a polarized-ion source[13-15] generally agree with our data within statistical errors. Our cross-section measurements have been compared with older, less abundant, but in general more accurate data[8,13,15-17] wherever possible. The angular distributions are in reasonable agreement, but in some instances there exist differences in the absolute

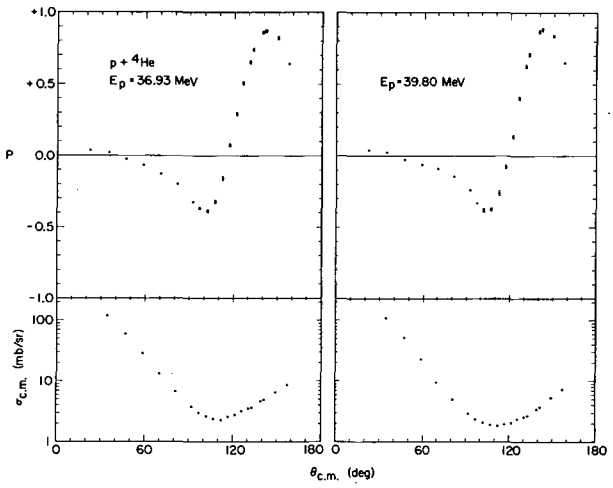

Fig. 1. Angular distributions of the proton polarization $p(\theta)$ and the differential cross section $\sigma(\theta)$ at 37 and 40 MeV.

(XBL 705-2764)

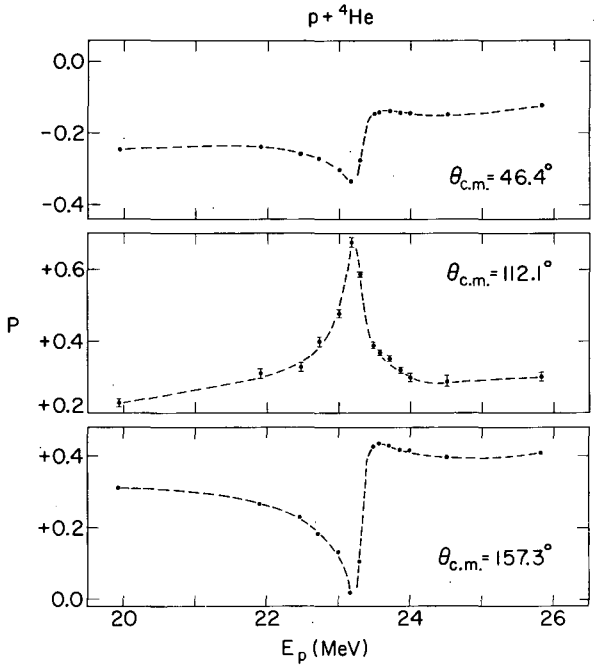

Fig. 2. Polarization excitation functions across the 23.4-MeV resonance corresponding to the $3/2^+$ level at 16.7 MeV in ^{5}Li. Only three of the fifteen angles investigated are presented. The dashed lines serve only as a guide to the eye.

(XBL 704-2678)

normalization of up to 10%. The quoted systematic normalization errors of the different sets of data can in general explain these discrepancies.

The measured polarization behaves very smoothly as a function of energy at all angles, including those which provide the best figure of merit for a polarization analyzer (i.e.,

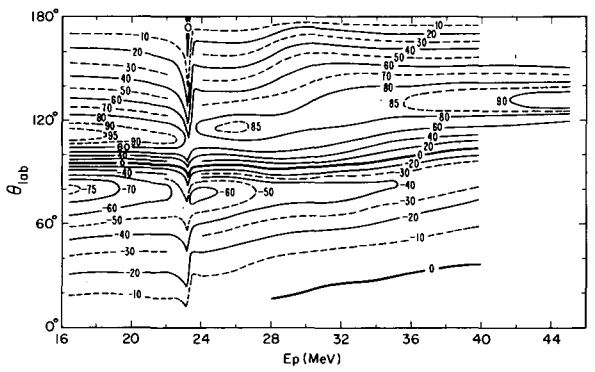

Fig. 3. Polarization contour map for p-^{4}He elastic scattering between 16 and 45 MeV. The part of the figure below 20 MeV has been drawn after Refs. 9 and 10.

(XBL 703-2603)

the negative and positive maxima near $\theta_{lab} = 80°$ and 125°, respectively). We believe that the amount and precision of our polarization data permit the calibration of an efficient polarization analyzer to better than 3% by simple interpolation in energy and angle (except of course in a 2-MeV wide region around the resonance near 23.4 MeV). In view of the internal consistency of our data, we find it doubtful that an energy-dependent phase-shift analysis could lead to uncertainties significantly lower than those of our data.

As shown in Fig. 3, a very weak and broad anomaly in the p-^{4}He polarization exists near 30 MeV. This energy corresponds to an excitation in ^{5}Li of approximately 22 MeV. As we have already mentioned, the anomaly is so weak that it is not observed in the p-^{4}He cross section.[6] This is in contrast to d-^{3}He elastic scattering where a strong "resonance-like" behavior has been found both with unpolarized[2] and polarized[3] deuterons. From these facts it must be concluded that the structure of ^{5}Li between 18- and 32-MeV excitation energy is not of p+^{4}He character as it is for the ground and first excited states. Some coupling to the p+^{4}He channel does exist, but the structure of ^{5}Li in this energy region is more likely of the d+^{3}He type. These experimental conclusions (which are by no means new) agree very well with recent theoretical calculations of ^{5}Li structure above the d+^{3}He threshold.[18]

Footnotes and References

*Condensed from LBL-280; submitted to Phys. Rev.

†Present address: Physics Department, Indiana University, Bloomington, Indiana 47401.

‡Present address: Physics Department, University of Basel, 4056 Basel, Switzerland.

§Present address: Sealy Mudd Laboratory, Los Angeles, California 90033.

1. T. Lauritsen and F. Ajzenberg-Selove, Nucl. Phys. 78, 1 (1966).

2. T. A. Tombrello, R. J. Spiger, and A. D. Bacher, Phys. Rev. 154, 935 (1967).

3. V. König, W. Grüebler, R. E. White, P. A. Schmelzbach, and P. Marmier, in Proceedings of the Third International Symposium on Polarization Phenomena in Nuclear Reactions, Madison, 1970, edited by H. H. Barschall and W. Haeberli (University of Wisconsin Press, Madison, 1970), p. 526.

4. L. Stewart, J. E. Brolley, and L. Rosen, Phys. Rev. 119, 1649 (1960).

5. W. Grüebler, V. König, A. Ruh, P. A. Schmelzbach, and R. E. White, Proc. Third Pol. Symp., ref. cit., p. 543.

6. S. N. Bunker, J. M. Cameron, M. B. Epstein, G. Paic, J. Reginald Richardson, J. G. Rogers, P. Tomas, and J. W. Verba, Nucl. Phys. A133, 537 (1969).

7. G. R. Plattner, T. B. Clegg, and L. G. Keller, Nucl. Phys. A111, 481 (1968).

8. P. W. Allison and R. Smythe, Nucl. Phys. A121, 97 (1968).

9. D. Garreta, J. Sura, and A. Tarrats, Nucl. Phys. A132, 204 (1969).

10. P. Schwandt, T. B. Clegg, and W. Haeberli, Nucl. Phys. A163, 432 (1971).

11. W. G. Weitkamp and W. Haeberli, Nucl. Phys. 83, 46 (1966).

12. E. T. Boschitz, M. Chabre, H. E. Conzett, E. Shield, and R. J. Slobodrian, in Proceedings of the Second International Symposium on Polarization Phenomena of Nucleons, Karlsruhe, Germany, 1965, edited by P. Huber and H. Schopper (Experienta Suppl. 12, 1966), p. 328; and Phys. Letters 15, 325 (1965).

13. P. Darriulat, D. Garreta, A. Tarrats, and J. Testoni, Nucl. Phys. A108, 316 (1968).

14. M. K. Craddock, R. C. Hanna, L. P. Robertson, and B. W. Davies, Phys. Letters 5, 335 (1963).

15. D. J. Plummer, K. Ramavataram, T. A. Hodges, D. G. Montague, A. Zucker, and N. K. Ganguly, Nucl. Phys. A174, 193 (1971).

16. S. M. Bunch, H. H. Forster, and C. C. Kim, Nucl. Phys. 53, 241 (1964).

17. M. K. Brussel and J. H. Williams, Phys. Rev. 106, 286 (1957).

18. P. Heiss and H. Hackenbroich, Nucl. Phys. A162, 530 (1971).

PHASE SHIFTS FOR p-^{4}He ELASTIC SCATTERING BETWEEN 20 and 40 MeV*

G. R. Plattner,† A. D. Bacher,‡ and H. E. Conzett

Phase-shift analyses of p-^{4}He elastic scattering are numerous and quite reliable for the energy region below 20 MeV (Refs. 1-3 and references therein). They reflect the abundance and high precision of the available data. Above the inelastic threshold near 23 MeV, both the quantity and quality of experimental data[4-8] on p-^{4}He scattering have, until recently, been inferior to the information available in the low-energy region. This has primarily been due to the lack of intense polarized beams. Analyses are further hampered: (1) by the increasing importance of higher partial waves, (2) by the need to consider complex rather than real phase shifts above the inelastic threshold, and (3) by the lack of detailed knowledge of inelastic processes leading to three or more particles in the final state. Though considerable effort has gone into the derivation of p-^{4}He phase shifts above 20 MeV,[5,7-14] these difficulties have led to inconsistent and contradictory results. In particular it has not been possible to deduce reliable information about the highly excited states of ^{5}Li from the previous analyses. Only the $3/2^+$ second excited state near 16.7-MeV excitation has been investigated with some precision.[7,8]

Our results show that our p-^{4}He polarization and cross-section data[15] above 20-MeV proton energy allow a consistent phase-shift analysis to be performed, which permits at least a qualitative discussion of the properties of possible states in ^{5}Li above 18-MeV excitation and also provides an improved parametrization of the $3/2^+$ second excited state.

Single-energy phase-shift analyses were carried out starting at 20 MeV. As a starting set of phase shifts, values extrapolated from the energy-dependent set of Ref. 2 were used. After a solution was found at one energy, the corresponding best-fit phase shifts were taken as starting values for a search on the data at the next higher energy. This procedure yielded satisfactory fits with seven parameters (real s, p, d, and f-wave phase shifts) at the first four energies up to the inelastic threshold near 23 MeV. Above this threshold, 14 parameters (complex s, p, d, and f-wave phase shifts) were used. In this manner, a smoothly energy-dependent set of phase shifts was obtained over the $3/2^+$ resonance corresponding to the second excited state of ^{5}Li. Since g waves are expected to become important above 30 MeV, the search was extended to include 18 parameters (complex s, p, d, f, and g-wave phase shifts), starting at 26 MeV. The quality of the fits was immediately improved and no problems were encountered in proceeding to 40 MeV. For the purpose of identification, the set of single-energy phase-shift solutions found in this manner will be called set I.

At this stage, smooth curves were drawn by hand through the set I phase shifts as a function of energy, and a second string of single-energy searches (now including g waves at all energies) was undertaken from 20 to 40 MeV with the smoothed, set I phase shifts as starting points. This resulted in the set II single-energy solutions, which not only were more smoothly dependent on energy, but also gave a better overall fit to the data. Set II was modified once more before arriving at the final results. An R-matrix calculation was performed to parametrize the complex $^2D_{3/2}$ phase shift between 20 and 32 MeV in an attempt to extract level parameters for the second excited state of ^{5}Li. Between 20 and 32 MeV we started from set II, but with the $^2D_{3/2}$ phase shift fixed at the values predicted by the R-matrix calculation. At energies above 32 MeV the $^2D_{3/2}$ parameters were initially set to values extrapolated from the R-matrix predictions at the lower energies. No problem was encountered in finding slightly modified solutions (set III), which represent the final result of our phase-shift analysis.

Two R-matrix calculations concerned with the influence of the $3/2^+$ second excited state in ^{5}Li on p-^{4}He elastic scattering have been published previously.[7,8] To understand why we have reexamined this effect, it is instructive to anticipate the final result of our R-matrix calculation as presented in Fig. 1. In this figure, the real phase $\delta = \mathrm{Re}(^2D_{3/2})$ and the absorption parameter $\eta = \exp(-2\ \mathrm{Im}(^2D_{3/2}))$ are shown. The solid lines correspond approximately to the empirical phase-shift parameters (i.e., to the set II values), whereas the dotted lines give a fair representation of the shape of a well-behaved, isolated resonance.[16] The unusual feature of our empirical $^2D_{3/2}$ phase shift lies in the "cut-off" of resonance effects in the real part on the high-energy side of the resonance. A similar, corresponding feature can be seen in our polarization data[15] at the same energy, so that there can be little doubt as to the existence of this effect.

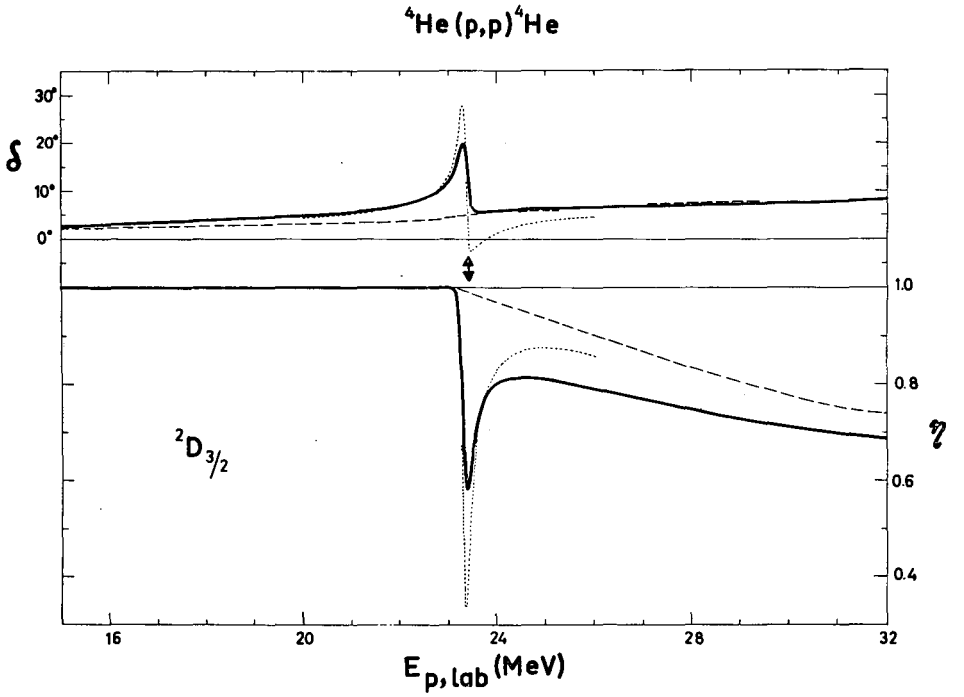

Fig. 1. The $^2D_{3/2}$ phase shift in the vicinity of the $3/2^+$ second excited state of ^{5}Li. The solid lines represent the result of an R-matrix calculation. The dashed lines show the background contribution. The dotted lines are obtained if resonance-background interference is neglected. The double arrow marks the resonance energy. (XBL 723-400)

In both previous investigations[7,8] of this resonance the R-matrix analysis has been oversimplified by complete neglect of resonance-background interference. As we will show, it is just this contribution which produces the peculiar resonance shape, so that a more sophisticated R-matrix analysis of the $^2D_{3/2}$ phase shift is called for.

Our analysis is based strictly on the formalism as presented by Lane and Thomas[17] and we use their notation. In order to calculate the $^2D_{3/2}$ phase shift from the assumed properties of the $3/2^+$ second excited state of ^{5}Li and of the nonresonant background, we have constructed the symmetric 3×3 (3-channel) R-matrix $R^{3/2}$ with elements

$$R_{cc'} = \frac{\gamma_c \gamma_{c'}}{E_\lambda - E} + R^0_{cc'}(E). \qquad (1)$$

The entrance and exit channel indices c and c' refer to the three channels:

(1) $p + {}^4He$ ($\ell = 2$, $s = 1/2$)

(2) $d + {}^3He$ ($\ell = 0$, $s = 3/2$)

(3) $d + {}^3He$ ($\ell = 2$, $s = 1/2$ and $3/2$)

The quantity E_λ is the c.m. characteristic energy of the $3/2^+$ level in the $p+{}^4He$ channel. The quantity γ_c is the reduced width amplitude of this level in channel c, and E designates the c.m. kinetic energy in the $p+{}^4He$ channel. The nonresonant background is represented by the parameters $R^0_{cc'}(E)$, which have been chosen to depend linearly on energy:

$$R^0_{cc'}(E) = R^0_{cc'} + (dR^0/dE)_{cc'}(E - 18.353). \qquad (2)$$

Thus $R^0_{cc'}(E)$ equals $R^0_{cc'}$ at 18.353 MeV, the c.m. energy of the first inelastic threshold. The matrix $R^{3/2}$ was then inserted into Eqs. VII, 1.5 and 1.6a of Ref. 17 and the collision matrix element $U_{11}{}^{3/2}$, corresponding to elastic scattering in the $^2D_{3/2}$ $p+{}^4He$ channel, was calculated. Finally, the real phase δ and the absorption parameter η, corresponding to the complex $^2D_{3/2}$ phase shift, were obtained from

$$\eta \exp(2i\delta + 2i\omega) = U_{11}^{3/2} \qquad (3)$$

where $\omega = \sigma_2 - \sigma_0$, the difference between the Coulomb phase shifts for $\ell = 2$ and $\ell = 0$.

The interaction radii a_c were chosen as $a_1 = 3.0$ fm ($p+^4$He channel), and $a_2 = a_3 = 5.0$ fm ($d+^3$He channels). To reduce the number of parameters, the following additional assumptions were made:

$R^0_{33}(E) = R^0_{22}(E)$, $R^0_{23}(E) = 0$, $R^0_{13}(E) = R^0_{12}(E)$.

We first tried to obtain a fit to an empirical background phase shift as determined by drawing a smooth curve (neglecting resonance effects) through the empirical values for the $^2D_{3/2}$ parameters δ and η. After a satisfactory background phase shift had been generated,

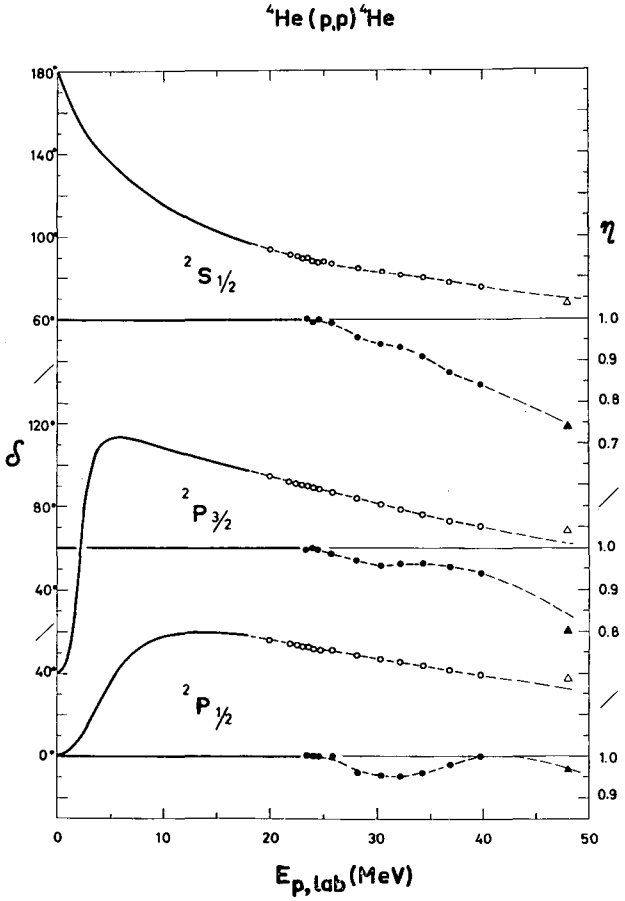

Fig. 2. The s- and p-wave phase shifts for p-^{4}He elastic scattering. The solid lines below 18 MeV represent the energy-dependent set of phase shifts of Ref. 2. Open and full circles are our own results for the real parts δ and the absoption parameter η, respectively. The triangles at 48 MeV indicate the results of Ref. 13.) (XBL 723-404)

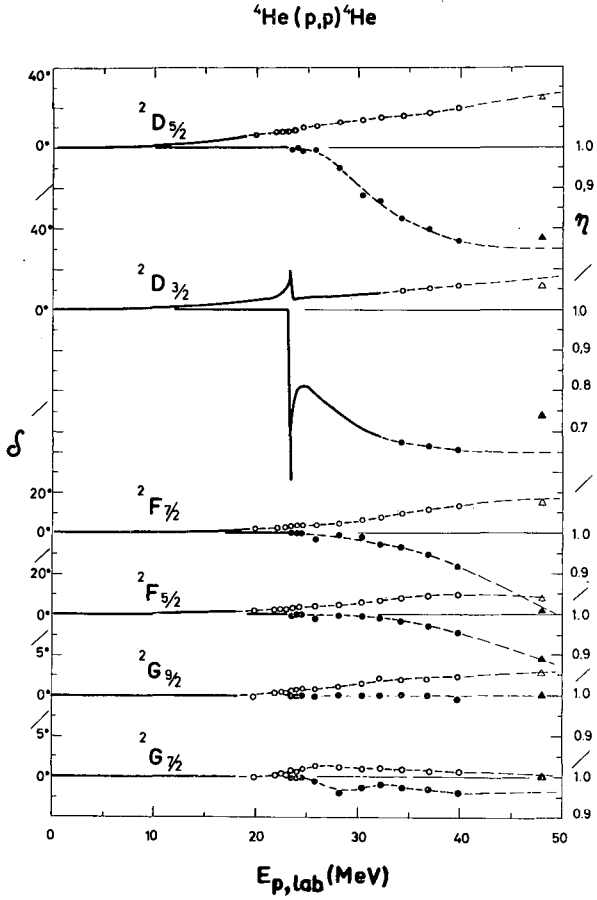

Fig. 3. The d-, f-, and g-wave phase shifts for p-^{4}He elastic scattering. See caption for Fig. 2 for explanation of symbols.

(XBL 723-403)

a set of $3/2^+$ level parameters was included in the calculation and a search was performed in an attempt to reproduce the complete $^2D_{3/2}$ phase shift. A good fit could be obtained both on and off resonance with little need for change in the background parameters determined previously. Since resonance and background interfere quite strongly, such a behaviour seems to imply that the background has reasonable properties. This in turn constitutes a strong a posteriori justification of the simplifying assumptions made.

The R-matrix parameters used in the calculation are given in Table I. In Fig. 1, both δ and η are plotted as a function of energy. The solid lines are the result of our calculation for both level plus background, while the dashed lines show the background only. The double arrow marks the resonance energy. The dotted lines demonstrate the importance of resonance-background interference. They show the result that one would predict from

Table I. R-matrix parameters[a] used in the analysis of the $3/2^+$ second excited state of ^{5}Li.

E_R	$E_X(^5\text{Li})$	$(\gamma_1)^2$	$(\gamma_2)^2$	$(\gamma_3)^2$	$(\theta_1)^2$	$(\theta_2)^2$	$(\theta_3)^2$	$(\theta_2)^2/(\theta_1)^2$	$\Sigma(\theta_i)^2$
23.39[b]	16.68 MeV	122 keV	1580 keV[c]	1580 keV	0.014[d]	0.765[d]	0.765[d]	55	1.55

R^0_{11}	$(dR^0/dE)_{11}$	R^0_{12}	$(dR^0/dE)_{12}$	R^0_{22}	$(dR^0/dE)_{22}$	a_1	a_2	a_3
0.468	0.008 MeV^{-1}	0.132	0.006 MeV^{-1}	0.187	-0.023 MeV^{-1}	3 fm	5 fm	5 fm

[a] The indices 1, 2, and 3 refer to the channels $p+^4He$ ($\ell = 0$), $d+^3He$($\ell = 0$), and $d+^3He$ ($\ell = 2$), respectively.

[b] Proton lab energy in the $p+^4He$ channel.

[c] The sign of this reduced width amplitude is negative.

[d] In units of the Wigner limit $3\hbar^2/2Ma^2$.

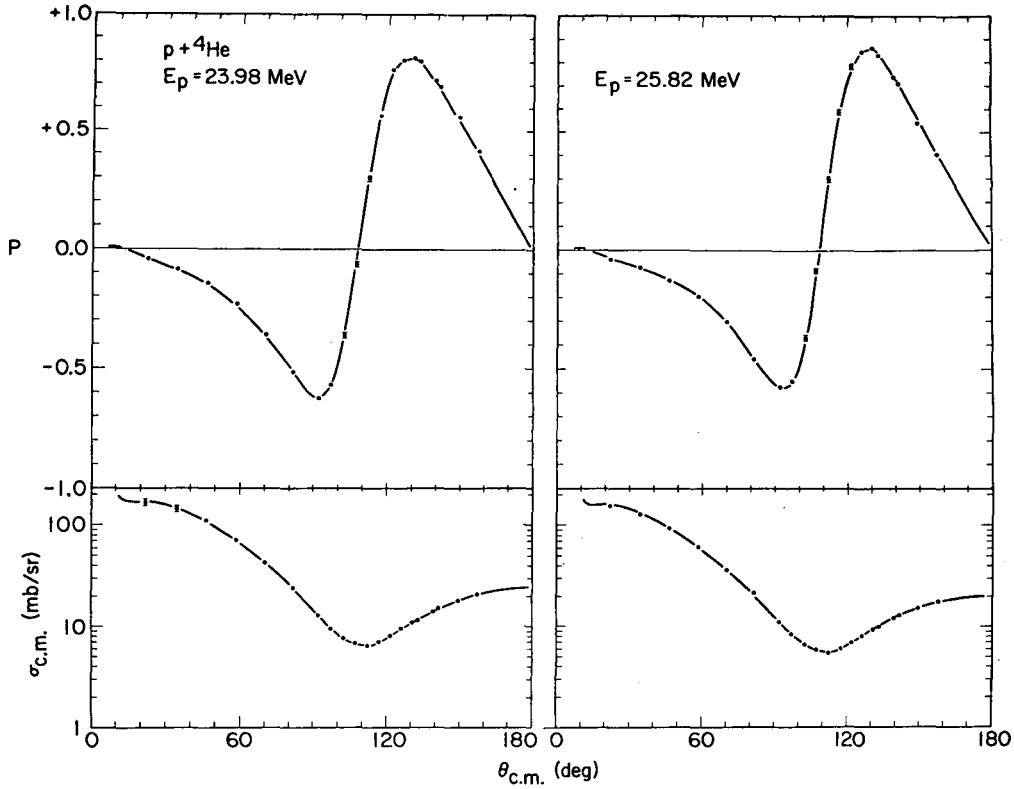

Fig. 4. Comparison at 24 and 26 MeV between our experimental data[15] and the corresponding curves calculated from our phase shifts.

(XBL 723-402)

our parameters as listed in Table I, if this interference were completely neglected, i. e. if one were to use the method[18] of Refs. 7 and 8. In contrast to our calculation, the strong "cut-off" effect that our data require is probably not reproducible with this method. In Figs. 2 and 3, the p-^{4}He phase shifts are shown as a function of energy from 0 to 50 MeV. In Fig. 4, fits to the experimental data are shown at two energies. In Fig. 5, fits to the polarization across the 23.4-MeV resonance are shown. In Fig. 6, the experimental polarization excitation function at $\theta_{c.m.} = 102.2^0$ is compared with the values calculated from our phase shifts. The broad anomaly centered around 30 MeV is well reproduced by the dashed line, which has been drawn through the calculated values.

Discussing the implications of our phase-shift results for the level structure of ^{5}Li, we should note that the weak anomaly discovered in our polarization measurements around 30 MeV (see Fig. 6) is not connected with a particular feature of any one phase-shift parameter, but rather seems to be caused by the rapid onset of absorption above the inelastic threshold. This result is in striking disagreement with a recent analysis[14] of p-^{4}He elastic scattering data between 25 and 29 MeV, where rapid variations with energy of both the $^2S_{1/2}$ and the $^2D_{5/2}$ phase shifts have been found and are interpreted as conclusive evidence for the existence of two excited states around 20 MeV in ^{5}Li with $J^\pi = 1/2^+$ and $5/2^+$. In a broader, less definite way we do agree, however, that the influence of highly excited states in ^{5}Li is probably seen in the p+^{4}He channel. The most striking feature of our phase shifts is certainly the dominance of absorption in the even partial waves. Around 30 MeV (corresponding to 22-MeV excitation in ^{5}Li), absorption in the $J^\pi = 1/2^+$, $3/2^+$, $5/2^+$, and $7/2^+$ scattering states amounts to 85% of the total inelastic cross section. This behavior can be understood qualitatively, if it is assumed that at these energies there exist in ^{5}Li very broad, overlapping levels of positive parity, which decay almost exclusively via the d+^{3}He and/or multiparticle-breakup channels. Recent calculations with a refined cluster model have

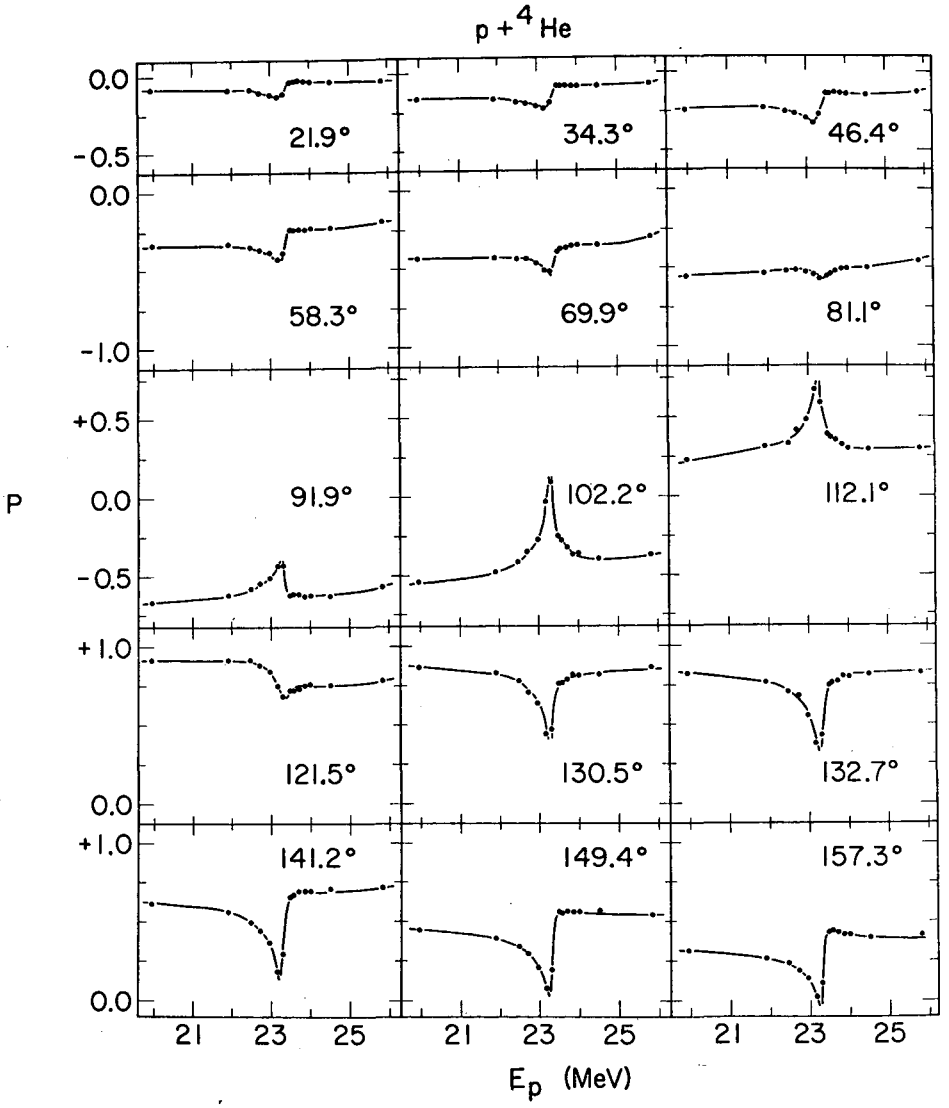

Fig. 5. Comparison of measured and calculated polarization excitation functions across the 23.4 resonance corresponding to the $3/2^+$ second excited state of ^{5}Li. The solid lines have been drawn through the values calculated from our single-energy phase shifts. (XBL 723-399)

indeed led Heiss and Hackenbroich[19] to predict the existence in ^{5}Li of a quartet of $T = 1/2$ states with $J^\pi = 1/2^+$, $3/2^+$, $5/2^+$, and $7/2^+$. These states are calculated to be of almost pure d-wave d+^{3}He character and are situated several MeV above the d+^{3}He threshold. Their nature is very similar to that of the $3/2^+$ second excited state of ^{5}Li, which is also reproduced in these calculations.[19,20] Additional evidence for positive-parity states in this energy range is found by Seiler[21] in an investigation of the ^{3}He(d, p)^{4}He reaction. He reports that a state with $J^\pi = 5/2^+$ near 20-MeV excitation and one with $J^\pi = 7/2^+$ near 22.5 MeV dominate this process. Our own investigation of p-^{4}He elastic scattering is not in contradiction with the possible existence of a $7/2^+$ level. In this scattering state we see an anomaly in the energy dependence of our phase shift ($^2G_{7/2}$). However, to deduce the existence of a $7/2^+$ level solely from these very weak fluctuations would not be justified.

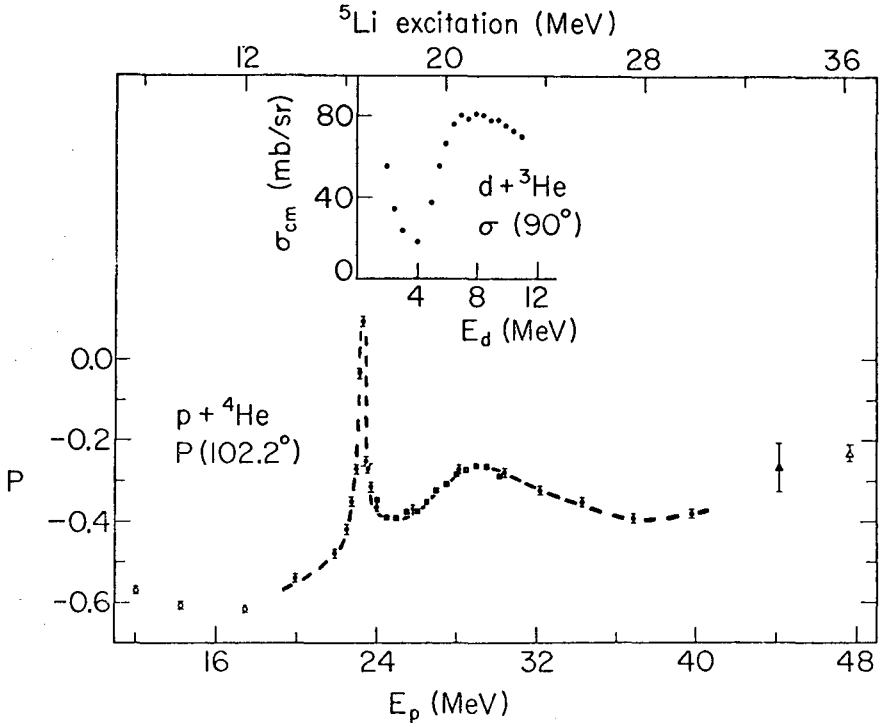

Fig. 6. Comparison between measured and calculated polarization at $\theta_{c.m.} = 102.2°$ across the broad anomaly near 30-MeV proton energy. Open circles are from Ref. 2, full circles and squares are our own data.[15] The full and open triangles represent data from Refs. 5 and 6, respectively.
(XBL 723-401)

Turning now to a discussion of the odd partial waves, we find that our p-wave phase shifts, which correspond to $J^\pi = 1/2^-$ and $3/2^-$, show some fluctations again in the absorptive parts, while the f-wave phases with $J^\pi = 5/2^-$ and $7/2^-$ are completely without structure. Empirical evidence for $J^\pi = 1/2^-$ and $3/2^-$ levels has been obtained from studies of the ^{3}He(d, p)^{4}He reaction,[21,22] of d-^{3}He elastic scattering,[23] of its mirror process d-T elastic scattering,[24] and of the ^{3}He(d, 2p)T and T(d, pn)^{3}T reactions.[25] The cluster-model calculation by Heiss and Hackenbroich[19] also generated such states and explains them as nucleon +^{4}He*(0$^+$ first excited state) cluster structures, which would decay mainly into multiparticle-breakup channels. The coupling to p+^{4}He channels should be very weak according to this model.

If all this tentative evidence for highly excited states in ^{5}Li is taken at face value, then the following qualitative picture of ^{5}Li (and mutatis mutandis of ^{5}He) emerges from the existing experimental information: Above the first inelastic threshold, near 16.5 MeV, a series of broad d+^{3}He cluster states appears. The first of these is the $3/2^+$ second excited state, which has been unambiguously identified. Its relatively small width is only a consequence of its position close to threshold. Its inherent character is that of a cluster state with a reduced width close to the Wigner limit. Above 18-MeV excitation, a quartet of d-wave d+^{3}He cluster states with $J^\pi = 1/2^+$, $3/2^+$, $5/2^+$, and $7/2^+$, and a doublet of p+^{4}He* cluster states with $J^\pi = 1/2^-$ and $3/2^-$ are predicted to exist.[19] Experimental evidence for all of these states is still inconclusive, despite claims to the contrary.[25]

Footnotes and References

*Condensed from LBL-269; submitted to Phys. Rev.

†Present address: University of Basel, Basel, Switzerland; supported by the Swiss National Science Foundation.

‡Present address: Indiana University, Bloomington, Indiana.

1. G. R. Satchler, L. W. Owen, G. L. Morgan, and R. L. Walter Nucl. Phys. A112, 1 (1968).

2. P. Schwandt, T. B. Clegg, and W. Haeberli, Nucl. Phys. A163, 432 (1971).

3. R. A. Arndt, L. D. Roper, and R. L. Shotwell, Phys. Rev. C3, 2100 (1971).

4. C. F. Hwang, D. H. Nordby, S. Suwa, and J. H. Williams, Phys. Rev. Letters 9, 104 (1962).

5. E. T. Boschitz, M. Chabre, H. E. Conzett, H. E. Shield, and R. J. Slobodrian, in Proceedings of the Second International Symposium on Polarization Phenomena of Nucleons, Karlsruhe, Germany, 1965, edited by P. Huber and H. Schopper (Experienta Suppl. 12, 1966), p. 328; and Phys. Letters 15, 325 (1965).

6. M. K. Craddock, R. C. Hanna, L. P. Robertson, and B. W. Davies, Phys. Letters 5, 335 (1963).

7. W. G. Weitkamp and W. Haeberli, Nucl. Phys. 83, 46 (1966).

8. P. Darriulat, D. Garreta, A. Tarrats, and J. Testoni, Nucl. Phys. A108, 316 (1968).

9. J. L. Gammel and R. M. Thaler, Phys. Rev. 109, 2041 (1958).

10. C. C. Giamati, V. A. Madsen, and R. M. Thaler, Phys. Rev. Letters 11, 163 (1963).

11. S. Suwa and A. Yokosawa, Phys. Letters 5, 351 (1963).

12. C. C. Giamati and R. M. Thaler, Nucl. Phys. 59, 159 (1964).

13. B. W. Davies, M. K. Craddock, R. C. Hanna, Z. J. Moroz, and L. P. Robertson, Nucl. Phys. A97, 241 (1967).

14. K. Ramavataram, D. J. Plummer, T. A. Hodges, and D. G. Montague, Nucl. Phys. A174, 204 (1971).

15. A. D. Bacher, G. R. Plattner, H. E. Conzett, D. J. Clark, H. Grunder, and W. F. Tivol, 4BL-280 (submitted to Phys. Rev.).

16. For a level with an elastic width $\Gamma_{el} < \frac{1}{2} \Gamma_{total}$, the resonating phase shift has this shape and does not pass through $\pi/2$ (see, e. g., Ref. 7).

17. A. M. Lane and R. G. Thomas, Rev. Mod. Phys. 30, 825 (1958).

18. These authors modify the single-level, no-background R-matrix expression of Ref. 17 by replacing the hard-sphere phase shift with a phenomenological, complex, nonresonant background parameter. This results in complete neglect of the resonance-background interference.

19. P. Heiss and H. Hackenbroich, Nucl. Phys. A162, 530 (1971).

20. P. Heiss and H. Hackenbroich, Phys. Letters 30B, 373 (1969).

21. F. Seiler, private communication.

22. W. Grüebler, V. König, A. Ruh, P. A. Schmelzbach, and R. E. White, Proceedings of the Third International Symposium on Polarization Phenomena in Nuclear Reactions, Madison 1970, edited by H. H. Barschall and W. Haeberli (University of Wisconsin Press, Madison, 1970), p. 543.

23. V. König, W. Grüebler, R. E. White, P. A. Schmelzbach, and P. Marmier, Proc. Third Pol. Symp., ref. cit., p. 526.

24. K. Kilian, H. Treiber, R. Strausz, and D. Fick, Phys. Letters 34B, 283 (1971).

25. D. Fick, H. Treiber, K. K. Kern, and H. Schroder, paper submitted to the Conference on the Nuclear Three-Body Problem, Budapest, Hungary, July 1971; and D. Fick, private communication.

MEASUREMENTS OF THE VECTOR ANALYZING POWER IN $\vec{d}$-^{4}He ELASTIC SCATTERING BETWEEN 15 AND 45 MeV

Ch. Leemann, H. E. Conzett, W. Dahme,* J. A. MacDonald, and J. P. Meulders†

As a consequence of the spin 1 of the deuteron, there exist four polarization-dependent contributions to the differential cross section in elastic $\vec{d}$-^{4}He scattering, corresponding to the vector and the three tensor polarization components describing a polarized deuteron beam. All four of these have been extensively investigated at energies up to ~ 12 MeV,[1,2,3] and there also exist somewhat less numerous measurements in the vicinity of 20 MeV.[4] These data have resulted in phase-shift analysis,[3,5,6] and, futhermore, at 11.5 MeV the vector analyzing power has been calibrated absolutely by comparison of double scattering and polarized beam data.[7]

The data near 20 MeV seemed to indicate a substantial reduction of the vector analyzing power as compared with lower energies, but this could only be a tentative conclusion because of the rather large uncertainties in the knowledge of the beam polarization. The present experiment was started to clarify this situation, and our early results showed that large values of the vector analyzing power were obtained up to 20 MeV, contrary to the results of Ref. 4. We then extended our measurements to the higher deuteron energies available from the Berkeley 88-inch cyclotron in order to establish a reliable vector-polarization analyzer for deuterons of energies above 12 MeV. So far, we have restricted ourselves to the use of a purely vector-polarized beam in which case the differential cross section can be written as:

$$\sigma(\theta, \phi) = \sigma_0(\theta)(1 + 3/2\, p_y A_y \cos\phi) \qquad (1)$$

where $\sigma_0(\theta)$ is the unpolarized cross section, θ, ϕ the polar and azimuthal scattering angles respectively, p_y the incident beam polarization and A_y the vector-analyzing power. The formula is based on a right-handed coordinate system with z-axis parallel to the incident deuteron momentum and the y-axis parallel to the beam polarization.

Data were taken in 5 MeV steps from 15 to 45 MeV at c.m. angles, θ, from 30° to 165°. At all angles the elastically scattered deuterons were detected using counter telescopes placed symmetrically to the left and right of the beam axis ($\phi = 0, \pi$). To distinguish deuterons from protons coming from the process $d + \alpha \rightarrow n + p + \alpha$, particle identification was used. A ^{4}He gas target at ~1 atmosphere pressure was used while the beam intensity on target was typically ~ 50 nA. A polarimeter placed downstream of the 36-in. scatter chamber served to monitor the relative beam polarization at each energy: Fig. 1 shows the measured asymmetries,

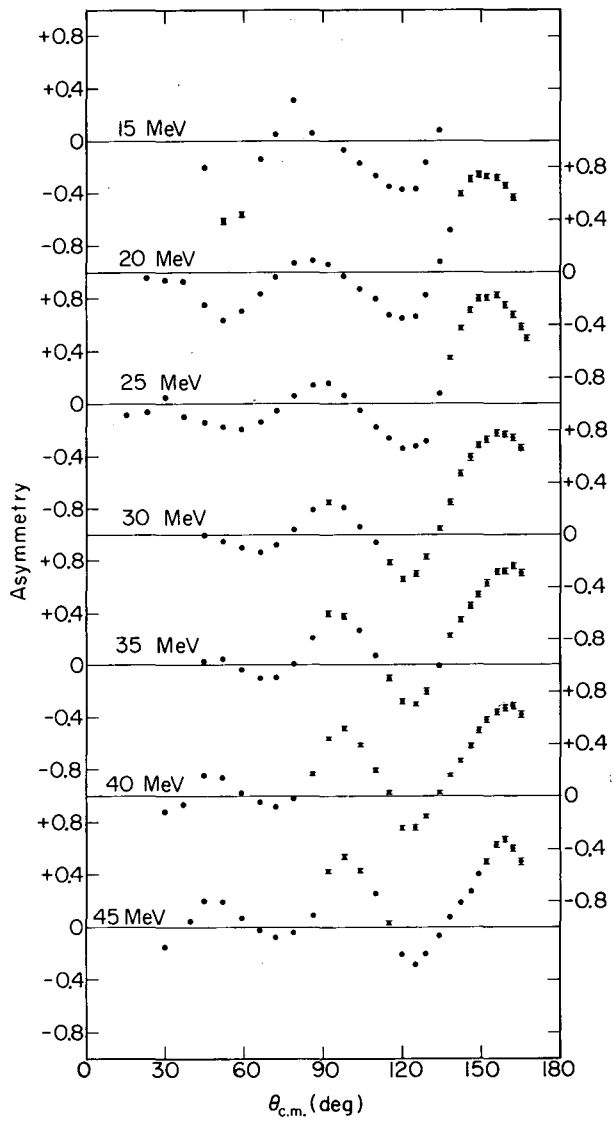

Fig. 1. Asymmetries in $\vec{d}$-^{4}He scattering. These values represent lower limits for the vector analyzing powers of $\vec{d}$-^{4}He scattering, as explained in the text. (XBL 723-2528)

$$\epsilon = [\sigma(\theta, 0) - \sigma(\theta, \pi)] / [\sigma(\theta, 0) + \sigma(\theta, \pi)]. \qquad (2)$$

Since the polarized ion source provides a beam with a theoretical maximum vector polarization of 2/3, it follows from Eq. (1) that the plotted asymmetries, in fact, represent lower limits for the analyzing power A_y.

Because of limitations imposed by the polarimeter construction, it was not feasible to determine an absolute value of beam polarization at each energy. Thus, the data of Fig. 1 are relative angular distributions. An improved polarimeter has been constructed which will make it possible to normalize our data to those at 11.5 MeV. However, our results already show conclusively that $\vec{d}$-^{4}He scattering is a useful analyzer for deuteron vector polarizations at energies up to 45 MeV.

We are very grateful to H. A. Grunder, R. M. Larimer, D. J. Clark, and J. J. Steyaert for assistance during various parts of the experiment.

Footnotes and References

*DAAD exchange student from the University of Munich, West Germany.

†Present address: Centre de Physique Nucléaire, Université de Louvain, Belgium.

1. V. König, W. Grüebler, P. A. Schmelzbach, and P. Marmier, Nucl. Phys. A134, 686 (1969).

2. V. König, W. Grüebler, P. A. Schmelzbach, and P. Marmier, Nucl. Phys. A148 380, (1970); also A148 381, (1970).

3. L. G. Keller and W. Haeberli, Nucl. Phys. A156 465, (1970), and references therein.

4. J. Arvieux, P. Darriulat, D. Garreta, A. Papineau, A. Tarrats, and J. Testoni, Nucl. Phys. A94 663, (1967).

5. P. Darriulat, D. Garreta, A. Tarrats, and J. Arvieux, Nucl. Phys. A94, 653, (1967).

6. P. A. Schmelzbach, W. Grüebler, V. König, and P. Marmier, Proceedings of the Third International Symposium on Polarization Phenomena in Nuclear Reactions, Madison 1970, p. 590.

7. V. S. Starkovich and G. G. Ohlsen, op. cit., p. 581.

ANALYZING POWER AND CROSS-SECTION MEASUREMENTS IN $\vec{p}$-Si ELASTIC SCATTERING BETWEEN 17 AND 20 MeV

H. E. Conzett, B. Frois,* R. Lamontagne,* Ch. Leemann, and R. J. Slobodrian*

Nuclear reaction mechanism and the structure of nuclear states have been studied extensively via proton-producing reactions such as (p, p'), (d, p), (^{3}H, p), (^{3}He, p), and (^{4}He, p). The experimental data consist predominantly of cross sections; but where particles with spin are involved, it is well known that additional observables must be measured in order to provide information for more adequate testing of the theoretical calculations. One such observable is the polarization of the outgoing proton, the determination of which requires a suitable polarization analyzer. Since these are secondary "beams" of protons, they are inevitably of very low intensity so that an analyzer with high efficiency coupled with good resolution is required.

The polarimeters most widely use to date consist of helium or carbon analyzers.[1,2] Both types have a low efficiency when high resolution is sought, and vice versa. The usefulness of silcon detectors as proton polarization analyzers was first pointed out by Miller.[3] Using an analyzer that is also a detector, it is a simple electronic problem to perform a coincidence between the pulse from the analyzer and the pulse from the left or right detectors, and subsequently to add them. This technique permits the use of thick analyzers without the corresponding appreciable loss in resolution, thereby increasing substantially the efficiency of the polarimeter. Recently, reports on two such polarimeters have been published.[4,5] The system described by Frois et al.[5] is intended for proton energies higher than 15 MeV, typically in the range between 15 and 30 MeV. It surpasses all other polarimeters in efficiency at comparable energy resolutions for protons of energy higher than 20 MeV. Since there has been a definite lack of data between 17 and 29 MeV, it was pointed out that accurate measurements of $\vec{p}$-Si analyzing powers and cross sections as functions of angle and energy were necessary in order to allow deter-

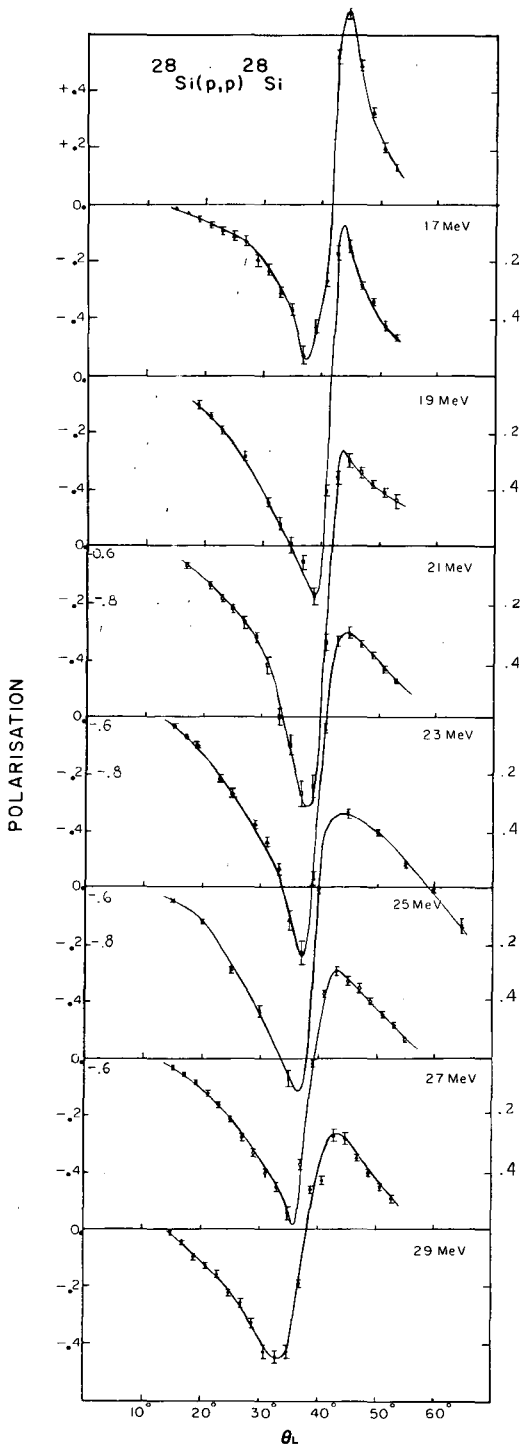

Fig 1. The analyzing power of Si for polarized protons between 17 and 29 MeV. The solid lines have been drawn to aid the eye.
(XBL 723-405)

minations of precise absolute values of proton polarizations with this apparatus. Some measurements have been made near 17 and 29 MeV,[6,7] but these data are not of sufficient accuracy and detail over the forward angles nor of sufficient extent in energy to permit achievement of the precision that is possible with the silicon polarimeter.

Thus, we have used the polarized proton beam[8] of the Berkeley 88-inch cyclotron to measure asymmetries in the scattering of polarized protons from silicon at 2-MeV intervals between 17 and 29 MeV inclusive. The beam polarization was monitored continuously with a helium polarimeter whose analyzing power was known from recent measurements.[9] Since the left-right scattering asymmetry is given by

$$(L-R)/(L+R) \equiv \epsilon = PA,$$

where P is the beam polarization and A the analyzing power of the scatterer, simultaneous determinations of the asymmetries in scattering from ^{4}He and Si result in:

$$\epsilon_{Si}/\epsilon_{He} = (PA_{Si})/(PA_{He}),$$

so that

$$A_{Si} = A_{He}\epsilon_{Si}/\epsilon_{He}$$

yields the desired analyzing powers. Cross sections for unpolarized $\vec{p}$-Si scattering are calculated from the sum (L+R) of the yields.

Our preliminary values of analyzing powers are shown in Fig. 1. A parametrization of the data by an optical-model analysis is under way, and should provide a means for a smooth interpolation of the data as a function of energy. These data show conclusively the good quality of silicon as a proton-polarization analyzer.

We are very grateful to R. de Swiniarski for his assistance during the experiment.

Footnote and References

*Summer visitor from Université Laval, Département de Physique, Québec, CANADA.

1. G. J. Lush, T. C. Griffith, and D. C. Imrie, Nucl. Instr. Methods 27, 229 (1964).

2. C. Tschalar, C. J. Batty, and A. I. Kilvington, Nucl. Instr. Methods 78, 141 (1970).

3. D W. Miller, Proceedings of the Second International Symposium on Polarization Phenomena of Nucleons (Birkauser, Basel 1966).

4. J. P. Martin and R. J. A. Levesque, Nucl. Instr. Methods 84, 211 (1970).

5. B. Frois, J. Birchall, R. Lamontagne, R. Roy, and R. J. Slobodrian, Nucl. Instr. Methods 96, 431 (1971).

6. D. J. Baugh, G. W. Greenlees, J. S. Lilly, and S. Roman, Nucl. Phys. 65, 33 (1965).

7. R. M. Graig, J. C. Dore, G. W. Greenlees, J. Lowe, and D. L. Watson, Nucl. Phys. 83, 493 (1966).

8. D. J. Clark, A. U. Luccio, F. G. Resmini, and H. Meiner, Proceedings of the Fifth International Cyclotron Conference, 1969 (Butterworth, London, 1971).

9. A. D. Bacher, G. R. Plattner, H. E. Conzett, D. J. Clark, H. Grunder, and W. F. Tivol. Proceedings of the Third Polarization Symposium, 1970 (University of Wisconsin Press, Madison, 1971), and LBL-280 (submitted to Phys. Rev.).

EXPERIMENT TO DETERMINE DEFORMATION PARAMETERS OF ^{28}Si BY SCATTERING OF POLARIZED PROTONS

H. E. Conzett, B. Frois,* R. Lamontagne,* R. J. Slobodrian,* and R. de Swiniarski†

In addition to the known large intrinsic quadrupole deformation of several s-d shell nuclei, more recent evidence has been presented for the existence of substantial hexadecapole (Y_4) deformations in ^{20}Ne, ^{28}Si, and ^{32}S.[1] The determinations of these Y_4 deformations resulted from coupled-channel analyses of cross sections for excitation of the 0^+, 2^+, 4^+ ground-state rotational bands by elastic and inelastic proton scattering. In this type of analysis the nuclear radius is given by

$$R = R_i\,(1 + \beta_2 Y_{20} + \beta_4 Y_{40} + \cdots),$$

where the β's are deformation parameters to be determined from fits to the experimental data, the Y's are spherical harmonics, and the R's correspond to the radii of the several components of the optical potential. The calculations were performed with a program that used a simplified form of the deformed spin-orbit potential,[2] and good fits to these data required substantial values of the deformation parameters β_2 and β_4. For example, the values for ^{20}Ne were $\beta_2 = 0.47$ and $\beta_4 = 0.28$, and the fit to the 4^+ data was much more sensitive to variations in β_4 than were the fits to the 0^+ and 2^+ angular distributions.

Subsequently, measurements were made of both cross-sections and analyzing powers in the scattering of 24.5-MeV polarized protons leading to the lowest 0^+, 2^+, and 4^+ states in ^{20}Ne and ^{22}He.[3] Coupled-channel calculations, using the simplified form of the deformed spin-orbit potential as before, failed to reproduce even the shapes of the analyzing-power angular distributions for the 2^+ and 4^+ states of ^{20}Ne.

Sherif and Blair[4] have shown that distorted-wave Born approximation (DWBA) fits to polarization in less strongly coupled nuclei could be significantly improved when the full Thomas form of the deformed spin-orbit potential was used, so this full Thomas form

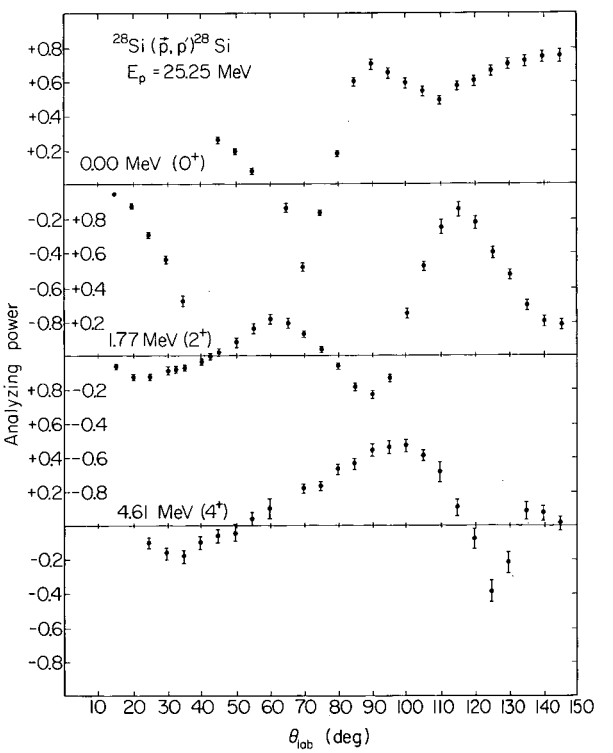

Fig. 1. Analyzing powers for 25-MeV proton scattering to the lowest 0^+, 2^+, and 4^+ states of ^{28}Si. (XBL 724-2687)

was included in the coupled-channel program. The resulting calculations were in considerable improved agreement with the ^{20}Ne analyzing-power data for the same β_2 and β_4 values deduced from the cross sections alone. Thus, the need for the full Thomas form was established.

Although inclusion of the full Thomas form in the calculation did not change the previously determined values of β_2 and β_4 for ^{20}Ne, it is not clear that would be the case for ^{28}Si and ^{32}S. Also, the β_4 values were determined less accurately for those two nuclei because of the lower quality cross-section data. Finally, a theoretical calculation[5] for β_4 for ^{28}Si gives a value of +0.05 as compared with the "experimental" value +0.25 ± 0.08 of Ref. 1, so it is clear that a redetermination of the deformation parameters for ^{28}Si is desirable.

We have, therefore, measured cross sections and analyzing powers of the ^{28}Si(p, p')^{28}Si* reaction leading to the lowest 0^+, 2^+, and 4^+ states. We used a beam of 25-MeV polarized protons[6] from the Berkeley 88-inch cyclotron, and the scattered protons were detected with eight Si(Li) detectors located symmetrically on opposite sides of the beam axis. Thus, left-right asymmetries and cross sections were measured at four scattering angles simultaneously. Analyzing powers were determined from the asymmetries as described before,[7] and Fig 1 shows these results. A coupled-channel calculation with the full Thomas form of the deformed spin-orbit potential, as described in Ref. 3, is in progress.

Footnotes and References

*Summer visitor from Université Laval, Département de Physique, Québec, CANADA.

†Summer visitor from Institut des Sciences Nucléaires de Grenoble, FRANCE.

1. R. de Swiniarski, C. Glashausser, D. L. Hendrie, J. Sherman, A D. Bacher, and E. A. McClatchie, Phys. Rev. Letters 23, 317 (1969).

2. A. G. Blair, C. Glashausser, R. de Swiniarski, J. Goudergues, R. Lombard, B. Mayer, J. Thirion, and P. Vaganov, Phys. Rev. C1, 444 (1970).

3. R. de Swiniarski, A. D. Bacher, F. G Resmini, G. R. Plattner, and D. L. Hendrie, LBL-201 (submitted to Phys. Rev. Letters).

4. H. Sherif and J. S. Blair, Phys. Letters 26B, 489 (1968).

5. A. L. Goodman, G. L. Struble, J. Bar-Touv, and A. Goswanri, Phys. Rev. C2, 380 (1970).

6. D. J. Clark, A. U. Luccio, F. G. Resmini, and H. Meiner, Proceedings of the Fifth International Cyclotron Conference, 1969 (Butterworth, London, 1971).

7. H. E. Conzett, B. Frois, R. Lamontagne, Ch. Leemann, and R. J. Slobodrian, Analyzing Power and Cross-Section Measurements in p-Si Elastic Scattering, preceding paper, this report.

MASSES OF LIGHT NUCLEI FAR FROM STABILITY*

J. Cerny

This review article indicates the progress that has been made in mass determinations of light nuclei far from the valley of beta-stability. Generally, high-isospin nuclei of mass $5 \leq A \leq 40$ were covered; such nuclei have been studied by in-beam multi-neutron transfer reactions induced by conventional projectiles and heavy ions, as well as through fragmentation reactions initiated by GeV projectiles.

Experimental results on $T_z = -3/2$ nuclei from ^{7}B through ^{37}Ca were discussed and tabulated; these masses were then compared with the predictions of the isobaric multiplet mass equation as well as to other theoretical mass predictions. Similarly, available data on highly neutron-excess nuclei from ^{8}He through ^{29}Mg were tabulated and used to evaluate the Garvey-Kelson mass relation. Finally, several useful extensions of present techniques for accurate mass measurements were noted, with particular emphasis given to those utilizing heavy ions as projectiles.

Footnote

*Abstracted from the Proceedings of the Fourth International Conference on Atomic Masses and Fundamental Constants, held at the National Physical Laboratory, Teddington, England, September 1971 (in press).

THE BETA-DELAYED PROTON EMISSION† OF ^{23}Al

R. A. Gough, R. G. Sextro, and J. Cerny

Recent mass measurements[1] have shown ^{23}Al to be the lightest, nucleon-stable member of the A = 4n + 3, $T_z = 1/2(N-Z) = -3/2$ mass series; however, no technique capable of characterizing the decay properties of these nuclides has been demonstrated. Using the ^{24}Mg(p, 2n) reaction, we have observed ^{23}Al through its beta-delayed proton emission. Extension of this approach to heavier $T_z = 0$ target nuclei should, in principle, permit the observation of several heavier members of this mass series which are predicted[2] to be nucleon stable (^{27}P through ^{35}K).

The external proton beam of the 88-inch cyclotron was used to induce the ^{24}Mg(p, 2n)^{23}Al reaction on 99.96% -enriched ^{24}Mg targets. Two independent experimental approaches were used. In the first of these, delayed protons from activity in the target were detected in a counter telescope mounted downstream from the target behind a slotted, rotating wheel. This wheel controlled the duration of the beam pulse and shielded the detectors during the beam-on intervals. Beam pulsing was achieved by modulating the cyclotron dee voltage; beam intensities of up to 8 μA on target were utilized. In these experiments a detector telescope, consisting of an 8-μm ΔE detector and a 50-μm E detector, fed a Goulding-Landis particle identifier. Any long-range particles were eliminated by a 50-μm reject detector. In order to observe low-energy protons (and α particles) singles spectra were recorded from the 8-μm detector as well as from an additional 14-μm detector. All detectors (except the ΔE) were cooled to -25° C. Accurate energy scales were obtained in this setup by scattering, from a thin Au foil, H_2^+ beams of 0.63 and 1.15 MeV/nucleon as measured in an analyzing magnet. (A 4-μm ΔE detector was used for this calibration.)

The second experimental configuration employed a helium-jet system[3] which swept nuclei recoiling from the target through a 0.48-mm diameter, 80-cm-long capillary and deposited them on a 550-μg/cm^2 Ni collector foil. At 1.2-sec intervals this foil was quickly (~ 25 msec) moved by a solenoidal stepping motor from the collection position to a position in front of a counter telescope. The telescope and its associated electronics were identical to those in the first setup except that it employed a 6-μm ΔE detector. In these experiments a continuous proton beam of up to 8 μA on target was utilized. By comparing the yields obtained in both experimental configurations (corrected for recoil-range effects), the efficiency of the helium-jet technique for collecting ^{23}Al was determined to be ~ 10%. This disadvantage was offset by the higher attainable geometry as well as by the improved energy resolution that was a result of the very thin layer of collected activity.

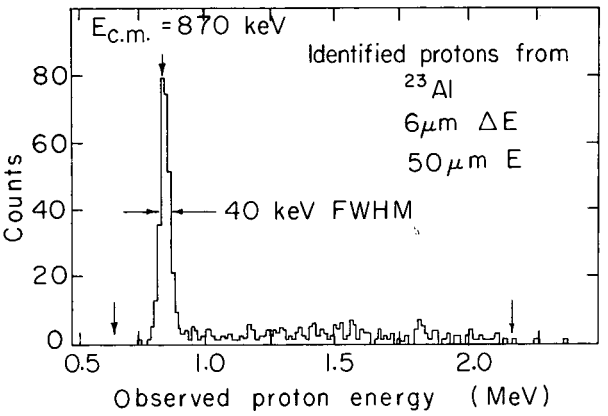

Fig. 1. An identified-proton spectrum arising from the bombardment of ^{24}Mg by 40-MeV protons, using the helium-jet technique. The vertical arrows designate the energy region over which protons could be observed.
(XBL7110-4530)

Figure 1 shows an identified-proton energy spectrum arising from the bombardment of ^{24}Mg with 40-MeV protons, using the helium-jet technique. Essentially no background is present arising from β-particle pileup. The dominant group in the spectrum has an energy of 870 ± 30 keV in the center-of-mass (c. m.) system. Higher-energy events (from 0.95 to 2.2 MeV lab) were observed in both experimental configurations. Although these events had a half-life consistent with that of the dominant group at 870 keV, their low yield precluded the assignment of other distinct transitions. The 870-keV group was observed to have a half-life of 470 ± 30 msec and was produced with a maximum cross section ≈ 220 nb. This half-life is consistent with the upper limit of 560 msec obtained from simple calculations using a log $\underline{ft}$ = 3.3 for the superallowed decay[4] of ^{23}Al and known log $\underline{ft}$ values for the first three allowed decays of its mirror nucleus ^{23}Ne.

To establish ^{23}Al as the source of this new activity, excitation-function data were acquired by using the slotted wheel technique. The experimental threshold for producing the 870-keV proton group was consistent with the

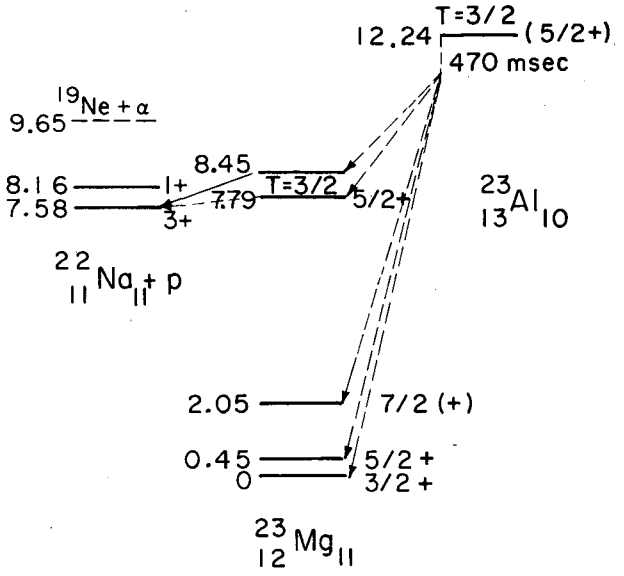

Fig. 2. A preliminary decay scheme for ^{23}Al. Energies are given in MeV. Decays that have not been directly observed are shown as dashed lines. (XBL 7110-4531)

expected value of 30.78 ± 0.08 MeV. However, the threshold for producing ^{20}Na via the ^{24}Mg(p,αn) reaction is only 24.99 ± 0.01 MeV and, although ^{20}Na is a well-known beta-delayed α emitter[5] with a half-life of 445.7 ± 3.1 msec,[6] it can emit beta-delayed protons ≲ 1 MeV. The ^{20}Na yield was measured from its 4.44 MeV α group, and detected via its ΔE loss, in two independent singles detectors of 8-μm and 14-μm thickness. The ratio of this yield to that of the 870-keV proton group varied by a factor of approximately 10 over an 8-MeV range of bombarding energy, thereby eliminating ^{20}Na as a possible source of the delayed protons.

A preliminary decay scheme for ^{23}Al is presented in Fig. 2. The assumed ground state spin of $5/2^+$ is based on its mirror ^{23}Ne; other data in the figure are taken from Refs. 7 and 8. For simplicity we have shown the 870-keV group decaying to the ground state of ^{22}Na. The protons, then, would originate from a heretofore unknown state at 8.45 MeV in ^{23}Mg which, if populated by allowed beta decay, is restricted to $J^\pi = 3/2^+, 5/2^+$, or $7/2^+$.

The superallowed beta decay of nuclides in the A = 4n + 3, T_z = - 3/2 mass series leads to levels in their daughters which are very close to the proton separation energy. The superallowed decay of ^{23}Al feeds the lowest T = 3/2 state in ^{23}Mg at 7.788 ± 0.025 MeV;[7] proton emission from this state would be isospin-forbidden and of low energy (209 ± 25 keV c.m.). Penetrability calculations alone show the width for this proton emission to be of the same order of magnitude as a typical 7.8-MeV M1 gamma ray in this mass region.[9] Although the possibility of observing these protons was, at best, marginal, an attempt was made using the helium-jet method and a 40-MeV proton beam. The low-energy proton group was sought in the spectrum from the 6-μm ΔE counter of the usual detector telescope (located on the same side of the collector foil as the deposited activity). In order to minimize the background of low-energy ^{16}O recoils formed in the decay of ^{20}Na (which was always present as a reaction by-product), an additional high geometry (3.3 sr) counter, located behind the collector foil, was placed in anticoincidence with the 6-μm detector. No experimental evidence for a 209-keV (c.m.) proton group was found; these results permit a very crude estimate[10] that $\Gamma_\gamma/\Gamma_p \gtrsim 50$ for the isospin-forbidden decay of the 7.79 MeV (T = 3/2) state of ^{23}Mg.

Heavier members of the A = 4n + 3, T_z = - 3/2 mass series are also expected to emit beta-delayed protons of low energy and can, in principle, be observed by using the techniques described in this work.

Footnotes and References

†Condensed from LBL-296.

1. J. Cerny, R. A. Mendelson, Jr., G. J. Wozniak, J. E. Esterl, and J. C. Hardy, Phys. Rev. Letters 22, 612 (1969).

2. I. Kelson and G. T. Garvey, Phys. Letters 23, 689 (1966).

3. R. D. Macfarlane, R. A. Gough, N. S. Oakey, and D. F. Torgerson, Nucl. Instr. Methods 73, 285 (1969).

4. J. C. Hardy and B. Margolis, Phys. Letters 15, 276 (1965).

5. R. M. Polichar, J. E. Steigerwalt, J. W. Sunier, and J. R. Richardson, Phys. Rev. 163, 1084 (1967).

6. D. H. Wilkinson, D. E Alburger, D. R. Goosman, K. W. Jones, E. K. Warburton, G. T. Garvey, and R. L. Williams, Nucl. Phys. A166, 661 (1971).

7. J. C. Hardy, H. Brunnader, J. Cerny, and J. Jänecke, Phys. Rev. 183, 854 (1969).

8. L. C. Haun and N. R. Roberson, Nucl. Phys. A140, 333 (1970).

9. S. J. Skorka, J. Hertel, and T. W. Retz-Schmidt, Nucl. Data A2, 347 (1966).

10. This estimate is based on a log ft = 3.3 for the superallowed decay (see Ref. 4) and the choice of a log ft = 5.0 for the decay branch leading to 870-keV protons, which was measured simultaneously [see N. B. Gove, in Nuclear Spin-Parity Assignments (Academic Press, New York, 1966), p. 83].

FINAL RESULTS ON THE PROTON RADIOACTIVITY OF $^{53}Co^{m}$

J. Cerny, R. A. Gough, R. G. Sextro, and J. E. Esterl

This report brings up to date our studies on the proton decay of $^{53}Co^{m}$.[1,2] Our earlier work has shown that $^{53}Co^{m}$ decays with a half-life of 243 ± 15 msec and that the 1.59 ± 0.03 MeV (c.m.) proton group arising from its decay is not in coincidence with positrons, thereby establishing its origin to be true proton radioactivity. Herein we report the results of our search for a proton-decay branch of 0.75 MeV (c.m.) leading to the first excited state of ^{52}Fe at 0.84 MeV as well as an improved estimate of the reduced width for the decay to the ^{52}Fe ground state.

Figure 1 presents an identified-proton energy spectrum from the decay of $^{53}Co^{m}$ produced via the $^{54}Fe(p,2n)$ reaction induced by 35-MeV protons. The use of a 4-μm ΔE detector permitted observation of protons down to an energy of ~0.4 MeV. These data set an upper limit of 1/250 for the ratio of protons to the $^{52}Fe^{*}$(0.84 MeV) state relative to the ^{52}Fe ground state. As noted previously,[1] the barrier penetrability for the proton group populating the $^{52}Fe^{*}$ state (an $\ell = 7$ decay) is ~ 6% of that to the ^{52}Fe ground state ($\ell = 9$). These results then set a limit for the relative reduced widths of γ_p^2(ground state)/$\gamma_p^2(2^+) > 15/1$.

We have improved our estimate of the absolute intensity of the proton decay of the ^{52}Fe ground state by calculating statistical model ratios for the relative cross sections $^{54}Fe(p,pn)^{53}Fe^{m}/^{54}Fe(p,2n)^{53}Co^{m}$ following the spin-dependent nuclear evaporation approach of Grover and Gilat.[3] (This calculation reproduces isomer cross-section ratios in the $^{16}O + ^{40}Ca$ reaction to better than ± 50%.) Figure 2 shows the results of these excitation-function calculations for both $^{53}Fe^{m}$ and $^{53}Co^{m}$; the theoretical results have been normalized to our observed excitation function[2] for production of $^{53}Co^{m}$. Taking Eskola's[4] value of ~ 5 mb for the peak cross section for the $^{54}Fe(p,pn)^{53}Co^{m}$ reaction, one finds the ratio $\sigma(^{53}Fe^{m})/\sigma$(proton activity) ≈ 11,000, while the theoretical result for $\sigma(^{53}Fe^{m})/\sigma(^{53}Co^{m})$ using peak cross sections is ≈ 165. This then leads to a partial branch of ~ 1.5% for the observed proton decay or a partial half-life of ~ 17 sec. Finally, since penetration through the Coulomb and centrifugal barriers leads to an expected half-life of ≈ 60 nsec for a reduced width $\gamma_p^2 = 1$, the above

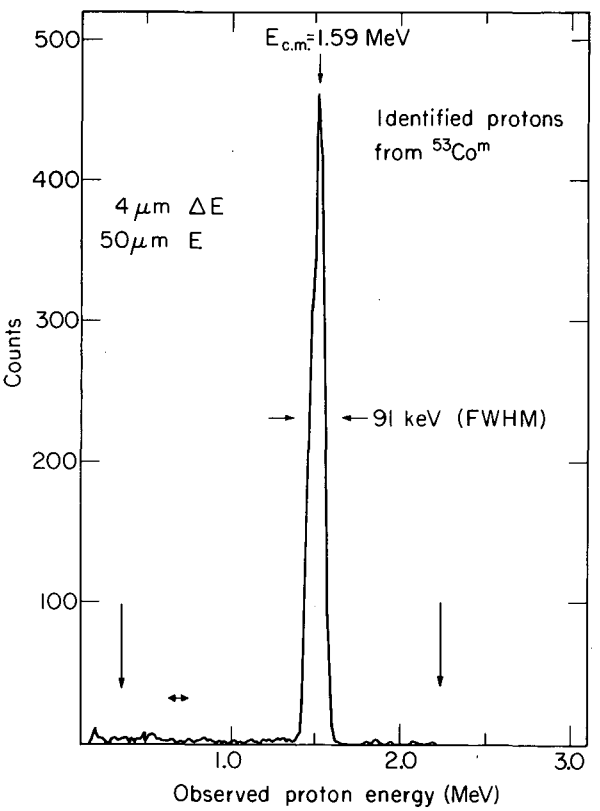

Fig. 1. An identified-proton spectrum arising from the bombardment of ^{54}Fe by 35-MeV protons. The vertical arrows denote the energy region over which protons could be observed, while the horizontal arrow indicates the location of any possible transitions to the $^{52}Fe^{*}$(0.84-MeV) state. (XBL 714-3232)

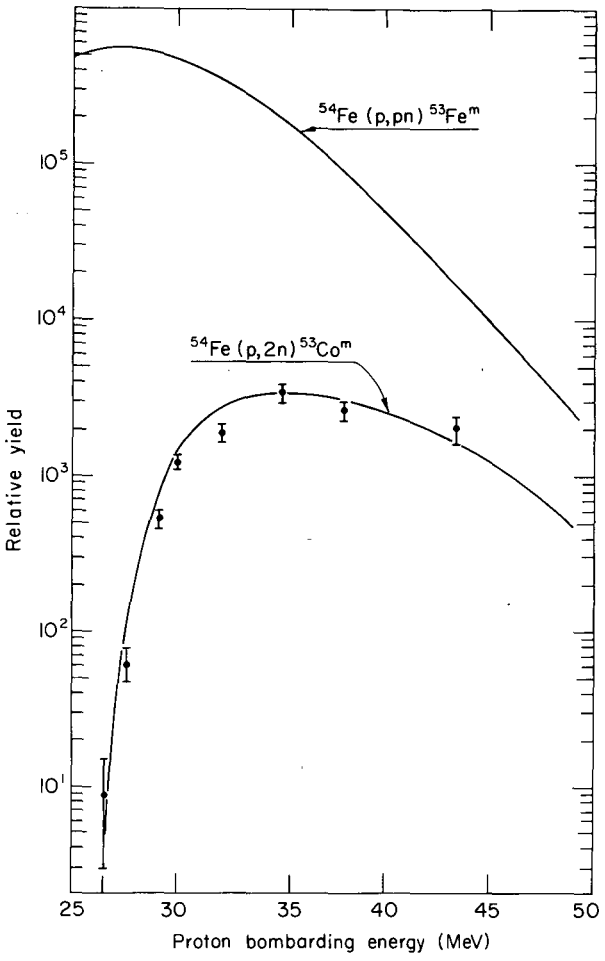

Fig. 2. Theoretical predictions for the production of $^{53}Fe^{m}$ and $^{53}Co^{m}$ employing the approach of Grover and Gilat.[3] The theoretical curves have been normalized to the experimental excitation function for the $^{54}Fe(p,2n)^{53}Co^{m}$ reaction. (XBL 7012-4203)

partial half-life implies $\gamma_p^2 \approx 4 \times 10^{-9}$ for this complex decay.

Figure 3 shows our decay scheme for $^{53}Co^{m}$. This isomer is presumed to be the mirror of the $19/2^-$, T = 1/2 isomer $^{53}Fe^{m}$; both isomeric states arise from the configuration $(f_{7/2})^{-3}$ and are due to the existence of large "spin gaps" in the level spectrum of the ground state configuration.[5] Unfortunately, meaningful theoretical predictions for the expected value of γ_p^2 in the $\ell = 9$ proton decay of such a state are difficult to obtain. However, our results on the ratio of the reduced widths for proton decay to the ground and first-excited states of ^{52}Fe should provide an additional test of such theoretical calculations.

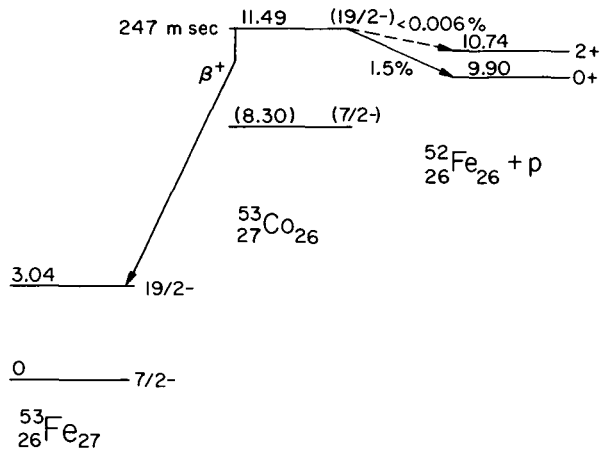

Fig. 3. The decay scheme of $^{53}Co^{m}$. (XBL 7012-4202)

References

1. K. P. Jackson, C. U. Cardinal, H. C. Evans, N. A Jelley, and J. Cerny, Phys. Letters 33B, 281 (1970).

2. J. Cerny, J. E. Esterl, R. A. Gough, and R. G. Sextro, Phys. Letters 33B, 284 (1970).

3. J. R. Grover and J. Gilat, Phys. Rev. 157, 802 (1967); J. Gilat, Brookhaven National Laboratory Report BNL-50246 (1970).

4. K. Eskola, Phys. Letters 23, 471 (1966); Ann. Acad. Sci. Fennicae A. VI 261, 7 (1967).

5. See J. Vervier, Nucl. Phys. A103, 222 (1967) and references therein.

HIGH-SPIN ASSIGNMENTS IN THE 1p-SHELL UTILIZING THE J-DEPENDENT (p,α) REACTION*

C. Maples and J. Cerny

Almost all previously reported (p,α) investigations below A = 60 have been restricted to measurements of the ground state and a few low-lying excited states. As such, the question of whether this pickup reaction, operating through its transferred angular momentum se-

lection rule $\vec{J}=\vec{L}+\vec{1}/2$, is useful as a spectroscopic tool in the lighter nuclei remains largely unanswered. We have studied the (p,α) reaction induced by 43.7- to 54.1-MeV protons on ^{12}C, ^{13}C, ^{14}N, ^{15}N, and ^{16}O, observing transitions to levels in the residual nuclei ranging from the ground state to 15 to 22 MeV in excitation. These data show that, in fact, a strong and consistent J-dependence, in accord with the above selection rule, is observed for both L = 1 and L = 3 transitions, permitting (within the scope of this paper) two definite spectroscopic assignments. J-dependent effects [first reported by Lee and Schiffer[1] for (d,p) reactions] have previously been noted for L = 1 (p,α) transitions on medium-mass nuclei (see, e.g., Refs. 2 and 3). Although a J-dependence for L = 3 transitions in both (p,α) reactions[3] and (α,p) reactions[4] has been predicted from distorted-wave Born approximation (DWBA) calculations, no definite experimental evidence for this has hitherto been reported.

These (p,α) reactions were investigated by using the proton beam of the Berkeley 88-inch spiral-ridge cyclotron at energies of 43.7 MeV on the ^{13}C, ^{14}N, and ^{15}N targets: 50.5 MeV on the ^{13}C target; and 54.1 MeV on the ^{12}C and ^{16}O targets. The experimental details have been described previously.[5] Alpha particles from the reaction were identified by a Goulding-Landis particle identifier. Gas targets of $^{16}O_2$, $^{15}N_2$ (enriched to 99%), $^{14}N_2$, and $^{13}CH_4$ (enriched to 93%), and a solid ^{12}C target were used. A representative spectrum of the $^{16}O(p,\alpha)^{13}N$ reaction, with an experimental resolution of approximately 190 keV is shown in Fig. 1. Transitions examined in all the residual nuclei yielded angular distributions, taken between approximately 10° and 80° center-of-mass (c.m.), on about 50 levels.

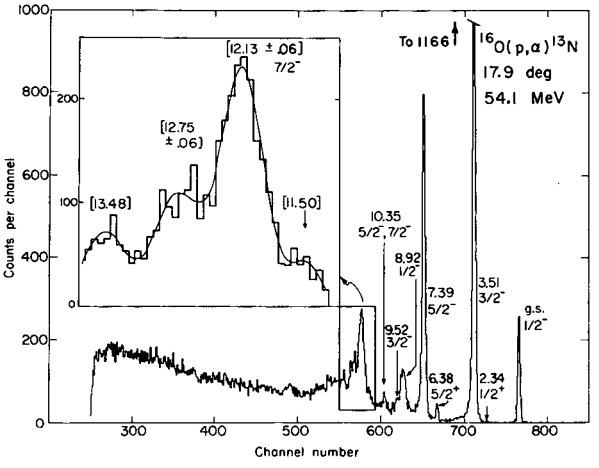

Fig. 1. The energy spectrum of the $^{16}O(p,\alpha)^{13}N$ reaction. The insert shows a four-Gaussian fit to the indicated region of the spectrum, after background subtraction.

(XBL 7012-4295)

This report will cover, with one exception, only those transitions for which a unique value for L and J is required by the selection rules. A detailed analysis of our results as well as a comprehensive discussion of the direct pickup character of these (p,α) reactions (at forward angles and at our bombarding energies) will be presented in a subsequent publication. A strong indication of a dominant pickup mechanism would be the highly selective population of "pure" p-shell final states[6] in all the residual nuclei. Such an effect was indeed observed. The strongest (p,α) transitions consistently populated only p-shell levels in the final nuclei with cross sections that were larger, by usually one or two orders of magnitude, than those to non-p-shell levels. In contrast to this, a knockout mechanism, for example, would have permitted some transitions to both types of levels, perhaps most strongly for reactions on the ^{12}C and ^{16}O targets [it would permit the incident proton to be captured into either the 1p or the (2s,1d)shell]. The spectrum in Fig. 1 particularly illustrates the differing relative cross sections for transitions to p-shell and non-p-shell final states.

Angular momentum selection rules restrict (p,α) transitions between p-shell levels to L = 1 (with J = 1/2 or 3/2) or L = 3 (with J = 5/2 or 7/2). Figure 2 shows some (p,α) angular distributions for which L = 1. While all the distributions peak toward zero degrees, there is little additional similarity between the J = 1/2 and 3/2 distributions. However, the uniformity and consistency of the angular distributions for a given J are pronounced. It is noteworthy that this uniformity persists even with differing kinematic effects and is generally preserved over a range of almost 18 MeV of excitation in the $^{15}N(p,\alpha)^{12}C$ reaction.

Transitions in which L = 3 are shown in Fig. 3.[7] The only consistent feature (an L-dependent effect) appearing in these distributions is that the first maximum no longer peaks toward zero degrees. The J-dependent effects are again apparent in the J = 5/2 and 7/2 distributions, although the differences are not as pronounced as in the previous L = 1 case. Although only one transition populated in these reactions was restricted solely to a J = 5/2 transfer [the $^{16}O(p,\alpha)^{13}N$(7.39 MeV, 5/2⁻) transition], at least four other transitions were observed to proceed predominatly through this mode.[8] One example of these is the $^{15}N(p,\alpha)^{12}C$(16.1 MeV, 2⁺, T = 1) transition. Simple spectroscopic arguments (employing in part the wave functions of Ref. 6) indicate that this transition should have a strong component of L = 3, J = 5/2 transfer, although

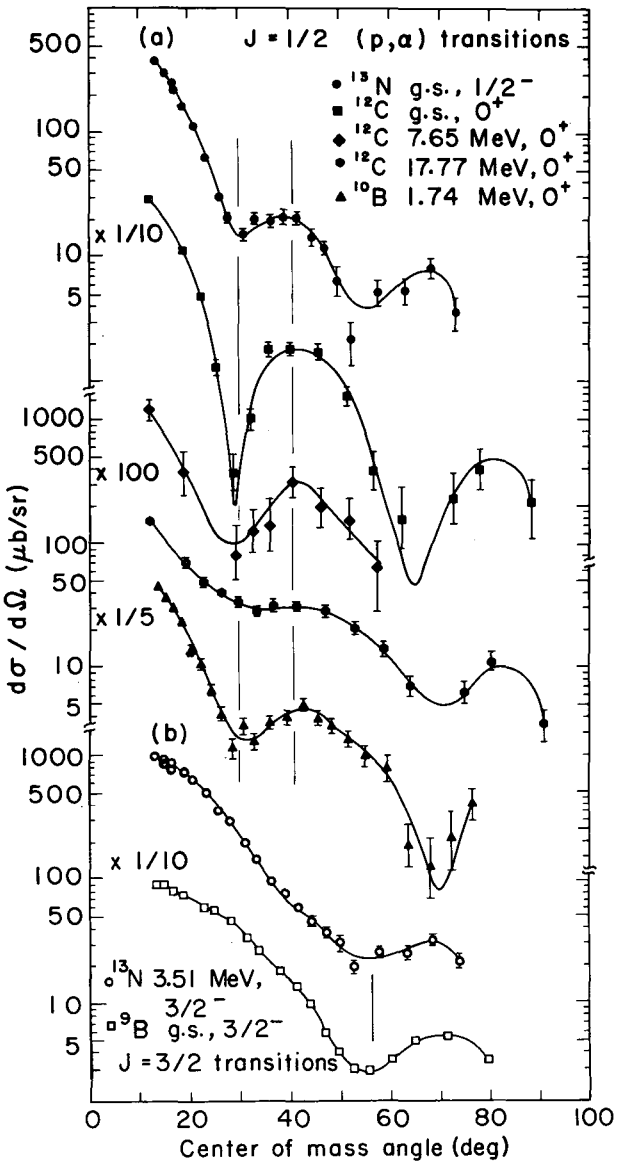

Fig. 2. Differential cross sections for various L = 1 (p,α) transitions: (a) J = 1/2 transitions; (b) J = 3/2 transitions. Where error bars are not shown, they are smaller than the size of the points. The curves represent least-squares fits to the data. Vertical lines have been added to facilitate comparisons.
(XBL 7110-4625)

L = 1, J = 3/2 transfer is also allowed. Since the angular distribution for this reaction (Fig. 3a) shows no obvious L = 1 character at forward angles, it can be taken as a further example of an essentially pure J = 5/2 transition. Of the final states populated in the J = 7/2 transitions, only the $^{12}C(4^+)$ and $^{10}B(4^+)$ were previously known (the small angle behavior of the transition to the ^{10}B state is well accounted for by a small admixture of an L = 1 component to an incompletely resolved neighboring level). The two remaining J = 7/2 transitions will be discussed below. The angular distributions of the strong transitions to all the other p-shell states are consistent with these four different J-dependent shapes, either singly or in an appropriate combination.

Distorted wave calculations were employed to determine whether the observed J-dependence was consistent, at least in general, with simple theory. Since the initial aim was only for a qualitative comparison, a local, zero-range calculation, using the point-triton approximation, was carried out by using the code DWUCK. [9] [Optical model parameters for the proton channel (including a spin-orbit term), the alpha channel, and the bound state (radius and diffuseness parameters only) were obtained from the literature. In the case of α-particle parameters it was often necessary to refit the elastic α-scattering data to obtain a deeper and more realistic real well potential (V_0) around 200 MeV.] In general, the DWBA fits qualitatively reproduce the shapes of the

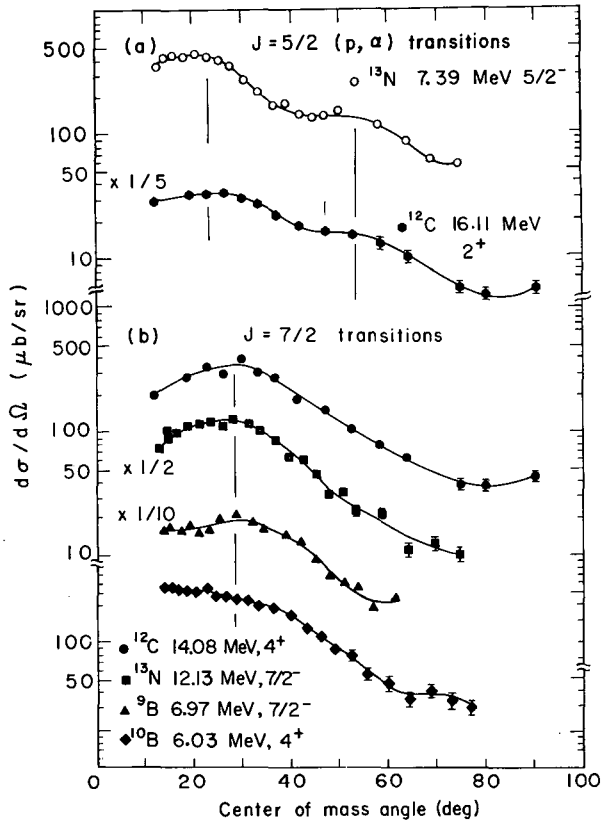

Fig. 3. Differential cross sections for various L = 3 (p,α) transitions: (a) J = 5/2 transitions; (b) J = 7/2 transitions. See caption for Fig. 2.
(XBL 7110-4626)

distributions and hence clearly predict the observed J-dependence. The relatively slight dependence of the distributions on kinematic effects was also reproduced by the calculations. The major deficiency of these calculations is that they consistently predict a more rapid decrease in the overall magnitude of the cross section (with increasing $\theta_{c.m.}$) than is observed.

Finally, this observed J-dependence permits us to make two definite spectroscopic assignments. The first of these is for the second strongest transition observed in the $^{12}C(p,\alpha)^{9}B$ reaction, which was to a level at 6.97 ± 0.06 MeV. This level, which has a width of approximately 2 MeV, accurately follows the kinematics of other ^{9}B levels and its excitation is consistent with a known $7/2^-$ state[10] in the mirror nucleus ^{9}Be at 6.6 MeV. The excitation of the 6.97 MeV level also corresponds well to a state reported at 7.1 ± 0.2 MeV in ^{9}B which was tentatively assigned[10] as $7/2^-$. Similarly, the third strongest transition in the $^{16}O(p,\alpha)^{13}N$ reaction was to a broad, hitherto unobserved, level ($\Gamma_{c.m.} \approx 300$ keV) at 12.13 ± 0.06 MeV (Fig. 1). The excitation energy of this state corresponds favorably with that of a state at 12.42 MeV in its mirror nucleus ^{13}C which has $J^\pi = 7/2^-$ (Ref. 5). The angular distributions for these (p,α) reactions to the ^{9}B and ^{13}N states, shown in Fig. 3b, are in agreement both with each other and with the known J = 7/2 transition shapes. Both distributions are also consistent only with the DWBA predictions for J = 7/2. Since these transitions proceed from 0^+ targets, unique $J^\pi = 7/2^-$ assignments are possible.

Footnotes and References

*Condensed from LBL-288.

1. L. L. Lee, Jr. and J. P. Schiffer, Phys. Rev. Letters 12, 108 (1964).

2. J. A. Nolen, Jr., C M. Glashausser, and M. E. Rickey, Phys. Letters 21, 705 (1966).

3. D. L. Dittmer and W. W. Daehnick, Phys. Rev. C 2, 238 (1970) and references therein.

4. L. L. Lee, Jr., A. Marinov, C. Mayer-Boricke, J. P. Schiffer, R. H. Bassel, R. M. Drisko, and G. R. Satchler, Phys. Rev. Letters 14, 261 (1965); R. O. Ginaven and A. M. Bernstein, Nucl. Phys. A154, 417 (1970).

5. D. G. Fleming, J. Cerny, C. C. Maples, and N. K. Glendenning, Phys. Rev. 166, 1012 (1968).

6. J. L. Norton and P. Goldhammer, Nucl. Phys. A165, 33 (1971); P. Goldhammer, private communication.

7. No L = 5 component in the transitions to the ^{12}C(14.08 MeV, 4^+) and ^{10}B(6.03 MeV, 4^+) final states is allowed under the assumptions of pure p-shell target nuclei and a pick-up mechanism.

8. Unfortunately, a pure J = 5/2 angular distribution cannot be observed in the $^{12}C(p,\alpha)^{9}B$ transition to the 2.3-MeV states due to the presence of an unresolved J = 1/2 component. This point will be discussed in our later publication.

9. P. D. Kunz, University of Colorado computer code DWUCK, unpublished (1967).

10. L. A. Kull and E. Kashy, Phys. Rev. 167, 963 (1968).

A HIGHLY NEUTRON-DEFICIENT VANADIUM ISOTOPE: ^{44}V†*

J. Cerny, D. R. Goosman,‡ and D. E. Alburger‡

With the exception of ^{16}F, all of the members of the A = 4n, $T_Z = (N - Z)/2 = -1$ series from ^{8}B through ^{40}Sc are nucleon stable and their decay properties have been fairly well established. However, no technique for investigating higher-A nuclei of this series has been demonstrated. We wish to report the observation of ^{44}V, following the $^{40}Ca(^{6}Li, 2n)$ reaction, by utilizing the weak beta-delayed particle emission frequently observed in the decay of nuclei in this mass series; in principle, extension of this approach to other heavy ions should permit observation of heavier unknown $T_Z = -1$ nuclei.

Mechanically chopped beams of 18.5- and 21.5-MeV ^{6}Li ions (3^+) from the second tandem of the Brookhaven National Laboratory three-stage MP tandem Van de Graaff facility were used to irradiate 0.86 mg/cm^2 natural calcium targets. Beam intensities incident on the target averaged 0.4 μA. The 21.5-MeV beam was employed to investigate the well-known beta-delayed α-particle emission of ^{20}Na[1] for orientation and calibration purposes: ^{20}Na was produced by the $^{16}O(^{6}Li, 2n)$ reaction on

oxygen target impurities. The 18.5-MeV beam was required to investigate ^{44}V, since this energy lies just below the threshold for the production of ^{20}Na which would otherwise present a severe background problem due to its prolific yield. (Due to the nucleon instability of ^{16}F, reactions on ^{12}C target impurities are of no concern.)

Simple calculations lead one to expect ^{44}V to be, most probably, a weak beta-delayed α-particle emitter with a half-life $\lesssim$ 150 msec. In order to detect fairly-low-energy α-particle groups in an intense beta background, a semiconductor telescope consisting of surface-barrier detectors was employed. This telescope utilized a 5-μ ΔE detector followed by a 31-μE detector and subtended a solid angle of 0.15 sr. The targets were placed at an angle of 30° to the beam while the telescope was positioned perpendicular to the beam axis.

A timing device triggered both the pneumatic beam interceptor and a shutter that dropped in between the target and the ΔE counter during the irradiation periods. Summed coincidence pulses between the two detectors were stored in a two-parameter analyzer as a function of time. As a further aid in reducing the background from beta-particle pile-up, only those events losing more than 600 keV in the ΔE detector were accepted.

Figure 1(a) presents data from the bombardment of the calcium target with 21.5-MeV ^{6}Li ions. Comparison of this α-particle spectrum with the results of Polichar et al.[1] shows that it is dominated by, and consistent with, the decay of ^{20}Na produced from oxygen target impurities. (The primary α-particle branch in this decay has a center-of-mass (c.m.) energy of 2.70 MeV; due to our relatively thick target, most of the yield of this group lies below the telescope cutoff.) Further, the observed half-life of these beta-delayed α particles agrees well with the known 446-msec half-life of ^{20}Na.[2]

Figure 1(b) presents an α-particle spectrum following the decay of the new isotope ^{44}V. A peak corresponding to a c.m. energy of 3.05 ± 0.20 MeV, after correction for energy loss in the target, dominates the observed spectrum. The data are consistent with the assumption that this fairly broad peak arises primarily from a single α-particle group and have been so treated; however, due to the low yield of this group and the various assumptions necessary for the energy analysis, the possibility that such a peak could arise from two moderately spaced α-particle groups cannot be completely eliminated. The half-life of this peak is 90 ± 25 msec and its production cross section is of the order of 100 nb.

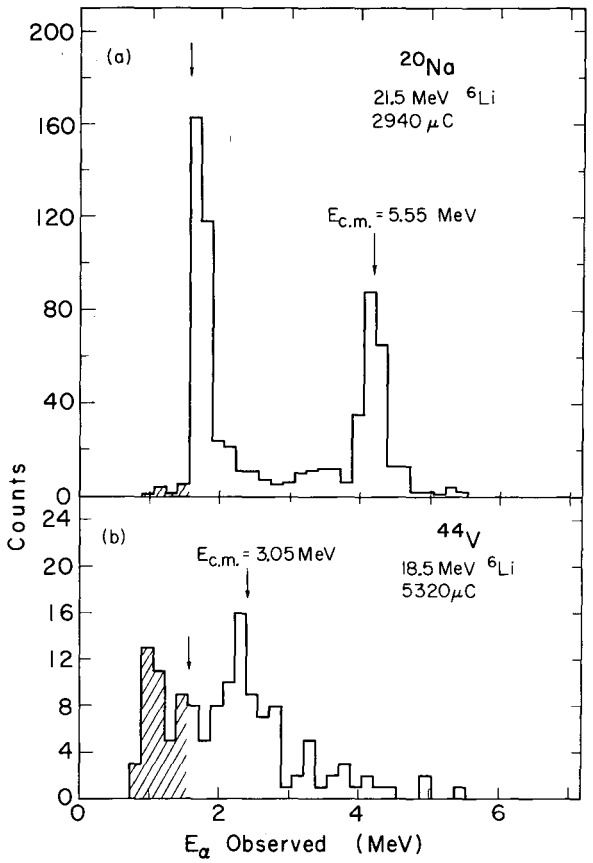

Fig. 1. (a) An α-particle spectrum following the decay of ^{20}Na produced by the $^{16}O(^{6}Li, 2n)$ reaction on oxygen target impurities. The center-of-mass energy of the major peak unaffected by the telescope cutoff is shown. (b) An α-particle spectrum following the decay of ^{44}V produced by the $^{40}Ca(^{6}Li, 2n)$ reaction. Cross-hatched events below the arrow at 1.6 MeV can only arise from β-particle pile-up. (XBL 719-4392)

Events in the shaded region arise from beta-particle pileup and have a half-life longer than one second.

This low yield for beta-delayed particle decay from ^{44}V coupled with the overwhelming yield of ^{20}Na from oxygen target impurities precluded determination of an excitation function for the $^{40}Ca(^{6}Li, 2n)^{44}V$ reaction. However, at this relatively low bombarding energy for ^{6}Li on calcium, no other nuclide including the unknown isotope ^{45}V can be formed which can be a source of beta-delayed α particles of this energy. (Unknown masses of relevant $f_{7/2}$ shell nuclei are taken from the predictions of Harchol et al.[3])

A preliminary decay scheme for ^{44}V is

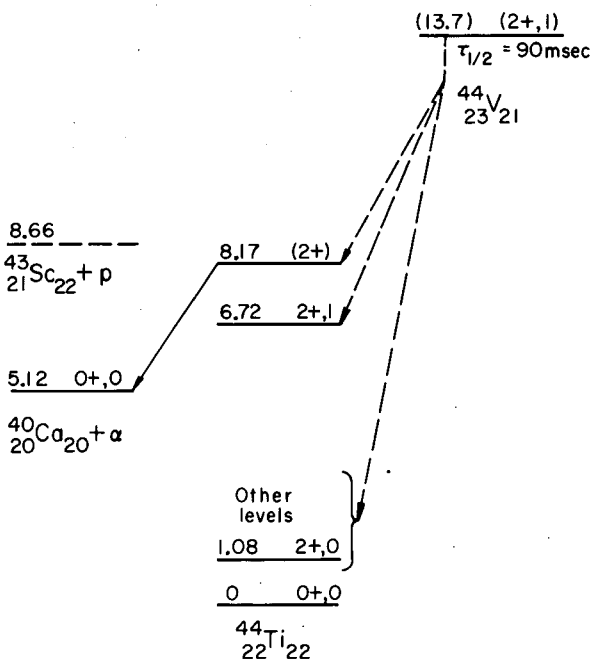

Fig. 2. A preliminary decay scheme for ^{44}V. Decays that have not been directly observed are shown as dashed lines. Energies are given in MeV. The spin-parity assignments are discussed in the text. (XBL 719-4393)

presented in Fig. 2. Data on ^{44}Ti were taken from Refs. 4 and 5. The spin and parity of ^{44}V are taken to be 2^+, based on its mirror nuclide ^{44}Sc.[6] (Similarly, based on this mirror comparison, one would also expect a beta-decaying isomer $^{44}V^m$ (6^+) of comparable half-life. For simplicity, we have attributed the observed decays to the ground state; several weak arguments, none of them convincing, favor this choice.) As can be seen in Fig. 2, the α particles must originate from a state at 8.17 MeV in ^{44}Ti which, if populated by allowed beta decay, is restricted to a J^π of 2^+ by angular momentum and parity conservation.[7] Superallowed beta decay populates the 2^+, T = 1 state at 6.72 MeV.[5] Even though this state is unstable to (isospin-forbidden) α-particle emission, penetrability calculations alone show that such α emission is far too slow to compete with γ-ray de-excitation; no evidence for any such α-particle group was observed in the ΔE singles spectra.

Footnotes and References

†Condensed from Physics Letters 37B, 380 (1971).

*The experimental work reported here was performed at Brookhaven National Laboratory where one of us (J. C.) was a Summer Visitor in the Physics Division for the first summer session of 1971.

‡Brookhaven National Laboratory, Upton, New York.

1. R. M. Polichar, J. E. Steigerwalt, J. W. Sunier, and J. R. Richardson, Phys. Rev. 163, 1084 (1967).

2. D. H. Wilkinson, D. E. Alburger, D. R. Goosman, K. W. Jones, E. K. Warburton, G. T. Garvey, and R. L. Williams, Nucl. Phys. A166, 661 (1971).

3. M. Harchol, A. A. Jaffe, J. Miron, I. Unna, and J. Zioni, Nucl. Phys. A90, 459 (1967).

4. J. J. Simpson, W. R. Dixon, and R. S. Storey, Phys. Rev. C4, 443 (1971).

5. N. Longequeue, J. P. Longequeue, and B. Vignon, Phys. Letters 32B, 596 (1970).

6. P. M. Endt and C. van der Leun, Nucl. Phys. A105, 1 (1967).

7. No isospin assignment is possible since the level scheme of ^{44}Ti is unknown and that of ^{44}Sc poorly characterized [see H. Ohnuma and A. M. Sourkes, Phys. Rev. C3, 158 (1971)] in the appropriate regions of excitation.

ISOSPIN-FORBIDDEN PARTICLE DEACY OF THE LOWEST T = 2 STATE OF ^{56}Ni

G. W. Goth,* R. A. Gough, H. L. Harney, and J. Cerny

Subsequent to the initial observation that isospin-forbidden particle decay accounts for almost all the width of the lowest T = 2 states of ^{20}Ne, ^{24}Mg, ^{28}Si, ^{32}S, and ^{40}Ca,[1] an additional measurement has been made of the isospin-forbidden particle decay of the first T = 2 state of ^{56}Ni. Measurements of the total widths of the T = 2 states of ^{20}Ne,[2] ^{24}Mg,[3] ^{28}Si,[4] and ^{32}S[5] have indicated that the total width ranges from 3×10^{-4} to 3×10^{-3} times the Wigner

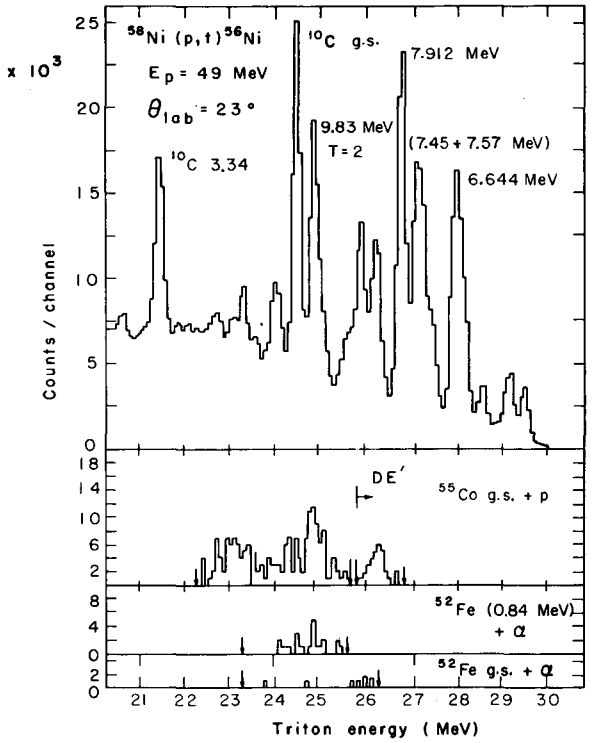

Fig. 1. Triton singles data containing the 0^+, T = 2 state(s) in ^{56}Ni, together with the summed projections of the coincidence data. Data to the right of the arrow labeled DE' in the proton spectrum are protons stopping in the ΔE-E-telescope. The vertical arrows indicate the cutoff energies determined by the kinematics and detector thicknesses. (XBL 716-3784)

limit. The maximum particle-decay energies (E_p^{max} = 2.6 MeV, E_α^{max} = 1.8 MeV) of the T = 2 state of ^{56}Ni and the high Coulomb and centrifugal barriers lead to a Wigner limit on the order of 3 keV for this state. The Weisskopf limit for an M1 γ transition to the first T = 1, $J^\pi = 1^+$ state (the excitation energy of which has not been experimentally determined, but which is expected to lie at about 8.09 MeV[6]) is 0.2 eV. If the ratio of the total width to the Wigner limit is the same for ^{56}Ni as it is for the lighter isotopes and the M1 transition is as strong as those seen in ^{20}Ne, ^{24}Mg, and ^{28}Si,[7] then γ decay might account for a substantial portion of the total width of the ^{56}Ni, T = 2 state. Studies of the M1 γ decay of T = 2 states also provide information concerning the matrix elements of the analogous Gamow-Teller beta decay.[8] Of particular interest are ΔT = 2 γ decays, which are strictly forbidden in the quark model of the nucleon;[9] the observation of such decays would be of considerable importance. Consequently, this experiment was undertaken to determine if

Table I. Summary of T = 2 branching ratio data for ^{56}Ni.

Mode	Net events	Branching[a] ratio (X100)	Normalized branching ratios
^{55}Co+p_0	34±7	95 ± 20	90
^{52}Fe+α_0	-2 ± 2	-5 ± 5	~0
^{52}Fe+α_1	5 ± 3	11 ± 7	10
Total		101 ± 28[b]	100

[a]Standard deviation includes only counting statistics.

[b]Standard deviation includes uncertainties in the number of triton counts and in the decay telescope solid angles (Ref. 1).

$\Gamma_{particle}$ was, in fact, substantially less than Γ_{total} for the T = 2 state of ^{56}Ni.

The ^{58}Ni(p, t)^{56}Ni reaction was used to populate the T = 2 state at 9.83 ± 0.1 MeV.[10] Coincidences between tritons forming the state and protons and α particles from its decay were measured in a system virtually identical

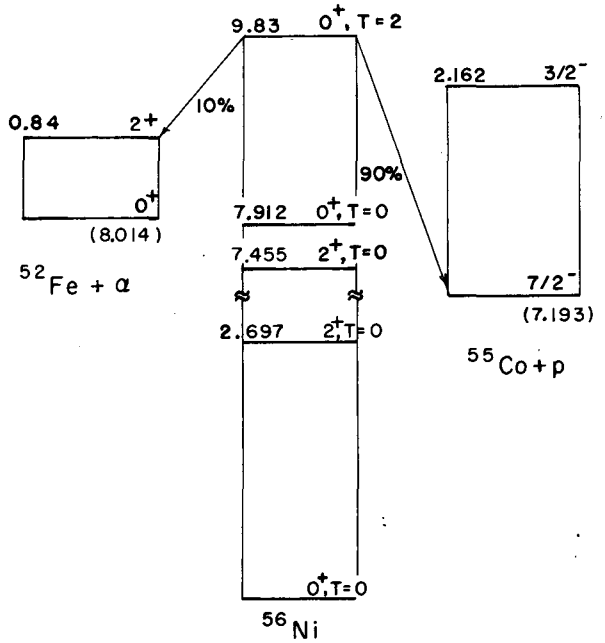

Fig. 2. Decay scheme of the lowest 0^+, T = 2 state(s) of ^{56}Ni. (XBL 716-3786)

to that described in Ref. 1. To prevent tritons from the $^{12}C(p,t)^{10}C$ (g. s.) contaminant reaction from overlapping with those from the $^{58}Ni(p,t)^{56}Ni(T=2)$ reaction, an incident beam energy of 49 MeV and a triton angle of 24° (c. m.) were chosen. The differential cross section populating this state at this angle is only 30 ± 5 μb/sr.

The data were analyzed as in Ref. 1. The triton singles spectrum and the coincidence spectra projected onto the triton energy axis are shown in Fig. 1. Branching ratio data are summarized in Table I and Fig. 2 illustrates the decay scheme of the $^{56}Ni(T=2)$ state.

A high-resolution study of $^{58}Ni(p,t)^{56}Ni$ at 40 MeV by R. Sherr et al.[11] recently revealed that the T = 2 state could be a triplet of 0^+ states all lying within about 100 keV. Their excitation energies are 9.915, 9.991, and 10.021 MeV; the first of these states is the strongest, the relative intensities being 1, 0.2, and 0.3. Moreover, states at 9.832- and 9.749-MeV excitation were also observed.[12] It is claimed in Ref. 12 that these last two states have spins $J \neq 0$. Unfortunately, all five of these states are contained in our peak labelled T = 2, due to the 250-keV resolution for tritons necessitated in this coincidence experiment. (See Fig. 1.) One can estimate from the data of Ref. 12 that the decay of the $T \neq 2$ states could account for at most 50% of our observed intensity. In order to take this into account, the errors quoted in Table I must be increased. We then find that (100^{+0}_{-50})% of the decay of the 0^+, T = 2 group of states in ^{56}Ni is via particle emission and that the branching ratio for proton emission is (90^{+10}_{-40})%.

Isospin-forbidden particle decay appears to account for a substantial fraction of the decay of the T = 2 state(s) of ^{56}Ni. It would therefore be difficult to observe any T = 2 γ decays from these states. Perhaps the ^{48}Cr T = 2 state at 8.77 ± 0.05 MeV[13] would be the best case in which to look for isospin-forbidden γ decay. The very low energies of the decay particles (E_p^{max} = 0.6 MeV, E_α^{max} = 1.1 MeV) lead one to expect a Wigner limit of about 0.2 eV, while $\Gamma_{\gamma(M1)}$ is likely to be about 0.2 to 0.4 eV, and $\Gamma_{\gamma(E2)}$, if it were allowed, would be ~ 1-3 eV.

Footnote and References

*Present address: Dept. of Chemistry, Washington University, St. Louis, Missouri.

1. R. L. McGrath, J. Cerny, J. C. Hardy, G. Goth, and A. Arima, Phys. Rev. C1, 184 (1970).

2. R. Bloch, R. E. Pixley, and P. Truöl, Phys. Letters 25B, 215 (1967).

3. F. Riess, W. J. O'Connell, D. W. Heikkinen, H. M. Kuan, and S. S. Hanna, Phys. Rev. Letters 19, 367 (1967).

4. K. A. Snover, D. W. Heikkinen, F. Riess, H. M. Kuan, and S. S. Hanna, Phys. Rev. Letters 22, 239 (1969).

5. S. Gales, M. Langevin, J. M. Maison, and J. Vernotte, C. R. Acad. Sc. Paris 271, 970 (1970).

6. W. G. Davies, J. E. Kitching, W. McLatchie, D. G. Montague, K. Ramavataram, and N. S. Chant, Phys. Letters 27B, 363 (1968).

7. S. S. Hanna in Isospin in Nuclear Physics (North-Holland, Amsterdam, 1969) p. 591.

8. E. K. Warburton and J. Weneser, in op. cit., p. 173.

9. A. de-Shalit, in Nuclear Reactions Induced by Heavy Ions, (North-Holland, Amsterdam 1970) p. 807.

10. J. Cerny, Ann. Rev. Nucl. Sci. 18, 27 (1968).

11. R. Sherr, W. Benenson, E. Kashy, D. Boyer, and I. Proctor, Bull. Am. Phys. Soc. 16, 1173 (1971).

12. D. Boyer, W. Benenson, E. Kashy, I. Proctor, and R. Sherr, Michigan State University preprint (1971).

13. O. D. Brill, A. D. Vongaĭ, V. S. Romanov, and A. R. Faĭziev, Sov. J. Nucl. Phys., 12, 138 (1971).

ALPHA-PARTICLE TRANSFER VIA THE (^{12}C, ^{8}Be) REACTION: APPLICATION TO STUDIES OF ^{16}O

G. J. Wozniak, K. H. Wilcox, H. L. Harney, and J. Cerny

With the advent of heavy-ion beams of sufficient energy, numerous α-transfer reactions[1] have been investigated as a means of studying four-particle correlations. In this paper we wish to report a simple technique for the detection of ^{8}Be which allows one to study four-particle four-hole states in ^{16}O via a new α-transfer reaction, (^{12}C, ^{8}Be).

The ^{8}Be nucleus in its ground state is unstable, with respect to breakup into two alpha-particles. It has a breakup energy of 92 keV and a mean lifetime of $\approx 10^{-16}$ seconds. Methods of identifying ^{8}Be that have been previously reported in the literature have relied on the separate detection of the two breakup α-particles: either their tracks have been observed in nuclear emulsions[2] or they have been recorded in coincidence in separate solid-state detectors.[3]

Our approach employs a conventional ΔE-E telescope plus particle identifier. If the two breakup alphas travel together through a counter telescope, they will be identified as a ^{7}Li. This can be seen as follows. The differential energy loss of a particle with charge z and velocity v in a given absorber may be written[4]

$$\frac{dE}{dx} = \frac{z^2}{v^2} f(v^2),$$

where f varies logarithmically (hence slowly) with v^2. We obtain for a ^{7}Li with energy E

$$\left(\frac{dE}{dx}\right)_{^{7}\mathrm{Li}} = \frac{9}{2E/7} f(2E/7),$$

and for two α particles, each of which carries half the energy E,

$$\left(\frac{dE}{dx}\right)_{^{8}\mathrm{Be}} = \frac{2\times 4}{E/4} f(E/4) .$$

Because of the approximate equality:

$$f(0.286E) \approx f(0.250\ E) = f_0,$$

we have

$$\left(\frac{dE}{dx}\right)_{^{7}\mathrm{Li}} = 31.5\ \frac{f_0}{E}$$

and

$$\left(\frac{dE}{dx}\right)_{^{8}\mathrm{Be}} = 32\ \frac{f_0}{E} .$$

The near equality of the last two expressions demonstrates that the two breakup alphas will be identified by their differential energy loss as a ^{7}Li. Similar results are obtained if an identifier of the power-law type is used.[5] Fortunately the Q value for the (^{12}C, ^{8}Be) reaction is often much larger than that of the (^{12}C, ^{7}Li) reaction on the same target. (For $T_z = 0$ targets, the difference is ≈ 15 MeV.) Thus the (^{12}C, ^{8}Be) reaction may be observed over a large range of excitation energy without contamination from the (^{12}C, ^{7}Li) reaction.

We have tested this approach for detecting ^{8}Be particles with the ^{12}C(^{12}C, ^{8}Be)^{16}O reaction. A ^{12}C beam of 62.6 MeV from the 88-inch cyclotron was used to irradiate carbon targets of 150-μg/cm^2 thickness. Particles were detected in two 4-counter telescopes consisting of silicon detectors whose thicknesses were 80μ, 50μ, 500μ, and 500μ. The fourth detector rejected particles which penetrated it. A particle identifier[5] was fed by the first three detectors. Our electronics were as described in Ref. 5, except for one major addition: Scattered ^{12}C ions, which were stopped in the first detector, saturated the linear amplifier, thus causing pileup problems. Saturating pulses were detected and eliminated by using an updating discriminator whose output inhibited the master gate of the identifier electronics for 4 μsec—the baseline recovery time of the linear amplifier.

Only a small fraction of the ^{8}Be particles emitted into its solid angle were detected by our setup. The two breakup alphas are confined to a cone (in the laboratory system) which is centered around the velocity vector $\vec{v}_8$ of the ^{8}Be which forms an angle γ given by

$$\gamma = 2 \arcsin \left(\frac{v_r}{2v_8}\right) .$$

Here v_r is the relative velocity of the two breakup alphas. This equation may be rewritten as

$$\gamma = 2 \arcsin \sqrt{\frac{Q}{E_8}} ,$$

where Q is the breakup Q value of the ^{8}Be ground state and E_8 is the laboratory energy of the ^{8}Be. For $E_8 = 40$ MeV we obtain $\gamma = 5.6°$. Our rectangular collimators sub-

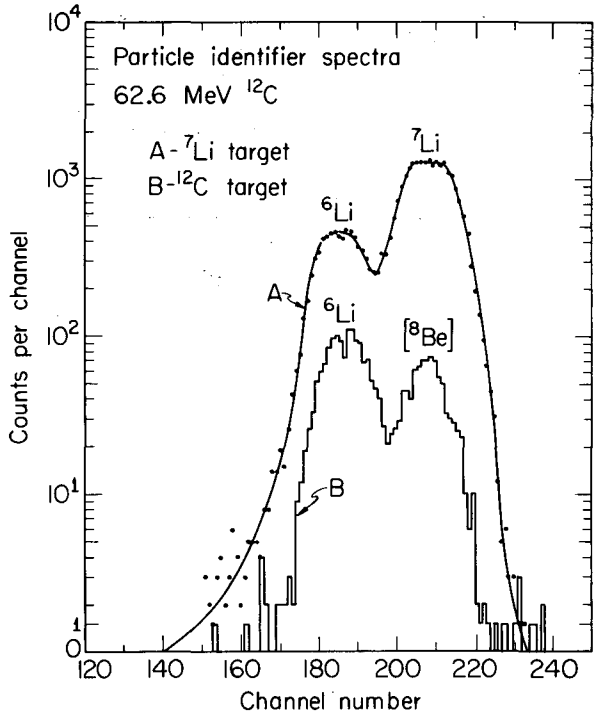

Fig. 1. Particle-identifier spectra showing the ^{6}Li and ^{7}Li events recorded at 14° from a ^{7}Li target (curve A) and the ^{6}Li and ^{8}Be events recorded at 24° from a carbon target (histogram B). (XBL 721-2174)

tended angles of 0.85° horizontally and 2.4° vertically. Hence, a ^{8}Be(g. s.) whose c. m. velocity vector $\vec{v}_8$ is within the solid angle of one of our telescopes has only a small probability that both of its breakup alphas fall inside the collimator. For our geometry we have calculated[6] a detection efficiency of about 1% for E_8 = 40 MeV. In contrast, our efficiency for detecting ^{8}Be* in its first excited state is calculated to be 1/25th as large, so that the "shadow-peaks" which usually occur in the spectra of heavy-ion reactions are much reduced.

Copious amounts of ^{6}Li and ^{7}Li reaction products formed by bombarding a 300-μg/cm^2 ^{7}Li target with a ^{12}C beam were used to calibrate the particle identifiers. Figure 1 presents particle identification spectra observed while irradiating first a ^{7}Li target (curve A) and second a ^{12}C target (curve B). The peak labelled ^{7}Li contains only genuine ^{7}Li events, which is verified by the corresponding energy spectrum in the upper half of Fig. 2, where only transitions to ^{12}C final states produced by the ^{7}Li(^{12}C, ^{7}Li)^{12}C reaction are seen.

The particle identification spectrum labelled (curve B) in Fig. 1 was produced by irradiating a carbon target and observing the reaction

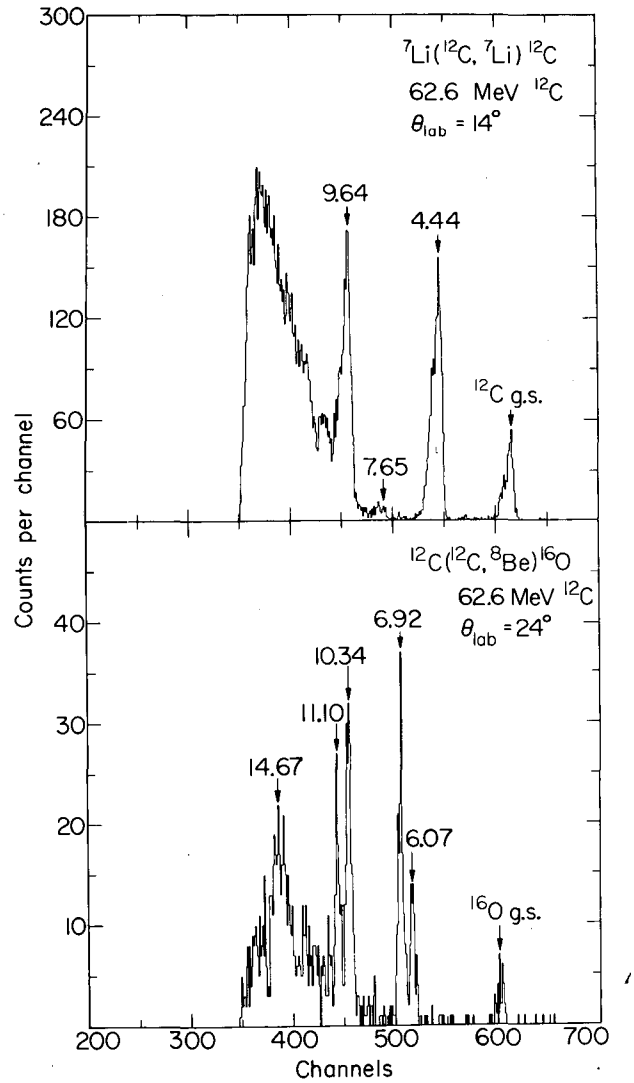

Fig. 2. The upper half shows the energy spectrum of ^{7}Li(^{12}C, ^{7}Li)^{12}C and corresponds to the ^{7}Li-peak of curve A in Fig. 1. The lower half is the spectrum of ^{12}C(^{12}C, ^{8}Be)^{16}O and corresponds to the [^{8}Be]-peak of histogram B in Fig. 1. The excitation energies given on the lower half of the figure are determined from this experiment. See also Table I. (XBL 721-2176)

products at θ(lab) = 24°. Due to the kinematics and the low-energy detector cutoff, no ^{7}Li's from the ^{12}C(^{12}C, ^{7}Li)^{17}F reaction could be observed at this angle. Thus the peak in curve B appearing in the ^{7}Li position contains only ^{8}Be-breakup events, and all the peaks in the corresponding energy spectrum in the lower half of Fig. 2 result from the ^{12}C(^{12}C, ^{8}Be)^{16}O reaction. The observed resolution was 500 keV FWHM, with the largest contributions arising

Table I. Summary of the results of the present experiment. The first two columns list the known states in ^{16}O according to Ref. 9. The third column gives the excitation energies which we determined for the observed states. The fourth column gives the observed cross sections as explained in the text.

States in ^{16}O according to Ref. 9		States in ^{16}O observed in the present experiment at $\theta_{(lab)} = 14°$	
E_x (MeV)	J^π	E_x (MeV)[b]	$(d\sigma/d\Omega)^a_{observed}$ (μb/sr)[c]
g.s.	0^+	-0.03	1.5
6.0502	0^+	6.07	8.2
6.13066	3^-		
6.9188	2^+	6.92	6.6
7.11867	1^-		
8.8717	2^-		
9.597	1^-		
9.8469	2^+		
10.353	4^+	10.34	16.0
10.952	0^-		
11.080	3^+		
11.096	4^+	11.10	7.6
11.26	0^+		
(11.44)	3^-		
⋮			
12.528	2^-		
⋮			
14.39	4^+		
(14.53)			
14.82	6^+	14.67	18.0
14.922	4^+		
⋮			
16.218	1^+		
16.23	6^+	16.27	13.0
16.30	$0(^-)$		
16.407	2^+		
⋮			

[a] Cross sections for populating ^{16}O final states are given in the c.m. system and are averages of several measurements.

[b] Errors are quoted in the text.

[c] The cross sections could be uniformly in error as much as 50%.

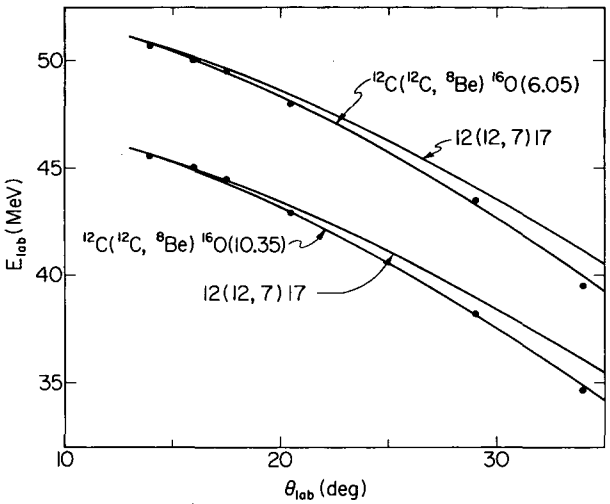

Fig. 3. Kinematics of the $^{12}C(^{12}C, ^{8}Be)^{16}O$ reaction as compared with the kinematics of a hypothetical reaction 12(12, 7)17. See explanation in the text. (XBL 721-2194)

from the target thickness (350 keV) and the kinematical spread (220 keV).

In order to provide further evidence that the observed reaction is the (^{12}C, ^{8}Be) reaction, we studied the energies of several ^{8}Be peaks as a function of the scattering angle. For two peaks the result is given in Fig. 3, along with two curves in each case: a) the kinematics of the reaction $^{12}C(^{12}C, ^{8}Be)^{16}O$ and b) the kinematics of a hypothetical reaction $^{12}C + ^{12}C \rightarrow$ mass 17 + mass 7 with the Q value adjusted to match both curves at the laboratory angle of 14°. The experimental points prove that we are indeed detecting mass-8 particles.

Provided the peaks in our spectra are due to the population of single states, we can determine their excitation energy to ±70 keV. In Table I we give the excitation energies and the cross sections at θ(lab) = 14° for the states in ^{16}O as determined from our experiment and compare them to the compilation of states from Ref. 7. The cross sections are given as $(d\sigma/d\Omega)_{observed}$, which is the number we measured, and does not include the correction for the ^{8}Be detection efficiency.

It appears that (^{12}C, ^{8}Be) is a "good" α-transfer reaction in that the four nucleons are transferred as a 0^+-cluster. This is apparent from comparing the (^{12}C, ^{8}Be) spectra to those from (^{7}Li, t), an example of an α-transfer reaction,[8] and to those from (^{10}B, ^{6}Li), an example of four-nucleon transfer without any pronounced selectivity.[9]

We do not observe the 2^- unnatural states at 8.87 and 12.53 MeV. Hence, it seems that only natural parity states are excited, as should be the case for an α-transfer reaction.

Our spectra are dominated by the rotational band based on the 6.050 MeV (0^+) state,[10] which contains the 6.919(2^+), 10.353(4^+), and 16.24(6^+) states; they have essentially 4p-4h character (see e. g., the introductory remarks of Ref. 11 and the references given therein). In addition to this band we observe two strong states:
(a) the 11.096(4^+) state, which shows up strongly in $^{14}N(\alpha, d)^{16}O$ and therefore was suggested[12] to have predominantly 2p-2h character;
(b) a broad (800 keV FWHM) state or a group of states at 14.73 MeV which probably contains the 6^+ state at 14.79 MeV observed in elastic α scattering[13] as well as in [12] $^{14}N(\alpha, d)^{16}O$. The population of the broad 5^- state at 14.6 MeV reported in Ref. 14 is unlikely, since it would be a member of the odd-parity, 3p-3h rotational band [containing the 9.6(1^-), 11.63(3^-), 14.6(5^-), and 20.8(7^-) states], and we do not find any evidence for the first two members of this band. These results are very similar to previous ones from the $^{12}C(^{7}Li, t)^{16}O$ reaction,[8,15] except that in the (^{12}C, ^{8}Be) reaction the 11.096(4^+) state is seen more strongly. Also, we do not know the relative population of the 6.050(0^+) and 6.131(3^-) states, since they are not resolved.

The four-nucleon transfer reaction[9] $^{12}C(^{10}B, ^{6}Li)^{16}O$ populates all the above-mentioned states, as well as states of comparable intensity at 8.872(2^-), 9.847(2^+), 13.258(3^-), 15.2, and 15.6. MeV.

In summary, this qualitative discussion suggests that (^{12}C, ^{8}Be) is a new α-transfer reaction.

References

1. K. Bethge, Ann. Rev. Nucl. Sci. 20, 255 (1970).

2. G. C. Deka and K. C. Deka, Can. J. Phys. 47, 227 (1969). (This artical contains references to the original identification of ^{8}Be in emulsions). J. J. Daetwyler, G. Czapek, and E. Jeannet, Helv. Phys. Acta 41, 251 (1968).

3. R. E. Brown, J. S. Blair, D. Bodansky, N. Cue, and C. D. Kavaloski, Phys. Rev. 138, B1394 (1965). P. Chevallier, F. Scheibling, G. Goldring, I. Plesser, and M. W. Sachs, Phys. Rev. 160, 827 (1967).

4. E. Segrè, Nuclei and Particles, (W. A. Benjamin, New York, 1965), p. 24.

5. G. Butler, J. Cerny, S. W. Cosper, and R. L. McGrath, Phys. Rev. 166, 1096 (1968).

6. H. L. Harney and G. J. Wozniak, FORTRAN-program EFFI, available on request.

7. F. Ajzenberg-Selove, Nucl. Phys. A166, 1 (1971).

8. F. Pühlhofer, H. G. Ritter, R. Bock, G. Brommundt, H. Schmidt, and K. Bethge, Nucl. Phys. A147, 258 (1970), and references therein.

9. K. D. Hildenbrand, H. H. Gutbrod, W. von Oertzen, and R. Bock, Nucl. Phys. A157, 297 (1970).

10. E B. Carter, G. E. Mitchell, and R. H. Davis, Phys. Rev. 133, B1421 (1964).

11. G. Bassani, G. Pappalardo, N. Saunier, and B. M. Traore, Phys. Letters 34B, 612 (1971).

12. M. S. Zisman, E. A. McClatchie, and B. G. Harvey, Phys. Rev. C2, 1271 (1970).

13. T. R. Ophel, S. D. Cloud, Ph. Martin, J. M. Morris, Phys. Letters 32B, 101 (1970).

14. K. P. Artemov, V. Z. Goldberg, I. P. Petrov, V. P. Rudakov, I. N. Serikov, and V. A. Timofeev, Phys. Letters 37B, 61 (1971).

15. J. R. Comfort, G. C. Morrison, B. Zeidman, and H. T. Fortune, Phys. Letters 32B, 685 (1970).

AN EXPLORATION OF THE (HEAVY-ION, ^{6}He) REACTION AS A TECHNIQUE FOR MASS MEASUREMENTS

G. J. Wozniak, K. H. Wilcox, H. L. Harney, and J. Cerny

Recently, the feasibility of using heavy-ion-induced reactions such as ^{40}Ca(^{12}C, t)^{49}Mn to measure the masses of unknown $T_z = (N-Z)/2 = -1/2$ nuclei in the $1f_{7/2}$ shell, has been reported.[1] We have attempted to extend this approach and have investigated the (^{12}C, ^{6}He) and (^{16}O, ^{6}He) reactions on ^{40}Ca as a possible technique for measuring the masses of the unknown $T_z = -1$ nuclei ^{46}Cr and ^{50}Fe. No masses of nuclides in this $A = 4n + 2$ series are known above ^{42}Ti.

A $^{12}C^{3+}$ beam from the 88-inch cyclotron with an intensity of 40 nA was used to irradiate self-supporting ^{7}Li(99.9%), and carbon targets of 500-, 125-, and 75-$\mu g/cm^2$ thickness respectively. The beam energy was measured with a high-resolution analysis magnet[2] and found to be 62.62 ± 0.03 MeV.

Two similar counter telescopes and electronic systems were simultaneously employed. The telescopes were mounted in an 18-inch diameter scattering chamber at 14° on opposite sides of the beam. Four phosphorus-diffused silicon transmission detectors were used in each telescope; signals from the fourth detector were used to reject particles traversing the first three. After a fast coincidence (50 nsec resolving time) among the first three detectors restricted the origin of all allowed events to a single beam burst, two particle identifications were performed and compared by using the signals from the two successive differential-energy loss detectors (an 80-μ $\Delta E2$ and a 56-μ $\Delta E1$) and the third 450-μ E detector.[3] Events in each system with acceptable identifications were sent via an analog-to-digital converter system to an on-line PDP-5 computer. Four parameters—the energy losses ($\Delta E2$, $\Delta E1$) in each of the first two transmission detectors, the total energy (E_T) deposited in the first three detectors, and the particle identification (PI)—were recorded for each event. Following the experiment each ^{6}He event was analyzed in detail.

Both counter telescopes subtended a solid angle of ~1 msr and were entirely enclosed by a thick tantalum shield, except for a collimated 120- × 200-mil entrance window. This shield was of critical importance in eliminating large high-frequency oscillations in our amplifiers. These oscillations were generated by the shower of low-energy electrons produced when the heavy-ion beam irradiated the target.

We monitored the elastic and inelastic scattering of the heavy ions to ensure constant beam energy (and beam type). Signals from the $\Delta E2$ detector were split after the preamplifier and one signal was fed into a $\Delta E2$-singles amplifier which had a dynamic range of 70 MeV. Since the cyclotron used carbon dioxide as its source gas and because $^{12}C^{3+}$ and $^{16}O^{4+}$ have an almost identical charge-to-mass ratio, mon-

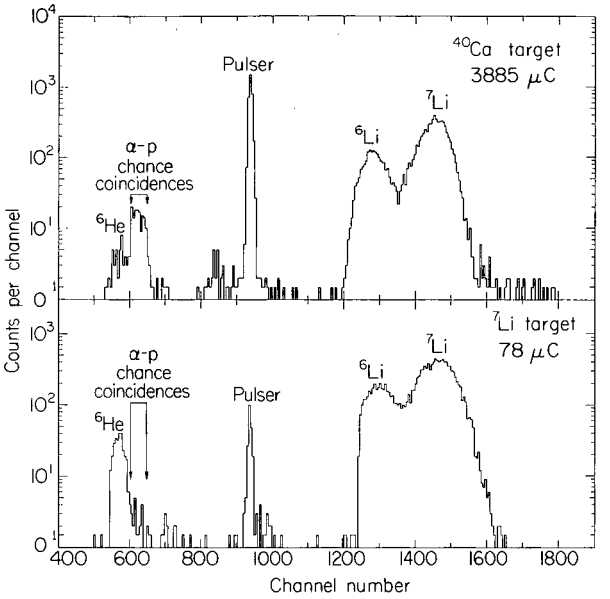

Fig. 1. Particle-identification spectra from 62.62-MeV ^{12}C-induced reactions on targets of ^{40}Ca (top) and ^{7}Li (bottom). The integrated charges given in the figure are based on fully stripped carbon ions. (XBL 721-2188)

itoring the beam energy was also a way to prove the beam was $^{12}C^{3+}$.

The reaction $^{7}Li(^{12}C, ^{6}He)^{13}N$ was used to calibrate the particle identifiers since it possesses a relatively high cross section (~3.6 μb/sr). Figure 1 presents particle-identification spectra from ^{12}C-induced reactions on the ^{7}Li and ^{40}Ca targets. Pileup from α-particle-proton chance coincidences falls just above the ^{6}He region in the identifier spectrum.[3] The calculated position of the α-p chance-coincidence peak is identical with the observed position and the α-p chance-coincidence rate from the ^{40}Ca target agrees within a factor of 2 with the one calculated from measured values of the α-particle and proton counting rates in our detector systems. Under our conditions, the ratio of α-p chance coincidence to ^{6}He events from the ^{40}Ca target is ~3.5/1. However, their two identifier peaks are well enough resolved that one can eliminate most of the α-p chance coincidences by requiring tight identification limits based on the ^{6}He reference peak from reactions on the Li target. The identifier peak labelled ^{7}Li in the top half of the figure includes a substantial fraction of ^{8}Be events (see the preceding paper in this Annual Report).

Lithium-6 and -7 data from the $^{7}Li(^{12}C, ^{6}Li)^{13}C$, $^{7}Li(^{12}C, ^{7}Li)^{12}C$ and $^{12}C(^{12}C, ^{6}Li)^{18}F$ reactions were used to establish an energy calibration. Our experimental resolution as observed from ^{18}F states was ~400 keV. In addition, the ^{18}Ne ground state populated by the $^{12}C(^{12}C, ^{6}He)$ reaction and the unresolved 3.51- and 3.55-MeV states in ^{13}N from the $^{7}Li(^{12}C, ^{6}He)$ reaction were used as calibration points (Fig. 2, b, and c). Using these energy calibrations and the expected mass-excess of ^{46}Cr of -29.53 ± 0.05 MeV, which was obtained from Coulomb energy systematics and theoretical calculations,[4] we have indicated the predicted position of the ^{46}Cr ground state in Fig. 2a. No evidence of population of the ^{46}Cr ground state is found in these data. The absence of background in the region of the predicted position of the ^{46}Cr ground state allows one to set an upper limit of 60 nb/sr for the differential cross section. The locations of the first three excited states of ^{46}Cr are also predicted, based on states in its mirror ^{46}Ti. Several events are present in the spectrum where one would expect the analogue of the second excited (4^+) state

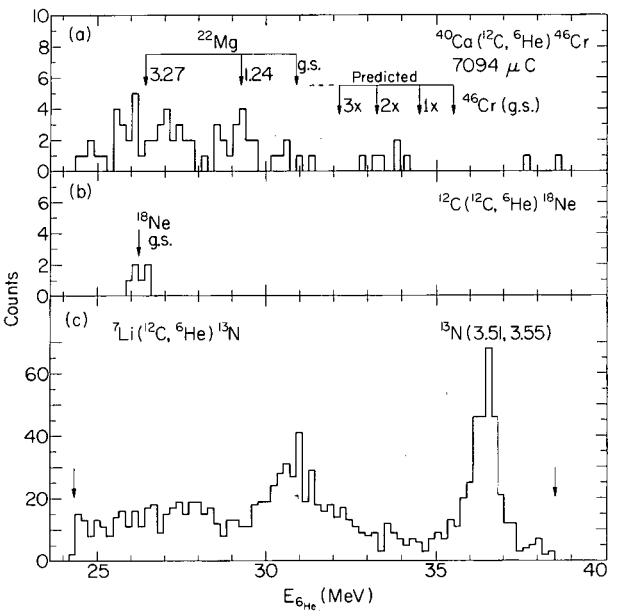

Fig. 2(a). A ^{6}He energy spectrum arising from the bombardment of ^{40}Ca by 62.62-MeV ^{12}C at 14° (lab). Energies given in MeV. The integrated charge shown assumes fully stripped carbon ions.

(b). A ^{6}He-energy spectrum from the $^{12}C(^{12}C, ^{6}He)^{18}Ne$ reaction at 14°. Possible transitions to the ^{18}Ne(1.89-MeV) state lie quite near the telescope cutoff.

(c). A ^{6}He energy spectrum from the ^{7}Li $(^{12}C, ^{6}He)$ ^{13}N reaction at 14°. The arrows indicate the region over which ^{6}He particles could be observed.

(XBL 721-2189)

in ^{46}Ti. Furthermore, one sees transitions to the ^{22}Mg ground state and several of its excited states from the (^{12}C, ^{6}He) reaction on oxygen target impurities.

The same detection system and method of analysis were used in an attempt to observe the ^{40}Ca(^{16}O, ^{6}He)^{50}Fe reaction. A 65.0-MeV $^{16}O^{3+}$ beam with an intensity of ~10 nA was used to irradiate a 100-μg/cm^2 natural calcium target on a 25-μg/cm^2 carbon backing. The ^{7}Li(^{16}O, ^{6}He)^{17}F reaction was used to calibrate the particle identifier. No events were observed at the predicted location of the ^{50}Fe ground state, for which the mass-excess is expected[4] to be - 34.49 ± 0.07 MeV. The upper limit for the differential cross section populating the ^{50}Fe ground state was determined to be 300 nb/sr.

These results demonstrate that while the ^{12}C(^{12}C, ^{6}He)^{18}Ne reaction has an observable cross section ($d\sigma/d\Omega$ = 1.2 μb/sr) at 14°(lab), the (^{12}C, ^{6}He) and (^{16}O, ^{6}He) reactions on ^{40}Ca have very low cross sections. Therefore, a large increase in beam intensity and a corresponding utilization of a more effective subnanosecond pileup-rejection system will be required before these heavy-ion reactions can be used to produce T_z = -1 nuclei in the $f_{7/2}$ shell.

References

1. J. Cerny, C. U. Cardinal, K. P. Jackson, D. K. Scott, and A. C. Shotter, Phys. Rev. Letters 25, 676 (1970).

2. A. D. Bacher, E. A. McClatchie, M. S. Zisman, T. A. Weaver, and T. A. Tombrello, Nucl. Phys. A181, 453 (1972).

3. G. W. Butler, J. Cerny, S. W. Cosper, and R. L. McGrath, Phys. Rev. 166, 1096 (1968).

4. M. Harchol, A. A. Jaffe, J. Miron, I. Unna, and J. Zioni, Nucl. Phys. A90, 459 (1967).

THE (α,2α) REACTION ON ^{44}Ca AND ^{40}Ca AT E_α = 90 MeV

J. D. Sherman and D. L. Hendrie

Preliminary results from the (α, 2α) reaction on the ^{40}Ca and ^{44}Ca isotopes are reported here. These targets have been chosen primarily because of the questions concerning the α-particle structure of these nuclei. Previous α knock-out reactions on targets with even a rather low density of states in the low-energy part of the residual nucleus spectrum have been bothered by poor energy resolution.[1] A major concern of this work is to maintain sufficient energy resolution so that low-lying residual states would be unambiguously resolved.

The 2α-coincident experiment was done with a 90-MeV α beam from the 88-inch cyclotron. Symmetric coplanar geometry has been used for all measurements. Figure 1 displays the pertinent kinematic variables. An independently movable counter was constructed for the 36-inch chamber which previously had only one independent remotely-controlled θ motion. The symmetric angles 25° - 25° to 70° - 70° can now be attained. The solid angles for the coincident detectors were nearly the same and equaled approximately 1.5 msr. This corresponded to a detector angular acceptance of 1.2°, assuming a point beam spot. The ^{40}Ca target thickness was 0.452 mg/cm^2 and that of ^{44}Ca was 0.390 mg/cm^2. Reaction particles were detected in identical counting systems composed of a 250-μm phosphorous-diffused transmission detector and a 3-mm Li-drifted Si stopping detector. The energy loss in the transmission detector was used to admit only Z = 2 particles into the coincident array. If all logical requirements are satisfied, the two summed energies and a TAC logic signal are transmitted to an on-line PDP-5 computer through a multiplexer-ADC system.[2]

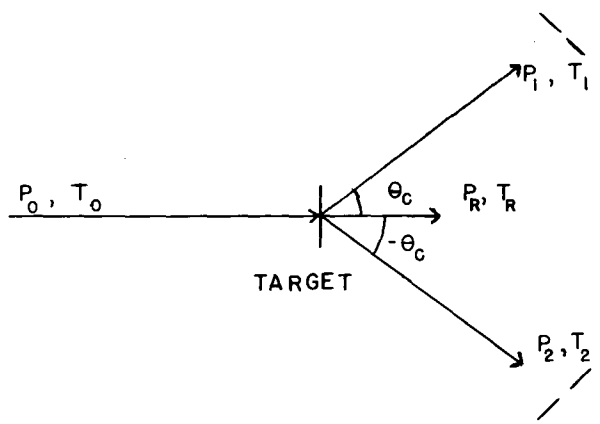

Fig. 1. Geometry and kinematic variables which are appropriate for a symmetric, coplanar experiment. (XBL 722-340)

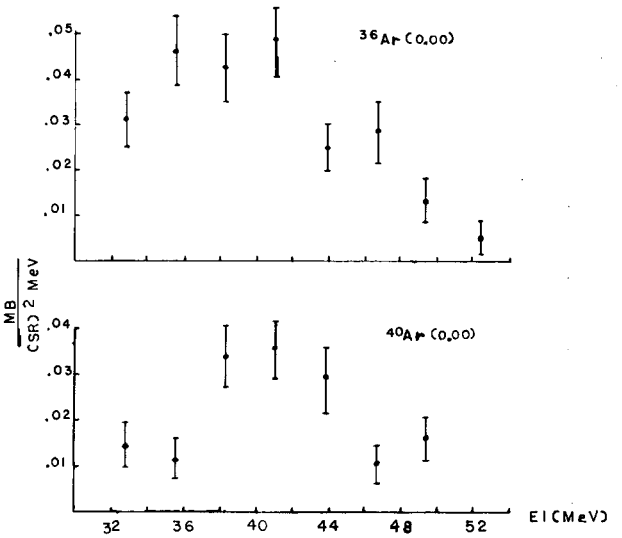

Fig. 2. Triple differential cross sections for the ^{36}Ar and ^{40}Ar ground state kinematic bands. (XBL722-344)

This experimental technique has yielded kinematic lines in the E1 + E2 vs E1 arrays of approximately 250 keV FWHM in the ^{36}Ar and ^{40}Ar residual nuclei. The E1 projections of transitions to ^{36}Ar and ^{40}Ar ground states at $\theta_c = 35°$ are given in Fig. 2. The lack of sharp peaks in this energy correlation indicates the absence of sequential mechanisms in this energy region, while the broad peak is characteristic of a direct reaction or quasi-elastic mechanism. Figure 3 illustrates the projection of the kinematic lines onto the summed energy axis. The various peaks correspond to states in residual nuclei characterized by the energy $T_1 + T_2 = T_0 + Q - T_R$. This energy notation is summarized in Fig. 1 Figure 3 indicates that oxygen is a serious contaminant in the Ca targets. Figure 3 also indicates very little excitation strength of ^{40}Ar excited states whereas ^{36}Ar excited states clearly stand out. These spectra have been analyzed up to approximately 5 MeV excitation. Relatively few Ar states have been identified since the random-chance background makes the identification of weak states difficult.

The results of integrating the E1 projection over the E1 energy range shown in Fig. 2 for peaks associated with ^{36}Ar and ^{40}Ar is given in Table I. The ground state transition to ^{36}Ar is seen to have slightly greater strength than the transition to the ^{40}Ar ground state. The major difference of transition strength lies in the population of excited states. Table I shows the low-lying excited states of ^{36}Ar are much more strongly populated than the corresponding region in ^{40}Ar. This indicates that in a cluster model, ^{40}Ca has significant parentage in ^{36}Ar [(excited state)+α] whereas most of the parentage in such a model for ^{44}Ca is in [^{40}Ar (g. s.)+α]. A review of parentage concepts in clustering has recently been published.[3] A unique assignment of excitation energy to a peak in ^{36}Ar at approximately 4.2 MeV has not been made, since there are several known levels[4] in ^{36}Ar near this energy. The last line in Table I provides a sum of the experimentally observed transition strengths of all observed ^{36}Ar states divided by a similar sum in ^{40}Ar. The ratios are given as a function of correlation angle. All errors are

Table I. Summary of triple differential cross sections integrated over the quasi-elastic region as a function of the correlation angle.

Residual nucleus	E^* (MeV)	$\int_{32.8}^{49.5} \left(\frac{d^3\sigma}{d\Omega_1 d\Omega_2 dE_1}\right) dE_1 \left(\frac{mb}{(SR)^2}\right)$ 25°	35°	45°
^{36}Ar	0.00	0.696±0.160	0.623±0.117	0.070±0.017
	1.97	0.663±0.146	0.207±0.063	0.039±0.023
	~4.2	0.423±0.113	0.158±0.055	0.012±0.007
^{40}Ar	0.00	0.652±0.157	0.383±0.095	0.063±0.027
	2.13	0.075±0.044	0.041±0.025	
$\frac{\Sigma^{E^*} {}^{36}\mathrm{Ar}(E^*)}{\Sigma^{E^*} {}^{40}\mathrm{Ar}(E^*)}$		2.45 ± 0.64	2.33 ± 0.64	1.92 ± 0.94

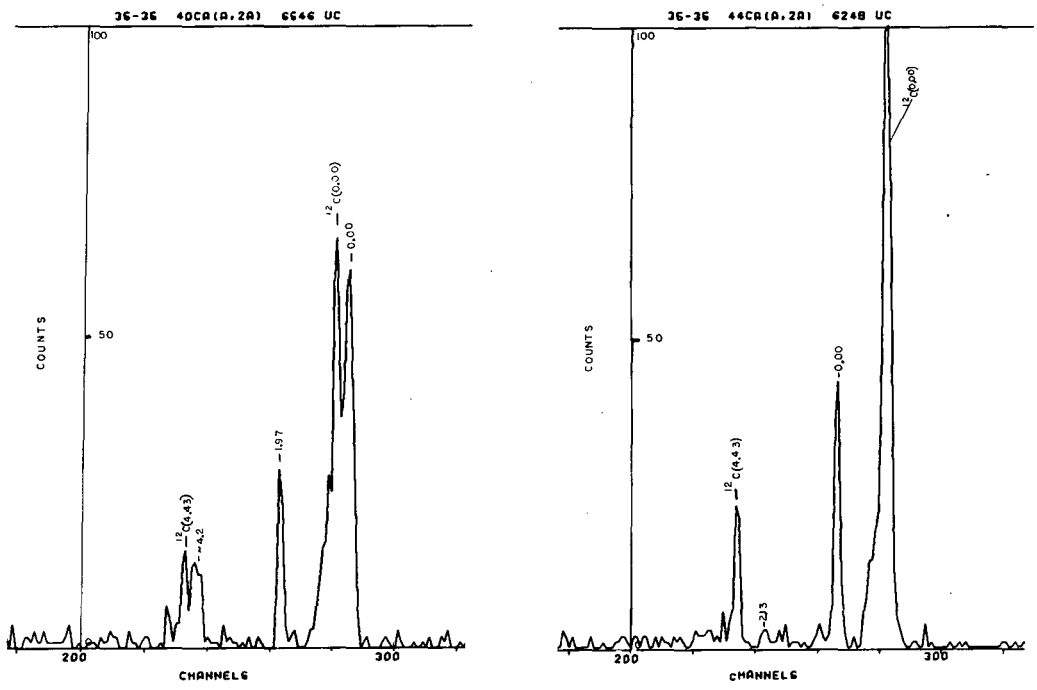

Fig. 3. Projection of kinematic bands observed in the $^{40}Ca(\alpha, 2\alpha)$ and $^{44}Ca(\alpha, 2\alpha)$ experiments onto the summed energy axis.
(XBL 722-343)

due to statistics. These results suggest that ^{40}Ca may contain a factor of approximately 2.2 more clusters than the ^{44}Ca nucleus.

The enhanced elastic scattering of $^{40}Ca(\alpha, \alpha_0)$ over $^{44}Ca(\alpha, \alpha_0)$ in the back hemisphere ($\theta_{lab} > 90°$) has been given considerable attention in recent work.[5,6] One theory[5] contends that the enhanced elastic differential cross-sections in ^{40}Ca arises from a scattering factor that lies outside the average optical-model potentials which fit this mass region. This factor is hypothesized to a repulsive α-cluster scattering from four-nucleon clusters in the ^{40}Ca nucleus. The second interpretation[6] claims that certain high ℓ values ($\gtrsim$ 12) which would normally be absorbed in the nucleus and hence contribute to the imaginary part of the optical model (OM) are instead scattered in the elastic channel. This ℓ-dependent cutoff in the imaginary part of the OM occurrs for smaller ℓ-values in ^{40}Ca than in ^{44}Ca because of different (α,η) Q values for these targets. Hence, the $^{40}Ca(\alpha, \alpha_0)$ cross section is expected to be enhanced over $^{44}Ca(\alpha, \alpha_0)$. The $^{40\text{-}44}Ca(\alpha, 2\alpha)$ results suggest there is an enhancement of α clustering in ^{40}Ca compared to ^{44}Ca, but it remains to be seen if the observed relative magnitudes of the α clustering can account for the $^{40\text{-}44}Ca(\alpha, \alpha_0)$ anomalies.

Besides offering the possibility of answering questions concerning α clustering in nuclei, it is hoped that good resolution $(\alpha, 2\alpha)$ experiments at medium α energies will stimulate a better theoretical understanding of the reaction mechanism. Considerable effort in this direction has already taken place.[3]

References

1. R. D. Plieninger, W. Eichelberger, and E. Velten, Nucl. Phys. A137, 20 (1969); G. Igo, L. F Hansen, and T. J. Gooding, Phys. Rev. 131, 337 (1963).

2. L. B. Robinson, F. Gin, and F. S. Goulding, Nucl. Instr. Methods 62, 237 (1968).

3. Daphne F. Jackson, Advan. Nucl. Phys. 4, 1 (1971).

4. P. M. Endt and C. Van Der Leuen, Nucl. Phys. A105, 255 (1967).

5. N. C. Schmeing, Nucl. Phys. A142, 449 (1970); G. Gaul, H. Lüdecke, R. Santo, H. Schmeing, and R. Stock, Nucl. Phys. A137, 177 (1969).

6. K. A. Eberhard, Phys. Letters 33B, 343 (1970).

AN INTERPRETATION OF THE STRONG AND WEAK 0^+ STATES EXCITED IN THE $^{142}Ce(p,t)^{140}Ce$ AND $^{140}Ce(p,t)^{138}Ce$ REACTIONS

J. D. Sherman, B. G. Harvey, D. L. Hendrie, M. S. Zisman, and B. Sørensen*

One year ago we reported our first experimental results from a spectroscopic study of the ^{140}Ce and ^{138}Ce nuclei by the (p,t) reaction.[1] We were interested in testing the predictions of pair vibration theory[2,3] at the N=82 closed neutron shell. We observed certain deviations from the harmonic theory[2,3] as did other experimenters[4] who studied various target nuclei with $A \geq 90$ by the (p,t) reaction. These experiments were performed at or near a closed neutron shell. The experimental objections to the harmonic theory in these cases can, perhaps, be summarized in two statements: first, the theory does not always yield the correct Q values for the states under consideration; and secondly, the transition strength is often split among a number of 0^+ levels. However, it was recognized[5] that the pair vibration state whose $J^\pi = 0^+$ could mix with other nuclear states of the same spin-parity. Such a model was developed and theoretical calculations were carried out for the Zr isotopes.[5] The results indicated a better agreement between experiment and theory. We have applied this model to the Ce experiment,[6] and we now describe these results.

Experimental details and the triton spectra were presented earlier,[1] and we will not repeat that discussion. Levels of $J^\pi = 0^+$ were of primary interest for the comparison between experiment and theory. Fortunately, angular distributions of two-neutron pick-up reactions with transferred angular momentum $\vec{L}_t = 0$ are quite characteristic at our proton energy. In our case the angular momentum condition $\vec{J}_t = \vec{L}_t + \vec{S}_t$ with the $\vec{L}_t = 0$ value leads to an immediate J^π assignment for the final state. Five $J^\pi = 0^+$ assignments were made in ^{140}Ce on this basis for excitations up to 6.36 MeV. These differential cross sections are given in Fig. 1. Two $\vec{L}_t = 0$ angular distributions were found in ^{138}Ce up to 3.62 MeV excitation, and these are given in Fig. 2. The solid curves are two-nucleon DWBA calculations in which one normalization has been used. The normalization will be discussed in more detail below.

The proposed model provides a framework in which the anharmonic pair vibration[7] may couple with other nuclear excitations characterized by $J^\pi = 0^+$. Henceforth this model is referred to as a "coupled anharmonic" (c.a.) theory. It differs from the harmonic theory in two ways. First, anharmonic theory permits interaction between the basic quanta of harmonic theory.[2] This may change (p,t) transition strengths significantly, but generally does

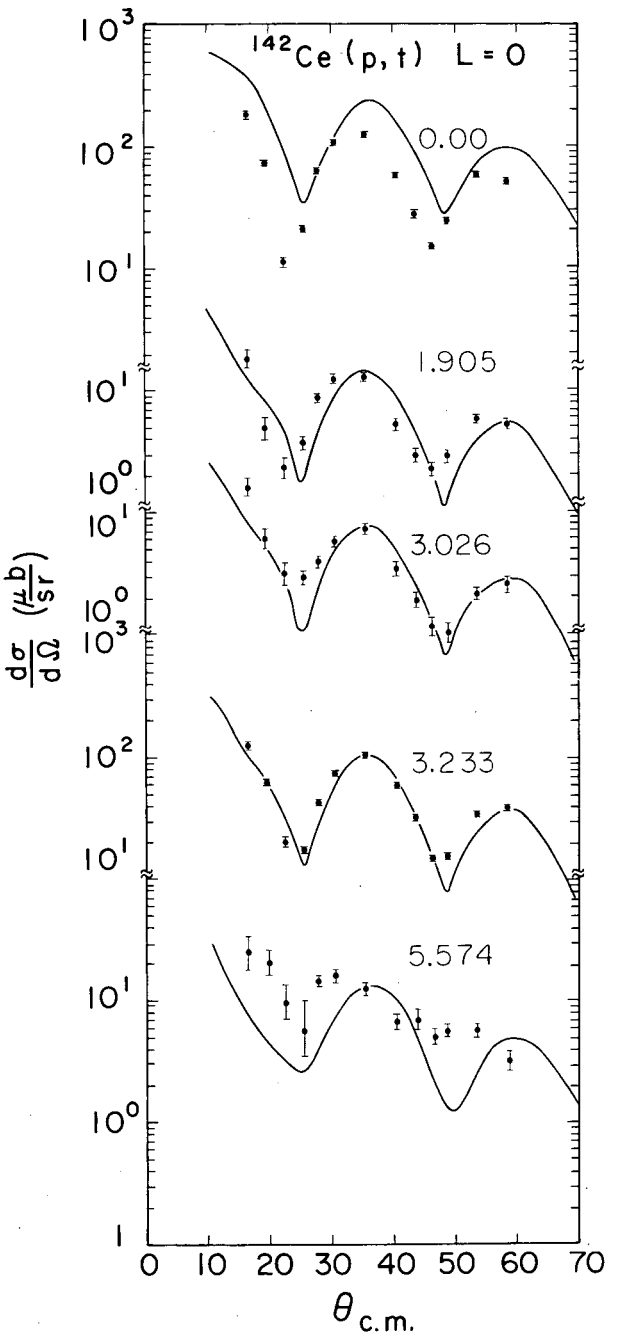

Fig. 1. Differential cross sections for $\vec{L}_t = 0$ transitions in ^{140}Ce. The solid curves are DWBA calculations. (XBL 7111-4825)

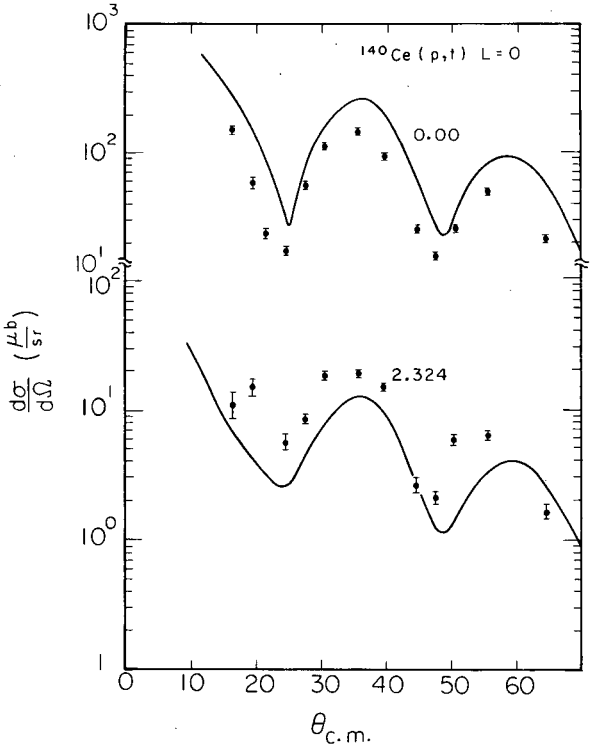

Fig. 2. Differential cross sections for $\vec{L}_t = 0$ transitions in ^{138}Ce. The solid curves are DWBA calculations. (XBL 7111-4826)

not affect excitation energies very much.[7] Second, the coupling part permits the wave function of a given nuclear state to be composed of fragments of a basis set, all of which have $J^\pi = 0^+$. This coupling may have the effect of making significant shifts away from the uncoupled harmonic (u. h.) theory's prediction for the pairing vibration energy.[5] The coupling also permits transitions to nuclear states which would have been forbidden in a one-step (p, t) reaction.[12] This coupling is then seen to dilute the transition strength to the pair vibration state, while allowing enhanced transitons to other nuclear states. This has often been the case experimentally.[4]

We shall now give a brief discussion of the basis set alluded to in the previous paragraph. Figure 3 provides a compact summary of all the components in the basis set. One component is the anharmonic pair vibration which is given the notation (0_-0_+). It's excitation energy is approximately 3.9 MeV. The ground state of ^{142}Ce has the notation (0_+) while the ^{138}Ce(g.s.) is noted by (0_-). Spin-parity 2^+ states in ^{138}Ce and ^{142}Ce at 0.796 and 0.64 MeV excitation, respectively, are given the notations (2_-) and (2_+). These can couple to give a multiplet of states in ^{140}Ce with J = 0 to 4 at $E_x = 5.33$ MeV in the u. h. model.[2] In the c. a. theory, a strong splitting between the (0_-0_+) and $(2_-2_+)_{0^+}$ components brings a main component of theoretical 0^+ excitation strength into energetic agreement with the experimentally observed 0^+ state at 3.23 MeV.[6]

The two multiple phonon states $(2^+ \otimes 2^+)_{0^+}$ and $(3^- \otimes 3^-)_{0^+}$ are also components of the basis set. These are given the notation $(2^2_{J=0})$ and $(3^2_{J=0})$ in Fig. 3. The one-phonon multipole vibrations are given the notations (2) and (3). Their excitations (1.59 MeV and 2.46 MeV) are from an inelastic alpha scattering experiment.[8] Four proton states of two quasi-particle nature[5, 6] complete the basis set. These are given the notations (0_1), (0_2), (0_3), and (0_4).

The mixing amplitudes are then calculated by diagonalizing the Hamiltonian

$$H = H_{sp} + H_p + H_2 + H_3$$

in the basis set described above. H_{sp} is the single-particle part, H_p the pairing force,[7] and $H_\gamma (\gamma = 2, 3)$ the separable multipole forces. A summary of the theoretical and experimental results is given in Fig. 3. Experiment is normalized to the 3.23-MeV state in ^{140}Ce, which can be associated with the expected pairing vi-

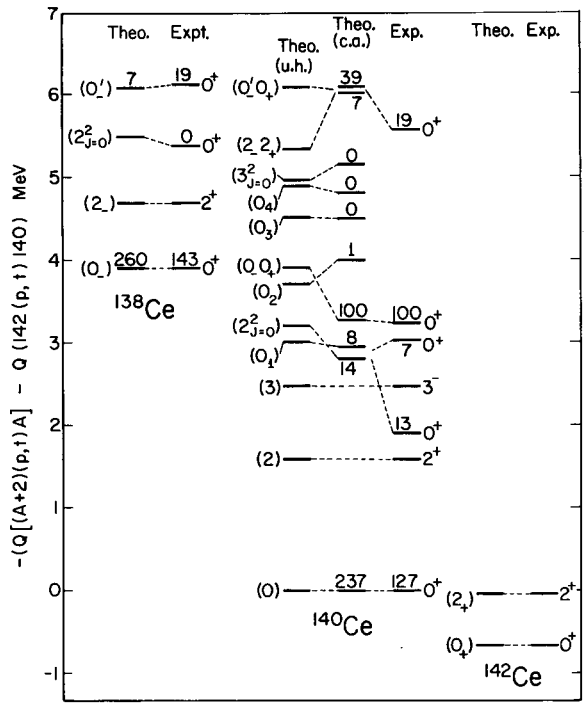

Fig. 3. Summary of calculated and experimental energies and (p, t) cross sections compared at the maximum near 35° for the selected states considered.
(XBL 719-4357)

bration.[9] Theory is similarly normalized with the optical model parameters for the DWBA calculations taken from the literature.[10,11] After carrying out this procedure, the theoretical ground state transitions are overestimated. These normalizations were reduced to 149 and 163 for ^{140}Ce(g.s.) and ^{138}Ce(g.s.), respectively, when a different set of optical model parameters still based on Refs. 10 and 11 were used. However, these parameters resulted in a poorer fit to the angular distributions. The dashed lines of Fig. 3 joining the u.h. theory to the c.a. theory indicate the dominant configurations of the c.a. wave functions.

The 0^+ states in ^{140}Ce at 5.57 MeV($0'_{-}0_{+}$) and in ^{138}Ce at 2.32 MeV ($0'_{-}$) may be understood as noncollective states predicted in Ref. 7. This is reasonable from an energetic viewpoint since the 2.32-MeV state in ^{138}Ce has very nearly the same energy above its ground state as the 5.57-MeV state in ^{140}Ce has above the pairing vibration.

Summarizing, the (p,t) reactions on the ^{142}Ce and ^{140}Ce isotopes have revealed, as in most previous cases for $A \geq 90$,[4] a $J^{\pi} = 0^+$ level structure that deviates significantly from harmonic p.v. theory. However, the described model calculation seems able to explain the redistribution of (p,t) strength from the harmonic p.v. to a number of low-lying states, to give a plausible reason for the large energy shift of the p.v., and for the occurrence of two 0^+ levels in ^{140}Ce(p,t) below the p.v. The 5.57-MeV state is likely to represent the first finding of a pair-analogue of a noncollective state that was predicted in Ref. 7.

Footnote and References

*The Niels Bohr Institute, University of Copenhagen, Denmark.

1. J. D. Sherman, B. G. Harvey, D. L. Hendrie, and M. S. Zisman, Nuclear Chemistry Division Annual Report for 1970, UCRL-20426, p. 82.

2. A. Bohr, Proc. Intern. Symp. on Nuclear Structure, Dubna, 1968; O. Nathan, ibid.

3. D. R. Bes and R. A. Broglia, Nucl. Phys. 80, 289 (1966).

4. J. B. Ball, R. L. Auble, and P. G. Roos, Phys. Letters 29B, 172 (1969); J. B. Ball, R. L. Auble, J. Rapaport, and C. B. Fulmer, Phys. Letters 30B, 533 (1969); K. Yagi, Y. Aoki, J. Kawa, and K. Sato, Phys. Letters 29B, 647 (1969); G. J. Igo, P. D. Barnes, and E. R. Flynn, Phys. Rev. Letters 24, 470 (1970).

5. Bent Sprensen, Nucl. Phys., in press.

6. J. D. Sherman, B. Sørensen, B. G. Harvey, D. L. Hendrie, and M. S. Zisman, submitted to Phys. Letters (LBL-227)

7. Bent Sørensen, Nucl. Phys. A134, 1 (1969).

8. E. T. Baker and R. S. Tickle, Phys. Letters 32B, 47 (1970).

9. K. Yagi, Y. Aoki, and K. Sato, Nucl. Phys. A149, 45 (1970).

10. F. D. Becchetti, Jr. and G. W. Greenlees, Phys. Rev. 182, 1190 (1969).

11. E. R. Flynn, D. D. Armstrong, J. G. Beery, and A. G. Blair, Phys. Rev. 182, 1113 (1969).

12. R. J. Ascuitto and N. K. Glendenning, Phys. Rev. C2, 1260 (1970).

ANOMALOUS BACKWARD α-SCATTERING

B. G. Harvey, D. L. Hendrie, J. Mahoney, J. Sherman, J. Steyaert, M. Zisman, G. Gaul,* R. Santo,* R. Stock,* and M. Bernas†

The elastic scattering of α-particles by ^{40}Ca, ^{39}K and ^{36}Ar at angles greater than 90° is anomalous in the sense that cross sections decrease more slowly than the exponential decay expected from diffraction scattering.[1-3] For ^{40}Ca, the phenomenon has been studied at energies from 18 to 42 MeV.

Two theories have been used to explain the anomalous scattering. According to the ℓ-dependent absorption model,[4,5] the absorption is reduced for partial waves exceeding the maximum angular momentum L_c that can be carried away by the dominant channels coupled to the elastic channel. The (α,n) reaction is considered to be the most important absorption channel. The different thresholds for (α,n) introduce an explicit isotope dependence.

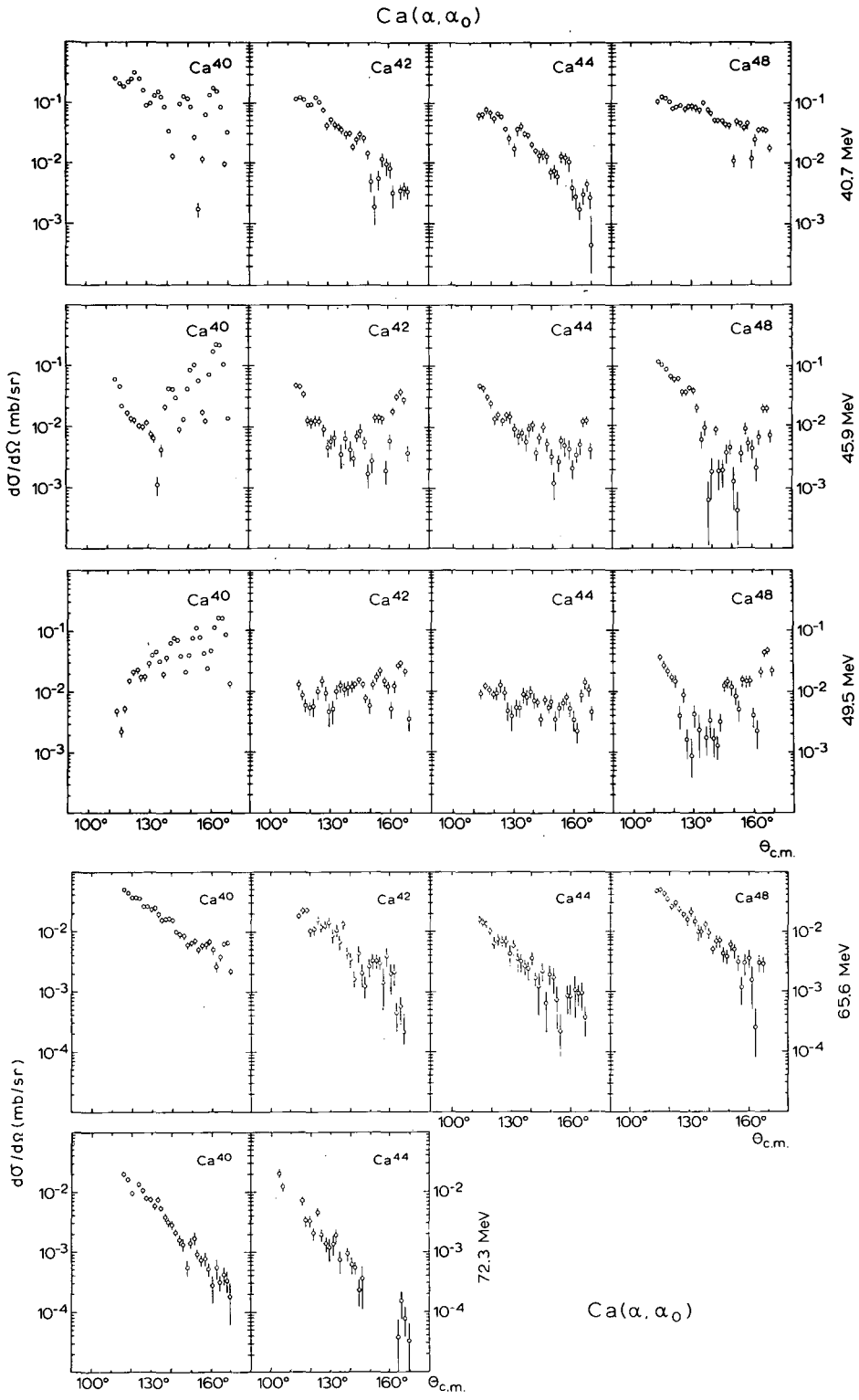

Fig. 1. Angular distributions for elastic scattering of α particles from $^{40,42,44,48}Ca$ at E_α = 40.7, 45.9, 49.5, 65.6, and 72.3 MeV.

(XBL 723-421)

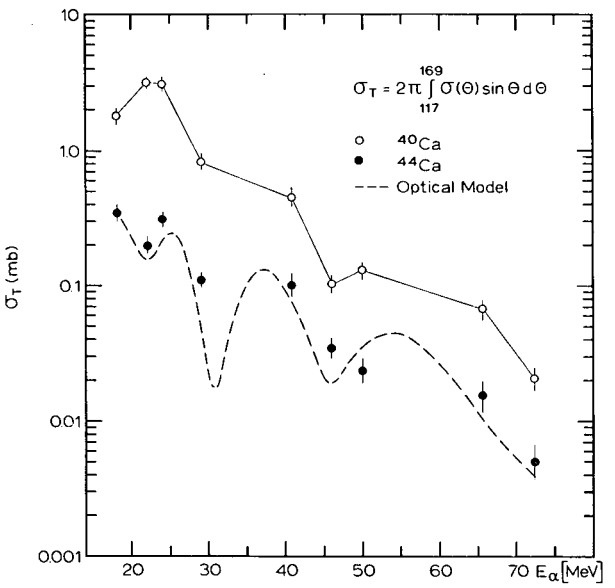

Fig. 2. Comparison of integrated backward-scattering cross sections for ^{40,44}Ca with optical model.

(XBL 723-342)

Good fits have been obtained for K, Ca and Ar at E_α = 24 MeV. The ℓ-dependent absorption effects should become less important, and finally disappear, at energies above about 40 MeV.

Alternatively, it has been suggested[2,6] that the anomalous scattering arises from an interaction between the α particle and a correlated T = 0 structure of four nucleons in the target. ^{40}Ca is known to have significant 4p-4h and 8p-8h components in its ground state.[7] The four (or eight) excited particles, mainly in the otherwise empty $f_{7/2}$ shell, are not hindered by the Pauli principle from adopting a highly correlated configuration that maximizes their mutual binding energy, but the neutrons already present in the $f_{7/2}$ shell in the Ca isotopes with A > 40 should hinder the formation of the correlated structure. Scattering should remain anomalously high in ^{40}Ca up to $E_\alpha \approx$ 100 MeV.

Backward scattering was measured at the 88-inch cyclotron for ^{40,42,44,48}Ca at five energies between 40.7 and 72.3 MeV. Above 49.5 MeV, the characteristic backward peaking in ^{40}Ca disappears (Fig. 1). Figure 2 shows the results of a quantitative test for the anomalous scattering. Optical model fits were made to the ^{44}Ca angular distributions. Experimental and optical-model cross sections were integrated from 117° to 160° (c. m.). Figure 2 shows that at all energies the ^{40}Ca cross section is 5 to 10 times greater than either ^{44}Ca or the optical model predictions.

The experimental results therefore favor the four-nucleon correlation model over the ℓ-dependent absorption, but clearly more experimental tests are required.

Footnotes and References

*Max Planck Institut für Kernphysik, Heidelberg.

†Institut de Physique Nucléaire, Orsay.

1. C R. Gruhn and N. S. Wall, Nucl. Phys. 81, 161 (1966).

2. G. Gaul, H. Lüdecke, R. Santo, H. Schmeing, and R Stock, Nucl. Phys. A137, 177 (1966).

3. A. Bobrowska, A. Budzanowski, G. Grotowski, L. Jarcyk, L. Miek, H. Niewodneczanski, A. Strzalkowski, and Z. Wrobel, Nucl. Phys. A126, 361 (1969).

4. R. A. Chatwin, J. S. Eck, D. Robson, and A. Richter, Phys. Rev. C1, 795 (1969).

5. D. Robson, Contributed paper to the Argonne Meeting on Heavy Ion Reactions (1971).

6. N. C. Schmeing, Nucl. Phys. A142, 449 (1970).

7. W. J. Gerace and A. M. Green, Nucl. Phys. A123, 241 (1969).

HIGH-SPIN PROTON STATES OBSERVED IN THE ^{90}Zr(a,t)^{91}Nb AND ^{92}Mo(a,t)^{93}Tc REACTIONS AT 50 MeV*

M. S. Zisman and B. G. Harvey

In recent years there have been many studies of proton configurations in the N = 50 nuclei ^{91}Nb and ^{93}Tc using the (^{3}He, d) reaction.[1-6] The states expected in proton transfer to ^{90}Zr and ^{92}Mo are $g_{9/2}$, $g_{7/2}$, $d_{5/2}$, $d_{3/2}$, $s_{1/2}$, and possibly $h_{11/2}$. The (^{3}He, d) reaction, however, preferentially populates the lower-angular-momentum states (i.e., ℓ = 0, 2) and

Table I. Levels observed in the $^{90}Zr(\alpha, t)^{91}Nb$ reaction at 50 MeV.

No.	(α, t) Levels observed[a] (MeV)	(α, t) Intensity[b] (mb)	$(^3He, d)$ Levels observed[c, d] (MeV)	$(^3He, d)$ ℓ_p[d]	$(^3He, d)$ C^2S[d]	^{91}Mo(g. s.)decay levels observed[e] (MeV)
1	0.0	3.441	0.0	4	0.918	---
2	(0.103)[f]	0.144	0.103	1	0.430	
3	1.29	0.038[g]	1.31	1	0.048[h]	
						1.581
4	1.60	0.073	1.60	1	0.078[h]	1.637
						1.791
5	1.82	0.069[g]	1.84	3	0.058[h]	
6	1.95 ± 0.04	Weak	1.96	2[h]	0.014[h]	
7	2.30	0.043[i]	2.34	1	0.017[h]	
8	2.39 ± 0.03	Weak				(2.391)[j]
9	2.53	0.032[i]				2.531
10	2.61	0.023[k]	2.62[l]		Weak[l]	2.631
						2.792
11	2.77	0.012[k]				
12	2.90	0.074	2.92[l]		Weak[l]	
13	3.01	0.036[m]				3.028
			3.07	2	0.035	
14	3.12 ± 0.04	Weak	3.11			3.149
						3.187
15	3.37	0.218	3.36	2	0.388	
16	3.65 ± 0.04	0.027[k]	3.66	2[h]	0.023[h]	
						3.837
						3.886
			3.92[n]		Weak[n]	3.916
			3.95			
			3.99			
			4.11	0	0.055	
17	4.18	0.107	4.18	(2)	0.020	4.179
			4.23	(2)	0.008	
			4.30	2	0.023	
			4.39	0	0.160	
			4.49	2	0.043	
			4.61	2	0.013	
			4.70	2	0.033	
18	4.77 ± 0.03	0.232[g]	4.77	4	0.343	
			4.80			
			4.85			
19	4.89 ± 0.03	0.096[g]	4.90			
			4.95	(0)	0.055	
			4.99			
20	5.02 ± 0.03	Weak	5.04	0	0.040	
21	5.14 ± 0.03	0.067[i]	5.17	(0)	0.080	
			5.24	2	0.133	
22	5.34 ± 0.03	Weak	5.33	0	0.090	
			5.44	2	0.165	
			5.57	(0)	0.035	
			5.64	0	0.060	
			5.74	0	0.020	
			5.80	0	0.120	
			5.86	0	0.045	
23	5.95 ± 0.05	(0.1)[o]	6.01	4	0.500	
24	6.09 ± 0.05	Weak	6.09	2	0.075	
			6.17	2	0.103	
			6.215[n]	(4)[n]	Weak[n]	

(Table I (continued)

[a]Excitation energy ±20 keV except as noted. The Q value for the reaction was assumed to be -14.643 MeV.

[b]Integrated from $\theta_{c.m.}$ = 12.5 to 57° except as noted.

[c]Excitation energy ±15 keV.

[d]Taken from Ref. 2 except as noted. All $\ell = 2$ levels up to 5.44 MeV are assumed $d_{5/2}$. All $\ell = 4$ levels except the ground state are assumed $g_{7/2}$.

[e]Taken from Ref. 8. Only those levels believed to be populated in the g.s. ($9/2^+$) decay are included. All energies ±1 keV or less. The upper limit for the decay is about 4.4 MeV.

[f]Not resolved.

[g]Integrated from $\theta_{c.m.}$ = 12.5 to 52°.

[h]Taken from Ref. 4. All $\ell = 1$ levels except 0.103 MeV are assumed $p_{3/2}$. The 1.85-MeV level is assumed $f_{5/2}$.

[i]Integrated from $\theta_{c.m.}$ = 12.5 to 36.5°.

[j]The existence of this level was uncertain.

[k]Integrated from $\theta_{c.m.}$ = 12.5 to 42°.

[l]Taken from Ref. 1.

[m]Integrated from $\theta_{c.m.}$ = 12.5 to 42°.

[n]Taken from Ref. 6.

[o]Observed at only three angles. The average differential-cross-section ratio to the 4.18-MeV level (~0.9) was used in obtaining the intensity.

thus is not a very efficient method for locating high-spin states such as $g_{9/2}$, $g_{7/2}$, or $h_{11/2}$. On the other hand, the large momentum transfer in the (α, t) reaction, compared with that in the (^{3}He, d) reaction, favors the excitation of high-angular-momentum proton states [$\vec{Q} \times \vec{R} \approx 6$ for the (α, t) reaction]. A comparison of the relative strengths of states observed in both the (^{3}He, d) and (α, t) reactions should, therefore, give some information on the location of $\ell = 4$ or 5 levels in ^{91}Nb and ^{93}Tc.

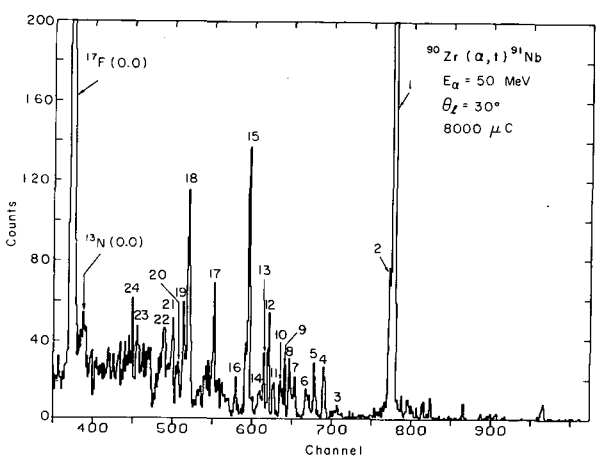

Fig. 1. Triton energy spectrum from the ^{90}Zr(α, t)^{91}Nb reaction at $\theta_\ell = 30°$. The peak numbers correspond to excitation energies given in Table I. (XBL 713-3116)

The experiment was performed with the 50-MeV α-particle beam of the Berkeley 88-inch cyclotron at a beam resolution, ΔE/E, of 0.04%. The targets were self-supporting metal foils of ^{90}Zr (enriched to 97.8%) and ^{92}Mo (enriched to 98.3%) whose nominal thicknesses were 0.20 and 0.30 mg/cm^2, respectively. Absolute cross sections are accurate only to ± 50% but relative cross sections for each target should be correct to ±15%. Tritons were detected with two counter telescopes each consisting of a 0.25-mm phosphorus-diffused silicon ΔE and 5-mm Si(Li) E detector and identified with a Goulding-Landis particle identifier.[7]

A triton spectrum of the ^{90}Zr(α, t)^{91}Nb reaction at $\theta_\ell = 30°$ is given in Fig. 1. The resolution is 50 keV full width at half maximum (FWHM). The spectrum is dominated by the $g_{9/2}$ ground state (level 1) which is a factor of 15 more intense than any other single level in the spectrum. The excitation energies of states observed in this work are given in Table I. The results agree, in general, with those of Vourvopoulos et al.[2]

Table II. Levels observed in the $^{92}Mo(\alpha,t)^{93}Tc$ reaction at 50 MeV.

	(α,t)		$(^3He,d)$[a]			$(^3He,d)$[b]		
No.	Levels observed[c] (MeV)	Intensity[d] (mb)	Levels observed (MeV)	ℓ_p	C^2S[e]	Levels observed (MeV)	ℓ_p	C^2S[e]
1	0.0	3.709	0.0	4	0.67	0.0	4	0.50
2	0.39	0.118	0.390 ± 0.010	1	0.30	0.396 ± 0.005	1	0.38
3	0.68	0.040	0.660 ± 0.020		Weak	(0.66)		Weak
4	1.18	0.019	1.190 ± 0.015	1	0.03, 0.01	1.21 ± 0.020	1	0.034, 0.015
5	1.42 ± 0.03	0.037						
6	1.51	0.044	1.500 ± 0.015	1	0.10, 0.04	1.500 ± 0.010	1	0.12, 0.052
7	1.78	0.055[f]	1.780 ± 0.020	1	0.12, 0.05	1.788 ± 0.010	1	0.11, 0.048
8	2.14	0.097	2.130 ± 0.020		Weak	2.134 ± 0.015	3	0.045[g]
9	2.59 ± 0.04	0.082	2.565 ± 0.020	2	0.04, 0.02	2.556 ± 0.015	2	0.037, 0.019
10	3.10	0.091						
			3.170 ± 0.020	(2)		3.147 ± 0.015	2	0.034, 0.018
11	3.36	0.390	3.360 ± 0.020	2	0.78, 0.38	3.343 ± 0.015	2	0.78, 0.41
12	3.58	0.064						
13	3.91	0.245	3.910 ± 0.020	2	0.09, 0.05	3.89 ± 0.020	(2)	(0.11, 0.06)
			4.110 ± 0.020	(0)	(0.15)	4.09 ± 0.030	0	0.23
14	4.15 ± 0.04	0.059[f]						
15	4.37	0.192[f]	4.43			4.39 ± 0.040		
16	4.47	0.066[h]						
17	4.67 ± 0.03	0.07[i]						
18	4.77 ± 0.03	0.087[i]	4.79			4.76 ± 0.030		
19	4.90	0.166[i]	4.92			4.88 ± 0.030		
			5.02					
20	5.20 ± 0.03	0.097[h]	5.18			5.170 ± 0.015	1	0.23, 0.083
			5.33			5.302 ± 0.015	2	0.059, 0.032
			5.49			5.50 ± 0.040	(2)	(0.051, 0.028)
			5.65			5.64 ± 0.040	2	0.035, 0.019
21	6.01 ± 0.03	0.16[h]				5.98 ± 0.040	(5)	(0.079)[j]
22	6.17 ± 0.03	0.17[h]				6.24 ± 0.040		
23	6.44 ± 0.04	0.11[h]						

[a] Taken from Ref. 1. No spectroscopic information is given for levels above 4.110 MeV.

[b] Taken from Ref. 5.

[c] Excitation energy ±20 keV except as noted.

[d] Integrated from $\theta_{c.m.}$ = 12.5 to 57° except as noted.

[e] When two values are listed the first corresponds to $j = \ell - 1/2$, the second to $j = \ell + 1/2$.

[f] Integrated from $\theta_{c.m.}$ = 12.5 to 52°.

[g] Assumed $f_{5/2}$.

[h] Integrated from $\theta_{c.m.}$ = 12.5 to 36.5°.

[i] Integrated from $\theta_{c.m.}$ = 15.5 to 52°.

[j] Assumed $h_{11/2}$.

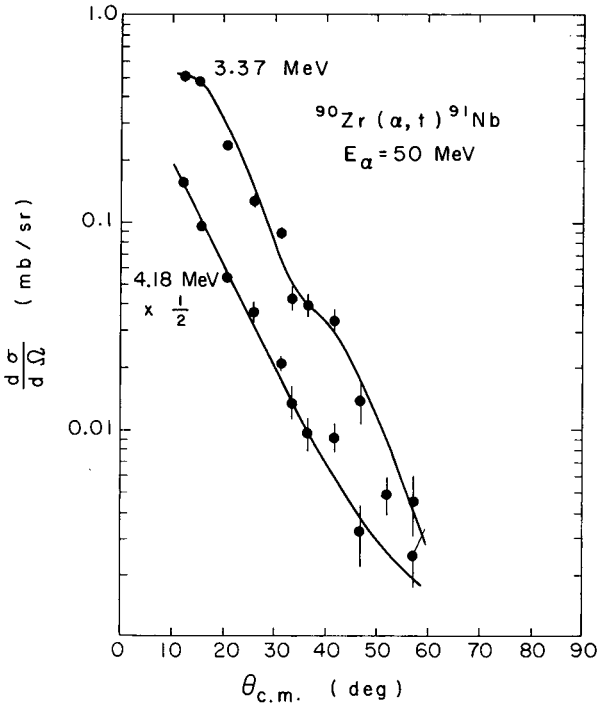

Fig. 2. Angular distributions of tritons from the ^{90}Zr(α, t)^{91}Nb reaction leading to the 3.37- and 4.18-MeV levels. Statistical errors are shown for each point. The curves have no theoretical significance. (XBL 713-3113)

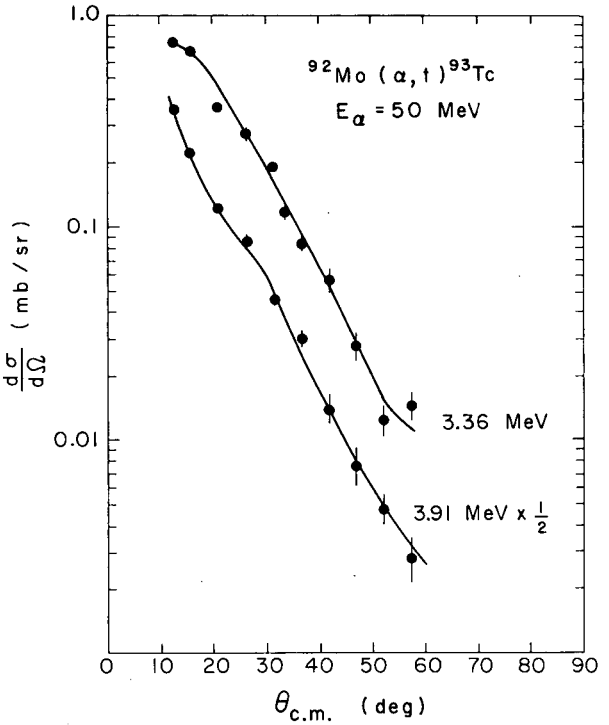

Fig. 4. Angular distributions of tritons from the ^{92}Mo(α, t) ^{93}Tc reaction leading to the 3.36- and 3.91-MeV levels. Statistical erros are shown for each point. The curves have no theoretical significance.

(XBL 713-3114)

Figure 2 shows angular distributions of two of the stronger final states (levels 15 and 17), both of which are assigned $\ell = 2$ in (^{3}He, d).[2, 6] The shapes of the two curves are slightly different at forward angles: the 3.37-MeV angular distribution flattens out while the 4.18-MeV angular distribution is steeper. This steep angular distribution shape is also observed for the ground and 4.77-MeV states, which are both assigned $\ell = 4$.[2, 6] Another discrepancy with the $\ell = 2$ assignment for the 4.18-MeV level comes from its strength: based on (^{3}He, d) spectroscopic factors,[2, 6] it is too strong relative to the 3.37-MeV level by a factor of between 14 and 20. Additional evidence for the existence of a high-spin level at this energy comes from a study of the ^{91}Mo($9/2^+$) β-decay[8] which populates a weak level at 4.179 ± 0.001 MeV. Consideration of β-decay selection rules suggests that $9/2^+$, $7/2^+$, or $11/2^-$ states are the most likely possibilities to be seen in (α, t). This would then correspond to $\ell = 4$ or $\ell = 5$ proton transfer.

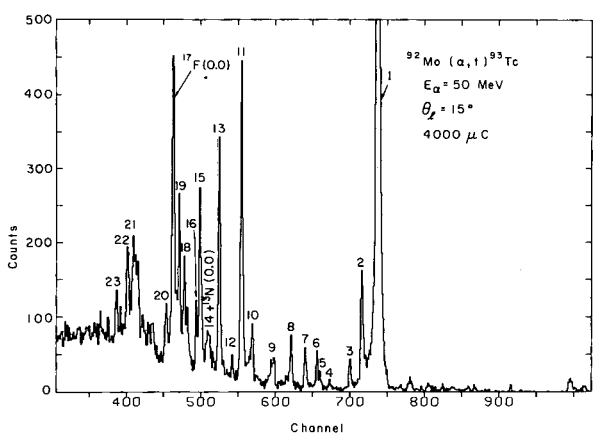

Fig. 3. Triton energy spectrum from the ^{92}Mo(α, t) ^{93}Tc reaction at θ_ℓ = 15°. The peak numbers correspond to excitation energies given in Table II. (XBL 713-3117)

A ^{92}Mo(α, t)^{93}Tc spectrum is shown in Fig. 3. The resolution is 55 keV (FWHM). Here too the spectrum is dominated by the ground state ($g_{9/2}$). A summary of the levels observed in this work is given in Table II. The excitation energies determined here agree generally with those found previously.[1, 5] In the ^{92}Mo(α, t) data, as was true for ^{90}Zr(α, t), there is one level, at 3.91 MeV, whose strength is inconsistent with its $\ell = 2$ assign-

ment.[1] The angular distribution of this state (level 13) and that of the 3.36-MeV $\ell = 2$ state (level 11) are shown in Fig. 4. The forward angle behavior of the 3.91-MeV level is different from that of the 3.36-MeV $\ell = 2$ state; it corresponds more closely to the shape of the $\ell = 4$ ground state. Moreover, the strength of the 3.91-MeV state relative to the 3.36-MeV state is 4 times that expected from the (^{3}He,d) spectroscopic factors.[1,5] Thus, based on the comparison of the (^{3}He, d) and (α, t) results, both the ^{91}Nb 4.18-MeV and ^{93}Tc 3.91-MeV states may be $\ell = 4$ or 5 proton levels.

Footnote and References

*Condensed from Phys. Rev. C 4, 1809 (1971).

1. J. Picard and G. Bassani, Nucl. Phys. A131, 636 (1969).

2. G. Vourvopoulos, R. Shoup, J. C. Fox, and J. B. Ball, in Nuclear Isospin (Academic Press, New York, 1969), p. 205.

3. H. Ohnuma and J. L. Yntema, Phys. Rev. 176, 1416 (1968).

4. M. R. Cates, J. B. Ball, and E. Newman, Phys. Rev. 187, 1682 (1969).

5. R. L. Kozub and D. H. Youngblood, Phys. Rev. C 4, 535 (1971).

6. K. T. Knöpfle, M. Rogge, C. Mayer-Böricke, J. Pederson, and D. Burch, Nucl. Phys. A159, 642 (1970).

7. F. S. Goulding, D. A. Landis, J. Cerny, and R. H. Pehl, Nucl. Instr. Methods 31, 1 (1964).

8. K. Hesse and E. Finckh, Nucl. Phys. A141, 417 (1970).

HIGH-SPIN LEVELS OF ^{92,93,94,96}Nb AND ^{94}Tc POPULATED WITH THE (α,d) REACTION AT 50 MeV*

M. S. Zisman and B. G. Harvey

The ^{90,91,92,94}Zr(α, d)^{92,93,94,96}Nb and ^{92}Mo(α, d)^{94}Tc reactions have been investigated with a 50-MeV α-particle beam from the Berkeley 88-inch cyclotron in order to search for high-spin states in the A = 90 mass region. As in previous (α, d) experiments,[1] the three criteria used to identify (α, d) states of the same configuration are: (a) large cross section in (α, d), (b) similar angular distribution, and (c) regular dependence of the Q-value for forming the level, Q_f, on mass number.

Large (α, d) cross sections were observed for two levels in each of the even-A niobium and technetium isotopes and for two multiplets in ^{93}Nb. Figures 1 and 2 show spectra for the ^{90}Zr(α, d)^{92}Nb and ^{92}Mo(α, d)^{94}Tc reactions at $\theta_\ell = 20°$. The resolutions were 50 and 65 keV full width at half maximum (FWHM), respectively. Summaries of levels seen in the two reactions are given in Tables I and II. In each spectrum the ground state and one excited state (2.58 MeV in ^{92}Nb, 2.68 MeV in ^{94}Tc) are strongly populated. Angular distributions for these strong levels are shown in Figs. 3 and 4. As can be seen, the two ground states and two excited states have very similar angular distributions. The ^{92}Nb ground state is known[2] to be 7^+ and the ^{94}Tc ground state has been assigned[3] 6^+ or 7^+. Based on the (α, d) results a 7^+ assignment is indicated, in agreement with shell model predictions.[4,5]

A summary of the Q values for formation of these two groups of levels in (α, d) is given in Table III. Neither of the two groups seen here displays the regular Q_f vs mass dependence seen previously.[1] It is clear that the

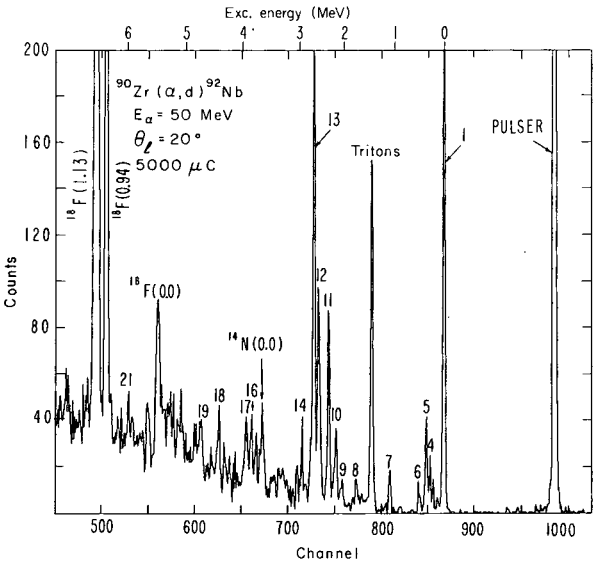

Fig. 1. Deuteron energy spectrum from the ^{90}Zr(α, d)^{92}Nb reaction at θ_ℓ = 20°. The peak numbers correspond to excitation energies given in Table I. (XBL 718-4112)

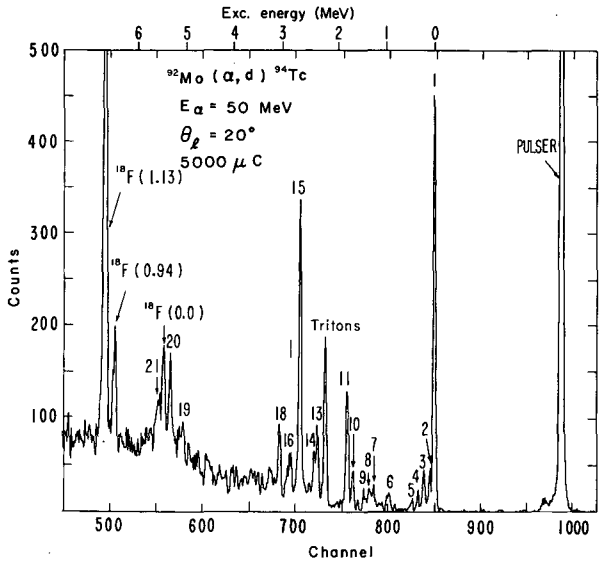

Fig. 2. Deuteron energy spectrum from the ^{92}Mo(α, d)^{94}Tc reaction at θ_ℓ = 20°. The peak numbers correspond to excitation energies given in Table II. (XBL 718-4113)

Table I. Levels observed in the ^{90}Zr(α, d)^{92}Nb reaction at 50 MeV.

No.	Levels observed[a] (MeV)	Intensity[b] (mb)
1	0.0	0.278
2	0.13	Weak
3	0.21	Weak
4	0.28	0.025
5	0.36	0.069
6	0.49	0.01
7	1.08	0.022
8	1.75	0.03
9	2.03	0.019
10	2.15	0.051
11	2.28	0.097
12	2.47	0.166[c]
13	2.58	0.345
14	2.81	0.047[c]
15	3.72	0.057
16	3.81	0.040
17	3.92	0.053
18	4.45	0.04[d]
19	4.83	0.05[d]
20	5.62	0.124
21	(6.0 ± 0.1)	--

[a] Excitation energy error ± 30 keV except as noted.

[b] Integrated from $\theta_{c.m.}$ = 12.4 to 56.8° except as noted.

[c] Integrated from $\theta_{c.m.}$ = 12.4 to 51.7°.

[d] Integrated from $\theta_{c.m.}$ = 12.4 to 31.1°.

Table II. Levels observed in the ^{92}Mo(α, d)^{94}Tc reaction at 50 MeV

No.	Levels observed[a] (MeV)	Intensity[b] (mb)
1	0.0	0.336
2	0.10	0.040
3	0.21	0.083
4	0.34	Weak
5	0.45	0.027
6	0.93	0.040
7	1.22	0.039
8	1.30	0.042
9	1.41	0.040
10	1.64	0.045
11	1.74	0.139
12	2.14	Weak
13	2.35	0.109[c]
14	2.43	0.04[d]
15	2.68	0.446
16	2.86	0.083
17	2.95	0.06
18	3.08	0.117
19	5.07	0.09[e]
20	5.24	0.183
21	5.38	0.197

[a] Excitation energy ± 30 keV.

[b] Integrated from $\theta_{c.m.}$ = 12.5 to 56.9° except as noted.

[c] Integrated from $\theta_{c.m.}$ = 12.5 to 41.6°.

[d] Integrated from $\theta_{c.m.}$ = 12.5 to 36.2°.

[e] Integrated from $\theta_{c.m.}$ = 12.5 to 51.9°.

lack of regularity in Q_f is not due to a failure of the reaction to selectively populate specific shell model configurations, since the 7^+ levels (which correspond to the levels labelled E_1 in Table III) have been identified in all but one case by other reactions.[2, 6, 7] Since both groups show the same Q-value dependence (i.e., the relative energy difference between the two groups remains nearly constant at about 2.4 MeV) it seems reasonable to associate the levels listed as E_2 in Table III with a specific shell-model state in spite of the irregular Q_f vs A dependence.

In this mass region there are a number of high-spin proton-neutron configurations which might be strongly populated in (α, d). For example, the $(\pi\, g_{9/2}, \nu d_{5/2})_{7^+}$ configuration is selectively populated in the (α, d) reaction in all of the cases studied here (see Table III). Other possible high-spin states, to which the higher (α, d) group might correspond, are

Table III. Q Values of Strong (α, d) states.

Final nucleus	E_1[a] (MeV)	Q_1[b] (MeV)	E_2 (MeV)	Q_2[b] (MeV)
^{90}Y	0.69[c]	-12.79	3.11[c]	-15.21
^{92}Nb	0.0	-13.03	2.58	-15.61
^{94}Tc	0.0	-13.37	2.68	-16.05
^{94}Nb	0.08	-12.89	2.42	-15.23
^{96}Nb	0.23	-12.60	2.38	-14.75

[a] $(\pi g_{9/2}, \nu d_{5/2})_{7^+}$ states. All levels except the ^{94}Tc ground state have been assigned 7^+ by other groups. See text.

[b] Ground state Q values taken from C. Maples, G. W. Goth, and J. Cerny, Nucl. Data A2, 429 (1966), except for ^{96}Nb, which is inferred from S. Antman, H. Petterson, and Y. Grunditz, Nucl. Phys. A110, 289 (1968) and S. Antman, Y. Grunditz, A. Johansson, B. Nyman, H. Petterson, and B. Svahn, Z. Physik 233, 275 (1970).

[c] Obtained from ^{88}Sr$(\alpha, d)^{90}$Y data, M. S. Zisman, E. A. McClatchie, and B. G. Harvey, Lawrence Radiation Laboratory Report UCRL-19530 (1970), p. 100 (unpublished).

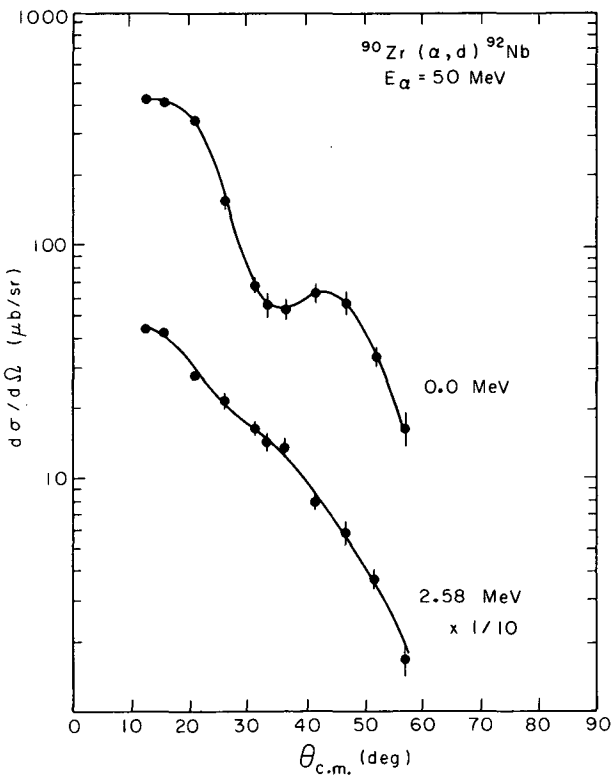

Fig. 3. Angular distributions of deuterons from the ^{90}Zr$(\alpha, d)^{92}$Nb reaction leading to the 0.0 and 2.58 MeV states. Statistical errors are shown for each point. The curves have no theoretical significance. (XBL 718-4102)

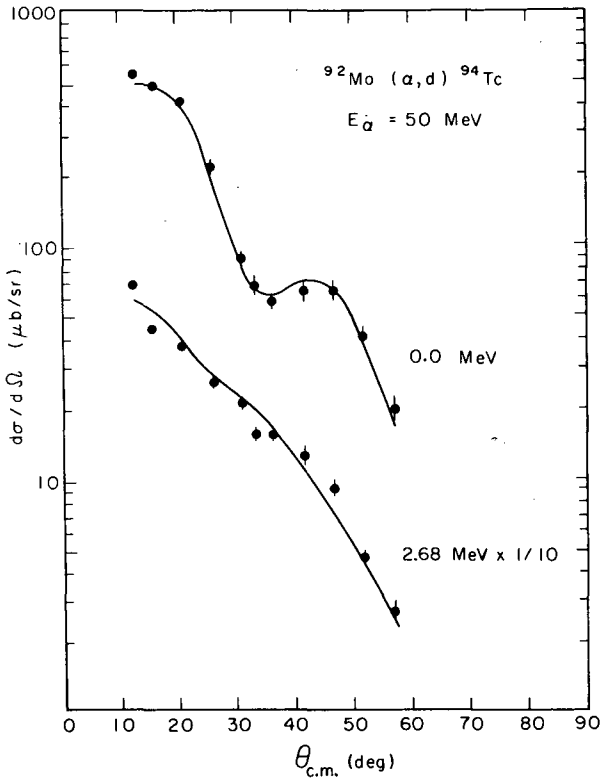

Fig. 4. Angular distributions of deuterons from the ^{92}Mo$(\alpha, d)^{94}$Tc reaction leading to the 0.0 and 2.68 MeV states. Statistical errors are shown for each point. The solid lines through the data points represent smooth curves drawn through the experimental angular distributions of the ^{90}Zr$(\alpha, d)^{92}$Nb reaction leading to the ground and 2.58-MeV states (see Fig. 3). (XBL 718-4105)

$(\pi g_{9/2}, \nu h_{11/2})_{10^-}$, $(\pi g_{9/2}, \nu g_{7/2})_{8^+}$, $(d_{5/2})^2_{5^+}$, $(\pi g_{7/2}, \nu d_{5/2})_{6^+}$, $(g_{7/2})^2_{7^+}$, and $(\pi g_{7/2}, \nu h_{11/2})_{9^-}$. In order to determine which possibilities are reasonable, simple shell-model calculations, based on the method outlinded by Brody and Moshinsky,[8] were performed with the code PHYLLIS.[9] A Gaussian potential employed by True[10] was used and the oscillator parameter was obtained by normalizing the calculation to the empirical residual interaction for the ^{92}Nb ground state, -0.679 MeV. This procedure yielded an oscillator parameter $\nu = 0.156$ fm^{-2}. Since the $h_{11/2}$ neutron level is actually in a different oscilla-

Table IV. Summary of shell model calculations for the two-particle states in ^{92}Nb.

Configuration	J^π	V_{RES}[a] (MeV)	E_x[b] (MeV)
$(\pi g_{9/2}, \nu d_{5/2})$	7^+	-0.678	0.0
$(\pi g_{9/2}, \nu h_{11/2})$	10^-	-1.263	>2.10
		(-1.472)[c]	(>1.89)[c]
$(\pi g_{9/2}, \nu g_{7/2})$	8^+	-1.098	2.35
$(d_{5/2})^2$	5^+	-1.129	3.75
$(\pi g_{7/2}, \nu d_{5/2})$	6^+	-0.543	5.66
$(g_{7/2})^2$	7^+	-1.268	7.70
$(\pi g_{7/2}, \nu h_{11/2})$	9^-	-0.975	> 7.90
		(-1.136)[c]	(> 7.74)[c]

[a]Calculated with a single oscillator parameter $\nu = 0.156$ fm^{-2} except as noted.

[b]Based on single-particle energies summarized in Table V.

[c]Calculated with oscillator parameters 0.156 and 0.184 fm^{-2} for the proton and neutron, respectively.

tor shell than the other particles, a modified calculation with different oscillator parameters for the two particles was performed using the code NAOMI.[9] The generalized transformation brackets are expanded in terms of standard Moshinsky brackets[8] using a formula derived by Gal.[11] The results of both calculations are given in Table IV. The single-particle energies required to calculate the excitation energies are taken from single-nucleon transfer data[12,13] and are listed in Table V.

Based on the results in Table IV, the most likely configurations for the ^{92}Nb 2.58-MeV level are $(\pi\, g_{9/2}, \nu\, h_{11/2})_{10^-}$ and $(\pi\, g_{9/2}, \nu\, g_{7/2})_{8^+}$. As can be seen in Table IV, the calculated interaction energies are quite similar for all of the configurations considered here. Thus, the predicted excitation energies depend strongly on the single-particle energies but are not particularly sensitive to the choice of oscillator parameters.

Table V. Single-particle energies for A = 91.

	^{91}Nb[a] (MeV)	^{91}Zr[b] (MeV)
$g_{9/2}$	0.0	--
$d_{5/2}$	4.20	0.04
$s_{1/2}$	5.27	1.66
$d_{3/2}$	6.43	2.76
$g_{7/2}$	5.52	2.77
$h_{11/2}$	--	>2.68

[a]Taken from Ref. 12.

[b]Taken from Ref. 13.

Footnote and References

*Condensed from LBL-226.

1. C. C. Lu, M. S. Zisman, and B. G. Harvey, Phys. Rev. 186, 1086 (1969).

2. T. S. Bhatia, W. W. Daehnick, and T. R. Canada, Phys. Rev. C 3, 1361 (1971).

3. N. K. Aras, E. Eichler, and G. G. Chilosi, Nucl. Phys. A112, 609 (1968).

4. K. H. Bhatt and J. B. Ball, Nucl. Phys. 63, 286 (1965).

5. J. Vervier, Nucl. Phys. 75, 17 (1966).

6. U. Gruber, R. Koch, B. P. Maier, O. W. B. Schult, J. B. Ball, K. H. Bhatt, and R. K. Sheline, Nucl. Phys. 67, 433 (1965).

7. J. R. Comfort, J. V. Maher, G. C. Morrison, and J. P. Schiffer, Phys. Rev. Letters 25, 383 (1970).

8. T. A. Brody and M. Moshinsky, Tables of Transformation Brackets (Gordon and Breach, New York, 1967).

9. M. S. Zisman, Shell Model Matrix Element Code (umpublished).

10. W. W. True, Phys. Rev. 130, 1530 (1963).

11. A. Gal, Ann. Phys. (N. Y.) 49, 341 (1968).

12. G. Vourvopoulos, R. Shoup, J. C. Fox, and J. B. Ball, in Nuclear Isospin, (Academic Press, New York, 1969), p. 205.

13. C. R. Bingham and M. L. Halbert, Phys. Rev. C2, 2297 (1970).

MULTIPOLE DEFORMATION OF ^{238}U

D. L. Hendrie, B. G. Harvey, J. R. Meriwether,* J. Mahoney, J. C. Faivre,† and D. G. Kovar

The ability to measure details of nuclear deformation to multipoles higher than quadrupole by means of α-particle inelastic scattering has been well demonstrated in permanently deformed rare earth nuclei.[1,2] Attempts to extend these measurements to the interesting actinide region of permanent deformations were thwarted by experimental difficulties—the inability of solid state detectors to resolve the more closely spaced energy levels in these nuclei. Meanwhile, several theoretical predictions for the Y_{40} moment of actinide nuclei and experimental results using other techniques have been published. The interest in the problem is intensified, because both theoretical predictions[2,3,4] and experimental results[5,6] show variations of up to one order of magnitude for the Y_{40} moment of uranium.

Our experiment measured the angular distributions in elastic and inelastic scattering of 50-MeV α particles by ^{238}U, utilizing the new magnetic spectrometer[7] for detection of the scattered alphas. Differential cross sections were measured for levels in the ground state rotational band up to 8^+. The target was made by evaporating 75 μg of uranium metal onto a 50-μg carbon backing. Beams of up to 1 μA were prepared by the high-resolution magnetic analysis system, delivered onto the target, and collected and measured in a Faraday cup. The quantity of beam on target was also monitored by a solid-state detector placed at 20° with respect to the incident beam. Detection

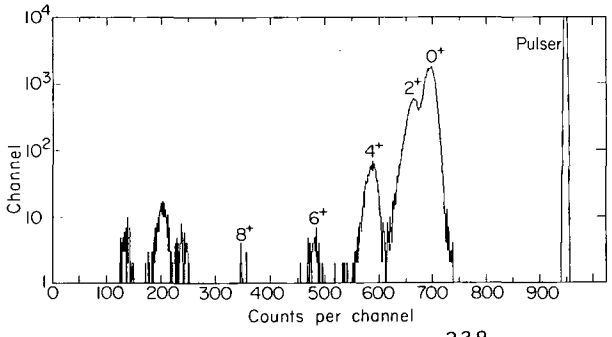

Fig. 1. Sample spectrum of the ^{238}U (α,α') reaction at 48° (lab). (XBL 723-2531)

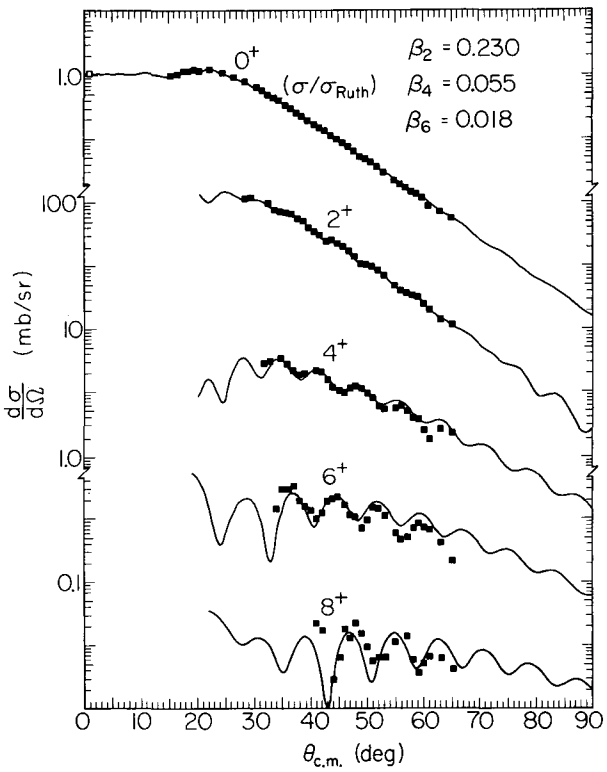

Fig. 2. Differential cross sections and coupled-channel calculations. The optical parameters for the calculations are the same as in Ref. 1. (XBL 723-2530)

of scattered alphas at the focal plane of the spectrometer was made by a position-sensitive silicon detector (1-cm high by 5-cm long) obtained from Nuclear Diodes, Inc. The energy resolution of the entire system was 16 keV at forward angles, changing slowly to 20 keV at the most backward angles, where target-thickness effects become more important.

The data were taken in two independent runs. Scattering from a target contamination of about 10% ^{182}W obscured the ^{238}U levels for several angles in the first run. This problem did not repeat in the second run; the results from the two runs reproduced well where

Table I. Table of deformation parameter for this work and in the recent literature. The parameters are defined by describing the nuclear surface as $R = R_0(1 + \beta_2 Y_{20} + \beta_4 Y_{40} + \beta_6 Y_{60})$. The radius common to all values in the table is $R_0 = 1.2\ A^{1/3}$ Fm.

β_2	β_4	β_6	Reference
0.23 ±0.01	0.055±0.01	-0.018±0.01	This work
0.23 ±0.01	$0.017\ \{^{+0.015}_{-0.030}\}$	-0.015	(p, p') Ref. 5
0.235±0.006	0.100±0.028	---	Coulomb excitation, Ref. 6
0.220	0.071	---	Theory, Ref. 2
0.200	0.075	---	Theory, Ref. 3
0.267	---	---	Average without β_4, Ref. 10

they could be checked. A sample spectrum from the second run is shown in Fig. 1. The resulting angular distributions are shown in Fig. 2. Also shown in Fig. 2 are the results of a coupled-channels calculation using the program of Glendenning.[8] Expansions and numerical sums were carried to convergence so that the only approximations involved in the calculation are those inherent in the model itself. The optical parameters chosen were the same as were used in the rare earth work;[9] varying these slightly did not change the values extracted for the deformation parameters. Estimate of the errors were made by making several independent calculations with altered parameters.

Table I lists the value of the deformation parameters obtained from our work and from other recent theoretical and experimental results. Our results are in fair agreement with the theories of Refs. 2 and 3, but disagree markedly with the two other experimental values.

Footnotes and References

*Permanent address: University of Southwestern Louisiana, Lafayette, La.

†Permanent address: CEN Saclay, France.

1. D. L. Hendrie, N. K. Glendenning, B. G. Harvey, O. N. Jarvis, H. H. Duhn, J. Saudinos, and J. Mahoney, Phys. Letters 26B, 127 (1968).

2. S. G. Nilsson, C. F. Tsang, A. Sobiczewski, Z. Szymanski, S. Wyech, C. Gustafson, I. L. Lamm, P. Möller, and B. Nilsson, Nucl. Phys. A131, 1 (1969); P. Möller, B. Nilsson, S. G. Nilsson, A. Sobiczewski, Z. Szymanski, and S. Wyech, Phys. Letters 26B, 418 (1968).

3. F. A. Gareev, S. P. Ivanova, and V. V. Pashkevich, Yad. Fig. 11 (1970) 1200 (Sov. J. Nucl. Phys. 11 (1970) 667).

4. R. R. Chasman, Phys. Rev. C1, 2144 (1970).

5. J. M. Moss, Y. D. Terrien, R. M. Lombard, F. Resmini, C. Brassard, and J. M. Loiseaux, Phys. Rev. Letters 26, 1488 (1971).

6. F. K. McGowan, C. E. Bemis, J. L. C. Ford, Jr., W. T. Milner, R. L. Robinson, and P. H. Stelson, Phys. Rev. Letters 27, 1741 (1971).

7. D. L. Hendrie, J. R. Meriwether, F. Selph, D. Morris, and C. Glashausser, BAPS 15, 650 (1970), and to be published.

8. N. K. Glendenning, Proceeding of the International School of Physics "Enrico Fermi," courseXL (Academic Press, New York, (1967).

9. N. K. Glendenning, D. L. Hendrie, and O. N. Jarvis, Phys. Letters 26B, 131 (1968).

10. K. E. C. Löbner, M. Vetter, and V. Honig, Nucl. Data 7, 495 (1970).

A STUDY OF SECOND-ORDER PROCESSES IN THE $^{238}U(p,t)^{236}U$ REACTION

D. G. Kovar, B. Mayer, M. Marinescu, B. G. Harvey, M. S. Zisman, F. G. Pühlhofer,
F. D. Becchetti, J. Mahoney, A. Giorni, R. J. Ascuitto, N. K. Glendenning, and B. Sørensen

There has been considerable interest in the importance of higher-order processes in one- and two-nucleon transfer reactions such as (p, d) and (p, t). In recent coupled-channels studies of transfer reactions on spherical nuclei Ascuitto, et al.[1] found that while the two-step processes via inelastic channels can be important, there was no conclusive evidence. In their more recent studies[2] on deformed nuclei, however, they found clear evidence for two-step processes which significantly affect both the magnitude and the angular distributions of the (p, t) cross sections for the 0^+, 2^+, and 4^+ members of the ground state rotational bands. While these results are impressive, it is of interest to determine whether one can use coupled channels to analyze data for higher members of the ground state band such as the 6^+ and 8^+ members, as well as members of excited bands.

In the present study we have investigated the $^{238}U(p,t)^{236}U$ reaction in order to obtain such information. Previous studies of the effect of inelastic channels have been confined mostly to nuclei with smaller mass numbers.[3] Here we extend the study to a heavier mass region. The experimental information on the deformation parameters for ^{238}U is available,[4] as are the nuclear structure calculations needed for the structure factors used in the calculations. The study is at present particularly interesting in view of the results of Maher et al.[5] from the study of (p, t) reactions in the actinide region (including ^{238}U) which revealed that the first 0^+_1 state (~900 keV) in these nuclei was populated unusually strong. These studies, made near the Coulomb barrier (E_p = 17 MeV), reported the angular distributions for only the 0^+ and 2^+ members of the g. s. and excited bands. The angular distributions were not fit well by the DWBA calculations. In the present study, made at a higher bombarding energy, angular distributions for the (p, t) reaction leading to members of the g. s. band up to 6^+ and to members of the excited-state band have been obtained. Tentative results are given here.

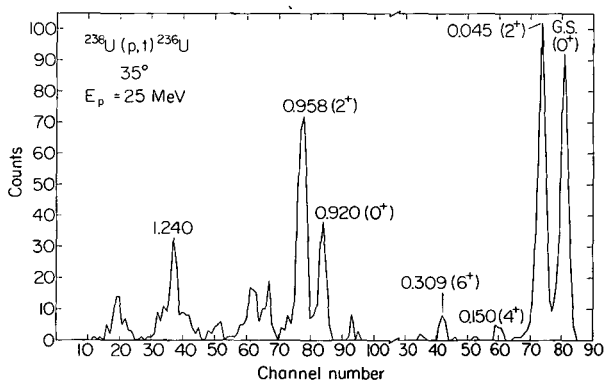

Fig. 1. The spectrum obtained at θ_L = 35° from the (p, t) reaction on ^{238}U with a proton beam of 25 MeV. (XBL 723-2533)

The $^{238}U(p,t)^{236}U$ reaction was studied by using a 25-MeV proton beam from the 88-inch cyclotron. A spot target (100 μg/cm^2) enriched to 99.9% ^{238}U on a 10-μg/cm^2 carbon foil was used. The tritons were momentum-analyzed in the Berkeley uniform field spectrometer[6] and detected by two 300-micron position-sensitive detectors (10 × 50 mm) situated in the focal plane to cover the excitation range in ^{236}U from the g. s. to 0.45 MeV and from 0.85 to 1.35 MeV. The position spectrum obtained at 35° is shown in Fig. 1. Typical energy resolutions of 15 to 20 keV were obtained.

The well known 0^+ (g. s.), 2^+(45 keV), 4^+ (150 keV), and 6^+(309 keV) members of the g. s. band, and the 0^+_1(920 keV) and 2^+_1(959 keV) members of the first excited band in ^{236}U were observed and their angular distributions obtained in 5° steps from 15° to 60° (Fig. 2). In addition, several other states not reported in the previous (p, t) study were observed at excitation energies above 1 MeV. Some of these states can be identified with levels populated in the $^{235}U(d,p)$ reaction.[7] A comparison of the angular distributions for the two 0^+ and the two 2^+ states (Fig. 2) reveals that while the maxima and minima remain in the same position, the oscillatory structure of the angular distributions for the excited band members appears to be significantly damped when compared to those of members of the g. s. band. A theoretical analysis of these results using the coupled-channels procedures of Ascuitto et al. is in progress.

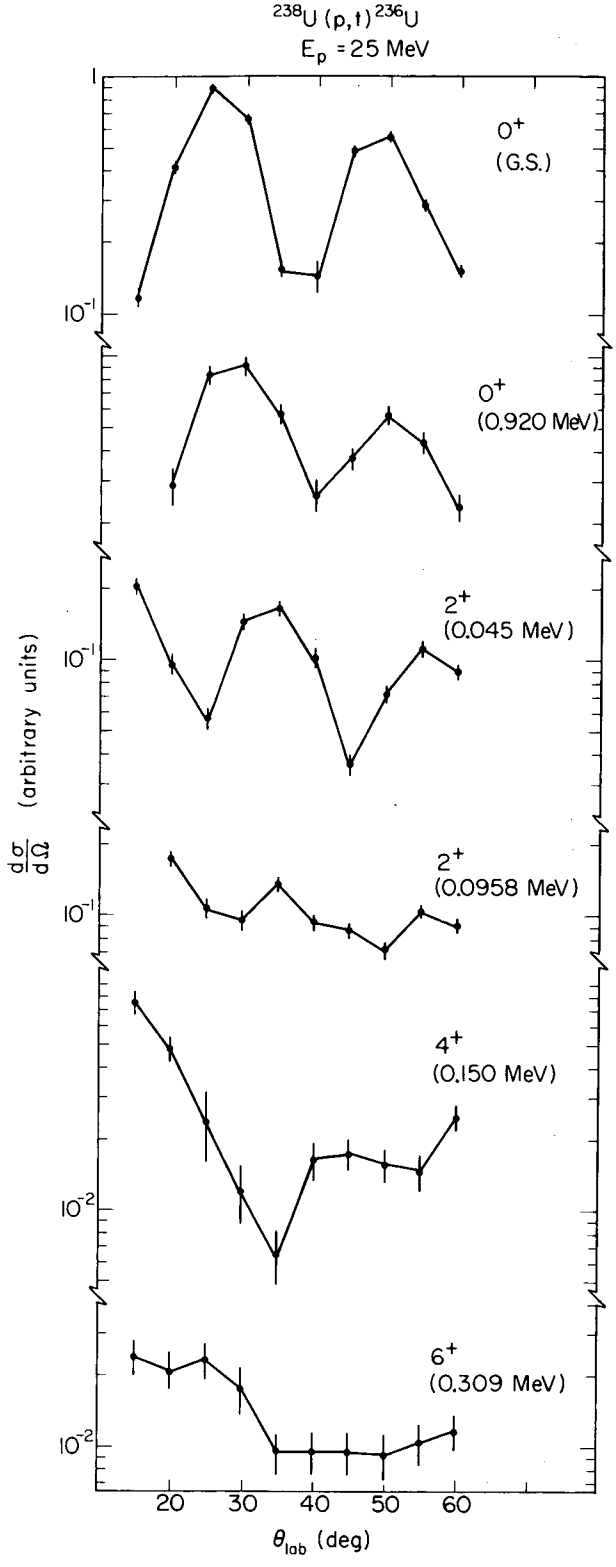

Fig. 2. Angular distribution obtained from the ^{238}U(p,t)U reaction at E_p = 25 MeV leading to the 0^+, 2^+, 4^+, and 6^+ members of the ground state band and to the 0^+ and 2^+ members of the first excited band.

(XBL 723-2532)

References

1. R. J. Ascuitto and N. K. Glendenning, Phys. Rev. C2, 1260 (1970); N. K. Glendenning in Proc. Int. Conf. on Properties of Nucl. States (U. of Montreal Press, Montreal, 1969).

2. R. J. Ascuitto, N. K. Glendenning, and B. Sørensen, UCRL-20426, p. 11; R. J. Ascuitto, N. K. Glendenning and B. Sørensen, LBL-248 (1971), to be published.

3. R. J. Ascuitto and N. K. Glendenning, Phys. Rev. C2, 1260 (1970).

4. D. L. Hendrie, private communication (1971).

5. J. V. Maher, J. R. Erskine, A. M. Friedman, J. P. Schiffer, and R. H. Siemssen, Phys. Rev. Letters 25, 302 (1970).

6. D. L. Hendrie, to be published.

7. B. E. F. Macefield and R. Middleton, Nucl. Phys. 59, 561 (1964).

INTERFERENCE EFFECTS IN HEAVY-ION INELASTIC SCATTERING

F. D. Becchetti, D. G. Kovar, B. G. Harvey, J. Mahoney, F. Pühlhofer, M. Zisman,
B. Mayer, M. Marinescu, J. R. Meriwether, S. W. Cosper, J. D. Sherman, and A. Giorni

At bombarding energies above the Coulomb barrier the forces responsible for inelastic transitions consist of a long-range Coulomb term and a short-range nuclear term. Since the sign and phases of these terms differ, one often observes interference effects.[1] Such phenomena are expected to be sensitive to the details of the nuclear force.[2] In heavy-ion inelastic scattering, the Coulomb and nuclear forces are comparable and interference effects are large.

A series of experiments using the ^{16}O beam from the 88-inch cyclotron has been initiated in order to study these effects. Scattered particles were detected and identified using a six-wire proportional counter in the focal plane of the magnetic spectrometer (see Sec. IV). The energy resolution was between 100 and 300 keV (FWHM). A spectrum for ^{16}O + ^{208}Pb at E_L = 104 MeV is shown in Fig. 1. The levels reported in (p, p) are also indicated together

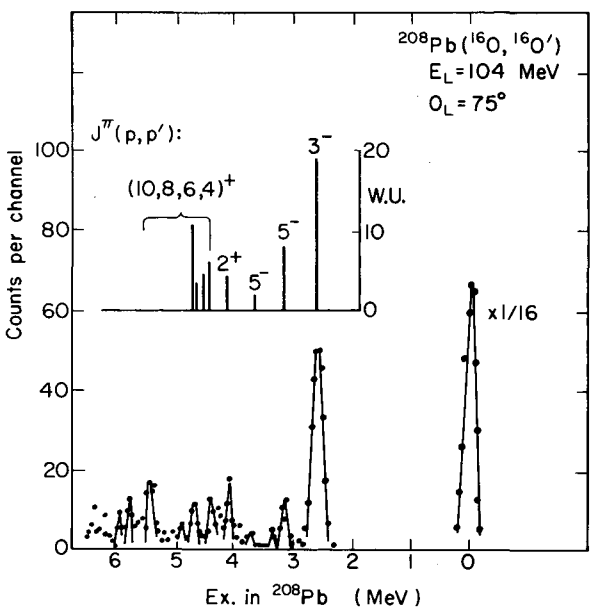

Fig. 1. An ^{16}O spectrum obtained from ^{16}O+ ^{208}Pb at E_L = 104 MeV. The counts vs position spectrum from a single wire of the focal-plane proportional counter is shown. The levels in ^{208}Pb observed in (p, p') are indicated along with the transition strengths.[3]
(XBL 723-2536)

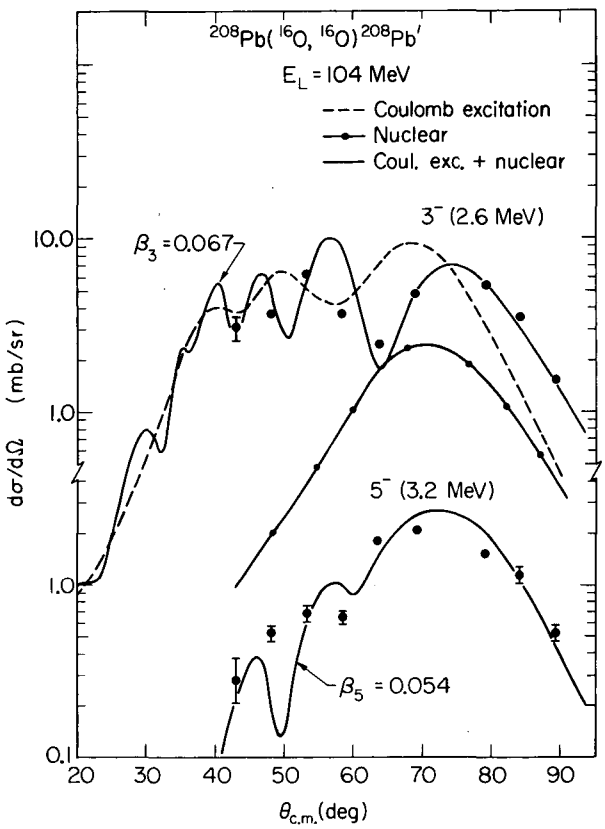

Fig. 2. A comparison of the experimental data with DWBA calculations, using nuclear and/or Coulomb excitation form factors. The values of β_L deduced are indicated. The values given in Ref. 3 are β_3 = 0.085 and β_5 = 0.051. (XBL 723-2534)

with the transition strengths in Weisskopf units.[3]

DWBA calculations for $^{208}Pb(^{16}O, ^{16}O)$ have been performed using a version of the program DWUCK[4] modified to use 140 partial waves. The form factor was taken to be the sum of the Coulomb excitation term and the first derivative of the optical model potential. The latter was of a Woods-Saxon form with V = -40 MeV, W = -15 MeV, R = 11 fm, and a = 0.5 fm and was chosen to fit the elastic scattering. The DWBA calculations are shown in Fig. 2 together with some preliminary data

for the 3^- - state at 2.6 MeV and the 5^- state at 3.2 MeV. It can be seen that interference effects play a dominant role, particularly for the 3^- state. The deformation parameters deduced are in reasonable agreement with other measurements.[3]

References

1. J. Alster, Phys. Rev. 141, 1138 (1966).

2. V. K. Lukyanov et al., Phys. Letters 29B, 535 (1969). G. R. Satchler, Phys. Letters 33B, 385 (1970). C. Leclercq-Willain, Nuclear Reactions Induced by Heavy Ions (North-Holland, Amsterdam, 1970), p. 453.

3. J. Saudinos et al., Phys. Letters 22, 492 (1966).

4. P. D. Kunz, unpublished.

STUDY OF THE $^{208}Pb(^{16}O, ^{17}O)^{207}Pb$ AND $^{208}Pb(^{16}O, ^{15}N)^{209}Bi$ REACTIONS AT 104 MeV

D. G. Kovar, F. D. Becchetti, B. G. Harvey, F. Pühlhofer, M. Zisman, J. Mahoney, A Giorni, M. Marinescu, B. Mayer, J. Sherman, S. Cosper, and J. Meriwether

There is at present considerable interest in the experimental information that can be obtained from the study of heavy-ion induced single-nucleon transfer reactions. The results of recent transfer reaction studies[1] on target nuclei with $A \leq 100$ have revealed that (a) the reactions are selective, populating essentially the same states populated in the equivalent light projectile reaction, and (b) the reactions show a definite Q dependence strongly affecting the transfer cross sections. While the Q dependence can be understood qualitatively in terms of a semiclassical model,[2] there remain questions concerning the applicability of existing theoretical techniques.[2, 3] There is evidence, for example, that multistep processes may be important.[4]

To further investigate these questions, single-nucleon transfer reactions on ^{208}Pb were studied using an ^{16}O beam [$E(^{16}O) = 104$ MeV] from the 88-inch cyclotron. The reaction products were momentum-analyzed in the uniform field spectrometer[5] and detected with a six-wire proportional counter described in detail elsewhere.[6] The total position spectrum included a large variety of reaction products whose separation and identification were made using time-of-flight and dE/dx information. Time-of-flight resolutions of 2 to 3% and dE/dx resolutions of 12 to 15% made possible the clean, if not complete, separation of the reaction products of interest.

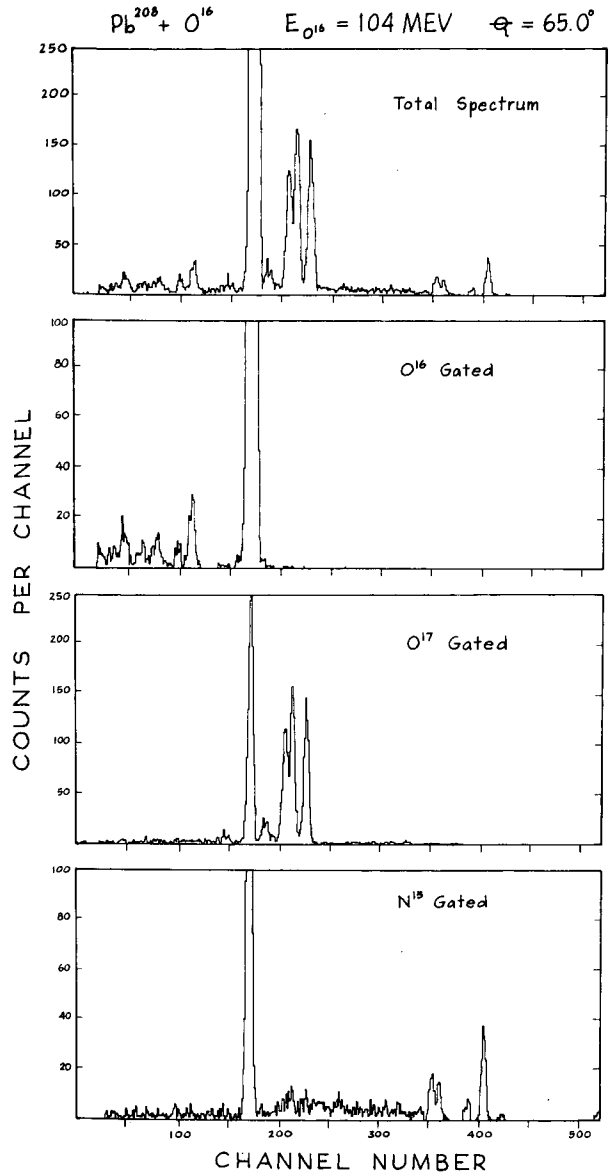

Fig. 1. The total position spectrum and the gated ^{16}O, ^{17}O, and ^{15}N spectra obtained at 65° in the laboratory from the reaction ^{16}O + ^{208}Pb at an energy $E(^{16}O) = 104$ MeV.
(XBL 721-55)

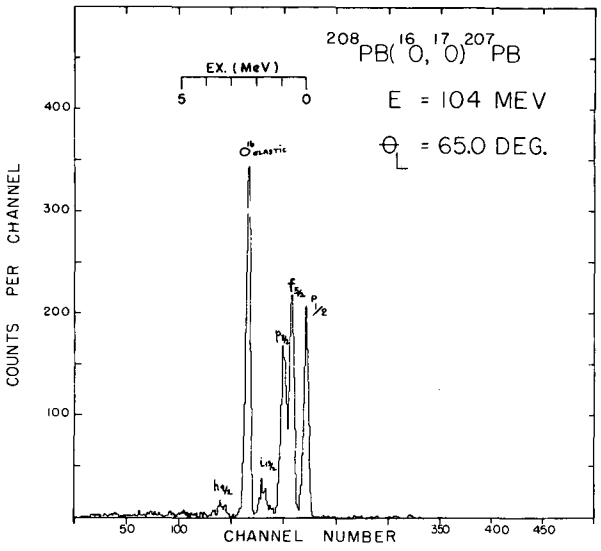

Fig. 2. Position spectrum of the neutron pickup reaction ^{16}O, ^{17}O on ^{208}Pb. The five observed "single-hole" states in ^{207}Pb are labelled. (XBL 721-89)

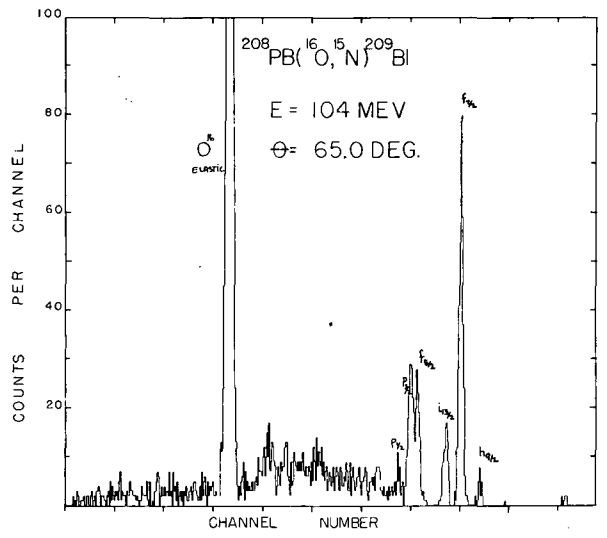

Fig. 3. Position spectrum of the proton-stripping reaction (^{16}O, ^{15}N) on ^{208}Pb. The six observed "single-particle" states in ^{209}Bi are labelled. (XBL 721-91)

In Fig. 1 we show the total position spectrum and the gated ^{16}O, ^{17}O, and ^{15}N spectra obtained at 65°. As can be seen, except for some leak-through of the ^{16}O elastic and some inelastic peaks, the particle separation is very good. Spectra for these reactions were obtained in the angular range 40° to 85° in 5° steps. Typical energy resolutions of 150 to 250 keV were observed.

In the ^{17}O gated spectra (see Fig. 2) we observed the population of all the known neutron single-hole states in ^{207}Pb with the exception of the $2f_{7/2}^{-1}$ state at 2.34 MeV excitation which is expected to be found exactly at the position of the ^{16}O leak-through peak. In addition to these states, we observed, as expected, states in the data built on the 0.871 MeV ^{17}O first excited state.

In the ^{15}N spectra (see Fig. 3) we observed the population of the six known proton single-particle states. At higher excitation there exists a background resulting either from some break-up phenomenon or from the population of a large number of unresolved levels in ^{209}Bi. Of additional interest in the (^{16}O, ^{15}N) reaction is the possibility of exciting the members of the well-known [$^{208}Pb(3^-) \times h_{9/2}$] septuplet at about 2.6-MeV excitation by means of a two-step inelastic process. Our results give no clear evidence that they are excited. However, these states might reasonably be expected to be significantly more weakly excited than the single-particle states and hence it is of interest to further pursue this question to establish an upper limit for these cross sections.

The angular distributions are at present being extracted and will be analyzed using DWBA with finite-range form factors. The results may be compared with those obtained at sub-Coulomb energies.[7]

References

1. F. D. Becchetti, N. Baron, P. R. Christensen, S. I. Manko, and R. J. Nickles, in Proceedings of the Conference on Heavy-Ion Physics, Dubna (1971); M.-C Lemaire, Nuclear Theory Course in the International Centre for Theoretical Studies, Trieste (1971); F. D. Becchetti, private communication (1972).

2. P. J. A. Buttle and L. J. B. Goldfarb, Nucl. Phys. A176, 299 (1971).

3. F. Schmittroth, W. Tobocman, and A. A. Golestaneh, Phys. Rev. C1, 377 (1970).

4. P. R. Christensen, F. D. Becchetti, S. I. Manko, and R. J. Nickles, Proceedings of the Conference on Heavy-Ion Physics, Dubna (1971).

5. D. L. Hendrie et al., to be published.

6. B. G. Harvey et al., Sec. IV, this report.

7. A. R. Barnett, W. R. Phillips, P. J. A. Buttle, and L. J. B. Goldfarb, Nucl. Phys. A176, 321 (1971).

THE Q-VALUE DEPENDENCE OF HEAVY-ION INDUCED TRANSFER REACTIONS

F. D. Becchetti*

In a series of experiments performed at the Niels Bohr Institute in Copenhagen, Denmark, the Q-value dependence for one- and two-nucleon transfer reactions between ^{16}O ions and several target nuclei, $40 \leq A \leq 100$, has been determined. The incident beam energy of 60 MeV (lab) corresponds to an energy 15 to 25 MeV above the Coulomb barrier.[1]

One finds that the neutron transfers have maximum cross sections when $Q \approx 0$, while the one- and two-proton stripping reactions, e.g. (^{16}O, ^{15}N) and (^{16}O, ^{14}C), peak at $Q \approx -5$ MeV and $Q \approx -10$ MeV, respectively. These results are consistent with those obtained by Diamond, et al.[2]

In the theory of sub-Coulomb heavy-ion reactions[3] the Q-value dependence is determined by the overlap of the semiclassical orbits of the projectiles in the incident and final channels. This overlap can be characterized by the difference in the apsidal distances

$$\Delta D(\theta) = D_f(\theta) - D_i(\theta)$$

where (1)

$$D_{i,f}(\theta) = (\eta_{i,f}/k_{i,f})(1 + \mathrm{cosec}\,\theta/2).$$

Here η and k are the Coulomb parameter and reduced wave number, respectively, and θ is the scattering angle. Equation 1 is expected to be valid provided $\eta_{i,f} >> k_{i,f} >> 1$ and $L << \ell_o$ where L is the angular momentum transfer and ℓ_o is the partial-wave ℓ

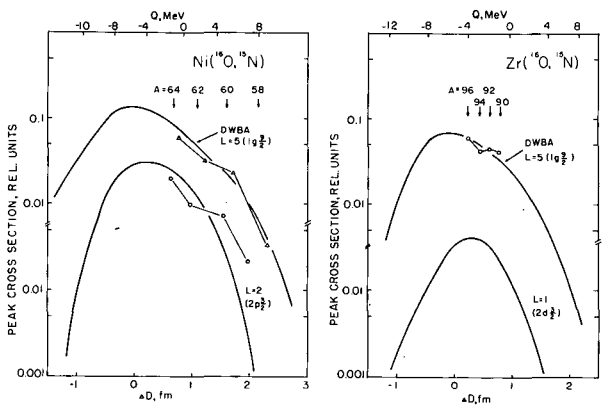

Fig. 1. The peak cross section for the (^{16}O, ^{15}N) reaction (60 MeV lab) on the Ni and Zr isotopes as function of $\Delta D(\theta)$ as defined in Eq. 1. (XBL 721-48)

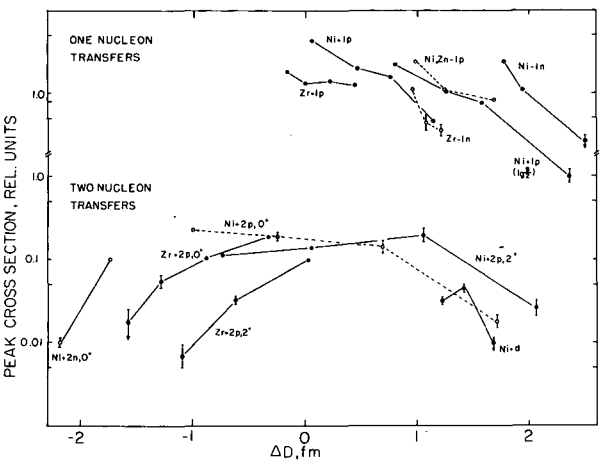

Fig. 2. The peak cross sections for some one- and two-nucleon transfer reactions as a function of $\Delta D(\theta)$. The incident energy is 60 MeV. The notation used is: $+1p = (^{16}O, ^{15}N)$, $-1p = (^{18}O, ^{19}F)$, $-1n = (^{16}O, ^{17}O)$, $+2p = (^{16}O, ^{14}C)$, $+2n = (^{18}O, ^{16}O)$, $+d = (^{16}O, ^{14}N)$. Where applicable, the experimental cross sections have been divided by the shell-model spectroscopic factors. Transitions are g.s. → g.s. unless otherwise indicated. (XBL 721-47)

value for a grazing collision. The experimental data presented here have $\eta \approx 25$, $k \approx 5$, $0 \leq L \leq 5$, and $\ell_o \approx 25$ so that Eq. (1) should be valid provided the theory is applicable when the incident energies are above the barrier.[1] The maximum overlap of semiclassical orbits occurs when[3]

$$\Delta D(\theta) \doteq 0$$

or (2)

$$Q \doteq E_i(Z_3Z_4/Z_1Z_2 - 1) \approx E_i(Z_t/Z_1),$$

where $Z_1(Z_3)$ and $Z_2(Z_4)$ are the projectile and target charges respectively, in the incident (final) channel, $Z_t = Z_2 - Z_1$, and E_i is the incident c.m. energy. Equation 2 neglects terms of the order (L/ℓ_o).

In Fig. 1 and 2 we present the experimental data for one- and two-nucleon transfers as a function of $\Delta D(\theta)$ as defined in Eq. 1. Also shown are DWBA calculations[4] for the (^{16}O, ^{15}N) reaction using a full finite range form factor.[5] It can be seen that the experimental results are consistent with Eq. 2 and also the

DWBA calculations. It thus appears that the sub-Coulomb theory may be applicable to the study of heavy-ion reactions above the barrier. Experiments in progress at the 88-inch cyclotron[6] will provide additional information on the Q-value dependence, and in particular, test the dependence on bombarding energy predicted by Eq. 2.

Footnote and References

*Work done in collaboration with P. R. Christensen, S. I. Manko, and R. J. Nickles

1. F. D. Becchetti, et al., in Proceedings of the Dubna Heavy Ion Physics Conference, 1971.

2. R. M. Diamond, et al., Phys. Rev. Letters 20, 802 (1968).

3. P. J. A. Buttle, and L. J. B. Goldfarb, Nucl. Phys. A176, 299 (1971). R. Broglia and A. Winther, to be published.

4. Program DWUCK, P. D. Kunz, unpublished.

5. Program RDRC, F. Schmittroth, W. Tobocman, and A. A. Golestaneh, Phys. Rev. C1, 377 (1970).

6. D. G. Kovar et al., previous paper.

^{3}He ACTIVATION ANALYSIS FOR S, Cl, K, AND Ca: EXCITATION FUNCTIONS

D. M. Lee and S. S. Markowitz

Experimentally determined excitation functions are useful for activation analysis and radioisotope production. In order to evaluate the feasibility of activation analysis or production of radionuclides by using a particular nuclear reaction, the excitation function has to be known.

In the present work, the excitation functions for ^{3}He nuclear reaction with light elements have been extended to the elements sulfur, chlorine, potassium, and calcium at incident ^{3}He energies from 5 to 20 MeV. The cross sections of the following nuclear reactions: $^{32}S(^3He, p)^{34m}Cl$, $^{35}Cl(^3He, \alpha)^{34m}Cl$, $^{37}Cl(^3He, 2p)^{38}Cl$, $^{37}Cl(^3He, 2n)^{38}K$, $^{39}K(^3He, 2\alpha)^{34m}Cl$, $^{39}K(^3He, \alpha)^{38}K$, and $^{40}Ca(^3He, \alpha p)^{38}K$, have been measured. Samples containing small known amounts of above elements were tested for the possible use of this method for quantitative determinations.

Targets were prepared by the separate vacuum evaporation of CaF_2, KI, $PbCl_2$, and pure sulfur, for the measurements of the excitation functions. For the subsequent analyses, samples were synthesized as thin targets or as thick ones. Thin targets were prepared either by vacuum evaporation or by settling the finely ground powder on a tantalum backing-foil from an ether suspension; the powder was fixed to the foil with a drop of dilute polystyrene in dichloroethylene. The thick targets were prepared by homogenizing a known small amount of material to be analyzed, with pure lead powder (approx 200 mg/cm^2) and then pressing the mixture into a thin disk.

Irradiations were performed at the Berkeley 88-inch cyclotron. The energy was first adjusted to 30 MeV before the ^{3}He impinged on the targets, and then a further energy degradation was achieved by using aluminum degrader foils. The length of bombardments varied between 8 to 15 min. and the average beam current was about 0.2 μA of ^{3}He. Thin targets were irradiated simultaneously at different energies by using stacked-foil technique; thick targets were irradiated one at a time with a thin standard in the same stack, or a thick standard from two successive irradiations. The decays of the ^{38}K(7.7 min), ^{38}Cl (37 min) and ^{34m}Cl (32 min) activities were followed by measuring the 2.17 MeV and 2.14 MeV γ-ray with a 30-cm^3 Ge(Li) detector coupled to a 1024 multichannel analyzer with a magnetic tape unit. The computer program SAMPO[1] was used for the numerical data analysis of the 2.14- and 2.17-MeV γ-ray peak. Data reduction was conveniently performed in an interactive on-line mode, employing cathode-ray-tube (CRT) display and teletype input and output.

A summary of experimental cross-section data obtained in this work is presented in Table I, and the excitation functions for each element are shown in Figs. 1 through 4. Results of sample analyses are shown in Table II; the average deviation from known values is about 5%. The cross sections for a particular nuclear reaction can be used to estimate the

Table I. Cross sections (in mb) for ^{3}He nuclear reactions on S, Cl, K, and Ca.

Average beam energy (MeV)	Energy interval (MeV)	^{32}S (^{3}He, p) ^{34m}Cl	^{35}Cl (^{3}He, α) ^{34m}Cl	^{37}Cl (^{3}He, 2p) ^{38}Cl	^{37}Cl (^{3}He, 2n) ^{38}K	^{39}K (^{3}He, α) ^{38}K	^{39}K (^{3}He, 2α) ^{34m}Cl	^{40}Ca (^{3}He, αp) ^{38}K
4.2	4.6-3.8	0.25						
4.6	5.0-4.3	1.1						
5.2	5.6-4.9	3.1						
6.3	6.6-6.1	11.1						
7.5	7.8-7.3	28.4	7.9	0	0.5	6.4		
8.2	8.4-8.1			0.1	3.8	8.2		0.36
8.7	9.0-8.4	35.2				9.8	0	
8.9	9.2-8.6		10.3	2.8				
10.1	10.3-9.4	34.2			9.1	10.2		5.9
10.6	10.9-10.4		12.1	13.4	9.3	9.9		
11.2	11.5-11.0		11.6	21.8	12.9			
11.9	12.1-11.6	31.0						
12.4	12.6-12.3				18.4	7.7	0	22.4
13.8	14.0-13.6	23.1	9.5	48.0	22.8			39.1
14.8	15.0-14.7		8.5	53.1	23.0	6.9	0.5	50.5
15.4	15.6-15.3	16.2	7.4	60.5				
15.9	16.0-15.7		7.8	62.2	22.6			
16.2	16.4-16.0					6.3	3.6	62.6
17.1	17.3-17.0	12.4	7.7	70.0				
18.0	18.1-17.8	10.3	6.7	75.0	20.1	6.1	7.1	72.1
18.8	19.0-18.6	9.7						
20.0	20.2-19.9	7.2	8.1	77.7	17.2	5.8	8.2	76.6
22.0	22.1-21.8	6.7						

Table II. Results of ^{3}He activation analyses.

Sample	Element sought	Product nuclide	Element (mg/cm^2) Present	Found	Dev. from known (%)
S	S	^{34m}Cl	0.211	0.205	-2.8
S + Pb	S	^{34m}Cl	1.121	1.202	+7.2
Saran-1	Cl	^{38}Cl	1.204	1.082	-10.0
Saran-2	Cl	^{38}Cl	0.985	0.902	-8.4
AgCl	Cl	^{38}Cl	0.753	0.802	+6.5
NaCl-1	Cl	^{38}Cl	0.211	0.207	-1.9
NaCl-2	Cl	^{38}Cl	1.081	1.025	-5.2
$PbCl_2$ + Pb	Cl	^{38}Cl	0.101	0.105	+4.0
KCl	Cl	^{38}Cl	1.345	1.306	-2.9
CaF_2-1	Ca	^{38}K	0.540	0.550	+1.8
CaF_2-2	Ca	^{38}K	0.258	0.261	+1.2
CaF_2-3	Ca	^{38}K	0.130	0.135	+3.8

Av. dev. ≈ 5%

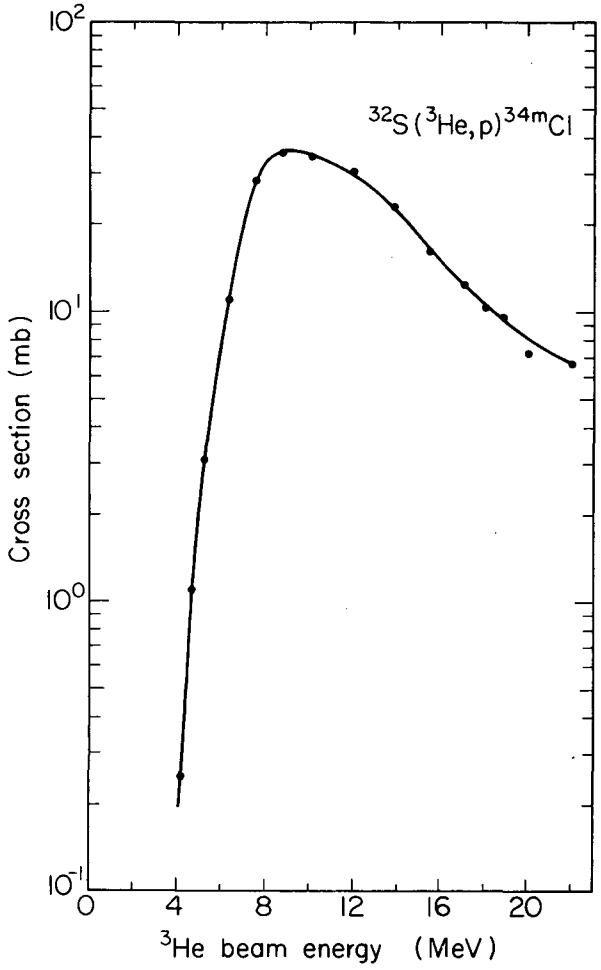

Fig. 1. Excitation function for the reaction $^{32}S(^{3}He, p)^{34m}Cl$. (XBL 723-2524)

Table III. Percent ^{38}K activity produced from K, Cl, and Ca.

^{3}He beam energy (MeV)	From elements[a]		
	K	Cl	Ca
8	90	9	1
10	51	16	33
15	10	10	80
20	7	5	88

[a]Equal weight of natural elements in a thin sample.

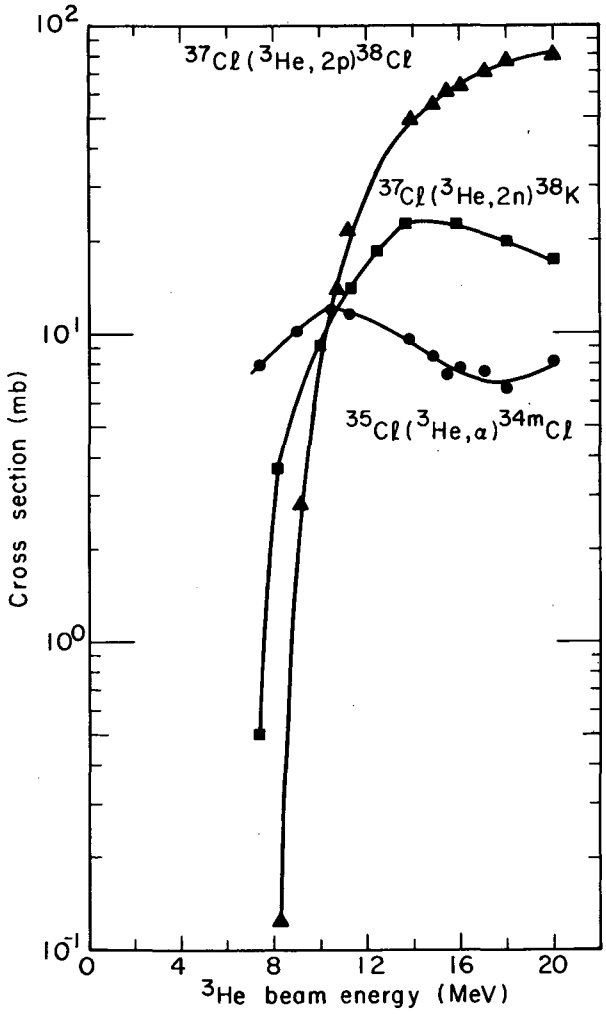

Fig. 2. Excitation functions for reactions ^{3}He + Cl.
- ▲ $^{37}Cl(^{3}He, 2p)^{38}Cl$
- ■ $^{37}Cl(^{3}He, 2n)^{38}K$
- ● $^{35}Cl(^{3}He, \alpha)^{34m}Cl$.

(XBL 723-2525)

sensitivity of the method. The detailed mathematical and statistical treatment has been discussed by Currie.[2] Applying Currie's "working expression" for an interference-free Ca determination by activation with 20-MeV ^{3}He, (1 μA current, 8-min irradiation time, starting count immediately after irradiation for 8 min and with a counting efficiency about 1%) we estimate the determination limit to be about 0.015 μg.

Relative activities for formation of the same reaction-product nuclide by more than one element are shown in Tables III and IV.

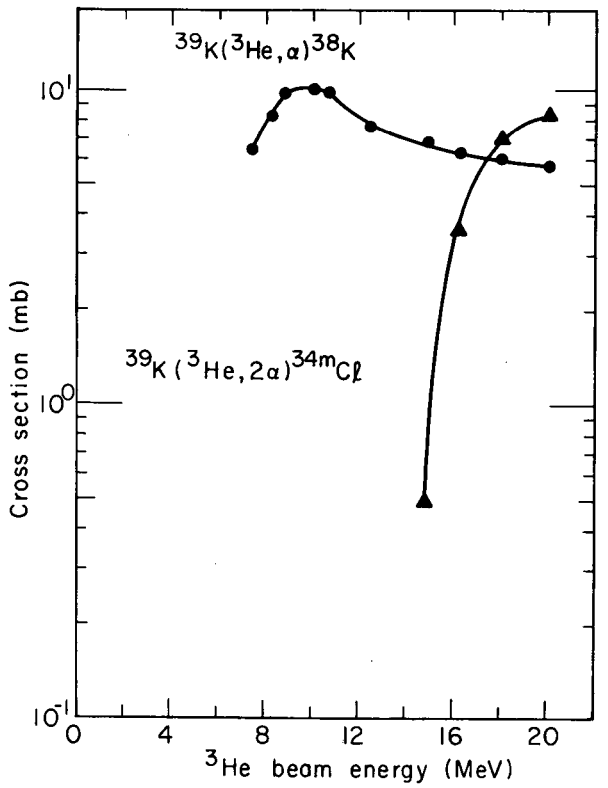

Fig. 3. Excitation functions for reactions ^{3}He + K.

● $^{39}K(^{3}He,\alpha)^{38}K$

▲ $^{39}K(^{3}He,2\alpha)^{34m}Cl$.

(XBL 723-2526)

Table IV. Percent ^{34m}Cl activity produced from Cl, S, and K.

^{3}He beam energy (MeV)	From elements[a]		
	Cl	S	K
8	16	84	0
10	19	81	0
15	24	73	3
20	30	36	34

[a]Equal weight of natural elements in a thin sample.

Chlorine can be determined unambiguously by detection of ^{38}Cl from ^{37}Cl (^{3}He, 2p) ^{38}Cl reaction, because no other element will produce ^{38}Cl under our conditions. However, for the determinations of Ca, K, and S, the interfering activities can not be completely eliminated. It is possible to minimize these interferences by the adjustment of bombarding energies. The extent of interference can be assessed also by knowning the ratio of production from the interfering element if it also produces another detectable activity in the same sample. For example, to determine Ca in the presence of K and Cl at 20-MeV ^{3}He bombarding energy, the ^{38}K activity produced from K and Cl can be estimated by the activity of ^{34m}Cl and ^{38}Cl.

The method can be applied successfully for determining Cl non-destructively with relative few interferences. In the case of samples containing low concentrations of K and Cl, the determination of Ca is also possible.

This research extends the applicability of

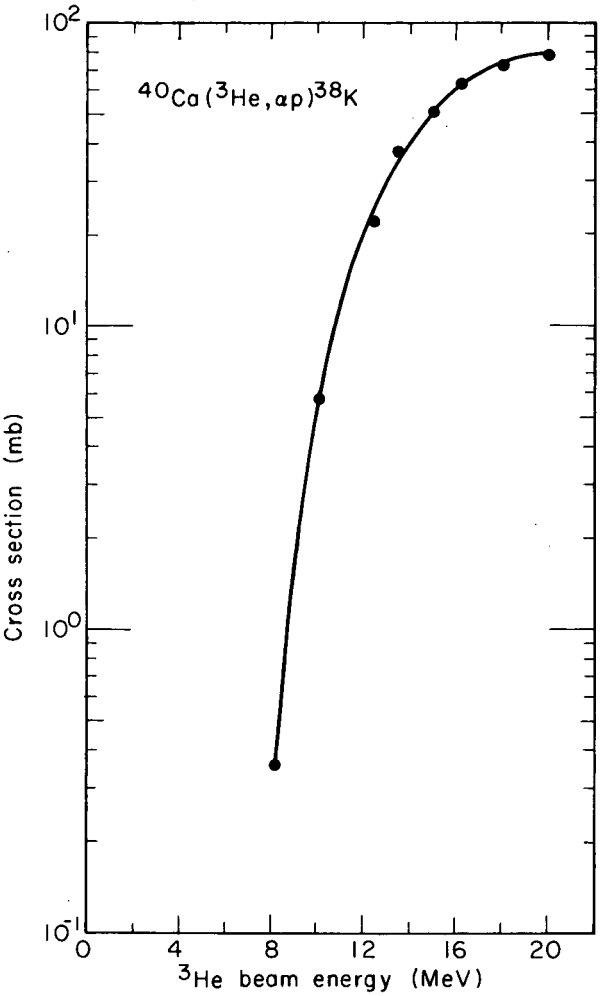

Fig. 4. Excitation function for the reaction ^{40}Ca (^{3}He, αp)^{38}K. (XBL 723-2527)

^{3}He activation analysis to elements not yet published in the literature.

References

1. J. T. Routi and S. G. Prussin, Nucl. Instr. Methods 72, 125 (1969).

2. L. A. Currie, Anal. Chem. 40, 586 (1968).

ENHANCEMENT OF DIRECT PROCESSES IN HEAVY-ION REACTIONS AT HIGH ANGULAR MOMENTA

F. G. Pühlhofer* and R. M. Diamond

Direct processes in reactions induced by ^{16}O and ^{20}Ne on ^{27}Al have been studied in the energy range from about 4 to 10 MeV/nucleon. Heavy-ion reactions at these energies are characterized by angular momenta between the interacting nuclei which may exceed the upper limit J_{cr} of the angular momentum of a compound nucleus.[1] J_{cr} indicates the angular momentum at which the fission barrier of the compound nucleus vanishes or becomes so small that its lifetime is comparable to the time typical for direct reactions. Therefore, compound-nuclear processes become more and more unlikely at higher bombarding energy. This has been shown experimentally for the reactions mentioned.[2] As a further consequence, one expects a corresponding increase of the cross sections for direct reactions, since the total reaction cross section is known to be approximately constant at energies far above the Coulomb barrier.[3]

The experiments were performed with ^{16}O and ^{20}Ne beams from the Hilac. Excitation functions were measured in large energy steps by observing γ rays from the residual nuclei in-beam and out-of-beam with Ge(Li) counters. Information about the momentum transferred in a particular reaction, and thus about the reaction mechanism was obtained from the Doppler effect and from measuring γ intensities as a function of target thickness. The experimental method turned out to be very effective, allowing the observation of many reaction products in a relatively short bombardment time.

A survey of all reaction products identified in the ^{20}Ne experiment is given in Fig. 1. The lines of nuclei with masses $A \geq 32$ are most intense at the lower bombarding energies. Their excitation functions and the recoil measurements show that they are formed in compound-nucleus reactions. At high bombarding energies (10 MeV/nucleon), the spectra are characterized by lines from nuclei with mass numbers between 18 and 28. Except for ^{23}Na, these nuclei are produced in reactions with small momentum transfer, i.e., in direct reactions. They have no appreciable recoil if they originate from the target nucleus, as for example ^{26}Al. Or, if they come from the projectile, they have its full velocity, thereby producing a strongly Doppler broadened line in the γ spectrum. This is the case with ^{21}Ne, which is mostly formed in a neutron pickup in the ^{20}Ne bombardment. The distribution of the reaction products also gives some hints as to the type of direct reactions occurring at high energies. Simple nucleon-transfer reactions seem to have the highest probability. Fragmentation processes are the most likely explanation for the observation of nuclei like ^{19}F or ^{18}F made from the target.

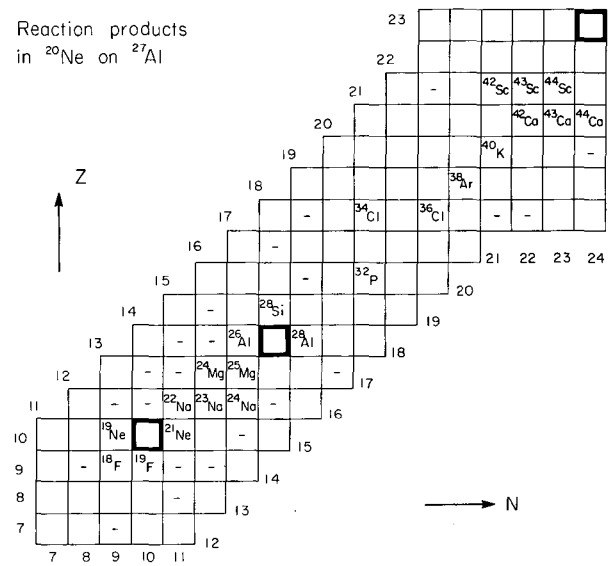

Fig. 1. Reaction products identified in the experiment with the ^{20}Ne beam. Projectile, target, and compound nucleus are indicated by dark squares. A minus sign indicates that a nucleus has not been observed, although it should be detectable in this experiment.
(XBL 7110-4532)

In Fig. 2 are given the excitation functions

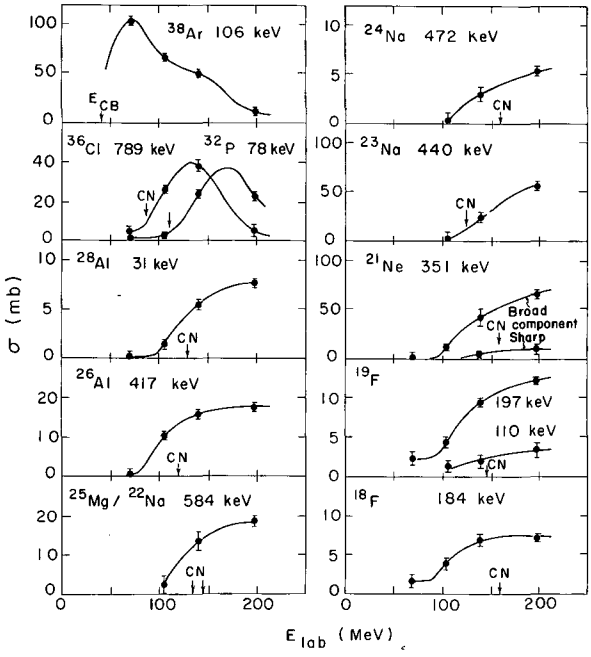

Fig. 2. Excitation functions measured for ^{20}Ne on ^{27}Al. The arrows labeled CN indicate the calculated threshold for compound-nucleus reactions. Error bars include only statistics and errors due to background subtraction. (XBL 7112-4876)

for γ rays from nuclei produced in the reaction ^{20}Ne on ^{27}Al. The results for nuclei with masses larger than 28 are typical for compound-nucleus reactions. Observed thresholds and maxima are in agreement with simple calculations. The excitation functions for the nuclei in the mass region A = 18 to 28 (except ^{23}Na and ^{26}Al) show a shape similar to each other, but different from those of the heavier products. A typical example is given by the broad component of the 351-keV line of ^{21}Ne. The excitation function shows a threshold at about 100-MeV beam energy. This is about 50 MeV below the threshold for compound-nucleus reactions involving emission of nucleons and α particles leading to the same nucleus.

The cross sections for direct reactions, exemplified by the excitation function for the neutron pick-up reaction leading to ^{21}Ne, do show the expected behavior, namely a strong increase by factors of 5 to 10 or more compared with the values below the threshold observed at about 100-MeV beam energy (for ^{20}Ne). This threshold indicates the point where the angular momenta for surface collisions begin to exceed the critical angular momentum, J_{cr}, of the compound nucleus. Thus, above 100 MeV, partial waves with angular momenta smaller than those for surface collisions be-

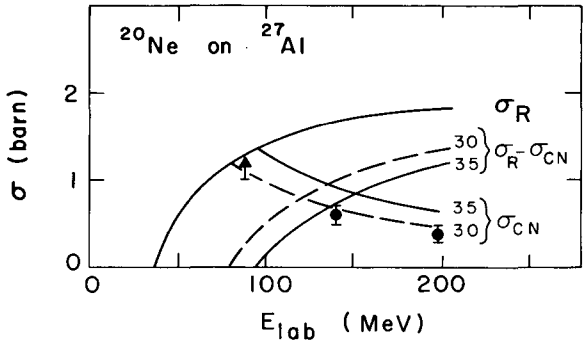

Fig. 3. Energy dependence of the reaction cross section, σ_R and of the total compound-nucleus cross section, σ_{CN}, for ^{20}Ne on ^{27}Al according to the sharp-cutoff model described in the text. The curve parameter is L_{cr}, the upper limit of the angular momentum of the compound nucleus. The data points for σ_{CN} are from Ref. 2. (XBL 7112-4874)

come increasingly available for direct reactions rather than leading to fusion. This concept is formulated more quantitatively by means of a sharp-cutoff model (see Fig. 3). Here, the reaction cross section, α_R, is calculated assuming that all collisions in which the two nuclei come within the range of the nuclear forces lead to a reaction. The total compound-nucleus cross section, σ_{CN}, follows from the assumption that all partial waves with an angular momentum smaller than $L_{cr} \approx J_{cr}$ lead to compound-nucleus formation. Figure 3 shows that the measured fusion cross sections[2] are consistent with $L_{cr} \approx 30\ \hbar$. The excitation functions for direct reactions are to be identified with the difference $\sigma_R - \sigma_{CN}$ and should therefore show an exactly complementary behavior. Our results (the threshold being at about 100 MeV) indicate a slightly higher limit ($L_{cr} = 35\ \hbar$). The discrepancy may be attributed to the fact that compound-nucleus formation follwed by fission has not been included in the cross section of Ref. 2.

Footnote and References

*On leave from the University of Marburg, Germany.

1. S. Cohen, F. Plasil, and W. J. Swiatecki, in Proc. of the Third Conf. on Reactions between Complex Nuclei, (University of California Press, Berkeley and Los Angeles, 1963), p. 325.

2. L. Kowalski, J. C. Jodogne, and J. M. Miller, Phys. Rev. 169, 894 (1968).

3. B. Wilkins and G. Igo, Third Conf. (see Ref. 1), p. 241.

ISOSPIN PROPERTIES OF THE GIANT DIPOLE RESONANCE

J. D. Vergados

The study of the giant dipole resonance (GDR) is a very interesting problem of nuclear structure. In particular, a microscopic description of the DGR, using realistic interactions, has become an attractive application of the shell model since the advancement of computer technology made it easier to use relatively complex Hilbert spaces. Furthermore, the effort in this direction has been motivated by the fact that many experimental techniques have become available for the study of the GDR [e.g., (p, γ) excitation functions].

The excitation energy of the GDR and the relevant-sum rules have already been understood in terms of the configuration mixing of the shell model. Recently the efforts have been centered on trying to understand the fragmentation of the GDR. The most consistent explanation of this fragmentation can be given in terms of the isospin quantum number (T), which retains its significance even in heavy nuclei.

If the ground state of the nucleus is characterized by isospin $T = T_z = 1/2\,(N-Z)$, then, since the dipole operator is essentially an isovector, the GDR is expected to split into two components with isospins T and T + 1 (in the case of N = Z nuclei, i.e., T = 0, only the T + 1 component appears). In a simple-minded picture[1] one expects the energy splitting to be

$$\Delta E = E(T+1) - E(T) = (V_1)_{eff}(T+1)/A, \quad (1)$$

where $(V_1)_{eff} \approx 3/5\ V_1$. V_1 is the strength of the Lane potential (~100 MeV) and is related to the symmetry energy U via the relationship $U = V_1\ T/A$. The dipole strength d is distributed between the two isospin components as follows:

$$d_{T+1}: d_T = (1-\alpha_1)/(T+\alpha_1);\ \alpha_1 = 1.5\ T\ A^{-2/3}. \quad (2)$$

Equations (1) and (2) provide a definite isospin dependence. They predict that for N = Z nuclei, only the T + 1 component is present, while for N - Z large (e.g., Pb region), the T + 1 component of the GDR almost disappears. In the intermediate cases both isospin components are present and fragmentation is expected. The above predictions should be checked by detailed shell-model calculation and experiment. However, since the excitation function shows fine structure and theoretically the dipole strength is shared by many eigenstates, some kind of averaging has to be devised. We have chosen to define $\bar{E} = \Sigma E_i \Gamma_i / \Sigma \Gamma_i$, where Γ_i is the radiative width of the state i with energy E_i.

For nuclei in Sr region ($T \approx 6$), we have already performed such calculations which have been published.[2] So we will not elaborate here except to state that they confirm the above predictions. The results are summarized in Table I.

For nuclei in the Pb region, such calculations are in progress, but the final results are not yet available. We intend to perform these calculations after the spurious motion has been rigorously removed.

Therefore, we will discuss, in detail, calculations[3] of nuclei with N - Z = 2 (T = 1), for which the strength is expected to be fragmented more or less evenly between the two isospin components. In particular, we will focus our attention on ^{42}Ca since this is a case where sufficient experimental information has become available.

For the initial (dipole) states, our shell-model space was allowed to include 2-particle (2p) and 3-particle--1-hole (3p - 1h) excitations in any of the $0d_{5/2}^{-1}$, $1s_{1/2}^{-1}$, $0d_{3/2}^{-1}$, $0f_{7/2}$, $1p_{3/2}$, $0f_{5/2}$, $1p_{1/2}$, and $0g_{9/2}$ orbitals. The unperturbed single-particle energies of -13.36, -9.66, -7.26, 0, 2.10, 6.00, 4.10, and 4.98 MeV, respectively, for both neutrons and protons were taken essentially from experiment. For the final states, we restricted ourselves to the 2p positive-parity states. The resulting matrices were 182×182 and 216×216 for the T = 2 and T = 1 dipole states, respectively.

The Kuo-Brown realistic effective interaction (bare matrix elements) was used, and the isospin-breaking Coulomb interaction was neglected. The calculation predicts (Figs. 1 and 2) $\bar{E}_T$ = 17.0 MeV, $\bar{E}_{T+1}$ = 19.6 MeV, V_1 = 52.5 MeV, which is in good agreement with experiment[3] ($\bar{E}_T$ = 17.4 MeV, $\bar{E}_{T+1}$ = 20.4 MeV, V_1 = 60 MeV) and the above simple model (see Table I). The calculation also shows that there is no appreciable dipole-quadrupole coupling, at least if the effects of deformation can be neglected.[3]

As a further example, we considered the case of ^{42}Sc, which is characterized by T = 1, T_z = 0. Then the dipole states are characterized by isospins T - 1, T, and T + 1. However, the $T \rightarrow T$ isovector dipole transition is strictly forbidden (the Clebsch-Gordon coefficient

Table I. Summary of calculations.

Nucleus	BE1($T_<$) $E_\gamma \leq 7.5$ MeV	BE1 $T_>$ e^2fm^2	BE1 $T_>$ e^2fm^2	BE1($T_>$) / BE1($T_<$)	$\frac{1}{T}$	α_1	$\frac{1}{T}\left\|\frac{b_{T+1}}{b_T}\right\|^2$	$\bar{E}_{T_<}$ (MeV)	$\bar{E}_{T_>}$ (MeV)	V_2(eff) (MeV)	BE1 $\frac{A}{NZ}$
^{88}Sr	2.77	31.8	2.76	0.087	0.167	0.450	0.086	15.67	19.47	48	1.60
^{90}Zr	2.94	32.9	3.78	0.114	0.200	0.373	0.117	15.18	19.66	67	1.65
^{89}Y	5.59	27.5	3.16	0.115	0.182	0.410	0.100	16.40	19.74	46	1.40
^{42}Ca	1.35	8.25	6.54	0.793	1.000	0.124	0.779	17.90	20.74	53	1.42

Experimentally (Carlos and Bergere):

$$\int \sigma_{T_>} \frac{dE}{E} \Big/ \int \sigma_{T_<} \frac{dE}{E} = 0.12 \pm 0.02 \quad \text{for } ^{88}Sr \text{ and } ^{90}Zr.$$

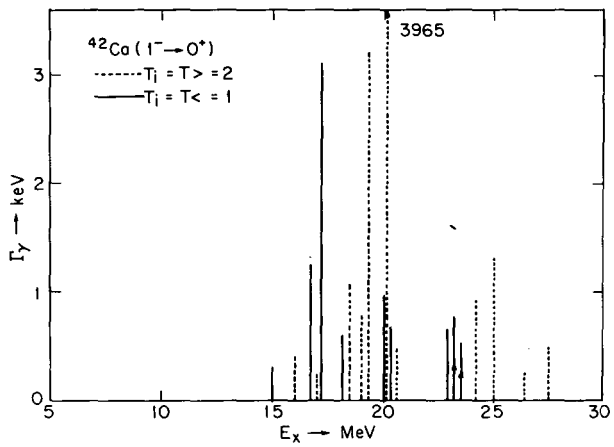

Fig. 1. Dipole transitions $^{42}Ca(1^- \rightarrow 0^+)$. Only widths $\Gamma_\gamma \geq 0.2$ keV are presented.
(XBL 7112-4867)

< T0 10 | T0 > vanishes). Therefore, the GDR now splits into two components which differ by two units of isospin, but the separation energy should be approximately twice the separation energy predicted by the effective symmetry energy.

The calculated total oscillator strength (14.88 e^2 fm^2) compares well with that of ^{42}Ca(14.79 e^2 fm^2). We also find d_{T+1} : d_{T-1} = 1.41 which is in excellent agreement with the above simple model (d_{T+1} : d_{T-1} = 1.40). However, the T = 0 strength is fragmented all over the place (Figs. 3 and 4). We get $\bar{E}(T+1)$ = 20.5 MeV and $\bar{E}(T-1)$ = 18.8 MeV, which yields ΔE = 1.7 MeV instead of the expected 3.7 MeV. However, if we used the BE1 strength, rather than the width, as weight is computing the average energy, we get ΔE = 5.6 MeV. The separation energy seems to be a sensitive function of the averaging method, especially when the strength is fragmented. Unfortunately, there are no experimental results here to compare the calculation with.

Since nuclei with $T \neq T_z$ will provide a further test for the isospin properties of the GDR, we plan to investigate another such nucleus (e.g. ^{14}N). Hopefully, the strength will be

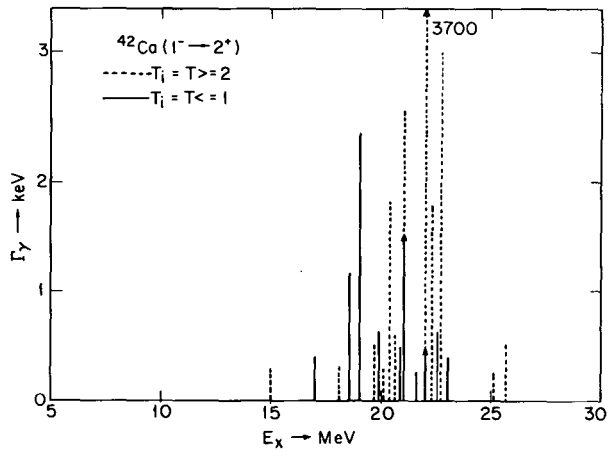

Fig. 2. Dipole transitions $^{42}Ca(1^- \rightarrow 2^+)$. Only widths $\Gamma_\gamma \geq 0.2$ keV are shown.
(XBL 7112-4868)

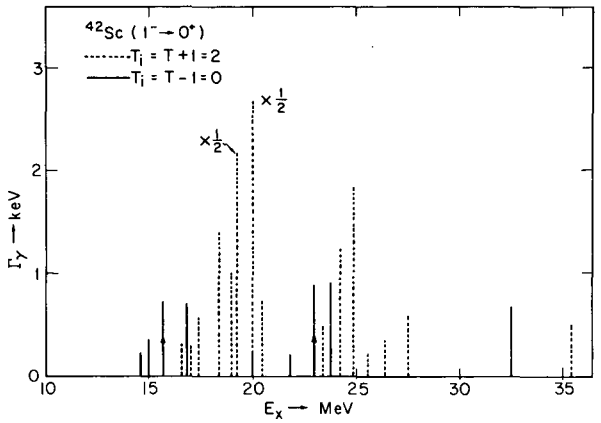

Fig. 3. Dipole transitions ^{42}Sc($1^- \rightarrow 0^+$). Only widths $\Gamma_\gamma \geq 0.2$ keV are shown.
(XBL 7112-4866)

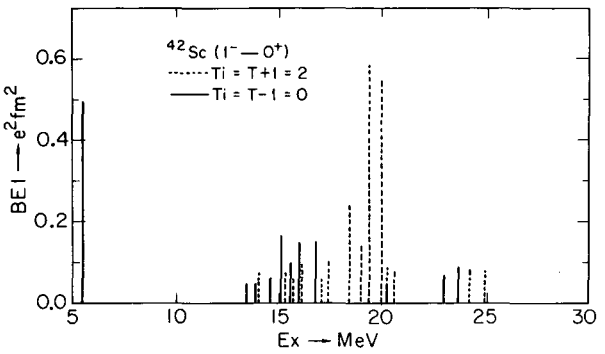

Fig. 4. Dipole transition strengths ^{42}Sc($1^- \rightarrow 0^+$). Only strengths BE1 ≥ 0.05 e^{2}fm^2 are shown.
(XBL 722-2350)

more concentrated, and the ambiguities of the averaging will not come in.

References

1. R. Ö. Akyüz and S. Fallieros, Phys. Rev. Letters 27, 1016 (1971).

2. J. D. Vergados and T. T. S. Kuo, Nucl. Phys. A168, 225 (1971); J. D. Vergados and T. T. S. Kuo, Phys. Letters 35B, 93 (1971).

3. E. Diener, J. Amman, P. Paul, and J. D. Vergados, Isospin Effects in the Giant Dipole Resonance in ^{42}Ca, LBL-602, 1972.

RADIATIVE π^- ABSORPTION IN NUCLEI

J. D. Vergados

The absorption of a π^- from an atomic orbit by the nucleus can serve as a very good probe for the study of the nucleus: First, because the pion wavelength (1.7 fm) is smaller than the nucleon wavelength, i.e., of the order of the range of nuclear forces. This means that a precise knowledge of the π-N interaction is less necessary than that of the N-N interaction. Second, because the captured pion is in a bound orbit around the nucleus. So one overcomes some of the problems associated with the continuum states involved in nuclear reactions.

Once a pion is absorbed, because of the tremendous energy which is released (roughly equal to the pion mass, i.e. $\approx$ 140 MeV) there are many channels which open up. Mostly, we have emission of neutrons and γ rays. However, it has been observed[1] that about 2% of the time, the pion capture is followed by emission of high-energy γ rays, i.e.,

$$\pi^- + A(N, Z) \rightarrow \gamma + A^*(N+1, Z-1).$$

So, superimposed on the continuum spectrum one sees very-well-resolved spikes; e.g. in ^{12}C peaks are observed at E_γ = 124.7, 120.3, and 117.0 MeV. These correspond to transitions in which the residual nucleus is left in the 1^+ (ground), 2^- (E_x = 4.46 MeV), and 1^- (E_x = 7.85 MeV) states, respectively. It is interesting that the final 1^-- and 2^--states are parents of the highly collective states in ^{12}C seen via a number of other reactions.

Two questions must be answered: Why the radiative π^- absorption proceeds with so high a probability (2%)? Why the nucleus prefers to go only to a specific number of states, at least at the high-energy portion of the γ-spectrum? Furthermore, it is interesting to compute the capture rates to a number of final states and compare them with experiment.

In order to answer these questions, one must "tackle" the following problems:

(a) The pion wave function must be known accurately. Hydrogenic wave functions will not be accurate enough because of distortions arising both from the Coulomb and strong interactions. The pion comes very close to the

nucleus, compared with the electron. So the nucleus cannot be treated as a point charge. Furthermore, it falls within the range of strong interactions, and its interaction with the nucleons must be taken into account. For this part of the problem, we rely on the collaboration of the atomic and nuclear physicist.

(b) The interaction responsible for this transition must be known. In constructing the effective interaction, we follow the well-known CGLN[2] prescription, which derives the effective interaction for the inverse process (pion photoproduction). The nonrelativistic limit of this Hamiltonian yields the following operator:

$$H(i) = 2\pi i \left[A\,\vec{\sigma}_i \cdot \hat{\epsilon} + B\,(\vec{\sigma}_i \cdot \hat{\epsilon})\,(\vec{q} \cdot \vec{k}) + C\,(\vec{\sigma}_i \cdot \vec{k})\,(\vec{q} \cdot \hat{\epsilon}) + iD\,\vec{q} \cdot (\vec{k} \times \hat{\epsilon}) \right], \quad (1)$$

where

$\vec{\sigma}_i$ is the spin of the ith nucleon

$\vec{q}$ is the pion momentum

$\vec{k}, \hat{\epsilon}$ are the momentum and polarization of the produced photon.

The coefficients A, B, C, D at zero momentum, are chosen to be:

$$A = -0.032\ M_\pi^{-2}, \quad B = 0.0075\ M_\pi^{-2},$$
$$C = -0.037\ M_\pi^{-2}, \quad D = -0.037\ M_\pi^{-2}.$$

The effective Hamiltonian to be sandwiched between the nuclear states is

$$Heff = \sum_{i=1}^{A} e^{-i\vec{k}\cdot\vec{r}_i}\, H(i)\, f^{n_0}_{\lambda_0}(r_i)\, Y^{\lambda_0}_{\mu_0}(\hat{r}_i),$$

where $\exp[-i\vec{k}\cdot\vec{r}_i]$ is a retardation factor and $f^{n_0}_{\lambda_0}(r_i)\, Y^{\lambda_0}_{\mu_0}(\hat{r}_i)$ is the pion wave function [$Y^{\lambda_0}_{\mu_0}(\hat{r}_i)$ is a spherical harmonic of rank λ_0].

We have made use of the impulse approximation. Furthermore, inside the nucleus, we might have to consider renormalization effects, i.e., the constants A, B, C, D may have to be modified.

(c) Since the radiative π^- absorption is a collective effect, the nuclear wave functions for the A(N, Z) and A^*(N+1, Z - 1) systems must be computed as accurately as possible. We have set up the computer programs which are going to compute these wave functions by diagonalizing fairly large shell-model matrices. So, configuration-mixing effects will be taken into account using realistic two-body interactions. The techniques of the calculation, coefficients of fractional parentage and Racah Algebra are well-known and will not be discussed here, nor will the formulas that yield the single-particle reduced-matrix elements, which are rather involved. Special care must be taken to guarantee that the transverse polarization of the photon is included. If the axis of quantization is in the k- direction, then $\hat{\epsilon}_Z = 0$. This restriction makes the formulas somewhat more complicated.

The pion-capture rate (in natural units) is given by

$$S = \frac{2k^2}{(2\lambda_0+1)}\,\frac{1}{2Ja+1}\int \frac{d\hat{k}}{4\pi} \sum_{\substack{M_a \\ M_b \\ \mu_0, \epsilon_i}} \left| \langle J_b M_b | H_{eff} | J_a M_a \rangle \right|^2 .$$

The formalism has completely been worked out but only tentative results are available for the reaction:

$$\pi^- + {}^6\mathrm{Li} \rightarrow \gamma + {}^6\mathrm{He}.$$

References

1. J. A. Bistirlich et al., Phys. Rev. Letters 25, 689 (1970).

2. C. F. Chew, M. L. Goldberger, F. E. Low, and Y. Nambu, Phys. Rev. 106, 1345 (1957).

MICROSCOPIC CALCULATIONS OF QUASI-ROTATIONAL STATES

C. W. Ma and C. F. Tsang

During the past few years, one of the most exciting phenomena in the deformed regions of nuclei is the experimental discovery of the quasi-rotational energy patterns which strongly deviate from the simple I(I + 1) rotational spectrum. A variety of models directed to understanding this problem have been suggested and are often capable of giving a good fit to the ex-

perimental spectrum. Among these, the empirical variable-moment-of-inertia model[1] (or the mathematically equivalent Harris' fourth-order cranking model[2]) probably stands out as the most popular one, which was found recently to have a very wide range of validity for the yrast states. In the VMI model, the energy of a state with spin I is given as

$$E_I = \frac{1}{2} C(J_I - J_0)^2 + \frac{I(I+1)}{2J_I} \qquad (1)$$

subjected to the minimization condition

$$\frac{\partial E_I}{\partial J_I} = 0. \qquad (2)$$

The two parameters C and J_0 are obtained by a least-square fit to the experimental data.

We are currently performing detailed microscopic calculations on the quasi-rotational states. Specifically, we calculate the moment-of-inertia, J_0, and the force constant, C, associated with the VMI model. The former can be calculated by the well-known second-order cranking formula, while the latter can be expressed as[3]

$$C = \left[\sum_i \frac{1}{C_i} \left(\frac{\partial J_0}{\partial X_i} \right)^2 \right]^{-1} \qquad (3)$$

where $\{X_i\}$ stand for the "vibrational" modes leading to the deviation from the I(I + 1) rule. The present calculation takes into account the symmetric quadrupole (ϵ) and hexadecapole (ϵ_4) centrifugal stretching, the proton (ν_n) and neutron (ν_p) Coriolis-anti-pairing and the fourth-order cranking[2](η) effects:

$$\frac{1}{C} = \frac{1}{C_{22}} \left(\frac{\partial J_0}{\partial \epsilon_2} \right)^2 + \frac{1}{C_{44}} \left(\frac{\partial J_0}{\partial \epsilon_4} \right)^2 + \frac{1}{C_{\nu_p}} \left(\frac{\partial J_0}{\partial \nu_p} \right)^2 + \frac{1}{C_{\nu_n}} \left(\frac{\partial J_0}{\partial \nu_n} \right)^2 + \frac{1}{C_\eta} \left(\frac{\partial J_0}{\partial \eta} \right)^2$$

Calculations on nuclei in the actinide region, the rare-earth region and the neutron-rich region (A ≈ 110), based on the new Nilsson wave function,[4] are under way.

Preliminary results show that the calculated moment-of-inertia of the ground state, J_0, in the rare-earth and actinide regions can be over-all reproduced, provided the pairing strength is chosen as G_0 = 18.0 MeV and G_1 = 7.4 MeV. This pairing force will give odd-even mass differences which are systematically smaller than the empirical values. It may be argued that effects other than pairing force may also contribute to the empirical odd-even mass difference. In particular, the kinetic energy contribution of 22/A MeV (due to the simple fact that there are two particles per level) appear to be able to account for the discrepancy.

References

1. M. A. J. Mariscotti, G. Scharff-Goldhaber, and B. Buck, Phys. Rev. 178, 1864 (1969).

2. S. M. Harris, Phys. Rev. 138, 509 (1965).

3. Chin W. Ma and John O. Rasmussen, Phys. Rev. C2, 798 (1970).

4. S. G. Nilsson, C. F. Tsang, A. Sobiczewski, Z. Szymanski, S. Wyech, C. Gustafson, I.-L, Lamm, P. Moller, and B. Nilsson, Nucl. Phys. A131, 1 (1969).

CORIOLIS EFFECTS IN THE YRAST STATES

F. S. Stephens and R. S. Simon

For a given angular momentum, the state of lowest energy in a nucleus is called the yrast state. For angular momenta lower than about 10 ħ, these states are reasonably well known and understood in most nuclei, but there is much less information about yrast states of considerably higher angular momentum. Recently, however, evidence[1,2] has been accumulating for a major change in the nature of the yrast levels in some deformed rare-earth nuclei somewhat below I = 20, and furthermore, at higher spin values a new very regular structure seems to develop.[1] If we confine ourselves to rotational nuclei, both because most of the above data relate to this type and because they are considerably easier to understand, then it seems reasonably clear that the primary new features at high angular momentum are the presence of strong centrifugal and Coriolis forces. There is experimental evidence[3] that in good rotors, such as ^{154}Sm, the centrifugal stretching up to spin 8 is very small, if it occurs at all. Although the stretching may well be appreciable

for larger spins, it seems unlikely to cause the major effects described above. On the other hand, any simple estimate indicates that the Coriolis effects can be very large, and furthermore, they are known to be involved in determining the yrast levels at rather low spins ($I \approx 10$) in some odd-mass rare-earth isotopes.[4] We have therefore attempted to evaluate the direct effects of the Coriolis force on the nuclear levels. By direct effects we mean those that result from the diagonalization of the Coriolis interaction among a given set of levels. This simple procedure does not take into account changes due to other types of interaction (centrifugal stretching, for example) nor more subtle effects of the Coriolis force, itself (the Mottelson-Valatin effect,[5] for example). Thus, while we cannot expect all the changes occuring in nuclei at high spins to be direct Coriolis effects, we can expect such effects to provide a background which is occuring and against which other changes might be identified. This work represents an attempt to understand this background; and a more complete report of it has been given elsewhere.[6]

In order to calculate the direct Coriolis effects in deformed even-even nuclei, we must decide which states to include in the calculation and which to omit. Fortunately, it turns out to be rather straightforward to select the important states; namely, the ones that lie low in energy and have large Coriolis interactions. As far as the energy is concerned, one can say that the 2 quasiparticle (2qp) states lie lowest--after the ground band (0qp)--then the 4qp states, etc., and apart from this it depends on the exact location of the fermi surface. The requirement for large Coriolis interactions is much more specific. It is well known that these effects are much the largest in the unique-parity high-j orbital within each shell. In the rare-earth region these shells would be the $i_{13/2}$ for neutrons and the $h_{11/2}$ for protons. Due to the fact that it is less-completely filled, the $i_{13/2}$ orbital turns out to be considerably more important than the $h_{11/2}$ in the rare-earth region. This suggests that it might be reasonable to consider the Coriolis effects among the states from the $i_{13/2}$ orbital explicitly, and to assume that the other states form an inert core that only rotates. This is the model we have chosen to explore and we have made rather extensive calculations involving up to 4 quasi particles in the $i_{13/2}$ orbital.

The results of these calculations have been discussed in some detail elsewhere;[6] so that here we will only give a brief summary. We find that at moderately high values of the spin ($I \lesssim 10$) a pair of $i_{13/2}$ particles tend to decouple from the core and align their angular momenta, $2j - 1$, with the rotational angular momentum of the core. This state, whether or not fully decoupled, lies very low in the 2 quasiparticle spectrum and generally intersects the rising ground state band somewhere between $I = 10$ and 20. Thus, our calculations suggest that the lowest-lying band changes character rather abruptly in this region to one where two particles—$i_{13/2}$ particles in the beginning of the rare-earth deformed region—are (or tend to be) decoupled from the core. If the Coriolis matrix elements are somewhat reduced over the a priori estimate, this picture fits rather well the experimental data on rotational spacings[2] and feeding following (HI, xn) reactions.[1] This method for carrying angular momentum with the minimum expenditure of energy combines that used by the deformed nuclei for lower spin values, rotation, with that used by the near-closed-shell nuclei, aligning high-j particles, and suggests that at least in some cases the combination is more efficient than either one separately.

Our calculations ignore any other significant changes that may be occurring in the nucleus as the angular momentum increases. It does not seem so likely that such other changes will totally prevent or submerge the tendencies of the Coriolis interaction, but they may certainly interrupt, delay or temporarily overshadow them. The Mottelson-Valatin effect[5] might represent an example of such a change. This is the phase transition caused by the Coriolis force from the state with pairing correlations to the one without, and is expected to occur rather suddenly at around $I = 20$. This effect is not the same as the decoupling that we are discussing, though both are related in that they have a common cause--the Coriolis force. In fact, the Mottelson-Valatin effect has also been suggested[2] as a possible cause of the observed change in the yrast levels around $I = 20$. If this is true then the decoupling which we have discussed would have to occur at still higher angular momentum. It is an interesting and challenging problem to try to determine whether the experimentally observed changes are due to decoupling, the Mottelson-Valatin effect, some combination of these two, or some other cause.

References

1. J. O. Newton, F. S. Stephens, R. M. Diamond, W. H. Kelley, and D. Ward, Nucl. Phys. A141, 631 (1970).

2. A. Johnson, H. Ryde, and J. Sztarkier, Phys. Letters 34B, 605 (1971).

3. R. M. Diamond, G. Symons, J. Quebert, K. Nakai, K. H. Maier, J. Leigh, and F. S. Stephens, submitted to Nuclear Physics.

4. K. A. Hagemann, S. A. Hjorth, H. Ryde, and H. Ohlsson, Phys. Letters 28B, 513 (1969).

5. B. R. Mottelson and J. G. Valatin, Phys. Rev. Letters 5, 511 (1960).

6. F. S. Stephens and R. S. Simon, Nuclear Physics, A183, 257(1971).

TEMPERATURE-DEPENDENT THOMAS-FERMI CALCULATION OF NUCLEAR PROPERTIES

W. A. Kupper*

The temperature dependence of nuclear properties can be investigated in the Thomas-Fermi approximation, using the expression for the free energy which is a simple extension of the zero-temperature ground state energy. It has been shown[1] that one can formulate a generalized T and chemical potential μ, in which the free energy is required to be stationary with respect to variations in the density, subject to the condition that the total number of particles remains constant.

The momentum-dependent phenomenological two-body interaction $V(r_{12}, p_{12})$ used in this work is that of Seyler and Blanchard[2] with coefficients chosen to roughly reproduce known nuclear properties.[3] Only symmetric nuclear systems (neutron and proton densities equal) that may be thought of as consisting of only one component are considered here.

The free energy can then be written

$$F = E - TS$$

$$= \int d\underline{r}_1 \frac{4}{(2\pi)^3} \int d\underline{P}_1 \rho(\underline{r}_1, \underline{P}_1) \left[\frac{\underline{P}_1^2}{2m} + \frac{1}{2} V(\underline{r}_1, \underline{P}_1) \right]$$

$$+ \frac{1}{\beta} \int d\underline{r}_1 \frac{4}{(2\pi)^3} \int d\underline{P}_1 \left[\rho(\underline{r}_1, \underline{P}_1) \ell n \rho(\underline{r}_1, \underline{P}_1) \right. \quad (1)$$

$$\left. + (1-\rho(\underline{r}_1, \underline{P}_1)) \ell n (1-\rho(\underline{r}_1, \underline{P}_1)) \right],$$

where

$$V(\underline{r}_1, \underline{P}_1) = -\frac{1}{2} \int d\underline{r}_2 \frac{4}{(2\pi)^3} \int d\underline{P}_2 \, V(r_{12}, \underline{P}_{12}) \rho(\underline{r}_2, \underline{P}_2) \quad (2)$$

is the potential energy of a nucleon with momentum P_1 located at $\underline{r}_1$, and

$$\rho(r_1, P_1) = \frac{1}{\exp\left\{\beta\left[\frac{P_1^2}{2m} + V(\underline{r}_1, \underline{P}_1) - \mu\right]\right\} + 1} \quad (3)$$

is the distribution function, which determines the density $\rho(\underline{r}_1)$ and the particle number A:

$$A = \int d\underline{r} \, \rho(\underline{r}) = \int d\underline{r} \frac{4}{(2\pi)^3} \int dP \, \rho(\underline{r}, \underline{P}). \quad (4)$$

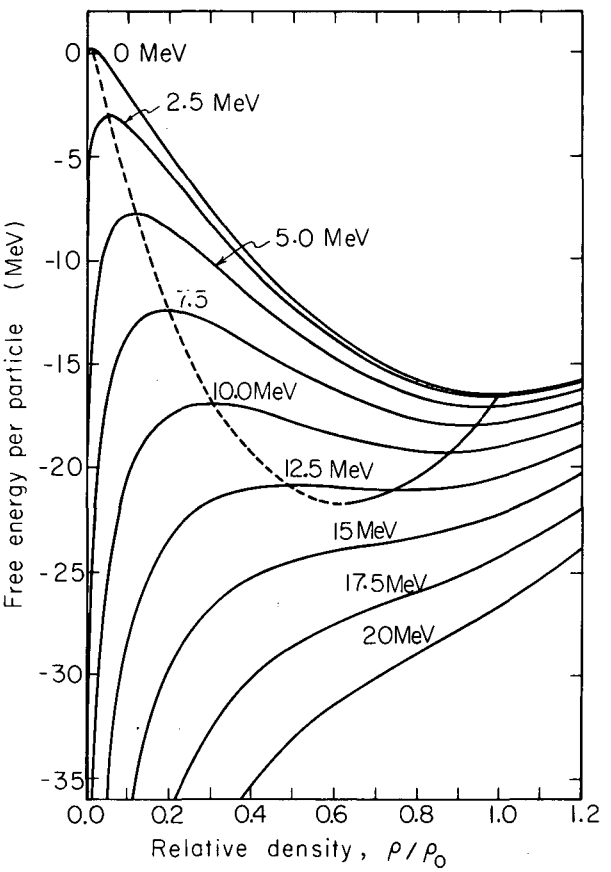

Fig. 1. The free energy per particle F/A as a function of the normalized density ρ_n for various temperatures. The locus of the stationary points – solid line for minima, dashed line for maxima – is shown in the same figure.

(XBL 723-2561)

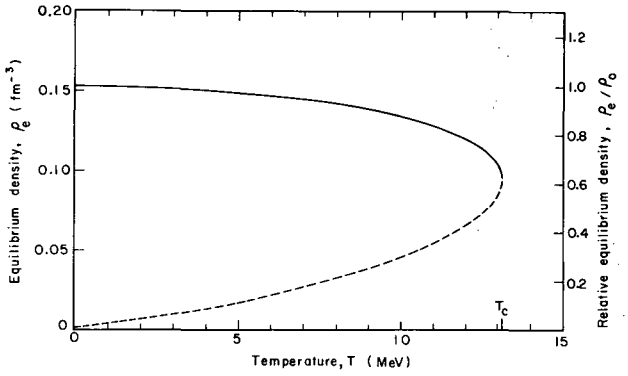

Fig. 2. The equilibrium density for nuclear matter as a function of temperature. The solid line represents minima, the dashed line maxima of F/A. T_c = 13.15 MeV is the critical temperature.

(XBL 723-2574)

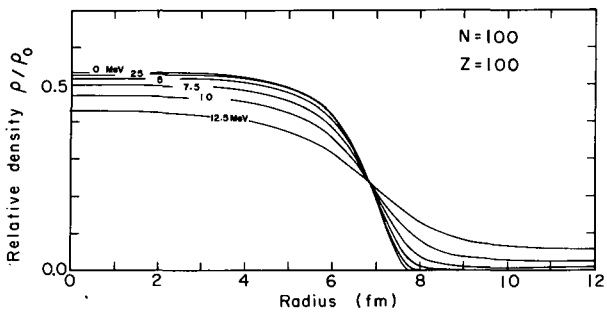

Fig. 3. Density distribution of a symmetric nucleus (N = Z) without Coulomb energy as a function of the radial distance for various temperatures (in MeV).

(XBL 723-2560)

Nuclear Matter. The equilibrium density of nuclear matter is found by minimizing the free energy per particle. Figure 1 shows F/A for several temperatures as a function of the normalized density $\rho_n = \rho/\rho_0$, where ρ_0 is the density of nuclear matter at zero temperature. The locus of the stationary points is given in the same figure. In Fig. 2, this locus is plotted against the temperature. With increasing temperature, the density of nuclear matter decreases. Beyond the critical temperature T_c = 13.15 MeV, no stable solution exists except the trivial one at zero density.

Finite Nuclei. Figure 3 shows the density distribution of a symmetric nucleus (N=Z=100) without Coulomb energy as a function of the radial distance. For an infinitely large nucleus, the central density would be that of nuclear matter. For large, but finite nuclei, the surface tension squeezes the central region, and the central density is increased above that of nuclear matter at the same temperature. The central density, as a function of temperature, shows the same characteristic behavior as the density of nuclear matter. At finite temperature, the solution consists of the original nucleus in equilibrium with a vapor whose density is characteristic of the temperature and nucleus being considered. With increasing temperature, the surface of the nucleus becomes more diffuse, and the characteristic radii of the nucleus, such as the mean-square radius, increase.

Footnote and References

*Visitor from Sektion Physik der Universität München, Munich, Germany.

1. N. D. Mermin, Ann. Phys. 21, 99 (1963).

2. R. G. Seyler and C. M. Blanchard, Phys. Rev. 131, 355 (1963).

3. W. D. Myers, Nucl. Phys. A145, 387 (1970).

THEORY OF NUCLEAR MAGNETIC RESONANCE DETECTED BY NUCLEAR RADIATIONS*

E. Matthias,† B. Olsen,‡ D. A. Shirley, J. E. Templeton,§ and R. M. Steffen‖

A comprehensive theoretical description was given for the effects of magnetic resonance on the angular distribution of radiation emitted from oriented nuclear states. The formulation was made in a general way. It may be applied to an ensemble of nuclei oriented by any method: For example, nuclear reactions, angular correlations, and low-temperature nuclear orientation may be treated. In fact, the theory can also be applied to optical-double-resonance experiments. Statistical tensors, designed to describe nuclear orientation in the "resonant" state, are defined by the equation

$$\rho_q^{\lambda}(0) \vec{z} = \sum_m (-1)^{I+m'} \langle I\text{-}m'Im|\lambda q\rangle \langle Im'|\rho(0)|Im\rangle, \quad (1)$$

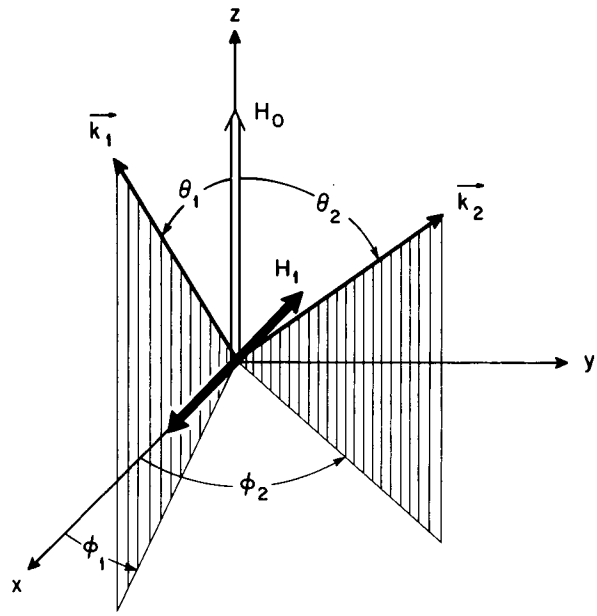

Fig. 1. Unit vectors $\vec{k}_1$ and $\vec{k}_2$ in the laboratory frame. (XBL 678-3906)

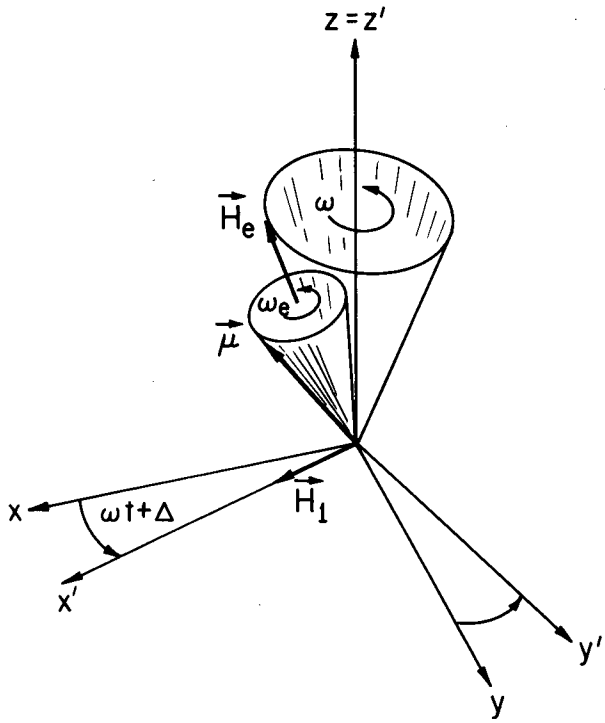

Fig. 2. Transformation from the laboratory frame S into the rotating frame S'(t). (XBL 711-2664)

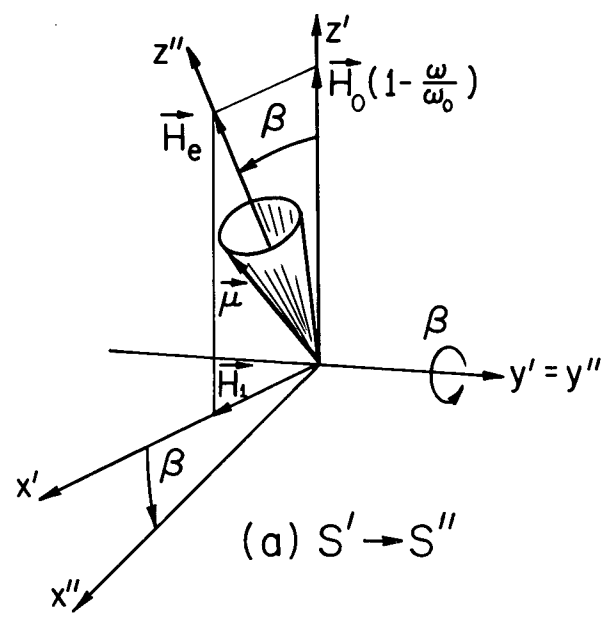

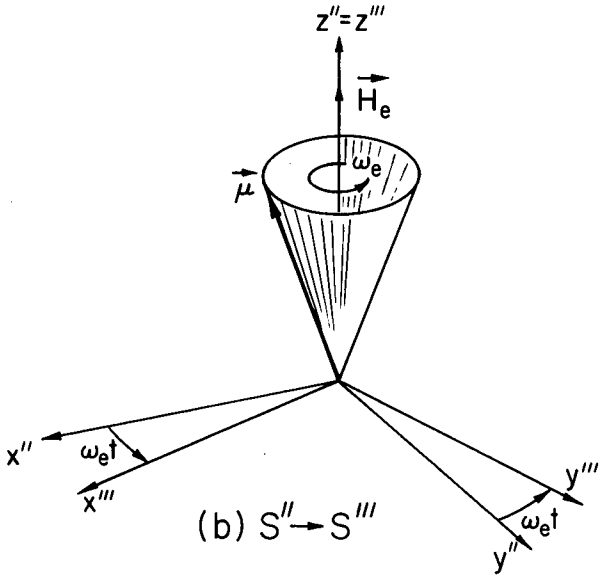

Fig. 3. Transformations (a) from the S' frame into the S'' frame, with $\vec{H}_e$ as the z'' axis, and (b) into S''', a second rotating frame. The S'' → S''' transformation transforms $\vec{H}_e$ to zero in the S''' frame. (XBL 711-2663)

where $\langle \mathrm{Im}' | \rho(0) | \mathrm{Im} \rangle$ is an element of the density matrix for the resonant state at time t = 0, and $\langle \mathrm{I\text{-}m'Im} | \lambda q \rangle$ is a Clebsch-Gordan coefficient. The problem at hand is to solve explicitly for the time-dependent angular distribution of radiation from a resonant state perturbed by a static field $\vec{H}_0$, taken along the z axis, and

an oscillatory field $\vec{H}_1$, taken along the x axis. The nuclei are initially oriented in an arbitrary direction k_1 and the detector is in an arbitrary direction k_2, as shown in Fig. 1.

The central problem in calculating the influence of an extranuclear perturbation on angular distributions or correlations is the computation of the time evolution of the density matrix $\rho(t)$ from a given initial state $\rho(0)$ for a specific perturbation Hamiltonian $\mathcal{H}$:

$$\rho(0) \xrightarrow{\mathcal{H}} \rho(t).$$

The time evolution of a density operator is given by the von Neumann equation

$$i\hbar\,\dot{\rho} = [\mathcal{H}, \rho] = \mathcal{H}\rho - \rho\mathcal{H}. \qquad (2)$$

The operators ρ and $\mathcal{H}$ must be defined in the same reference frame.

Solutions of Eq. (2) are found by introducing the time-evolution operator $\Lambda(t)$, which represents a time-dependent unitary transformation of the density matrix ρ:

$$\rho(t) = \Lambda(t)\,\rho(0)\,\Lambda(t^{+}). \qquad (3)$$

The density matrix $\rho(t)$ is a solution of Eq. (2) if $\Lambda(t)$ satisfies the Schrödinger equation

$$\frac{\partial \Lambda(t)}{\partial t} = -\frac{i}{\hbar}\,\mathcal{H}(t)\,\Lambda(t). \qquad (4)$$

If the operator $\mathcal{H}$ does not contain the time t explicitly or if a reference frame can be found such that $\mathcal{H}$ does not depend on t, the solution of Eq. (4) is

$$\Lambda(t) = \exp(-i\mathcal{H}t/\hbar), \qquad (5)$$

and $\rho(t)$ has the simple form

$$\rho(t) = \exp(-i\mathcal{H}t/\hbar)\rho(0)\exp(+i\mathcal{H}t/\hbar. \qquad (6)$$

Although $\mathcal{H}$ is time dependent in the laboratory frame S, a series of three rotational transformations into the rotating frame S', the tipped frame S'', and the doubly rotating frame S''', defined by Figs. 2 and 3, yield a time-independent Hamiltonian. The transformations can be written in terms of the D matrices as

$$\rho_0^{\lambda}(t) = \rho_0^{\lambda}(0)\,\vec{k}_1 \sum_{\substack{q q' p p' \\ q\,q'}} D^{(\lambda)}_{0q}(0, -\theta_1, -\phi_1) D^{(\lambda)}_{qq'}(\Delta, 00)$$
$$\times D^{(\lambda)}_{q'p}(0, \beta, 0) D^{(\lambda)}_{pp'}(-\omega_e t, 0, 0) D^{(\lambda)}_{p'\bar{q}}(0, -\beta, 0)$$
$$\times D^{(\lambda)}_{\bar{q}q'}(-\omega t - \Delta, 0, 0) D^{(\lambda)}_{q'0}(\phi_2, \theta_2, 0). \qquad (7)$$

This may be compared to the general expression for a time-dependent statistical tensor

$$\rho^{\bar{\lambda}}_{\bar{q}}(t)\,\vec{z} = \sum_{\lambda, q} G^{q\bar{q}}_{\lambda\bar{\lambda}}(t)\,\vec{z}\;\rho^{\lambda}_{q}(0)\,\vec{z},$$

where we have introduced the perturbation coefficient

$$G^{q\bar{q}}_{\lambda\bar{\lambda}}(t)\vec{z} = \sum_{m', \bar{m}} (-1)^{2I+\bar{m}'+m'} \langle I\text{-}\bar{m}'I\bar{m}\,|\bar{\lambda}\bar{q}\rangle \langle I\text{-}m'Im\,|\lambda q\rangle$$
$$\times \langle \bar{m}\,|\Lambda(t)\,|m\rangle \langle \bar{m}'\,|\Lambda(t)|\,m'\rangle. \qquad (8)$$

The angular distribution of radiation is given by

$$W(\theta_1\phi_1\theta_2\phi_2; \vec{H}_0\ t) = \sum_{\lambda} B_{\lambda}(I)\,A_{\lambda}(X_2)\Gamma_{\lambda}(t), \qquad (9)$$

where the orientation parameters are defined by

$$B_{\lambda}(I) = (2I+1)^{1/2}\,\rho_0^{\lambda}(0)\vec{k}_1, \qquad (10)$$

and the response functions are related to the perturbation coefficients by

$$\Gamma_{\lambda}(t) = \frac{4\pi}{2\lambda+1} \sum_{q, \bar{q}} G^{q\bar{q}}_{\lambda\lambda}(t)\,Y_{\lambda q}(\theta_1, \phi_1)\,Y_{\lambda,\bar{q}}(\theta_2, \phi_2). \qquad (11)$$

Response functions for tensor rank $\lambda = 1$ are given in Table I for several important geometries.

Another approach to the theory of radiative detection can be made by generalizing the torque equation, familiar from NMR theory,

$$\frac{d\vec{M}}{dt} = \gamma\,\vec{M}\times\vec{H}; \qquad (12)$$

where $\vec{M}$ is the magnetization. This leads to the generalized torque equation

$$\frac{d\vec{K}}{dt} = \gamma\,\vec{K}\times\vec{H}, \qquad (13)$$

which governs the time-evolution of the symmetry axis of the oriented ensemble of nuclei, $\vec{K}(t)$. At time $t = 0$, $\vec{K}(0) = \vec{k}_1$. If the angle $\eta(t)$ is defined by

TABLE I. Response function $\Gamma_1(t) = \vec{K}(t) \cdot \vec{k}_2$ for selected geometries. The angles are defined in Fig. 1.

No.	θ_1	ϕ_1 (deg)	θ_2	ϕ_2	$\Gamma_1(t) = \vec{K}(t) \cdot \vec{k}_2$
1	0	0	180	0	$-G_{11}^{00} = -\cos^2\beta - \sin^2\beta \cos\omega_e t$
1	0	0	0	0	$G_{11}^{00} = \cos^2\beta + \sin^2\beta \cos\omega_e t$
2	0	0	90	90	$-(i/\sqrt{2})(G_{11}^{01} + G_{11}^{0-1}) = \sin\beta\cos\beta\sin(\omega t + \Delta)(1 - \cos\omega_e t) - \sin\beta\cos(\omega t + \Delta)\sin\omega_e t$
3	0	0	90	0	$(1/\sqrt{2})(-G_{11}^{01} + G_{11}^{0-1}) = \sin\beta\cos\beta\cos(\omega t + \Delta)(1 - \cos\omega_e t) + \sin\beta\sin(\omega t + \Delta)\sin\omega_e t$
4	0	0	90	45	$\frac{1}{2}(-G_{11}^{01} + G_{11}^{0-1} - iG_{11}^{01} - iG_{11}^{0-1}) = \sin\beta\cos\beta(1 - \cos\omega_e t)\sin(\omega t + \Delta + \frac{1}{4}\pi)$ $- \sin\beta\sin\omega_e t\cos(\omega t + \Delta + \frac{1}{4}\pi)$
5	90	45	0	0	$\frac{1}{2}(-G_{11}^{10} + G_{11}^{-10} + iG_{11}^{10} + iG_{11}^{-10}) = \sin\beta\sin\omega_e t\cos(\Delta + \frac{1}{4}\pi)$ $+ \sin\beta\cos\beta(1 - \cos\omega_e t)\sin(\Delta + \frac{1}{4}\pi)$
6	90	135	0	0	$\frac{1}{2}(G_{11}^{10} - G_{11}^{-10} + iG_{11}^{10} + iG_{11}^{-10}) = \sin\beta\sin\omega_e t\sin(\Delta + \frac{1}{2}\pi)$ $- \sin\beta\cos\beta(1 - \cos\omega_e t)\cos(\Delta + \frac{1}{4}\pi)$
7	0	0	135	90	$-(1/\sqrt{2})G_{11}^{00} - \frac{1}{2}i(G_{11}^{01} + G_{11}^{0-1}) = (1/\sqrt{2})[\sin\beta\cos\beta\sin(\omega t + \Delta)(1 - \cos\omega_e t)$ $- \sin\beta\cos(\omega t + \Delta)\sin\omega_e t - \cos^2\beta - \sin^2\beta\cos\omega_e t]$
8	45	90	0	0	$(1/\sqrt{2})G_{11}^{00} + \frac{1}{2}i(G_{11}^{10} + G_{11}^{-10}) = (1/\sqrt{2})[\sin\beta\sin\omega_e t\cos\Delta + \cos^2\beta + \sin^2\beta\cos\omega_e t$ $+ \sin\beta\cos\beta(1 - \cos\omega_e t)\sin\Delta]$
9	90	0	90	180	$\frac{1}{2}(-G_{11}^{11} + G_{11}^{1-1} + G_{11}^{-11} - G_{11}^{-1-1}) = \cos\beta\sin\omega_e t\sin\omega t - \sin(\omega t + \Delta)\cos\omega_e t\sin\Delta$ $+ (\cos^2\beta\cos\omega_e t - \sin^2\beta)\cos(\omega t + \Delta)\cos\Delta$
10	90	0	90	135	$\frac{1}{4}\sqrt{2}(-G_{11}^{11} + G_{11}^{1-1} + G_{11}^{-11} - G_{11}^{-1-1} + iG_{11}^{11} + iG_{11}^{1-1} - iG_{11}^{-11} - iG_{11}^{-1-1})$ $= \cos\beta\sin\omega_e t\sin(\omega t + \frac{1}{4}\pi) - \cos\omega_e t\sin(\omega t + \Delta + \frac{1}{4}\pi)\sin\Delta$ $- (\sin^2\beta + \cos^2\beta\cos\omega_e t)\cos(\omega t + \Delta + \frac{1}{4}\pi)\cos\Delta$
11	90	45	90	135	$\frac{1}{2}(G_{11}^{1-1} + G_{11}^{-11} + iG_{11}^{11} - iG_{11}^{-1-1}) = \cos\beta\cos\omega t\sin\omega_e t$ $+ \cos\omega_e t\sin(\omega t + \Delta + \frac{1}{4}\pi)\cos(\Delta + \frac{1}{4}\pi)$ $- (\sin^2\beta + \cos^2\beta\cos\omega_e t)\cos(\omega t + \Delta + \frac{1}{4}\pi)\sin(\Delta + \frac{1}{4}\pi)$
12	90	45	90	0	$\frac{1}{4}\sqrt{2}(G_{11}^{11} - G_{11}^{1-1} - G_{11}^{-11} + G_{11}^{-1-1} - iG_{11}^{11} + iG_{11}^{1-1} - iG_{11}^{-11} + iG_{11}^{-1-1})$ $= -\cos\beta\sin\omega_e t\sin(\omega t + \frac{1}{4}\pi) - \sin(\omega t + \Delta)\cos\omega_e t\cos(\Delta + \frac{1}{4}\pi)$ $+ (\sin^2\beta + \cos^2\beta\cos\omega_e t)\cos(\omega t + \Delta)\sin(\Delta + \frac{1}{4}\pi)$
13	90	90	90	45	$\frac{1}{4}\sqrt{2}(G_{11}^{11} + G_{11}^{1-1} + G_{11}^{-11} + G_{11}^{-1-1} - iG_{11}^{11} + iG_{11}^{1-1} - iG_{11}^{-11} + iG_{11}^{-1-1})$ $= -\cos\beta\sin\omega_e t\sin(\omega t + \frac{1}{4}\pi) + \cos\omega_e t\cos\Delta\cos(\omega t + \Delta + \frac{1}{4}\pi)$ $+ [\sin^2\beta + \cos^2\beta\cos\omega_e t]\sin(\omega t + \Delta + \frac{1}{4}\pi)\sin\Delta$

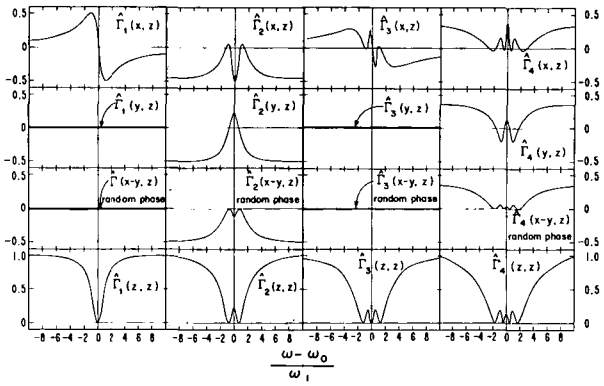

Fig. 4. Line shapes in the saturation limit $\omega_1\tau \to \infty$, with $\vec{k}_2$ along $\vec{z}$ and $\vec{k}_1$ along $\vec{x}$ with $\Delta = 0$ (top row), along y with $\Delta = 0$, in the x-y plane with Δ random, and along $\vec{z}$ (bottom row). (XBL 687-3315)

$$\cos\eta(t) = \vec{k}_2 \cdot \vec{K}_S(t), \qquad (14)$$

then the angular distribution of radiation is given by

$$W(k_1, k_2, t) = \sum_\lambda \rho_0^\lambda(0)_{\vec{k}_1} A_\lambda(X_2) P_\lambda(\cos\eta(t)). \qquad (15)$$

This theory leads to some very unusual resonance line shapes, especially when the phase angle Δ between $\vec{k}_1$ and the oscillatory field is held fixed. Typical cases are shown in Fig. 4

Footnotes and References

*Condensed from Phys. Rev. A4, 1626 (1971), UCRL-18413.

†Present address: I. Physikalisches Institut, Freie Universität Berlin, Boltzmannstrasse 20, 1 Berlin 33, Germany.

‡Present address: Institute of Physics, University of Uppsala, Thumbergsvägen 7, Uppsala 12, Sweden.

§Present address: Oxford Instrument Corp., 100 Cathedral St., Annapolis, Md. 21401.

‖Department of Physics, Purdue University.

THE IMPORTANCE OF INDIRECT TRANSITIONS ON (p,t) REACTIONS ON DEFORMED NUCLEI

R. J. Ascuitto,* N. K. Glendenning, and B. Sørensen†

The mechanism involved in a nuclear reaction is pictured in one of two ways: 1) either a compound nucleus is formed involving the rapid sharing of the incident energy through many collisions, followed by its eventual decay when sufficient energy again becomes concentrated on one or several particles so that they can escape; or 2) a single reaction takes place in which only those nucleons are involved that are needed to change the target ground state into a nearby and closely related final state. The latter reaction, referred to as a direct one, has proved enormously valuable in nuclear spectroscopy since Butler first postulated it to explain the forward-peaked angular distributions populating low-lying states in (d, p) reactions. That all nuclear reactions should fit so neatly into one or the other of these very different categories does seem implausible, however. It has been known for some time that the excitation of intermediate states in inelastic scattering is important for deformed nuclei, though not so important for vibrational nuclei, except for any state whose structure forbids or inhibits its direct production in a single interaction (such as 2-phonon states). In the past several years we have been investigating the question of whether higher-order processes in nucleon transfer reactions are important.[1-8] The processes that we expect are most important are those in which an excited state is produced by an inelastic collision and is followed by the transfer reaction to the final state, together with these interactions in reverse order. Such processes, when important, will involve inelastic transitions to states that are enhanced, and the final states for which the multiple-step processes are important will be those that have a considerable fraction of their parentage based on such collective excited states. Thus the spectroscopy of a different class of states is opened up, namely those whose main parent is a collective state as compared with those most extensively studied up till now, which have the target ground state as main parent. Naturally the former states, on the average, appear higher in the energy spectrum; but since the theoretical analysis has, until now, assumed that any direct reaction proceeds in a single step, undoubtedly many analyses

have yielded misleading information.

Very recently, in the ^{176}Yb(p, t) reaction, we reported what we consider to be the firmest evidence for strong higher-order processes in direct reactions; and the way in which the higher-order processes interfere with the single-step direct transition to bring about agreement with experiment is strong evidence of the correctness of the reaction mechanism.[6]

We have refined and extended the calculations reported in the last annual report so that nuclei at both ends of the rare earth region, for which β_4 has opposite signs, have been treated—and now at two typical bombarding energies. There is much evidence from various sources that the rotational model provides a good description of these nuclei. This implies the existence of an intrinsic state from which all two-nucleon transfer amplitudes to the ground band of the neighboring nucleus can be computed. This is in contrast to spherical nuclei, where the various states of different spin are independent of each other. We may thus have a high degree of confidence that relative cross sections can be computed correctly if the reaction mechanism is properly treated. This indeed turns out to be the case where, with an accuracy unprecedented in reaction theory, the cross sections to the 0^+, 2^+, 4^+, and 6^+ members of the ground band are reproduced, as shown in Fig. 1. However, this comes about only because the many higher-order routes of producing these states were included in the calculation. Especially for the higher spins, the higher-order processes were more important than the first-order ones, traditionally treated by the DWBA. This is demonstrated in detail for the 4^+ state in Fig. 2, where it can be seen that the direct transition, usually used to describe direct reactions, is smaller than the three indirect processes shown and smaller also than the experimental cross section. In both cases we studied—i. e., in a nucleus near both ends of the rare-earth region (both positive and negative β_4) and at two different energies—the interference among the different processes was destructive but of different magnitude for each state in a given nucleus, and also different in the two nuclei for the same spin state. The interference of the various routes, which was between amplitudes of comparable magnitude, did, however, bring about the remarkable agreement mentioned, and is the strongest confirmation that higher-order processes in transfer reactions are of importance for a correct description, and that they can be computed with satisfactory accuracy. This success supports the conclusions that we reached elsewhere[4] for spherical nuclei where, however, direct

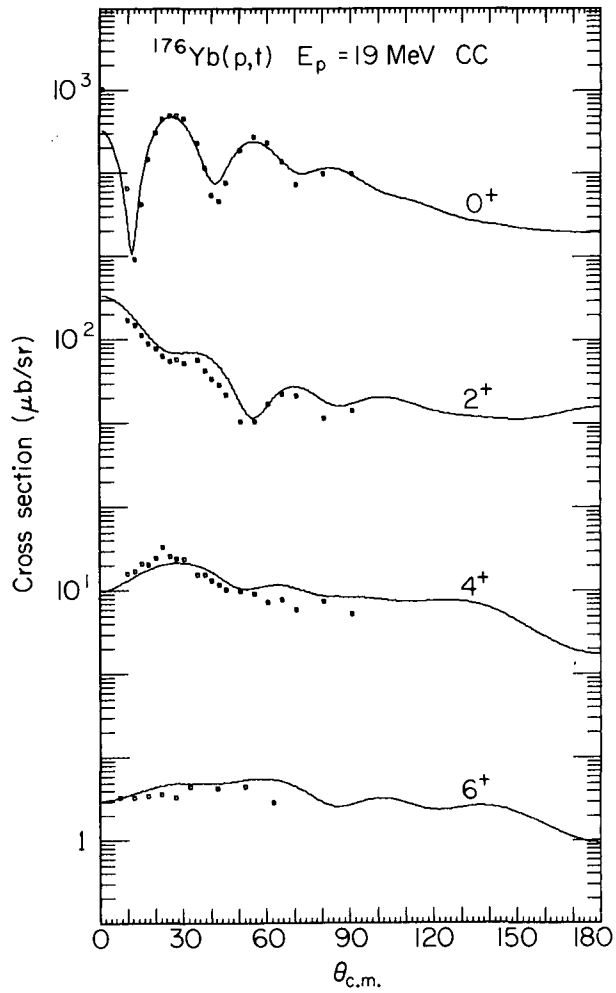

Fig. 1. Complete calculation for the ground-band members of ^{174}Yb produced in the (p, t) reaction. Calculations include all inelastic and reaction transitions connecting all four states in both nuclei. The 0^+ is normalized to the data and the same normalization was used for the others. The experimental values of the deformation parameters β_2, β_4, β_6 were used. (XBL 718-4185)

confirmation from experiment was not possible, both because of the lack of data and because the nuclear structure information was more tenuous. We claim, therefore, on the basis of this work, that we have demonstrated that our calculation of higher-order processes is correct, and on the basis of that other work that they are important in spherical nuclei, though less dramatic in producing changes in angular distributions computed for the direct transition.

We emphasize that at each step of the cal-

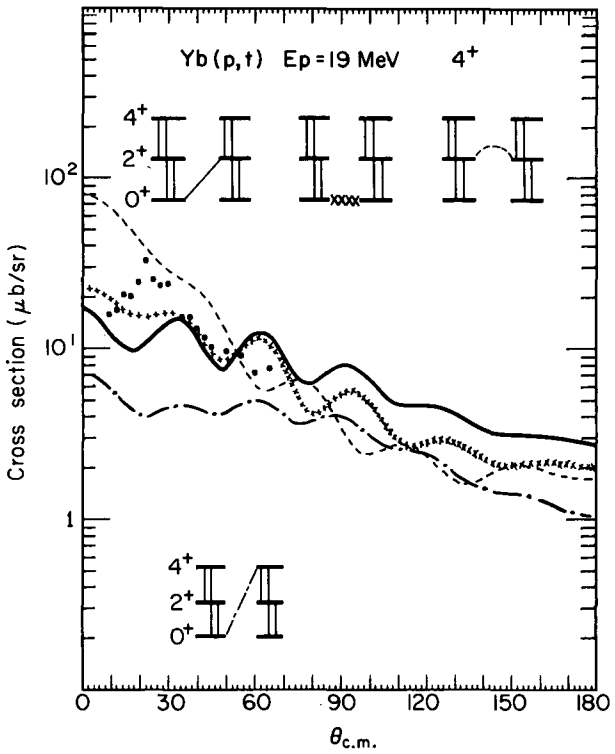

Fig. 2. Cross sections for the 4^+ state at 19 MeV corresponding to several of the many individual transfer processes indicated in the insets. (XBL 718-4196)

culation we made the physically reasonable choices of parameters, and had we not been rewarded with success, we would not have known what else to try.

Contrary to suggestions made elsewhere,[9,10] it seems to us that the (p,t) reaction is not a good way of determining higher multipoles in the nuclear shape. This suggestion was made on the assumption that the reaction could be described by its direct transition alone. As we have seen, the direct transition to the 4^+ state, from which it might be hoped to determine β_4, is smaller than many of the higher-order processes. The higher-order processes, since they go through an intermediate state, involve, dominantly, lower multipoles than the direct. Thus sensitivity to higher multipoles in the shape is weak.

Footnotes and References

*Present address: Wright Nuclear Structure Laboratory, Yale University, New Haven, Connecticut.

†Present address: The Niels Bohr Institute, University of Copenhogen, Denmark.

1. R. J. Ascuitto and N. K. Glendenning, Phys. Rev. 181, 1396 (1969).

2. N. K. Glendenning, in Proceedings of the International Conference on the Properties of Nuclear States (University of Montreal Press, Montreal, 1969).

3. R. J. Ascuitto and N. K. Glendenning, Phys. Rev. C2, 415 (1970).

4. R. J. Ascuitto and N. K. Glendenning, Phys. Rev. C2, 1260 (1970).

5. R. S. Mackintosh and N. K. Glendenning, Nucl. Phys. A168, 575 (1971).

6. R. J. Ascuitto, N. K. Glendenning, and B. Sørensen, Phys. Letters 34B, 17 (1971); and LBL-248, to be published in Nucl. Phys.

7. T. Tamura, D. R. Bes, R. A. Broglia, and S. Lansdowne, Phys. Rev. Letters 25, 1507 (1970) and errata, ibid. 26, 156 (1971).

8. R. J. Ascuitto, N. K. Glendenning, and B. Sørensen, Nucl. Phys. A170, 65 (1971).

9. K. Kubo, R. A. Broglia, C. Riedel, and T. Udagawa, Phys. Letters 32B, 29 (1970).

10. R. A. Broglia, C. Riedel and T. Udagawa, Nucl. Phys. A135, 561 (1969).

QUANTUM MECHANICAL TREATMENT OF PARTICLE TRANSFER BETWEEN HEAVY IONS NEAR THE COULOMB BARRIER IN THE PRESENCE OF COULOMB EXCITATION*

R. J. Ascuitto† and N. K. Glendenning

In the collision, at energies near the Coulomb barrier, between an ion such as oxygen and a deformed nucleus such as samarium, the probability that the deformed nucleus is left in an excited state is very high. Indeed it is near unit probability that the nucleus is in the 2^+ state.[1] In the treatment of particle transfer between the colliding ions, it is there-

fore essential that inelastic processes be included in the description. Now, there is no difficulty in formulating the quantum mechanical description of Coulomb excitation. Indeed, the Coulomb and nuclear forces were treated on an equal basis in a very accurate description of 50-MeV alpha scattering on rare earth nuclei which yielded the first information on higher multipoles in the nuclear shape.[2] There, however, the Coulomb field was much weaker than the nuclear field. In the typical Coulomb excitation experiment the reverse is true; and then while the theory is the same as before, the numerical problems become critical. The Coulomb field being the strong one, and the quadrupole Coulomb field falling off with distance so slowly as $1/r^3$, the differential equations describing the collision have to be integrated to great distance, R (hundreds of fermis) and corresponding large angular momenta ($\ell_m \approx kR$, i.e., hundreds). For this reason Coulomb excitation can and has been treated semiclassically, so long as the energy is sufficiently low that nuclear interaction does not take place; the enormous experimental literature on Coulomb excitation has been based on such a treatment.[1]

With the burgeoning interest in heavy-ion reactions, a semiclassical theory of particle transfer has been developed in analogy to the Coulomb excitation theory.[3] One might think at first, if Coulomb excitation is important in these transfer reactions, that the same difficulties as to large interaction regions and high partial waves will be present here also. This is in fact not the case and can be understood as follows: At Coulomb or sub-Coulomb energies the ions are prevented from interpenetrating by the Coulomb barrier. (Quantum mechanically we know that there is a small but finite probability for this. In such cases massive rearrangement will result and the particles are lost to the particular simple transfer of one or several nucleons that we envision.) Particles can be exchanged between the ions in slightly more distant collisions, however, because of the finite probability of their being found beyond the nuclear surface, where their wave functions are described by exponentially decaying tails. However, because of the exponential decay of the tails, the probability of transfer falls off rapidly with distance. So there is some region bounded on the lower side by the sum of the radii $R_1 + R_2$ of the two ions and some larger, but not so much larger, radius R_3, where the product of the two exponential tails—the particle bound in one nucleus and then transferred to the other—produces negligible probability that the transfer takes place. This outer radius for particle transfer is certainly only several fermis larger than $R_1 + R_2$. On the other hand, because of the slowly decreasing Coulomb field, Coulomb excitation between states in the target nucleus as mentioned earlier can take place even at several hundred fermi beyond $R_1 + R_2$. However, any such collision with impact parameter R, which is much larger than $R_1 + R_2$, cannot contribute to the transfer of particles between the ions. Therefore only such partial waves are relevant for the transfer of particles which lie within $\ell \leq R_3/k$. (The radial wave function corresponding to angular momentum ℓ increases from zero and has its first maximum near $R = \ell/k$, where k is the wave number of relative motion.) Higher partial waves, while they may excite the target, will not give rise to particle transfer!

The above argument establishes that particle transfer reactions between heavy ions, even when Coulomb excitation of an excited state has a high probability, is governed by a much more modest number of partial waves than the Coulomb cross section, namely those corresponding to the nuclear region, $\ell \leq R_3/k$. However, Coulomb excitation of the nucleus among the above limited number of partial waves is still possible and implies, because of the slow fall-off of the Coulomb field, that the equations describing the reaction will have to be integrated to distances considerably in excess of the nuclear region, though much smaller than the distance required to describe Coulomb excitation alone.

For the above reason it is feasible to do a fully quantum mechanical treatment of particle transfer reactions between heavy ions at Coulomb energies when Coulomb excitation is present so that transfer can take place from excited states.

In the paper[4] of which this is an abstract, we have formulated the above problem by using our source term technique.[5] We use the following symbols to denote the reaction:

$$D + A \rightarrow P + B$$

$$D = P + N \ , \quad B = A + N \ .$$

Here D and P are the incoming and outgoing ions and N is the transferred particle, which may be a single nucleon, or several. Then, in the notation of Ref. 4, the coupled equations governing the reaction are

$$(T_d - E_d)\, u_d^{\pi I}(R_d) + \sum_{d'} V_{dd'}^{\pi I}\ u_{d'}^{\pi I}(R_d) = 0$$

$$(T_p - E_p)\, w_p(R_p) + \sum_{p'} V_{pp'}^{\pi I}\, w_{p'}(R_p) = \sum_d \rho_{dp}(R_p).$$

Here ρ is a source term which contains the

information on the transfer leading from a typical channel d of the initial partition to channel p in the final partition. We have evaluated the source term under certain assumptions that are discussed fully in Ref. 4, where the detailed form of ρ is also given. Briefly we are able to treat a finite range interaction, but at the expense of limiting the validity of the source to energies below or near the Coulomb barrier, where the transfer takes place dominantly in the tail region of the bound state wave functions. The equations are sufficiently general to account for Coulomb excitation of all four nuclei involved in the reaction, with particle transfer taking place between all states in the initial and final partition.

Footnotes and References

*Condensed from LBL-233.

†Present address: Wright Nuclear Structure Laboratory, Yale University, New Haven, Connecticut.

1. K. Alder and A. Winther, editors, Coulomb Excitation (Academic Press, New York and London, 1966.

2. N. K. Glendenning, in Proc. Int. School of Physics, "Enrico Fermi", Course XL, 1967 (Academic Press, New York, 1919); D. L. Hendrie, et al. Phys. Letters 26B, 127 (1968).

3. R. A. Broglia, T. Kammuri, and A. Winther, in Proc. International Conf. on Heavy Ion Physics, Dubna (Preprint from Niels Bohr Institute).

4. R. J. Ascuitto and N. K. Glendenning, LBL-233.

5. R. J. Ascuitto and N. K. Glendenning, Phys. Rev. 181, 1396 (1969), and Phys. Rev. C2 415 (1970).

DROPLET-MODEL PREDICTIONS FOR THE VALLEY OF BETA STABILITY

W. D. Myers

In the course of a program to determine the best set of coefficients for use in a droplet-model[1] mass formula, we have undertaken a comparison between the properties of the experimental valley of β stability and the properties predicted by the droplet model. The latest nuclear mass table was used[2] and following the procedure employed by previous investigators,[3] we simply fit parabolas to isobaric sequences. Our study differs from previous work in that we corrected the experimental masses for "shell effects" and the "Wigner term" before determining the β-stability parameters so as to remove the scatter introduced into these quantities by nondroplet-model effects.

The three quantities determined for each A value are: the value of the mass at the bottom of the valley V_A, the value of the neutron excess at the bottom $Y_A = (N - Z)_{min}$, and the curvature of the parabola C_A. The differences between these quantities and a reference set (obtained from a liquid-drop-model formula similar to that used by Kodama[3]) are plotted as points in Fig. 1. Clearly, the shell effects were imperfectly removed since some scatter remains.

The smooth lines represent the droplet-

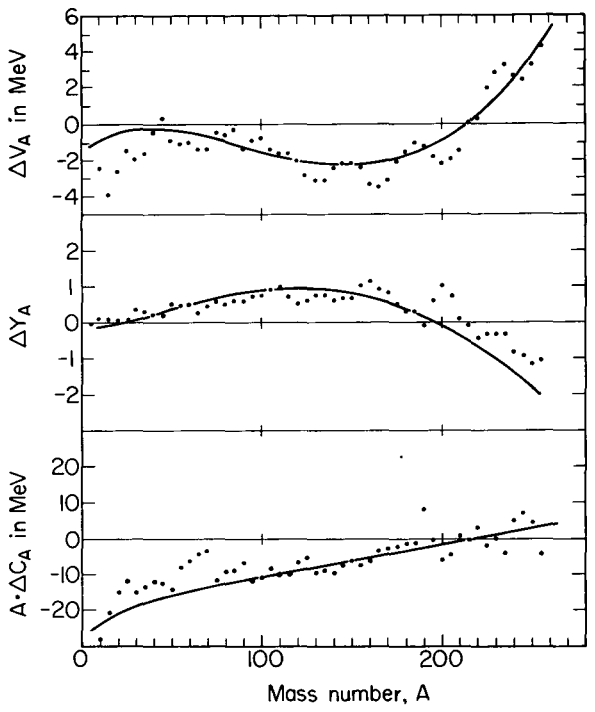

Fig. 1. (XBL 723-2535)

model predictions for these quantities using the parameters

a_1 = 15.938	J = 30.372	K = 240
a_2 = 20.628	Q = 17.889	L = 29
a_3 = 0	r_o = 1.176	M = 295.

Some features to note in this figure are the sharp reduction in stability at the end of the periodic table as the mass V_A turns upward, and the tendence toward N = Z nuclei shown by the downward trend of ΔY_A.

References

1. W. D. Myers and W. J. Swiatecki, Ann. Phys. 55, 395 (1969).

2. A. H. Wapstra and N. B. Gove, Nuclear Data Tables 9, 265 (1971).

3. An early reference is E. S. Green, Nuclear Physics (McGraw-Hill, New York, 1955); a more recent one is T. Kodama, Prog. Theor. Phys. 45, 1112 (1971).

DROPLET-MODEL FISSION BARRIERS

W. D. Myers and R. W. Hasse*

Preliminary work[1] on the calculation of fission barriers has been extended to include all droplet-model effects.[2] The Nix shapes[3] are employed in a program that searches for the droplet-model saddle points. In addition, a much faster approximation has been developed that permits one to quickly compare the barriers predicted for a particular set of droplet-model coefficients with the substantial number of experimental data that are available. Such a comparison is shown in Fig. 1. The circled points represent the experimental values[4] that are corrected for ground state shell effects and the crosses represent the droplet-model barriers calculated for the set of coefficients given in the previous report. The lack of agreement in the Pu region reflects the preliminary nature of this set of coefficients.

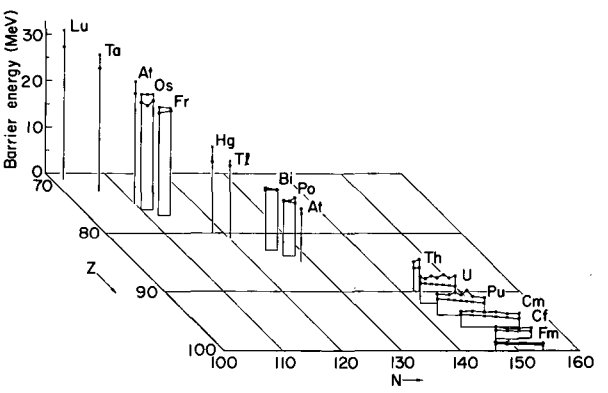

Fig. 1. (XBL 723-2680)

The program that permits quick approximate comparisons of the type shown employs the one-dimensional y-family of shapes (the family of liquid-drop-model saddle-point shapes where y = 1 - x, x being the fissility parameter). In addition, tabulated values of the six shape dependences B_s, B_c, B_k, B_r, B_v, and B_w are employed to reduce computation time.

The figure is plotted in perspective because the single fissility parameter x of liquid-drop-model fission theory no longer serves to uniquely determine the barrier. In the droplet model, the barrier is a more complicated function of N and Z.

The droplet model includes surface symmetry effects and this leads to the interesting result that the predicted barriers for a particular isotopic sequence remain relatively constant, or even (for some choices of the coefficients such as the one shown) decrease with increasing neutron number. Another feature of the droplet-model barriers is that agreement between experiment and theory no longer requires a value of the radius constant r_0 in disagreement with results obtained from electron scattering.[5] Over quite a range of variation of the other parameters in the theory, we find that a single value of the radius constant can be determined that simultaneously gives a good fit to masses, a good fit to barriers, and agreement with nuclear charge radii.

Footnotes and References

*Present address: Institut für Theoretische Physik der Universität Heidelberg.

1. R. W. Hasse, Ann. Phys. 68, 377 (1971).

2. W. D. Myers and W. J. Swiatecki, UCRL-19543, January 1970.

3. J. R. Nix, Ann. Phys. 41, 52 (1967).

4. From Ref. 1 and S. G. Thomson, private communication.

5. W. D. Myers and W. J. Swiatecki, Nucl. Phys. 81, 1 (1966).

SEARCH FOR SUPERHEAVY ELEMENTS IN NATURE

E. Cheifetz,* R. C. Jared, E. R. Giusti, and S. G. Thompson

In recent years various estimates and calculations have been made which suggest the possibility that nuclei having atomic numbers in the region 108-114 may be sufficiently stable to exist in nature.[1-3] These nuclei are expected to decay either directly by spontaneous fission, or by alpha and/or beta emission to give products that would undergo spontaneous fission. The production in nature of such long-lived superheavy nuclei could come about via the r-process[4] or by fission of neutron-rich heavy ions in the vicinity of neutron stars.[5] On the basis of the present knowledge of fission barriers and spontaneous fission decay of heavy elements, the possibility of production of the superheavy elements in nature can neither be excluded nor be established; thus the field has been open for experiments aimed at discovering minute quantities of these elements in nature.

Estimates by Nix[6] based on liquid-drop dynamical calculations and simple extrapolation based on the behavior of the kinetic energy release and mass differences between fissioning nuclei and the fragments of a wide variety of nuclei indicate that on the average ~230 MeV of kinetic energy should be liberated in the fission of the superheavy nuclei and that about ten neutrons should be emitted in such fission events. The evaporation of such a large number of neutrons with average energies of 2 to 3 MeV is unique and is a very sensitive indication of the presence of superheavy elements in a sample. Furthermore, these evaporated neutrons would have sufficient energy to escape from a large sample and enter a counting chamber.

We have used a large gadolinium-loaded liquid scintillation detector as a method for detecting events in which several neutrons are emitted. The detector is a tank of dimensions $62 \times 62 \times 125$ cm which holds the liquid scintillator with a center well of dimensions 11.4×105 cm, for the samples to be counted.

Neutrons produced by any source placed at the center of the chamber enter the liquid and are thermalized by collisions with the hydrogen in the solution and eventually are either captured by the gadolinium or leak out of the tank. The (η, γ) reaction in the gadolinium produce ≈ 9 MeV of γ energy, the energy usually being shared by several γ rays. The electrons created by the reactions of these γ rays with the liquid, produce scintillations which are seen by a few of the photomultipliers.

The distribution in time for neutron capture is broad and has a peak at about 10 μsec after the neutrons are emitted. About 90% of all the captured neutrons are detected within the interval 1 to 36 μsec after their production. In this way individual members of a burst of energetic neutrons are separated in time for convenient electronic multiplicity counting.

Due to the large volume of samples it is impossible to trigger the system with the fission fragments; therefore, the system is designed to be triggered by the first neutron or the prompt γ rays from any fission event.

The detection of an event is obtained the following way: A pulse from the counting chamber triggers a gate that is 35- μsec long and delayed by 0.5 μsec. (The delay is to insure that all of the prompt γ rays from a fission event have been emitted.) During the 35-μsec gate interval all tank pulses are counted by a scaler. At the end of the 36-μsec period the digital information in the scaler is stored. Then the scaler is reset. The next tank pulse defines a new 36-μsec gate interval. A more detailed description of the electronics and counting chamber was given at the Leysin conference.[7]

A spectrum of multiplicity in the range 0–15 is thus obtained. The system is capable of monitoring a burst of neutrons where the counting period can be activated either by the prompt γ-rays or the first neutron captured.

When the system operates with any neutron or gamma signal as the main trigger, it is sensitive to the environmental radiation which consists of γ rays from natural sources (e.g., U, Th, and K) and cosmic rays and the products of their reactions in matter. The γ rays that arise from natural sources appear in general as single random pulses. Accidental coincidence between these random pulses yields a distribution which is represented by a Poisson probability function

$$P(N) = \frac{8.64 \times 10^4 (CT)^{N+1} \exp(-CT)}{N!\,T}, \quad (1)$$

where P(N) is the number of events observed per day in which N pulses follow a single random trigger appearing at a rate of C/sec within a gate length of T(sec) after each pulse. At the operating gate length of 35 μsec and a count rate of 600 counts/sec, less than 0.5 events per day appearing as multiplicity four or more are expected by the above probability function.

The experimental equipment was placed in a 250-m deep [500-meter-water-equivalent (M. W. E.)] tunnel to reduce the cosmic-ray background. The situation in regard to cosmic rays underground was reviewed by E. P. George.[8] At the depth of the tunnel the only significant component of the cosmic rays that can induce multiple neutron emission is that of energetic μ-mesons.

Gorshkov and Zyabkin[9] have studied neutron production induced by μ mesons at a depth of 150 M. W. E. and estimate that at a depth of 800 M. W. E. the total of neutron production in lead is $\sim 10^{-8}$ neutrons/g sec. Less than 10% of the neutrons are produced from stopped negative μ mesons for which $\bar{\nu} = 1.8$ in lead whereas 90% of the neutrons are produced from inelastically scattered μ mesons with $\bar{\nu} > 10$ and thus could register efficiently in our chamber as significant events. Assuming $\bar{\nu} = 10$ we expect a rate of 50 high-multiplicity events for a sample of 50-kg lead in 250 h.

The passage of μ mesons in the detector liquid causes an ionization of ~2 MeV/cm of path length, thus a μ meson entering the sample can be identified by its high energy loss. If a high-energy inelastically scattered μ meson comes into the tank from the vertical direction through the sample tube it must traverse at least 20 cm of the scintillating liquid at the bottom of the tank depositing more than 30 MeV in the tank.

Since neutron capture in gadolinium gives a total of 9 MeV of γ-ray energy, it was possible to eliminate some of the μ meson-induced high multiplicity events by rejecting the events which produce a signal that had an energy greater than 9 MeV. Nevertheless the neutron multiplicities which are induced in the sample by energetic neutrons, produced by inelastic collisions outside the chamber, cannot be rejected nor can the μ-meson-induced neutron multiplicities detected in the chamber but originating outside it be eliminated.

The operation of the system was monitored continuously by chart recorders that monitored the rate of single pulses coming from the tank and the time distribution of events that were of multiplicity four or more. In addition an efficiency of the system to detect neutrons was measured twice a week and was generally found to be stable at the ~65% level. Any variation of over 2% in the efficiency and consequently in the single count rate, was corrected by adjusting the threshold discriminator levels. This occurred several times during about one year of running.

Results of the observed multiplicity distribution measured with a sample of pure tungsten and with an empty chamber are shown in Figs. 1 and 2. The results are plotted on a semilog scale with the abscissa being the multiplicity and the ordinate N! × counts. In this way the multiplicity distributions due to the singles rate, which is the dominant component up to N = 3, appear as a straight line. The counts that are above this line in these figures are background events due to cosmic rays or their products.

The results of many samples that were placed in the detector are summarized in Tables I-IV.

The tables describe the sample, its weight, and the period of measurement. Under the heading of "Counts" are presented three different experimental numbers. The column headed by "4" lists the total observed events with multiplicity of four. The column headed by "4 Ran" is the estimated value at random multiplicities

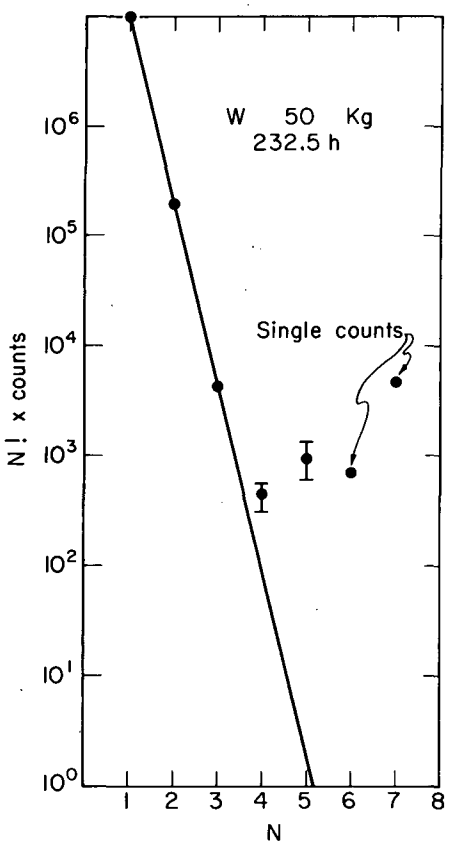

Fig. 1. The multiplicity distribution for metallic tungsten sample. The abscissa N is the observed multiplicity (i.e., number of events following a trigger). The ordinate is N! × counts of the Nth multiplicity. The straight line represents the contribution of random multiplicities. (XBL 714-3245)

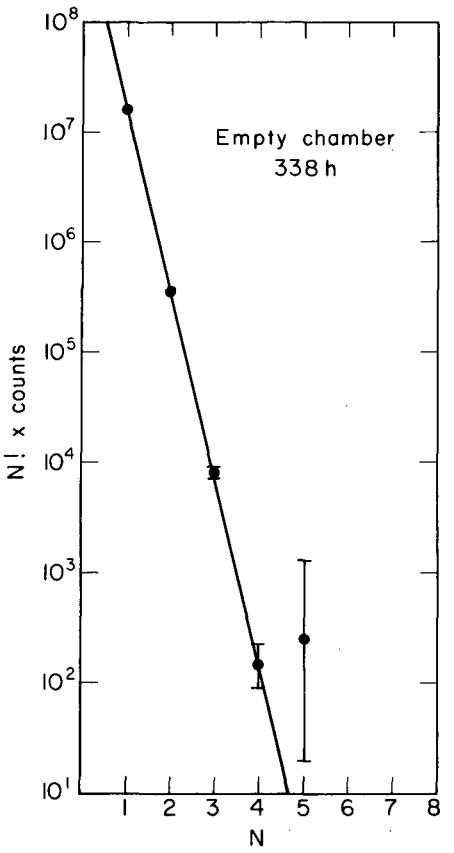

Fig. 2. The multiplicity distribution of the detector without any sample.
(XBL 714-3244)

in the "4" column. This value was inferred from linear extrapolation of the counts having multiplicities of 1, 2, and 3. The column "5^+" contains all the observed events having multiplicities of 5 and above. The "Normalized" column in Tables I, II, and III presents counts normalized to 50-kg samples and 250 hour counting periods at multiplicities four or more after subtraction of the "Empty-Chamber" count rate and the random multiplicities:

$$\text{"Normalized"} = \left\{ \frac{(4) - (4\text{RAN}) + (5+)}{\text{Time}} \times 250 - \frac{\text{Empty chamber counts} \times 250}{\text{Time}} \right\} \times \frac{50}{\text{Weight}} \quad (2)$$

The "Normalized" results thus represent the additional counts of multiplicities four or more that are due to the presence of the sample. Thus activity could be caused either by cosmic rays or by spontaneous neutron emission.

The value of $T_{1/2}$ conc. represents the apparent half-life of the major components of

Table I. Metallic samples and empty chamber.

	Sample		Weight (kg)	Time (h)	Counts 4	Counts 4 Ran	Counts 5^+	Normalized counts/50 kg-250h	$T_{1/2}$/conc. 10^{22} y
1		W	55	233	18	4	10	20 ±6	16
2		Hg	45	189	13	2	5	20 ±5	15
3		Pb	91	91	2	1	5	9 ±5	32
4		Pt	168	163.5	6	2	4	25 ±9	12
5		Cu	60	192	8	3	0	2 ±4	50
6	a	Empty		330	6	6	2	1.5 ±2	
7	a	Empty		168	7	3	2	9 ±5	
8	a	Empty		338	19	13	1	5 ±4	
6-8	a	Total		844	32	22	5	4 ±2	
9		U[b]	0.0107	21.5	29	1	2	1.66×10^{6}	1.5×10^{-4}
10		U	0.0106	30.5	81	1	9	3.44×10^{6}	0.7×10^{-4}

[a]Empty chamber "Normalized" column is normalized to 250 h counting time and not by weight.

[b]The uranium in sample 9 was shielded by 1 in. of lead capsule inside the chamber.

Table II. Samples

	Sample	Weight (kg)	Time (h)	Counts 4	Counts 4 Ran	Counts 5^+	Normalized counts/50 kg-250h	$T_{1/2}$ conc. 10^{22} y
11	Hg Ore	21.2	251	16	4	2	24 ± 12	12
12	Gold nuggets	36	335	21	5	3	11 ± 6	28
13	Pt Ore	20	380	19	10	5	13 ± 7	24
14	Bi Ore	14.3	360	57	21	6	84 ± 24	3
15	Manganese nodules	7	192	23	9	2	120 ± 57	9
16	Moon rocks	3	781	44	18	8	99 ± 58	17
	Steel cans	27						
17	Cu Ore	10	279	9	8	1	-20 ± 22	
18	Water filters	10	118	8	4	0	23 ± 22	60
19	Air filters		90	5	2	0		
20	California soil	9	170	15	4	2	83 ± 25	
21	Pegmatite	13.5	310	31	19	4	26 ± 26	
22	Tenaya Pegmatite	<337	135	237	4			
23	Tioga Pegmatite	<122	132	570	570	11		

Table III. Lead ores and lead processing.

	Sample	Weight (kg)	Time (h)	Counts 4	Counts 4 Ran	Counts 5^+	Normalized counts/50 kg-250h	$T_{1/2}$ conc. 10^{22} y
24	Galena 1	20	256	35	3	7	86 ± 18	3.4
25	Galena 2	23	77	12	2	3	92 ± 28	3.2
26	Bunker Hill Galena	25	122	6	2	1	12 ± 12	24
27	Bunker Hill Bullion	90	120	14	3	6	17 ± 5	17
28	Low grade Galena	15	46	5	1	0	45 ± 36	6.5
29	Homemade lead	75	240	13	5	4	6 ± 3	48
30	Slag 1 50 % [a]	34	70	5	1	0	15 ± 13	
31	Slag 2 50% [a]	25	185	11	2	5	30 ± 12	
32	Galena 3	17	112	3	1	0	2 ± 13	145
33	Galena 4	17	94	4	1	1	20 ± 20	15
34	Thullium fraction	7	188	18	5	1	104 ± 50	3

[a] These samples were produced from 135 kg of lead ore (see text). Samples 30 and 31 are only 50% of the slag produced.

Table IV. Selby lead smelting and refining plant.

Number	Sample	Weight (kg)	Time (h)	Counts 4	Counts 4 Ran	Counts 5^+	Normalized counts/250h
35	Lead bullion	50	48	2	1	2	12 ± 10
36	Blast furnace slag	19.5	76	8	4	3	12 ± 11
37	Cintering dust (I)	16.1	65	2	2	1	4 ± 8
38	Cintering dust (II)	7.2	108	7	3	0	12 ± 5
39	Blast furnace slag II	12.5	87	1	1	0	-1 ± 3
40	Dust from As, Sb, Sn, Cu removal	5	114	10	3	3	18 ± 8
41	Dust of tin dross	13.1	72	5	2	0	6 ± 6
42	Bismuth fraction	55	74	4	1	2	13 ± 8

the sample assuming that all "Normalized" events are real.

Table I presents results obtained with chemically refined samples or an empty chamber. These samples form a background for heavy elements. Samples 9 and 10 are reagent-grade uranium metal. The result shows that the excess counts in any of our samples assumed to be due to cosmic rays corresponds to the counting rate given by ~10 ppm of uranium.

Table II shows the results of various samples: Sample 11 was Hg ore, 80% cinnabar, from the Great Western Mine, Middletown, California; Sample 12 was gold nuggets, 95% gold, from the collection of Sierra County, California; Sample 13 was Pt ore, 67% Pt, from Goodnews Bay Mining Company, Alaska; Sample 14 was a composite of Bi ore from Colorado, Tanzania, Saxony, Cornwall, and Bolivia; Sample 15 was manganese nodules from the Mid-Atlantic ridge; Sample 16 was moon rocks from the first United States flight to the moon; Sample 17 was Cu ore from the South Pacific area; Sample 18 was activated charcoal and sand from a local water plant that was used to filter ~ 1100 gallons of drinking water; Sample 19 was an air filter flown by a plane that filtered 290 000 ft^3 of air; Sample 20 was soil from a pasture in Martinez, California; Sample 21 was pegmatites from the Sierra Nevada Mountains of California at Tioga Pass and Tenaya Lake.

A chemical separation was made on the pegmatites to obtain Samples 22 and 23. The chemical procedure used was to grind the rock to about 100 mesh and then to leach the rock with a mixture of 2 parts aqua regia and 1 part water. The resulting solution of sand and acid was stirred four times during a period of not less than 12 h (temperature 20 to 25°C). At the end of the leaching, the acid mixture was decanted off and two water rinses followed. The resulting liquid was then evaporated to near dryness so that the volume would fit in the counting chamber. Of the material dissolved from the rock, 66% was present in the sample counted. Sample 22 consisted of leached material from 338 kg of pegmatitic rock from Tenaya Lake, California, and Sample 23 was leached material from 122 kg of pegmatitic rock from Tioga Pass, California.

Table III shows the results of lead ores and lead processing. Special attention was paid to lead because of the results of Flerov et al.[10] The first lead ore sample that was checked (Sample 24) showed significant excess neutron activity so a second sample was prepared (Sample 25) at a location 5 miles from Lawrence Berkeley Laboratory to reduce the possibility of contact with spontaneous fission sources. The second sample also showed excess neutron activity. Both samples were ≈ 80% galena obtained by the Materials Science and Engineering Department of the University of California at Berkeley about 30 years ago from the Bunker Hill mines in Idaho. The uranium concentration was determined but could not account for all of the observed activity. Samples 26 and 27 were then obtained from Bunker Hill, Idaho, but gave negative results. In addition 9 samples were collected at the lead smelting and refining plant at Crockett, California. The samples were taken from most of the locations at which chemical fractionation occurs at the plant. No significant activity was found in any of these samples as is shown in Table IV (35 counts per 250 hr would be positive). Sample 28 was low-grade galena ore (≈ 30% galena) chosen to determine if the excess neutron activity was in the

rock or galena of Samples 24 and 25.

An attempt was made to concentrate the activity in ~200 kg of high-grade lead ore that had shown a positive indication. The process chosen for the separation was the reduction of the galena by iron. PbS + Fe → Pb + FeS at 1100°C. The products of the reaction were easily separated into three components: lead bullion, slag with iron, slag with sodium borate. All three of these samples gave negative results. Samples 32 and 33 were taken from the same ore and gave negative results. It is possible that the activity could have been due to very slight contaminations by ^{252}Cf that occurred despite the strict precautionary measures taken.

In conclusion, we have been unable to find any evidence to support the existence of superheavy elements in nature.

Footnotes and References

*Present address: Weizmann Institute of Science, Rehovoth, Israel.

1. S. G. Nillson, C. F. Tsang, A. Sobiczewski, Z. Szymanski, S. Wycech, C. Gustafson, T. Lamm, P. Möller, and B. Nilsson, Nucl. Phys. A131, 1 (1969).

2. M. Bolsterli, E. O. Fiset, J. R. Nix, and J. L. Norton, Phys. Rev. Letters 27, 681 (1971).

3. Yu. A. Muzychka, V. V. Pashkevich, and V. M. Strutinsky, Sov. J. Nucl. Phys. 8, 417 (1969).

4. E. M. Burbidge, G. R. Burbidge, W. A. Fowler, and F. Hoyle, Rev. Mod. Phys. 29, 547 (1957).

5. M. Kowalski and Br. Kuchowicz, Phys. Letters 30B, 79, (1969).

6. J. R. Nix, Phys. Letters 30B, 1 (1969).

7. E. Cheifetz, E. R. Guisti, H. R. Bowman, R. C. Jared, J. B. Hunter, and S. G. Thompson, CERN Report 70-30, 709 (1970).

8. E. P. George, Observation of Cosmic-Rays Underground and their Interpretation, Progress in Cosmic Ray Physics, edited by J. G. Wilson, North Holland 1952, p. 393.

9. G. V. Gorshkov and V. A. Zyabkin, Yad. Fiz. 12, 340 (1970). [(English translation) Sov. J. Nucl. Phys. 12, 189 (1971)].

10. G. N. Flerov, N. K. Skobelev, G. M. Ter-Akopyan, V. G. Subbotin, B. A. Gvozdev, and M. P. Ivanov, JINR D6-4554 (1969).

POSSIBLE HEAVY-ION REACTIONS LEADING TO SUPERHEAVY NUCLEUS FORMATION

W. J. Swiatecki* and C. F. Tsang

The existence of an island of stability in the region of proton number 114 and neutron number 184 has been predicted by many groups[1-5] over the past few years. Though many suggestions have been advanced for the production of such superheavy nuclei, detailed studies of the production processes are not yet available. In the present work we consider in a semiempirical approach, one of the most probable ways of producing superheavy nuclei, i.e., by means of heavy-ion reactions using projectiles that will be available through the SuperHilac at Berkeley.

The study is based on the most recent detailed predictions of the island of stability supplied by Nix and collaborators[5] at Los Alamos. In Fig. 1, their calculated half-lives are shown in units of years. The major decay in electron capture is marked out by arrows. Half-lives in excess of 10^5 years are found near the Z = 110, N = 184 region. If a compound nucleus is formed in the region where α decay is dominant, there is a good chance that one will be able to observe a series of three or four alphas with energies in the 7- to 13-MeV region. In the calculations of half-lives, the spontaneous fission half-life is most uncertain because of our lack of knowledge concerning the penetrability of the fission barrier in spontaneous fission. If a pessimistic view is taken that the spontaneous fission half-lives in these calculations were overestimated by a factor of 10^{10}, then results are obtained as shown in Fig. 2. The longest half-life found is in excess of one year and the picture still looks good for the observation of superheavy nuclei once they are made.

To make the superheavy nuclei, the heavy-ion reactions should ideally aim at a compound nucleus somewhat to the northeast of the center of the island of stability at Z = 114 and N = 184. In Fig. 3, the available landing

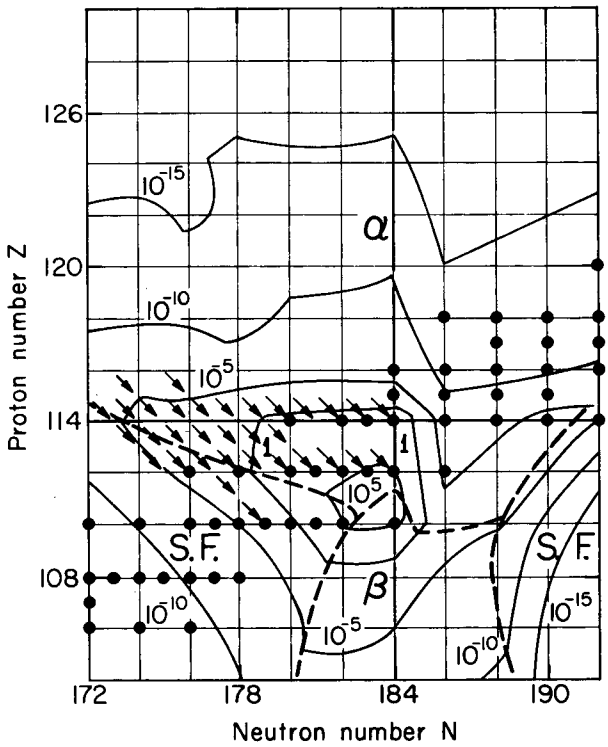

Fig. 1. Half-life contours (numbers in units of years) in the region of Z = 114 and N = 184. The broken lines divide the region into portions, in each of which the dominant decay mode is indicated. Nuclei whose dominant decay is electron-capture are denoted by arrows in the direction of their decay.

(XBL 724-2762)

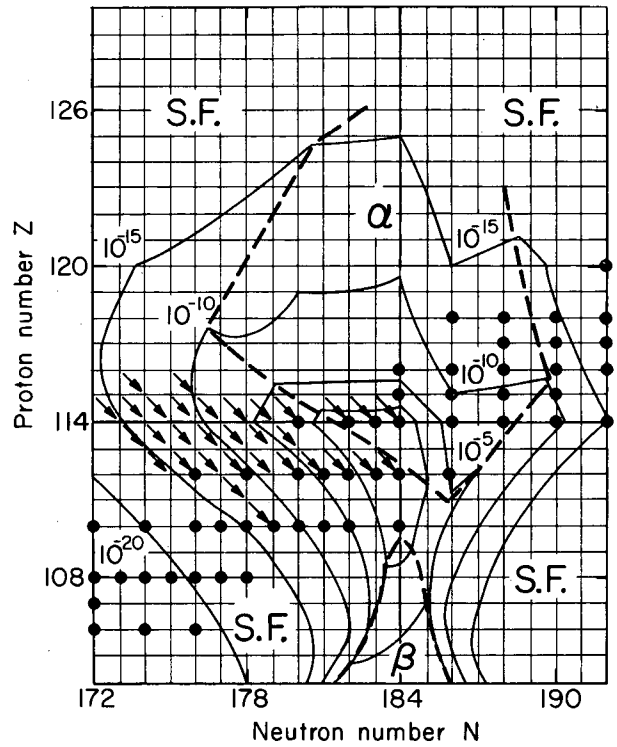

Fig. 2. Same as Fig. 1, but the spontaneous fission half-lives from Ref. 5 are arbitrarily cut down by a factor of 10^{10}.

(XBL 724-2763)

places near the center of the island are shown. The cases that require ^{252}Cf and ^{250}Cm targets that are not yet available are pointed out. In particular, one may note that with Ge isotopes as projectiles on ^{232}Th, one lands at Z = 122 and N = 180, 182, 183, 184, and 186. In terms of half-lives as shown in Figs. 1 and 2, this is one of the few favorable cases which decays by successive alpha-emission, reaching relatively long-lived isotopes of elements 110 and 112 by electron capture.

The compound nucleus formed is necessarily in a very excited state. There is a chance that the excited compound nucleus will fission immediately and no superheavy nucleus remain. On the other hand, there is also a chance that the excited compound nucleus will emit several neutrons, typically four, taking off most of its excitation energy. Moretto[6] has made a detailed study of such fission-neutron-emission competition. We made a rough estimate of the survival of superheavy nuclei by neutron emission. The approximate region within which the survival

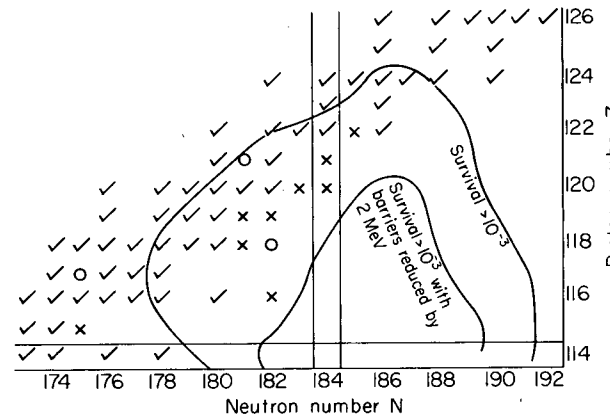

Fig. 3. Available landing places in heavy-ion reactions. These are designated by √, X, or o. The latter two symbols denote landing places that cannot be reached without ^{250}Cm or ^{252}Cf targets respectively. The longer solid curve marks out the region where the probability of the compound nucleus surviving four successive neutron-fission competition is expected to be in excess of 10^{-3}. This region will be decreased to the area indicated if the calculated fission barrier is arbitrarily cut down by 2 MeV. (XBL 724-2764)

probability may be expected to exceed 10^{-3} is marked out in Fig. 3. Two estimates are made, one with the nominal values of fission barriers deduced from the Los Alamos shell corrections and the other representing the pessimistic arbitrary assumption that barriers were overestimated by 2 MeV. (When the barrier is cut down by 2 MeV, the original curve representing survival probability of 10^{-3} is estimated to have a survival probability of approximately 10^{-5}.) The reaction of Ge on Th, as well as that of ^{48}Ca on ^{248}Cm (landing at z = 116, N = 180) are among the more favorable cases looking apart from ^{250}Cm and ^{252}Cf targets. If these targets became available, one would stand a better chance with the landing places 116^{182}, 118^{182}, 120^{184}.

The above discussion assumes that the compound nucleus is already formed. There are still many uncertainties concerning the fusion probability of the projectile and target nuclei. In particular, a large viscosity of nuclear matter in the fusion dynamics might cut down the formation probability tremendously. In Figs. 4 and 5, the first few stages of the fusion of ^{76}Ge and ^{232}Th are shown in an end-on collision as well as a broadside-on collision. (The broadside-on collision is expected to leave an excitation energy some 80 MeV higher than the end-on collision because of the higher Coulomb energy involved.) The saddle point shape of the compound nucleus is also shown. If the configuration of the projectile and target nucleus on collision falls to a large extent within the saddle point shape of the compound nucleus one is attempting to form, then only a small amount of nuclear matter flow is able to bring the system within the potential well of the compound nucleus ground state, and the fusion probability might then be close to unity. The results shown in the figures suggest that there remains much uncertainty as regards the compound nucleus formation probability. The broadside collisions appear to be somewhat more favorable (but would end up with more excitation).

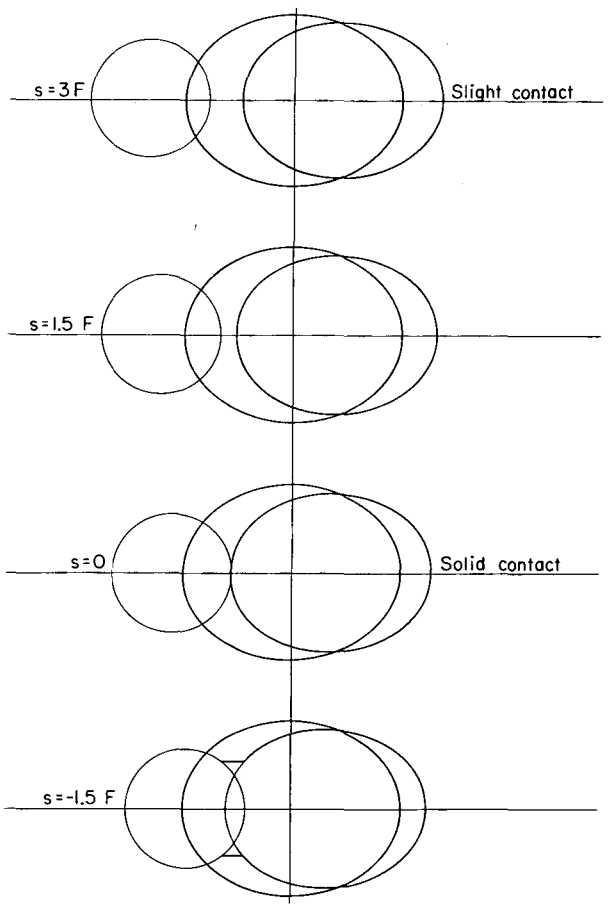

Fig. 4. End-on collision of ^{76}Ge on ^{232}Th. The circle on the left represents the half-density contour shape of the ^{76}Ge projectile. The ellipse on the right represents the half-density contour shape of the ^{232}Th target. The saddle point shape of the compound nucleus to be formed is shown as another ellipse with its center of mass at the center of mass of the colliding projectile and target. Four stages of the collision are shown. In the first stage, the separation s between the half-density contours of the projectile and target is 3 fermi. At this separation, the tails of the density distributions are just beginning to overlap. In the second stage, s = 1.5 fermi, and the overlap of the densities is more pronounced. In the third stage, s = 0, and "solid contact" is made; beyond this point, the nuclear density in the region of the overlap would begin to exceed the nuclear matter value. In order to avoid this, nuclear matter must flow out of the region of overlap into a ring-shaped space surrounding it. This is indicated in the fourth stage with s = -1.5 fermi, and the overlap of the densities is more pronounced. In the third stage, s = o, and "solid contact" is made; beyond this point, the nuclear density in the region of the overlap would begin to exceed the nuclear matter value. In order to avoid this, nuclear matter must flow out of the region of overlap into a ring-shaped space surrounding it. This is indicated in the fourth state with s = -1.5 fermi. Beyond this stage, the further development in time of the fusing system would depend critically on inadequately known features of nuclear dynamics, in particular, on nuclear viscosity. (XBL 724-2765)

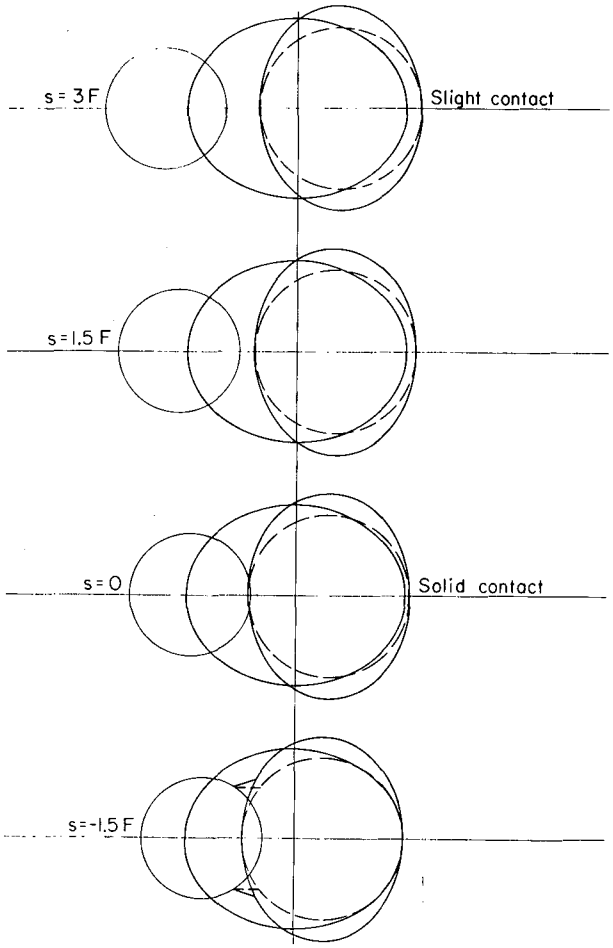

Fig. 5. Same as Fig. 4 with the broadside-on collision. In the lowest figure, the broken curve indicates the configuration when looking along the axial-symmetric axis of ^{232}Th nucleus. (XBL 724-2766)

We may summarize by giving an estimate of the cross section of superheavy nucleus formation based on various controlling effects. Start with a geometric cross section of 10^{-24} cm^2. Assume that the compound nucleus can support at most 20 $\hbar$ units of angular momentum. This requirement cuts down cross sectioning by 10^{-2}. Assume that the compound nucleus formation occurs with a probability of 10^{-1} (with an uncertainty of +1 to $-\infty$ in the exponent). Finally, assume that in the neutron-fission competition, the survival probability is 10^{-3}. The final cross section could then be in the neighborhood of 10^{-30} cm^2. It would be unlikely to be greater than 10^{-27} or 10^{-28} cm^2. It could be vanishingly small (less than 10^{-35}, say) if the compound nucleus formation were inhibited by excessive nuclear viscosity.

Footnotes and References

*Theoretical Physics Group, LBL.

1. W. D. Myers and W. J. Swiatecki, Nucl. Phys. 81, 1 (1966).

2. H. Meldner, Arkiv Fysik 36, 593 (1967). P. A. Seeger, Arkiv Fysik 36, 217 (1967).

3. S. G. Nilsson, C. F. Tsang, A Sobiczewski, Z. Szymanski, S. Wycech, C. Gustafson, I. L. Lamm, P. Möller, and B. Nilsson, Nucl. Phys. A131, 1 (1969).

4. M. Brack, J. Damgaard, H. C. Pauli, A. Stenholm-Jensen, V. M. Strutinsky, and C. Y. Wong, to be published in Rev. Mod. Phys.

5. M. Bolsterli, E. O. Fiset, J. R. Nix, and J. L. Norton, to be published in Phys. Rev.

6. L. G. Moretto, to be published in Nucl. Phys.

SHELL-MODEL CALCULATIONS OF FISSION DECAY WIDTHS AND PROBABILITIES IN SUPERHEAVY NUCLEI

L. G. Moretto

The possible existence of magic or near magic regions about the proton number Z = 114 and the neutron number N = 184 has led to a great amount of theoretical study on the stability of superheavy elements. By means of the Strutinski procedure, the nuclear potential energy surfaces have been calculated as a function of deformation. Nuclear masses, fission barriers, alpha and beta decay energies have been predicted. In particular, very large fission barriers are expected with consequently long spontaneous fission lifetimes.[1-3]

However, the analysis of the potential energies alone does not allow one to draw any definite conclusion concerning the possibility of synthesizing superheavy elements.[4] Two more aspects of the problem must be considered. The first concerns the possibility of the coalescence of the target and a very heavy ion into a compound nucleus. Very little is known about this aspect. The second, which is the object of this paper, concerns the stability of the superheavy compound nuclei towards fission. It has been shown in a preceding paper[5] that

the ground state shell effects are gradually washed out with increasing excitation energy. This is very relevant as far as the stability of the superheavy compound nuclei is concerned. In contrast with lower Z elements, the fission barrier of superheavy elements is generated exclusively by shell effects. The excitation energy, by effectively reducing the fission barrier, may substantially compromise the stability of superheavy compound nuclei. In order to investigate this problem, we have evaluated, on the basis of the shell model and of the BCS Hamiltonian, the nuclear deformation probability for different excitation energies. We have shown[5, 6] that the deformation probability can be expressed as follows:

$$P(E, \epsilon)\, d\epsilon = \frac{\sqrt{2\pi m}}{h} A'^{-1/2} \rho(E - V(\epsilon), \epsilon)\, d\epsilon,$$

where ϵ is the nuclear deformation, m is the inertial mass associated with the motion along the collective coordinate, E is the excitation energy, $V(\epsilon)$ is the potential energy, and

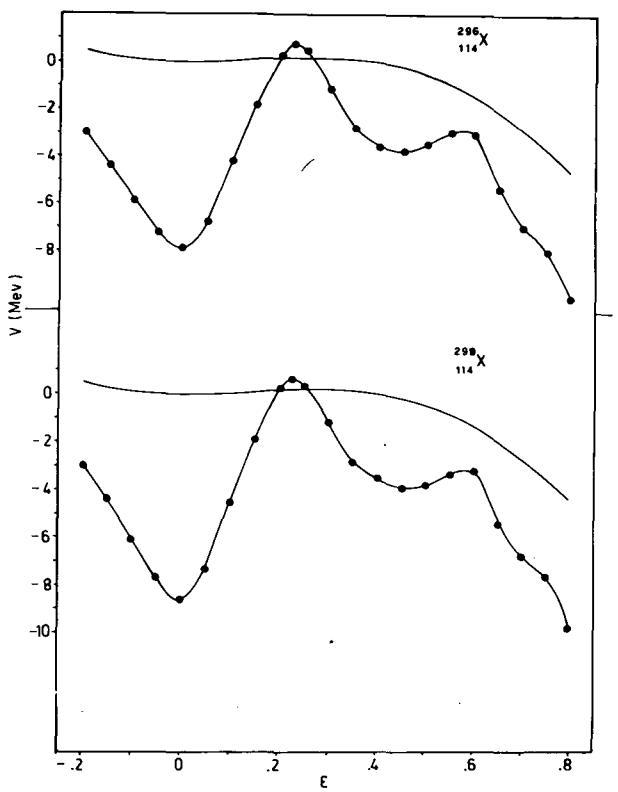

Fig. 1. Fission barriers for the nuclei $^{296}_{114}X$ and $^{298}_{114}X$ calculated on the basis of the Nilsson model. The black dots represent the potential energies calculated by means of the Strutinski procedure; the solid line represents the liquid-drop potential energy. (XBL 725-833)

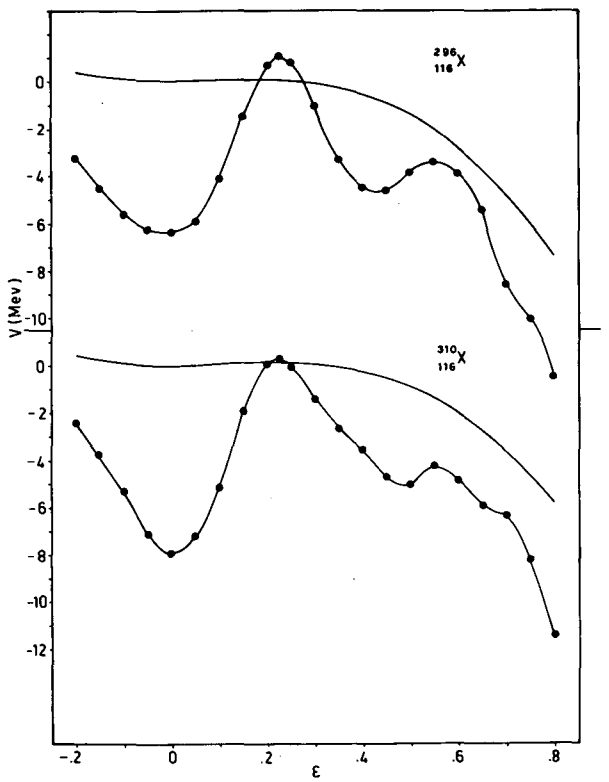

Fig. 2. Fission barriers for the nuclei $^{296}_{116}X$ and $^{310}_{116}X$ calculated on the basis of the Nilsson model. The black dots represent the potential energies calculated by means of the Strutinski procedure; the solid line represents the liquid-drop potential energy. (XBL 725-828)

$$A' = \left[\frac{d\ell n\, \rho(x, \epsilon)}{dx}\right]_{x = E - V(\epsilon)}.$$

Calculations of the fission barriers and of the deformation probabilities have been performed on the basis of the Nilsson model. In Figs. 1 and 2 the potential energy profiles are presented for the nuclei $^{296}_{114}X$, $^{298}_{114}X$, $^{296}_{116}X$, $^{310}_{116}X$ as obtained from the Strutinski procedure. Large barriers are seen to develop close to the doubly magic nucleus with Z = 114, N = 184.

In Fig. 3 the natural logarithm of a quantity proportional to the deformation probability is presented for $^{296}_{116}X$. This calculation is performed by evaluating the level density from the Nilsson diagram and the BCS Hamiltonian. At low-excitation energies a sharp peak centered about sphericity is visible. This is what could be called the compound nucleus peak. Since the system can undergo fission, the probability

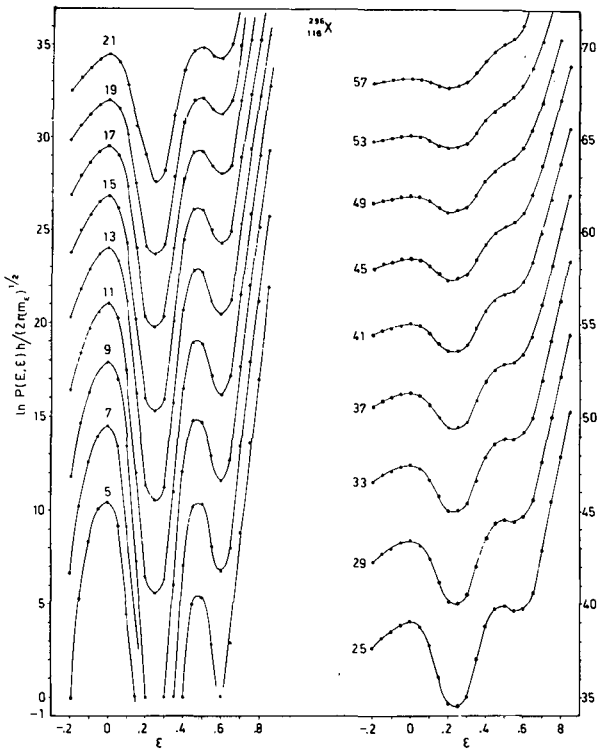

Fig. 3. Deformation probabilities at different excitation energies for $^{296}_{116}X$ on the basis of the Nilsson model. The quantity $P(E,\epsilon)\hbar/(2\pi m_\epsilon)^{1/2}$ has the dimension $MeV^{-1/2}$. (XBL 725-821)

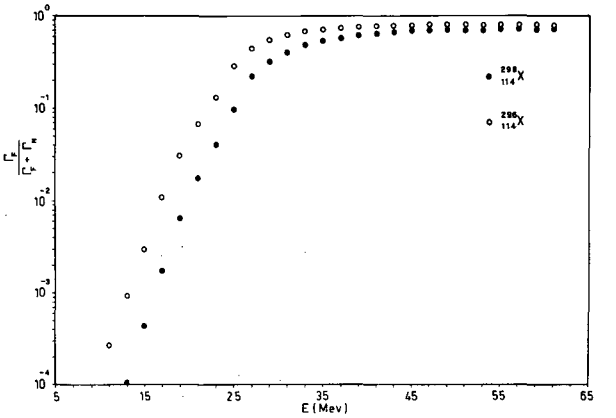

Fig. 4. First chance fission probabilities for $^{296}_{114}X$ and $^{298}_{114}X$. (XBL 725-830)

does not ever go to zero at any prolate deformation. The deepest minimum of probability along this coordinate represents the transition state or the stage which controls the flow of probability towards fission and determines the fission width.

In all the cases it can be seen that, as the excitation energy increases, the compound nucleus peak becomes less sharp and less defined while the transition-state probability steadily increases. At sufficiently high energies the deformation probability becomes so uniform with deformation that the definition of a compound nucleus does not seem possible any longer. The shell effects have completely disappeared at this stage and the consequences ought to be visible in the fission probability. The first chance fission probability $\Gamma_F/\Gamma_F + \Gamma_N$ can be obtained by calculating Γ_F from the probability of deformation at the transition state and by evaluating Γ_N at the equilibrium deformation of the residual nucleus. Examples of such calculations are shown in Figs. 4, and 5 for the nuclei listed above.

It can be noticed that very small fission probabilities are observed at low excitation energy, consistent with the fact that fission barriers substantially exceed the neutron binding energies. However, at moderate excitation energies the fission probabilities grow quickly to very substantial values, in some cases above 0.9. This is due to the washing out of the shell effects, which was illustrated above. A fission probability above 0.9 is predicted by the uniform model for a difference $B_N - B_F \approx 6$ MeV. Since the neutron binding energies are about 6 MeV, it can be said that for some of these nuclei at the moderate excitation energy of ~35 MeV the effective fission barrier is already very close to zero. The cases presented here are rather favorable. Calculations performed for other nuclei further

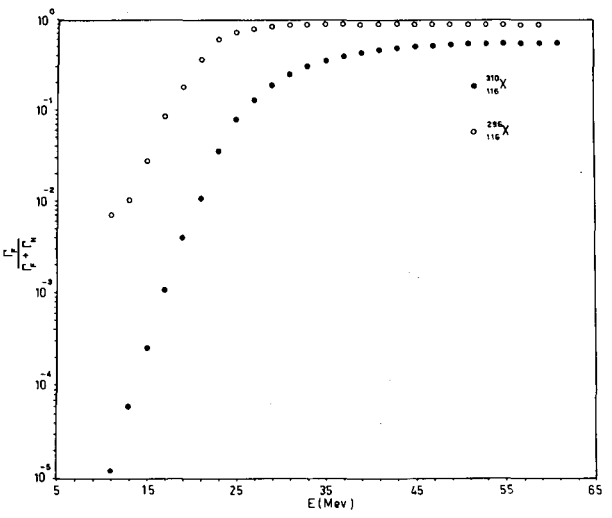

Fig. 5. First chance fission probabilities for $^{296}_{116}X$ and $^{310}_{116}X$. (XBL 725-825)

removed from the magic region indicate, in some cases, a fission probability as high as 0.95 over substantial energy ranges. Again it is to be stressed that the first chance fission probability should not be confused with the much larger total fission probability which accounts for the fission competition during the overall evaporation cascade. Still one has to recognize that even a survival factor of 10% per evaporation stage yields a reasonable overall survival factor of 10^{-4} for a loss of four neutrons.

In conclusion, it seems that even allowing for the disappearance of shell effects with excitation energy, the predicted survival factor, at the compound nucleus stage, should be better than that measured in the actinide region.

References

1. Yu. A. Muzychka, V. V. Pashkevich, and V. M. Strutinski, Yad. Fiz. 8, 716 (1960).

2. S. G. Nilsson, C. F. Tsang, A. Sobiczewski, S. Wychech, G. Gustafson, I. L. Lamm, P. Moeller, and B. Nilsson, Nucl. Phys. A131, 1 (1969).

3. J. R. Nix, LA-DC-12488, April 15, 1971.

4. L. G. Moretto, Phys. Letters 34B, 191 (1971).

5. L. G. Moretto and R. Stella, Phys. Letters 32B, 558 (1970).

6. L. G. Moretto, LBL-228, August 1971.

TRANSITIONS IN ODD A AND ODD-ODD ISOTOPES PRODUCED IN THE PROMPT FISSION OF ^{252}Cf

E. Cheifetz,* R. C. Jared, S. G. Thompson, and J. B. Wilhelmy

In past studies we have reported on transitions in ground state bands of prompt even-even fission products.[1-3] In this report we present preliminary assignments of γ-ray transitions to specific odd A and odd-odd isotopes produced in the spontaneous fission of ^{252}Cf. The experimental procedure which consists of three- and four-parameter measurements of γ rays, x rays and prompt fission-product kinetic energies, has been described in previous publications,[1-3] and therefore details will not be included here. Basically, the kinetic energies of the fragments are used to determine the mass of the isotopes, the x rays are used to identify their atomic numbers, and the γ rays give information on the nuclear properties. Our previous studies have been successful in identifying the ground state bands in even-even products for two primary reasons:

1) The angular momentum of the primary fission products ($\sim 7\hbar$) results in a condition strongly favoring population of the ground state band at around the 6^+ or 8^+ member[4] followed by an easily identifiable cascade of transitions as the band deexcites, and

2) even-even nuclei have very regular systematics in their energy-level spacings[5] which enables prediction of the location of the members of the ground state band and, therefore, confidence is obtained in the transition assignments if the observed level spacings are close to those predicted. However, these favorable conditions do not exist in the odd A and odd-odd fission-product isotopes. The angular momentum dissipation can be spread over inter- as well as intra-band transitions therefore eliminating the strong regularly spaced γ rays in the spectrum. Of equal importance is the unpredictability of the nuclear-level spacings in the odd A and odd-odd isotopes. This lack of regular systematics results in less confidence in assignments of band spacings in these nuclei.

Even with these limitations we feel it is possible to make reasonably positive assignments of some of the observed prompt γ rays to specific odd A and odd-odd isotopes. The unfortunate situation currently is that the existing tabulations of prompt transition assignments to specific isotopes[6-9] have some errors in isotope assignments. Though most of the assignments are probably correct, the incorrect assignments result in a loss of confidence in prompt-fission spectroscopy and therefore retard incorporation of these data into the main body of spectroscopic information. With the improvements of the x-ray analysis techniques,[1,2,3,6,8,9] the atomic number assignments have become, for favorable cases, very reliable. The major difficulty for strong transitions is now in the mass identification. The masses are calculated from the measured kinetic energies of the fragments and utilize predetermined neutron emission distributions.[10] The mass resolution using these techniques is approximately 4 to 6 amu (FWHM), which is rather poor.

But even with this resolution, centroids of mass distributions for strong transitions can be readily determined to ±0.2 amu accuracy. This should be adequate for making positive mass assignments. The difficulty is that the calculational procedure for obtaining the masses relies on an accurate energy calibration for heavy ions stopped in solid state detectors[11] and more importantly on the details of the neutron evaporation for specific isotopes. These neutron-multiplicity measurements have been performed only as averages as a function of energy release in fission.[10] Therefore, average corrections are being applied to specific isotopes. This can introduce errors of over 1 amu in the mass determination of certain isotopes.

To eliminate these problems we try to utilize transitions in predetermined even-even isotopes for internal mass calibration points. The mass calculational procedure, even though it biases the assignment for some isotopes, is a smooth function and accurate results can be obtained for non-even-even nuclei by interpolation between these known isotopes. An example of this procedure is shown in Fig. 1 for transitions from three adjacent isotopes of Mo (104, 105, 106). The plotted points represent observed intensities of three separate γ rays as a function of mass interval. These γ rays have been established through x ray-γ ray coincidence[1,3,8,9] as being associated with Mo

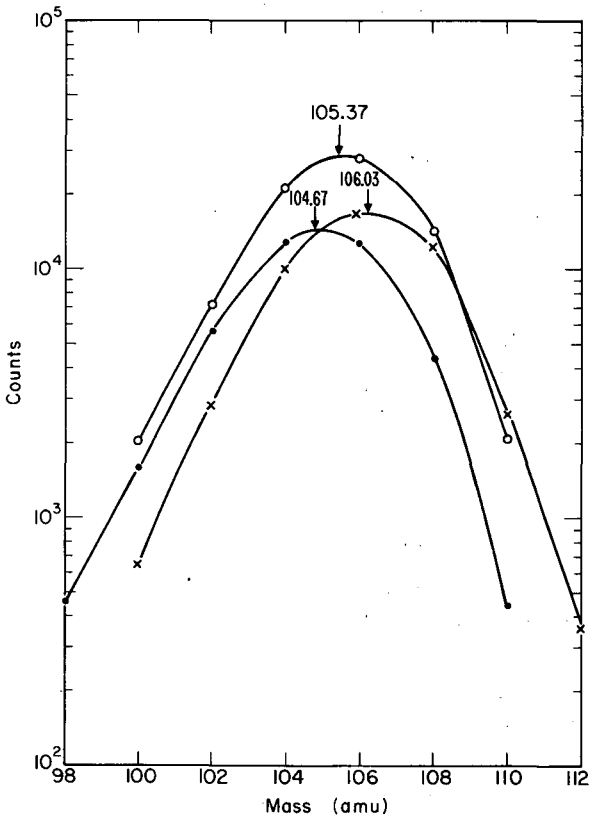

Fig. 1. Mass determination for three transitions associated with Mo isotopes. Plotted are the observed intensities of the γ rays in various mass intervals. The γ rays are: ^{104}Mo $2^+ \rightarrow 0^+$ 192.3 keV, o ^{105}Mo 95.0 keV, x ^{106}Mo $2^+ \rightarrow 0^+$ 171.7 keV. The centroids of the distributions are shown on the plot.

Table I. Assignment of prompt-fission gamma rays to specific odd A and odd-odd isotopes.

Isotope	Energy (keV)	Isotope	Energy (keV)
^{99}Zr	53.6	^{112}Rh	60.6
^{105}Mo	94.9	^{115}Pd	48.8
	138.2		
	144.8	^{136}I	87.4
	246.8		
	283.0	^{140}Cs	51.0
	418.2		78.9
^{107}Tc	71.8	^{143}Ba	117.6
^{108}Tc	123.2	^{145}Ba	112.7
^{109}Tc	69.4	^{144}La	90.9
^{109}Ru	74.3	^{145}La	100.1
	98.3		
		^{146}La	114.6
^{111}Ru	63.0		
	76.1	^{151}Pr	52.6
	104.0		
	150.4		
	167.0		
	358.1		
^{110}Rh	58.9		

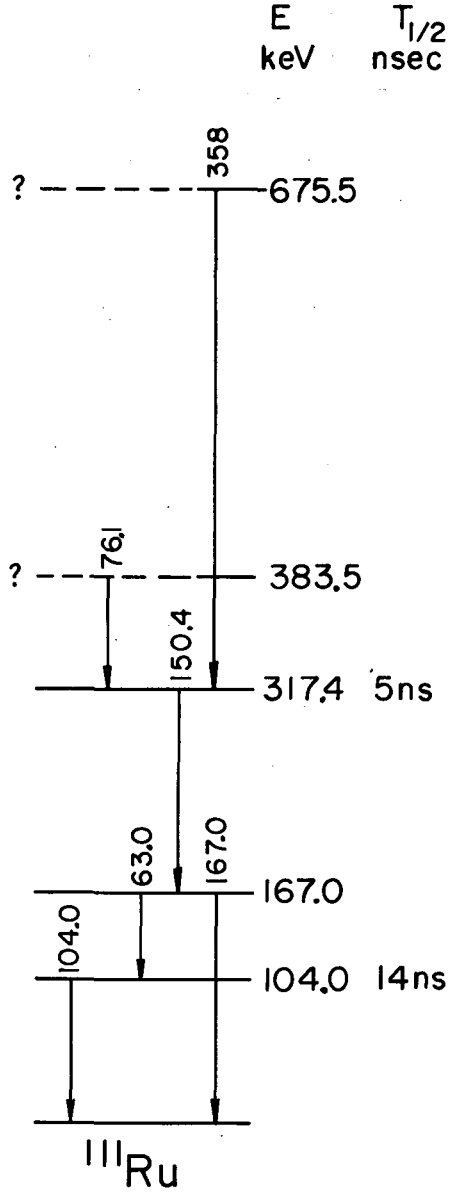

Fig. 2. Tentative level scheme for ^{111}Ru. (XBL 713-3073)

isotopes. The observed mass distribution for each of these transitions is quite wide (~ 5 amu FWHM) but the centroids can be well established. From coincidence studies and decay scheme systematics, two of the transitions have been shown to be associated with ^{104}Mo and ^{106}Mo.[1,3] These transitions have centroids in the mass distribution at A = 104.67 and A = 106.03 respectively.

The other transition which is also from a Mo isotope has a mass centroid at A = 105.37 and is therefore assigned to ^{105}Mo. Similar considerations have been applied to other transitions observed in the prompt γ-ray spectra. For cases which are reasonably intense and relatively free of other γ-ray contaminants, good mass determinations are possible.

The long-term objective in these experiments is to determine nuclear level properties of the prompt-fission isotopes, but as of now the complexity of the γ-ray spectra and the relatively poor mass resolution obtained from fragment kinetic energy measurements have precluded these determinations except for even-even isotopes. Gamma ray-gamma ray coincidence measurements will be useful in establishing level structures, and we have performed such measurements. An example of a tentative decay scheme for ^{111}Ru is shown in Fig. 2. These transitions have been shown to be associated with Ru x rays and to have mass distributions consistent with mass 111. The order of the transitions is determined from intensity considerations, lifetime determinations,[7] and γ-γ coincidence measurements. Unfortunately, even with this information we are unable to make reliable spin assignments to the levels.

Even though, at this time, we are unable to make level scheme determinations for odd A and odd-odd isotopes, we feel it is useful to establish the first step in this procedure—the accurate assignment of transitions to specific isotopes. Table I contains a partial list of such assignments. These assignments are made by using the x-ray and mass determinations described above. Additional experiments are now being performed to improve the quality of the data so that more assignments can be made.

Footnote and References

*Present address: Weizmann Institute of Science, Rehovoth, Israel.

1. E. Cheifetz, R. C. Jared, S. G. Thompson, and J. B. Wilhelmy, Phys. Rev. Letters 25, 38 (1970).

2. J. B. Wilhelmy, S. G. Thompson, R. C. Jared, and E. Cheifetz, Phys. Rev. Letters 25, 1122 (1970).

3. E. Cheifetz, R. C. Jared, S. G. Thompson, and J. B. Wilhelmy, in Proceedings of the International Conference on the Properties of Nuclei Far From the Region of Beta-Stability, Leysin, Switzerland, 1970 (CERN, Geneva, 1970), Vol. 2, p. 883.

4. J. B. Wilhelmy, E. Cheifetz, R. C. Jared, S. G. Thompson, H. R. Bowman, and J. O. Rasmussen, submitted to Phys. Rev. (preprint LBL-256).

5. M. A. J. Mariscotti, G. Scharff-Goldhaber, and B. Buck, Phys. Rev. 178, 1864 (1969).

6. R. L. Watson, J. B. Wilhelmy, R. C. Jared, C. Rugge, H. R. Bowman, S. G. Thompson, and J. O. Rasmussen, Nucl. Phys. A141, 449 (1970).

7. W. John, F. W. Guy, and J. J. Wesolowski, Phys. Rev. C2, 1951 (1970).

8. F. F. Hopkins, G. W. Phillips, J. R. White, C. F. Moore, and P. Richard, Phys. Rev. C4, 1927 (1971).

9. F. F. Hopkins, J. R. White, G. W. Phillips, C. F. Moore, and P. Richard, to be published in Phys. Rev.

10. H. R. Bowman, J. C. D. Milton, S. G. Thompson, and W. J. Swiatecki, Phys. Rev. 126, 2120 (1962); Phys. Rev. 129, 2133 (1963).

11. H. W. Schmitt, W. E. Kiker, and C. W. Williams, Phys. Rev. 137, B837 (1965).

INFLUENCE OF SHELLS AND PAIRING IN THE FISSION PROBABILITIES OF NUCLEI BELOW RADIUM

L. G. Moretto, S. G. Thompson, J. Routti, and R. C. Gatti

A large body of experimental information on fission cross sections for nuclei lighter than radium is now available.

Preliminary analysis of the fission probabilities on the basis of the Fermi gas level density has shown that fission barriers can be reliably obtained.

Difficulties arise when one attempts to fit the fission probabilities over a rather large energy interval. Close to the shell region, the ratio a_f/a_n between the level density parameters in the fission width and in the neutron width can be as large as 1.4 and decreases to ~ 1.0 with increasing excitation energy. This behavior is attributed to the presence of shell effects in the neutron width and their washing out with excitation energy. Experimental studies of fission fragment angular distributions in ^{210}Po and ^{211}Po seemed to indicate large pairing effects at the saddle point.

In order to investigate shell effects in the neutron width and pairing effects in the fission width, realistic level densities have been incorporated in the calculation.[1-3] The level density employed in the neutron width is calculated on the basis of the Nilsson model and pairing is accounted for by means of the BCS Hamiltonian. The level density used in the fission width is calculated on the basis of the uniform model and the BCS Hamiltonian. Angular momentum effects are accounted for throughout the calculation. No free parameters are included in the neutron width. The harmonic oscillator shell spacing $\hbar\omega_0$ has been assigned the value 41 $A^{-1/3}$. The free parameters in the fission width are the following: 1) fission barrier B_f, 2) single particle level density at the saddle point g_f, 3) gap parameter Δ, 4) barrier penetration. The experimental fission cross sections are transformed into fission probabilities by dividing them by a reaction cross section calculated from the optical model. In order to obtain the first-chance fission probability, one should correct for higher order fission and for non-compound nucleus reactions. The evaluation of these corrections is rather uncertain; however, they are expected to cancel out to some extent. Therefore, no correction has been performed and the fitting has been carried out up to 70 MeV and 120 MeV excitation energy.

The fitting has been performed in three modes:

1) All the parameters free. The fits are quite good; however, rather large fluctuations in the barrier penetrabilities are obtained where data close to the barrier are not available.

2) The barrier penetrability is fixed at its average value of 1 MeV. The fits are essentially as good as in 1).

3) Since the saddle point gap parameters obtained in 1) and 2) are smaller than the average observed in ground state nuclei, they were fixed just at this value ($\Delta = 11\ A^{-1/2}$). The fits are very poor, indicating that within the formalism used here, such large values are not acceptable.

Table I. Parameters obtained from the analysis of fission probabilities. [a]

Reaction	Ref.	B_f (MeV)	g_f (MeV^{-1})	Δ (MeV)	χ^2_{LOG} [b]
$_{83}Bi^{209} + _2He^4 \rightarrow _{85}At^{213}$	c	17.0	7.67	0.38	0.060
$_{82}Pb^{208} + _2He^4 \rightarrow _{84}Po^{212}$	c	19.5	7.36	0.06	0.027
$_{82}Pb^{207} + _2He^4 \rightarrow _{84}Po^{211}$	c	19.7	7.08	0.84	0.001
$_{82}Pb^{206} + _2He^4 \rightarrow _{84}Po^{210}$	c	20.5	7.42	0.60	0.030
$_{83}Bi^{209} + _1H^1 \rightarrow _{84}Po^{210}$	c	21.4	7.33	0.17	0.024
$_{82}Pb^{208} + _1H^1 \rightarrow _{83}Bi^{209}$	c	23.3	7.55	0.22	0.020
$_{82}Pb^{206} + _1H^1 \rightarrow _{83}Bi^{207}$	c	21.9	7.63	0.11	0.035
$_{79}Au^{197} + _2He^4 \rightarrow _{81}Tl^{201}$	c	22.3	7.57	0.39	0.051
$_{79}Au^{197} + _1H^1 \rightarrow _{80}Hg^{198}$	c	20.4	7.43	0.68	0.015
$_{75}Re^{187} + _2He^4 \rightarrow _{77}Ir^{191}$	d	23.7	7.16	0.05	0.003
$_{75}Re^{185} + _2He^4 \rightarrow _{77}Ir^{189}$	d	22.6	6.84	0.10	0.023
$_{74}W^{184} + _2He^4 \rightarrow _{76}Os^{188}$	e	24.2	6.89	0.54	0.005
$_{74}W^{183} + _2He^4 \rightarrow _{76}Os^{187}$	e	22.7	6.84	0.83	0.004
$_{74}W^{182} + _2He^4 \rightarrow _{76}Os^{186}$	e	23.4	6.66	0.43	0.006
$_{73}Ta^{181} + _2He^4 \rightarrow _{75}Re^{185}$	c	24.0	6.51	0.60	0.008
$_{71}Lu^{175} + _2He^4 \rightarrow _{73}Ta^{179}$	d	26.1	6.53	0.99	0.002
$_{69}Tm^{169} + _2He^4 \rightarrow _{71}Lu^{173}$	d	28.0	6.17	0.87	0.003

[a] The barrier penetrations have been set equal to 1.0 MeV.

[b] $$\chi^2_{LOG} = \frac{1}{N} \sum_{K=1}^{N} [LOG(Exp._K) - LOG(Theor._K)]^2$$

[c] A. Khodai-Joopary, Ph. D. thesis, UCRL-16489, July 1966.
[d] G. M. Raisbeck and J. W. Cobble, Phys. Rev. 153, 1270 (1967).
[e] L. G. Moretto, R. C. Gatti, and S. G. Thompson, UCRL-17989, Nuclear Chemistry Division Annual Report, January 1968, p. 141.

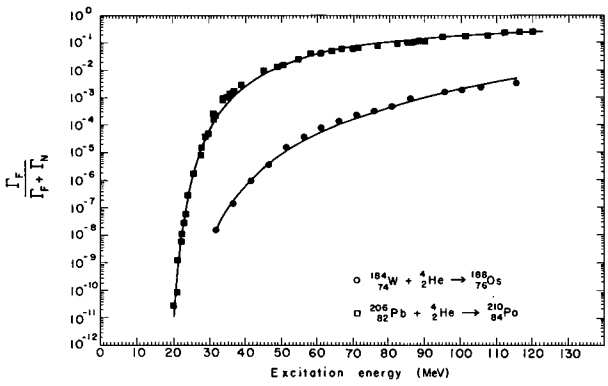

Fig. 1. Theoretical fits to the experimental fission probabilities of ^{188}Os and ^{210}Po. The parameters obtained from the fitting procedure are reported in Table I. (XBL 721-15)

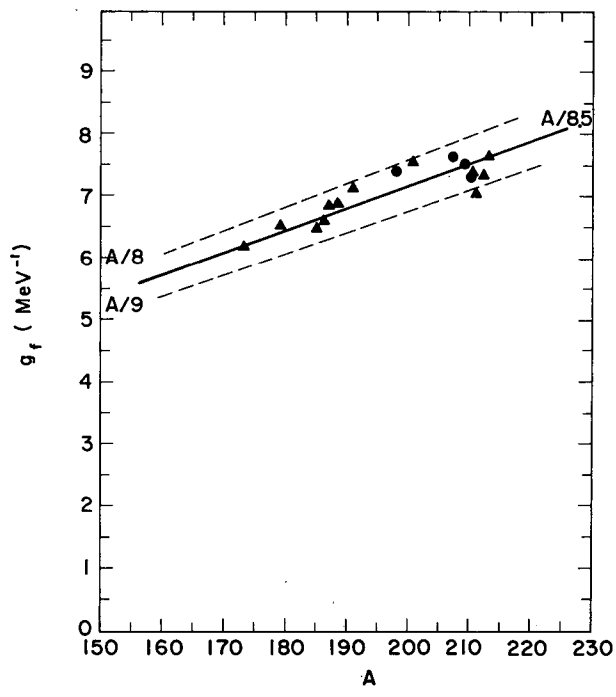

Fig. 2. Experimental fission barriers corrected for the ground state shell effects. The solid line represents the liquid-drop prediction. (XBL 721-14)

In Fig. 1 examples are shown of typical fits. The fission barriers as obtained in mode 2) are presented in Fig. 2, together with the ground state shell effects and the liquid-drop prediction. It can be seen that the experimental fission barriers can be obtained by adding the ground state shell effect to the liquid-drop barrier. [4]

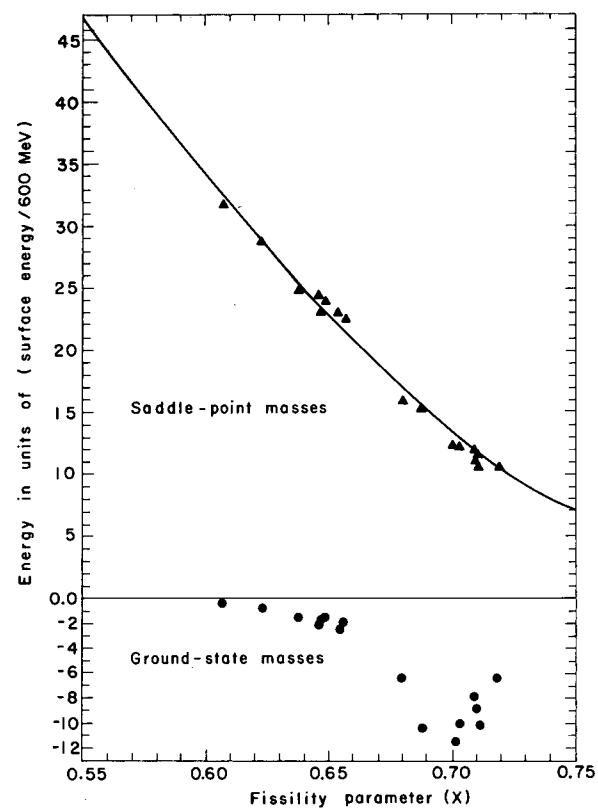

Fig. 3. Saddle point densities of doubly degenerate single particle levels. The values cluster about a line corresponding to a = A/8.5. (XBL 721-16)

In Fig. 3 the saddle-point single-particle level densities are shown as a function of A. The expected linear dependence with A is clearly seen. The experimental values cluster around the line corresponding to a = A/8.5 and are bracketed by the lines corresponding to a = A/9 and a = A/8. No particular structure is seen in going through the ^{208}Pb shell, indicating that the Nilsson model accounts for the shell effects satisfactorily.

The summary of the parameters obtained from the data fitting is presented in Table I.

As a conclusion, it seems that: 1) the fission barriers are well understood, 2) the Nilsson model accounts for the shell effects in Γ_n and their disappearance with excitation energy, 3) pairing at the saddle point is either small or some physical effect not accounted for in the present formalism is artificially lowering pairing.

References

1. L. G. Moretto, R. Stella, V. Caramella Crespi, Energia Nucleare 7, 436 (1970).

2. L. G. Moretto, LBL-219, August 1971; to be published in Nucl. Phys.

3. L. G. Moretto, LBL-228, August 1971; to be published in Nucl. Phys.

4. W. D. Myers and W. S. Swiatecki, Nucl. Phys. 81, 1 (1966).

PROMPT GAMMA-RAY SPECTRA FROM PRODUCTS FORMED IN THE SPONTANEOUS FISSION OF ^{252}Cf†

J. B. Wilhelmy, E. Cheifetz,* R. C. Jared, and S. G. Thompson

The purpose of this report is to present information on how to obtain and use a magnetic tape on which is recorded γ-ray spectral information in coincidence with the prompt fission of ^{252}Cf. These data have been obtained from three- and four-parameter measurements of γ rays and K x rays in coincidence with fission fragment pairs (see Fig. 1). From analysis of these data information has been obtained on the ground state bands of even-even fission products,[1-3] on the mass and charge distribution in fission,[4] and on the primary fragment angular momentum.[5] In the experiments, ~ 2×10^8 multiparameter coincidence events have been recorded. This quantity of data has therefore precluded the possibility of presenting all of the experimental information in published form. Since, to a large extent these data are unique, we propose to make available, on request, a magnetic tape containing the spectral information so that interested potential users will have access to the data for any analysis which they would care to perform. The details of how to obtain the tape and a compilation of data necessary for utilizing the information is presented in the main report[6] for which this is a summary.

The tape contains γ-ray spectra for selected mass intervals (in one case also Z intervals). The masses were calculated from the measured kinetic energies of the fragments, using the predetermined mass-dependent neutron emission distribution[7] and the Schmitt, Kiler, and Williams mass-dependent energy calculation procedure.[8] This method consists of first obtaining a rough energy calibration from the measured fragment kinetic-energy pulse-height spectrum,

$$E = a \cdot x + b, \qquad (1)$$

where x is the recorded fragment kinetic-energy channel number and a and b are constants,

$$a = 24.40/(P_L - P_H),$$

$$b = 103.77 - a \cdot P_L,$$

with P_L and P_H being the centroids of the light and heavy fission-fragment kinetic-energy peaks. Conservation of momentum requires

$$M_{1P} = \frac{252}{(1 + E_{1P}/E_{2P})}$$
$$M_{2P} = 252 - M_{1P}. \qquad (2)$$

M_i and E_i denote mass in amu and energy in MeV of the ith fragment. The subscript P denotes preneutron emission quantities. In the

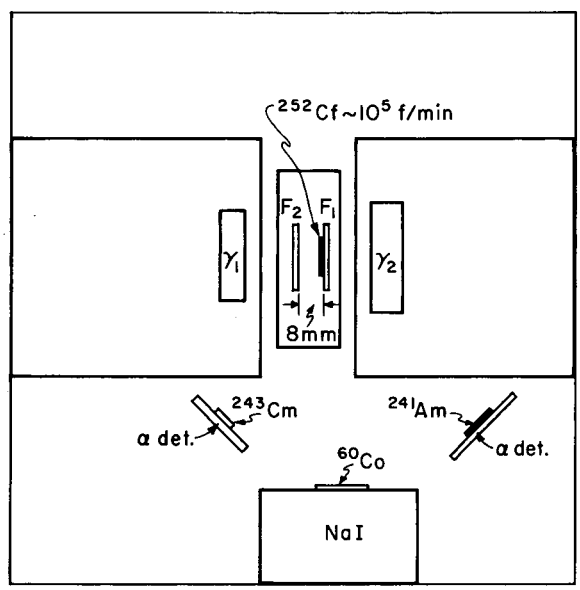

Fig. 1. General schematic representation of the detector configuration. Detectors F_1 (with electrodeposited ^{252}Cf) and F_2 measured kinetic energies of the fragments. Detectors γ_1 and γ_2 measured energies of γ rays and/or x rays. The sources and detectors indicated in the bottom of the figure were used for external stabilization of the photon detectors. (XBL 703-2403)

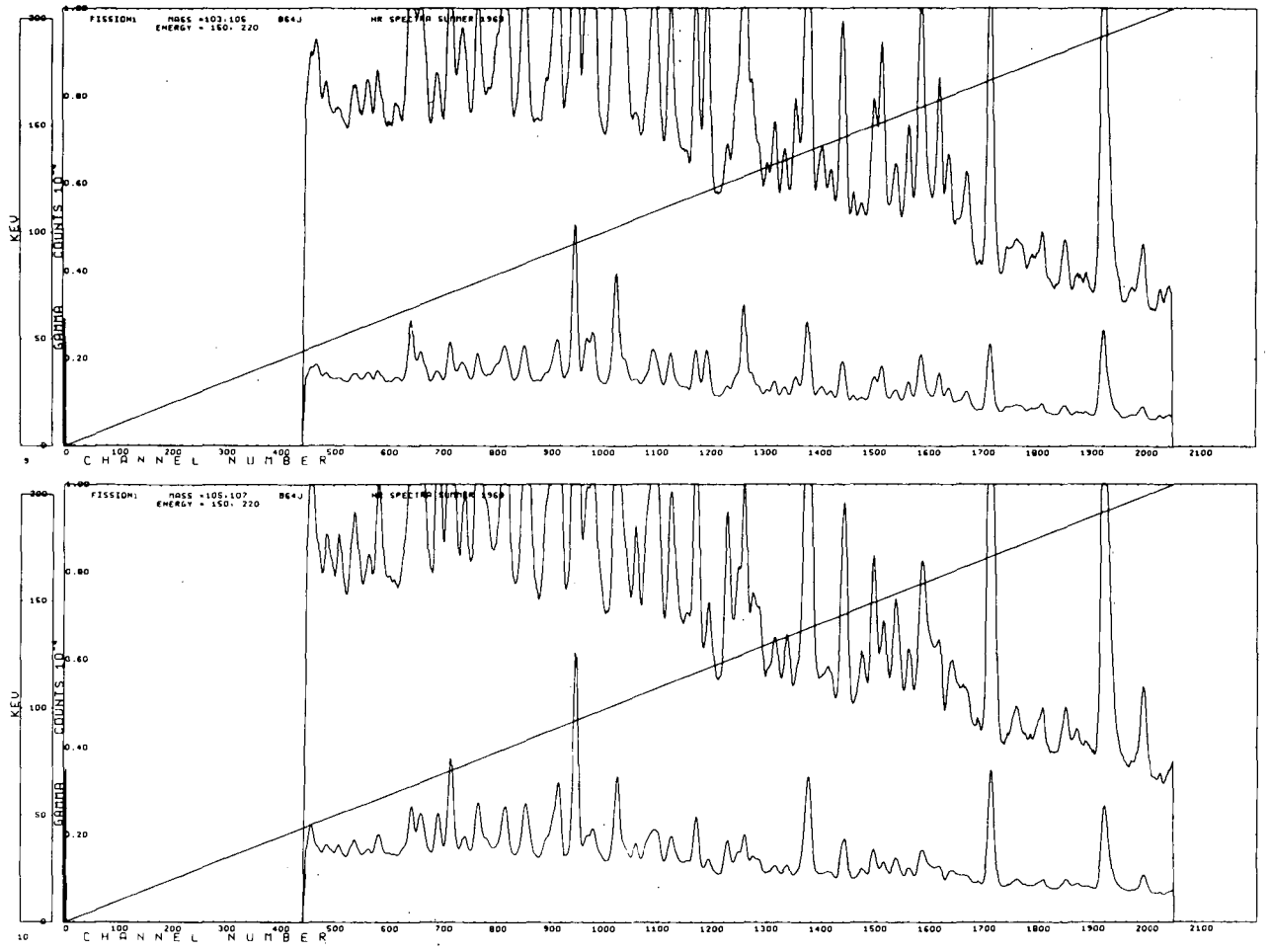

Fig. 2. An example of portions of mass-sorted γ-ray spectra recorded in Experiment 1 (HR). The top spectrum is for transitions from fission products stopped in fragment detector F_1 having masses between 103-105 and the bottom spectrum is for the mass internal 105-107. The straight line is for energy calibration. Each spectrum is plotted twice with the top spectrum being equal to the bottom spectrum multiplied by 5.

(XBL 708-1785)

first calculation E_{1P} and E_{2P} are approximated by

$$E_T = E_{1P} + E_{2P} \approx E_1 + E_2. \qquad (3)$$

The values of M_{1p} and M_{2P} are then corrected for the average number of emitted neutrons ($\bar{\nu}$) using the experimental results of $\bar{\nu}(M, E_T)$ presented by Bowman et al.[7] This correction has the form

$$M_1 = M_{1P} - \bar{\nu}_1 (M_{1P}, E_T)$$

$$M_2 = M_{2P} - \bar{\nu}_2 (M_{2P}, E_T). \qquad (4)$$

Using these values of M_1 and M_2, the mass-dependent energy calibration[8] is evaluated:

$$E_i = (24.0203 + 0.03574\, M_i) \frac{X}{P_L - P_H} - (24.0203 + 0.0374\, M_i) \frac{P_L}{P_L - P_H} + 0.1370\, M_i + 89.6083. \qquad (5)$$

The values of E_{iP} are then calculated:

$$E_{iP} = E_i(1 + \nu_i/M_i). \quad (6)$$

The new values of E_{1P} and E_{2P} are entered into Eq. (2) for continuation of the iterative process. This is repeated until the mass values resulting from the consecutive iterations differ by less than 0.05%. These calculations are performed only once for each allowed channel combination (a total of 10 000 possibilities) and the results are stored in an array in the computer program used for the data analysis. The event-by-event mass assignments are then obtained from the experimental fragment kinetic-energy results by interpolation in the array. After the mass of each event is determined, the recorded coincident γ-ray (or K x-ray) channel is incremented in the γ-ray (or K x-ray) spectrum corresponding to the appropriate mass interval. The spectral information is stored in 38 discrete mass intervals (each 2 amu wide) covering the fission product distribution from A = 87 to A = 163.

The magnetic tape which we will provide contains sorted spectral information for six different experimental configurations. These individual experiments provide data which are useful over varying energy ranges and detector geometries. A brief description of each experiment is given below, with our designation shown in parenthesis.

Experiment 1 (HR)

This is a three-parameter measurement of γ rays in coincidence with fission fragments. The γ-ray detector used was a 1-cm^3 Ge(Li) detector having resolution of ~ 1 keV at 122 keV and was located in position γ_2 (see Fig. 1). The experimental data covered a usable energy range of from 40 to 400 keV. An example of the mass-sorted spectra from this experiment is shown in Fig. 2.

Experiment 2 (G6)

Two three-parameter measurements were recorded in the same experiment; these experiments are designated "G6" and "COAX". In the G6 experiment a 6-cm^3 Ge(Li) detector was used having resolution of 1.6 keV at 279 keV and was located in position γ_1 (Fig. 1). The data cover a usable energy range of 60 to 1400 keV.

Experiment 3 (GX)

The data recorded in this experiment represent the γ-ray portion of three- and four-parameter measurements in which γ rays and K x rays were recorded. The γ-ray detector had a 6-cm^3 volume with resolution of ~ 1.6 keV at 279 keV and was located at position γ_1 (Fig. 1). The usable energy range in this experiment was 60 to 1400 keV.

Experiment 4 (COAX)

The data presented in this experiment were recorded at the same time as the data presented in Experiment 2. In this case a 35-cm^3 coaxially drifted Ge(Li) γ-ray detector with resolution of 2.5 keV at 279 keV was used. This crystal was located in position γ_2 and had a usable energy range of 150 to 1900 keV.

Experiment 5 (HRF2)

This experiment presents the same three-parameter data recorded in Experiment 1. In this case, however, the data is presented for mass intervals relative to the fragments stopping in fragment detector F_2 (see Fig. 1). For all other presented results the mass intervals are relative to fragments stopping in detector F_1. The sorting is performed in this manner so that transition lifetime information can be extracted from the γ-ray intensity measurements. By observing, over the same mass intervals, the intensity of a specific γ ray in the "HR" and "HRF2" experiments and by knowing the velocity of the fragment and the geometry of the detectors, it is possible to estimate the transition lifetime. Transition lifetimes in the 0.2- to 2-nonosecond region, which we have extracted using this technique, are presented in Refs. 1-3.

Experiment 6 (Z)

This experiment presents γ-ray data obtained in a four-parameter experiment in which two fragment energies were recorded in coincidence with γ rays and K x rays. The γ rays were recorded by using the detector described in Experiment 3. In this experiment the data are presented in 27 spectra each labeled by an atomic number (Z = 37 to 63). These atomic numbers were established by placing windows on the appropriate energy interval containing the Kα x rays of each element.

Footnotes and References

†Condensed from LBL-255, November 1971.

*Present address: Weizman Institute of Science, Rehovoth, Israel.

1. E. Cheifetz, R. C. Jared, S. G. Thompson, and J. B. Wilhelmy, Phys. Rev. Letters 25, 38 (1970).

2. J. B. Wilhelmy, S. G. Thompson, R. C. Jared, and E. Cheifetz, Phys. Rev. Letters 25, 1122 (1970).

3. E. Cheifetz, R. C. Jared, S. G. Thompson, and J. B. Wilhelmy, in Proceedings of the International Conference on the Properties of Nuclei Far From the Region of Beta Stability, Leysin, Switzerland, 1970 (CERN, Geneva, 1970) Vol. 2, p. 883.

4. E. Cheifetz, J. B. Wilhelmy, R. C. Jared, and S. G. Thompson, Phys. Rev. C4, 1913 (1971).

5. J. B. Wilhelmy, E. Cheifetz, R. C. Jared, S. G. Thompson, H. R. Bowman, and J. O. Rasmussen, submitted to Phys. Rev. (preprint LBL-256).

6. J. B. Wilhelmy, E. Cheifetz, R. C. Jared, S. G. Thompson, LBL-255, November 1971.

7. H. R. Bowman, J. C. D. Milton, S. G. Thompson, and W. J. Swiatecki, Phys. Rev. 126, 2120 (1962); Phys. Rev. 129, 2133 (1963).

8. H. W. Schmitt, W. E. Kiler, and C. W. Williams, Phys. Rev. 137, 837 (1965).

INTERPRETATION OF MASS ASYMMETRY IN FISSION BASED ON DEFORMATION ENERGY SURFACES*

C. F. Tsang and J. B. Wilhelmy

One of the most readily observed properties of the fission process has been the determination of the mass distribution of the resultant fission products. Until very recently all low-energy induced fission studies of actinide nuclei have shown mass distributions that were strongly asymmetric. A characteristic measurement of the asymmetry is the ratio of the yield of fission products corresponding to the peak of the mass distribution compared with the yield of products at the valley. Experimental peak-to-valley ratios have been tabulated for low-energy induced fission of actinide nuclei[1] and these results invariably show them to be strongly asymmetric and have the property that as the excitation energy is increased in the fissioning nucleus, the peak-to-valley ratio decreases. Recently an apparently anomalous case has been discovered in which the thermal-neutron induced fission of ^{257}Fm has resulted in a strongly symmetric mass distribution.[2] These results are even more striking because other current experimental studies have shown that the mass distribution for the spontaneous fission of the adjacent even-even isotope ^{256}Fm is asymmetric.[3]

Many attempts have been made to theoretically interpret the fission mass distribution but none, so far, have been successful for quantitative predictions. The liquid-drop model analysis[4] predicts the mass distribution to be symmetric in all cases. Very often the asymmetry has been qualitatively explained as the result of strong shell effects in the residual fission product nuclei. Recently a tractable theoretical interpretation of the mass distribution was proposed by Möller and Nilsson[5] in which they have shown that in the actinide region, the second fission barrier has a lower total energy for asymmetric mass division. A schematic representation of the total deformation energy surface of an actinide nucleus is shown in Fig. 1. The multidimensional aspects of the surface are reduced by combining the two symmetric coordinates (ϵ_2 and ϵ_4) and the two asymmetric coordinates (ϵ_3 and ϵ_5). The surface shows that the ground state, first fission barrier, and secondary minimum have their lowest energy along the symmetric axis (labeled SYM). However, the calculations show that in the outer barrier region there is a mountain top on the symmetric axis and the saddle point is located at an asymmetric deformation. Also shown in Fig. 1 are cross sections of the deformation energy surface through the symmetric axis and an asymmetric axis in the second barrier region. The cross section through the symmetric axis shows the now-familiar double-peaked fission barrier. On the other hand, the cross section through the asymmetric axis shows that the deformation energy surface clearly prefers an asymmetric deformation near the second barrier.

Our interpretation of mass asymmetry is based on a quasi-static analysis of the system at the second saddle point. We make the simple assumption that the probability of symmetric or asymmetric fission is related to the excitation energy of the system relative to the deformation energy surface of the symmetric and asymmetric outer fission barrier. When the excitation energy is positive with respect to the barriers then we take the probability for asymmetric and symmetric fission to be proportional to the local level density above the asymmetric saddle point and the

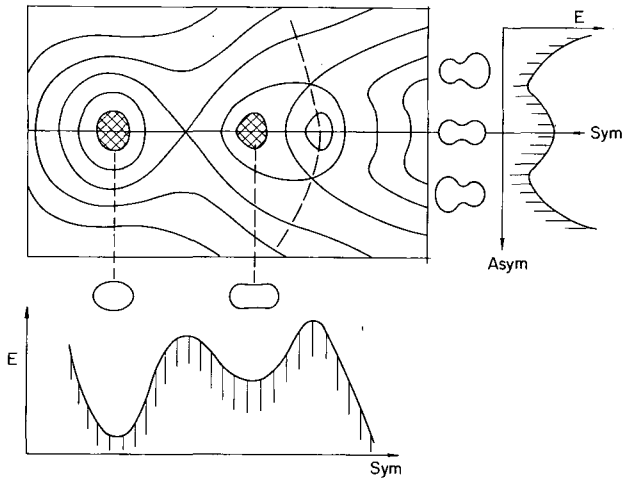

Fig. 1. Schematic representation of a deformation energy surface as a function of symmetric and asymmetric deformations. For details, see text. (XBL 719-4270)

symmetric mountain top respectively. This probability is evaluated by using the simplest Fermi gas level-density formula:

$$P_a = c \exp\left(2\sqrt{a'(E_T - E_a)}\right), \qquad (1)$$

$$P_s = c \exp\left(2\sqrt{a(E_T - E_s)}\right),$$

where P_a and P_s are the probability for asymmetric and symmetric division respectively, E_T is the excitation energy, E_a and E_s are the energies of the asymmetric saddle point and the symmetric mountain top, and a' and a are the level-density parameters for the asymmetric and symmetric cases. In the Fermi gas model the level-density parameters are proportional to the number of particles (A) and can therefore be formally written as

$$a' = \chi' A; \; a = \chi A .$$

By making these substitutions in Eq. (1) and taking the ratio of the probability of asymmetric to symmetric fission, we get, on a slight rearrangement,

$$1 = 2\sqrt{\chi'}\,\frac{\sqrt{A(E_T - E_a)}}{\ell n\, Pa/Ps} - 2\sqrt{\chi}\,\frac{\sqrt{A(E_T - E_s)}}{\ell n\, Pa/Ps} . \qquad (2)$$

A plot of $\sqrt{A(E_T - E_a)}/\ell n(P_a/P_s)$ against $\sqrt{A(E_T - E_s)}/\ell n(P_a/P_s)$ should be linear if χ and χ' are constants. To make such a plot it is necessary to evaluate the various quantities in the ordinate and abscissa. The ratio P_a/P_s is taken to be the experimentally determined[1] peak-to-valley ratio, E_T is the excitation in the fissioning nucleus, and the energy of the asymmetric saddle point is taken as the empirical barrier height of the outer fission barrier. These empirical values have been derived from the analyses of experimental data by Bjørnholm,[6] Britt et al.,[7] and Back et al.[8] Where experimental data is not available we have used the semiempirical values of Pauli and Ledergerber.[9] The values of the symmetric barrier heights (E_s) were obtained by adding the theoretically calculated[5,10,11] energy difference between the symmetric and asymmetric fission barriers ($E_s - E_a$) to the above-mentioned empirical values for the asymmetric barriers. Thus, this energy difference is the only number we get directly from the theory.

These values were used to calculate the ordinate and abscissa for Eq. (2), and Fig. 2 presents a plot of this data based on the Möller-Nilsson[5] deformation-energy surfaces. The data with large excitation energy have large values of the ordinate and abscissa. As can be seen, these data define a reasonable

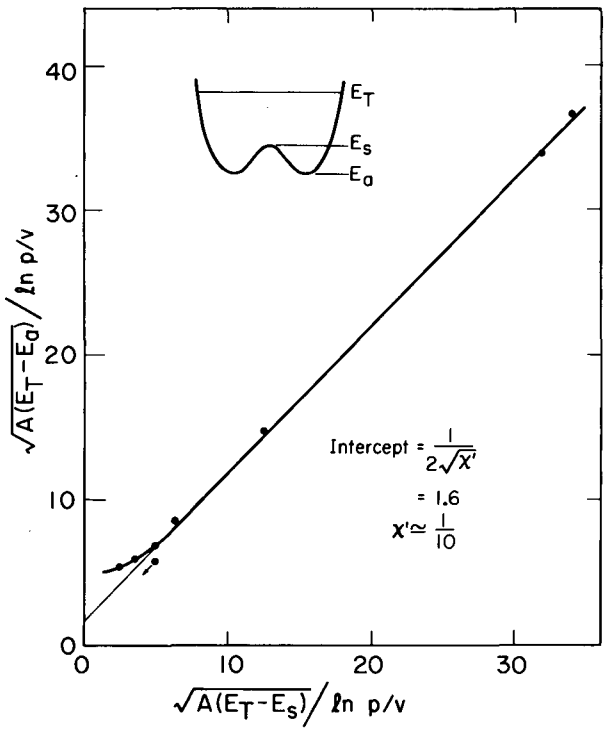

Fig. 2. Correlation obtained by plotting data using Eq. (2) for cases in which the excitation energy in the fissioning nucleus is above both the asymmetric saddle point and the symmetric mountain top.[5] The line is drawn to smoothly join data points. (XBL 719-4272)

straight line, with some deviation at the low-energy end. The magnitudes of χ and χ' are determined from the line. They are found to be equal (which is reasonable, since, when the excitation energy is large the effect of the energy difference between the symmetric mountain top and the asymmetric saddle point becomes less significant) and of value ~ 1/10. This gives for the level-density parameter in the Fermi gas model, a = A/10, which is in good agreement with the value obtained from analysis of neutron-capture resonances and of other nuclear reactions where a is typically determined to be between A/8 and A/12. For low-energy points, both χ and χ' are seen to be no longer constant as a function of energy. Since the smooth curve bends up from the straight line as one goes to decreasing values on the abscissa, this means that the value of χ' is decreasing which implies a decrease in the number of levels when the energy is close to the deformation-energy surface.

Using these results we are now in a position to make an estimate of the peak-to-valley ratio for the thermal-neutron induced fission of ^{257}Fm. The values[12, 5, 9] of E_T, E_s, and E_a are 6.5, 3.5, and 3.3 MeV respectively. Using the values of χ and χ' from Fig. 2 and rearranging Eq. (2), we obtain a prediction for the peak-to-valley ratio of ~1.8. This compares well with the experimental value of 1 (i.e., symmetric fission) since the range of values of peak-to-valley ratios which are experimentally known is from 1 to $\gtrsim$750. Th uncertainties in theory are more than enough to account for the difference of 1.8 from 1. The physical reason why we predict close-to-symmetric fission in this case is that the energy difference between the asymmetric saddle point and symmetric mountain top is small (only 0.2 MeV) so that at the neutron binding energy, 3.2 MeV above the barrier, its effect is not large. In other cases such as U and Pu, the difference is about 2 MeV and this has a significant effect on the mass distribution for excitation energies corresponding to thermal-neutron induced fission. In this argument, we can predict that the thermal-neutron induced fission of ^{255}Fm will also be symmetric (even though spontaneous fission of ^{256}Fm is found to be asymmetric).

In cases when the excitation energy is below the barriers (for example, spontaneous fission) we interpret the probability for asymmetric and symmetric fission to be given by the probability of penetrating the fission barriers along the symmetric and asymmetric paths. These probabilities are given by the standard WKB penetration formula

$$P_a = c' \exp -2 \sqrt{\frac{2\beta'}{\hbar^2} A^{5/3}(E_a - E_T)}\, d\epsilon \ ,$$
$$P_s = c' \exp -2 \sqrt{\frac{2\beta}{\hbar^2} A^{5/3}(E_s - E_T)}\, d\epsilon \ , \qquad (3)$$

where $\beta' A^{5/3}$ is the inertia parameter for penetrating the asymmetric saddle, and $\beta A^{5/3}$ is that for the symmetric mountain. On taking the ratio of probabilities, the penetration from the ground state to the second minimum that is common to both cancel out, and we need only consider the penetration from the secondary minimum to the emerging point of the barrier by way of the asymmetric and symmetric paths.

For the analysis of the peak-to-valley ratios by using Eq. (3), there are two parameters to be obtained: the asymmetric and symmetric inertia parameters. Until recently there has only been one radiochemical result of the peak-to-valley ratio for spontaneous fission, which is the case of ^{252}Cf (~ 750). The other spontaneous fission results are given only as lower limits. As a reasonable number, we have assumed the inertial parameter for asymmetric fission was the same as that obtained by Nilsson et al.[13] from an analysis of spontaneous fission half-lives. Their value is:

$$\sqrt{\frac{2\beta'}{\hbar^2}} = 0.3390 \text{ MeV}^{-1/2}. \qquad (4a)$$

The value for the symmetric inertial parameter can then be obtained from Eq. (3) by fitting the ^{252}Cf peak-to-valley ratio. This gives a value of:

$$\frac{2\beta}{\hbar^2} = 0.3747 \text{ MeV}^{-1/2} \ . \qquad (4b)$$

With these values it is now possible to predict peak-to-valley ratios for all spontaneously fissioning even-even nuclei. Results of the analysis are shown in Table I. Thus the peak-to-valley yield for the spontaneous fission of ^{256}Fm is calculated to be 43, which agrees reasonably well with the experimental value[3] of ~12. The physical reason why the spontaneous fission of ^{256}Fm is asymmetric is that even though the energy difference between the asymmetric saddle point and the symmetric mountain top is small, in the case of tunneling under the barrier it is felt quite strongly. This is to be contrasted with the case of the thermal-neutron induced fission of ^{257}Fm, where the energy difference is just as small, but its effect is very little when the

Table I. Experimental and calculated values of peak-to-valley ratios for spontaneously fissioning nuclei.

Nucleus	Peak yield/valley yield Experimental	Calculated
^{238}U	$> 500^a$	8×10^6
^{240}Pu	$> 270^a$	7×10^5
^{242}Cm	$> 700^a$	2.4×10^4
^{244}Cm	$> 5\times10^{3\,b}$	2×10^4
^{252}Cf	$\sim 750^a$	Fitted
^{256}Fm	$\sim 12^b$	43

[a]Ref. 1.
[b]Ref. 3.

excitation energy is substantially above the barrier. In this argument, we can predict that the spontaneous fission of ^{258}Fm is asymmetric, even though the thermal-neutron induced fission of ^{257}Fm is found to be symmetric.

In this study we have correlated quantitatively the peak-to-valley ratios of the mass yield distributions of all even-even fissioning nuclei. We are able to understand the apparently anomalous case of the symmetric thermal-neutron induced fission of ^{257}Fm. We have also made a study of radium fission which yields a triple-peaked mass yield distribution. The results can be understood within our picture.

Footnote and References

*Condensed from LBL-254. Published in Nucl. Phys. A184, 417 (1972).

1. H. R. von Gunter, Actinides Rev. 1, 275 (1969).

2. W. John, E. K. Hulet, R. W. Lough, and J. J. Wesolowski, Phys. Rev. Letters 27, 45 (1971).

3. K. F. Flynn, E. T. Horwitz, C. A. Bloomquist, R. F. Barnes, R. K. Sjoblom, and L. E. Glendenin, submitted to Phys. Rev.

4. W. J. Swiatecki and S. Cohen, Ann. Phys. (N. Y.) 22, 406 (1963); J. R. Nix, Nucl. Phys. A130, 241 (1969).

5. P. Möller and S. G. Nilsson, Phys. Letters 31B, 283 (1970); also private communication (1971).

6. S. Bjørnholm, in Proceedings of the Conference on Transuranium Elements--The Mendeleev Centennial (Robert A. Welch Foundation, Houston, 1969), p. 447.

7. H. C. Britt, S. C. Burnett, B. H. Erkkila, J. E. Lynn, and W. E. Stein, Phys. Rev. C4, 1444 (1971).

8. B. B. Back, J. P. Bondorf, G. A. Otroschenko, J. Pederson, B. Rasmussen, Nucl. Phys. A165, 449 (1971).

9. H. C. Pauli and T. Ledergerber, Nucl. Phys. A175, 545 (1971).

10. J. R. Nix, Private communication (1971); M. Bolsterli, E. O. Fiset, J. R. Nix, and J. L. Norton, submitted to Phys. Rev. C (Los Alamos Scientific Laboratory Report LA-DC-12817).

11. M. Brack, Jens Damgaard, H.-C. Pauli, A. Stenholm-Jensen, V. M. Strutinsky, and C. Y. Wong, On Nuclear Shell Effects (to be published in Rev. Mod. Phys.)

12. W. D. Myers and W. J. Swiatecki, Nucl. Phys. 81, 1 (1966); Lawrence Radiation Laboratory Report UCRL-11980 (1965).

13. S. G. Nilsson, C. F. Tsang, A. Sobiczewski, Z. Szymanski, S. Wycech, G. Gustafson, I. L. Lamm, P. Möller, and B. Nilsson, Nucl. Phys. A131, 1 (1969).

A USE OF ^{252}Cf FOR FISSION-FRAGMENT MEASUREMENTS

R. C. Jared and J. A. Harris

The fission process has long been used as a method for producing neutron-rich isotopes. These neutron-rich isotopes have been used to study radioactive decay schemes. Until

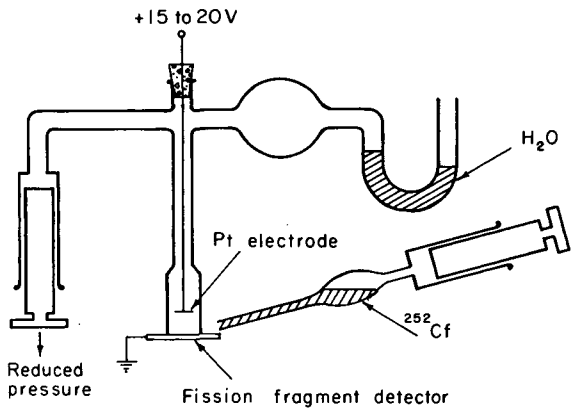

Fig. 1. The plating cell for ^{252}Cf. The liquids were added or removed by the syringe on the right by using vacuum or pressure from the syringe on the left as an aid.
(XBL 721-2138)

recently, very few conclusive assignments were made on prompt γ radiation from fission. The measurements of decay schemes of fission products have been limited to nuclei that have undergone beta decay and have sufficiently long half-lives to permit application of chemical separation techniques.

A typical fission experiment would consist of two fission-fragment detectors facing each other with a ^{252}Cf source in the middle mounted on a very thin foil so that both fission-fragment kinetic energies can be measured. The masses of the fission fragments are calculated from these energies. In addition to the fission detector, a γ detector is usually positioned close to the source to obtain gammas that are in coincidence with calculated masses. The main problem with the above experimental configuration is that the γ rays emitted from the moving fragments are broadened and shifted as a result of the Doppler effect. This effect can be minimized by stopping the fragment in times much shorter than the lifetimes of the γ rays.

An obvious solution to the problem is to stop one of the fission fragments immediately after fission in one of the fragment detectors and then observe the γ rays. This was accomplished by electrodepositing the californium on a detector. The stopping time of the fragments is ~ 10^{-12} sec; therefore, lines with half-lives greater than 10^{-10} sec can be clearly identified. This technique was used to identify 30 decay schemes for prompt even-even isotopes in the fission of ^{252}Cf.[1,2]

Experiment

The electrodepositing of ^{252}Cf was accomplished in the cell shown in Fig. 1 A phosphorus diffused Si detector (200-500Ω/cm) was mounted at the bottom of the cell. The ^{252}Cf was made chemically pure by being processed through a cation exchange column. The sample was then placed in 0.001 M HNO_3 and transferred to the plating apparatus.

Electrodepositing of ^{252}Cf was done under the following conditions. A Si detector was used as the cathode, and Pt wire as the anode. The 0.001 M HNO_3 solution with ^{252}Cf was introduced into the system by applying a slight vacuum to the cell, which was done by means of a syringe attached as shown on the left-hand side of Fig. 1. Voltage was applied and the sample was allowed to plate for 10 to 15 min, after which time NH_4OH was introduced into the system, converting the sample to the hydroxide form. The detector was then removed and thoroughly washed with alcohol, and allowed to dry under a heat lamp.

Results

The detector showed no deterioration from the plating procedure, but the life of the detector due to radiation damage was reduced by a factor of 5. This reduction in lifetime was probably due to microscopic nonuniformity in the plated californium.

Conclusion

In conclusion, the overall effect of the plating was to reduce the useful life of the fission-fragment detector, but this was far outweighed by the ability to stop the fission fragment within ~ 10^{-12} sec of fission, thereby eliminating for all practical purposes Doppler-shifted lines in the γ-ray spectrum of ^{252}Cf.

References

1. E. Cheifetz, R. C. Jared, S. G. Thompson, and J. B. Wilhelmy, Phys. Rev. Letters, 25, 38 (1970).

2. J. B. Wilhelmy, S. G. Thompson, R. C. Jared, and E. Cheifetz, Phys. Rev. Letters, 25, 1122 (1970).

3. R. M. Latimer, Electrodepositing Procedure (unpublished).

Rb and Cs ISOTOPES AND CROSS SECTIONS FROM 40- TO 60-MeV PROTON FISSION OF ^{238}U, ^{232}Th, AND ^{235}U†

B. L. Tracy, J. Chaumont, R. Klapisch, J. M. Nitschke, A. M. Poskanzer, E. Roeckl, and C. Thibault

On-line mass spectrometer techniques for the separation of Rb and Cs have been used to detect products from the 40- to 60-MeV proton-induced fission of ^{238}U, ^{232}Th, and ^{235}U. New isotopes were observed, half-lives measured, and isotopic cross section distributions determined.

Briefly, the experimental arrangement involves having the target in the ion source, where energetic fission fragments are caught in heated graphite foils from which Rb and Cs diffuse very quickly. They are ionized easily by surface ionization, accelerated, and then analyzed with a mass spectrometer (90° deflection, 30 cm radius). Individual ions are detected at the collector by means of an electron multiplier.

This apparatus was installed in an external beam of the Grenoble cyclotron. The current of the proton beam bombarding the target of about 2 μA was pulsed by blocking the ion source to give 100 msec of beam with a repetition period of 1 to 10 sec.

To measure short half-lives, two methods were used:

A) Differential scanned diffusion. In this method, $i_0(t)$ is the diffusion-limited time dependence of the ion current following a proton irradiation when the mass spectrometer is set on a stable or long-lived isotope. If another measurement is performed on a short-lived isotope, radioactive decay will be an additional limiting factor to the ion current and we shall thus have $i(t) = i_0(t) \exp(-\lambda t)$. From the ratio i/i_0 the radioactive decay constant can be obtained. In fact $i(t)$ and $i_0(t)$ are monitored at fixed regular intervals by means of a periodic triangular modulation of the ion accelerating potential in order to discriminate the signal from the time-dependent background.

B) Beta-decay measurements. The electron multiplier, normally used to count ions, can detect beta rays emitted by nuclei accumulated on the first dynode with an efficiency of about 20%. With the mass spectrometer set at a particular mass, nuclides are collected on the dynode during the proton irradiation and for 130 msec afterwards. At this time, t_0, the ion beam is switched off and the decay of the accumulated activity is recorded. This method not only gives the half-life of the respective Rb or Cs isotope but also allows the observation of the beta-decay descendants. From an analysis of the initial activities information can be gained on whether the second half-life belongs to the daughter or granddaughter. The results are given in Table I. ^{99}Rb, ^{98}Sr, and $^{145,146}Cs$ are new isotopes.

The isotopic distributions of Rb and Cs independent yields were measured with high precision. The Rb isotopic distributions have a Gaussian shape, but those of Cs are somewhat asymmetrical. As the proton bombarding energy increases, the neutron-excess

Table I. Measured half-lives in milliseconds.

Mass	Element	Diffusion	Beta decay	Best value	Previous work
96	Rb	207 ± 3		207 ± 3	230 ± 20
97	Rb	176 ± 6	175 ± 8	176 ± 5	135 ± 10
	Sr		≲200	≲200	400 ± 300
	Y		1110 ± 140	1110 ± 140	1110 ± 30
98	Rb	140 ± 8	96 ± 27	136 ± 8	
	Sr		845 ± 43	850 ± 50	
	Y		≲300	≲300	
99	Rb	76 ± 5		76 ± 5	
145	Cs	559 ± 28	613 ± 100	563 ± 27	
146	Cs	189 ± 11		189 ± 11	

sides of the distributions remain approximately fixed while the neutron-deficient sides shift to lower mass numbers. The distributions also show significant variations with the neutron-to-proton ratio of the target.

All the isotopic cross sections show a significant odd-even structure, with the formation of even neutron isotopes being favored. The effect is more pronounced for the neutron-rich isotopes. A similar structure is found to occur in Rb and Cs distributions from fission induced by thermal neutrons, 155-MeV protons, and 24-GeV protons, as well as in the Na and K cross sections from 24-GeV proton reactions with a variety of targets.

This structure is more evident if one analyzes the data by a method of third differences. Let L_0, L_1, L_2, and L_3 be the natural logarithms of the relative isotopic yields at the mass numbers A, A + 1, A + 2, and A + 3. We then define the third difference for this mass interval as

$$D_3 \equiv (-1)^A [(L_3 - L_0) - 3(L_2 - L_1)]/8. \quad (1)$$

If L_0 to L_3 lie on a parabola (i.e., the data are Gaussian), then it is easily shown that the third difference is exactly zero. Suppose now that the logarithms of the yields of odd-mass isotopes all lie above a smooth parabola by an amount Δ, and those of even-mass isotopes all lie below this curve by an equal amount. Then, it can be shown that $D_3 = +\Delta$. Thus if the yields of odd-mass isotopes are favored, the third differences will be consistently greater than zero and will give directly the average fractional odd-even effect for each interval of four masses. The resulting third differences for all Rb distributions are shown in Fig. 1. The experimental data of J. Chaumont[1] have been used to compute the third differences from fission by thermal neutrons, 155-MeV protons, and 24-GeV protons. From these graphs it is evident that a small but significant odd-even effect exists in all of the Rb isotopic distributions measured up to the present. This effect varies more or less smoothly with mass number, but shows no apparent dependence on target or bombarding energy. The effect is 10% or higher for the most neutron-rich isotopes, but levels off to a value of about 2% near the maxima of the distributions. Some graphs show a tendency to increase on the neutron-deficient side, but this is not reproduced in all cases.

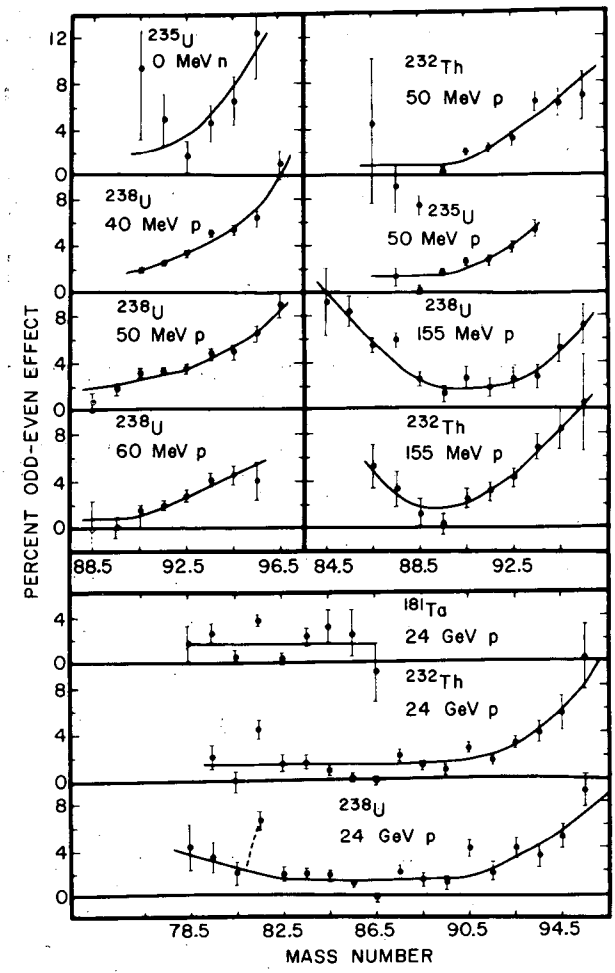

Fig. 1. Percent odd-even effect in the Rb distributions. The third difference for each mass interval A to A + 3 is plotted at the midpoint of this interval, i.e., at mass A + 1.5. In each case a smooth curve has been drawn by eye through the computed points. Open circles represent third differences containing one or more interpolated or extrapolated yields. These points have been given less weight when drawing the smooth curve. (XBL 724-780)

An odd-even effect which favors even-neutron species in the isotopic distribution could have two possible origins:

1) A preference in the nuclear division itself for fragments with even numbers of neutrons, because of the higher Q values involved.

2) A tendency for odd-neutron prompt fragments to evaporate slightly more neutrons than even-neutron prompt fragments.

In the first case, neutron emission from the prompt fragments will tend to smear out

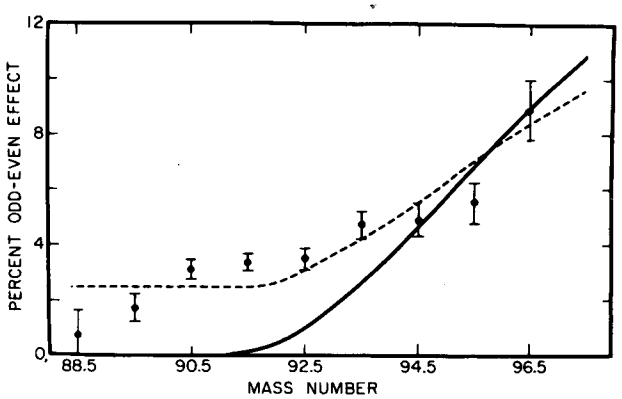

Fig. 2. Analysis of the odd-even effect in the Rb distribution from the fission of ^{238}U by 50-MeV protons. The points are computed from the experimental data, and are the same as in Fig. 1. The solid curve shows the results of the calculation for $\bar{\nu} = 1.6$, a pairing effect of ± 18% in the prompt yields, and no pairing effect in the neutron emission; the dashed curve is for $\bar{\nu} = 1.6$, a pairing effect of ± 12% in the prompt yields, and a ± 2.5% effect in the neutron emission.
(XBL 724-781)

any structure originally present at the moment of scission. However, this structure will tend to be preserved on the neutron-rich side of the isotopic distribution. This is because the yields of the neutron-rich fragments are decreasing very quickly with increasing neutron number, and neutron evaporation from higher mass isotopes has very little effect on the observed yield of the isotope at mass A. Expressed differently, the observed yields of the neutron-rich isotopes result from events in which very few if any neutrons are emitted. On the other hand, near the maximum of the isotopic distribution, the yields of adjacent isotopes are about equal, and neutron emission from higher-mass isotopes becomes more effective in smearing out pairing structure. In the second case, a pairing effect in the neutron emission leads to a structure which is nearly constant with mass.

A preliminary calculation has been performed of the odd-even effect in the Rb distribution from ^{238}U at 50 MeV and is shown in Fig. 2. We conclude that the odd-even effect in the Rb and Cs distributions can be accounted for by a 10 to 15% neutron pairing effect in the prompt yields and a 2 to 3% pairing effect in the neutron emission.

From the mean mass numbers of the Rb and Cs distributions, the average total number of emitted neutrons has been estimated for each reaction. This information, together with other results on neutron emission as a function of fragment mass, has allowed the mean mass numbers to be corrected for prompt neutron emission. These corrected values differ by about one mass unit from the values predicted by the unchanged charge density (UCD) mechanism and are consistent with the same mechanism of charge division as that operating in thermal neutron fission.

Footnote and References

†Condensed from Phys. Letters 34B, 277 (1971) and Phys. Rev. C5, 222 (1972). Work performed at the Centre de Spectrométrie de Masse du C. N. R. S., 91-Orsay, France, where one of the authors (AMP) was a Guggenheim Fellow, and another (JMN) was employed.

1. J. Chaumont, Thesis, Faculté des Sciences Orsay (1970).

SEARCH FOR γ TRANSITIONS EMITTED IN THE FORMATION OF A FISSION ISOMER

D. Benson, Jr., C. M. Lederer, and E. Cheifetz*

The phenomenon of isomeric states decaying by fission was first discovered by Polikanov.[1] It was first suggested by Strutinsky,[2] and is now generally accepted,[3,4] that nuclei exhibiting fission isomerism undergo fission after being trapped briefly in a secondary minimum in the potential-energy surface. A probable[4] mechanism by which fissioning isomeric states could be populated involves γ decay in the second potential well after evaporation of neutrons from the compound nucleus.

In our search for γ rays preceding delayed fission we chose to study the reaction $^{238}U(\alpha, 2n)^{240m}Pu$. This reaction has a relatively high ratio of isomeric to prompt fission[4] (4.4×10^{-5} at $E_\alpha = 25$ MeV). With a half-life[4] of 3.8 ± 0.3 nsec the isomer decay can be observed between bursts of the 25-MeV α beam at the 88-inch cyclotron.

A target consisting of 0.6 mg/cm^2 UO_2 on a 0.2 mg/cm^2 carbon foil was mounted at 45° to the beam. Fission fragments were detected

by a 450-mm^2 surface barrier Si detector on one side of the target, at about 100° to the beam. The target was viewed on the opposite side through a thin Al window by a 5-cm^3 Ge(Li) γ-ray detector. Both detectors were placed close to the target to maximize geometric efficiencies.

The arrival time of the beam burst was derived from the zero-crossover point on the cyclotron rf voltage. A bi-level time pickoff system was used with the Si detector. The lower threshold provided fast timing of the fission events, while the upper threshold rejected the more abundant pulses from scattered α particles. Gamma-ray timing was obtained from a leading-edge discriminator on the preamplifier output. The time delays between the beam burst and a fission event, T_{Bf}, and between a γ ray and a fission event, $T_{\gamma f}$, were measured, as well as E_γ. Baseline stabilization of the T_{Bf} signal corrected for any rf phase drift[5] during long runs. The $T_{\gamma f}$ signal was compensated[6] for energy dependence of the γ timing.

Most of the width of the T_{Bf} curve (Fig. 1) is due to the time structure of the beam burst. This width does not permit complete separation of delayed from prompt fission. However, it was possible to set a window on the T_{Bf} signal, as shown in Fig. 1, such that about 17% of the events in the window should be due to the isomer. This amounts to an enhancement of 4×10^3 relative to the overall isomer/prompt ratio.

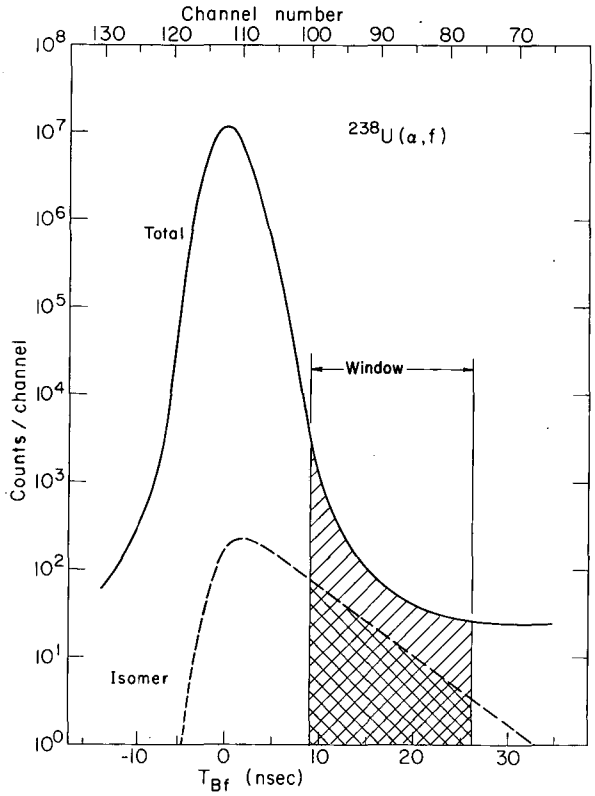

Fig. 1. Time distribution of fission relative to beam bursts. The dashed line indicates isomer activity calculated for a 3.8-nsec half-life with overall isomer/prompt-fission ratio of 4.4×10^{-5}. (XBL 721-2035)

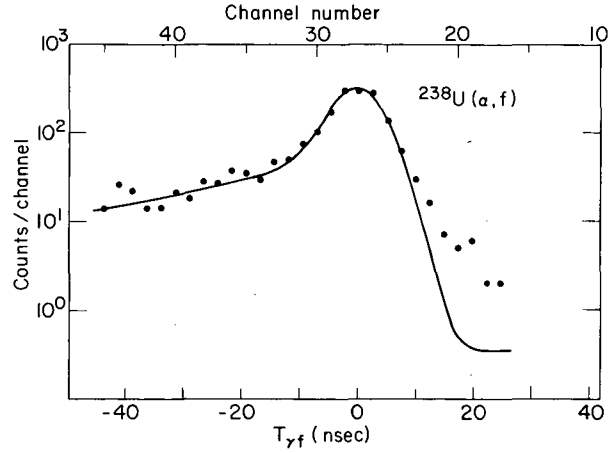

Fig. 2. Time distribution of fission relative to γ rays for all γ energies above 25 keV. The plotted points correspond to events for which T_{Bf} falls within the delayed fission window (Fig. 1). The solid curve, obtained with no restrictions on T_{Bf}, is normalized to the points in the vicinity of the peak.
(XBL 721-2033A)

The two parameters E_γ and $T_{\gamma f}$ were stored serially on magnetic tape for every fission-γ coincidence event that also fell within the T_{Bf} window. One out of every 100 events falling outside the window was also stored; marker flags distinguished these events from those gated by the T_{Bf} window. A total of 5×10^8 fission events were counted during the 36-hour measurement. The results are shown in Fig. 2. The plotted points correspond to events for which T_{Bf} fell within the delayed fission window, while the solid curve, normalized to the points near the peak, was obtained with no restrictions on T_{Bf}. The excess of γ-delayed fission coincidences, evident from the right-hand portion of Fig. 2, totals 57 ± 8 counts. These counts cannot be related to the time structure of the beam bursts (because the timing of a true fission-γ coincidence is independent of the beam time structure), but may be ascribed to one or more of the following effects:

(1) Gamma rays emitted in the formation of the 3.8-nsec isomer.
(2) Chance coincidences between (apparently)

delayed fission fragments and prompt γ rays emitted during the same beam burst by another nucleus.

(3) Tailing in the time-response curve of the fission detector.

At the observed counting rates we would expect 47^{+21}_{-18} chance coincidences between prompt γ rays and those fission events occurring within the T_{Bf} window. The validity of this estimate for effect (2) was checked in a separate experiment, in which fission fragments were counted in chance coincidence with prompt γ rays from the preceding beam burst. Thus chance coincidences alone can account for the observed excess of fissions delayed with respect to the γ rays; an upper limit of 36 counts can be ascribed to the effect (1) we have sought to observe. Since chance coincidences alone can account for the data, the spurious effect (3) due to tailing in the fission detector time-response curve is apparently small. We have attempted to check this conclusion by repeating the experiment with the ^{232}Th + 25-MeV α reaction, which produces no known fission isomer. However, an increased chance coincidence rate, due to a poorer time structure of the beam, makes these results inconclusive.

In summary, our results give no definite evidence for γ rays feeding isomeric fission. If the isomeric state is 2.6 MeV above the ^{240}Pu ground state,[4] the maximum energy available for γ decay would be 5.4 MeV. From the gross γ detection efficiency (photopeak plus Compton), we conclude that an average of < 2 γ-ray photons precede isomeric fission of ^{240}Pu. This low γ multiplicity may indicate a "special" channel for formation of the isomer, possibly via compound states of low angular momentum.

The energy spectrum of prompt γ rays coincident with (apparently) delayed fission reveals no discrete lines. Table I gives limits on possible discrete photon transitions as a function of energy. The low intensity in the Pu K x-ray region (100 keV) indicates that the isomeric state is not populated by transitions that are strongly K-converted. The present results do not rule out possible rotational transitions in the second well, since these would be converted strongly in the L and higher shells.

Table I. Limits on the intensities of possible discrete photon transitions preceding delayed fission.

E_γ (keV)	Maximum γ's per fission isomer
50 - 120	0.2
175	0.3
250	0.5
300	0.7
400	1.0

Footnote and References

*Present address: Weizmann Institute of Science, Rehovoth, Israel.

1. S. M. Polikanov, V. A. Druin, V. A. Karnaukhov, V. L. Mikheev, A. A. Pleve, N. K. Skobelev, V. G. Subbotin, G. M. Ter-Akop'yan, and V. A. Fomichev, Zh. Eksp. Teor. Fiz. 42, 1464 (1962) [transl.: Sov. Phys. – JETP 15, 1016 (1962)].

2. V. M. Strutinsky, Nucl. Phys. A95, 420 (1967).

3. S. Bjornholm and V. M. Strutinsky, Nucl. Phys. A136, 1 (1969); S. G. Nilsson, C. F. Tsang, A. Sobiczewski, Z. Szymanski, S. Wycech, C. Gustafson, I. L. Lamm, P. Möller, and B. Nilsson, Nucl. Phys. A131, 1 (1969).

4. H. C. Britt, S. C. Burnett, B. H. Erkkila, J. E. Lynn, and W. E. Stein, Phys. Rev. C4, 1444 (1971).

5. C. M. Lederer, J. M. Jaklevic, and J. M. Hollander, Nucl. Phys. A169, 449 (1971).

6. J. M. Jaklevic, F. M. Bernthal, J. O. Radeloff, and D. A. Landis, Nucl. Instr. Methods 69, 109 (1969).

A NEW SEMIEMPIRICAL LEVEL DENSITY FORMULA WITH PAIRING AND SHELL EFFECTS

A. Gilbert, R. C. Gatti, S. G. Thompson, and W. J. Swiatecki

The original Bethe[1] formula for the nuclear level density ρ is

$$\rho = C \exp (2\sqrt{aU}),$$

where U is the excitation energy and a is proportional to A, the number of nucleons.

Using the Bethe formula to fit neutron resonances, with a as an adjustable parameter, one finds systematic odd-even and shell effects in a. Newton[2] and Gilbert and Cameron,[3] among others, showed that the odd-even effect could be accounted for by subtracting from U the odd-even mass difference, and that shell effects in a could be related to the shell term of the mass formula.

In the high-energy limit, Rosenzweig[4] and Gilbert[5] found that for a periodic scheme of single-particle states the level density has the form

$$\rho \sim \exp [2\sqrt{a(U+\Delta)}] ;$$

Δ is related to shell structure and has maximum negative value at closed shells.

In order to incorporate all these effects we have devised the following semiempirical level density formula:

$$\rho(U) = C \exp (2\sqrt{a_{eff}U'}),$$

where $a_{eff} = \alpha A(1 + \frac{\Delta}{U'+K})$;

$$U' = U + E_0,$$

where E_0 is the odd-even term of the Myers-Swiatecki[6] mass formula;

$$\Delta = S - E_d,$$

where S is the experimental shell correction to the Myers-Swiatecki[6] mass formula and E_d is the deformation energy. C is a constant; α and K are adjustable parameters.

Neutron resonance data are being used to

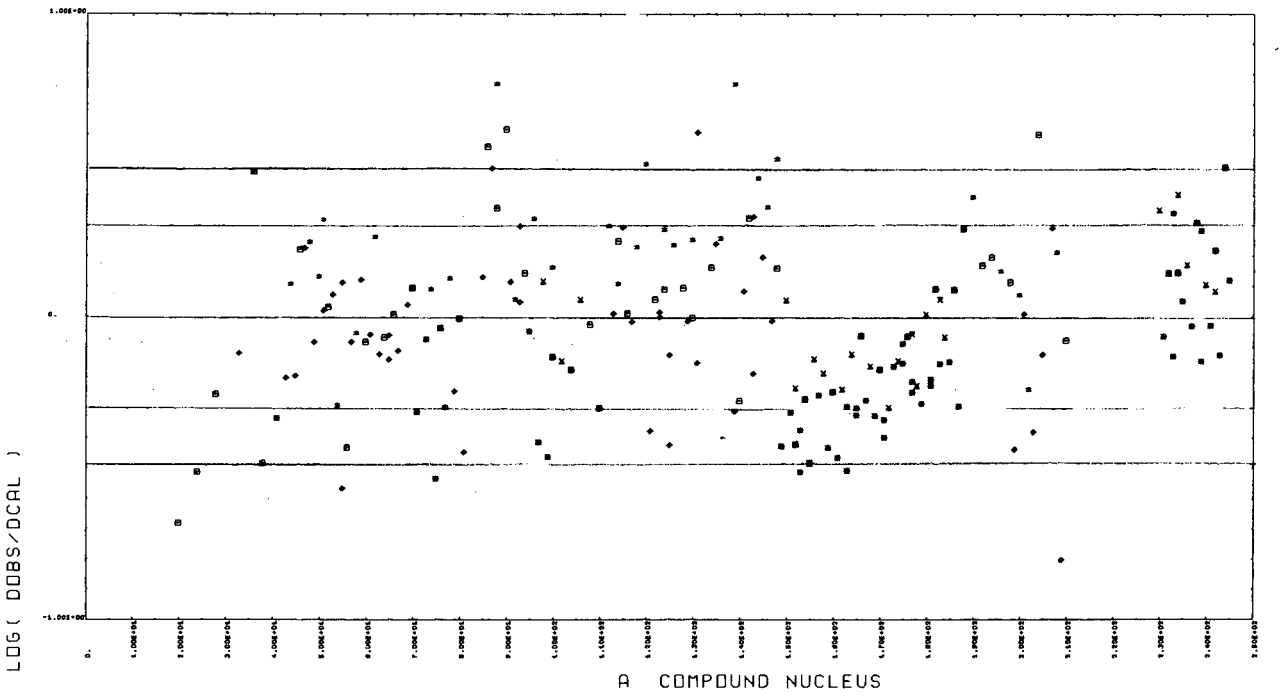

Fig. 1. The logarithmic ratio of observed to calculated neutron resonance spacing with α = 0.125 and K = 12.0 MeV versus the number of nucleons. (XBL 724-678)

determine α and K. Our compilation of resonance data was derived from the Brookhaven neutron cross section work (BNL-325), supplemented by the Nuclear Data Sheets, the work of Baba,[7] and some recent references.

Figure 1 is a logarithmic plot of the ratio of observed and calculated neutron resonance spacings with α = 0.125 and K = 12.0 MeV; 75% of the points are within a factor of 2, 18% are between a factor of 2 and 3 off, 7% are off by over a factor of 3 (but well within a factor of 10).

Some systematic discrepancies are of concern, particularly near the N = 50 shell and in the rare-earth region. Preliminary indications from Myers and Swiatecki are that these discrepancies may be related to problems in the mass formula. Final fitting of parameters will await completion of the new Myers-Swiatecki mass formula.

We plan to use our semiempirical level density formula to fit high-energy fission cross-section data.[8]

References

1. H. Bethe, Phys. Rev. 50, 332 (1936).

2. T. D. Newton, Can. J. Phys. 34, 804 (1956).

3. A. Gilbert and A. G. W. Cameron, Can. J. Phys. 43, 1446 (1965).

4. N. Rosenzweig, Phys. Rev. 108, 817 (1957); and Phys. Letters 22, 307 (1966).

5. A. Gilbert, UCRL-18095, February 1968.

6. W. D. Myers and W. J. Swiatecki, Nucl. Phys. 81, 1 (1966).

7. H. Baba, Nucl. Phys. A159, 625 (1970).

8. A. Khodai-Joopari, Fission Properties of Some Elements Below Radium (Ph. D. thesis), UCRL-16489, July 1966.

A NOVEL APPROACH TO THE EVAPORATION OF COMPLEX FRAGMENTS

L. G. Moretto

The neutron evaporation process has been described by Weisskopf[1] on the basis of the detailed balance equation. The neutron decay width is usually written as:

$$\Gamma d\epsilon = \frac{2m}{\pi^2 \hbar^2 \rho(E)} \sigma_{inv}(\epsilon)\, \epsilon\, \rho^*(E - B_N - \epsilon)\, d\epsilon,$$

where $\rho(E)$ is the compound nucleus level density at the excitation energy E; B_N, m, and ϵ are the neutron binding energy, the neutron mass, and the neutron kinetic energy respectively; $\rho^*(E - B_N - \epsilon)$ is the level density of the residual nucleus; and σ_{inv} is the cross section for the inverse process.

The same expression is also frequently used for describing the emission of complex particles. The inverse cross section is either taken from the experimental particle-induced reaction cross section, or, equivalently from an optical model calculation. This may be correct in the case of neutron emission but may be seriously in error for more complex particles. In fact the inverse cross section has no direct fundamental meaning, but it is introduced in order to provide a rough estimate of the inverse probability:

$$P_{inv} \approx \frac{\sigma_{inv} \times \text{particle velocity}}{\text{normalization volume}}.$$

Therefore the use of an experimental cross section or of an optical model cross section may lead to a gross misrepresentation of the number and the relevance of the degrees of freedom (especially the collective ones) involved in the process. A way to account specifically for the relevant degrees of freedom is offered by the transition state method, used, for instance, for the evaluation of the fission widths. If a highly asymmetric mass splitting is considered, the critical shape, corresponding to the fission saddle point, is highly necked-in and the mass asymmetry degree of freedom can be considered frozen. This critical point in the potential energy can be called the ridge point, in analogy with the saddle point, because it is found on a slope of the potential energy curve versus the mass asymmetry (Fig. 1a).

In order to illustrate this approach, let the liquid-drop model be used for the potential-energy calculation and the ridge point shapes be searched for among those allowed by the parametrization described below.

The ridge point configuration is represented as a sphere (small fragment) in contact with the pole of a spheroid with variable eccentricity $\mathcal{Z}$ (large fragment). The small fragment is assumed to be without internal de-

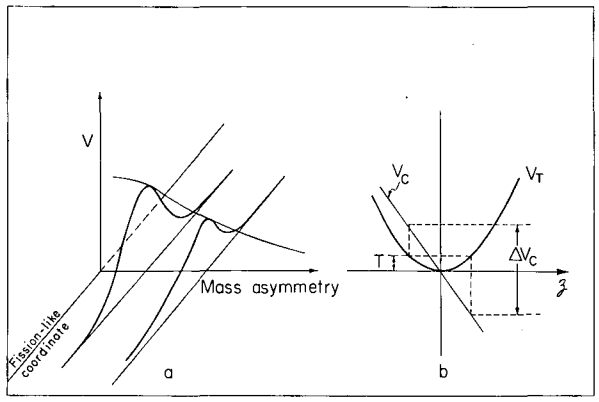

Fig. 1 (a) Schematic representation of the potential energy of a nucleus versus a fission-like coordinate and a mass asymmetry coordinate. Two paths towards decay at different mass asymmetry show the passage through the ridge point.

(b) Total potential energy V_T and Coulomb interaction energy V_C versus the deformation of the large fragment. A fluctuation in the total potential energy of the order of the temperature T produces a fluctuation in the Coulomb interaction energy ΔV_C, which can be very large. (XBL 721-2027)

grees of freedom and with only zero intrinsic spin: it is allowed to oscillate in a doubly degenerate mode ω about the pole of the spheroid. This approximation may be reasonably good for fragments like ^{4}He, ^{12}C, ^{16}O, ^{20}Ne and for temperatures at the ridge point lower than the first excited state of the small fragment. The first observation which can be made is the closeness (in the model, the coincidence) of the ridge point and of the splitting point. Therefore the distribution of the dynamical quantities of the two points can be taken to be the same.

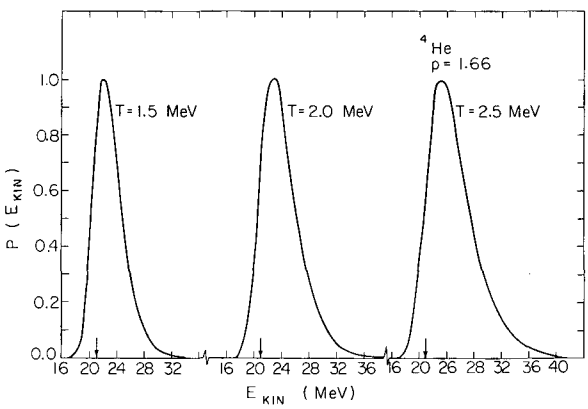

Fig. 2. Kinetic energy distribution predicted for the emission of ^{4}He from ^{236}U at different temperatures. (XBL 721-2029)

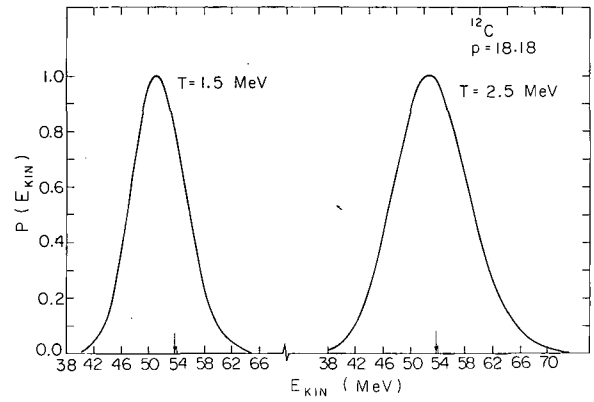

Fig. 3. Kinetic energy distribution predicted for the emission of ^{12}C from ^{236}U at different temperatures. (XBL 721-2031)

The second observation is that the large fragment, at the ridge point, has a prolate deformation—the larger, the higher the charge of the fragment. This implies that fragments can be emitted below the nominal Coulomb barrier (Coulomb interaction energy of two touching spheres).

The third observation concerns an amplification effect in the kinetic energy spectrum (Fig. 1b). The total potential energy and the Coulomb interaction energy can be expanded up to second and first order respectively in the deformation coordinate ζ of the large fragment about the ridge point:

$$V_T = k\zeta^2,$$

$$V_C = c\zeta.$$

As can be seen in Fig. 1, an excursion in potential energy of the order of the tempera-

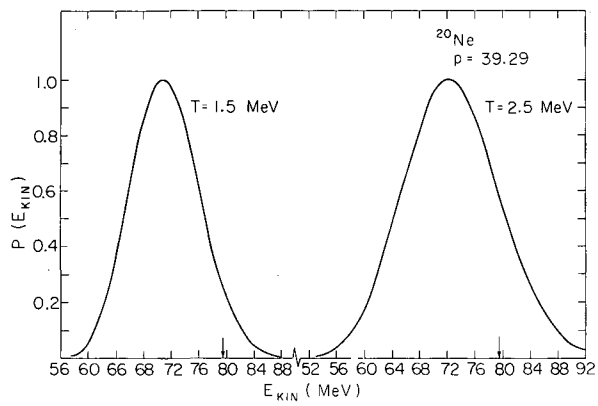

Fig. 4. Kinetic energy distribution predicted for the emission of ^{20}Ne from ^{236}U at different temperatures. (XBL 721-2030)

ture along the coordinate z corresponds to an excursion in Coulomb interaction energy and eventually in kinetic energy given by the relation:

$$(\Delta V_c)^2 \propto pT,$$

where T is the ridge temperature and $p = c^2/k$. All of these features are contained in the differential decay width:

$$\Gamma = \frac{dz\, 2\pi\omega\, d\omega}{2\pi\rho(E)h^2}\, \rho^*(E - B - 2\omega^2 - kz^2 - \epsilon - \frac{p_z^2}{2m_z} - \frac{p_\omega^2}{2m_\omega})$$

$$2\pi\, p_\omega\, dp_\omega\, dp_z\, d\omega\,,$$

where ρ^* is the level density at the ridge point; ϵ is the ridge point kinetic energy; p_z, p_ω, m_z, m_ω are the momenta and inertial masses along the coordinates z and ω; B is the ridge point height; and E is the excitation energy.

The final kinetic energy distribution in the center of mass is given by the expression

$$P(x)\, dx \propto (2x-p) \exp(-\frac{x}{T})\, \mathrm{erfc}\, \frac{p-2x}{2\sqrt{pT}}$$

$$+ 2\sqrt{\frac{pT}{\pi}} \exp(-\frac{p^2 + 4x^2}{4pT}),$$

where $x = E_k - E_0$, E_k is the kinetic energy, and E_0 is the Coulomb interaction energy of the two fragments at the ridge point.

It is interesting to notice that for the case of neutron emission ($p = 0$, $E_0 = 0$) the distribution reduces to a Maxwellian

$$P(E_k)\, dE_k \propto E_k \exp(-\frac{E_k}{T})\, dE_k,$$

in agreement with the standard theory. Substantially different results are obtained for more complex fragments. In Figs. 2, 3, and 4 the kinetic energy distributions are obtained for the emission of ^{4}He, ^{12}C, ^{20}Ne from the compound nucleus ^{236}U. It can be seen that, with increasing charge of the fragment, the distribution changes from Maxwellian to Gaussian and that the widths of the distribution for the same temperature greatly increase with the parameter p. Some of the features predicted by the present formalism, like the emission below the Coulomb barrier and the large widths of the kinetic energy distributions seem to be visible in the particle spectra obtained in the bombardment of ^{238}U with 6-GeV protons.[2,3] No definite conclusions are possible because of the very complicated modes of decay involved in such a high-energy reaction. Experimental research at smaller excitation energies is now being planned.

References

1. V. F Weisskopf, Phys. Rev. 52, 295 (1957).

2. A. M. Poskanzer, G. W. Butler, and E. K. Hyde, Phys. Rev. C3, 882 (1970).

3. E. K. Hyde, G. W. Butler, and A. M. Poskanzer, Phys. Rev. C9, 1759 (1971).

BASIC FORMULATION OF NUCLEAR LEVEL DENSITY CALCULATIONS

A. Gilbert, R. C. Gatti, and G. L. Struble

The calculation of the nuclear level density requires a knowledge of the grand partition function

$$Z = \mathrm{Tr}\, e^{-\beta H},$$

where H is the Hamiltonian of the system.

In this work we derive a variational principle for the grand partition function which is an extension of the well-known minimum principle for the ground state energy of a quantum mechanical system.

The variational principle is based on Peierls' theorem[1] and the Bogoliubov inequality.[2,3]

Peierls' theorem[1] says that

$$Z = \mathrm{Tr}\, e^{-\beta H} \geq \sum_k e^{-\beta \langle k | H | k \rangle},$$

where $|k\rangle$ is an arbitrary set of orthonormal states.

In other words, if H_d is the diagonal part of the Hamiltonian in some representation, then

$$\mathrm{Tr}\, e^{-\beta H} \geq \mathrm{Tr}\, e^{-\beta H_d}.$$

If any Hamiltonian operator is written as $H = H_0 + H_1$, we can make use of the Bogoliubov inequality[2,3]

$$\ln \mathrm{Tr}\, e^{-\beta(H_0 + H_1)} \geq \ln \mathrm{Tr}\, e^{-\beta H_0} - \beta \frac{\mathrm{Tr}(H_1 e^{-\beta H_0})}{\mathrm{Tr}\, e^{-\beta H_0}} .$$

These two theorems combined give a lower bound Z_1 for Z, which is then maximized.

The diagonal terms of a general nonrelativistic Hamiltonian with two-body forces can be written as

$$H_d = U + \sum_\alpha W_\alpha n_\alpha + 1/2 \sum_{\alpha\gamma} W_{\alpha\gamma} n_\alpha n_\gamma .$$

The n_α are number operators equal to $a_\alpha^+ a_\alpha$, a_α^+ and a_α being creation and destruction operators. U, W_α, $W_{\alpha\gamma}$ depend on the choice of representation.

Bogoliubov's choice for H_1 is

$$H_1 = 1/2 \sum_{\alpha\gamma} W_{\alpha\gamma} (n_\alpha - f_\gamma)(n_\gamma - f_\gamma),$$

where the f_α are adjustable parameters. Then the lower bound for Z is given by

$$\ln Z_1 = -\beta U + \sum_\alpha \ln (1 + e^{-\beta E_\alpha}) - \frac{\beta}{2} \sum_{\alpha\gamma} W_{\alpha\gamma} \frac{1}{\left(e^{\beta E_\alpha} + 1\right)\left(e^{\beta E_\gamma} + 1\right)} + \beta \sum_{\alpha\gamma} W_{\alpha\gamma} \frac{f_\gamma}{e^{\beta E_\gamma} + 1} ;$$

$\ln Z_1$ depends on the parameters f_α and on the choice of representation. The maximization of $\ln Z_1$ with respect to f_α can be carried out quite generally, yielding

$$f_\alpha = \frac{1}{e^{\beta E_\alpha} + 1} .$$

In this work the variational principle is applied to the case of a two-body Hamiltonian under the special Bogoliubov transformation. The results give a generalization of the usual temperature-dependent BCS pairing theory.

References

1. T. D. Schultz, Nuovo Cimento Ser. 10, 8, 943 (1958).

2. N. N. Bogoliubov, D. N. Zubarev, and I. A. Tserkovnikov, Sov. Phys. -Dokl. 2, 535 (1957).

3. M. Girardeau, J. Math. Phys. 3, 131 (1962).

STATISTICAL DESCRIPTION OF A PAIRED NUCLEUS WITH THE INCLUSION OF ANGULAR MOMENTUM

L. G. Moretto

The statistical properties of a paired nucleus have been studied as a function of the temperature T and of the angular momentum projection on the z axis M. [1,2]

The B. C. S. Hamiltonian can be written in its second quantization forms as follows:

$$H = \sum_{\pm k} \epsilon_k a_k^\dagger a_k - G \sum_{kk'} a_{-k'}^\dagger a_{k'}^\dagger a_k a_{-k} , \qquad (1)$$

where ϵ_k are the single-particle energy levels, $a_k^\dagger$ and a_k are the single-particle creation and annihilation operators, and G is the pairing strength.

The boundary conditions can be immediately introduced in the Hamiltonian by performing the substitution:

$$H \to H - \lambda N - \gamma M, \qquad (2)$$

where N is the number of particles, M the angular momentum z projection, and λ and γ are Lagrange multipliers to be determined. In this form the Hamiltonian can be approximately diagonalized by means of the Bogoliubov method. [3] The Hamiltonian in its diagonal form is:

$$H = \sum (\epsilon_k - \lambda - E_k) + \sum n_k^+ (E_k - \gamma m_k) + \sum n_k^- (E_k + \gamma m_k) + \frac{\Delta^2}{G} , \qquad (3)$$

where $E_k = [(\epsilon_k - \lambda)^2 + \Delta^2]^{1/2}$ are the quasiparticle excitations; n_k^+, n_k^- are the

occupation numbers of the quasiparticles with positive and negative spin projection respectively; m_k are the single-particle spin projections; and the quantity Δ, called the gap parameter, is given by the gap equation

$$\sum \frac{1 - n_k^+ - n_k^-}{E_k} = \frac{2}{G}, \tag{4}$$

where E_k is defined as above.

The Grand Partition function, which summarizes the statistical properties of the system, is given by

$$e^{\Omega} = \mathrm{Tr}\, e^{-\beta H'}, \tag{5}$$

where

$$\Omega = -\beta \sum (\epsilon_k - \lambda - E_k) + \sum \ln[1 + \exp -\beta(E_k - \gamma m_k)] + \sum \ln[1 + \exp -\beta(E_k + \gamma m_k)] - \beta \frac{\Delta^2}{G}, \tag{6}$$

where $\beta = 1/T$ is the inverse of the temperature. The quantities $\Delta, \beta, \lambda, \gamma$ are related by the gap equation:

$$\sum \frac{1}{2E_k} [\tanh \tfrac{1}{2} \beta(E_k - \gamma m_k) + \tanh \tfrac{1}{2} \beta(E_k + \gamma m_k)] = \frac{2}{G}. \tag{7}$$

The first integrals of the system can be obtained from the Grand Partition function:

$$N = \sum \left\{1 - \frac{\epsilon_k - \lambda}{2E_k} [\tanh \tfrac{1}{2}\beta(E_k - \gamma m_k) + \tanh \tfrac{1}{2} \beta(E_k + \gamma m_k)]\right\}, \tag{8}$$

$$M = \sum m_k \left[\frac{1}{1 + \exp \beta(E_k - \gamma m_k)} - \frac{1}{1 + \exp \beta(E_k + \gamma m_k)}\right], \tag{9}$$

$$E = \sum \epsilon_k \left\{1 - \frac{\epsilon_k - \lambda}{2E_k} [\tanh \tfrac{1}{2} \beta(E_k - \gamma m_k) + \tanh \tfrac{1}{2} \beta(E_k + \gamma m_k)]\right\} - \frac{\Delta^2}{G}. \tag{10}$$

The system of Eqs. (7) through (10) defines the quantities $\Delta, \beta, \lambda, \gamma$ as a function of the boundary conditions. The entropy is given by the expression

$$S = \sum \ln[1 + \exp -\beta(E_k - \gamma m_k)] + \sum \ln[1 + \exp -\beta(E_k + \gamma m_k)] + \beta \sum \frac{E_k - \gamma m_k}{1 + \exp \beta(E_k - \gamma m_k)} + \beta \sum \frac{E_k + \gamma m_k}{1 + \exp \beta(E_k + \gamma m_k)}. \tag{11}$$

The level density of the system is given by

$$\rho(E, N, M) = \frac{\exp S}{(2\pi)^{3/2} D^{1/2}}, \tag{12}$$

where

$$D = \det \left| \frac{\partial^2 \Omega}{\partial \alpha_i \partial \alpha_j} \right|, \tag{13}$$

and $\alpha_1 = \beta$, $\alpha_2 = \beta\lambda$, $\alpha_3 = \beta\gamma$. In order to illustrate the interrelation between temperature, pairing gap, and angular momentum the formalism can be applied to a uniform spectrum of doubly degenerate single-particle levels of density g and of average spin projection m.

For $T = 0$ ($\beta = \infty$) Eqs. (7) and (9) can be integrated to yield the zero temperature dependence of the gap parameter on angular momentum:

$$\Delta = \Delta_0 \left(1 - \frac{M}{M_c}\right)^{1/2}, \tag{14}$$

where Δ_0 is the gap parameter for $T = 0$ and $M = 0$. The gap parameter decreases with increasing angular momentum (Fig. 1) and the pairing correlation is destroyed for $M = M_c$, where:

$$M_c = g\, m\, \Delta_0. \tag{15}$$

The reason for the pairing breakdown with increasing angular momentum is related to the blocking effect generated by the quasiparticle

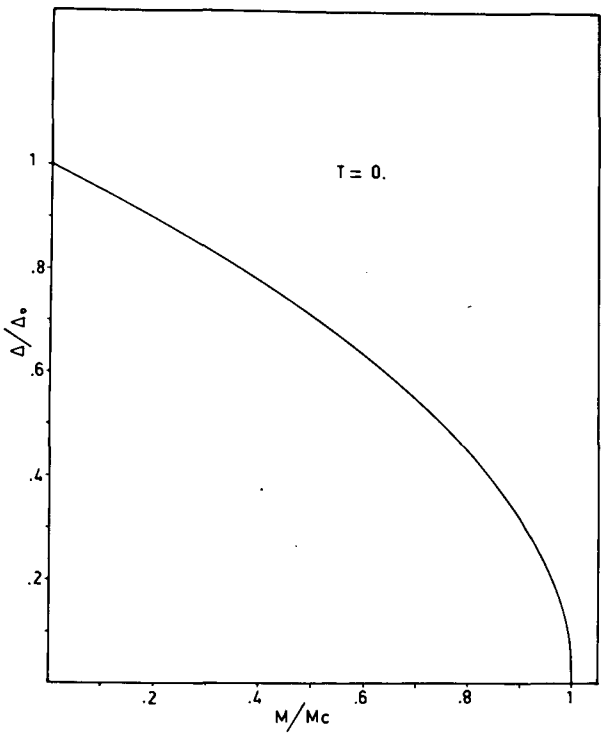

Fig. 1. Dependence of the gap parameter Δ upon the angular momentum M at zero temperature. Δ_0 is the gap parameter for T = 0, M = 0, and M_c is the critical angular momentum above which $\Delta = 0$.

(XBL725-831)

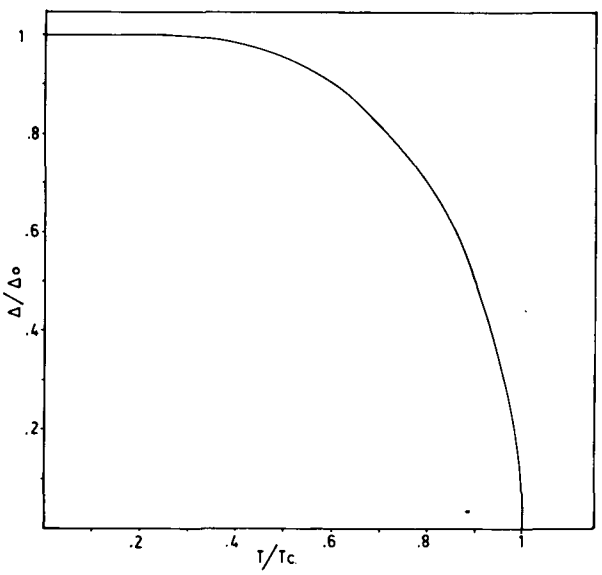

Fig. 2. Dependence of the gap parameter Δ upon the temperature T at zero angular momentum. T_c is the critical temperature above which $\Delta = 0$.

(XBL725-832)

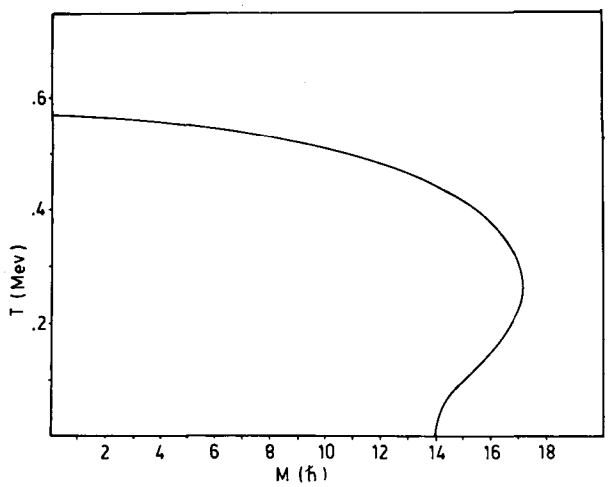

Fig. 3. Dependence of the critical temperature upon angular momentum: the parameters used in the calculation are: Δ_0 = 1 MeV, g = 7 MeV^{-1}, m = 2ħ.

(XBL725-823)

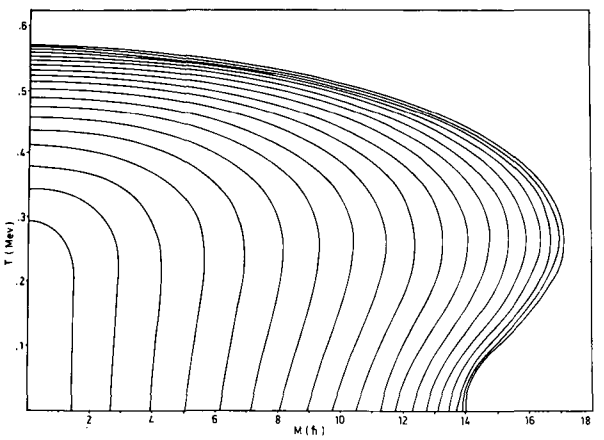

Fig. 4. Contour map of the gap parameter as a function both of temperature and angular momentum. The spacing in Δ between two successive lines is 0.05 MeV from Δ = 1.0 MeV to Δ = 0.1 MeV. The outer line corresponds to Δ = 0 MeV.

(XBL725-826)

excitations on which angular momentum is built up.

Pairing is also destroyed by an increase in temperature (Fig. 2). The gap parameter goes to zero at the critical temperature T_c:

$$T_c = \frac{2\Delta_0}{3.50}.$$

The critical temperature depends upon angular momentum as is shown in Fig. 3. A peculiar feature of this function is its double value for values of M between M_c and 1.22 M_c. In this interval at T = 0 the system is unpaired; when the temperature increases up to the lower critical temperature, pairing sets in until, above the higher critical temperature, pairing disappears again. This effect, which can be called "thermally assisted pairing correlation," is simply explained by the antiblocking effect of temperature. The tight strongly blocking quasiparticle structure typical of the zero temperature is spread out to a less blocking configuration when the temperature increases. The thermally assisted pairing correlation is visible also for values of $M < M_c$. In Fig. 4 the lines of equal Δ are shown in the T, M plane: it can be seen that, for any non-zero value of M, the gap parameter Δ starts increasing with temperature, goes through a maximum, and finally goes to zero.

The effect of angular momentum on entropy can be seen in Fig. 5 where the entropy is plotted versus angular momentum—in constant-temperature steps.

By setting T = 0 in Eqs. (7), (9), and (10) the equations for the yrast line are obtained:

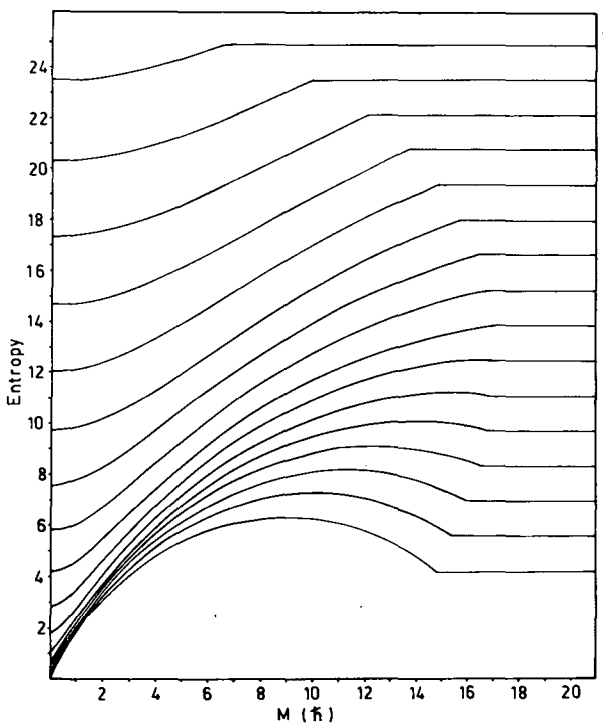

Fig. 5. Entropy as a function of angular momentum for a set of equally spaced temperatures.

(XBL725-829)

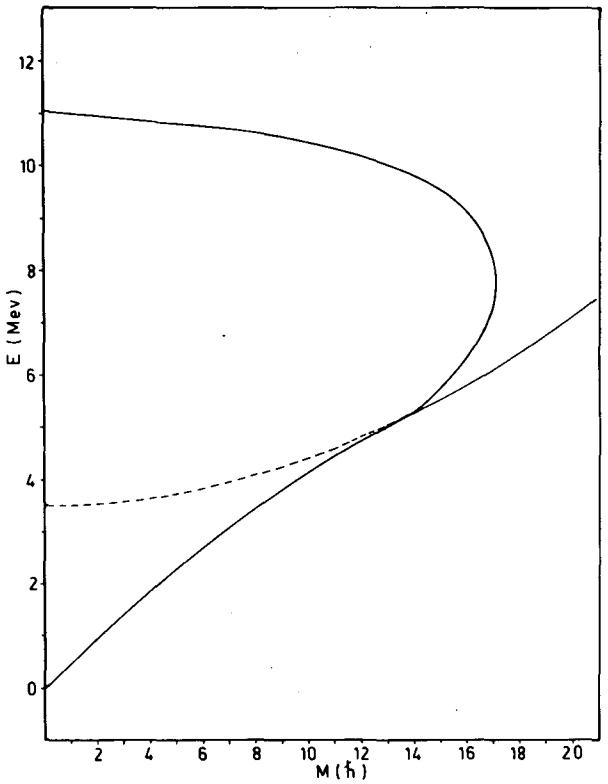

Fig. 6. Critical energy (upper line) and yrast line (lower line) as a function of angular momentum. The dashed line, which merges into the yrast line at $M = M_c$ is the yrast line for the unpaired system. The difference in energy between the dashed line and the lower solid line represents the condensation energy due to pairing.

(XBL725-827)

$$E_{yrast} = \frac{1}{2} g \Delta_0^2 \frac{M}{M_c}\left(2 - \frac{M}{2M_c}\right) \text{ for } M < M_c$$

$$= \frac{1}{2} g \Delta_0^2 + \frac{M^2}{4m^2 g} \text{ for } M > M_c .$$

In Fig. 6 the lower line represents the yrast line and the intermediate dashed line represents the yrast line that can be obtained for zero pairing. The energy difference between the two curves represents the condensation energy at each value of angular momentum. The upper curve represents the upper boundary of the paired region.

References

1. L. G. Moretto, Phys. Letters 35B, 129 (1971).

2. LBL-219, August 1971.

3. N. N. Bogoliubov, Zh. Eksp. Teor. Fiz. 34, 41 (1958); ibid. 34, 51 (1968); Nuovo Cimento 7, 794 (1958).

DEFORMATION IN EXCITED NUCLEI AND DISAPPEARANCE OF SHELL EFFECTS WITH EXCITATION ENERGY

L. G. Moretto

Ground state nuclei are known to have a well-defined deformation, which corresponds to the minimum in the potential energy surface as a function of a set of deformation parameters. The only uncertainty in the ground state deformation is related to the quantum mechanical fluctuations due to the zero-point motion. The same considerations do not apply to an excited system; if the statistical assumption is valid, the nucleus should be able to explore all the deformations that are allowed by the excitation energy. Therefore an excited nucleus is characterized by a distribution in deformations or by a function that will be called deformation probability.

This function can be calculated if one assumes full statistical coupling between the internal and the collective degrees of freedom.[1,2]

Let ϵ be a collective nuclear coordinate, $V(\epsilon)$ the potential energy function, E the excitation energy. At any deformation ϵ, the available excitation energy is $E_T = E - V(\epsilon)$. This available energy can be shared in many ways between the internal degrees of freedom and the collective one. The semiclassical statistical probability for a given partitio is:

$$P(x,\epsilon)\, d\epsilon\, dp = \rho(x)\, \frac{d\epsilon\, dp}{h} ,$$

where x is the fraction of the available excitation energy taken up by the internal degrees of freedom, $\rho(x)$ is the nuclear level density, p is the conjugate momentum associated with the coordinate ϵ, and h is the Planck constant. In order to obtain the total probability at the deformation ϵ one must integrate over all the energy partitions:

$$P_T(E_T,\epsilon)\, d\epsilon = \frac{d\epsilon}{h} \int \rho\left(E_T - \frac{p^2}{2m}\right) dp,$$

where m is the inertial mass for the motion along ϵ. The integration limits are $\pm \sqrt{2m\, E_T}$. Because of the rapid decrease of the integrand with increasing $|p|$ the limits can be substituted with $\pm\infty$. By expanding the logarithm of the level density about E_T and retaining terms up to the second order, the integrand reduces to a Gaussian which can be integrated explicitly:

$$P_T(E_T,\epsilon)\, d\epsilon = \frac{\sqrt{2\pi m}}{h}\, A'^{\,-1/2}\, \rho(E_T)\, d\epsilon,$$

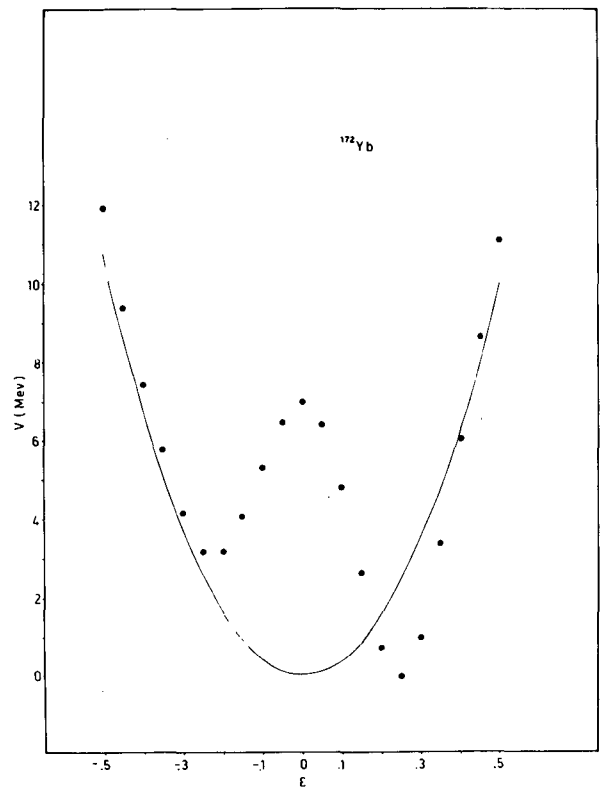

Fig. 1. Potential energy as a function of the deformation parameter ϵ for ^{172}Yb calculated from the Nilsson diagram by means of the Strutinski procedure (black circles). The continuous line represents the liquid-drop energy.

(XBL725-815)

where

$$A' = \left[\frac{d\ln\rho(x)}{dx}\right]_{x=E_T} .$$

The approximations associated with the evaluation of the integral correspond to the passage from the energy-preserving microcanonical ensemble to the constant-temperature canonical ensemble. In particular the quantity A' can be identified with the inverse of the temperature $1/T$.

In order to obtain a realistic estimate of the deformation probability it is necessary

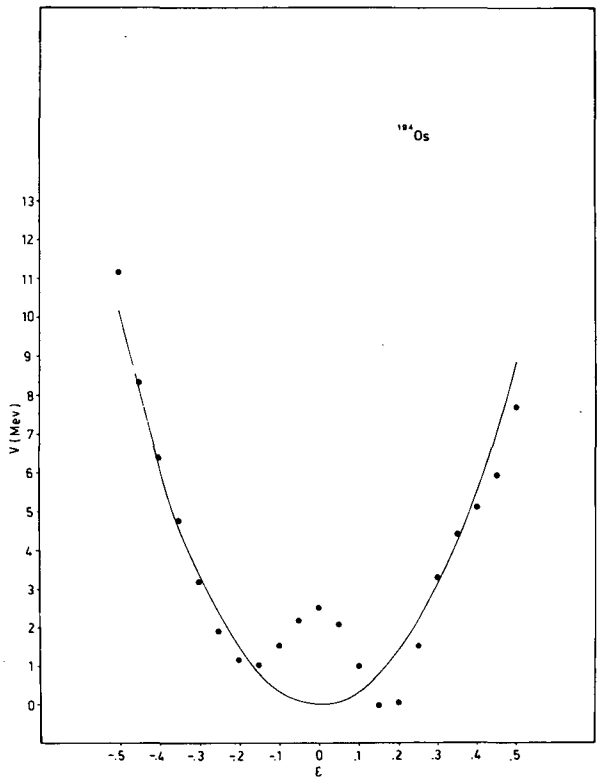

Fig. 2. Same as in Fig. 1, but for ^{284}Os.

(XBL725-818)

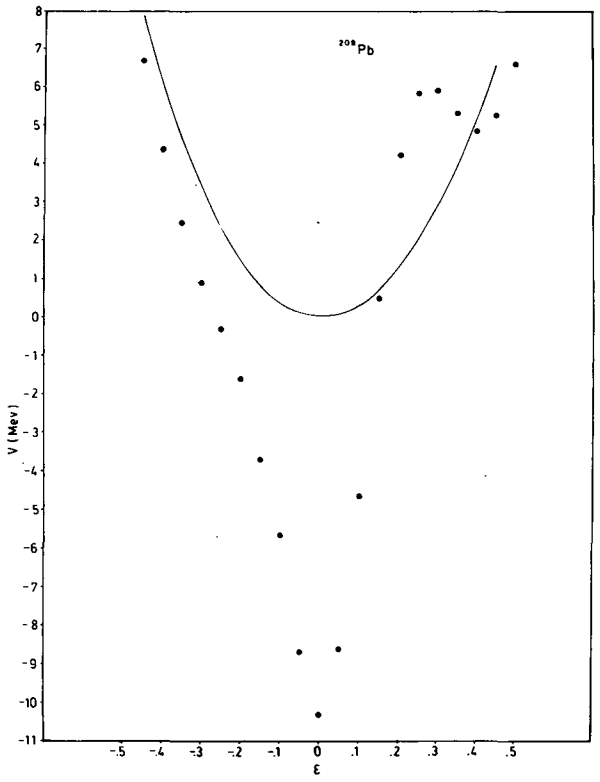

Fig. 3. Same as in Fig. 1, but for ^{208}Pb.

(XBL725-819)

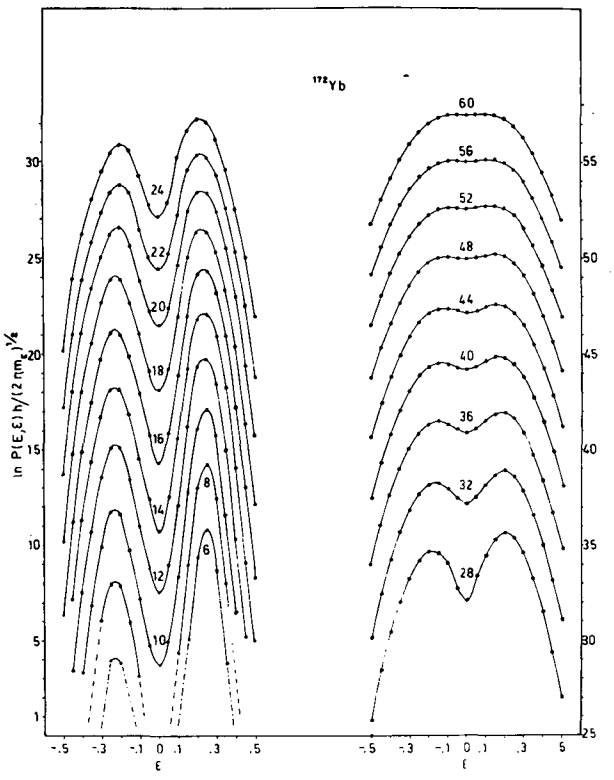

Fig. 4. Natural logarithm of the deformation probabilities (see text for details) at different excitation energies for ^{172}Yb. The labeling of each curve is in MeV.

(XBL725-820)

to be able to calculate accurately both the potential energy $V(\epsilon)$ and the level density $\rho(\epsilon, E_T)$.

The first quantity can be obtained by means of a procedure suggested by Strutinski.[3] The second quantity can be evaluated on the basis of the same shell model and B. C. S. Hamiltonian as described elsewhere.[2,4]

In Figs. 1, 2, and 3 the potential energies versus deformation are shown for the nuclei ^{174}Yb, ^{184}Os, ^{208}Pb. The first two nuclei appear to be deformed in their ground state while the third is spherical. In Figs. 4, 5, and 6 the logarithm of a quantity proportional to the deformation probability is plotted for different excitation energies. For the nuclei

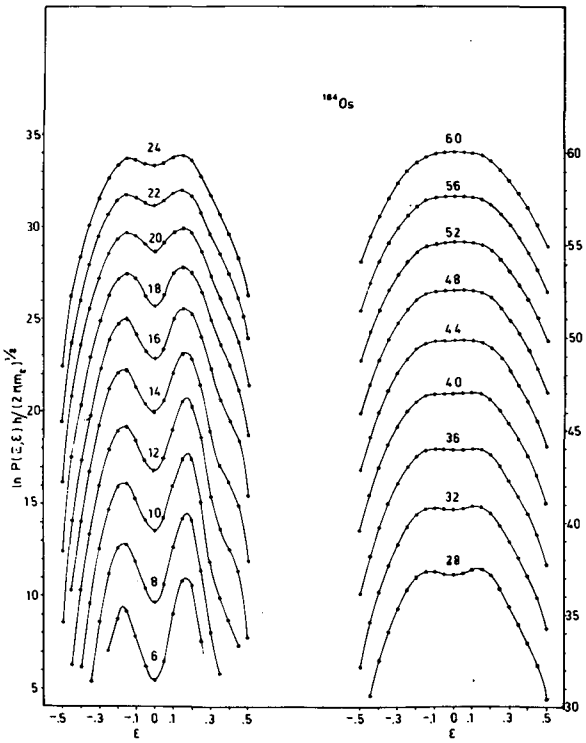

Fig. 5. Same as in Fig. 4, but for ^{184}Os.

(XBL725-822)

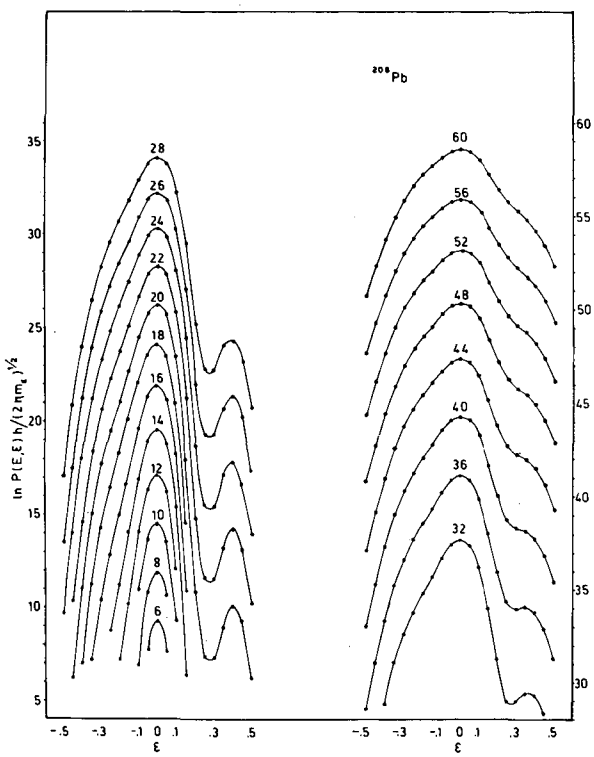

Fig. 6. Same as in Fig. 4, but for ^{208}Pb.

(XBL725-824)

^{174}Yb and ^{184}Os the deformation probabilities show, at the lowest excitation energies, a sharp peak in correspondence with the ground state deformation. A secondary peak is also present at the position of the oblate minimum. A deep minimum in probability separates the two peaks. As the energy increases, the two peaks become broader, tend to get closer and to equalize their height, while the minimum which separated them progressively fills in. Eventually, first for ^{184}Os then for ^{174}Yb, all the structure disappears and the deformation probability seems to reflect the liquid-drop potential energy without any recollection of the strong shells visible in the true potential energy. These calculations show in a dramatic way how the shell structure is washed out by excitation energy. In particular, deformed nuclei are seen to become spherical at high excitation energy with high probability for fluctuations about sphericity.

Concerning the doubly magic ^{208}Pb, the deformation probability peaks at sphericity at all energies. The excitation energy tends to broaden the peak substantially, until at the highest excitation energies, the deformation probability curve looks rather similar to that of the other two nuclei.

References

1. L. G. Moretto and R. Stella, Phys. Letters 32B, 558 (1970).

2. L. G. Moretto, LBL-228, August 1971.

3. V. M. Strutinski, Nucl. Phys. A95, 420 (1967).

4. L. G. Moretto, LBL-219, August 1971.

NOTE ON THE DISAPPEARANCE OF SHELL EFFECTS WITH EXCITATION ENERGY AND THE STRUTINSKI SMOOTHING PROCEDURES

L. G. Moretto

Recent numerical calculations performed on the basis of the shell model have shown the influence of shell effects on level densities and their disappearance with excitation energy. [1-3] It has been shown by Kahn and Rosenzweig[4] that the entropy of a system characterized by a periodically bunched single-particle spectrum at high energy has the same form as in the equidistant model:

$$S = 2\sqrt{a\,E_x},$$

where $E_x = E - \Delta E$. The quantity ΔE is an energy shift which has been identified with the ground state shell effect.

By analogy some authors have assumed that a similar behavior is to be expected for the entropy calculated on the basis of the shell model. In particular it has been claimed that plots of S^2 versus E have become linear at moderate excitation energy and the intercept of ΔE with the E axis has been identified with the shell effects. [5-7]

We will first show that the above assumption is not justified, even for uniform models where the single-particle level density is not constant. We shall then discuss the mechanism by which the shell structure is washed out in the Strutinski procedure and in the statistical calculation. Finally we shall illustrate the theoretical conclusions with numerical calculations.

a) Let us consider a system characterized by the single-particle level density g(e). We expand g(e) about the chemical potential μ up to second order and calculate the logarithm of the Grand Partition function:

$$\Omega = \beta\frac{\mu^2}{2}\,g(\mu) - \beta\frac{\mu^3}{3}\,g'(\mu) + \beta\frac{\mu^4}{8}\,g''(\mu) + \frac{7}{360}\,\frac{\pi^4}{\beta^3}\,g''(\mu) + \frac{\pi^2}{6\beta}\,g(\mu),$$

where β is the inverse of the temperature.

The particle number N, energy E, and entropy S can be obtained immediately:

$$N = \mu g(\mu) - \frac{1}{2}\mu^2 g'(\mu) + \frac{\pi^2}{6\beta^2}\,g'(\mu) + \frac{1}{6}\mu^3 g''(\mu)$$

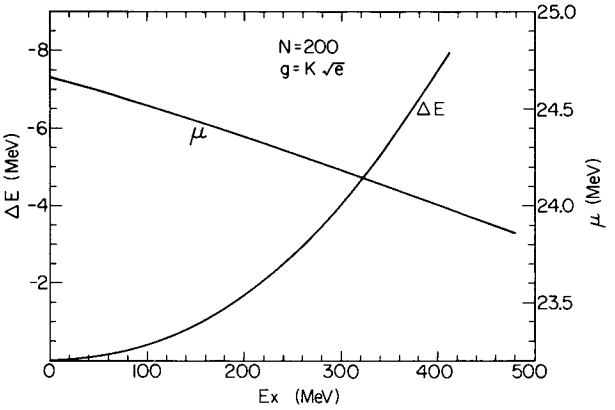

Fig. 1. Intercept ΔE and chemical potential μ versus excitation energy for a Fermi gas ($g = k\sqrt{e}$) of 200 particles.

(XBL 7112-4977)

$$E_T = \frac{1}{2}\mu^2 g(\mu) - \frac{1}{6}\mu^3 g'(\mu) + \frac{1}{24}\mu^4 g''(\mu) + \frac{\pi^2}{6\beta^2}\,g(\mu) + \frac{\pi^2}{6\beta^2}\,\mu g'(\mu) + \frac{7}{120}\,\frac{\pi^4}{\beta^4}\,g''(\mu),$$

$$S = \frac{\pi^2}{3\beta}\,g(\mu)\left[1 + \frac{7}{30\beta^2}\,\pi^2\,\frac{g''(\mu)}{g(\mu)}\right].$$

It can be seen that only if $g'(\mu) = g''(\mu) = 0$ then μ = constant,

$$E_T - E_0 = E = \frac{\pi^2}{6\beta^2}\,g \quad \text{and} \quad S = \frac{2a}{\beta} = 2\sqrt{aE}.$$

Only in this case is a linear dependence of S^2 vs E obtained. If $g'(\mu) > 0$ then μ is decreasing with excitation energy. In other words the chemical potential is attracted towards the regions of low single-particle level density. In Fig. 1 the behavior of μ and ΔE is shown for a Fermi gas ($g = k\sqrt{e}$). It can be seen that ΔE starts from zero and goes toward ever-increasing negative values, simulating a shell effect increasing with energy.

b) The single-particle level density, as obtained by a shell model, can be considered as composed of a smooth component and a rapidly fluctuating component, the latter being

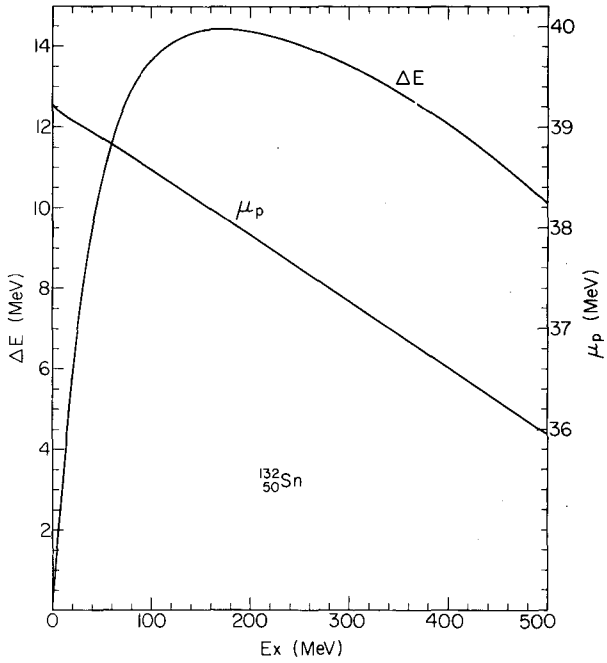

Fig. 2. Intercept ΔE and proton chemical potential μ_p versus excitation energy for ^{132}Sn. (XBL 7112-4976)

due to the shell structure. The smoothing in the Strutinski procedure is performed by a Gaussian:

$$g(e) = \frac{1}{\gamma\sqrt{\pi}} \sum F_k \exp\left(-\frac{e_k - e}{\gamma}\right)^2 .$$

The quantity F_k has the purpose of retaining the smooth trend of the level density undistorted. The statistical procedure smoothes out the spectrum by means of the function:

$$f(x) = \frac{4}{\beta}\,\mathrm{sech}^2\,\frac{1}{2}\,\beta x,$$

$$g(e) = \frac{4}{\beta} \sum \mathrm{sech}^2\,\frac{1}{2}\,\beta(e_k - e) .$$

The two smoothing functions are very similar and the parameters β and γ are connected by the relation:

$$\gamma = \frac{2.12}{\beta} .$$

Once the shell structure is washed out, the smooth but not constant component of the level density is left.

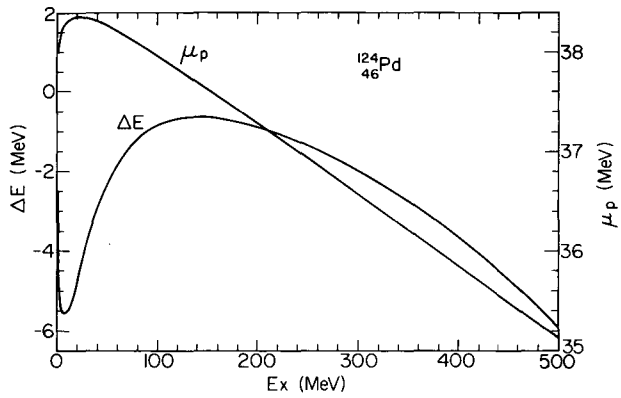

Fig. 3. Same as in Fig. 2, but for ^{124}Pd. (XBL 7112-4978)

c) In Figs. 2 and 3 the quantities ΔE and μ are shown for a magic and a non-magic nucleus. The chemical potential first senses the low level density at the shell and then is attracted by the lower level density deeper in the well. The intercept ΔE varies rapidly at low energies while the shell structure is washed out, then the effect of the smooth component of the level density takes over and the intercept decreases slowly. It can be observed that ΔE never becomes a constant, which implies that S^2 never becomes linear with E.

References

1. L. G. Moretto, R. Stella, and V. Caramella Crespi, Energia Nucleare 17, 436 (1970).

2. L. G. Moretto and R. Stella, Phys. Letters 32B, 558 (1970).

3. L. G. Moretto, LBL-228, August 1971.

4. P. B. Kahn and R. Rosenzweig, Phys. Rev. 187, 1193 (1969).

5. V. S. Ramamurthy, S. K. Kataria, and S. S. Kapoor, preprint.

6. V. S. Ramamurthy, S. S. Kapoor, and S. K. Kataria, Phys. Rev. Letters 25, 386, (1970).

7. J. R. Huizenga, in Proceedings of the International Conference on Statistical Properties of Nuclei, August 23-27, 1971, to be published.

II. Chemical and Atomic Physics

Atomic and Molecular Spectroscopy

Hyperfine Interactions

Photoelectron Spectroscopy

OPTICAL ZEEMAN SPECTRA OF Am^{3+}, Cm^{3+}, AND Nd^{3+} IN CaF_2

J. J. Stacy, N. Edelstein, R. D. McLaughlin, and J. Conway

It is well established that when a trivalent rare earth ion is incorporated into CaF_2, several kinds of sites are created as a consequence of the various modes of compensation of the excess positive charge. The resultant sharp line spectra are very complex due to the superposition of spectra belonging to specific sites.[1] We have used a superconducting magnet (maximum field 67 kG) to study the Zeeman effect of Am^{3+}, Cm^{3+}, and Nd^{3+} in CaF_2. The axis of rotation was parallel to the given crystal direction and perpendicular to the magnetic field.

The [110] Zeeman rotation patterns for two Nd^{3+} absorption lines at ~ 7300 Å are shown in Fig. 1. It is apparent from the angular variation that the symmetry of the lines is tetragonal. In particular the 70° to 110° split between the angles at which the lines merge is characteristic of tetragonal symmetry.[2] The relation of the zero field lines to the Zeeman components can be seen in Fig. 2, which shows the splitting of the lines as a function of magnetic field strength. The Zeeman components of the two tetragonal lines repel one another as the magnetic field is increased. This interaction can be thought of as a "crystal Paschen-Bach effect."

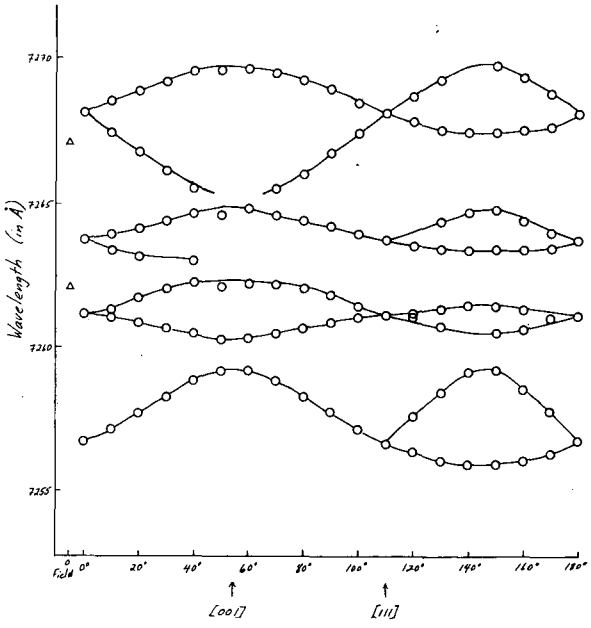

Fig. 1. Optical Zeeman rotation pattern for 0.1 wt% Nd^{3+}-CaF_2, rotation about [$\bar{1}$10] direction ($^4S_{3/2}$; $^4F_{7/2}$ manifold).
(XBL 7111-1669)

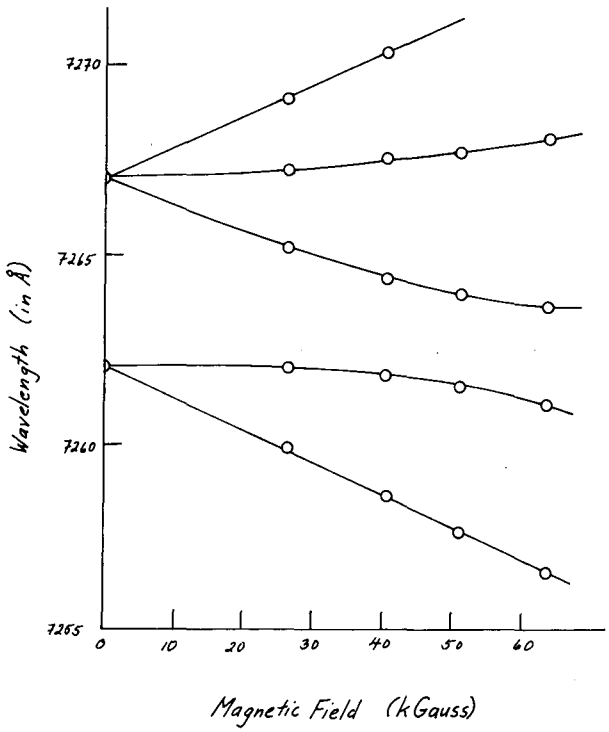

Fig. 2. Splitting of absorption lines as a function of magnetic field strength ($^4S_{3/2}$; $^4F_{7/2}$ manifold).
(XBL 7111-1670)

Three additional tetragonal Nd^{3+} lines at 6263 Å, 7356 Å, and 7962 Å could be positively identified. However, only one tetragonal line could be identified for Am^{3+}-CaF_2 and for Cm^{3+} - CaF_2. No lines due to symmetries other than tetragonal could be identified.

Although only a single Am line could be investigated, valuable information was gained about the thermoluminescence of Am. This Am absorption at 5223 Å corresponds to one of the high-temperature thermoluminescence emission lines observed by Edelstein, Easley, and McLaughlin,[3] and hence confirms Merz and Pershan's[4] proposal that such thermoluminescence is due to tetragonal sites.

References

1. M. J. Weber and R. W. Bierig, Phys. Rev. 134, A1492 (1964).

2. C. W. Rector, B. C. Pandey and H. W. Moos, J. Chem. Phys. 45, 171 (1966).

3. N. Edelstein, W. Easley, and R. D. McLaughlin, Advances in Chemistry Series 71 (American Chemical Society Publications, Washington, D. C., 1967), p. 203.

4. J. L. Merz and P. S Pershan, Phys. Rev. 162, 217 (1967); ibid. 162, 235 (1967).

ABSORPTION SPECTRUM OF URANIUM FORMATE, ENERGY LEVEL SCHEME OF URANIUM (+3)*

J. Drozdzynski† and J. G. Conway

The absorption spectrum of uranium(+3) formate mixed in Halowax (index of refraction = 1.635) has been studied at room, liquid nitrogen, and liquid helium temperatures in the wavelength range 2500 to 45000 Å. Twelve well-separated levels were identified, and a least-square fitting was used to derive the electrostatic, spin-orbit, and configuration parameters. A RMS deviation of 20 cm^{-1} was obtained with parameters of E^1 = 2779, E^2 = 14.1, E^3 = 272, ζ_{5f} = 1656, α = 17.5, β = 479 and γ = 1000 cm^{-1} (held constant).

Intensity calculations were attempted. Matrix elements $U^{(\lambda)}$ were calculated for us by Dr. W. T. Carnell of Argonne National Laboratory.

Footnotes

*The complete report will appear in the J. Chem. Phys. 56, 883 (1972). Also available as LBL-218.

†Fulbright-Hays Fellow; Committee on International Exchange of Persons. Permanent address: Institute of Chemistry, University of Wroclaw, Wroclaw, Poland.

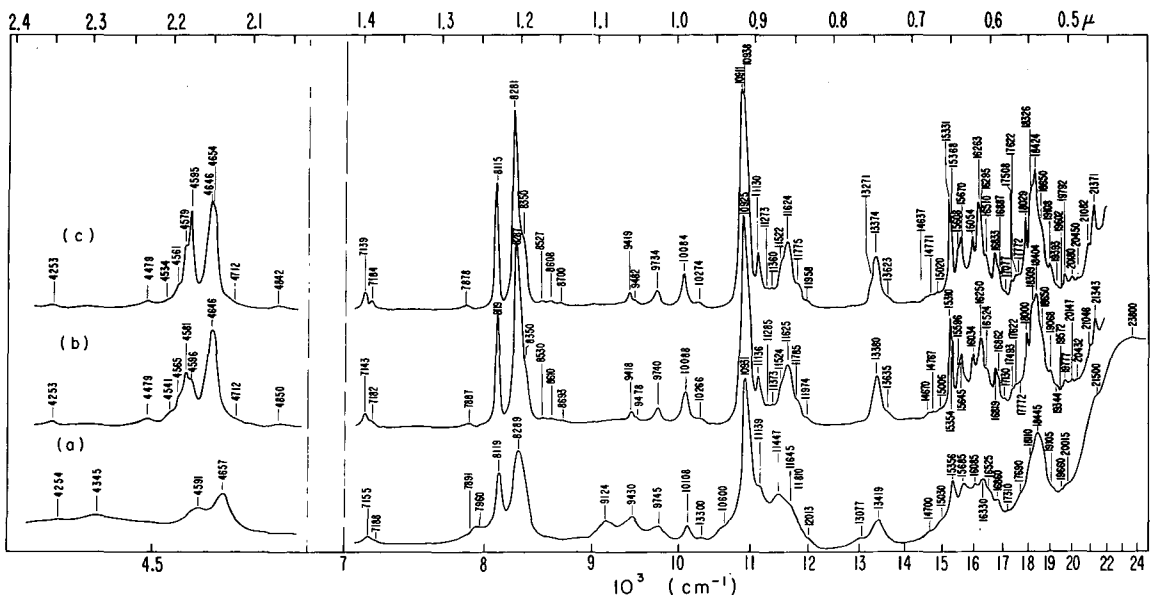

Fig. 1. Absorption spectrum of $U(HCOO)_3$: (a) at 298°K, (b) 77°K, (c) 4°K.
(XBL 717-3933)

THE ABSORPTION SPECTRUM OF $PmCl_3$ IN $LaCl_3$*

W. Baer, S. P. Davis, and J. G. Conway

The absorption spectrum of a single crystal of $LaCl_3$ containing approximately 0.1% $PmCl_3$ was photographed between 3,000 and 9,000 Å. Polarization spectra at liquid helium and liquid nitrogen temperatures were taken. Groups of lines or multiplets were found. Starting with parameter values interpolated from Nd^{+3} and Sm^{+3}, a least-square fitting process was begun for electrostatic, spin-orbit and crystal-field parameters. The matrix elements for crystal-field parameters of the ^5I, ^5F, ^5S were calculated, and from an analysis of the levels, fitting of crystal-field parameters were obtained for $^5I_4$, $^5S_2$, $^5F_1$, $^5F_2$, $^5F_3$. The best values for the parameters are $F_2 = 358$, $F_4 = 36$, $F_6 = 4.06$, $\zeta_{4f} = 1020$, $B_0^2 = 145$, $B_0^4 = 320$, $B_0^6 = -650$, $B_6^6 = 450$ cm^{-1}.

Footnote

*W. Baer, The Crystal Spectrum of Promethium 3^+ in $LaCl_3$ (Ph. D. Thesis), September 1971 (unpublished).

SPIN-OFF OF THE DYSPROSIUM WORK

J. G. Conway and E. F. Worden

With the publication of the energy levels and wavelength lists of dysprosium I and II, there have been a number of workers who have found the data useful. We published this work realizing that there was more to do, but the pressure of other analysis work was such that we felt we were not ready to complete it. The data was sent to the French group before publication. So far, they have two publications extending the analysis, and Spector has used some of the levels in a treatment of a special problem in a configuration of the heavy rare earths. A group at Los Alamos has used the levels in a treatment of vapor pressure data of dysprosium metal. Ross at Rollins College has been able to assign his isotope shift data to the configurations found. Brewer, Martin, VanderSluis and Nugent have all used the configuration and level information in their various treatments of the systematics of rare earth spectra. Howard, of Kitt Peak, has used the wavelengths to extend the identification of Dy in the sun by a factor of three to four. Such a large use of these data in a short time is surprising and encouraging.

HIGH-IONIZATION STUDIES OF URANIUM

G. V. Shalimoff

The spectrum of ionized uranium has been obtained in the vacuum ultraviolet region, using a sliding-spark source. A McPherson 3-meter vacuum spectrograph and Kodak SWR plates were used to photograph spectra at various excitation currents.

From survey plates taken with a 10-meter vacuum spectrograph at the National Bureau of Standards, the region 500 to 2000 Å is very rich in lines at all excitation levels from 100 to 900-A peak current. To date over 1200 lines have been measured in the region of 1070 to 1750 Å for a 200-A peak excitation exposure. Visual separation of the various stages of ionization is made by observing the changes of intensity of the lines in the spectra photographed at different excitation currents.

Although the spectra are photographed with an adjacent reference spectrum from a copper hollow-cathode lamp, it has been difficult to measure the spectrum lines accurately because of shifts of the lines at the various excitation conditions. Some of this is due to expected Stark effects, but a more serious source of random shift is apparently due to our optical setup, and tests are underway to correct or eliminate it.

ON THE METASTABLE DISSOCIATION OF THE CH^+ ION PRODUCED BY ELECTRON IMPACT*

A. S. Newton and A. F. Sciamanna

Several investigations have been made on the occurrence of metastable ions in small molecules.[1-4] These have concentrated on the region above mass 12. Below mass 12, Melton and Rosenstock[2] saw only the results of collision-induced transitions. Recently Lorquet, Lorquet, Momigny, and Wankenne[5] observed the metastable dissociation of CH^+ from C_2H_2 and HCHO. The present investigation confirms the metastable dissociation of CH^+ but the energetics differ from those of Lorquet et al.[5] and this leads to a different interpretation of the source of the metastability of this ion.

These experiments were performed on a Dempster-type mass spectrometer Model 21-103B. In Fig. 1 are shown peaks in the mass range 8.5-12 in the mass spectra of CH_4, CD_4, C_2H_2, and C_2D_2. In Table I are shown the transitions leading to these respective peaks. In Fig. 2 is shown the variation of peak sensitivity (peak intensity/pressure) with pressure for $(M/q)^* = 11.077$ from CH-containing compounds and of $(M/q)^* = 10.286$ from CD-containing compounds. It is apparent that each of these shows a well-defined peak sensitivity at zero pressure, indicating the bulk of each respective peak is of unimolecular origin at moderate pressures. In Fig. 3 are shown the variations of peak sensitivity with pressure of various transitions of CD_x^+ formed from C_2D_6.

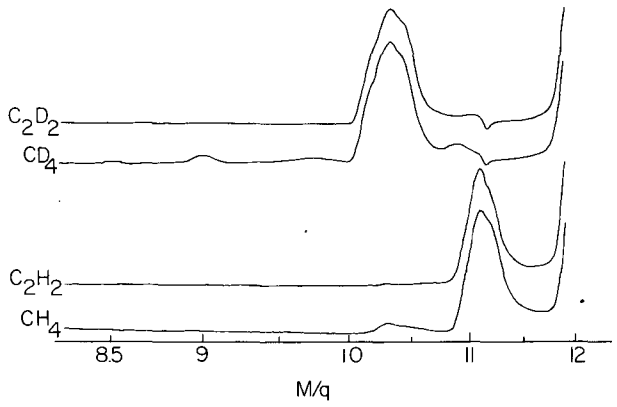

Fig. 1. Mass spectra of CH_4, CD_4, C_2H_2, and C_2D_2 in the mass region 8.5 to 12 amu. Conditions: all at 50 μm inlet pressure except CD_4 at 80 μm. Collector slitwidth 1.5 mm; V_e = 70 V nominal, I_e = 38 μA. Voltage scan with MV_A = 30 600. Focus maximized for metastable peaks. (XBL 721-4)

$(M/q)^* = 10.286$ and $(M/q)^* = 9.000$ show definite unimolecular components. $(M/q)^* = 10.889$ probably has a unimolecular component but the sensitivity is low. $(M/q)^* = 8$ shows no unimolecular component. The unimolec-

Table I. Dissociation process of CH_x ions leading to apparent metastable ion peaks below $(M/q)^* = 12$.

Process	Type[a]	$(M/q)^*$ CH_x	$(M/q)^*$ CD_x
1) $CH^+ \rightarrow C^+ + H$	(m)	11.077	10.286
2) $CH_2^+ \rightarrow C^+ + H_2$	(m)	10.286	9.000
3) $CH_3^+ \rightarrow CH^+ + H_2$	(m)?	11.267	10.889
4) $CH_3^+ \rightarrow C^+ + (3H)$	(c)	9.600	8.000
5) $CH_4^+ \rightarrow CH^+ + (3H)$	(c)	10.563	9.800
6) $CH_4^+ \rightarrow C^+ + (4H)$	(c)	9.000	7.200

[a](m) = metastable ion plus collision-induced component observed.
(c) = only collision-induced dissociation observed.

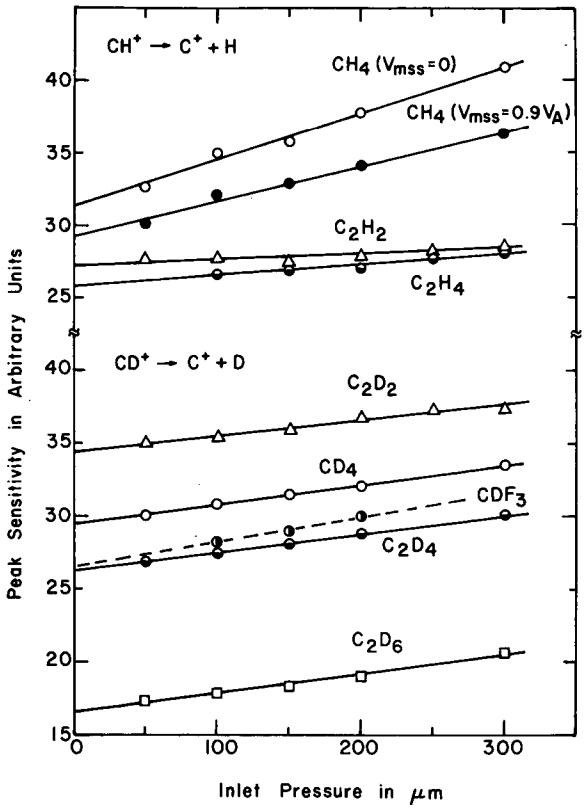

Fig. 2. Variation of peak sensitivity with pressure of metastable peak at $(M/q)^* = 11.077$ from various sources of $CH^+(m)$ and $(M/q)^* = 10.286$ from various sources of $CD^+(m)$. Peak sensitivities have been adjusted for clarity of presentation. Conditions: $V_A = 3000$ V, $V_e = 70$ V, $I_e = 38$ μA. Focus maximized for $(M/q)^* = 10.286$ peak. (XBL 721-2)

ular components of the 9.000 and 10.889 peaks were of too low intensity for further investigation.

The $(M/q)^* = 11.077$ and $(M/q)^* = 10.286$ from the transitions

$$CH^+(m) \rightarrow C^+ + H \quad (1)$$

$$CD^+(m) \rightarrow C^+ + D \quad (2)$$

were studied in detail. The kinetic energy release in the metastable dissociation of $CH^+(m)$ was 1.1 ± 0.3 eV and of $CD^+(m)$ was 1.4 ± 0.3 eV as shown in Table II. These values were determined by the change in peak width with ion accelerating voltage.[6]

When formed from the parent compounds by fast fragmentation processes in the ion source, $CH^+(m)$ and $CD^+(m)$ can also possess initial kinetic energy. This initial kinetic energy was

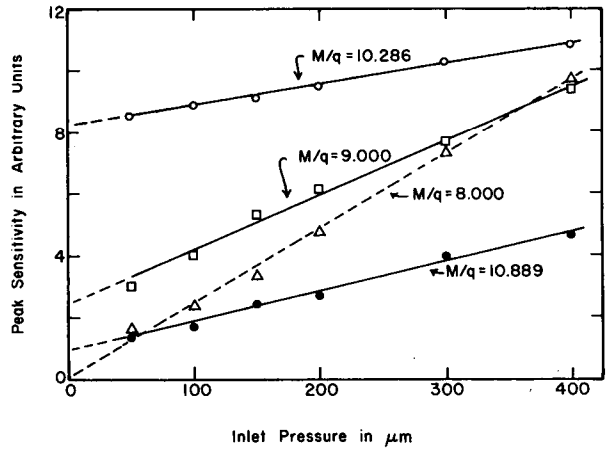

Fig. 3. Variation of peak sensitivity with pressure of various metastable peaks in the mass spectrum of C_2D_6. Conditions: $MV_A = 30\,600$, $V_e = 70$ V, $I_e = 38$ μA. Focus maximized for $(M/q)^* = 10.286$ peak. (XBL 721-1)

Table II. Kinetic energy release in the metastable fragmentation of $CH^+(m)$ and $CD^+(m)$ from various sources.

Compound	T^a $CH^+ \rightarrow C^+ + H$	T^a $CD^+ \rightarrow C^+ + D$
C_2H_2	1.1 ± 0.3	
C_2D_2		1.4 ± 0.2
C_2H_4	1.1 ± 0.2	
C_2D_4		1.1 ± 0.3
CH_4	(b)	
CD_4		1.4 ± 0.3
CHF_3	1.3 ± 0.5	
CDF_3		1.4 ± 0.3
$CHCl_3$	1.1 ± 0.3	
CH_2Cl_2	1.1 ± 0.3	

[a] Probable errors include estimates of errors in measuring width of peaks as well as reproducibility with various voltage differences.

[b] Value not recorded owing to interference from $(M/q)^* = 11.267$.

determined by the negative repeller cutoff method[7] as shown in Fig. 4. The results from various compounds are shown in Table III.

The half-life of the metastable dissociation

Table III. Initial kinetic energy (KE) of CH^+(m) and CD^+(m) formed by 70-eV electron impact with various source molecules.

Source	Initial KE (eV) CH^+(m) or CD^+(m)	T (init.)
CH_4	0.3 ± 0.1	Indeterminate
CD_4	0.6 ± 0.2	Indeterminate
C_2H_2	1.3 ± 0.2	2.6 ± 0.4
C_2D_2	0.7 ± 0.2	1.4 ± 0.4
CDF_3	~3.2 ± 0.4	Indeterminate

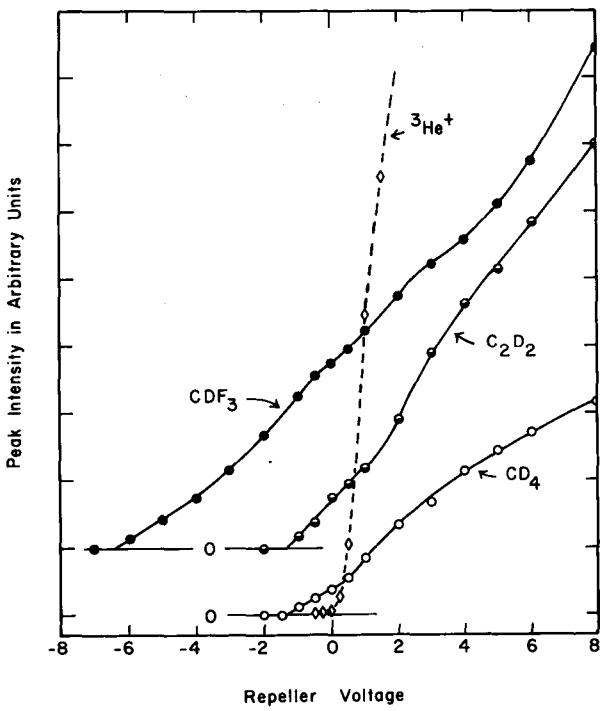

Fig. 4. Negative repeller cutoff curves for the metastable peak at $(M/q)^*$ = 10.286 in the mass spectra of CD_4, C_2D_2, and CDF3. Conditions: Magnetic scan, V_A = 3000 V, V_e = 70 V, I_e = 38 μA. Inlet pressure: CD_4 = 175 μm, C_2D_2 = 120 μm, CDF_3 = 300 μm. Zero intensities have been offset for clarity of presentation. (XBL 721-6)

was determined by the variation of the peak intensity with ion accelerating voltage and comparison with the discrimination calculated for various half-lives.[8] The observed intensities must be corrected for two factors. 1) The beam width at the collector is wider than the collector slitwidth, so the integrated intensity (approximated by peak width in amu multiplied by the peak height) must be used. 2) The initial kinetic energy of CH^+(m) or CD^+(m) causes discrimination losses at the ion-source exit slit. These corrections were calculated by the method of Berry.[9]

In Figs. 5 and 6 are shown the results of the half-life determination. The circles are the observed points and correspond to about 0.1-μsec half-life. Correction for change in peak width with V_A raises this value to 0.15 to 0.17 μsec. A further correction for initial kinetic energy raises the value to 0.5 to 0.8 μsec. This last correction assumes all CH^+(m) and CD^+(m) to possess the maximum initial kinetic energy determined. This is almost certainly not true and there is a distribution of initial kinetic energy values in each case. Assuming over-correction for initial kinetic energy, the best value of the half-life for CH^+(m) or CD^+(m) is 0.4 ± 0.2 μsec. Lorquet et al.[5] report 0.1 μsec for the half-life of this metastable transition.

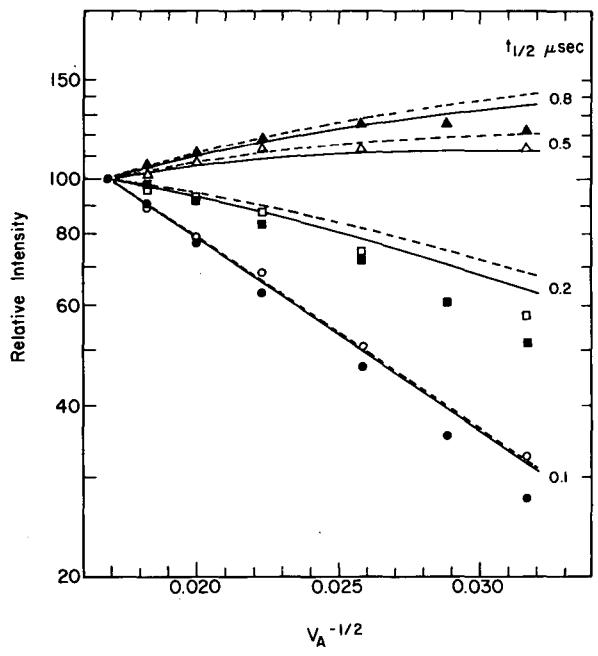

Fig. 5. Ion accelerating-voltage discrimination curves for the metastable peak at $(M/q)^*$ = 11.077 from CH_4 and $(M/q)^*$ = 10.286 from CD_4. Lines calculated for the half-lives shown for the transitions $CH^+ \rightarrow C^+ + H$, solid lines; and $CD^+ \rightarrow C^+ + D$, dashed lines. Observed points: open circles, CH_4; filled circles, CD_4. Points corrected for peak width: open squares, CH_4; filled squares, CD_4. Points further corrected for initial kinetic energy: open triangles, CH_4; filled triangles, CD_4. (XBL 721-7)

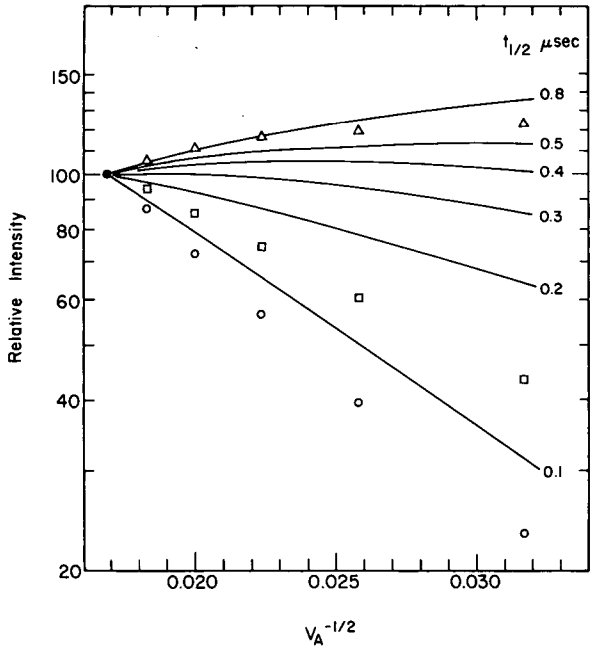

Fig. 6. Ion accelerating-voltage discrimination curves for the metastable peak at $(M/q)^* = 11.077$ in the mass spectrum of C_2H_2. Lines calculated for the half-lives shown. Observed points, circles; corrected for metastable peak width, squares; corrected for peak width and initial kinetic energy of $CH^+(m)$, triangles.
(XBL 721-8)

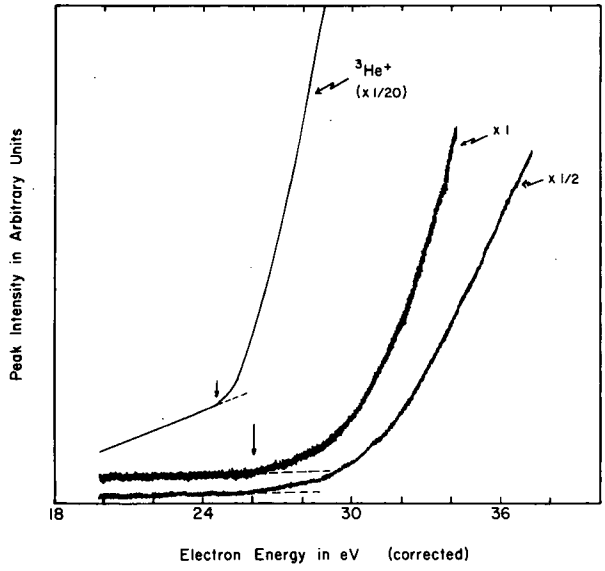

Fig. 7. Ionization efficiency curves for the $(M/q)^* = 10.286$ peak from C_2D_2 at two sensitivity levels. $^3He^+$ standard for calibrating energy scale. The background at $M/q = 3$ below 24.6 eV is due to a small HD^+ background produced when deuterated compounds are introduced into the ion source.
(XBL 721-9)

Table IV. Energetics of formation of the metastable ions CH^+ and CD^+ from various sources.

Compound	Products[a]	Diss. limit (calc)[b], eV	T^c eV $CH^+(m)$	AP, eV (calc)	AP^d, eV (obs)	Standard
CH_4	$[C^+ + H] + H + H_2$	23.99	~1.4	25.4	31.0 ± 1	He^+
CD_4	$[C^+ + D] + D + D_2$	23.99	1.4	25.4	30 ± 1	$^{22}Ne^+$
C_2H_2	$[C^+ + H] + CH$	24.78	1.1	25.9	26.9 ± 0.5	He^+
C_2D_2	$[C^+ + D] + CD$	24.78	1.4	26.2	26.2 ± 0.5	$^{22}Ne^+$ $^3He^+$
C_2D_4	$[C^+ + D] + D + CD_2$	26.74	1.1	27.8	30.3 ± 0.5	$^{22}Ne^+$

[a] Bracketed species appear as the metastable ion.
[b] Assuming C^+ in the $^2P^o_{1/2}$ ground state. For C^+ in the ^4P first excited state add 5.33 eV.
[c] This is the kinetic energy of fragmentation of the metastable ion. Other fragmentations are assumed to occur with zero kinetic energy release at the AP.
[d] All AP's from the initial break compared to the initial break in the standard.

Appearance potential determinations on the metastable ion peak at $(M/q)^* = 10.286$ from C_2D_2 are shown in Fig. 7. The appearance of the $^3He^+$ ion is used as an energy standard, though this has an interference from HD^+ formed in the ion source when deuterated compounds are introduced.

Appearance potentials from various source molecules together with calculated appearance potentials, assuming the minimum energy fragmentation path, are shown in Table IV. From CH_4 and CD_4, the appearance potential is ~ 5 eV above that calculated to the lowest dissociation limit. From C_2H_2 and C_2D_2, however, the agreement between the observed and the calculated value is quite good and shows definitely that $CH^+(m)$ dissociates to the lowest dissociation limit.

$$CH^+(m) \rightarrow C^+(^2P^o_{1/2}) + H(^2S). \quad (3)$$

Lorquet et al.[5] found an appearance potential of 34 eV for $CH^+(m)$ from C_2H_2 and postulated the dissociation limit to be to the $C^+(^4P)$, which is 5.33 eV above the first limit. The data on C_2H_2, C_2D_2, and C_2D_4 show this cannot be the case. The above authors[5] calculated potential energy curves for many states of CH^+. Only two of their states are in the energy region consistent with dissociation to the lowest limit. The $b\,^3\Sigma^-$ is crossed ~1.6 eV above the dissociation limit by the $c\,^3\Sigma^+$ state. This crossing is forbidden by the selection rule $\Sigma^+ \not\rightarrow \Sigma^-$. The $b\,^3\Sigma^+$ state can radiate to the $a\,^3\Pi$ state by an allowed transition. The half-life for predissociation may be determined by the partial half-life for depopulating the $b\,^3\Sigma^+$ state by radiation to the $a\,^3\Pi$ state.

Footnote and References

*Short version of LBL 295; to be submitted to J. Chem. Phys.

1. V. H. Dibeler and H. M. Rosenstock, J. Chem. Phys. 39, 1326 (1963).

2. C. E. Melton and H. M. Rosenstock, J. Chem. Phys. 26, 568 (1957).

3. Ch. Ottinger, Z. Naturforsch. 20, 1232 (1965).

4. L. P. Hills, M. L. Vestal, and J. H. Futrell, J. Chem. Phys. 54, 3824 (1971).

5. A. J. Lorquet, J. C. Lorquet, J. Momigny, and H. Wankenne, J. Chim. Phys. Supplement pp. 64-68, 1970 (20th Meeting Soc. Chim. Phys., Paris, May 1969).

6. A. S. Newton and A. F. Sciamanna, J. Chem. Phys. 44, 4327 (1966).

7. A. S. Newton, A. F. Sciamanna, and G. E. Thomas, Int. J. Mass Spectrom. Ion Phys. 5, 465 (1970).

8. A. S. Newton and A. F. Sciamanna, J. Chem. Phys. 52, 327 (1970).

9. C. E. Berry, Phys. Rev. 78, 597 (1950).

ELECTRON IMPACT EXCITATION FUNCTIONS OF RADIATING AND METASTABLE STATES OF CARBON MONOXIDE*

A. S. Newton and G. E. Thomas

One technique for obtaining electron impact excitation functions for long-lived metastable states of atoms and molecules is the crossed electron and neutral beam technique. The metastables produced by electron impact are detected via their ability to eject an electron from a metal surface placed downstream from the collision region in the path of the neutral beam.[1] Photons higher in energy than the work function of the metal detector can also be measured. By pulsing the electron beam and by using time-of-flight (TOF) techniques, the two signals can be measured independently.[2]

The molecular beam apparatus and the electron gun used in this study have been described previously by Clampitt and Newton.[2] The only significant change in the apparatus was that an EMI 9603 Be-Cu electron multiplier was used as the detector. This multiplier had an effective photoelectric work function of 5.1 eV, measured by using a deuterium light source and a monochromator. The distance between the electron gun and the detector was 10.7 cm. The data-gathering system has been described by Thomas and Vogelsberg.[3] To record the photon curve, the data count gate was opened only during the electron pulse. For the metastable curve, the count gate was delayed for 60 μsec and was then opened to intercept the majority of the TOF distribution of the CO metastables. The time between electron pulses

was 1 msec.

The electron energy scale was calibrated by using the threshold for metastable argon atoms at 11.62 eV. It is estimated that the energy scale established in this fashion was accurate to ±0.2 eV.

Figure 1 shows the excitation function for metastable states produced by electron impact on CO. The excitation threshold was found to be 5.9 eV as compared with the spectroscopic value of 6.01 eV. The shape of the curve agrees quite well with the initial portion of a metastable CO curve recently published by Borst and Zipf.[4] It is, however, quite different from the curve measured by Olmsted, Newton, and Street.[5] Referring to Krupenie's compilation of spectroscopic data on CO,[6] the only state which could contribute to the metastable signal in the region immediately above 6 eV is the a $^3\Pi$ state.

Figure 2 shows the excitation function obtained for the production of prompt radiation of energy greater than 5.1 eV from CO. An unusual feature of this curve is the sharp peak observed at threshold. The onset of the curve is at 7.4 eV and the peak occurs at 8.3 eV. The width at half height of the peak is 0.9 eV, including the broadening caused by the energy spread of the electrons from the thoriated iridium filament. There is a second strong emission threshold at ~11 eV. It is also apparent that there is weak emission below 11 eV that is probably not connected with the peaked feature, but the threshold of this emission is obscured. It is not possible in the present instrument to measure the wavelength distribution of the emitted light.

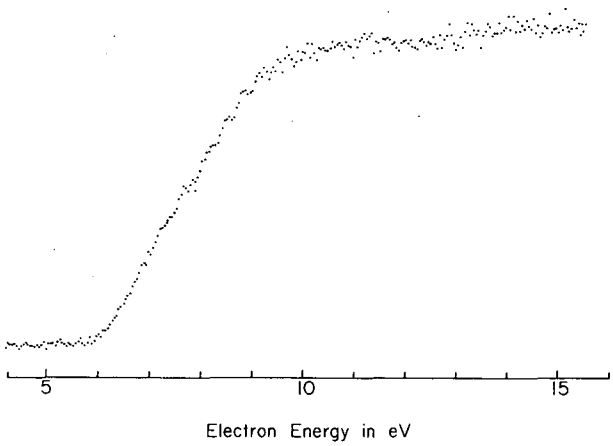

Fig. 1. Excitation function for production of long-lived metastable states of CO.
(XBL 716-1162)

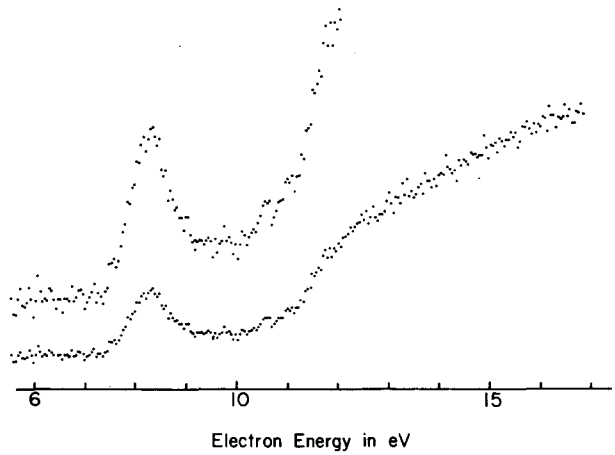

Fig. 2. Excitation function for the production of prompt photons of energy > 5.1 eV from CO.
(XBL 716-1160)

The strong emission above 11 eV can have several sources. The A $^1\Pi$ state has a threshold at 8.03 eV and should rise gradually as the energy increases. In the "3A" system of CO($c\ ^3\Sigma^+ \rightarrow a\ ^3\Pi$), the upper state has an excitation potential of 11.1 eV.[7] The series of high-lying $^1\Sigma^+$ states listed by Krupenie[6] ($B\ ^1\Sigma^+$, $E_0\ ^1\Sigma^+$ and $C\ ^1\Sigma^+$) can decay either via allowed transitions to the $A\ ^1\Pi$ state, which in turn can decay to the $X\ ^1\Sigma^+$ ground state, or via a direct transition to the ground state.

The sharp peak at 8.3 eV in the photon ex-

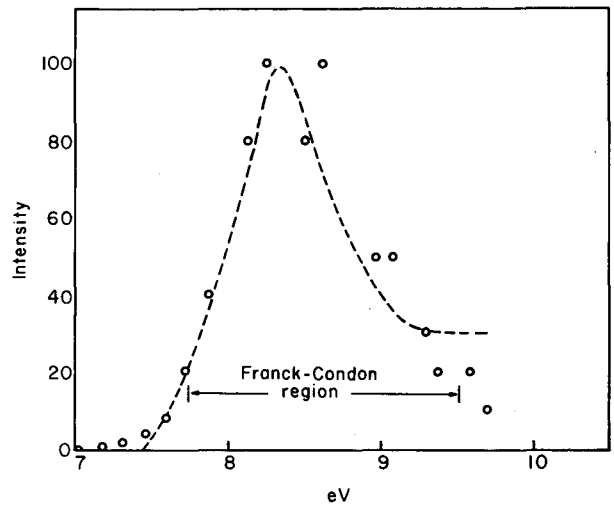

Fig. 3. Excitation function for the production of prompt photons from CO (dashed curve) compared to photon absorption intensities for the forbidden $a'\ ^3\Sigma^+ \leftarrow X\ ^1\Sigma^+$ transition (points from Ref. 8).
(XBL 716-1161)

citation efficiency curve is more difficult to explain. The only known states of CO accessible to Franck-Condon transition below 8 eV are the a $^3\Pi$ and the a' $^3\Sigma^+$ (Ref. 6). The a $^3\Pi$ state can be eliminated from consideration on the basis of its long radiative lifetime.[4] Its excitation function should resemble that of CO in Fig. 1. Furthermore, this state becomes inaccessible to a Franck-Condon transition from the ground state above 7 eV, and no new phenomena preceded by direct excitation of this state should occur above this energy.

To interpret the peaked feature as arising from a direct transition to the a' $^3\Sigma^+$ state, followed by the decay of this a' state to the ground state, is also difficult. Figure 3 compares the peak observed here with the optical absorption envelope for the transition a' $^3\Sigma^+ \leftarrow$ X $^1\Sigma^+$ observed by Herzberg and Hugo.[8] It is clear that the a' state passes through the Franck-Condon region in the appropriate energy range. It would be expected that the electron impact peak would be broadened if direct excitation were involved.

An alternative that is consistent with the present data is that selected vibrational levels of the a' state are being populated via a resonant state. This could certainly account for the narrow width of the excitation function. The a' state can radiate to the metastable a $^3\Pi$ via a dipole-allowed transition (the Asundi system). No radiations directly to the X $^1\Sigma^+$ ground state have been observed. The present observations would demand that the branching ratio for depopulation of the a' state by direct radiation to the ground state be an appreciable fraction of the total population.

An improbable source of the light is by direct excitation to the A $^1\Pi$ state which radiates to the ground state (Fourth Positive bands). The threshold for this state is at 8.03 eV, well above the observed threshold of 7.4 eV and outside the experimental error in establishing the energy scale. Further, there is no precedent in which the electron impact excitation of an allowed state exhibits resonance behavior. Excitation of the A $^1\Pi$ state accounts for the low-intensity light in the 9- to 11-eV region of Fig. 2.

If the a' $^3\Sigma^+$ state populated via a resonant state is not the source of the radiation, it seems necessary either to postulate an unknown[6] and unpredicted[9] state of CO in the appropriate energy range, or to consider the possibility of photon emission proceeding via a long-lived ($\sim 10^{-8}$ sec) CO^- state at the observed energy and the unstable $^2\Pi$ ground state of CO^-. This is the dielectronic attachment process.[10] The ground state of CO^- has been observed in electron scattering experiments[11] and its potential energy curve has been estimated by Boness, Hasted, and Larkin.[12] Chantry[13] has shown that there are excited states of CO^- which have dissociation limits of 9.62 eV [$C(^3P) + O^-(^2P)$] and 10.88 eV [$C(^1D) + O^-(^2P)$], and Stamatovic and Schultz[14] have shown still a third state with the dissociation limit of 9.84 eV [$C^-(^4S) + O(^3P)$]. Both the states leading to $O^-(^2P)$ have their maximum yield near the threshold with the kinetic energy of O^- equal to zero.[13] One can therefore assume that these are not repulsive states and that there are bound levels of these states below the dissociation limit that lie within the Franck-Condon region. The fate of these levels is not known.

In order to clarify the nature of the peaked feature observed here it would be useful to measure the wavelength distribution of the emitted light and to search for a resonance in CO in the energy range between 7 and 8 eV.

Footnote and References

*Condensed version of Chem. Phys. Lett. 11, 171 (1971).

1. R. Dorrestein, Physica 9, 447 (1942).

2. R. Clampitt and A. S. Newton, J. Chem. Phys. 50, 1997 (1969); Lawrence Radiation Laboratory Report UCRL-18032.

3. G. E. Thomas and F. E. Vogelsberg, Rev. Sci. Instr. 42, 161 (1971).

4. W. L. Borst and E. C. Zipf, Phys. Rev. A3, 979 (1971).

5. J. Olmsted III, A. S. Newton, and K. Street, J. Chem. Phys. 42, 2321 (1965).

6. P. H. Krupenie, "The Band Spectrum of Carbon Monixide," Natl. Std. Ref. Data Ser., Natl. Bur. Std. (US), NSRDS-NBS 5 (1966).

7. O. S. Duffendack and G. W. Fox, Astrophys. J. 65, 214 (1927).

8. G. Herzberg and T. J. Hugo, Can. J. Phys. 33, 757 (1955).

9. S. V. O'Neal and H. F. Schaeffer III, J. Chem. Phys. 53, 3994 (1970).

10. H. S. W. Massey, Negative Ions, 2nd ed. (Cambridge University Press, Cambridge, 1950), p. 43.

11. H. Ehrhardt, L. Langhans, F. Linder, and H. S. Taylor, Phys. Rev. 173, 222 (1968).

12. M. J. W. Boness, J. B. Hasted, and I. W. Larkin, Proc. Roy. Soc. (London) A305, 493 (1968).

13. P. J. Chentry, Phys. Rev. 172, 125 (1968).

14. A. Stamatovic and G. J. Schultz, J. Chem. Phys. 53, 2663 (1970).

SPECTROGRAPHIC INVESTIGATION OF THE LIGHT PRODUCED BY IMPACT OF 8.3-eV ELECTRONS ON CO

A. S. Newton, A. F. Sciamanna, and G. V. Shalimoff

The observation of an apparent resonant fast photon emission from CO when impacted with 8.3-eV electrons has led to no firm conclusion regarding the source of these photons.[1] An attempt has therefore been made to measure the wave length distribution of this radiation. It is known that the bands must lie between 2430 Å (5.1 eV) and 1494 Å (8.3 eV).

A vacuum system was built onto a 3-meter McPherson vacuum spectrograph. The effective aperture of this spectrograph is about f22. For the electron gun, the detector from an EAI Quad 250B residual gas analyzer was installed in the vacuum system. The ion gun on this unit was constructed with open apertures to both the quadrupole analyzer-multiplier unit and, in the opposite direction, to the spectrograph. In order to prevent metastable molecules and/or ions striking the multiplier, a 1-mm-thick fluorite window was installed between the gun and the quadrupole analyzer. Carbon monoxide was introduced to the gun through a thin-wall 1/16-in.-o.d. stainless steel tube held in place on one of the open side walls of the gun with a BeN spacer. The CO traveled across the ion gun perpendicular to the electron beam and out the other side. Because of the geometry of the system, the CO was not introduced as a true molecular beam through the electron gun. While this gun is purported to operate at 500 to 1000 μA of electron current, at low electron energies (5 to 15 eV), the filament life even at 250 μA was found to be short (sometimes less than 24 hours). The electron beam was collimated with a weak magnetic field (~280 gauss).

In operation the electron energy scale was roughly calibrated by measuring the light intensity on the Be-Cu multiplier through the fluorite window and quadrupole lens system. The rise at ~11 eV in the work of Newton and Thomas[1] was compared with the similar rise in this system. The resonant feature at 8.3 eV was not observed. Its position on the electron energy scale was estimated by the position of the rise at 11 eV.

Exposures for 24 hours with a 2-mm slit

Table I. Cameron bands observed in electron impact of 8.0-eV electrons with CO.[a]

Observed band head Å (± 1 Å)	Intensity[b]	Cameron band head[2] Å	Transition v' - v''
1927.9	w	1928.0	2 - 0
1991.8	m	1992.1 (1992.7)	1 - 0
2061.4	m	2061.8	0 - 0
2156.5	s	2157.1	0 - 1
2177	vvw	2177.3	1 - 2
2258.5	w	2257.7	0 - 2
2280	w	2280.5	1 - 3

[a] 250 μA of 8.0-eV electrons, 2-mm slit, 70 hours. Plate center at 2000 Å.

[b] w = weak, m = medium, s = strong, vvw = very very weak.

Table II. Unidentified bands or lines observed in electron impact of 8.3-eV electrons with CO.[a]

Observed wave length Å (± 2 Å)	Energy, eV	A $^1\Pi$ band Possible interferences v' - v''
1744	7.109	5 - 7, 2 - 5
1731	7.162	1 - 4
1621	7.648	Clear
1611 (?)[b]	7.695	4 - 4
1538	8.061	Clear
1478	8.388	5 - 2, 2 - 0
1473	8.416	Clear
1928 (Cameron)[c]		
1922 (Cameron)		
2061 (Cameron)		

[a] 250 μA of 8.3-eV electrons, 2-mm slit, 70 hours. Plate centered at 1750 Å.

[b] The existence of this line is open to doubt because of a scratch on the plate.

[c] Three Cameron bands shown established the wavelength scale.

opening to the spectrograph and with electron energies from 11 to 25 eV showed only the Fourth Positive bands from CO, A $^1\Pi \rightarrow$ X $^1\Sigma^+$. Between 1600 and 2400 Å some 35 bands due to this transition were observed.

Exposure for 70 hours with 250 μA of 8.0-eV electrons and with the plate centered at 2000 Å showed 7 bands in the forbidden Cameron system, a $^3\Pi \rightarrow$ X $^1\Sigma_g^+$. These bands are shown in Table I.

Exposure for 70 hours with 250 μA of 8.3-eV electrons with the plate centered at 1750 Å resulted in the recording of three of the Cameron bands along with seven very weak lines which were barely visible on the plate. These are shown in Table II. As yet no identification of these bands has been made, nor could they be duplicated, as later experiments at this level of current always resulted in filament burnout within less than 24 hours.

The observation of Cameron bands in the region of 7 to 9 eV was a disappointment. The radiative lifetime of the a $^3\Pi$ state of CO is now estimated[3] to be ~1 msec, and it was hoped that the open sides of the ion source would lead to their removal before they could radiate. From the rate of leak, the volume of the system, and the equilibrium pressure, one can estimate that the mean life of a CO molecule in the vacuum chamber is ~0.1 sec. Therefore all molecules excited to the a $^3\Pi$ state radiate in the vacuum chamber (or undergo de-excitation at a wall). Since the recording and electron beam are continuous, a buildup occurs to a steady-state level of a $^3\Pi$ molecules, some of which can radiate in the electron gun or in front of the spectrograph slit. In the experiments of Newton and Thomas, this buildup did not occur, since the electron beam was pulsed 10 μsec on and 1 msec off. Recording of photons only occurred during the electron-on cycle. This pulsed operation discriminates against the Cameron bands. It is, however, not possible to use pulsed operation with photographic recording.

References

1. A. S. Newton and G. E. Thomas, Chem. Phys. Lett. 11, 171 (1971).

2. P. H. Krupenie, Natl. Stand. Ref. Data Ser., NSRDS-NBS 5, July 16, 1966.

3. W. L. Borst and E. C. Zipf, Phys. Rev. A3, 979 (1971).

γ-IRRADIATION OF ACTINIDE IONS IN CaF_2

J. J. Stacy, N. Edelstein, R. D. McLaughlin, and J. Conway

When small amounts of rare-earth ions are incorporated into CaF_2, they replace the calcium ions; however, since they are most stable in the trivalent state, a valence mismatch occurs which must be compensated. This gives rise to rare-earth ions in cubic, tetragonal, trigonal, or lower symmetries depending upon the mechanism of charge compensation.[1] We have used optical absorption and thermoluminescence measurements to study the effects of γ-irradiation on trivalent actinide ions in CaF_2.

When Np^{3+}-CaF_2 is γ-irradiated at 0°C or at room temperature, an intense broad absorption appears throughout the visible spectral region and three new groups of sharp lines appear. These latter features are due to Np^{4+}. The rate of decay of Np^{3+} is proportional to the rate of growth of Np^{4+}. The rate of decay of Np^{3+}, however, is not first order, which implies that the oxidation mechanism is not direct ionization.

CaF_2 crystals containing Pu^{3+} and Cm^{3+} show similar behavior, i.e., they are oxidized to the tetravalent state by room temperature γ-irradiation. However, Am^{3+}, like all of the lanthanides,[2] is reduced to the divalent state.[3] U^{3+}-CaF_2 is not yet well understood because there is considerable controversy about the assignment of U^{2+} and U^{4+} in CaF_2.[4,5]

When Np^{3+}-CaF_2 is γ-irradiated at 77°K, the most pronounced effect is the appearance of three new intense Np^{3+} absorption lines. Since these lines do not appear in the room temperature irradiation, it must be inferred that γ-irradiation at 77°K produces a new Np^{3+} site.

Intense broad absorptions also appear when An^{3+}-CaF_2 crystals are γ-irradiated. These are shown in Fig. 1. The most striking feature is that the broad band maxima occur at approximately the same wavelengths for all of the actinides (except Am, which behaves like a lanthanide). These absorptions are undoubtedly related to the defects of the lattice and are therefore assigned to color centers.

Thermoluminescent glow curves for these actinide ions (and for comparison the lanthanides Er, Ho, and Tm) have been measured between 100° and 300°K and are shown in Fig. 2. These are remarkably similar, with glow peaks occurring at nearly the same temperatures for all of the ions. High resolution

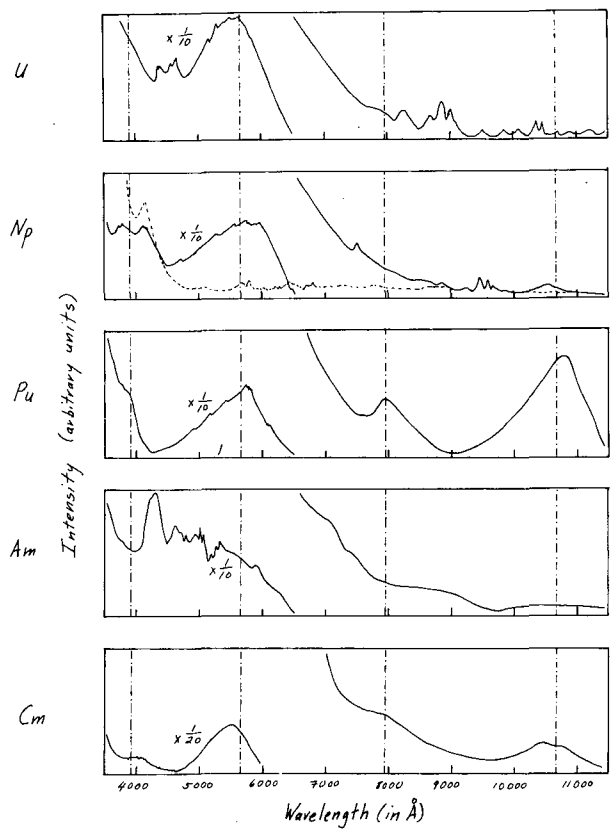

Fig. 1. Broad absorption spectra of An^{3+}-CaF_2 after 3 h γ-irradiation. The vertical dotted lines indicate the position of absorption maxima. Typically the unirradiated spectra are very weak, as shown by the dotted lines for Np. (XBL 7111-1682)

measurements of the spectra of the thermoluminescence show that the emission is identical to the fluorescence of the trivalent ions, and determines the site symmetry of the emitting ion. There is evidence that the glow emission below 300°K originates from trivalent actinide ions in cubic sites.

The data presented above can be explained by a simple model. Irradiation at 77°K produces hole traps and electrons which are localized near cubic An^{3+} ions. Heating allows a hole to diffuse to the site of a localized electron. The hole and extra electron recombine, leaving an excited trivalent actinide ion. Decay of this ion to its ground state results in the observed thermoluminescence. When

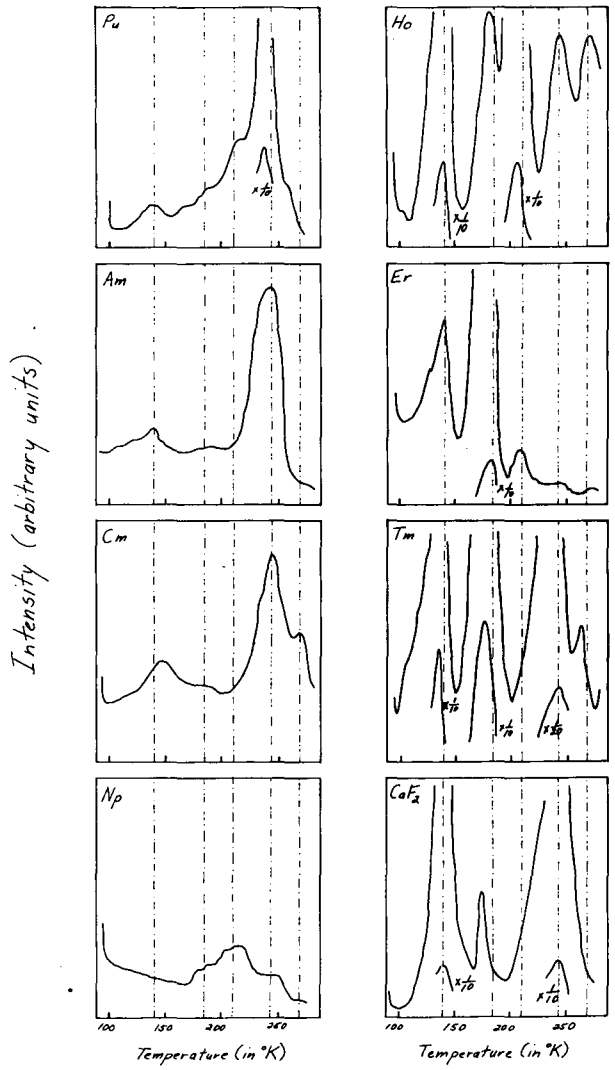

An^{3+}-CaF_2 crystals are irradiated at 300°K, the actinide ion is oxidized to the tetravalent state. Subsequent heating allows electrons which had become trapped in the lattice to recombine with the An^{4+} ions. The decay of the newly formed An^{3+} ion to its ground state results in the observed thermoluminescence.

References

1. M. J. Weber and R. W. Bierig, Phys.Rev. 134, A1492 (1964).

2. J. L. Merz and P. S. Pershan, Phys. Rev. 162, 217 (1967); ibid. 162, 235 (1967).

3. N. Edelstein, W. Easley, and R. McLaughlin, J. Chem. Phys. 44, 3130 (1966).

4. R. McLaughlin, U. Abed, J. G. Conway, and E. H. Huffman, J. Chem. Phys. 53, 2031 (1970).

5. W. A. Hargreaves, Phys. Rev. 156, 331 (1967).

Fig. 2. Thermoluminescence of Ln^{3+}-CaF_2. All irradiations were at 77°K for 30 min in a ^{60}Co source. The dotted lines indicate the positions of glow peak maxima.

(XBL 7111-1657)

ZERO-FIELD SPLITTINGS OF TRIPOSITIVE Cm IN $SrCl_2$ AND ThO_2

W. Kolbe, N. Edelstein, M. M. Abraham,* and C. B. Finch*

The actinide ions with half-filled shells (Cm^{3+} and Am^{2+}; Ac core, $5f^7$) exhibit cubic crystal field splittings in CaF_2 and $SrCl_2$ which are at least two orders of magnitude larger than their lanthanide analogs.[1,2] These splittings were determined from an EPR measurement of the g value anisotropy of the Γ_6 ground state caused by Zeeman mixing of the Γ_8 excited state. In this paper we report similar measurements for Cm^{3+} in ThO_2[3] and SrF_2, and for Am^{2+} in SrF_2. In addition we have measured the g value anisotropy of the thermally populated Γ_7 excited state of the ground J = 7/2 manifold of Cm^{3+} in $SrCl_2$. In the latter case this measurement together with the earlier one,[2] establishes the values of the crystal field parameters b_4 and b_6.

The crystals used in these experiments were grown as described previously.[1,2] Measurements were made using a Varian Associates model E-12 35-GHz bridge. The magnetic field was produced by a 12-inch electromagnet which was rotatable about a vertical axis, and was measured by an Alpha Scientific NMR gaussmeter monitored by a frequency counter. For measurements at 4.2°K the samples were immersed in liquid helium. The excited state Γ_7 measurements were done at a temperature of approximately 25°K which was obtained by flowing cold He gas over the sample and cavity.

For actinide ions, spin-orbit coupling effects are large and only J, the total angular momentum quantum number, remains as a good quantum number. In the absence of the mixing of various J levels by the crystal field (a very good approximation in this case) the J = 7/2 ground state splits up into 2 doublets, Γ_6 and Γ_7, and one quartet, Γ_8. The Zeeman term causes an admixture of the Γ_8 state into the Γ_6 and Γ_7 levels with the result that these formally isotropic states exhibit an anisotropy which can be related to the zero-field crystal field splittings. The applicable Hamiltonian is

$$\mathcal{H} = g_J \mu_8 \vec{H} \cdot \vec{J} + B_4(0_4^0 + 50_4^4) + B_6(0_6^0 - 210_6^4) . \quad (1)$$

The magnetic field was rotated in a plane approximately normal to the [110] crystalline axis and the data were fitted at each point by a least-squares routine which diagonalized the 8×8 matrix generated by the Hamiltonian of Eq. (1). To compensate for crystal misalignment, the three angles necessary to specify the orientation of the magnetic field with respect to the crystal axes were also varied. We believe the small discrepancy between our present data and earlier work is due to a slight crystal misorientation. Table I lists the values for the crystal field splittings of all $5f^7$ ions measured to date.

The measured $\Gamma_7 - \Gamma_8$ splitting for Cm^{3+} in $SrCl_2$ agrees with the previously estimated values obtained from intensity measurements taken as a function of temperature. From the measured splittings, we calculate for Cm^{3+} in $SrCl_2$:

$$b_4 = 60B_4 = -0.66 \pm 0.03;$$

$$b_6 = 1260B_6 = -0.077 \pm 0.006.$$

The data presented here follow the trends

Table I. Zero field splittings of the $5f^7$ ions in various crystals.

Crystal	Ion	Γ_6-Γ_8 (cm^{-1})	Γ_8-Γ_7 (cm^{-1})	g_J	Reference
$SrCl_2$	Cm^{3+}	5.13 ± 0.05	15.3 ± 0.4	1.928 ± 0.002	This work
SrF_2	Cm^{3+}	11.2 ± 0.4		1.9257 ± 0.001	This work
CaF_2	Cm^{3+}	13.4 ± 0.5		1.926 ± 0.001	1
ThO_2	Cm^{3+}	15.5 ± 0.3		1.9235 ± 0.002	This work
$SrCl_2$	Am^{2+}	5.77 ± 0.48		1.9283 ± 0.0008	2
SrF_2	Am^{2+}	15.2 ± 0.4		1.9254 ± 0.001	This work
CaF_2	Am^{2+}	18.6 ± 0.5		1.926 ± 0.001	1

observed for the analogous ions ($4f^7$) in the lanthanide series. The relative magnitudes of the crystal field splittings are similar for the two series. The main difference is the much larger absolute magnitude of the splittings in the $5f^7$ ions. As shown previously a large part of this splitting is due to intermediate coupling effects.[1] For Cm^{3+} in all the crystals (assuming $b_6 << b_4$) the point charge model predicts the correct sign for b_4. However, the measured b_6 for Cm^{3+} (and Gd^{3+}) in $SrCl_2$ is of the opposite sign to that predicted by this simple model. Presumably the mechanisms discussed by Wybourne[4] and others[5] for the lanthanide ions are applicable here and are responsible for these discrepancies.

Footnotes and References

*Oak Ridge National Laboratory, Oak Ridge, Tennessee.

1. N. Edelstein and W. Easley, J. Chem. Phys. 48, 2110 (1968).

2. M. M. Abraham, L. A. Boatner, C. B. Finch, R. W. Reynolds, and H. Zeldes, Phys. Rev. B1, 3555 (1970).

3. M. M. Abraham, C. B. Finch, and G. W. Clark, Phys. Rev. 168, 933 (1968).

4. B. G. Wybourne, Phys. Rev. 148, 317 (1966).

5. B. F. Kim and H. W. Moos, Phys. Rev. 161, 869 (1967).

BIS(1,3,5,7-TETRAMETHYLCYCLOOCTATETRAENE) URANIUM (IV) AND BIS(1,3,5,7-TETRAMETHYLCYCLOOCTATETRAENE) NEPTUNIUM (IV); PROTON MAGNETIC RESONANCE SPECTRUM AND THE QUESTION OF f-ORBITAL COVALENCY

A. Streitwieser, Jr.,* D. Dempf,* G. N. LaMar,* D. G. Karraker,† and N. Edelstein

Our previously published[1] analysis of the observed large upfield shift for bis(cyclooctatetraene)uranium (IV), $(COT)_2U$, uranocene, indicated a large positive net contact shift that suggests some form of covalency; however, in the absence of data relating to the type of ligand MO (σ or π) containing the delocalized spin, no attempt was made to evaluate the possible role of f-orbitals in such covalency. Methyl substitution provides a useful technique for characterizing the spin-containing ligand. For spin in π-orbitals it is well known that an attached ring proton and methyl proton exhibit contact shifts of comparable magnitude but of opposite sign; for spin in in-plane or σ-orbitals, these shifts are of the same sign with the ring proton shift 3 to 5 times larger than the methyl shift.[2] To apply this approach to the uranocene case we have prepared and characterized bis(1,3,5,7-tetramethylcyclooctatetraene)-uranium (IV) and neptunium (IV), $(TMCOT)_2$ U and $(TMCOT)_2Np$. These compounds were prepared in a similar fashion to the parent compounds[3,4] except the TMCOT ligand prepared as described by de Mayo and Yip[5] was used. The TMCOT compounds had similar properties to the COT compounds except for greater solubility in organic solvents. An attempt was made to prepare $(TMCOT)_2Pu$, but it appeared that Pu(IV) was reduced by the ligand to Pu(III).

The proton NMR spectrum of a THF-d_8 solution of $(TMCOT)_2U$ was recorded as a function of temperature on a Varian HA-100 operating in the HR mode with variable frequency modulation. Two peaks with intensities of 3:1 were observed and can be assigned to the methyl and ring protons, respectively. The observed shifts at room temperature, referenced against TMCOT, are given in Table I together with that observed for $(COT)_2U$. The ring proton shifts and their temperature dependences are virtually the same for both complexes.[6] The proton NMR spectrum of a toluene-d_8 solution of $(TMCOT)_2Np$ was recorded at 37°C. The corresponding proton peaks of the methyl group (linewidth ~2000 Hz) were much broader than for the U complex. The shifts are listed in Table I.

The known structure[7] of $(COT)_2U$ and an extrapolated structure based upon ionic radii for $(COT)_2Np$ plus the assumption of a freely rotating methyl group were used to calculate the geometric factors.[8] The calculated dipolar shifts of the various protons were subtracted from the experimental shifts to give the net contact shifts listed in Table I. The hyperfine coupling constants A_F are also given.[9] The derived contact shifts are of opposite sign for the methyl and ring protons and their ratios [-0.5 for (TMCOT)U and

Table I. Chemical shifts and hyperfine coupling constants for $(TMCOT)_2U$, $(COT)_2U$ in THF, and $(TMCOT)_2Np$ in toluene

	$(TMCOT)_2U$		$(COT)_2U$	$(TMCOT)_2Np$	
	ring-H	methyl-H	ring-H	ring-H	methyl-H
Shifts[a]					
Observed	+41.3	+ 6.0	+42.6	+41.5 ± 2	- 9.9
Dipolar	+ 7.9	+23.6	+ 7.9	+ 5.2	+13.2
Contact	+33.4	-17.6	+34.7	+36.3 ± 2	-23.1
A_F[b]	+ 0.98	- 0.52	+ 1.02	+ 0.95	- 0.61

[a]Shifts in ppm, referenced against the uncomplexed diamagnetic TMCOT and COT. U data given at 298°K, Np data at 310°K.

[b]Hyperfine coupling constants in MHz; estimated accuracy ±25%.

-0.6 for (TMCOT)Np] are indicative of systems having considerable π spin density.[10] These results strongly suggest that the spin density in our ligands is primarily in π-MO's; indeed, application of the McConnell equation, $A = QP/2S$, with $Q = -63$ MHz, indicates in excess of 0.1 unpaired electron per ligand ring. Although the coupling constants are approximately the same for $U(TMCOT)_2$ and $Np(TMCOT)_2$, the U complex has only two unpaired electrons (three for the Np complex) which suggests stronger covalency for $U(TMCOT)_2$.[11] The high magnitude of this delocalized spin density compared with that observed in more ionic lanthanide and actinide complexes implies a high degree of covalency and raises the question of f-orbital involvement in such covalency.

Direct delocalization of f-electrons into a vacant ligand π-MO would give proton shifts of opposite sign to those observed.[1] A more plausible mechanism is charge transfer from filled ligand π-MO's to vacant f-orbitals; because of exchange interaction the transfer of spin parallel to the spin on the metal ion is energetically more favorable and would leave net positive spin density on the ligand as observed.[12] Donation of ligand electrons into empty 7s, 7p, or 6d orbitals will also produce the correct sign but it is less likely because of their relatively high energies. Exchange polarization of filled metal orbitals will also give the correct sign but the magnitudes calculated and observed for other lanthanide and actinide compounds[13] appear to be much smaller than in the uranocenes. The present interpretation is consistent with the Mössbauer isomer shift in $(COT)_2Np$[5] and does not disagree with the simple MO formulation presented earlier.[3,14] We hope that a more detailed model will result from further experimental and theoretical studies in progress.

Footnotes and References

*Department of Chemistry, University of California, Berkeley.

†E. I. De Pont de Nemours and Company, Savannah River Laboratory, Aiken, So. Carolina.

1. N. Edelstein, G. N. LaMar, F. Mares, and A. Streitwieser, Jr., Chem. Phys. Letters 8, 399 (1971).

2. S. E. Anderson, Jr., and R. S. Drago, J. Am. Chem. Soc. 92, 4244 (1970); M. F. Rettig and R. S. Drago, J. Am. Chem. Soc. 91, 3432 (1969); R. Prins, J. Chem. Phys. 50, 4804 (1969); H. P. Fritz, H. J. Keller, and K. E. Schwarzhans, Z. Naturforsch. B23, 298 (1968).

3. A. Streitwieser, Jr., and U. Muller-Westerhoff, J. Am. Chem. Soc. 90, 7364 (1968).

4. D. G. Karraker, J. A. Stone, E. R. Jones, Jr., and N. Edelstein, J. Am. Chem. Soc. 92, 4841 (1970).

5. P. de Mayo and R. W. Yip, Proc. Chem. Soc. London 84 (1964).

6. At $1/T = 0$ the methyl proton shift extrapolates to a non-zero intercept greater than that for the ring proton shift. At present we have no explanation for this observation.

7. (a) A. Audeef, K. N. Raymond, K. O. Hodgson, and A. Zalkin, Inorg. Chem., in press; (b) A. Zalkin and K. N. Raymond, J. Am. Chem. Soc., 91, 5667 (1969); (c) The refined structure of $U(COT)_2$ (Ref. 7a) has greatly reduced the uncertainty in the calculation of the dipolar shifts due to structural uncertainties. For this reason the numbers given in Table I differ slightly from those given in Ref. 1. Small variations of the $C-CH_3$ distances have little effect on the results.

8. The geometric factors of the ring H and methyl H for $(TMCOT)_2U$ are -0.0020×10^{24} cm^{-3} and -0.0059×10^{24} cm^{-3}, respectively; for the ring H and methyl H of $(TMCOT)_2Np$ the factors are -0.0024×10^{24} cm^{-3} and -0.0061×10^{24} cm^{-3} respectively.

9. Similar assumptions as discussed in Ref. 1 were used to calculate the $(TMCOT)_2Np$ coupling constants.

10. D. R. Eaton and W. D. Phillips, Adv. Magnetic Resonance 1, 103 (1965).

11. G. N. LaMar et al., Inorg. Chem., in press.

12. J. Owen and J. H. M. Thornley, Repts. Prog. Phys. 29, 675 (1966).

13. R. E. Watson and A. J. Freeman, Phys. Rev. Letters 6, 277 (1961); J. M. Baker and W. B. J. Blake, Phys. Letters 31A, 61 (1970); W. Kolbe and N. Edelstein, Phys. Rev. Nov. 1, 1971; M. T. Eastman, H. G. Hecht, and W. B. Lewis, J. Chem. Phys., in press.

14. The one-electron MO description in Ref. 3 should be regarded as one of several configurations because of the mixing of f-orbitals resulting from spin-orbit coupling.

HIGH-RESOLUTION MÖSSBAUER SPECTROSCOPY WITH THE 6.2-keV GAMMA RAYS OF ^{181}Ta

G. Kaindl* and D. Salomon

There are only two Mössbauer levels with lifetimes in the microsecond region for which gamma resonance has been observed: the 93-keV state of ^{67}Zn ($T_{1/2}=9.3\,\mu sec$)[1] and the 6.2-keV state of ^{181}Ta ($T_{1/2}=6.8\,\mu sec$).[2] In both cases the natural widths of the recoilless γ rays are comparable ($\Gamma=\hbar/\tau=4.9\times10^{-11}$ eV for ^{67}Zn and $\Gamma=6.7\times10^{-11}$ eV for ^{181}Ta). The ultimate resolution which may eventually be obtained in a Mössbauer measurement of hyperfine interactions (of electric monopole, magnetic dipole, and electric quadrupole type) is mainly determined by the natural linewidth of the Mössbauer resonance and by the size of the nuclear parameters involved ($\Delta\langle r^2\rangle$, μ, and Q, respectively). Since all of these parameters are rather large for the ^{181}Ta resonance, and especially much larger than those of the ^{67}Zn resonance, the 6.2-keV γ transition of ^{181}Ta is the top candidate for high-resolution Mössbauer spectroscopy applied to hyperfine interaction studies.

The present paper reports on a major improvement towards this goal: we have for the first time observed large isomer shifts of the Mössbauer absorption line between sources of ^{181}W diffused into single crystals of the 3d, 4d, and 5d transition metals, and absorbers of Ta metal, $KTaO_3$ and TaC. Single crystals were used to insure high-purity hosts and to preclude preferential diffusion along grain boundaries. The observed isomer shifts cover a range of 104 mm/sec, corresponding to 16 000 times the natural linewidth $W_0=2\Gamma=2\hbar/\tau$, or 1500 times the total minimum experimental linewidth obtained up to now.[3] Part of the results of this work has already been published.[4]

The measurements were performed at room temperature with a sinusoidal electromechanical velocity drive[6] and a 2048-channel multichannel analyzer. The experimental technique and the procedure used for preparing the sources were similar to those described previously.[5] In the present experiment, however, the ^{181}W activity, after deposition on the single-crystalline metal samples, was reduced in an atmosphere of H_2 at 850°C prior to diffusion under high vacuum at temperatures up to 2400°C. The resulting W concentration is estimated to be less than 1 at.% for all sources. The Ta metal absorber (4 mg/cm^2 thick) was the same one used in our previous work.[5] The $KTaO_3$ absorber (5 mg/cm^2) was prepared from finely powdered 99.9% pure $KTaO_3$ by sedimentation in a polystyrene-benzene solution on a 1/4-mil-thick Mylar foil. The same preparation technique was used for the TaC absorber.[7]

Some typical velocity spectra are shown in Fig. 1. Dispersion-modified Lorentzian lines[2,5] were least-squares fitted to the spectra. The large range of the observed isomer shifts is clearly exhibited. Table I sum-

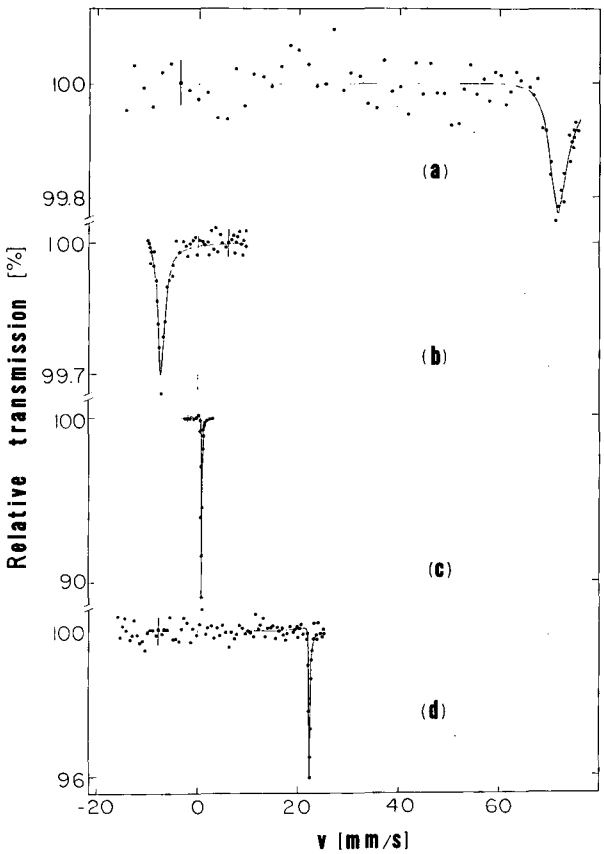

Fig. 1. Absorption spectra of the 6.2-keV γ rays of ^{181}Ta: (a) absorber: TaC, (b) absorber: $KTaO_3$, (c) absorber: Ta metal; all three measured with a ^{181}W(W) source; (d) absorber: Ta metal, source: ^{181}W(Mo). Adjacent points were added for the plots, and the solid curves represent the result of the least-squares fit.
(XBL 721-2156)

marizes the experimental results. The errors quoted for the isomer shifts include a possible 0.5% inaccuracy of the absolute velocity calibration of the drive. The quoted isomer shifts are given relative to a Ta metal absorber: in all cases where they have been measured with the respective sources versus a Ta metal absorber they are given with opposite sign from the measured Doppler shifts. The amplitudes of the dispersion term 2ξ, resulting from the least-squares fits, agree for all spectra within statistical error with our previously published value of $2\xi = 0.30 \pm 0.01$. [5]

A graphical representation of the observed isomer shifts is given in Fig. 2. The isomer shifts measured for ^{181}Ta in lattices of the transition metals cover a range of 36 mm/sec.

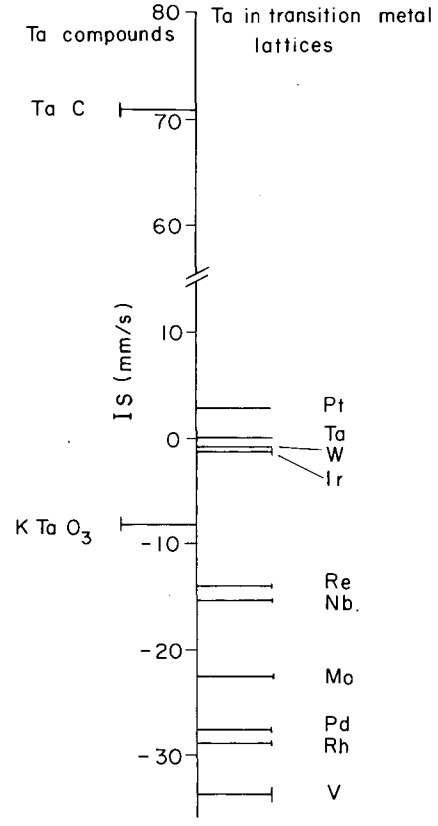

Fig. 2. Graphical representation of observed isomer shifts. (XBL 721-2247)

As can be seen, those found for the cubic 5d metals (Ta, W, Ir, and Pt) are rather small, while those obtained for the cubic 4d metals (Nb, Mo, Pd, and Rh) cover a wider range from -15.26 mm/sec (Nb) to -28.80 mm/sec (Pd). The value found for the 3d element V is again larger (-33.6 mm/sec). A calibration of the ^{181}Ta isomer shifts has not yet been established. From a comparison with isomer shifts measured for other Mössbauer γ rays of isotopes of the 3d, 4d, and 5d transition elements, especially of ^{57}Fe, ^{99}Ru, ^{193}Ir, and ^{197}Au, the following conclusions may be drawn:

1) The change of the mean square nuclear charge radius $\Delta^2\langle r^2\rangle = \langle r^2\rangle_e - \langle r^2\rangle_g$ is negative for the 6.2-keV γ transition, and of the order of -10^{-2} fm^2. The negative sign is also favored by the measured ratio of the electric quadrupole moments of the excited state and the ground state ($Q_e/Q_g = 1.133 \pm 0.010$ [12]), from which it follows, that the intrinsic quadrupole moment of the excited state is smaller than that of the ground state.

2) As in the cases of Ru metal and Ir metal, [8] the isomer shift found for Ta metal

Table I. Summary of experimental results for the isomer shifts IS (given relative to a Ta metal absorber) and the total experimental linewidths W

Source lattice	W [mm/sec]	IS [mm/sec]
V	7.7 ±2.6	-33.6 ±0.7
Nb	0.30 ±0.04	-15.28±0.10
Mo	0.22 ±0.03	-22.50±0.13
Rh	3.2 ±0.5	-28.80±0.25
Pd	2.7 ±0.6	-27.55±0.25
Ta	0.184±0.006	-0.075±0.004
W	0.112±0.002	-0.860±0.008
Re	0.60 ±0.04	-13.99±0.09
Ir	1.60 ±0.12	- 1.84±0.10
Pt	0.50 ±0.08	+ 2.81±0.06
Absorbers		- 8.11 0.15
$KTaO_3$	1.5 ±0.2	- 8.11±0.15
TaC	2.4 ±0.4	+ 70.8±0.5

lies close to that of the pentavalent state ($KTaO_3$). Since the isomer shifts found for isotopes of the transition elements imbedded into the lattices of transition metals cover typically a range which corresponds to roughly a difference of 1 in the formal oxidation state, we may expect that the isomer shifts for other Ta compounds will not exceed by much the present range of 100 mm/sec. Anyway, Ta compounds exist only in three formal oxidation states (III, IV, V), with the pentavalent state being the most stable.

The superior resolution which can be obtained in applications of isomer shift measurements with the 6.2-keV γ rays to solid state or chemical problems is demonstrated in Table II. There we compare the presently observed total ranges of isomer shifts, the natural linewidths W_0, and the current best experimental linewidths W for those Mössbauer transitions that have good resolution for isomer shift studies. As can be seen, the ideal resolution (represented by Q_1) as well as the presently reached experimental resolution (represented by Q_2) are for the ^{181}Ta resonance more than an order of magnitude higher than for all other Mössbauer resonances presently in use.

Acknowledgment: The authors would like to thank Prof. D. A. Shirley for his constant interest in this work, and Dr. N. H. Krikorian, Los Alamos Scientific Laboratory, for the supply of high-purity TaC.

Footnote and References

*Miller Fellow, 1969-1971.

1. H. de Waard and G. T. Perlow, Phys. Rev. Letters 24, 566 (1970).

2. C. Sauer, E. Matthias, and R. L. Mössbauer, Phys. Rev. Letters 21, 961 (1968), and references therein.

3. G. Wortmann, Phys. Letters 35A, 391 (1971).

4. D. Salomon, G. Kaindl, and D. A. Shirley, Phys. Letters 36A, 457 (1971).

Table II. Total range of observed isomer shifts R, natural linewidth $W_0 = 2\hbar/\tau$, presently best experimental linewidth W, and quality factors $Q_1 = R/W_0$ and $Q_2 = R/W$ for several Mössbauer transitions with good resolution for isomer shift measurements.

Isotope	Gamma-ray energy [keV]	IS range R [mm/sec]	W_o [mm/sec]	W [mm/sec]	$Q_1 = \frac{R}{W_0}$	$Q_2 = \frac{R}{W_0}$
^{181}Ta	6.2	104	0.0064	0.069	16 200	1500
^{237}Np	59.5	106	0.073	1.1	1450	96
^{99}Ru	90	2.5	0.147	0.28	17	9
^{57}Fe	14.4	2.5	0.195	0.24	13	10
^{193}Ir	73.1	7	0.594	0.70	12	10
^{119}Sn	23.9	7	0.619	0.8	11	9

5. G. Kaindl and D. Salomon, Phys. Letters 32B, 364 (1970).

6. G. Kaindl, M. R. Maier, H. Schaller, and F. Wagner, Nucl. Instr. Methods 66, 277 (1968).

7. The TaC used has a cubic lattice parameter $a_0 = 4.4561 \pm 0.0006$ Å, suggesting a formula $TaC_{0.99}$. N. H. Krikorian, Los Alamos Scientific Laboratory, private communication (1971).

8. G. Kaindl, D. Kucheda, W. Potzel, F. E. Wagner, U. Zahn, and R. L. Mössbauer, in Hyperfine Interactions in Excited Nuclei, edited by G. Goldring and R. Kalish (Gordon and Breach, 1971), p. 595.

9. F. E. Wagner, Technische Universität München, private communication (1971).

10. T. Danon, in Chemical Applications of the Mossbauer Effect, edited by V. I. Goldanskii and R. H. Herber (Academic Press, New York, 1968), p. 159.

11. G. Kaindl, D. Salomon, unpublished results.

12. G. Kaindl and D. Salomon, this report, next paper.

ELECTRIC QUADRUPOLE SPLITTING OF THE 6.2-keV GAMMA RAYS OF ^{181}Ta IN RHENIUM METAL

G. Kaindl* and D. Salomon

From the preceding paper the extreme sensitivity of the 6.2-keV γ resonance of ^{181}Ta to small changes of the total electron density at the nucleus is obvious.[1] Its inherent resolution for magnetic hyperfine studies has already previously been demonstrated by measurements of the magnetic moment of the excited state in externally applied magnetic fiel of the order of 1.5 to 3.0 kOe.[2,3] Likewise a very high resolution is expected for the measurement of electric quadrupole interactions (EQI) due to the large electric quadrupole moment of the ground state of ^{181}Ta, $Q(7/2) = +(3.9 \pm 0.4)$b.[4] The present paper reports on a measurement of the electric quadrupole splitting of the 6.2-keV γ rays of ^{181}Ta in sources of ^{181}W diffused into single-crystal rhenium metal. This is the first application of the ^{181}Ta γ resonance to nuclear quadrupole interaction studies. From the completely resolved split spectra, the sign and magnitude of the electric field gradient (EFG) at the ^{181}Ta site in rhenium metal, the ratio of the quadrupole moments of the excited state to that of the ground state, and the isomer shift of ^{181}Ta(Re) relative to Ta metal are derived.

The experimental technique employed was very similar to the one described in the preceding paper.[1] From a high-purity single crystal of rhenium metal ($\rho_{300}/\rho_{4.2} = 10\,500$),[5] oriented to within 1° by reflection of coherent light on an etched surface and subsequently by the Laue backscattering method, thin disks (about 1 mm thick) were cut with a spark cutter parallel and perpendicular to the [0001] axis. The ^{181}W activity was diffused into the Re metal disks at a temperature of 2500°C in high vacuum (10^{-7} Torr). The same Ta metal absorber and the same Mössbauer spectrometer were used as in our previous work.[1]

The velocity spectra obtained are presented in Fig. 1. As the 6.2-keV transition has pure E1 character with the spin sequence $9/2 \rightarrow 7/2$, the hyperfine spectrum resulting from an EQI alone consists of 11 hyperfine components, of which 7 are $\Delta m = \pm 1$ transitions, 3 are $\Delta m = 0$ transitions and 1 is a mixed transition. In the diagrams of Fig. 2 the dependence of the line positions on the ratio of the quadrupole moments $Q(9/2)/Q(7/2)$ is presented for an axially symmetric EFG, with the direction of observation perpendicular (a) and parallel (b) to its axis. By observing the emission spectrum parallel and perpendicular to the [0001] axis of the single-crystal ^{181}W(Re) sources, the assignment of individual transitions to the observed lines could be done uniquely.

Both Mössbauer spectra were simultaneously least-squares fitted with a superposition of dispersion modified Lorentzian lines:

$$N(v) = N(\infty) \left\{ 1 - \sum_{i=1,11} \frac{A(i)\,(W/2)^2}{[v - v_0(i)]^2 + (W/2)^2} \times \left[1 + 2\xi \frac{v - v_0(i)}{W/2} \right] \right\},$$

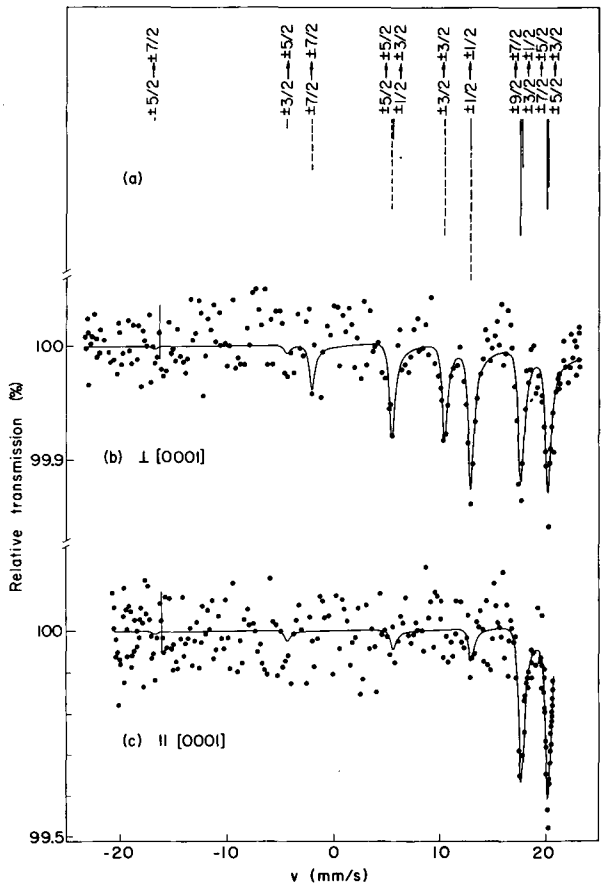

Fig. 1. Velocity spectra of the 6.2-keV γ rays of ^{181}Ta in rhenium metal versus a Ta metal absorber, with direction of observation parallel (c) and perpendicular (b) to the [0001] axis , respectively.

(XBL 7111-4691)

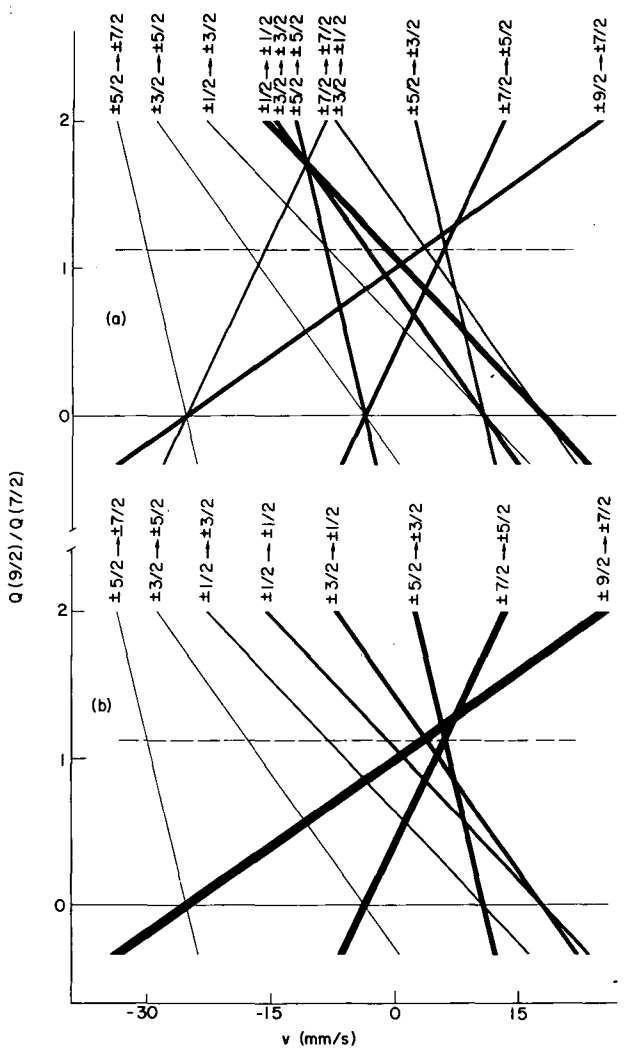

Fig. 2. Dependence of the line positions expected for the 9/2(E1)7/2 ground state transition in ^{181}Ta on the ratio of the quadrupole moments Q(9/2)/Q(7/2) for an axially symmetric electric field gradient: (a) perpendicular to the axis of the EFG, and (b) parallel to it. The widths of the lines are proportional to the intensities of the components.

(XBL 7111-4750)

where the amplitude 2ξ of the dispersion term was set equal to $2\xi = 0.30$.[3] [N = number of counts, W = experimental linewidth (FWHM), v = Doppler velocity, A(i) and $v_0(i)$ = amplitude and position of the ith component, respectively]. The z component of the axially symmetric electric field gradient eq, Q(9/2)/Q(7/2), the isomer shift IS, W/2; and for each of the two spectra, N(∞) and an amplitude factor A_{tot}, describing the total summed effect, were used as free parameters for the 8-parameter fit. Within statistical accuracy the measured spectra are in agreement with the assumption of an axially symmetric EFG, expected from the point symmetry of the hexagonal rhenium lattice.

The results of the least-squares-fit analysis are presented in Table I, with negative signs for IS and $e^2qQ(7/2)$, since the measured interactions occurred in the source. The observed linewidth W = 0.60±0.04 mm/sec reflects a considerable line-broadening, only part of which is due to geometrical broadening (about 0.1 mm/sec for the solid angle $\Omega = 4\pi/500$ used). Because of the line-broadening, the total resonance effect A_{tot}, summed over all components, is rather small (~1%) in both spectra.

With the electric quadrupole moment of the $7/2^+$ ground state Q(7/2) = + (3.9±0.4)b,[4] values for the electric quadrupole moment of

Table I. Summary of experimental results obtained by a simultaneous least-squares fit of spectra (b) and (c).

isomer shift IS	$-(14.00 \pm 0.10)$	mm/sec
$Q(9/2)/Q(7/2)$	1.133 ± 0.010	
$e^2q\,Q(7/2)$	$-(2.15 \pm 0.02)$	10^{-6} eV
linewidth W	0.60 ± 0.04	mm/sec
effect A_{tot}	$1.30 \pm 0.18\%$	Spectrum(b)
	$0.94 \pm 0.18\%$	Spectrum(c)

the 6.2-keV state and for the EFG eq at the ^{181}Ta nucleus in rhenium metal can be derived. Using our experimental value

$$Q(9/2)/Q(7/2) = 1.133 \pm 0.010,$$

we obtain

$$Q(9/2) = +(4.4 \pm 0.5)\text{b}$$

for the quadrupole moment of the $9/2^-$ excited state and

$$eq = -(5.5 \pm 0.5) \times 10^{17}\ \text{V/cm}^2$$

for the EFG at ^{181}Ta(Re) at room temperature.

The ground state and the 6.2-keV state of ^{181}Ta have been classified as intrinsic proton states with the Nilsson assignments $7/2^+[404]$ and $9/2^-[514]$, respectively.[6] Assuming the same intrinsic quadrupole moment for both states, the Nilsson model predicts a value of $Q(9/2)/Q(7/2) = 1.17$, which is slightly larger than our experimental value of 1.133 ± 0.010. Neglecting band mixing, we obtain for the ratio of the intrinsic quadrupole moments Q_0 a value of $Q_0(9/2)/Q_0(7/2) = 0.97 \pm 0.01$.

Our value for the EFG at ^{181}Ta in rhenium metal may be compared with the results of nuclear specific heat[7] and nuclear acoustic resonance[8] measurements for pure rhenium metal. In agreement with our result, the sign of the EQI was reported negative.[7] From the quadrupole coupling constant for ^{185}Re in rhenium metal and the quadrupole moment of the ground state of ^{185}Re[$Q(^{185}\text{Re}) = +(2.3 \pm 0.9)$b[9]], a value of $eq = -(4.9 \pm 1.9) \times 10^{17}$ V/cm^2 can be derived for the EFG in rhenium metal at 4.2°K. This value is in good agreement with our room-temperature result for ^{181}Ta(Re), though of less accuracy due to the large error in the value for $Q(^{185}\text{Re})$. The only other 5d element for which the EFG has been measured as an impurity in rhenium metal is osmium: $eq = -(3.3 \pm 0.6) \times 10^{17}$ V/cm^2 at 4.2°K.[10] In all three cases the EFG's are negative; for a quantitative comparison, however, a measurement of the EFG of Ta(Re) at 4.2°K is highly desirable. It may be noted that a measurement of the temperature dependence of the EFG of Ta(Re) can be achieved over an unusually large temperature region by using the 6.2-keV γ resonance of ^{181}Ta.

We would like to thank Prof. D. A. Shirley and Dr. H. Haas for valuable discussions, and Dr. B. B. Triplett for the rhenium metal single crystal.

Footnote and References

*Miller Fellow, 1969-1971.

1. D. Salomon and G. Kaindl, preceding paper and references therein.

2. C. Sauer, E. Matthias, and R. L. Mössbauer, Phys. Rev. Letters 21, 961 (1968).

3. G. Kaindl and D. Salomon, Phys. Letters 32B, 364 (1970); D. Salomon and G. Kaindl, Nuclear Chemistry Division Annual Report for 1970, Lawrence Radiation Laboratory Report UCRL-20426, p. 215.

4. L. Lindgren, Arkiv Fysik 29, 553 (1965).

5. B. B. Triplett, University of California, Berkeley, private communication.

6. U. Hauser, Nucl. Phys. 24, 488 (1961).

7. P. E. Gregers-Hansen, M. Krusius, and G. R. Pickett, Phys. Rev. Letters 27, 38 (1971), and references therein.

8. J. Buttet and P. K. Baily, Phys. Rev. Letters 24, 1220 (1970).

9. J. Kuhl, A. Steudel, and H. Walter, Z. Physik 196, 365 (1966).

10. F. E. Wagner, Technische Hochschule München, Germany, private communication.

NMR ON ORIENTED ^{196}Au AND ^{198}Au IN NICKEL

F. Bacon, G. Kaindl,* H.-E. Mahnke,† and D. A. Shirley

Induced magnetic hyperfine fields at dilute impurities in the ferromagnetic host lattices Fe, Co, and Ni have been measured for a large number of elements,[1] and play a significant role for hyperfine interaction studies. Despite this the theoretical understanding of the origin of these fields is still rather poor. Until recently the fields were considered as arising entirely from a Fermi contact interaction. By a study of the hyperfine anomaly between the first excited state and the ground state of ^{193}Ir in Fe[2] as well as Co and Ni,[3] using the Mössbauer effect, non-contact contributions to the effective hyperfine fields were derived. A similar approach was made for Au(Fe), by studying the hyperfine anomaly between the ground states of ^{198}Au and ^{199}Au in iron with the NMR-ON technique.[4] For an understanding of these non-contact fields, an accurate study of their variation for Fe, Co, and Ni is of crucial importance. We have therefore used the NMR-ON technique to determine the non-contact part of the induced hyperfine field for Au(Ni).

Using the NMR-ON technique, we have determined the magnetic hyperfine interactions $\mu H/I$ for the 2$^-$ ground states of ^{196}Au and ^{198}Au in nickel, and compared them with the one measured for ^{197}Au(Ni) by the NMR spin-echo method.[5] Since the magnetic moments of all three nuclear states have been determined with great precision,[6,7,8] we can derive from our data values for the hyperfine anomalies $^{196}\Delta^{197}_{Ni}$ and $^{197}\Delta^{198}_{Ni}$ for Au in a nickel lattice; since in addition the hyperfine anomalies $^{1}\Delta^{2}_{c}$ for these pairs of isotopes have also been measured with great precision for pure contact interaction (free atoms),[6,7] we can determine contact (H_c) and non-contact (H_{nc}) contributions to the hyperfine field from the two different hyperfine anomalies $^{1}\Delta^{2}_{c}$ and $^{1}\Delta^{2}_{Ni}$. The two anomalies are related by

$$^{1}\Delta^{2}_{Ni}\, H^{(2)}_{eff} = {}^{1}\Delta^{2}_{c}\, H^{(2)}_{c},$$

where $H^{(2)}_{eff} = H^{(2)}_{c} + H^{(2)}_{nc}$ is the total hyperfine field at isotope 2.

The carrier-free ^{196}Au and ^{198}Au activities, produced by bombardment of a Pt target containing 36.2% ^{196}Pt and 44.4% ^{198}Pt with 18-MeV deuterons, and subsequent chemical separation, was electroplated on a high-purity nickel foil. After repeated melting of the nickel in an H_2 atmosphere, a thin foil (~20 000 Å) was produced and contact-cooled by the copper fin of an adiabatic demagnetization apparatus, which uses CMN as a cooling salt. Gamma rays were detected along the external polarizing field of 1 kOe with a NaI(Tl) detector.

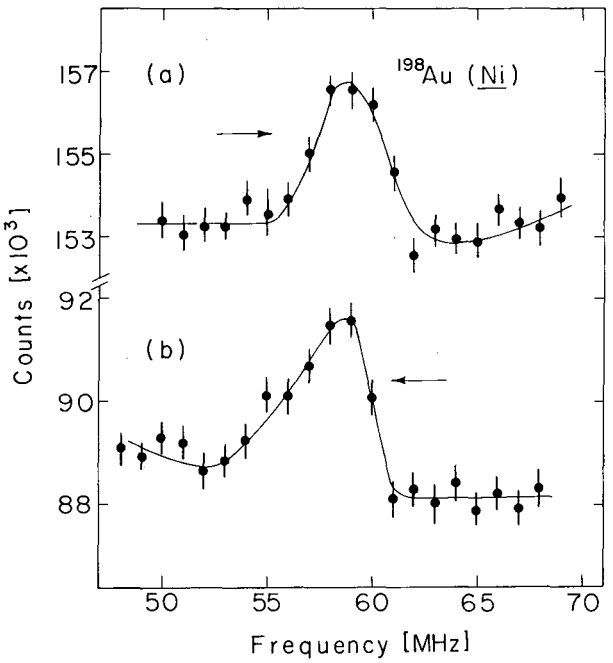

Fig. 1. Frequency dependence of the intensity of the 412 keV γ rays, observed along the polarizing field direction, for increasing (a) and decreasing (b) frequencies, respectively. The rf field was modulated with 100 Hz over a bandwidth of 1.4 MHz, and the total time span between adjacent points was 4.25 min.
(XBL 721-2153)

A typical result of the NMR-ON experiment is presented in Fig. 1, where the frequency dependence of the intensity of the 412-keV γ rays, following the β decay of ^{198}Au is plotted for increasing (a) and decreasing (b) rf frequency. Despite the fact that the frequency was varied in steps of 1 MHz with a total time span of 4.25 min between adjacent data points, the resonance curves measured for increasing and decreasing frequencies are shifted against each other. This is due to the rather long nuclear spin-lattice relaxation time T_1', which was determined as $T_1' = 3 \pm 1$ min, using a single exponential fit.[8] Similar resonance curves were measured simultaneously for the 356-keV γ rays, following the EC decay of ^{196}Au. Since the magnetic moment of ^{196}Au and ^{198}Au differ by only 0.33(26)%[6] and also the hyperfine anom-

aly $^{196}\Delta^{198}_{c}$ was found to be zero within the limits of error,[6] we give the average of the resonance frequencies derived from the ^{196}Au and ^{198}Au data:

$$\nu = 58.4 \pm 0.3 \text{ MHz}.$$

Using $\mu(196) = 0.5823(14)$ n.m. and $\mu(198) = 0.5842(4)$ n.m. for the 2$^-$ ground states of ^{196}Au and ^{198}Au,[6,7] we derive a value for the magnetic field

$$|H_{eff}^{196,198}| = 262.3 \pm 1.3 \text{ kOe}.$$

With the magnetic field determined by the spin-echo method for a sample of less than 2 at.% ^{197}Au(Ni), $H_{eff}^{197} = -294 \pm 6$ kOe,[6] we derive

$$^{197}\Delta^{198}_{Ni} = +12.1 \pm 2.3\%$$

for the hyperfine anomaly $^{197}\Delta^{198}$ in nickel. The comparison with $^{197}\Delta_c{}^{198} = +8.53 \pm 0.08\%$[7] leads to a non-contact field of

$$H_{nc} = +110 \pm 70 \text{ kOe},$$

with the contact fields being

$$H_c^{197} = -404 \pm 70 \text{ kOe and } H_c^{196,198} = -372 \pm 70 \text{ kOe}.$$

The rather large error is mostly due to the 2% error in the value for H_{eff}^{197}. It is our hope that this value can be improved by using a smaller Au concentration in nickel.

The present result is compared with all the other available data on the non-contact parts of hyperfine fields in Fe, Co, and Ni in Table I. The error bars are still too large to draw conclusions, but in all cases the non-contact fields are positive, and there seems to be some indication that they increase from Ni to Fe.

Table I. Summary of experimental results for non-contact contributions to the induced hyperfine fields at Au and Ir in Fe, Co, and Ni.

Impurity	Host lattice	N_{nc} [kOe]	Ref.
Au	Fe	+270 ± 70	4
Au	Ni	+110 ± 70	Present work
Ir	Fe	+335 ± 200	2
Ir	Fe	+155 ± 90	3
Ir	Co	+149 ± 80	3
Ir	Ni	+ 52 ± 50	3

Footnotes and References

*Miller Fellow, 1969-1971.

†On leave from Hahn-Meitner Institutue, Berlin, Germany.

1. T. A. Koster, and D. A. Shirley, in Hyperfine Interactions in Excited Nuclei, edited by G. Goldring and R. Kalish (Gordon and Breach, 1971), p. 1239.

2. G. J. Perlow, W. Henning, D. Olsen, and G. L. Goodman, Phys. Rev. Letters 23, 680 (1969).

3. F. E. Wagner and W. Potzel, in Hyperfine Interactions in Excited Nuclei, edited by G. Goldring and R. Kalish (Gordon and Breach, 1971), p. 681.

4. R. A. Fox and N. J. Stone, Phys. Letters 29A, 341 (1969).

5. M. Kontani and J. Itoh, J. Phys. Soc. Japan 22, 345 (1967).

6. S. G. Schmelling, V. J. Ehlers, and H. A. Shugart, Phys. Rev. C2, 225 (1970).

7. H. Dahmen and S. Penselin, Z. Physik 200, 456 (1967).

8. F. Bacon, J. A. Barclay, W. D. Brewer, D. A. Shirley, and J. E. Templeton, UCRL-20465 (1971).

MAGNETIC HYPERFINE FIELDS AT BISMUTH IN IRON AND NICKEL

F. Bacon, H. Haas,* G. Kaindl,† and H.-E Mahnke‡

Magnetic hyperfine fields on impurities in ferromagnetic host metals have been studied in the past for a large number of elements, but so far only very few experimental data are available for the heavy elements with $Z > 80$. Recently the discrepancy in the measured fields for lead in Fe (Co and Ni) has been clarified by means of the time-differential perturbed angular correlation technique (DPAC)[1] and by channeling experiments.[2] In this context the fields at bismuth became of increased interest. We report here on measurements of the magnetic

fields at bismuth in Fe and Ni by thermal equilibrium nuclear orientation of ^{204}Bi.

The ^{204}Bi activity ($T_{1/2}$ = 11.3 h) was produced by the ^{206}Pb(p, 3n)^{204}Bi reaction with 30-MeV protons on a 99.8% enriched $^{206}PbSO_4$ target. The carrier-free ^{204}Bi activity, obtained by anion exchange separation, was precipitated with 50 mg $Fe(OH)_3$ carrier, heated to form the mixed oxides, and reduced in hydrogen at 800°C. The samples were quickly melted in a hydrogen stream without excessive loss of activity and quenched to room temperature in less than 10 sec. The ^{204}Bi(Ni) sample was prepared in a similar way.

Together with a ^{60}Co(Fe) thermometer the Bi samples were attached with Bi-Cd solder to the copper fin of an adiabatic demagnetization apparatus. Using CMN as a cooling salt, the lowest temperatures reached were 0.005°K. A superconducting Helmholtz pair, operated in persistent mode, was employed to magnetize the samples in a field of 4 kOe. Gamma ray spectra parallel and perpendicular to the polarizing field were taken during the warm-up of the samples over a typical period of 8 hours with high-resolution Ge(Li) detectors. After background and decay corrections, the anisotropies were obtained for the 899-, 912-, and 984-keV γ lines of ^{204}Pb as well as for the ^{60}Co γ lines. Figure 1 shows the temperature dependence of the anisotropy of the 984-keV γ transition in ^{204}Pb measured with the ^{204}Bi(Fe) sample. The data were least-squares fitted for a nuclear spin I = 6, using the hyperfine interaction $|\mu H|$ and an amplitude factor as free parameters. All the measured samples were also investigated at room temperature by DPAC of the 1274-keV state of ^{204}Pb ($T_{1/2}$ = 290 nsec), using the 912 to 375-keV γ cascade, in order to check the samples. In all cases the same fields as previously observed for sources of ^{204m}Pb in Fe and Ni were obtained. The insert in Fig. 1 shows as an example the spin rotation of the 1274-keV state as observed with one of our ^{204}Bi(Fe) samples. The modulation frequency obtained from a least-squares fit corresponds to an internal field at the Pb nucleus of +262 ± 5 kOe, in very good agreement with the result quoted in Refs. 1 and 3.

Due to the intermediate 9^- state in ^{204}Pb ($T_{1/2}$ = 66.9 min) the anisotropies of the 899- and 912-keV γ lines do not necessarily have to show the same temperature dependence as the one of the 984-keV γ transition. This transition is not fed by the 9^- state, of ^{204}Pb, while about 60% of the 912-keV γ transition and less than 15% of the 899-keV γ transition occurs via the 9^- state. However, the effects of a reorientation of the 9^- state on the temperature dependence of the anisotropies of the 912-keV and 899 keV γ rays can be neglected, because of the much smaller hyperfine interaction expected

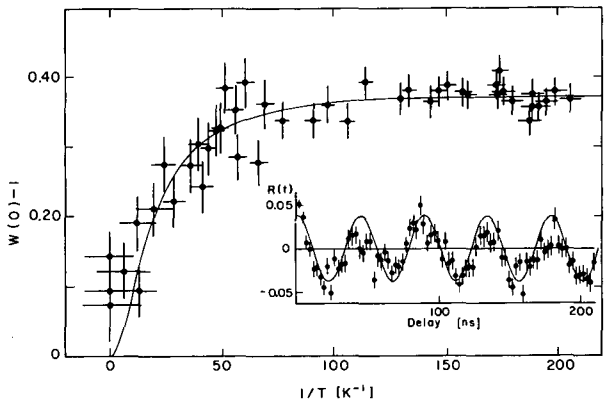

Fig. 1. Temperature dependence of W(0) - 1 for the 984 keV γ rays, emitted from the polarized ^{204}Bi(Fe) source. The insert shows the spin rotation of the 1274 keV state of ^{204}Pb, measured with the same sample at room temperature. The solid curves are the results of least-squares fits. (XBL 7112-4942)

for this state as compared with the ^{204}Bi ground state. Within statistical accuracy the least-squares fits of the anisotropy curves for the three γ lines yield the same values for the magnetic splitting. As a final result the mean values for ^{204}Bi(Fe) and ^{204}Bi(Ni) are given in Table I.

The results of recent channeling experiments on Tl, Pb, and Bi impurities in an iron lattice[2] provide evidence that the hyperfine field of 262 kOe measured for Pb(Fe) is associated with the substitutional site for lead. We therefore may conclude from our DPAC results for ^{204}Pb(Fe), measured on the same samples as used for our orientation work, that our field value for ^{204}Bi(Fe) is also associated with the substitutional site. The same argument applies for Bi(Ni).

Our value for the hyperfine field for ^{204}Bi(Ni) can be compared with the result of a previous IPAC measurement on ^{211}Bi(Ni), using an ^{227}Ac(Ni) source: H_{hf} = + 160 ± 30 kOe.[5] This

Table I. Magnetic hyperfine fields on Bi in iron and nickel at temperatures T < 0.1°K.

Host	$\lvert\mu H\rvert$ (10^{-18} erg)	H_{hf} (kOe)
Fe	25.4 ± 2.9	1180 ± 130
Ni	7.0 ± 0.8	325 ± 35

value is smaller than our result by a factor of 2. The ratio of the hyperfine fields found in the present experiment for Fe and Ni hosts agrees very well with the ratio of the magnetic moments per atom of the ferromagnetic host lattices. If we assume the positive sign for our field values, they agree rather well with the predictions from the phenomenological theory of Balabanov and Delyagin,[6] namely +935 kOe for Bi(Fe) and +255 kOe for Bi(Ni), respectively.

We would like to thank Prof. D. A. Shirley for valuable discussions.

Footnotes and References

*Present address: Hahn-Meitner Institute, Berlin, Germany.

†Miller Fellow, 1969-1971.

‡NATO Fellow, 1970-1972.

1. H. Haas, to be published.
2. L. C. Feldman, E. N, Kaufman, D. W. Mingay, and W. M. Augustyniak, Phys. Rev. Letters 27, 1145 (1971).

3. T. A. Koster and D. A. Shirley, UCRL-20411.

4. M. F. Martin, Nuclear Data Sheets B5, 601 (1971).

5. F. C. Zawislak and D. D. Cook, Bull. Am. Phys. Soc. 14, 1171 (1969).

6. A. E. Balabonov and N. N. Delyagin, Sov. Phys.-JETP 27, 752 (1968).

NUCLEAR MAGNETIC RESONANCE ON ORIENTED PLATINUM-195m IN IRON

F. Bacon, G. Kaindl,* H.-E. Mahnke,† and D. A. Shirley

Nuclear magnetic resonance on oriented nuclei (NMR-ON)[1] provides precise information on the magnetic splitting of nuclear sublevels ($\mu H_{eff}/I$). On the other hand, the magnetic hyperfine interaction (μH_{eff}) results from an analysis of the temperature dependence of γ-ray anisotropies. By a combination of both measurements the spin of the nuclear state can therefore be obtained directly. The present paper reports on the first application of this method to an isomeric state, in determining the spin of the 259-keV state ($T_{1/2}$ = 4.1 d) of ^{195}Pt. In addition, the magnetic moment of the isomeric state and the mixing ratio of the 98.8-keV γ transition of ^{195}Pt were derived.

The ^{195m}Pt activity was produced by neutron irradiation of 57% enriched ^{194}Pt metal in a neutron flux of 2.5×10^{15} n/cm^2 sec for a period of two weeks. Thin foils (≈ 20.000 Å thick) containing 1 at.% Pt in an iron matrix were prepared after melting the ^{195m}Pt under a hydrogen atmosphere with high-purity iron, already containing a matched amount of ^{60}Co activity, to be used for thermometry. The low temperature technique was the same as described in the previous paper. For the NMR-ON experiment an rf field H_1 was applied perpendicular to H_{ext}, and the amplitude of H_1 was measured by a pickup coil.

Figure 1 shows the results of the NMR-ON experiment. The temperature of the sample increased during the run from $1/T = 145 \pm 5\ K^{-1}$ to $125 \pm 5\ K^{-1}$, causing the sloping background noticeable in Fig. 1b. Despite a total time span of 3.5 min between adjacent data points, the resonance curves measured for increasing vs decreasing frequencies in steps of 1 MHz are shifted relative to each other by more than 1 MHz. This is due to the rather long nuclear spin-lattice relaxation time T_1' for ^{195m}Pt(Fe), which was determined in a separate experiment[2] to be $T_1' = 10 \pm 1$ min at a temperature of $1/T = 150 \pm 5\ K^{-1}$, using a single-exponential fit.[3] The observed resonance effect represents a 30% destruction of the γ-ray anisotropy. The same resonance curves were simultaneously observed for the 129-keV γ rays of ^{195}Pt. The possibility of heating by a coil resonance was excluded since the γ-ray anisotropy of the 158-keV γ rays, originating from the decay of ^{199}Au that was also present in our sample, did not show any frequency effect. From the results in Fig. 1 we determine the resonance frequency as

$$\mu H_{eff}/h \cdot I = 89.5 \pm 0.5 \text{ MHz}.$$

In a separate experiment the temperature dependence of the anisotropies of the 99-keV and 129-keV γ rays of ^{195}Pt were measured at angles of 0 and 90 degrees relative to the polarizing field. During the warmup of the samples over a typical period of 7 h, spectra were taken continuously for periods of 15 min. The anisotropy of the ^{60}Co γ lines was used for thermometry. The data shown in Fig. 2 are the results of three individual demagnetizations of the same

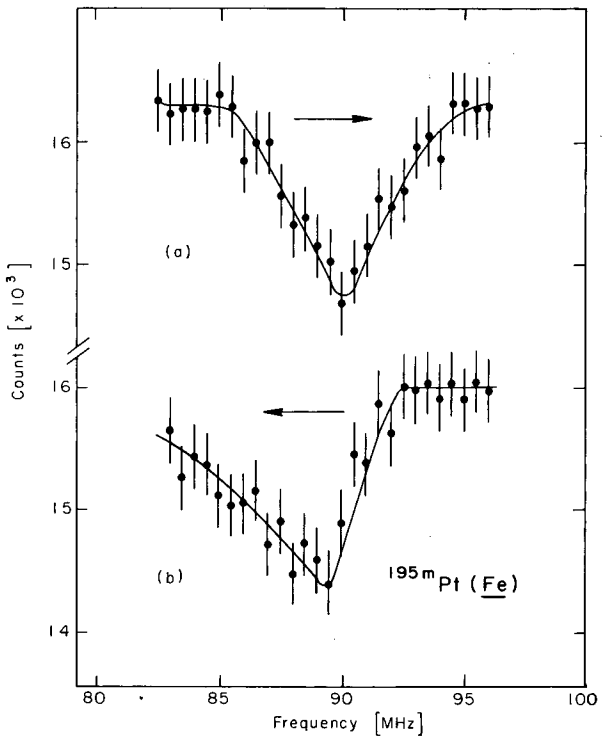

Fig. 1. Frequency dependence of the 99-keV γ-ray intensity, observed in the direction of the polarizing field H_{ext} = 1 kOe, for (a) increasing and (b) decreasing frequency, respectively. The rf frequency was modulated with 100 Hz and a bandwidth of 1 MHz, and the rf amplitude was 0.8 Oe. The time span between neighboring points is 3.5 min.
(XBL 7112-4940)

^{195m}Pt source. The anisotropy curves were least-squares fitted with

$$W(\theta) = 1 + \sum_{k=2,4} B_k U_k F_k Q_k P_k(\cos\theta).$$

In the analysis of the anisotropy of the 129-keV γ rays the influence of the 129.6-keV M4 γ transition was taken into account. With the branching ratios of Ref. 4, and the conversion coefficient $\alpha_{exp} = 1.76 \pm 0.19$ for the 129.8-keV E2 transition[5], and α_{th} = 1230 for the 129.6 M4 transition,[6] the ratio of the γ intensity of the M4 transition to that of the E2 transition at 129 keV was found to be 0.029. Using this value, the anisotropy curve of the 129-keV γ rays, shown in Fig. 2b, was fitted with μH_{eff} as a single parameter, and various values for the spin I of the isomeric state. As expected the results obtained for μH are independent of the assumed spin within the limits of error, clearly demonstrating that from anisotropy curves only a value for the magnetic moment can be obtained. Only for a spin I = 13/2 does $(\gamma H)_{NO}$ agree with $(\gamma H)_{NMR}$. The sensitivity of the method is shown by a plot of the ratio $(\gamma H)_{NO}/(\gamma H)_{NMR}$ versus the assumed spin, given in the insert of Fig. 2.

The anisotropy curve of the 98.8-keV γ rays (Fig. 2a) was least-squares fitted with the E2/M1 mixing ratio δ (in the definition of Biedenharn and Rose, Ref. 7) as the single free parameters, taking $\mu \cdot H/I$ from the NMR experiment. This leads to a value of

$$\delta = -(0.16 \pm 0.02)$$

for the mixing ratio of 98.8-keV γ transition. The absolute value of δ is in good agreement with previous measurements[8,9], but the negative sign is opposite to the one given by Ref. 9.

For a derivation of the magnetic moment of the $13/2^+$ state we use the hyperfine field $H_{hf} = -(1280 \pm 26)$ kOe, measured for the $1/2^-$-

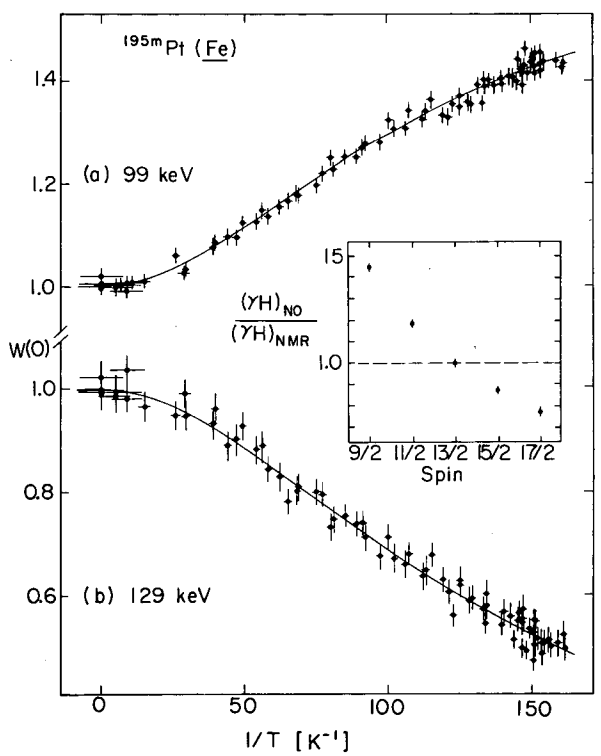

Fig. 2. Temperature dependence of the γ-ray anisotropy $W(\theta = 0) - 1$ of the (a) 99-keV and (b) 129-keV γ rays of ^{195}Pt(Fe) for H_{ext} = 4 kOe. The solid curves are the results of least-squares fit procedures (see text). In the insert the ratio $(\gamma H)_{NO}/(\gamma H)_{NMR}$ is plotted versus the value of the assumed spin.
(XBL 721-2226)

ground state of ^{195}Pt in iron.[10] This leads to

$$\mu(13/2) = (\pm)\ (0.597 \pm 0.015)\ \text{n.m.}$$

for the magnetic moment of ^{195m}Pt, with the negative sign assumed from systematics. The error is mostly due to the 2% uncertainty in the value for the hyperfine field. A correction for a possible hyperfine anomaly between the $13/2^+$ isomeric state and the $1/2^-$ ground state has not been applied. In the neighboring odd mercury isotopes ^{195}Hg and ^{197}Hg, however, the hyperfine anomalies between the $13/2^+$ isomeric states and the $1/2^-$ ground states have been measured[11]: $^{195m}\Delta^{195} = +0.91 \pm 0.02\%$ and $^{197m}\Delta^{197} = +0.97 \pm 0.07\%$. A hyperfine anomaly of this size can also be expected between the analogous states of ^{195}Pt. Thus the quoted value for $\mu(13/2)$ should perhaps be decreased by 1%.

Our result for the spin of the isomeric state, $I = 13/2$, confirms the spin assignment made on the basis of the M4 multipolarity of the 129.6-keV isomeric transition.[12] For ^{195m}Pt a neutron configuration $(i_{13/2})^{13}(f_{5/2})^4$ outside of the $N = 82$ core and the filled $f_{7/2}$ and $h_{9/2}$ neutron shells is expected, since the $p_{3/2}$, $p_{1/2}$, $f_{5/2}$, and $i_{13/2}$ levels lie very close together, and hence the neutron pairs are expected to fill the states of higher angular momentum first due to the pairing energy. Following the core-polarization approach of Arima and Horie[13] we obtain for this neutron configuration a value of -0.64 n.m. for the magnetic moment, in rather good agreement with our experimental result. The magnetic moment may be compared with the known magnetic moments of other $13/2^+$ states in neighboring even-odd nuclei[11,14]: ^{193}Hg [$\mu = -1.0416(3)$ n.m.], ^{195}Hg [$\mu = -1.0280(2)$ n.m.], ^{197}Hg [$\mu = -1.0112(3)$ n.m.], and ^{205}Pb [$\mu = -0.975(39)$ n.m.]. Going from Pt to Hg, the effect on the magnetic moment of two additional protons that are filling up the $d_{3/2}$ shell, is obviously quite drastic and much larger than expected on the basis of the single-particle model with configuration mixing.

Footnotes and References

*Miller Fellow, 1969-1971.

†On leave from Hahn-Meitner Institut, Berlin.

1. E. Matthias and R. J. Holliday, Phys. Rev. Letters 17, 897 (1966).

2. F. Bacon, G. Kaindl, H.-E. Mahnke, and D. A. Shirley, to be published.

3. F. Bacon, J. A. Barclay, W. D. Brewer, D. A. Shirley, and J. E. Templeton, Phys. Rev. 5B, 2397 (1972).

4. R. Schöneberg, D. Gföller, and A. Flammersfeld, Z. Physik 203, 453 (1967).

5. T. Fink and N. Benczer-Koller, Nucl. Phys. A138, 337 (1969).

6. R. S. Hager and E. C. Seltzer, Nuclear Data Tables A4, 1 (1968); O. Dragoun, Z. Platjner, and F. Schmutzler, Nuclear Data Tables A9, 119 (1971).

7. L. C. Biedenharn and M. E. Rose, Rev. Mod. Phys. 25, 729 (1953).

8. B. Ahlesten and A. Bäcklin, Nucl. Phys. A154, 303 (1970); L. Grodzins, R. R. Borchers, and G. B. Hagemann, Nucl. Phys. 88, 474 (1966).

9. D. Ashery, A. E. Blaugrund, and R. Kalish, Nucl. Phys. 76, 336 (1966).

10. M. Kontani and J. Itoh, J. Phys. Soc. Japan 22, 345 (1967).

11. P. A. Moskowitz, C. H. Lin, G. Fulop, and H. H. Stroke, Phys. Rev. C4, 620 (1971).

12. Nuclear Data Sheets, NRC 61-4-94.

13. A. Arima and H. Horie, Progr. Theor. Phys. 12, 623 (1954).

14. K. H. Maier, J. R. Leigh, and R. M. Diamond, Nucl. Phys. A176, 497 (1971).

MAGNETIC MOMENT OF THE 12$^-$ ISOMER OF ^{196}Au*

F. Bacon, G. Kaindl,† H.-E. Mahnke,‡ and D. A. Shirley

High-spin isomers with large magnetic moments and long lifetimes are especially suitable for the technique of thermal equilibrium nuclear orientation. Using the induced large hyperfine fields in iron, high saturation of the nuclear polarization can be easily reached.[1] Thus, the determination of the magnetic hyperfine interaction from the temperature dependence of the γ-ray anisotropy becomes independent of uncertainties in factors influencing the

absolute magnitude of the anisotropy. This technique was applied to a measurement of the magnetic moment of the 12^- isomer of ^{196}Au ($T_{1/2}$ = 9.7 h) to test the interpretation as $[\pi h_{11/2}, \nu i_{13/2}]12^-$ shell-model configuration.[2]

The carrier-free ^{196m}Au activity was produced by the ^{196}Pt(d, 2n) reaction with 18-MeV deuterons on isotopically enriched platinum foils and subsequent ethyl acetate-HCl solvent extraction.[3] Thereafter, the ^{196m}Au was electroplated in high-parity iron or nickel foils already containing carrier-free ^{60}Co used for thermometry. Foils of ^{196m}Au ^{60}Co Fe (or Ni) were then made from the electroplated foils by melting, rolling, and annealing. These foils were contact-cooled by the copper fins of an adiabatic demagnetization apparatus, which used cerium magnesium nitrate, to temperatures in the 8 millidegree K range. Polarization was obtained by applying a 4-kOe field parallel to the plane of the foil.

During the warmup period of the foils, counting data for the 148- and 188-keV γ rays of ^{196m}Au and the ^{60}Co γ rays were measured at 0- and 90- degree angles relative to the polarizing field with high-resolution Ge(Li) detectors. After background and decay corrections, a least-squares fit of the data to the angular distribution function[1]

$$W(\theta) = 1 + \sum_{k=2,4} B_k U_k F_k Q_k P_k(\cos\theta)$$

gave the results for the magnetic hyperfine interaction, μH, listed in Table I. The ratio of the magnetic hyperfine interactions for iron and nickel agree within error with the ratio of the hyperfine field of ^{197}Au in iron and nickel.[4]

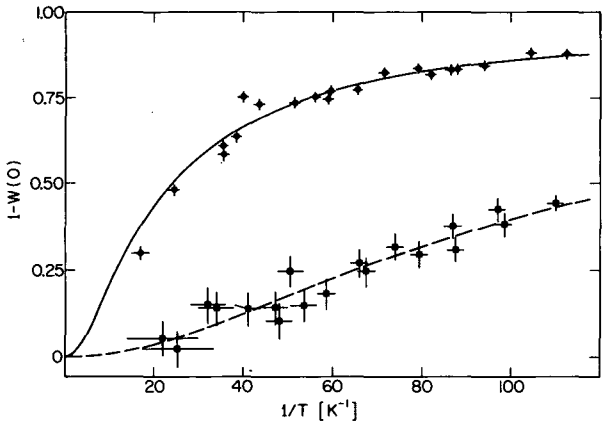

Fig. 1. Temperature dependence of 1 - W(0) for the 148-keV γ rays of ^{196m}AuFe (circles) and ^{196m}AuNi (squares). (XBL 719-4341)

Figure 1 shows the temperature dependence of 1 - W(0) for the 148-keV γ rays for ^{196m}AuFe (circles) and ^{196m}AuNi (squares). The solid curve is the result of a least-squares fit with two free parameters, the hyperfine interaction and an amplitude factor, to the anisotropy data. Whereas the dashed curve, the ^{196m}AuNi data, is a one-parameter fit of μH with the amplitude factor fixed from the ^{196m}AuFe fit. The different procedure was necessary because, in the latter case, saturation is not fully reached and therefore the two parameters would be completely correlated. The importance of reaching full saturation is thus clearly demonstrated.

A value for the magnetic moment of the 12^- state can be determined from the measured values of μH by taking into account the hyper-

Table I. Summary of experimental results for two different samples of ^{196m}Au(Fe) (a and b) and one sample of ^{196m}Au(Ni), obtained from the temperature dependence of the anisotropy of the 148-keV γ rays.

Host lattice	θ (deg)	$\lvert\mu H\rvert$ [10^{-18} erg]	$\lvert\mu H\rvert_{average}$ [10^{-18} erg]
Fe	0 (a)	31.8 ± 1.6	
Fe	90 (a)	27.3 ± 3.1	30.6 ± 1.2
Fe	0 (b)	30.0 ± 2.4	
Ni	0	6.0 ± 0.4	
			6.4 ± 0.4
Ni	90	7.4 ± 0.7	

fine anomalies known to exist for other gold isotopes.[5-7] Using the Bohr-Weisskopf theory[8] extended to odd-odd nuclei, we find that the calculated anomalies, $^{196m}\Delta^{197} = -12.2\%$ and $^{196m}\Delta^{198} = -2.3\%$, agree to within 20% with the measured ones for ^{196,197,198}Au. From the measured hyperfine field of ^{197}Au and ^{198}Au in iron,[4] the corrected values for the magnetic moment lead to a weighted average value of $\mu = \pm 5.35 \pm 0.20$ n.m. for the 12^- state. Theoretically, this state should have the shell-model configuration $(\pi h_{11/2}, \nu i_{13/2})\, 12^-$.[2] The magnetic moment of such a state is easily calculated. The proton contribution to the nuclear moment can be calculated following the spin polarization procedure of Arima and Horie[9] which yields $\mu = 6.7$ n.m. The neutron configuration as an $i_{13/2}$ state is experimentally well established and we take the measured moment of ^{195m}Hg ($\mu = 1.03$ n.m.[10]) for its contribution. One then gets the coupled moment for this configuration as $\mu = 5.67$ n.m., in good agreement with the measured value, assuming the positive sign. The experimental value for the magnetic moment of the 12^- state therefore provides strong evidence for the correctness of the assumed shell-model configuration.

We wish to thank Mrs. Winifred Heppler for preparing the carrier-free gold activity.

Footnotes and References

*Condensed from Phys. Letters 37B, 181 (1971).

†Miller Fellow, 1969-1971.

‡NATO Fellow on leave from the Hahn-Meitner Institute, Berlin, Germany.

1. D. A. Shirley, Ann. Rev. Nucl. Sci. 16, 89 (1966).

2. A. H. Wapstra, P. F. A. Goudsmit, J. F. W. Jansen, J. Konijn, K. E. G. Lobner, G. J. Nijgh, and S. A. de Wit, Nucl. Phys. A93, 527 (1967).

3. J. F. Emery and G. W. Leddicotte, Nucl. Sci. Series, NAS-NS 3036 (1961).

4. T. A. Koster and D. A. Shirley, Table of Hyperfine Fields, UCRL-20411 (1970).

5. P. A. Vanden Bout, V. J. Ehlers, W. A. Nierenberg, and H. A. Shugart, Phys. Rev. 158, 1078 (1967).

6. R. A. Fox and N. J. Stone, Phys. Letters 29A, 341 (1969).

7. S. G. Schmelling, V. J. Ehlers, and H. A. Shugart, Phys. Rev. C2, 225 (1970).

8. A. Bohr and V. F. Weisskopf, Phys. Rev. 77, 94 (1950).

9. A. Arima and H. Horie, Progr. Theor. Phys. 12, 623 (1954).

10. P. A. Moskowitz, C. H. Lin, G. Fulop, and H. H. Stroke, Phys. Rev. C4, 620 (1971).

SPIN AND MAGNETIC MOMENT OF THE 18.7-h ISOMER OF ^{200}Au

F. Bacon, G. Kaindl,* H.-E. Mahnke,† and D. A. Shirley

It has been suggested that the recently discovered 18.7-h isomer of ^{200}Au[1] is analogous to the 12^- state of ^{196}Au on which we reported earlier.[2] We used nuclear orientation techniques combined with NMR-ON to test this assumption by determining the spin and magnetic moment of ^{200m}Au.

The ^{200}Au isomer was produced by the ^{198}Pt(α, pn) reaction with 35-MeV α particles on a Pt metal target containing ^{198}Pt in an enrichment of 44.4%. Samples of ^{200m}Au in iron and nickel were prepared in a similar way as described in Ref. 2, in which we also gave a description of the experimental setup and procedure used for measuring nuclear orientation. For the NMR-ON experiment an rf field was applied to the sample perpendicular to the external magnetic field.

The anisotropy as a function of temperature was measured for the six strongest γ lines (181, 256, 368, 498, 580, and 760 keV) following the β decay of ^{200m}Au. As a typical example, Fig. 1 shows the temperature dependence of the anisotropy of the 368-keV γ transition of ^{200m}Au(Fe) (circles) and ^{200m}Au(Ni) (squares). The solid lines represent least-squares fit of the data by

$$W(\theta) = 1 + \sum_{k=2,4} U_k F_k B_k Q_k P_k(\cos\theta).$$

Since very little is known about the multipolar-

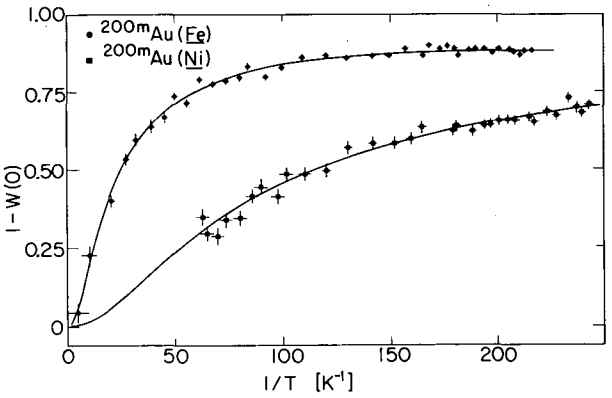

Fig. 1. Temperature dependence of 1 - W(0) for the 368-keV γ rays of ^{200m}Au(Fe) (circles) and ^{200m}Au(Ni) (squares).
(XBL 7112-4965)

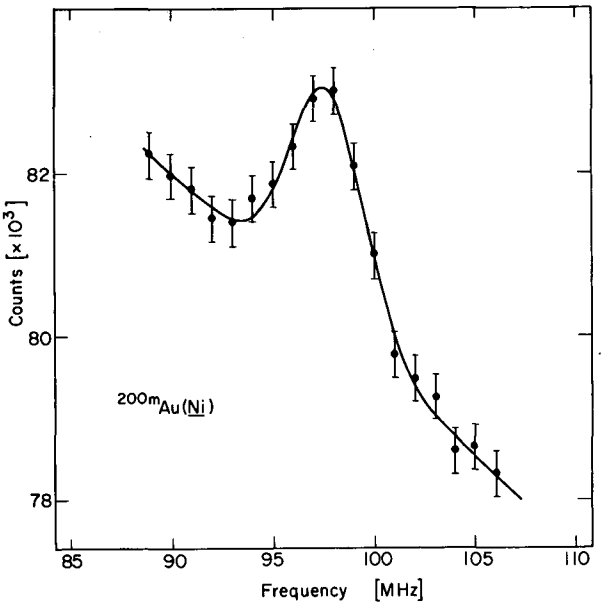

Fig. 2. Frequency dependence of the summed intensity of the 498-, 580-, and 760-keV γ rays of ^{200m}Au(Ni) observed along the external field H_{ext} = 1 kOe. (XBL 7112-4963)

ities of the transitions involved, the products $U_k F_k$ (k = 2, 4) were determined by fitting 0° and 90° spectra of ^{200m}Au(Fe) simultaneously. With these values of $U_k F_k$ the fit procedure for the nickel data assuming various spin values yielded the hyperfine interaction μH_{eff} for ^{200m}Au(Ni) given in column 2 of Table I.

Figure 2 shows the result of the NMR-ON experiment on ^{200m}Au(Ni). The summed counting rate of the 498-, 580-, and 760-keV γ rays observed along the external field is plotted versus the rf field was frequency modulated with 100 Hz over a bandwidth of 1 MHz and had an amplitude of 0.5 mOe. The resonance frequency was determined to be

$$\nu = \frac{\mu H_{eff}}{\mu I} = 97.7 \pm 0.2 \text{ MHz}.$$

No resonance was detected with the modulation frequency switched off, ruling out the possibility of a warming up of the sample by a coil resonance. Agreement between the NMR-result ($\mu H_{eff}/I$) and the value of the hyperfine interaction (μH_{eff}) determined from the anisotropy data is obtained only for a spin I = 12 (see column 3 of Table I).

With the recently measured hyperfine field for ^{198}Au in Ni $H_{hf} = -(262.5 \pm 1.3)$ kOe,[3] we derive a value for the magnetic moment of the isomeric state of ^{200}Au of

$$\mu = \pm 5.86 \pm 0.03 \text{ n.m.}$$

The agreement in spin and magnetic moment [$\mu(^{196m}\text{Au}) = (+) 5.35 \pm 0.20$ n.m.[2]] strongly supports the suggested analogy to the 12^- isomeric state of ^{198}Au.

Table I. Summary of fit results for μH_{eff} obtained from the anisotropy curves for ^{200m}Au(Ni), assuming various values for the spin of the isomeric state.

I	μH_{eff} (10^{-18} erg)	$(\mu H)_{NO}/(\mu H)_{NMR}$
11	7.73 ± 0.23	1.073 ± 0.030
12	7.81 ± 0.23	0.995 ± 0.030
13	7.89 ± 0.23	0.934 ± 0.030

Footnotes and References

*Miller Fellow, 1969-1971.

†NATO-Fellow on leave from Hahn-Meitner Institute, Berlin, Germany.

1. K. Sakia and P. J. Daly, Nucl. Phys. A118, 361 (1968).

2. F. Bacon, G. Kaindl, H.-E. Mahnke, and D. A. Shirley, Phys. Letters 37B, 181 (1971) and this report.

3. F. Bacon, G. Kaindl, H.-E. Mahnke, and D. A. Shirley, to be published.

A TEMPERATURE-INDEPENDENT SPIN-LATTICE RELAXATION TIME IN METALS AT VERY LOW TEMPERATURES*

F. Bacon, J. A. Barclay,† W. D. Brewer,‡ D. A. Shirley, and J. E. Templeton§

Nuclear magnetic resonance in oriented nuclei (NMR/ON), in which resonance is detected through the distribution of nuclear radiations, was suggested by Bloembergen and Temmer[1] and first observed in nuclei oriented by thermal equilibrium methods by Matthias and Holliday.[2] It was used to study relaxation in ferromagnetic metals,[3] a phenomenon that has also been studied by nonresonant methods.[4]

In 1964 Cameron et al.[5] suggested that, for nuclei relaxing in a metal through interaction with conduction electrons, the spin-lattice relaxation time T_1 will approach a constant value at temperatures low enough that the magnetic quantum γH is larger than kT. This effect was observed by Brewer et al., who reported it in abbreviated form in 1968.[6] A summary of a detailed theoretical discussion of this result is given below.

Let us assume that spin-lattice relaxation occurs via an interaction with the conduction electrons, of the form

$$A\vec{I}\cdot\vec{S} = AS_zI_z + \frac{A}{2}[S_+I_- + S_-I_+], \quad (1)$$

and that first-order perturbation theory is applicable. Here $\vec{S}$ is an effective electron-spin operator that can be related to either the orbital or spin operator of conduction electrons, or to both. The discussion below is quite general, requiring only that the nuclei relax by exchanging energy with a degenerate Fermi gas, via magnetic dipole transitions. If the nuclear energy levels are equally spaced by $h\nu$ and the $|m=-I\rangle$ state lies lowest, we may write for the transition probabilities between states $|m\rangle$ and $|m+1\rangle$

$$W_{m,m+1} = B\left|\langle m+1|I_+|m\rangle\right|^2 \times \int_0^\infty f(\epsilon)\,[1-f(\epsilon-h\nu)]\,d\epsilon,$$

$$W_{m+1,m} = B\left|\langle m|I_-|m+1\rangle\right|^2 \times \int_0^\infty f(\epsilon)\,[1-f(\epsilon+h\nu)]\,d\epsilon. \quad (2)$$

Here B is a constant that contains various numerical factors including the density of states at the Fermi energy, and $f(\epsilon)$ is the Fermi-Dirac distribution function

$$f(\epsilon) = [e^{(\epsilon-\epsilon_F)/kT_L}+1]^{-1},$$

where L denotes the lattice. After evaluating the matrix elements and the integrals we find

$$W_{m,m+1} = Bh\nu\,[I(I+1) - m(m+1)/[e^{x_L}-1],$$

$$W_{m+1,m} = Bh\nu[I(I+1) - m(m+1)/[1-e^{-x_L}], \quad (3)$$

where $x_L = h\nu/kT_L$. It is easily shown, by choosing $I=1/2$, substituting into Eq. (3), and comparing with the rate equations in the high-temperature limit, that $B=(2kC)^{-1}$, where C is the high-temperature Korringa constant ($T_1T = C$).

The appearance of the Bose-Einstein distribution function $1/[e^{x_L}-1]$ in $W_{m,m+1}$ suggests that the above transition probabilities should possess an interesting analogy with the radiation problem. Of course this is also expected because the states $|m\rangle$ and $|m+1\rangle$ could be connected by the emission and absorption of photons. We can rewrite $W_{m+1,m}$ as follows:

$$W_{m+1,m} = (h\nu/2kC)[I(I+1)-m(m+1)][1/(e^{x_L}-1)+1]$$
$$= W_{m,m+1} + (h\nu/2kC)[I(I+1)-m(m+1)].$$

Thus the downward transition probability

contains two parts, a temperature-dependent part which is equal to the upward probability (in analogy to stimulated emission and absorption) and a temperature-independent part, analogous to spontaneous emission. Here temperature plays a role analogous to the occupation of the radiation field in photon processes. The appearance of stimulated and spontaneous transition probabilities is in fact a general property of transitions whose quanta of excitation obey Bose statistics and are thus more likely to enter states that are already occupied. That the quanta exchanged in magnetic relaxation obey Bose statistics is clear not only from Eq. (3) but from the fact that a relaxation process is accompanied by a conduction electron spin-flip, i.e., an "excitation" of spin 1. This is even more apparent in the case of quadrupole relaxation, in which relaxation processes are accompanied by emission or absorption of lattice phonons that clearly obey Bose statistics. At absolute zero there are no more lattice phonons to absorb, but a nucleus can still relax by exciting a phonon; i.e., spontaneous emission remains.

It is useful to define a set of parameters $\{p_m\}$ that measure the deviation of the diagonal density-matrix elements ρ_m from their equilibrium values ρ_m^0,

$$p_m = \rho_m - \rho_m^0 .$$

Since $\dot{\rho}_m = 0$ at equilibrium, the master equation may be written

$$\dot{p}_m = \sum_n (p_n W_{nm} - p_m W_{mn} . \qquad (4)$$

Under the $(A/2)[S_+ I_- + S_- I_+]$ interaction, only transitions to the states $n = m \pm 1$ are allowed. It is instructive to regard $\dot{p}_m$ and p_m as components of $(2I+1)$-dimensional vector with entries labeled in the order $m = I, I-1, \cdots -I$ (or we can use the corresponding label λ which runs from zero to $2I$). Then Eq. (4) can be written

$$\vec{\dot{p}} = \overline{\overline{F}}\, \vec{p}, \qquad (5)$$

where $\overline{\overline{F}}$ is a "tridiagonal" matrix with nonzero elements:

$$F_{mm} = W_{m,m-1} + W_{m,m+1} = -W\{[I(I+1) - m(m-1)] + [I(I+1) - m(m+1)]\, e^{-x_L}\},$$

$$F_{m-1,m} = W_{m,m-1} = W[I(I+1) - m(m-1)],$$

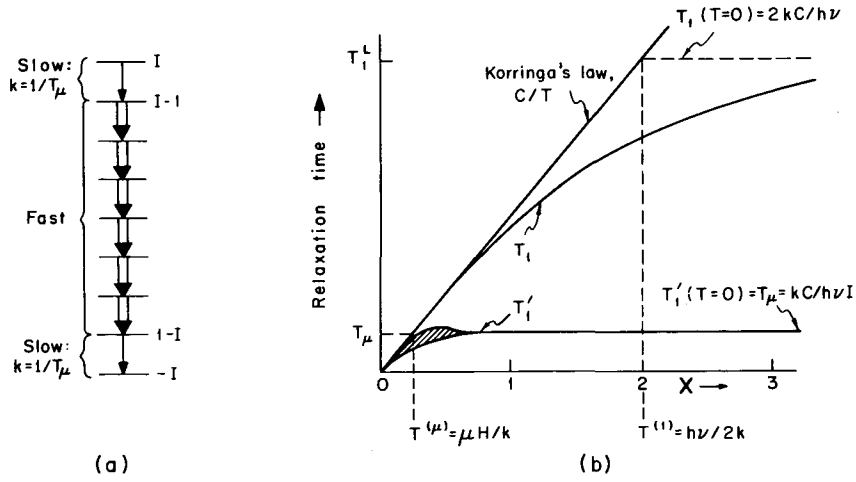

Fig. 1. Comparison of relaxation time T_1 and T_1'. Diagram (a) at left represents relative rates of transitions between levels, showing "bottleneck" effect of slower rates between topmost and bottommost pairs of levels, which leads to an effective relaxation time close to T_μ at relatively high temperatures. Diagram (b) at right shows temperature behavior of T_1 and T_1', illustrating the saturation of the latter at a relatively high-temperature $T^{(\mu)}$. By similar triangles one sees that $T^{(\mu)}/T^{(1)} = 2I$.

(XBL 714-3374)

$$F_{m,m-1} = W_{m-1,m} = W[I(I+1) - m(m-1)]e^{-x_L}.$$

Here $W = h\nu[2kC(1-e^{-x_L})]^{-1}$. The factor e^{-x_L} in the "upward" transitions assures that detailed balance obtains at equilibrium.

The general solution of Eq. (5) has the form

$$\vec{p}(t) = e^{-\overline{\overline{F}}t}\,\vec{p}(0). \qquad (6)$$

If $\overline{\overline{F}}$ has orthonormalized eigenvectors $\vec{\eta}^{(\lambda)}$ and corresponding eigenvalues k_λ ($\lambda = 0\ 1 \cdots 2I$), then a matrix $\overline{\overline{U}}$ with columns of the eigenvectors $\eta^{(\lambda)}$ diagonalizes $\overline{\overline{F}}$:

$$\overline{\overline{U}}^{-1}\,\overline{\overline{F}}\,\overline{\overline{U}} = \overline{\overline{K}}, \quad \text{where } \overline{\overline{K}}_{\lambda m} = k_\lambda \delta_{\lambda m}.$$

Using $\overline{\overline{U}}$, Eq. (6) can be rewritten as

$$\vec{p}(t) = \overline{\overline{U}}\, e^{-t\overline{\overline{K}}}\, \overline{\overline{U}}^{-1}\, \vec{p}(0), \qquad (7)$$

or, in component form,

$$p_m(t) = \sum_\lambda \overline{\overline{U}}_{m\lambda}\, e^{-k_\lambda t} \sum_{m'} \overline{\overline{U}}^{-1}_{\lambda m'}\, p_{m'}(0). \qquad (8)$$

At very low temperatures $x_L \to \infty$, $Q \to 0$ and $\overline{\overline{F}}$ approaches the limiting form

$$\overline{\overline{F}}_{LT} = -\frac{h\nu}{kC} \begin{pmatrix} I & 0 & & & & & \\ -I & 2I-1 & 0 & & & & \\ & 1-2I & 3I-3 & \ddots & & & \\ & & \ddots & \ddots & 0 & & \\ & & & & 1-2I & I & 0 \\ & & & & & -I & 0 \end{pmatrix}.$$

The matrix $\overline{\overline{F}}_{LT}$ is singular, and thus non-diagonalizable. The roots k_λ of its characteristic equation $|\overline{\overline{F}}_{LT} - k_\lambda \overline{\overline{I}}| = 0$ may be used, however, to find the limiting values of the eigenvalues of the general transition matric $\overline{\overline{F}}$ at low temperatures. These roots are simply the diagonal elements of $\overline{\overline{F}}_{LT}$. Thus the low-temperature limiting decay constants are, for integral I: 0 (appearing once), $I(h\nu/kC)$, $(2I-1)(h\nu/kC)$, $\cdots$ $\frac{I(I+1)}{2}(h\nu/kC)$ (each appearing twice). The two smallest nonzero rate constants, having the values $h\nu I/kC$ will tend to determine the rate of change of all observables

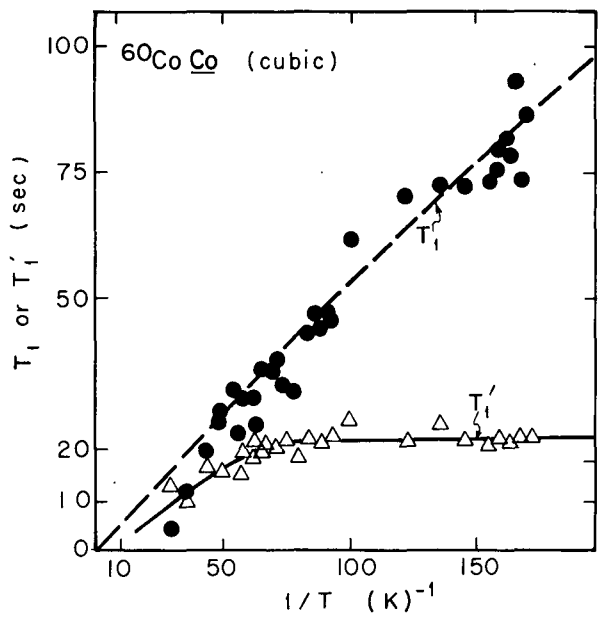

Fig. 2. Relaxation data for ^{60}CoCo at low temperature. The multiexponential fit T_1 points are indicated by circles. The single-exponential fit T_1' points are shown as triangles. The dashed curve shows the expected hyperbolic tangent dependence of T_1. The solid curve is simply an empirical curve drawn through the T_1' data. (XBL 714-3378)

as the lattice temperature approaches absolute zero, provided that secular equilibrium is established. In most practical experimental situations the initial conditions will lead to secular equilibrium rather quickly, and T_1', as obtained from a single-exponential analysis, will closely approach its low-temperature limiting value

$$\lim_{T \to 0} T_1' = kC/h\nu I \equiv T_\mu$$

at a relatively high temperature. We shall call T_μ the magnetic spin-lattice relaxation time. In the low-temperature limit T_μ plays a role which is similar to, but more general than, that of T_1 in the high-temperature limit.

The physical situation is depicted in Fig. 1. The experimental realization of a constant T_1' is illustrated for the typical case of ^{60}Co in a lattice of cubic cobalt in Fig. 2.

Footnotes and References

*Condensed version from Phys. Rev. 5B, 2397 (1972).

†Present address: Department of Physics,

Monash University, Clayton, Victoria, Australia.

‡Present address: 1. Physikalisches Institute, Freie Universität Berlin.

§Present address: Oxford Instrument Corp., 100 Cathedral St., Annapolis, Maryland 21401.

1. N. Bloembergen and G. M. Temmer, Phys. Rev. 89, 883 (1953).

2. E. Matthias and R. J. Holliday, Phys. Rev. Letters 17, 897 (1966).

3. J. E. Templeton and D. A. Shirley, Phys. Rev. Letters 18, 240 (1967).

4. See, e.g., N. J. Stone, A Review of Recent Developments in Low Temperature Nuclear Orientation, Hyperfine Interactions in Excited Nuclei, edited by G. Golding and R. Kalish (Gordon and Breach, 1971).

5. J. A. Cameron, I. A. Campbell, J. P. Compton, and R. A. G. Lines, Phys. Letters 10, 24 (1964).

6. W. D. Brewer, D. A. Shirley, and J. E. Templeton, Phys. Letters 27A, 81 (1968).

THE INTERNAL MAGNETIC FIELD OF MERCURY IN NICKEL

H.-E. Mahnke*

Magnetic hyperfine fields at mercury in ferromagnetic host metals have already been determined using time-integral perturbed angular correlation techniques (IPAC).[1] The determination of the effective field (H_{eff}) in an IPAC experiment, however, is based on the assumption that the angular correlation measured, e.g., in diamagnetic surroundings, is perturbed only by H_{eff} and is not attenuated by other processes; also, such field values only represent averages with respect to time and lattice location. Therefore time-differential (DPAC) measurements not only improve the accuracy but also check the assumptions on which the interpretation of an IPAC result is based.

The DPAC experiment was performed on the 2.4-nsec state in ^{199}Hg in nickel using the $3/2^-$(50 keV)$5/2^-$(158 keV)$1/2^-$ γ-ray cascade which follows the β^- decay of ^{199}Au. The $5/2^-$ state has one of the shortest half-lives ever used for time-differential studies. Carrier-free ^{199}Au activity was obtained in the standard ethyl acetate separation from neutron-activated Pt, and was electroplated onto nickel. Foils prepared from melted samples were magnetized between the pole tips of a permanent magnet (H_{ext} = 2 kOe).

Figure 1 shows a typical modulation spectrum measured with a 4-detector system. The solid line represents a least-squares fit of the data by $R(t) = a + b \cos 2(\theta - \omega_L t)$. The Larmor period was determined as

$$T_L = 25.8 \pm 1.3 \text{ nsec.}$$

Using the known g factor of $g = +0.404 \pm 0.032$[2,3] hyperfine field for mercury in nickel, corrected for H_{ext}, of

$$H_{hf} = -(124 \pm 12) \text{ kOe}$$

is derived, where the negative sign was confirmed by measuring a modulation spectrum with 135° detector geometry. Actually the g factor of the 2.4-nsec state was determined in a time-integral PAC experiment using ^{199}Tl(Au) sources;[3] but since the angular correlation coefficients were determined in the same source, possible systematic errors were avoided. The amplitude of the observed modulation agrees with an estimated value based on the angular correlation coefficients for the γ-γ cascade and the experimental factors like solid angle and time resolution which reduced the ideal angular correlation appreciably. It

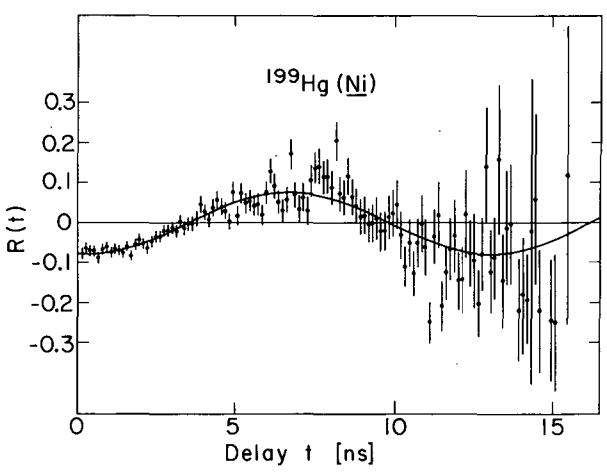

Fig. 1. Spin precession spectrum of ^{199}Hg ($5/2^-$ state) in nickel. (XBL 7112-4966)

can therefore be concluded that all mercury nuclei produced in the ^{199}Au decay are affected by the same field and that this field is associated with the substitutional position in the nickel lattice.

Footnote and References

*NATO Fellow, 1970-1972.

1. F. C. Zawislak, D. D. Cook, and M. Levanoni, Phys. Letters 30B, 541 (1969).

2. V. S. Shirley, in Hyperfine Interactions in Excited Nuclei, edited by G. Goldring and R. Kalish (Gordon and Breach 1971), p. 1255.

3. L. Grodzins, R. W. Bauer, and H. H. Wilson, Phys. Rev. 124, 1897 (1961).

ON THE INFLUENCE OF MOLECULAR GEOMETRY, ORIENTATION, AND DYNAMICS ON ANGULAR CORRELATION PATTERNS FROM ROTATIONALLY LABELED MACROMOLECULES*

D. A. Shirley

In order to determine the sensitivity of gamma-ray angular correlation patterns from solute macromolecules labeled with "rotational tracers" such as ^{111m}Cd, a theoretical study was made of the behavior expected under certain conditions. A nucleus of spin 5/2, acted upon by an axially symmetric electric field gradient, and bound to a rod-like macromolecule, was considered. Under static conditions (no molecular rotation), the time-dependent correlation pattern is quite sensitive to molecular orientation and, for oriented molecules, to the angle between the axis of the field-gradient tensor and the molecular axis. A general equation and results for selected geometric configurations are given. When molecular rotation is allowed, a classical model is applicable if the rotation is sufficiently slow. This model is used to calculate relaxation curves for several geometrical configurations under the condition that the macromolecules rotate about their long axes. These curves are found to have considerable diagnostic value.

Let us consider a system, such as a macromolecule in solution, that is labeled with a nucleus bound to a specific site such that it experiences quadrupole coupling. We assume further that the nucleus decays from an initial nuclear level to an intermediate level of spin I, emitting a γ quantum (γ_1). While in this intermediate level the nucleus interacts with extranuclear fields. The interaction, described by a hyperfine-structure Hamiltonian K, starts acting at the instant of formation of the intermediate level (time t = 0) and continues to act until this level decays by emission of the second γ quantum (γ_2). The nuclear mean-life τ_N is usually in the 10^{-8}–10^{-6} sec range in cases for which the rotational tracer method is most useful. Both γ_1 and γ_2 are detected and recorded, as is the time interval between their emission. The three processes involving the intermediate level—formation, perturbation, and decay—are separable. The angular correlation between the two quanta γ_1 and γ_2, emitted in the directions $\vec{k}_1$ and $\vec{k}_2$, respectively, is given by

$$W(\vec{k}_1, \vec{k}_2, t) = \frac{e^{-t/\tau_N}}{4\pi\tau_N}\left[1 + A_{22}\Gamma_2(\vec{k}_1, \vec{k}_2, t)\right], \quad (1)$$

where the response function $\Gamma_2(k_1, k_2, t)$ has the form

$$\Gamma_2(\vec{k}_1, \vec{k}_2, t) = \sum_q \sum_m \begin{pmatrix} I & I & 2 \\ m'-m & & q \end{pmatrix}^2 \times e^{3i(m^2-m'^2)\omega_Q t}\, Y_2^q(\theta_1, \phi_1)^*\, Y_2^q(\theta_2, \phi_2). \quad (2)$$

Here ω_Q is the fundamental quadrupole frequency.

For I = 5/2, the explicit expression for the response function is

$$\Gamma_2(k_1, k_2, t) = \tfrac{1}{4}[3\cos^2\theta_1 - 1][3\cos^2\theta_2 - 1]$$
$$+ 3\cos\theta_1 \sin\theta_1 \cos\theta_2 \sin\theta_2 \sin\theta_2 \cos(\phi_2 - \phi_1)$$
$$\times [\tfrac{2}{7}\cos\omega_0 t + \tfrac{5}{7}\cos 2\omega_0 t] + \tfrac{3}{4}[1 - \cos^2\theta_1]$$
$$\times [1 - \cos^2\theta_2]\cos 2(\phi_2 - \phi_1)[\tfrac{9}{14}\cos\omega_0 t + \tfrac{5}{14}\cos 3\omega_0 t].$$

Here $\omega_0 = 6\omega_Q$, and the z axis is taken along the symmetry direction of the electric field gradient tensor. This will be called the atomic frame, and the Cartesian axes in this frame will be denoted by xyz.

In rotational tracer experiments the tracer

nuclei are bound to macromolecules. We consider cylindrically symmetrical molecules, with the molecular coordinate frame xyz chosen with the symmetry axis along Z. The molecules are taken to be oriented at angle δ with respect to an external field $\vec{E}$, and the angle between Z and z is denoted by β. Two experimental geometries were considered:

$$\vec{E} \parallel \vec{k}_1 = -\vec{k}_2 \quad \text{(Geometry 1')}$$

and

$$\vec{E} \perp \vec{k}_1 = -\vec{k}_2 \quad \text{(Geometry 2')}.$$

The relationships among the directions $\vec{k}_1$, $\vec{E}$, $\vec{Z}$, and $\vec{z}$ are shown for Geometry 2' in Fig. 1. By using the cosine law and averaging over angles, general expressions were derived for the statistical response functions $\bar{\Gamma}_2(t)_{1'}$ and $\Gamma_2(t)_{2'}$. Curves were plotted for four cases:

Case I: $\vec{E} \parallel \vec{Z} \parallel \vec{z}$,

Case II: $\vec{E} \parallel \vec{Z} \perp \vec{z}$,

Case III: $\vec{E} \perp \vec{Z} \parallel \vec{z}$,

Case IV: $\vec{E} \perp \vec{Z} \perp \vec{z}$.

By combining these four cases with Geometries 1' and 2', a total of eight configurations can be constructed. These are designated by the notation I1', I2', etc. The angles describing these eight configurations are set out in Table I.

Table I. Classification of the configurations.

Configuration	β	δ	θ_1	Static curve
I 1'	0	0	0	A
I 2'	0	0	$\pi/2$	B
II 1'	$\pi/2$	0	$\pi/2$	B
II 2'	$\pi/2$	0	$0-\pi$	C
III 1'	0	$\pi/2$	$\pi/2$	B
III 2'	0	$\pi/2$	$0-\pi$	C
IV 1'	$\pi/2$	$\pi/2$	$0-\pi$	C
IV 2'	$\pi/2$	$\pi/2$	$0-\pi$	D

The eight configurations yield only four distinct curves. These curves, labeled A, B, C, and D, have the forms

$$\bar{\Gamma}_2(t)_A = 1,$$

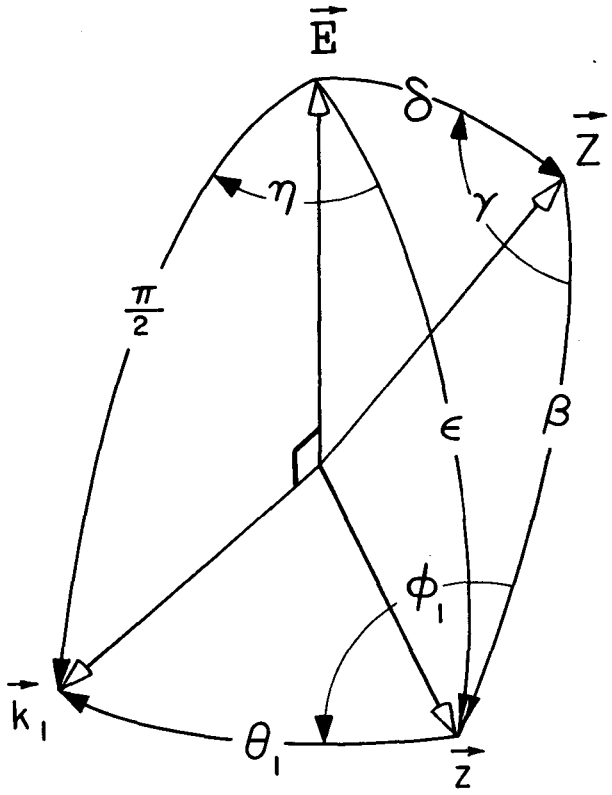

Fig. 1. Geometrical relationship of vectors in Geometry 2'. (XBL 7011-4148)

$$\bar{\Gamma}_2(t)_B = \frac{1}{4} + \frac{27}{56}\cos\omega_0 t + \frac{15}{56}\cos 3\omega_0 t,$$

$$\bar{\Gamma}_2(t)_C = \frac{11}{32} + \frac{129}{448}\cos\omega_0 t + \frac{15}{56}\cos 2\omega_0 t + \frac{45}{448}\cos 3\omega_0 t,$$

$$\bar{\Gamma}_2(t)_D = \frac{49}{256} + \frac{1443}{3584}\cos\omega_0 t + \frac{15}{64}\cos 2\omega_0 t + \frac{615}{3584}\cos 3\omega_0 t.$$

These four curves A through D are distributed among configurations I1' through IV2' as indicated in the last column of Table I. They are plotted in Fig. 2 for intercomparison. In assessing the diagnostic value of $\Gamma_2(t)$, we note that either Geometry, 1' or 2', would suffice to distinguish among Cases I, Cases II or III, and Case IV, but that II and III are undistinguishable.

Further differentiation among the configurations is possible in the long-correlation-time limit. By introduction of a classical (adiabatic) model and the use of random-walk techniques, relaxation curves of the form

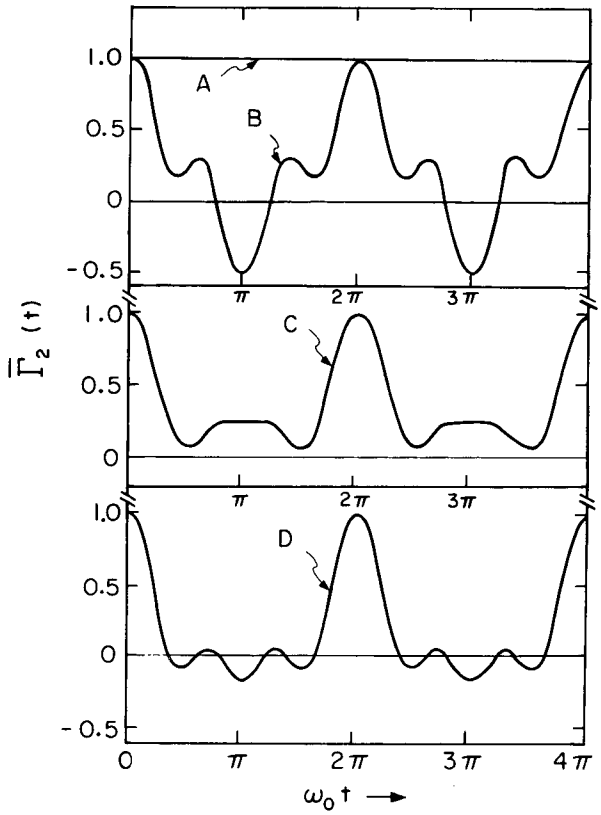

Fig. 2. The curves A through D describing $\Gamma_2(t)$ for statically oriented molecules. (XBL 7011-4151)

$$\bar{\Gamma}_2(t)_{III2'} = \frac{11}{32} + \frac{3}{8} e^{-t/\tau_c}\left[\frac{2}{7}\cos\omega_0 t + \frac{5}{7}\cos 2\omega_0 t\right] + \frac{9}{32} e^{-\frac{4t}{\tau_c}}\left[\frac{9}{14}\cos\omega_0 t + \frac{5}{14}\cos 3\omega_0 t\right],$$

for example, were calculated. These curves

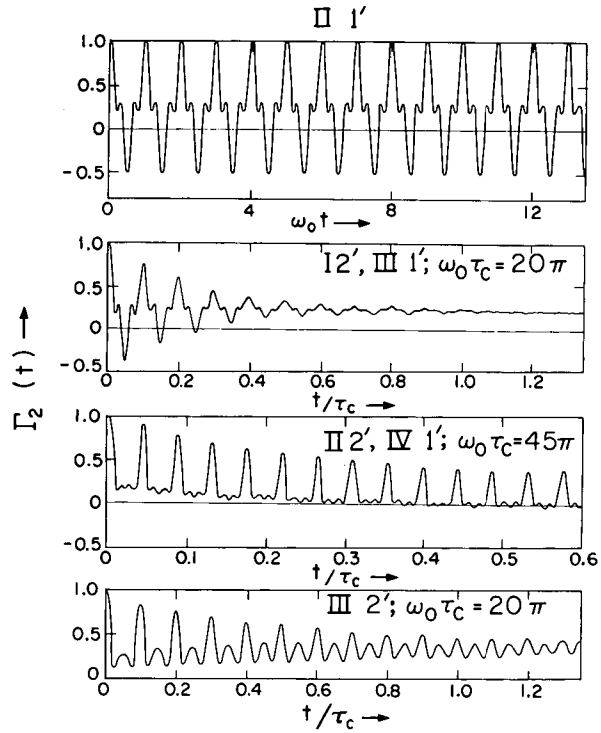

Fig. 3. Relaxation curves for various configurations. (XBL 7011-4149)

are shown in Fig. 3. Their diagnostic value is obvious. Clearly relaxation studies will yield further information about macromolecules. Thus gamma-ray angular correlations appear to hold considerable promise for the elucidation of certain static and dynamic properties of biological systems.

Footnote

* Condensed version of a paper that appeared in J. Chem. Phys. 55, 1512(1971).

K-ELECTRON BINDING ENERGY SHIFTS IN FLUORINATED METHANES AND BENZENES: COMPARISON OF A CNDO POTENTIAL MODEL WITH EXPERIMENT*

D. W. Davis, D. A. Shirley, and T. D. Thomas†

Shifts in 1s electron binding energies can yield valuable information about electronic charge distributions in molecules. The origins of core-level binding-energy shifts are well understood, and the shifts have been interpreted with various degrees of sophistication,[1,2] from valence-bond models to ab initio calculations on hole states.[3] Good correlations between measured shifts and other parameters have been obtained in nearly every case. Until now, however, a hiatus has existed between experiment and theory that has, in most cases, rendered a completely satisfactory interpretation impractical. Only ab initio calculations have yielded quantitative predicted shifts that were both in agreement with experiment and free of empirical parameters. Although it is adequate to use ground state orbital energies from ab initio results together with Koopmans' theorem to predict shifts, the expense of these calculations hampers their use in investigations involving large numbers of sizable molecules. It would be desirable to be able to predict core-level binding-energy shifts from one of the simpler "intermediate-level" molecular orbital approaches, such as the CNDO model.[4]

In this report we describe a possible solution to the above problem. For four fluorinated methanes and six fluorinated benzenes good agreement was obtained within each group between observed shifts in the carbon and fluorine 1s binding-energies and shifts in the electrostatic potentials at the carbon and fluorine nuclei, as calculated from CNDO wave functions. To a good approximation, shifts in the Coulomb potentials experienced by the nuclei and by the 1s electrons are equivalent. Since both CNDO calculations and the integrations required for evaluating the potentials require very little computer time, it appears feasible to predict core-level binding-energy shifts by this method for essentially any case of interest.

The measurements were made as described previously.[5] The calculations were done as follows:

(1) For each molecule a CNDO calculation was carried out, yielding molecular orbitals ψ_i expressed in terms of atomic orbitals ϕ_i, $\psi_j = \sum_i C_{ji} \phi_i$.

(2) The contribution of the occupied valence orbitals of the molecule to the electrostatic potential energy, V, at each carbon and fluorine nucleus was evaluated. The portion of this energy arising from occupied valence orbitals on the parent atom was, in each case, evaluated directly by calculating matrix elements of r^{-1}. The portion arising from the other atoms in each molecule was evaluated in two different ways, each based on CNDO populations: a point charge calculation, and evaluation of r^{-1} integrals by retaining only the diagonal matrix elements between atomic orbitals at the same center. The reason for choosing these approaches will be discussed in a later publication. The numerical results of the two calculations are quite close.

(3) The difference between the binding energies of electrons in 1s orbitals of a given element in two different sites was taken as (minus) the difference between the potential energies V calculated for the two sites, $\Delta E = -\Delta V$. Basch[6] has discussed the validity of this approach.

Theory and experiment are compared in Table I. Agreement within each group (methane derivatives and benzene derivatives) seems to be comparable to that obtained from ground state ab initio calculations.[1,5,7] This is not too surprising, as we have calculated the quantity of interest (ΔE_B) directly, rather than as a small difference between two large energies. There has been other evidence that the CNDO approximation gives orbital populations consistent with observed binding-energy shifts. For example, a plot of binding energies vs CNDO "atomic charges" shows about the right slope.[2] A point-charge analysis based on CNDO populations also shows a good correlation with experiment after suitable empirical parameters were determined by least-squares fitting.[1] The CNDO-potential described here has not been used previously to predict shifts. Schwartz[8] used the same approach with extended-Hückel wave functions, obtaining shifts that were much larger than experiment, in agreement with the well-known fact that the Hückel model exaggerates polarization effects.

Footnotes and References

*From LBL-216 (to be published in Journal of Chemical Physics).

†Present address: Department of Chemistry, Oregon State University, Corvallis, Oregon.

1. K. Siegbahn, C. Nordling, G. Johansson, J. Hedman, P. F. Hedén, K. Hamrin, U. Gelius, T. Bergmark, L. O. Werme, R. Manne, and Y. Baer, ESCA Applied to Free Molecules (North Holland, Amsterdam, 1969).

Table I. Carbon and fluorine 1s electron binding-energy shifts.

Compound	ΔE(carbon 1s), in eV[a]			ΔE(fluorine 1s), in eV[b]		
	Calculated, (point charge)	Calculated, diagonal plus p-p' elements	Experimental[c]	Calculated, (point charge	Calculated, diagonal plus p-p' elements	Experimental[c]
fluorobenzene, C_F[d]	2.30	2.84	2.43(4)	0.07	0.16	-0.04(10)
C_H	0.33*[e]	0.36*	0.39(3)			
o-difluorobenzene, C_F	2.49	2.93	2.87(6)	0.08	0.15	0.33(15)
C_H	0.72*	0.64*	0.72(4)			
m-difluorobenzene, C_F	2.68	3.26	2.92(6)	0.48	0.55	0.26(11)
C_H	0.29*	0.47*	0.70(5)			
p-difluorobenzene, C_F	2.38	2.88	2.74(6)	0.29	0.35	0.26(15)
C_H	0.63	0.65	0.76(4)			
1,3,5-trifluoro-benzene, C_F	3.21	3.85	3.02(9)	0.70	0.91	0.47(13)
C_H	0.50	0.48	0.56(13)			
hexafluorobenzene	3.75	4.45	3.57(9)	1.75	1.82	1.34(10)
methyl fluoride	2.58	2.97	2.8(2)	---	---	---
difluoromethane	4.99	5.58	5.55(5)	1.07	0.82	0.73(5)
fluoroform	7.32	8.54	8.3(2)	2.09	1.60	1.7(2)
carbon tetrafluoride	9.52	11.14	11.0(2)	3.11	2.37	2.6(2)

[a] Carbon shifts in fluorinated methanes and benzenes are referred to methane and benzene, respectively. The two scales disagree by 0.9 eV.

[b] All fluorine shifts are referred to methyl fluoride.

[c] Error in last place given parenthetically.

[d] Here C_F and C_H are carbons directly bonded to fluorine and hydrogen, respectively.

[e] Asterisk denotes weighted average over inequivalent carbons. Experimentally only one C_F and one C_H peak was seen in each case.

2. J. M. Hollander and D. A. Shirley, Ann. Rev. Nucl. Sci. 20, 435 (1970).

3. M. Schwartz, Chem. Phys. Letters 5, 50 (1970).

4. J. A. Pople, D. P. Santry, and G. A. Segal, J. Chem. Phys. 43, S129 (1965).

5. D. W. Davis, J. M. Hollander, D. A. Shirley, and T. D. Thomas, J. Chem. Phys. 52, 3295 (1970).

6. H. Basch, Chem. Phys. Letters 5, 337 (1970).

7. H. Basch and L. C. Snyder, Chem. Phys. Letters 3, 333 (1969(.

8. M. E. Schwartz, Chem. Phys. Letters 7, 78 (1970).

HIGH-RESOLUTION X-RAY PHOTOEMISSION SPECTRUM OF THE VALENCE BANDS OF GOLD*

D. A. Shirley

Electronic band structures are of fundamental importance in understanding properties of metals. A knowledge of the valence-band density of states of a metal can in principle yield considerable information about that metal's band structure. X-ray photoemission experiments, in which valence electrons are ejected from the specimen by photons from a monochromatic source and energy-analyzed in an electron spectrometer, yield spectra that are closely related to the valence-band density of states. The extent to which these photoemission spectra and the density of states can be directly compared is still somewhat uncertain, however.

In this paper the high-resolution x-ray photoemission spectrum is compared with lower-energy photoemission spectra and with band-structure results. The following questions are at least partially answered:

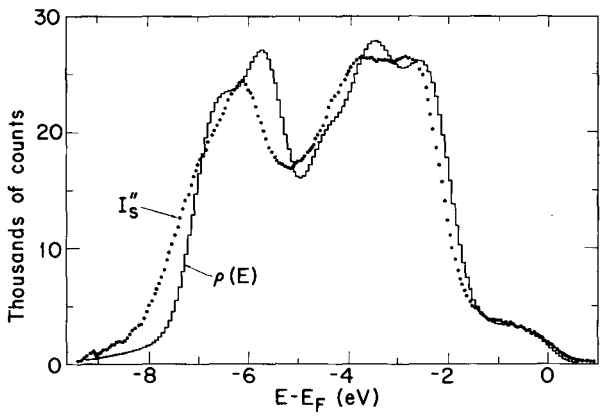

Fig. 1. Comparison of the corrected experimental spectrum I''_S with broadened density-of-states function ρ(E) from the relativistic KKR band-structure calculation of Connolly and Johnson. (XBL 7111-4854)

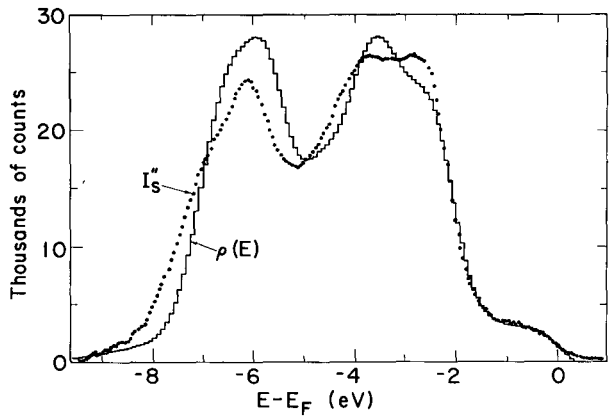

Fig. 2. Comparison of I''_S with broadened density-of-states function ρ(E) from the relativistic APW band-structure calculation of Christensen and Seraphin. (XBL 7111-4857)

(1) Do ultraviolet photoelectron spectroscopy (UPS) results approach x-ray photoelectron spectroscopy (XPS) data as the uv photon energy increases toward the upper end of the readily available energy range (~40 eV)?

(2) It is meaningful to compare XPS spectra directly with valence-band densities of states, or are matrix-element modulation effects so large as to obviate such comparisons?

(3) Can XPS spectra establish the necessity for relativistic band structure calculations in heavy elements?

(4) Are XPS spectra sensitive enough to distinguish critically among different theoretical band-structure calculations?

Table I. Comparison of gold d-band parameters.

Description	ΔE_B(eV)[a]	ΔE_d(eV)[d]	$E_F - E_d$(eV)[c]	Reference
KKR	0.79	5.25[d] (5.18)	1.89[d] (1.93)	3
RAPW	0.54	5.54 (5.58)	1.56 (1.41)	8
RAPW	0.78	4.90 (4.92)	2.21 (2.20)	7
RAPW	0.85	5.07 (5.12)	2.17 (2.04)	4
Interpolation	0.92	5.67 (5.64)	2.34 (2.18)	5
Experiment	---	5.24	2.04	This work

[a] FWHM of Poisson broadening function by which theoretical band-structure histogram were multiplied.

[b] FWHM of d-band.

[c] Energy difference from Fermi level to a point halfway up the higher-energy d-band peak.

[d] Values in parentheses were taken from smoothed curves. Values without parentheses were evaluated before smoothing. Accuracy is 0.1 eV.

A gold single crystal of 99.9% purity was cut to provide samples with (100), (110), and (111) faces. These were polished, etched, and annealed. Spectra were taken, at room temperature and in a sample chamber pumped to about 10^{-7} Torr, on a Hewlett-Packard ESCA spectrometer. This spectrometer employs monochromatized aluminum $K\alpha_{1,2}$ (1486 eV) radiation: it should in principle be possible to reduce the previously obtainable instrumental resolution[1,2] of 1.0 eV by a factor of 2 or more. The observed spectrum in fact shows a definite improvement over earlier spectra.

After background and scattering corrections were made, the results were compared directly with several broadened theoretical density-of-states functions. The following conclusions were drawn: (i) Relativistic band structure calculations are required to fit the spectrum. (ii) Both the KKR calculation of Connolly and Johnson[3] (Fig. 1) and the RAPW calculation by Christensen and Seraphin[4] (Fig. 2) give density of states results that (after broadening) follow the experimental curve closely. (iii) Full Slater exchange is required: fractional (2/3 or 5/6) exchange[5-7] gives d-band densities of states that are far too wide. (iv) Eastman's[8] 40.8-eV ultraviolet photoemission spectrum is similar to the x-ray spectrum, suggesting little dependence on photon energy above 40 eV. (v) Both (ii) and (iv) imply an absence of strong matrix-element modulation in the photoemission spectrum.

Footnote and References

*Condensed version of a paper submitted to Physical Review.

1. C. S. Fadley and D. A. Shirley, J. Res. Natl. Bur. Std. 74A, 543 (1970).

2. Y. Baer, P. F. Hedén, J. Hedman, M. Klasson, C. Nordling, and K. Siegbahn, Physica Scripta 1, 55 (1970).

3. J. W. D. Connolly and K. H. Johnson, MIT Solid State and Molecular Theory Group Report No. 72, 19 (1970) (unpublished); and private communication.

4. N. E. Christensen and B. O. Seraphin, Phys. Rev. B, to be published.

5. N. V. Smith and M. U. Traum, Spin Orbit Coupling Effects in the Ultraviolet and X-Ray Photoemission Spectra of Metallic Gold, in Electron Spectroscopy, edited by D. A. Shirley (North-Holland, Amsterdam, 1972).

6. M. G. Ramchandani, J. Phys. C, Solid State Phys. 3, S1 (1970).

7. S. Kupratakuln, J. Phys. C, Solid State Phys. 2, S109 (1970).

8. D. E. Eastman, Phys. Rev. Letters 26, 1108 (1971).

SPLITTING IN NITROGEN AND OXYGEN 1s PHOTOELECTRON PEAKS IN TWO PARAMAGNETIC MOLECULES: SPIN DENSITY IMPLICATIONS*

D. W. Davis and D. A. Shirley

Multiplet splitting of core-level peaks in x-ray photoelectron spectra, arising from exchange interactions between unpaired core and valence electrons, has been reported previously for molecular O_2 and NO[1,2] and for compounds of Mn and Fe.[3,4] In every case the magnitude of the multiplet splitting, ΔE, was found to be in good agreement with approximate theoretical estimates,[5] and it was concluded that the splitting was qualitatively understood. Better theoretical values for ΔE(NO) are now available, however. These values were derived from "frozen orbital" Hartree-Fock calculations on NO itself[6,7] and also from direct Hartree-Fock calculations[7] on the four NO^+ final states that can be formed by removing a single 1s electron from $NO(^2\Pi_{1/2})$. In this note we report high-precision experimental values for ΔE(NO). In addition, values of ΔE are reported for di-t-butylnitroxide. These latter data illustrate the efficacy of x-ray photoelectron spectroscopy in measuring spin density distributions in polyatomic free radicals.

All samples were run as gases on the Berkeley iron-free double-focusing $\pi\sqrt{2}$ spectrometer, as described earlier.[8] The current stepping interval of 0.1mA was equivalent to 0.14 eV for the N 1s peak and 0.13 eV for the O 1s peak. Sufficient data were taken to achieve good statistical accuracy (i.e., up to 6000 counts in the peak channel). At least two spectra were taken for each case, to demonstrate reproducibility. Careful least-squares fits were made, using both Gaussian and Lorentzian peak shapes, in order to extract values of ΔE from the unresolved peaks. The values of ΔE so obtained were essentially independent of the peak shape chosen. They were also insensitive to whether the doublet intensity ratio was fixed at 3 or allowed to vary. The final values, which are quoted in Table I, were all derived from Lorentzian fits, with the intensity ratio fixed at 3. A comparison run on N_2 gas gave a symmetrical N 1s peak of width 0.974 ± 0.025 eV FWHM.

The NO splittings given in Table I show good agreement with the Hartree-Fock final state calculations,[7] which are, however, 0.06 eV (or three standard deviations) low in each case. The frozen orbital calculations[6,7] also give fairly good estimates for ΔE, although the final-state calculations are distinctly favored by our data.

In a free atom whose valence electrons are coupled to spin S, the multiplet splitting of the 1s peak can be estimated as

$$\Delta E = (2S + 1)H_x,$$

where H_x is the 1s electron-valence electron exchange integral. In a free radical the unpaired electrons are bound in molecular orbitals that are distributed over the atoms. In the crudest approximation, using an LCAO basis set and neglecting all two-center integrals (including overlap), the total population of unpaired electrons can be approximately partitioned among the atoms, with a fraction f_i assigned to the ith atom. In this approximation we would expect multiplet splitting

$$\Delta E^i \approx f_i H_x^i (2S+1)$$

for the ith atom. Using this relation, and assuming that $H_x^N \approx H_x^O$, we may infer from Table I that most of the unpaired spin in the $p\Pi$ antibonding orbital of NO is on the N atom. With some refinement, multiplet splittings may give a more direct measure of spin density distributions than do hyperfine structure constants.

The splittings in di-t-butylnitroxide, when compared to those in NO, suggest that the spin density on the oxygen atom is essentially unchanged, but that the N atom loses spin density in the larger molecule, apparently to the alkyl groups. This is not surprising, as the unpaired electron is presumably in a delocalized antibonding orbital. By contrast the large reductions in binding energy of both the N 1s and

Table I. Binding energies and splittings of 1s electrons (in electron volts).

Case[a]	Binding energy	Linewidth (FWHM)	Measured splitting, ΔE	ΔE from final-state calculations	ΔE from frozen orbital estimates		ΔE (expt) hedman et al.
N̲O($^1\Pi$)	411.5(5)[b]	0.93(2)[c]	1.412(16)	1.35[d]	1.23[d]	1.26[e]	1.5
N̲O($^3\Pi$)	410.1(5)						
NO̲($^1\Pi$)	543.6(5)	0.91(2)	0.530(21)	0.48[d]	0.73[d]	0.77[e]	0.7
NO̲($^3\Pi$)	543.1(5)						
dtb N̲O($^1\Pi$)	406.9(5)	1.13(4)	0.539(42)				
dtb N̲O($^3\Pi$)	406.4(5)						
dtb NO̲($^1\Pi$)	536.7(5)						
dtb NO̲($^3\Pi$)	536.2(5)	0.88(3)	0.448(26)				
Methyl C	290.3(5)	1.16(5)					
Tertiary C	291.4(5)						

[a]The atom losing a 1s electron is underlined. Assumed final-state symmetry is denoted parenthetically, and "dtb" means "di-tertbutyl."

[b]Standard deviation in the last digit is given parenthetically. Absolute values of binding energies are accurate to only 0.5 eV.

[c]In fitting each group, linewidths were constrained to be equal.

[d]Ref. 7.

[e]Ref. 6.

the O 1s electrons in di-t-butylnitroxide demonstrate quite conclusively a net flow of electron charge from the alkyl group to the NO group. This conclusion is corroborated by increases in the binding energies of 1s electrons in the tertiary carbon atoms, as compared to the usual values of 290.2 eV for the tertiary alkyl carbon, indicating oxidation of these carbon atoms.

We are indebted to Dr. M. P. Klein for the sample of di-t-butylnitroxide.

Footnotes and References

1. J. Hedman, P. F. Hedman, C. Nordling, and K. Siegbahn, Phys. Letters 29A, 178 (1969).

2. K. Siegbahn, C. Nordling, G. Johansson, J. Hedman, P. F. Hedman, K. Hamrin, V. Gelius, T. Bergmark, L. O. Werme, R. Manne, and Y. Baer, ESCA Applied to Free Molecules (North Holland, Amsterdam, 1969).

3. C. S. Fadley, D. A. Shirley, A. J. Freeman, P. S. Bagus, and J. V. Mallow, Phys. Rev. Letters 23, 1397 (1969).

4. C. S. Fadley and D. A. Shirley, Phys. Rev. A2, 1109 (1970).

5. These estimates, which usually give ΔE as proportional to an exchange integral, are discussed in Refs. 1-4.

6. M. E. Schwartz, Theoretica Chemica Acta 19, 396 (1970).

7. P. S. Bagus and H. F. Schaefer III, to be published in J. Chem. Phys., 1971.

8. D. W. Davis, J. M. Hollander, D. A. Shirley, and T. D. Thomas, J. Chem. Phys. 52, 3295 (1970).

A COMPARISON OF VALENCE-SHELL AND CORE-IONIZATION POTENTIALS OF ALKYL IODIDES

J. A. Hashmall,* B. E. Mills, D. A. Shirley, and A. Streitwieser, Jr.

It has recently been shown that the lone-pair ionization potentials (IPs) of alkyl iodides, bromides, and chlorides correlate well the Taft's σ^* values (as used with the Hammett equation)[1] and even better with each other.[2] Similar correlations have been found between the iodide lone-pair IPs and those of a series of other alkyl substituted groups.[3] Figure 1 plots and Table I lists the iodine $5p_{1/2}$ IPs[2] of a series of alkyl halides as well as the shifts in IP of the iodine $3d_{5/2}$ level (relative to a trifluoromethyl iodide reference) with which we wish to compare them. These latter values were obtained with the Berkeley iron-free spectrometer[4] using Mg Kα x rays (1253.6 eV) on a mixture of sample and reference gases. Figure 2 gives examples of spectra in the best and worst cases.

Inspection of Fig. 1 will indicate that the core $3d_{5/2}$ IP is more sensitive to variations in the alkyl group than is the $5p_{1/2}$ level. This can be understood if one realizes that the change of substituent group results in a change of electron density in the C-I bond and that this bond is, on the average, closer to the $3d_{5/2}$ orbital than to the $5p_{1/2}$, with consequent greater effect on the core level. This is illustrated in Fig. 3.

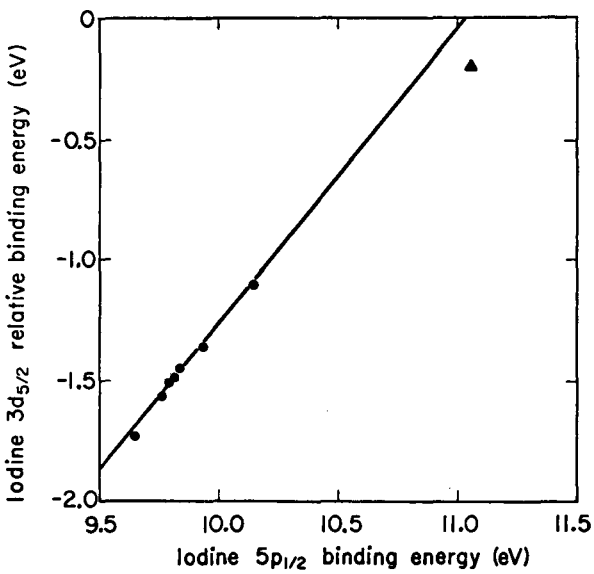

Fig. 1. Relative iodine $3d_{5/2}$ binding energy vs iodine $5p_{1/2}$ binding energy, and least-squares straight line fit (slope = 1.22 ± 0.05) of all points except that for HI (Δ).
(XBL 717-3928)

Table I. Summary of the iodine $5p_{1/2}$ binding energies and relative $3d_{5/2}$ binding energies for alkyl iodides.

R in RI	$5p_{1/2}$ binding energy[a] (eV)	$3d_{5/2}$ chemical shifts[b] (eV)
Methyl	10.14	1.10 ± 0.03
Ethyl	9.93	1.36 ± 0.03
n-propyl	9.83	1.45 ± 0.04
n-butyl	9.81	1.49 ± 0.04
n-pentyl	9.78	1.51 ± 0.03
i-propyl	9.75	1.57 ± 0.03
t-butyl	9.64	1.73 ± 0.05
Hydrogen	11.05	0.20 ± 0.04

[a] All errors ± 0.02 eV.

[b] Relative to trifluoromethyl iodide.

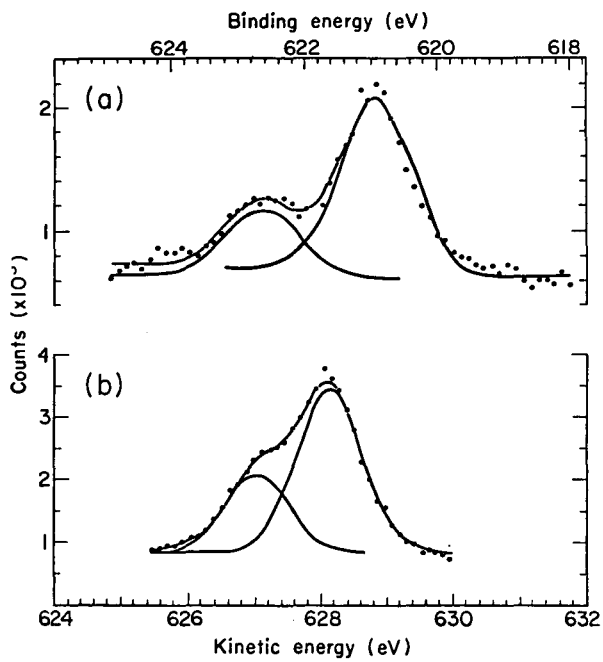

Fig. 2. Resolved photoelectron spectra of iodine $3d_{5/2}$ electrons from trifluoromethyl iodide with (a) tert-butyl iodide and (b) methyl iodide. Radiation was Mg Kα x rays.
(XBL 717-3929)

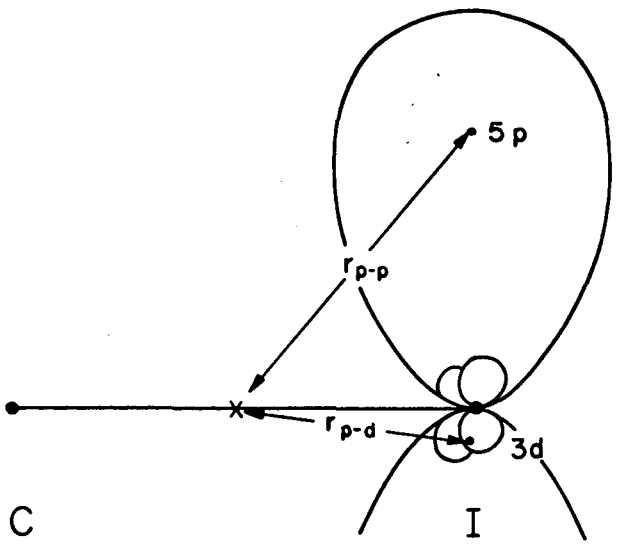

Fig. 3. Diagram of the C-I bond length in relation to the average position of the 5p and 3d electrons. Note that r_{p-p}, the distance between the center of the C-I bond and the expected position of the 5p electron, is considerably longer than r_{p-d}. (XBL 717-3930)

Figure 1 also shows that $5p_{1/2}$ IP of HI is larger than might be predicted from the alkyl results. Indeed, the HI $5p_{1/2}$ binding energy is about 0.14 eV greater than expected because the orbital is unable to hyperconjugate. In the alkyl iodides, hyperconjugation is possible with the σ orbitals of the alkyl group, resulting in destabilization of the iodine 5p levels. This effect is of the same order as that calculated by Brogli and Heilbronner.[5] There is the further implication in the fit of all of the alkyl iodides to a single line that the hyperconjugative interaction with C-C bonds must be approximately the same as with C-H bonds.

The present example demonstrates the unique advantages of using both valence-shell and core photoelectron spectroscopy to elucidate the causes for chemical shifts of ionization potentials. We are continuing our studies of ionization potentials, using these complementary techniques.

Footnote and References

*Present address: Department of Chemistry, Georgetown University, Washington, D. C. 20007

1. R. W. Taft, Steric Effects in Organic Chemistry, edited by M. S. Newman (John Wiley, New York 1956), Chap. 13.

2. F. Brogli, J. A. Hashmall, and E. Heilbronner, Helv. Chim. Acta, in press.

3. B. J. Cocksey, J. H. D. Eland, and C. J. Danby, J. Chem. Soc. (B), 790 (1971).

4. C. S. Fadley, S. B. M. Hagstrom, M. D. Klein, and D. A. Shirley, J. Chem. Phys., 48 (8), 3779 (1968).

5. F. Brogli and E. Heilbronner, Helv. Chim. Acta, in press.

X-RAY PHOTOELECTRON SPECTROSCOPY OF THE FLUORINE K LEVEL IN SIMPLE FLUORIDE COMPOUNDS*

R. G. Hayes† and N. Edelstein

Since x-ray photoelectron spectroscopy came into relatively common use two or three years ago, a rather large number of studies of core-level binding energies in solid compounds has appeared.[1] The primary object of such studies has been the correlation of core-electron binding energies with parameters such as the oxidation state or the charge of the atom bearing the core level. Such correlations have met with some success despite the fact that the binding energy of a core level is known not to be a local property of the system, but depends on attributes of the system away from the atom bearing the core level. It has been shown, from calculations on atoms and small molecules, that the binding energy of a core level can only be calculated accurately from independent calculations of the total energy of the ground state of the system and of the state containing a hole in the core level.[2] Such an elaborate calculation is necessary because the electronic system relaxes on core ionization. It is also known, however, that, at least in some systems, the binding-energy shifts of a core level correlate well with the orbital energies of the core level in the ground state of the various molecules, which means that the change in energy due to relaxation is nearly independent of the system in which the atom with a core vacancy is found.[3] Thus, for a comparison of the energies of a given core hole state among various systems, one may use the orbital energy of the core orbital. Finally, it has been shown, and it is clear

Table I.* Fluoride 1s binding energies, point-charge potentials, and corrected potentials at fluoride sites of various ionic fluorides.

Compound	$E_B(F^-)$ (Au N_{VII} = 94.0 eV)	$E_B - E_B(NaF)$	$V_{P.C.}$	V_{corr}	$V_{corr} - V_{corr}(NaF)$
LiF	686.3	0.9	12.45	8.34	-0.3
NaF	685.4	(0.0)	10.89	8.64	(0.0)
$KMgF_3$[a]	686.5	1.1	11.69	10.86	2.22
MnF_2[b]	686.1	0.7	12.61	11.30	2.66
CaF_2	686.3	0.9	1535	11.01	2.37
SrF_2	685.7	0.3	14.48	12.77	4.13
BaF_2	685.2	-0.2	13.53	10.67	2.03
LaF_3[c]	685.3	-0.1	9.20(I)	2.54	-6.10
			11.29(II)	4.52	-4.12
			8.18(III)	3.28	-5.36
YbF_3[d]	686.7	1.3	10.40(I)	5.58	-3.06
			11.21(II)	6.53	-2.11
UF_4[e]	685.4	0.0	(11.5)	$(9.5-\Delta V_u)$	$0.9-\Delta V_u$

*All units are eV.

[a]Crystal structure from R. W. G. Wycoff, Crystal Structures, Vol. II (John Wiley, New York, 1965), p. 390.

[b]Crystal structure from J. W. Stout and S. A. Read, J. Am. Chem. Soc. 76, 5279 (1954).

[c]Crystal structure from A. Zalkin, D. H. Templeton, and T. E. Hopkins, Inorg. Chem. 5, 1466 (1966).

[d]Crystal structure from A. Zalkin and D. H. Templeton, J. Am. Chem. Soc. 75, 2453 (1953).

[e]Crystal structure from A. C. Larson, R. B. Root, Jr., and D. T. Cromer, Acta. Cryst. 17, 555 (1964).

There are seven distinct kinds of fluorides. Their point-charge potentials range from 11.24 to 12.03 V.

from general agreements, that the dependence of the orbital energy on surroundings is given quite accurately by the electrostatic potential at the nucleus bearing the core level due to all the other nuclei and electrons other than the core electrons of interest.[4] At this point we can discuss attempts to correlate core binding energies with charges. The potential at a nucleus will be proportional to the charge on the atom having that nucleus only if the potential due to the rest of the system is proportional to the charge on the atom in question. Furthermore, the constant of proportionality will be the same for all systems having the atom in question only if the effect on the potential of transferring charge from the atom of interest to the rest of the system is the same for all systems. It is not likely that such would be the case, so one should attempt a more careful analysis of the relationship between core binding energies and charges.

Before discussing the analysis of binding energies in solids further it is well to make some observations about the studv of core binding energies in solid materials. The quantity one would wish to measure is the energy necessary to remove an electron into the vacuum. This quantity is not accessible, however, as has been pointed out.[1] Instead, one can measure the binding energy of the sample with respect to the vacuum level of the spectrometer material or, if one knows the work function of the spectrometer material, with

respect to the common Fermi levels of spectrometer and sample. Since, in a pure insulator, the Fermi level lies in the middle of the gap, the difference in vacuum levels can, in principle, be obtained if the gap is known and if the photoelectric threshold of the insulator is known, as well as the work function of the spectrometer material. These quantities are in general not known. Also the presence of impurities, or of damage centers, in the insulator can move the Fermi level and make the above arguments invalid.

The simplest approach to the analysis of core-level binding energies in solids, similar to the calculations of potentials which have been carried out for molecules, is one in which the potential due to other atoms is approximated by the point-charge Madelung potential. The contribution of electrons on the atom in question can then be handled by calculating the binding energy of the core level in the free atom and various free atom and setting the difference in orbital energy equal to the difference in potential. Such calculations have been discussed.[5] They are clearly much more rudimentary than the corresponding calculations in molecules, though, which do not use the point-charge approximation and which, in fact, include multi-center integrals.[6]

Any attempt to refine the simple point-charge calculation, in order to assess the magnitude of the corrections or to compare the agreement of the calculations with experiment, requires the study of substances of simple structure, since otherwise the corrections become difficult, if not impossible, to carry out. It is important, of course, to study the same atom in a number of environments because it is only binding-energy shifts that we are able to obtain. Finally, one needs reasonably good wave functions for all the atoms in the various compounds. Our choice of compounds for the study of binding energies and their correlation with calculated potentials has been the simple fluorides.

The compounds we have studied are available commercially. Spectra were from powders, except those from CaF_2, SrF_2, BaF_2, and LaF_3, which were from pieces of single crystals. The crystals, in general, gave narrower lines.

All spectra were studied on the Berkeley iron-free spectrometer by using a thin layer of gold evaporated over the sample as a reference.[7] The binding energy of the N_{VII} of gold with respect to the Fermi surface was taken to be 84.0 eV.[8]

The data were recorded on magnetic tape and were then analyzed by fitting the data in the least-squares sense, using a program described elsewhere.[9] The uncertainty in the binding energy in the least-squares fit was typically about ±0.05 eV. In duplicate runs of the same compound on different days, however, the results scattered by about ±0.3, which may be taken as the precision of our data for practical purposes.

The binding energy of the fluorine K level in the various compounds we have studied appears in Table I.

Table I also includes the results of an analysis of the expected binding energies, assuming the compounds to be completely ionic. The analysis was performed by, first, calculating the point-charge Madelung potential at the fluoride site (or sites, if there were several inequivalent fluorides), using a modification of the program described by Pickens.[10] These results, referred to the fluoride ion of NaF (in which the point charge Madelung potential is 10.89 v.) appear in column 4 of Table I, labeled $V_{\text{point charge}}$.

The results of the point-charge Madelung potential calculation were corrected approximately for the fact that the atoms are not, in fact, point charges. The pairwise potentials between the fluoride ion of interest and all other ions within 4 Å of the reference fluoride ion were calculated exactly, assuming the two atoms to be described accurately by free-ion Hartree-Fock functions. The functions used for the heavier cations were minimum-basis-set functions calculated for the free ions.[13]

The salient fact about the experimental fluoride-ion binding energies is their constancy. As one sees, the binding energies of fluoride in the various compounds we have studied are the same to within about 1.5 V. The calculations reflect this constancy only in part. Among the compounds of lighter elements, for which better wave functions are available (NaF, CaF_2, LiF, MnF_2, and $KMgF_3$), the rms deviation of the calculations from the measured binding energies is 1.27 V. This is hardly more than the expected uncertainty in binding energies due to solid state effects, but it is somewhat disconcerting that all the calculated shifts, except that of LiF, are too large. Furthermore, the point-charge Madelung calculations give nearly as good an account of the trends in binding energies. The rms deviation of the point-charge predictions from the observations is 1.56 V, but this is dominated entirely by the large deviation from CaF_2. On the whole, the agreements of both the point-charge calculations and the more elaborate calculations are not significantly better than the simpler calculations and the data show no evidence of significant covalency.

Table II. Linewidths of the fluorine K level and of the Au reference level in various fluoride compounds.

	ΔE_F (eV)	ΔE_{Au} (eV)
NaF	2.12	2.19
LiF	2.38	2.27
CaF_2	1.72	2.51
SrF_2	1.59	1.98
BaF_2	1.43	2.88
LaF_3	1.29	2.75
YbF_3	1.91	2.91
UF_4	1.77	2.06

The only systems displaying substantial negative deviations are LaF_3 and YbF_3, which could be corrected by assuming fluorine charges of -0.43 and -0.72 respectively. The rare-earth fluorides are not considered to be especially covalent, though. On the other hand, UF_4 is expected, on chemical grounds, to be rather covalent, but there is no evidence for covalency from the fluoride binding energies. We have no wave function for U^{4+}, but the cor rection can hardly be larger than 1 eV per uranium and each fluoride has two uranium neighbors. The result is sure to come within 1 eV of the observations.

It would appear that the negative deviations are an artifact produced in systems with small cations by errors in the F-F potential. LiF is a less severe example of such a component.

The structures of low symmetry permit crystallographically inequivalent fluorides, which have different potentials, as shown in Table I. The presence of more than one kind of fluoride is nowhere apparent in the data. No compound showed more than one peak from the fluoride 1s. There is not even a hint of broadening of the peaks of YbF_3, LaF_3, or UF_4. The widths of the fluoride peaks are hard to correlate in any quantitative way because the factors influencing the width of a peak are hard to unravel, but the widths of the fluoride peaks in several compounds, along with the widths of the gold peaks, shown in Table II substantiates our point. All widths are full widths at half maximum from fits of the data to Gaussian lines.

Our data suggest that all the fluorides we have studied are very highly ionic. The deviations of the binding energies from the predictions of a completely ionic model are within the combined uncertainty of the measurements and the calculations in most cases. There are, however, a few disconcerting facts. The constancy of the observed binding energies is rather surprising, and the fact that compounds with crystallographically distinct fluorides, calculated to be subjected to different potentials, show no evidence of more than one type of fluoride, is equally disconcerting. We must assume that in these compounds the electronic structure adjusts itself, in ways more subtle than described by our calculations, to yield a potential at the fluorides which is very nearly the same among various compounds.

We conclude that the compounds must all be quite ionic and that our calculations are not sufficiently subtle to reproduce the details of the potential at the fluorides, which is very nearly independent of compound and of crystallographic inequivalence.

Footnote and References

*Published in Electron Spectroscopy, edited by D. A. Shirley (North-Holland, Amsterdam, 1972).

†Permanent address: Chemistry Department, University of Notre Dame, Notre Dame, Indiana.

1. A recent review which considers some of these studies is J. M. Hollander and D. A. Shirley, Ann. Rev. Nucl. Sci. 20, 435 (1970).

2. P. S. Bagus, Phys. Rev. 139, A619 (1965); M. E. Schwartz, Chem. Phys. Letters 5, 50 (1970).

3. D. W. Davis, J. M. Hollander, D. A. Shirley, and T. D. Thomas, J. Chem. Phys. 52, 3295 (1970).

4. M. E Schwartz, Chem. Phys. Letters 6, 631 (1970).

5. a) K. Siegbahn et al., ESCA, Atomic Molecular and Solid State Structure Studied by Means of Electron Spectroscopy (Almqvist and Wiksells, Stockholm, 1967); b) C. S. Fadley, S. B. M. Hagstrom, M. P. Klein, and D. A. Shirley, J. Chem. Phys. 48, 3779 (1968).

6. M. E. Schwartz, Chem. Phys. Letters 7, 78 (1970).

7. G. Kaindl (private communication).

8. C. S. Fadley and D. A. Shirley, J. Res. Natl. Bur. Stand. 14A, 543 (1970).

9. C. S. Fadley (Ph. D. dissertation), Lawrence Radiation Laboratory Report UCRL-19535 (1970).

10. W. Van Gool and A. G. Piken, J. Material Sci. 4, 95 (1969).

11. E. Clementi and A. D. McLean, Phys. Rev. 133, A419 (1964).

12. E. Clementi, I. B. M. Journal Res. Dev. Suppl. 9, 2 (1965).

13. E. Clementi, D. L. Raimondi, and W. P. Reinhardt, J. Chem. Phys. 47, 1300 (1967).

CHEMICAL SHIFTS OF CORE-ELECTRON BINDING ENERGIES IN OSMIUM COMPOUNDS

G. Kaindl*

The recent development of x-ray photoelectron spectroscopy (ESCA)[1] has made it possible to measure binding energies of atomic core electrons with a precision that can detect shifts arising from differences in the chemical environment of the atom under study. These chemical shifts of core-electron binding energies (CS) are related to the isomer shifts (IS) of Mössbauer γ rays. The IS is proportional to the difference of the total electron density at the nucleus, which may vary through direct contributions of the valence electrons and indirectly by their shielding effects on s-type core electrons. The binding energies of core electrons, on the other hand, vary by effects of the molecular charge distribution on mainly the Coulomb potential acting on the core levels. The present paper reports on a study of chemical shifts of the 4f binding energies of Osmium in a series of divalent through octovalent Osmium compounds.[2] The complementary relationship between CSs and ISs is discussed on the basis of a comparison of the CS data with Mössbauer ISs of the 36.2-keV γ rays of ^{189}Os, measured for the same series of Os compounds.[3,4]

The standard features of the experimental technique employed are described elsewhere.[5] The samples studied were prepared by dusting the finely powdered Os compounds onto double-sided adhesive tape. Mg-Kα x rays were used to irradiate the samples, and the momentum distribution of the expelled photoelectrons was analyzed using the LBL iron-free spectrometer. Special care was taken to correct for the effects of electrical charging of the samples on the kinetic energy of the photoelectrons. Pseudoshifts of the photoelectron lines of up to 1.5 eV due to these charging effects were found. They were corrected for by depositing a thin layer of Au (about 5 Å thick) on top of each sample, and using the Au 4f lines for reference. Such a thin layer of Au does not noticeably influence the photoelectron spectrum of the underlying material, besides diminishing slightly its intensity. No changes in the line positions of the Os 4f lines were found as a function of the thickness of the Au layer from ~ 5 to ~20 Å within 0.5 eV. Instead of Au we have also used Pt as a deposit, and the CS's determined in this way agree with those determined with Au deposits within 0.05 eV. During this work the results of a similar study on charging effects, also using the method of noble metal deposition, came to our attention.[6]

Figure 1 shows some typical photoelectron spectra of the 4f levels of Os in $K_4[Os(CN)_6]$, $K_2[OsCl_6]$, and $K[OsO_3N]$. The experimental results are summarized in Table I; a graphical representation of the CSs relative to $K_4[Os(CN)_6[$ is given in Fig. 2. The quoted error bar of 0.1 eV represents the highest scattering of CS values found during repeated independent measurements. The following conclusions can be drawn from the data:

1) The chemical shifts can be arranged according to the formal oxidation state of Os, which may therefore be regarded as the main parameter to influence the binding energy.

2) On an average the 4f binding energy of Os increases by ~ 1 eV per unit increase in the formal oxidation state.

3) Possible differences in the contribution of the Madelung energy of the positive hole formed in the photoelectric process[5] to the observed shifts are obviously small enough for this series of highly covalent compounds, in order not to obscure the observed systematics.

Even though a quantitative interpretation of the observed shifts would have to involve MO calculations, a comparison with the results of relativistic free-ion Dirac-Fock calculations[7] reveals some interesting features. Using Koopman's theorem, the Dirac-Fock calculations show that upon removal of one 5d

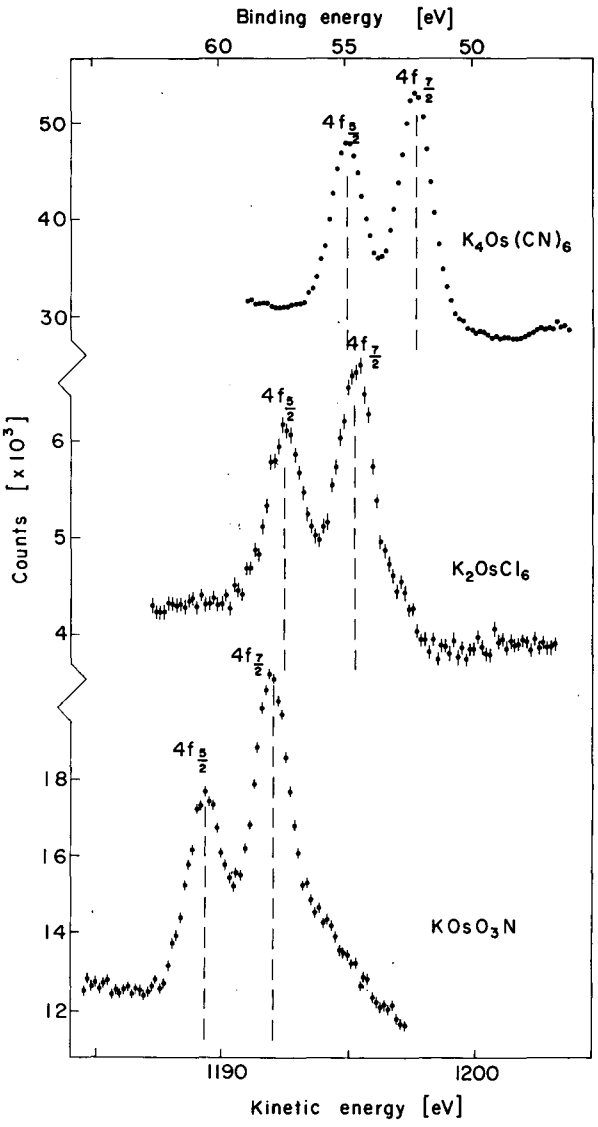

Fig. 1. X-ray photoelectron spectra of the 4f levels of Os in $K_4[Os(CN)_6]$, $K_2[OsCl_6]$, and $K[OsO_3N]$. The line positions corrected for charging effect are given by the dashed lines. (XBL 7011-4116)

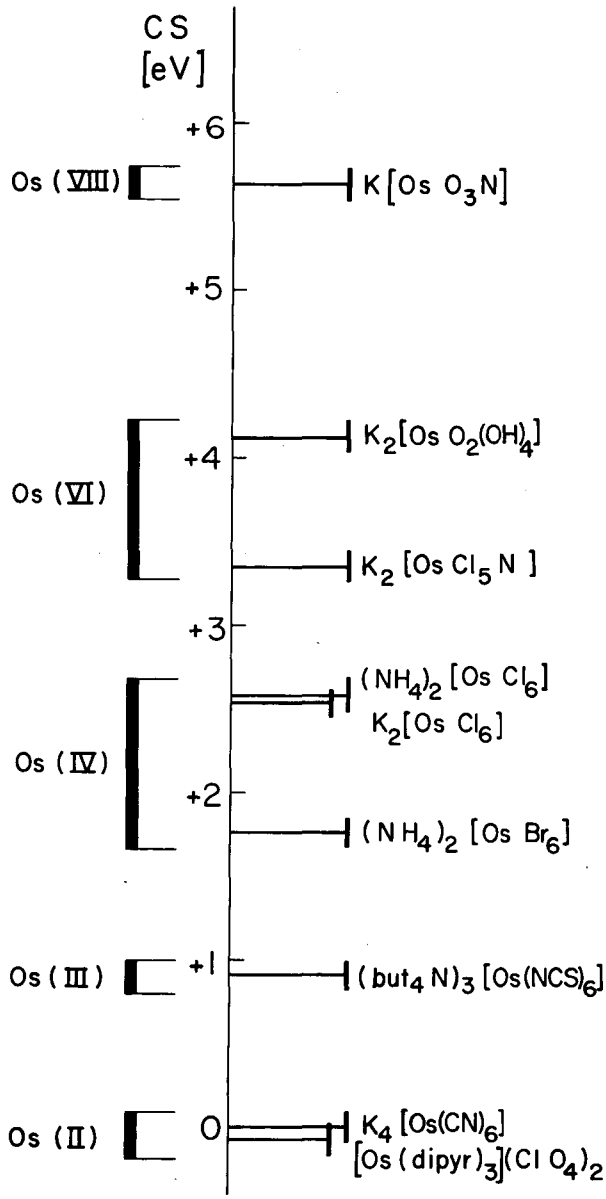

Fig. 2. Graphical representation of the CSs of the 4f binding energies of Os, relative to that of $K_4[Os(CN)_6]$, for all of the Os compounds studied. (XBL 713-3186)

electron the 4f binding energy of a free Os ion increases by 14 to 19 eV, depending on the 5d configuration. The small size of the experimental shifts (~ 1 eV), even after taking into account the contribution of the Madelung energy, reflects the fact that only a small fraction of an electron charge is actually removed from the Os atom when increasing its formal oxidation state by one. This is in agreement with what is expected from the principle of electroneutrality for these highly covalent compounds.

The experimental relationship between the CSs and the Mössbauer ISs is given in Fig. 3, where the ISs of the 36.2-keV γ rays of ^{189}Os are plotted versus the CSs of the Os 4f binding energies. The dashed curve represents the relationship resulting from the results of the free-ion Dirac-Fock calculations for different 5d configuration of the Os ions, with arbitrary scales on both axes. Qualitatively, such a free-ion-like picture

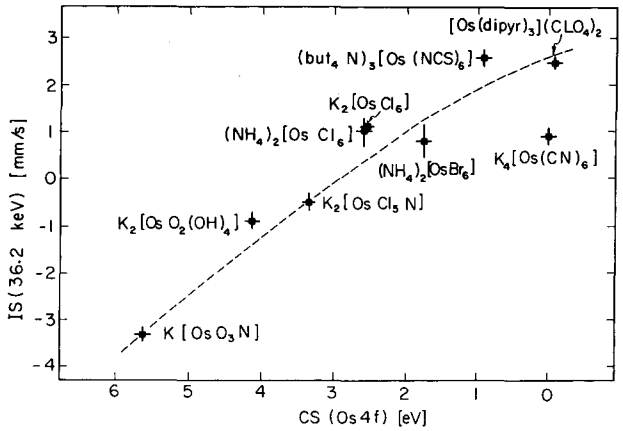

Fig. 3. Isomer shifts (IS) of the 36.2-keV γ rays of ^{189}Os, given relative to the ^{189}Ir(Ir) source, plotted versus the chemical shifts (CS) of the 4f binding energies of Os, given relative to $K_4[Os(CN)_6]$. (XBL 721-2155)

describes the overall features of the observed correlation rather well. A very similar conclusion has been drawn on the basis of d-electron shielding arguments from the systematics of Mössbauer isomer shifts for compounds of the d-transition elements.[4] Deviations from this simple free-ion like correlation are expected from the influence of covalency effects, like backbonding. Backbonding is especially pronounced for CN^-, NO^+, and (dipyr) ligands, which posses empty π^* orbitals, that can form π^* bonds with metal orbitals of the right symmetry. In the resulting MOs the d-electron density at the metal will be considerably reduced. This d transfer from metal to ligand is coupled with a synergic σ-charge transfer from ligand to metal, increasing the covalency in the σ bonds, in agreement with the principle of electroneutrality. Both coupled charge transfers will increase the total electron density at the nucleus, by a decrease of the shielding effect of the d electrons and by a direct contribution of the atomic s-type population of the σ-bonding orbitals, respectively. In contrast to this, the effects of the two synergically coupled charge transfers on the 4f binding energy have opposite signs, and therefore will not change it much. This explains the position of the points for $K_4[Os(CN)_6[$ and $[Os(dipyr)_3](ClO_4)_2$ in the plot of Fig. 3. Obviously covalency effects have rather different effects on the systematics of Mössbauer ISs and ESCA CSs giving rise to a complementary relationship between both.

The author is indebted to Drs. D. A. Shirley, Ursel Zahn, F. E. Wagner, J. B. Mann, and Mr. G. A. Apai.

Table I. Chemical shift (CS) of 4f binding energies of osmium for various osmium compounds relative to $K_4[Os(CN)_6]$.

Compound	Formal oxidation state of osmium	Chemical shift CS, in eV
$K[OsO_3N]$	Os(VIII)	+5.64 ± 0.10
$K_2[OsO_2(OH)_4]$	Os(VI)	+4.13 ± 0.10
$K_2[OsCl_5N]$		+3.35 ± 0.10
$K_2[OsCl_6]$	Os(IV)	+2.54 ± 0.10
$(NH_4)_2[OsCl_6]$		+2.58 ± 0.10
$(NH_4)_2[OsBr_6]$		+1.76 ± 0.10
$(but_4N)_3[Os(NCS)_6]$	Os(III)	+0.91 ± 0.10
$[Os(dipyr)_3](ClO_4)_2$	Os(II)	-0.07 ± 0.10
$K_4[Os(CN)_6]$		0.0

Footnote and References

*Miller Fellow, 1969-1971.

1. K. Siegbahn et al., ESCA, Atomic, Molecular and Solid State Structure Studied by Means of Electron Spectroscopy, (Almqvist and Wiksells, Stockholm, 1967).

2. G. Kaindl, Bull. Am. Phys. Soc. 15, 1359 (1970).

3. The IS data were partly measured during the author's stay at the Technische Universität München; for more recent data the author is indebted to Dr. F. E. Wagner.

4. G. Kaindl, D. Kucheida, W. Potzel, and F. E. Wagner, in Hyperfine Interactions in Excited Nuclei, edited by G. Goldring and R. Kalish (Gordon and Breach, 1971), p. 595.

5. C. S. Fadley, S. B. M. Hagstrom, P. P. Klein, and D. A. Shirley, J. Chem. Phys. 48, 3779 (1968).

6. D. J. Hnatowich, J. Hudis, M. L. Perlman, and R. C. Ragaini, Brookhaven National Laboratory Report BNL-15407 (1971).

7. J. B. Mann, Los Alamos, private communication (1971).

III. Physical, Inorganic, and Analalytical Chemistry

X-Ray Crystallography

Physical and Inorganic Chemistry

Radiation Chemistry

Chemical Engineering

Molecular Structure

Applications to Interdisciplinary Research

THE CRYSTAL STRUCTURE OF VANADYL SULFATE TRIHYDRATE

H. Ruben, A. Zalkin, and D. H. Templeton

A recent nuclear magnetic resonance study[1] of the coordination of vanadyl complexes in solution indicated that the vanadyl oxygen and four waters of coordination form a square pyramid in which the vanadium atom lies somewhat above the equatorial plane, and it also suggested that a fourth oxygen coordinates weakly to the vanadium and is in a position opposite the vanadyl oxygen. A crystal structure determination was undertaken to see if these conclusions would be consistent with the geometry in a hydrated vanadyl salt crystal. The salt we used for this study, vanadyl sulfate trihydrate, was a selection of convenience rather than design, since it was available commercially. The resulting structure determination confirms the postulated coordination geometry of Wuthrich and Connick,[1] and in particular the presence of a weakly coordinated water. Recently Ballhausen, Djurinskij, and Watson[2] reported the crystal structure determination of vanadyl sulfate pentahydrate, and our results are also in good agreement with theirs on the vanadium coordination geometry.

Crystals of $VO(SO_4)\cdot 3H_2O$ were obtained from Fairmount Chemical Company, in a bottle labeled $VOSO_4$. The crystals are blue and form fairly regular faces in a typical prismatic monoclinic form. The crystals are hygroscopic and required encapsulation in glass capillaries for examination. Sharp extinctions were observed under the polarizing microscope. The space group is $P2_1/c$ with cell dimensions $\underline{a} = 7.390 \pm 0.002$, $\underline{b} = 7.471 \pm 0.004$, $\underline{c} = 12.212 \pm 0.004$ Å, and $\underline{\beta} = 108.80 \pm 0.03°$, at 23°. A density measurement by flotation in a bromoform-ethylene chloride mixture gave a value of 2.03 g/cm^3. The calculated x-ray density, assuming four formula units per unit cell, is 2.11 g/cm^3. There is one formula unit in the asymmetric cell. There were 3080 θ-2θ scan data collected with an automatic diffractometer, using Cu Kα x rays and a scintillation counter.

The positions of vanadium, sulfur, and three oxygen atoms were deduced from a three-dimensional Patterson function. A Fourier analysis based on phases calculated from the partial structure revealed the positions of the remaining non-hydrogen atoms. After several cycles of least-squares refinements, a difference Fourier was calculated from which all six hydrogen atoms were located. Refinements were continued with anisotropic temperature factors for the non-hydrogen atoms. The final R value is 0.030 for 1128 data, and 0.035 for all 1246 data (includes zero weighted data); R_2 is equal to 0.035, and the standard deviation of a reflection of unit weight is 0.98.

The vanadium atom is in the interior of a distorted octahedron consisting of the vanadyl oxygen, the three water oxygen, and two sulfate oxygen atoms. Figure 1 shows this octahedron. The vandium atom is displaced 0.36 Å from a least-squares plane consisting

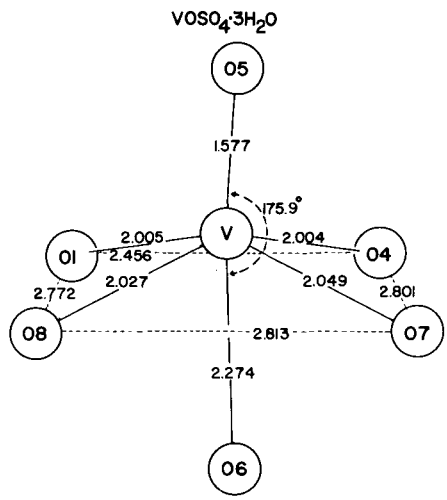

Fig. 1. Coordination octahedra about vanadium in vanadyl sulfate trihydrate.

(XBL 693-334)

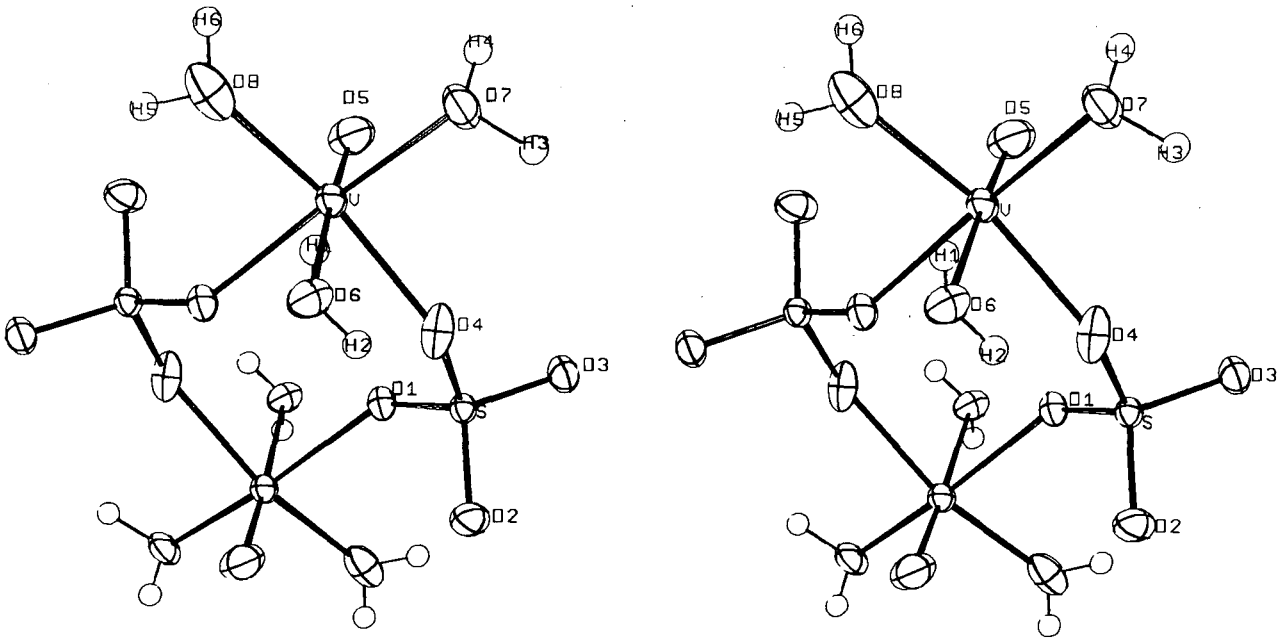

Fig. 2. Stereoscopic view of the dimer substructure in vanadyl sulfate trihydrate.
(XBL 693-324)

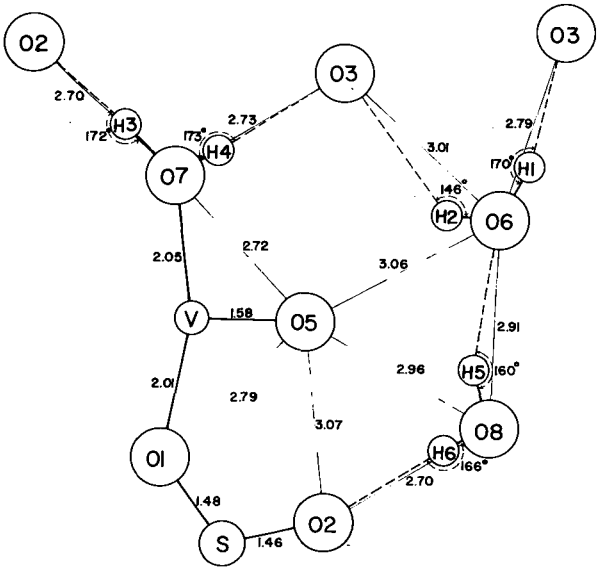

Fig. 3. Hydrogen bonding scheme and vanadyl-oxygen environment in vanadyl sulfate trihydrate. (XBL 693-328)

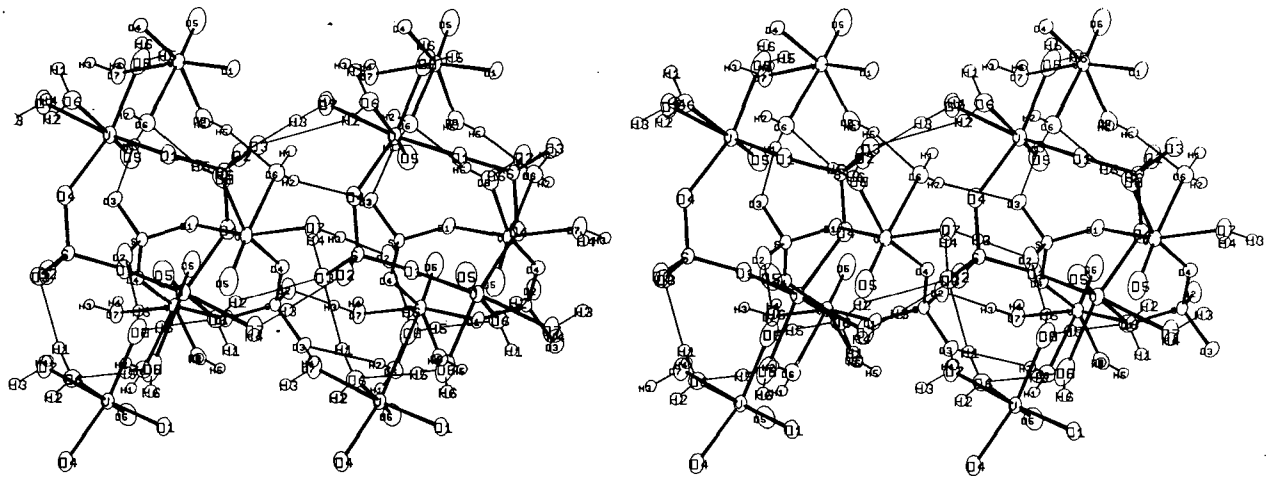

Fig. 4. Stereoscopic view of the hydrogen bonding in vanadyl sulfate trihydrate.
(XBL 693-327)

of atoms O(1), O(4), O(7), and O(8), and is displaced in the direction of its vanadyl oxygen. The V - O(6) distance, which is at least 0.2 Å longer than any of the other V - O distances in the octahedron, corresponds to a weak coordination in the axial position opposite the vanadyl oxygen.

The sulfate ion has the expected tetrahedral geometry; the average S-O bond distance is 1.470 Å (uncorrected for thermal libration) with an average deviation of 0.008 Å. When a librational correction is made, assuming the oxygen atoms to ride on the sulfur atom, the average becomes 1.479 Å with an average deviation of 0.007 Å.

A novel dimer substructure consisting of two formula units is found in this crystal. Two vanadyl octahedra are alternately linked to two sulfate tetrahedra about a crystallographic center of symmetry. Figure 2 shows a stereographic view of the dimer. The individual dimers are bound to each other by an intricate system of hydrogen bonds which involves all of the hydrogen atoms in the structure. Figure 3 shows a schematic diagram of the hydrogen bonding. Figure 4 shows a stereoscopic view of the bonding network.

References

1. K. Wüthrich and R. E. Connick, Inorg. Chem. 7, 1377 (1968).

2. C. J. Ballhausen, B. F. Djurinskij, and K. J. Watson, J. Am. Chem. Soc. 90, 3305 (1968).

THE CRYSTAL STRUCTURE OF $(C_2H_5)_4NCo(B_7C_2H_9)_2$, A SALT OF THE COBALT DERIVATIVE OF THE $(B_7C_2H_9)^{-2}$ CARBORANE LIGAND*

D. St. Clair,† A. Zalkin, and D. H. Templeton

A new polyhedral transition metal complex containing the $(B_7C_2H_9)^{-2}$ ligand was prepared by Hawthorne and George,[1] who deduced its structure on the basis of NMR data and chemical analysis. The anion, $Co(B_7C_2H_9)_2^-$, 2,2'-commo-bis[nonahydro-dicarba-2-cobalta-closo-decaborate](1-), is shown without hydrogen atoms in Fig. 1. It is a sandwich compound of cobalt (formal oxidation state +3) with two carborane polyhedral fragments. Carbon is in position 1 and in either position 6 or position 9 (Fig. 1). Positions 6 and 9 are chemically equivalent in each cage, but enantiomeric, and isomerism is possible depending on the relationship of the carbon atoms in the two cages of a complex.

We have made an x-ray diffraction analysis of the structure of tetragonal crystals of the tetraethylammonium salt of $Co(B_7C_2H_9)_2^-$.

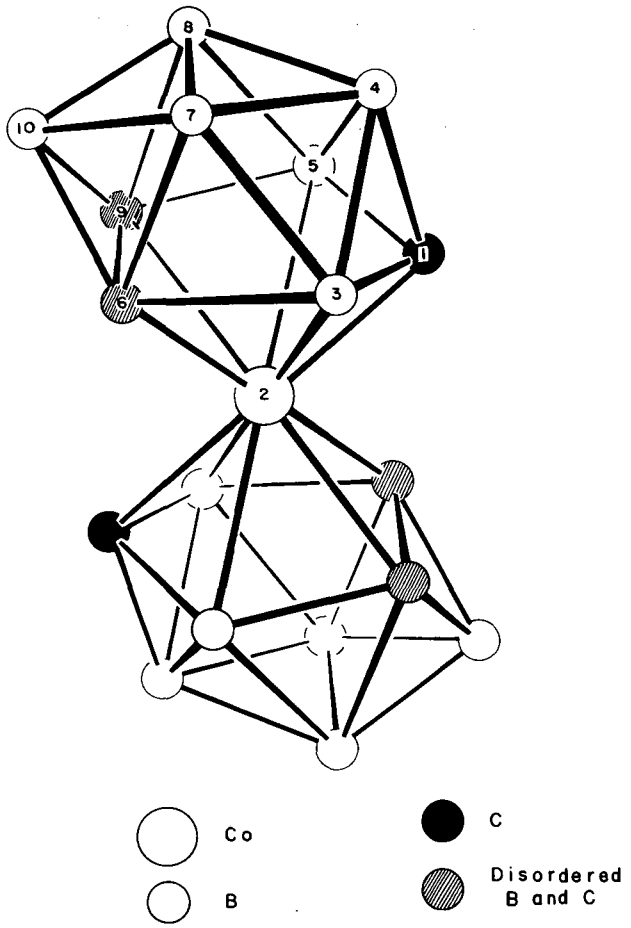

Fig. 1. Skeletal drawing of the $Co(B_7C_2H_9)_2^-$ anion. (XBL 6810-6061)

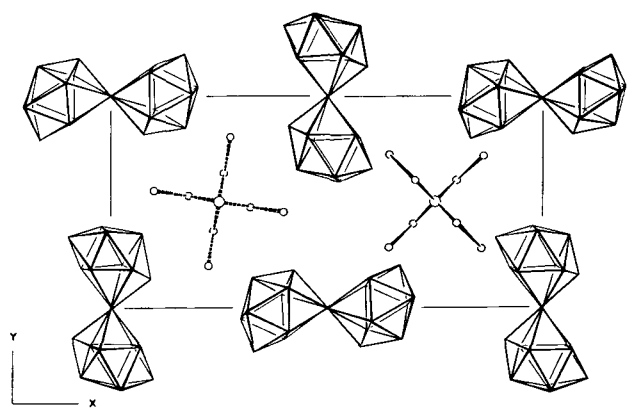

Fig. 2. Crystal structure of the tetraethylammonium salt of $Co(B_7C_2H_9)_2^-$. (XBL 6811-6118)

This study confirms the structural features found by Hawthorne and George,[1] but fails to resolve the isomer problem because disorder is present.

The crystals are tetragonal, space group P4/n, with a = 16.556(6), c = 8.580(4) Å at 24°C. The density measured by flotation, 1.13 g/cm^3, agrees with 1.15 g/cm^3 calculated for four molecules of $[(C_2H_5)_4N][Co(B_7C_2H_9)_2]$ per cell.

The structure determination, based on measurements of 926 independent, non-zero reflections, was not straightforward. By a combination of Fourier, least-squares, and trial-and-error methods we located all of the atoms except hydrogen and convinced ourselves that disorder exists. Carbon atoms are either at position 6 or at position 9 in each cage, and half of the tetraethylammonium ions have a choice of configurations. We failed to determine the hydrogen positions. For the final structure, R was reduced to 0.097 with anisotropic thermal parameters.

The structure of the anion may be described in terms of the bicapped square antiprism. Two vertices (positions 1 and 10), and bonds to them, may be described as polar. The other positions may be described as tropical, and bonds among them as tropical or equatorial. The tropical bonds connect positions 2, 3, 4, and 5, or 6, 7, 8, and 9. Average bond lengths (excluding atoms involved in disorder) are: Co-C = 1.93, Co-B = 2.15, B-C (polar) = 1.60, B-B (polar) = 1.73, B-B (tropical) = 1.88, B-B (equatorial) = 1.83 Å.

Figure 2 indicates the packing of the molecules in the crystal. The disorder in the cages has little effect on the external shapes of the anions. The disordered cations, indicated by broken lines, may be as shown or may be inverted. In either case, the positions in this projection are the same.

Footnotes and Reference

*Condensed from UCRL-18910; Published in Inorg. Chem. 11, 377 (1972).

†Present address: Shell Oil Co., Wood River, Illinois.

1. M. F. Hawthorne and T. A. George, J. Amer. Chem. Soc. 89, 7114 (1967).

THE CRYSTAL AND MOLECULAR STRUCTURE OF METHYL PHEOPHORBIDE WITH APPLICATIONS TO THE CHLOROPHYLL ARRANGEMENT IN PHOTOSYNTHETIC LAMELLAE*

M. S. Fischer,† D. H. Templeton, A. Zalkin, and M. Calvin

Lack of sufficiently large crystals has hindered x-ray diffraction studies of chlorophyll. We became interested in methyl pheophorbide a ($C_{36}H_{38}N_4O_5$, Fig. 1) because of its structural similarity to chlorophyll and the availability of crystals. It differs from chlorophyll a only by having two hydrogen atoms rather than magnesium in the center and a methyl ester rather than a phytyl ($C_{20}H_{39}$) ester on a side chain. The crystal structure was determined from measurements of diffraction intensities of 1662 independent non-zero reflections.

The unit cell dimensions (at room temperature, ~23°) are $\underline{a} = 8.035 \pm 0.004$, $\underline{b} = 28.531 \pm 0.020$, $\underline{c} = 7.320 \pm 0.004$ Å, and $\beta = 110.96 \pm 0.06°$. A density of 1.25 ± 0.01 g/cm^3 was obtained from flotation in aqueous solutions of $ZnBr_2$, KBr, and NaI. The calculated density is 1.285 for a formula weight of 606.7, Z = 2, and V = 1567 Å^3.

The structure was found by a trial-and-error method and was refined by least squares. Final parameter shifts were less than 0.1 σ with R = 0.053. The highest peak in a final ΔF map is 0.15 e/Å^3. Extensive calculations by Fourier methods convinced us that the two hydrogen atoms at the center of the molecule are distributed among four positions (on the four nitrogen atoms), but probably not with equal probability. Bond distances were determined to an accuracy of about 0.01 Å (except for hydrogen).

The central ring system is nearly flat (Fig. 2), while the side chains are not. The packing of the molecules in the crystal is shown in Fig. 3. Parallel molecules, tipped 16° from the b axis and related by a and c translations, are packed in a pseudohexagonal array. Such layers, related by the screw axes, are stacked in the b direction. Within the layer, the plane of each molecule is 3.49 and 3.52 Å from the planes of its nearest neighbors.

On the basis of these results and other physical evidence, we have speculated concerning the structure of chlorophyll as it exists in the plant. Figure 4 shows the configuration in a proposed model.

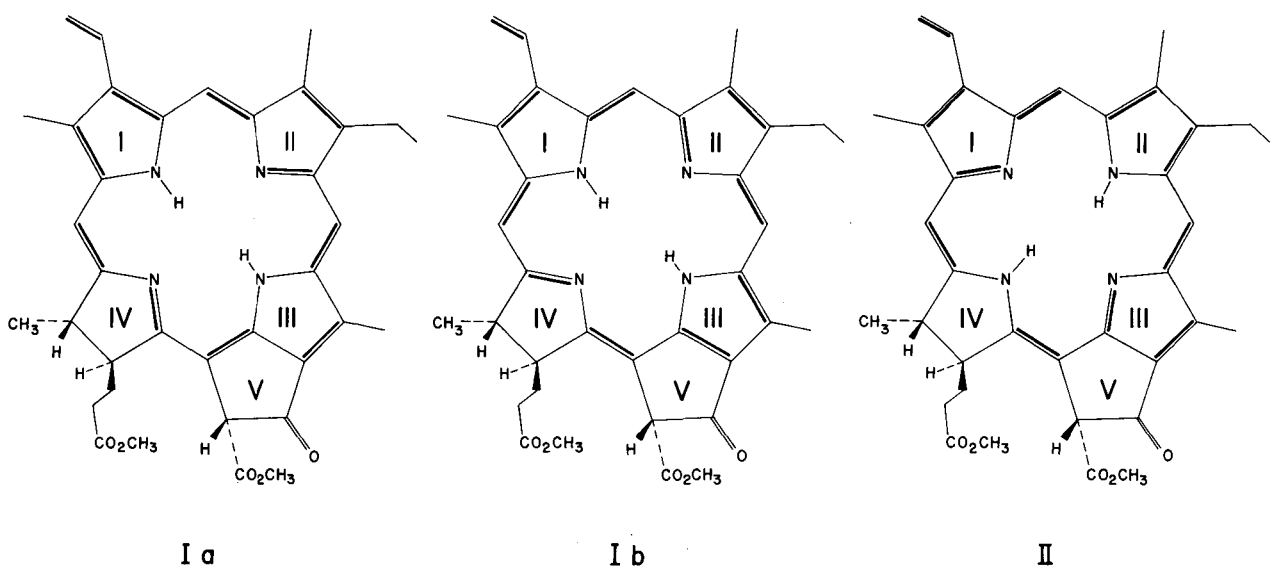

Ia Ib II

Fig. 1. Three resonance structures of two tautomers of methyl pheophorbide a.
(XBL 696-727)

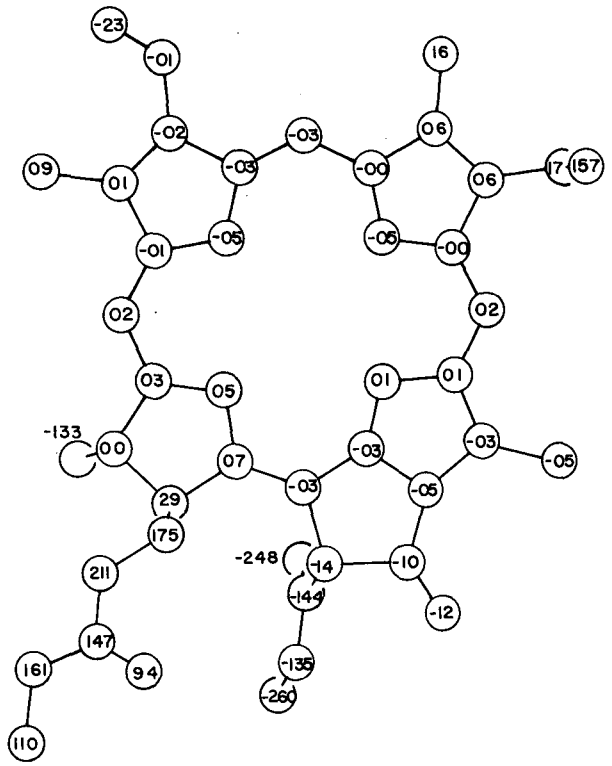

Fig. 2. Deviations (×100 in Å) of atoms from a plane. (XBL 698-1332)

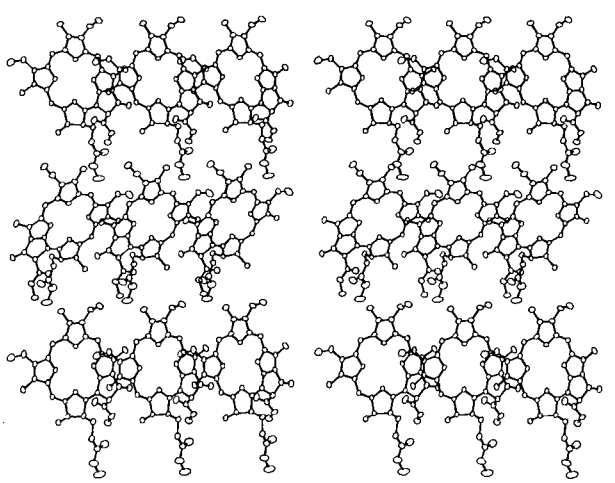

Fig. 3. Stereoscopic view of the crystal structure of methyl pheophorbide; a axis horizontal, b axis vertical. (XBL 698-1331)

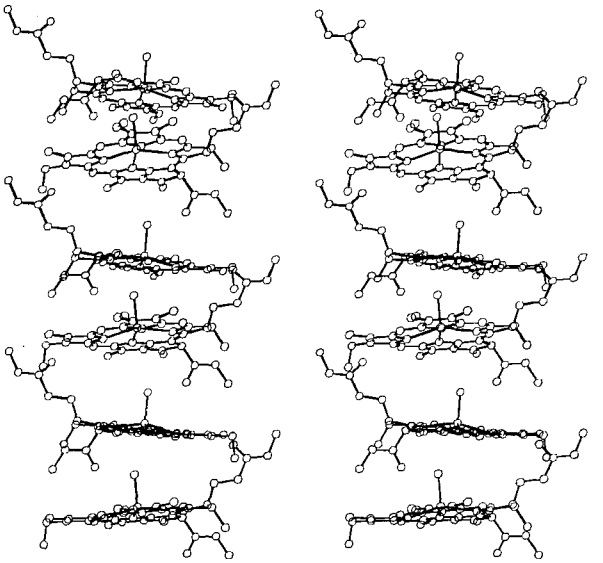

Fig. 4. Stereoscopic view of a proposed model of a chlorophyll-water polymer which might exist in photosynthetic lamellae. Only the first carbon atom of each phytyl group is shown. (XBL 6910-5918)

Footnotes

*Condensed from UCRL-19524; to be published in J. Amer. Chem. Soc.

†Present address: Department of Physiological Chemistry, Medical School, University of Wisconsin, Madison, Wisconsin.

CRYSTAL AND MOLECULAR STRUCTURE OF CHLOROMERCURINAPHTHALENE-1-SULFONYL FLUORIDE, A POSSIBLE PROTEIN LABEL, AND CRYSTAL DATA FOR THE 4, 1-ISOMER

M. S. Fischer,* D. H. Templeton, and A. Zalkin

Fenselau et al.[1] have proposed that chloromercurinaphthlenesulfonyl fluorides, $C_{10}H_6HgClSO_2F$, be employed as heavy-atom labels for x-ray structural work on proteins. The sulfonyl fluoride, the reactive group of the label, has been demonstrated to react with the hydroxyl group of the serine residue of the active site of the protein chymotrypsin.[2] In the synthesis of several of the isomers, an amino group is converted to a diazonium salt and then replaced by the chloromercuric group. A single-crystal x-ray analysis was undertaken to determine whether or not the actual isomer was the expected one and to obtain a detailed structure that would be of use in structure studies of so-labeled protein crystals.

Samples of the 4,1- and 7,1- derivatives were crystallized from dioxane; both are monoclinic. The cell dimensions for the 7,1 derivative are a = 9.725(3), b = 6.836(3), c = 8.351(3) Å, and β = 90.99(3)° in space group $P2_1/m$. The 4,1 derivative is in space group C2, Cm, or C2/m and has dimensions a = 17.50(6), b = 4.92(2), c = 13.13(5) Å, and β = 104(1)°. Densities were determined by flotation in mixtures of 1,2-dibromoethane and 1,1,2,2-tetrabromoethane and are 2.64 ± 0.02 g/cm^3 for both derivatives. We measured 1055 intensities of the 7,1 derivative with a card-controlled diffractometer, using θ-2θ scan technique and Mo Kα x rays. The heavy-atom structure was solved with the use of the three-dimensional Patterson function; the light atoms were found in subsequent difference Fourier maps. Some disorder difficulties were encountered with respect to the sulfonyl group, and the results seemed to indicate that a fluorine and an oxygen occupy positions across a mirror plane such that one

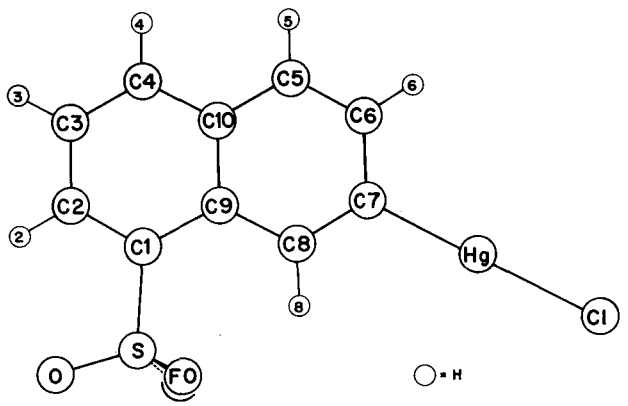

Fig. 1. Numbering scheme for 7-chloromercurinaphthalene-1-sulfonyl fluoride.
(XBL 6910-5731)

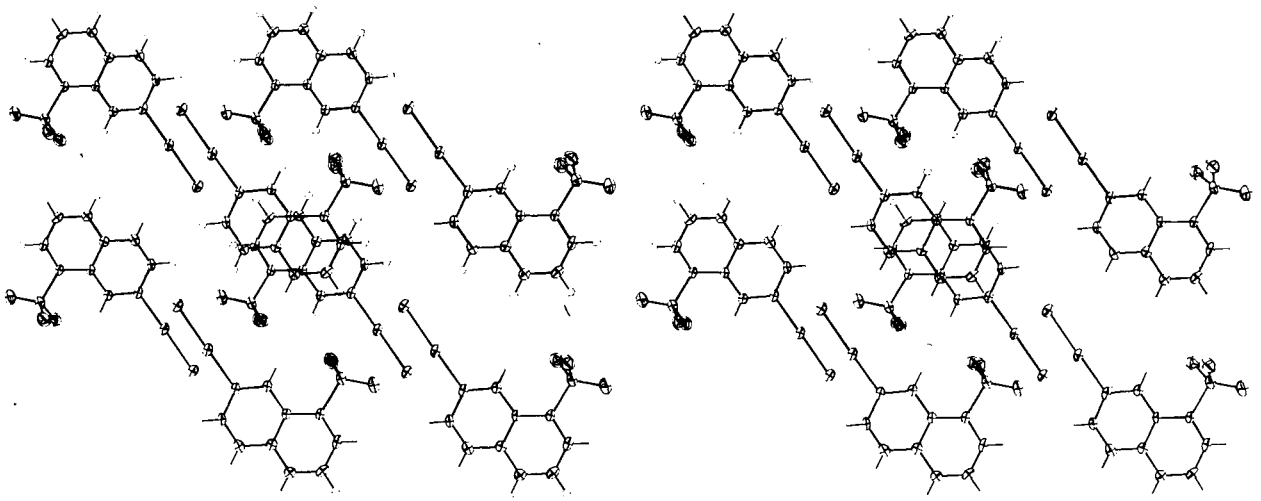

Fig. 2. Stereoscopic view of the packing of 7-chloromercurinaphthalene-1-sulfonyl fluoride looking down the b axis.
(XBL 6910-5730)

must assume 50% occupancy for each. The molecule is shown diagrammatically in Fig. 1 with the disorder indicated. The atomic coordinates were refined until the maximum shift was less than 1% of its standard deviation. The final R value is 0.0269 for the 1034 observed and 0.0281 for the 1055 zero and nonzero data.

We have confirmed that the crystal is composed of molecules of the 7,1-isomer of chloromercurinaphthalenesulfonyl fluoride as was originally expected. The molecule lies on the mirror plane, a special position of space group $P2_1/m$. The molecules pack in sheets in the ac plane. The naphthalene rings in the sheets are related by centers of symmetry in such a way that there is almost complete overlap of rings in adjoining sheets (see Fig. 2). The sheets are separated by a distance of $\frac{1}{2}$ c 3.418 Å. The Hg-Cl and Hg-C distances are 2.303(3) and 2.033(8) Å respectively, and the near-linear C1-Hg-C bond angle is 179.3(3)°.

Footnote and References

*Present address: Dept. of Physiological Chemistry, Medical School, University of Wisconsin, Madison, Wisconsin.

1. A. Fenselau, D. Koenig, D. E. Koshland, Jr., H. G. Latham, Jr., and H. Weiner, Proc. Nat. Acad. Sci. U. S. A. 57, 1670 (1967).

2. H. Weiner, and D. E. Koshland, Jr. (1965), J. Mol. Biol. 12, 881.

TWO ISOSTRUCTURAL CYCLOOCTATETRAENE DIANION π-COMPLEXES OF THE 5f TRANSITION SERIES: THE CRYSTAL AND MOLECULAR STRUCTURE OF URANOCENE, $U(C_8H_8)_2$ AND THOROCENE, $Th(C_8H_8)_2$†

A. Avdeef,* K. N. Raymond,* K. O. Hodgson* and A. Zalkin

Following the initial characterization of bis(cyclooctatetraenyl) uranium (uranocene) by Streitwieser and Müller-Westerhoff,[1] the synthesis and chemical properties for a number of 4f and 5f transition-series π complexes containing cyclooctatetraene dianion (COT^{-2}) have been reported.[2-6] It was originally postulated that uranocene has a π-sandwich structure and that symmetry-allowed overlap of the 5f orbitals with the ligand molecular orbitals could contribute to the bonding.[1] Our preliminary report[7] showed the structure of uranocene to be a true π-sandwich complex with D_{8h} molecular symmetry. The question of f-orbital participation in bonding has since become the subject of much renewed interest and speculation. Mössbauer studies on bis(cyclooctatetraenyl) neptunium[3] and proton magnetic resonance studies of uranocene[8] and the substituted uranocene, bis(1,3,5,7-tetramethylcyclooctatetraene)uranium,[6] appear to confirm the presence of at least some π interaction between ligand molecular orbitals and metal 5f orbitals. Little is known of the structures of these π-carbocyclic complexes and knowledge of the precise molecular structure is necessary in order to interpret their spectral and magnetic properties. The recently reported structure of $[Ce(C_8H_8)Cl \cdot 2\ OC_4H_8]_2$ is the only other structural report for an actinide or lanthanide compound containing COT^{-2}.[9]

After the characterization of uranocene, the analogous thorium complex was synthesized.[2] Its physical and chemical properties were so different from those of uranocene that there was question as to whether the complex had the same π-sandwich structure. A structural study was begun in order to determine if the two complexes were indeed isostructural.

Single crystals of both compounds suitable for x-ray analysis were obtained by vacuum hot tube sublimation of the pure powdered material. The highly oxygen-sensitive crystals were sealed in thin-walled quartz capillaries under a dry argon atmosphere; a small amount of Kel-F grease was used as an adhesive.

The uranocene crystal selected for data collection was a deep-green regular parallelepiped. The monoclinic cell parameters are a = 7.084, b = 8.710, c = 10.631 Å, and β = 98.75°. The calculated density is 2.29 g/cm^3 for two molecules in the unit cell of space group $P2_1/c$. Intensity data were collected manually by using the stationary-crystal stationary-counter method with Mo Kα x rays. A total of 543 non-zero unique reflections, $I > \sigma(I)$, were obtained and corrected for absorption.

A bright-yellow crystal of thorocene which extinguished sharply in polarized light was chosen for data collection. The cell param-

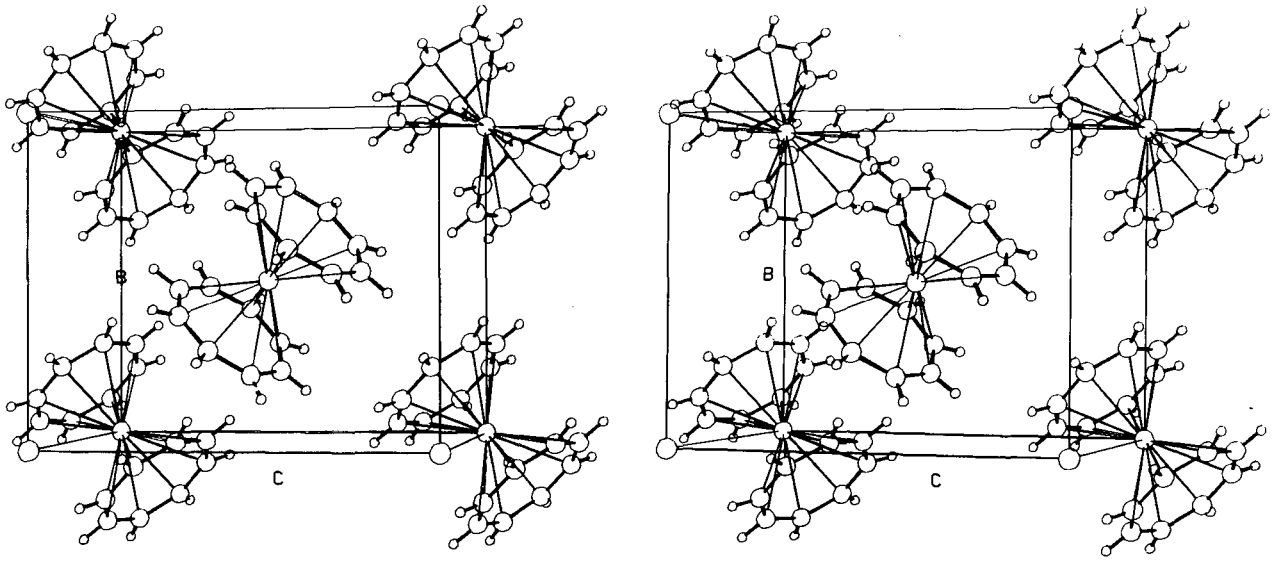

Fig. 1. A stereoscopic packing diagram of uranocene viewed normal to the yz plane. The origin is at the lower back left.
(XBL 702-346)

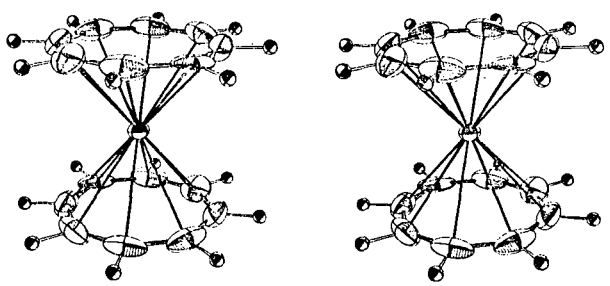

Fig. 2. A stereoscopic diagram of thorocene. Thermal ellipsoids are drawn at the 40% probability contour and the calculated hydrogen positions are included with β values of 1.0 $Å^2$. The numbering in the upper COT ring increases counterclockwise from C_4, the carbon at the far left in the upper ring.

eters are a = 7.058, b = 8.819, c = 10.704 Å and β = 98.44°. The calculated density is 2.22 g/cm^3 for two molecules in the unit cell of space group $P2_1/c$. The intensity data were collected with an automatic Picker diffractometer using a θ-2θ scan mode and monochromatized Mo Kα radiation. A total of 730 unique reflections with $I > 3\sigma(I)$ were obtained and corrected for absorption.

The structure of uranocene was solved by using Patterson techniques. With two formula units per unit cell, the uranium atom can be located unambiguously at the orgin with $\bar{1}$ (C_i) site symmetry. A three-dimensional Patterson map easily confirmed the heavy-atom positions. The remainder of the map, however, was dominated by Fourier ripple peaks around the origin and no uranium-carbon vectors could be discerned. In order to remove Fourier ripple peaks associated with the origin peak of the Patterson map, an origin-removed sharpened Patterson function was calculated. The resultant map showed large peaks and relatively little ripple. The largest eight peaks in the map for vectors with reasonable uranium-carbon bond lengths were all approximately 2.6 Å in length and represented the eight different U-C vectors. These peaks clearly showed the sandwich structure of the molecule. The coordinates obtained from the Patterson map, used directly in a least-squares refinement (with all atoms isotropic), converged in several cycles. Since the hydrogen atoms could only be approximately located in difference Fourier maps, their positions were estimated by assuming a trigonal planar geometry about the carbon atoms and C-H bond lengths of 1.0 Å. In the final anisotropic refinement, the hydrogen atom contributions to the structure factors were calculated from these fixed positions with isotropic thermal parameters. The model converged to give a final R factor of 2.1%.

Solution of the structure for thorocene followed directly from the uranocene results. Trial atomic positions with isotropic thermal

parameters from uranocene were used in a least-squares refinement with the thorocene data. The refinement converged in three cycles. Hydrogen atom positions were calculated as described for uranocene. In the final anisotropic least-squares refinement the structure factor contributions from these fixed hydrogen positions were included. The final R factor was R = 2.07%.

In the crystal structures of uranocene and thorocene, there are two molecules per unit cell. The heavy atoms occupy the symmetry-related positions 0 0 0 and 1/2 1/2 1/2 with $\bar{1}$ (C_i) site symmetry. A stereoscopic packing diagram of uranocene viewed normal to the yz plane is shown in Fig. 1. The molecules alternate in a herringbone motif up the two-fold screw axis, parallel to b. The molecular eight-fold axis which passes through the center of the two rings and the uranium atom makes an angle of 40.9° with the b axis in uranocene and 44.6° with the b axis in thorocene. The crystal structures show no unusually short intermolecular non-bonded distances.

A stereo view of the thorocene molecule is shown in Fig. 2. The molecular structure consists of a central metal atom symmetrically π-bonded to two COT^{-2} rings which are related by the inversion center at the heavy atom. In uranocene, the uranium-carbon bonds are equal within experimental error and average 2.647(4) Å. The thorium-carbon bonds in thorocene are slightly longer and average 2.701(4) Å. The mean ring-to-ring distance along the molecular eight-fold axis is 3.847(10) Å in uranocene and 4.007(3) Å in thorocene. The mean C-M-C angle for adjacent carbons in the dianion ring is 30.5(3)° in uranocene and 29.7(2)° in thorocene. Carbon-metal-carbon angles, where the two carbons are separated by three ring atoms and are on opposite sides of the dianion ring, average 86.80(13)° for uranocene and 84.22(16)° for thorocene. These angles and distances, along with the planarity of the dianion ring, establish almost exact D_{8h} molecular symmetry for the π-sandwich structures. The thermal motion of the heavy atoms is nearly isotropic.

The cyclooctatetraene dianions in both compounds are planar and have average C-C bond lengths of 1.393(13) and 1.386(9) Å in uranocene and thorocene, respectively. The planarity of the ring and the mean bond lengths and angles demonstrate the aromatic nature of the 10-π electron dianion rings in these structures.

The general features of the bonding in thorocene and uranocene, as established by this study, are substantially identical. Questions regarding the relative importance of f orbital involvement in the bonding of these compounds and how this may affect the relative reactivities of compounds such as thorocene and uranocene cannot be directly answered by structural studies alone. It was observed by Streitwieser and Yoshida that thorocene, in contrast to uranocene, is easily solvolyzed in solvents which can act as Lewis bases.[2] The degree to which f orbital back bonding explains the chemical differences

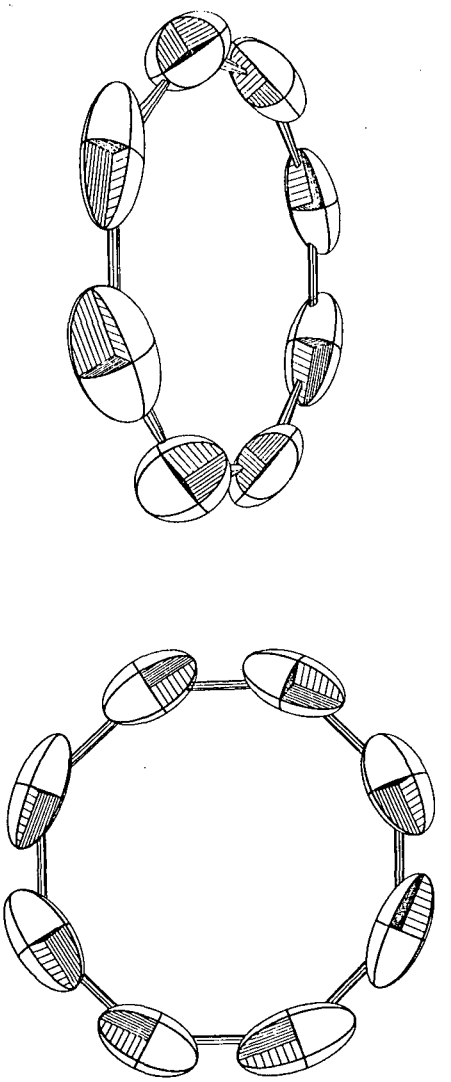

Fig. 3. The cyclooctatetraene dianion ring carbon atoms in thorocene viewed perpendicular to the plane of the ring are shown on the left. The right view is rotated 65°. The numbering sequence increases sequentially in a clockwise direction from the upper right carbon atom, C_1, in both rings.

in this series remains to be established by the magnetic resonance and spectroscopic studies which are in progress.

Footnotes and References

†Condensed from a report published in Inorganic Chemistry 11, 1083 (1972).

*Dept. of Chemistry, University of California, Berkeley.

1. A. Streitwieser, Jr., and U. Muller-Westerhoff, J. Amer. Chem. Soc. 90, 7364 (1968).

2. A. Streitwieser, Jr. and N. Yoshida, J. Amer. Chem. Soc. 91, 7528 (1969).

3. D. G. Karraker, J. A. Stone, E. R. Jones, Jr., and N. Edelstein, J. Amer. Chem. Soc. 92, 4841 (1970).

4. F. Mares, K. O. Hodgson, and A. Streitwieser, Jr., J. Organometal. Chem. 24, C68 (1970).

5. F. Mares, K. O. Hodgson, and A. Streitwieser, J. Organometal. Chem. 28, C24 (1971).

6. A. Streitwieser, Jr., D. Dempf, G. N. Lamar, and N. Edelstein, submitted for publication.

7. A. Zalkin and K. N. Raymond, J. Amer. Chem. Soc. 91, 5667 (1969).

8. N. Edelstein, G. N. Lamar, F. Mares, and A. Streitwieser, Jr., Chem. Phys. Letters 8, 399 (1971).

9. K. O. Hodgson and K. N. Raymond, Inorg. Chem. 10, (1971).

THE CRYSTAL STRUCTURE OF FERRIC AMMONIUM SULFATE TRIHYDRATE, $FeNH_4(SO_4)_2 \cdot 3H_2O$†

K. J. Palmer,* R. Y. Wong,* and K. S. Lee*

Large crystalline lumps of ferric ammonium alum, $FeNH_4(SO_4)_2 \cdot 12H_2O$, obtained from a bottle labeled "Analytical Reagent" for the purpose of preparing standard solutio of ferric ion, were observed to be encrusted with a granular material. When the alum was dissolved in water the granular material remained as a residue. Microscopic examination revealed that it consisted of a mixture of faintly mauve prisms and colorless hexagonal plates. The optical properties of these two types of crystals were determined but did not lead to the identification of either one. An x-ray powder pattern of the hexagonal crystals was found to agree with that recorded for ferric ammonium sulfate. The powder pattern of the prismatic crystals did not agree with any of the powder data available to us. Chemical analysis proved that the prismatic crystals contained iron. Because of our general interest in coordination chemistry, we decided to determine the structure of this previously unreported iron salt. The results of this determination prove that the prismatic crystals are $FeNH_4(SO_4)_2 \cdot 3H_2O$. The optical properties have been published separately.[1]

The crystals are in the monoclinic space group $P2_1/c$ with cell dimensions $a = 9.982(5)$, $b = 10.156(5)$, $c = 9.504(5)$ Å, and $\beta = 94.95(5)°$; 1690 intensity data were obtained manually by the stationary-crystal, stationary-counter method using Mo $K\alpha$ x rays.

A three-dimensional Patterson function was interpreted in a straightforward way and led to approximate positions for the iron and four oxygen atoms. Least-squares refinement, interspersed with Fourier difference calculations, led to the evaluation of the parameters of all 15 heavy atoms in the asymmetric unit. After a series of refinements a Fourier difference map was calculated from which approximate parameters for the ten hydrogen atoms were determined. After a correction for secondary extinction was made the R factor became 0.038 for the 1504 data whose intensities were greater than their standard deviations. All non-hydrogen atoms were assigned anisotropic temperature factors.

The ferric ion is coordinated to six oxygen atoms which form a distorted octahedron. The arrangement of the four sulfate groups and the two water molecules about the iron atom is shown in Fig. 1. The nitrogen atom and the third water oxygen, O(11), are not shown, but can be seen in Fig. 2. The structure has continuous chains composed of alternate iron atoms and the S(2) sulfate groups running parallel to the c axis. These chains are bridged by the coordinate bonding of the S(1) sulfate group to iron atoms in adjacent chains. The six thermally corrected Fe-O distances vary between 1.979 and 2.014 Å with an average value of 1.997 Å. The O-Fe-O angles indicate that the octahedron of oxygen atoms about the

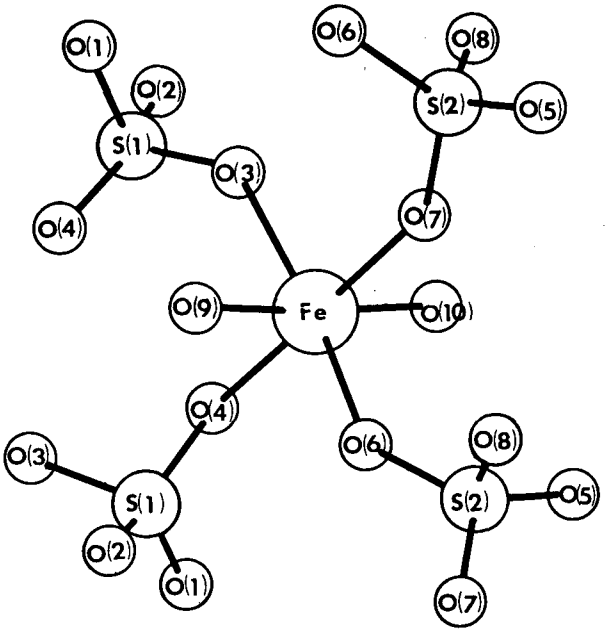

Fig. 1. Coordination of four sulfate and two water oxygen atoms around an iron atom. The numbering system used is shown.
(XBL 724-728)

Fe atom is somewhat distorted; i.e., bond angles that would ideally be 90° vary from 84.1 to 96.7°. There are two crystallographically distinct sulfate groups in this structure. The average value for all S-O bond lengths found is 1.468 Å when uncorrected for thermal motion and 1.478 Å after correction; these numbers are in excellent agreement with previously determined values.[2] The packing and bonding are illustrated in Fig. 2, which is a projection onto the (101) plane. The ammonium and water molecules form hydrogen bonds as shown by the dashed lines. There are ten hydrogen bonds in the asymmetric unit.

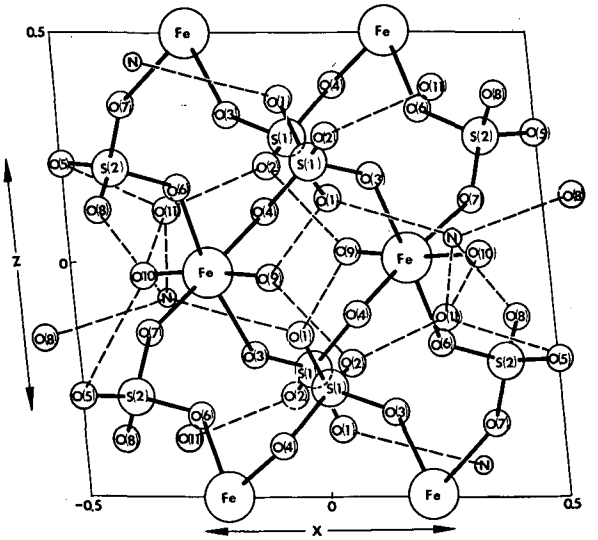

Fig. 2. Packing and bonding in $FeNH_4(SO_4)_2 \cdot 3H_2O$. This is a projection onto the (101) plane. Hydrogen bonds are shown as dashed lines. O(9), O(10) and O(11) are water oxygen atoms.
(XBL 724-279)

Footnotes and References

†This research was undertaken while K. J. P. was stationed at the Lawrence Berkeley Laboratory, Berkeley, California and was supported in part by the U. S. Atomic Energy Commission. Published in Acta Cryst. B28,236(1972).

*Western Regional Research Laboratory, Agricultural Research Service, U.S. Department of Agriculture, Berkeley, California 94710.

1. F. T. Jones, K. J. Palmer, R.S.F. Young, The Microscope 15, 480 (1967).

2. A. Zalkin, H. Ruben, and D. H. Templeton, Acta Cryst. 17, 235 (1964).

THE EFFECTS OF ION CHARGE ON ION-EXCHANGE RESIN SELECTIVITY

J. Bucher, B. Chu, and R. M. Diamond

It is often mentioned in ion exchange publications that for strongly acid cation or strongly basic anion resins, ion selectivity goes up the higher the charge on the ion. Such a rule is implicitly founded on a Coulomb's law interaction between the exchanging ions and the resin-fixed ion, and so is a natural consequence of ion-exchange models based on the importance of ion pairing in the resin phase.[1-3] But the opposite behavior, a decrease in resin affinity with increasing ionic charge, would be the rule if, as has also been proposed,[4-5] ion-water interactions, rather than ion-resin ion contacts, were the most important factors in the exchange. The higher-charged ion has a larger hydration energy, a greater need for hydration, than the lower-charged one; and since the best hydration is obtained in the dilute external phase rather than in the concentrated resin phase, the higher-charged ion goes into the aqueous solution preferentially, forcing the other ion into the less desirable resin phase.

What then is the experimental resolution of this question? Before answering this, one should note the effect of "electroselectivity" in this problem. That is, as discussed in Ref. 6, the Donnan potential of the ion-exchange resin, created by the tendency of the counter ions to diffuse into the solution and so leave a slight imbalance of charge in the resin, acts on the counter ions with a force proportional to the ionic charge. Thus, the counter ion of higher charge is more strongly attracted by the ion exchanger. And because the Donnan potential increases with dilution of the external solution and with increasing concentration of the resin-fixed ions, the attraction for the higher-charged ions follows the same pattern. Since, in most ion-exchange operations the external solution is dilute compared with the resin phase, this leads to the empirical observation that resins prefer the ion of higher charge. But, in fact, if the external solution is made quite concentrated, this order can be reversed. This type of selectivity, called electroselectivity, is not intrinsic to the exchanger, but follows merely from the difference in ionic charge of the two ions and the difference in concentration of the two phases.

However, in the equilibrium,

$$nA' + \overline{B}^n \rightleftharpoons n\overline{A}' + B^n, \qquad (1)$$

where the superscript bar represents the resin phase, and ion type A is univalent (for simplicity) with ion type B n-valent, the value of the equilibrium quotient, or selectivity coefficient, for Eq. (1),

$$K_{B/A} = \frac{[\overline{B}]\,[A]^n}{[\overline{A}]^n[B]}, \qquad (2)$$

where brackets indicate concentrations, does give a direct measure of the intrinsic selectivity even for heterovalent exchanges. A complication is that the value of $K_{B/A}$ may vary with resin composition. To circumvent this, the ions to be compared can be in tracer quantities in the presence of macro amounts of a third ion which thus dominates the composition in both phases. Experimentally it is more convenient to measure $K_{B/A}$ for one tracer ion at a time in the presence of the same macro species.

Obviously it would be best to compare (tracer) ions of similar size and structure, though differing in charge, so as to minimize all effects other than that of the charge on the selectivity. For this reason, tracer ReO_4^-, WO_4^{2-}, and CrO_4^{2-} were measured vs Cl^- as the macro anion, and tracer $Cr(CN)_6^{3-}$, $Co(CN)_6^{3-}$, and $Fe(CN)_6^{4-}$ were determined vs macro concentrations of CN^-. Values of D, the distribution ratio of the tracer anion,

$$D = \frac{(\text{counts/g of resin})}{(\text{counts/ml of solution})}, \qquad (3)$$

were measured for each tracer ion over a range of macro-anion concentrations to show

Table I. Selectivity coefficients for tracer anions on Dowex-1.

Tracer anion of charge n	Macro anion	K	$K^{1/n}$
ReO_4^-	Cl^-	570	570
WO_4^{2-}	Cl^-	0.10	0.32
CrO_4^{2-}	Cl^-	0.23	0.48
$Cr(CN)_6^{3-}$	CN^-	2.0	1.3
$Co(CN)_6^{3-}$	CN^-	22	2.8
$Fe(CN)_6^{4-}$	CN^-	0.073	0.52

that D did vary with the appropriate power of the macro-anion concentration, and then these values were converted to $K_{B/A}$ with the values of the resin capacity (per g of resin) and the external solution concentration (in molarity). Table I lists the values of the equilibrium quotients found. Actually, there is some uncertainty as to the most appropriate way to compare heterovalent exchanges. A fairer comparison than the values of K directly, might be $K^{1/ab}$ so that the equilibrium is normalized to one equivalent of exchange; these values are also listed. It can be seen from either set of values that there is a marked decrease in resin selectivity with an increase in the charge on the anion.

So at least with a strongly basic resin, electrostatic ion pairing in the resin phase does not determine the order of selectivity. On the contrary, resin selectivity appears to go with the inverse order of the hydration energies of the ions. This is, in fact, what would generally be expected from a model for ion-exchange selectivity based on the difference in hydration of an ion between the two phases, as the latter should be roughly proportional to ion hydration energy in pure water itself, at least for lowly and moderately cross-linked resins.

References

1. J. L. Pauley, J. Am. Chem. Soc. 76, 1422 (1959).

2. F. E Harris and S. A. Rice, J. Chem. Phys. 24, 1258 (1956).

3. H. P. Gregor, J. Belle, and R. A. Marcus, J. Am. Chem. Soc. 77, 2713 (1955).

4. B. Chu, D. C. Whitney, and R. M. Diamond, J. Inorg. Nucl. Chem. 24, 1405 (1962); B. Chu, Thesis, Cornell University, Ithaca, N. Y. (1959).

5. G. Eisenman, Biophys. J. Suppl. 2, 259 (1962).

6. F. Helfferich, Ion Exchange, (McGraw-Hill, New York, 1962), p. 156.

INFRARED SPECTRAL EVIDENCE ON THE NATURE OF THE TRIOCTYLPHOSPHINE OXIDE COMPLEXES OF $HReO_4$ AND $HAuCl_4$

J. J. Bucher and R. M. Diamond

In examining the extraction of the strong acids $HReO_4$ and $HAuCl_4$ by dilute solutions (< 0.1 M) of trioctylphosphine oxide (TOPO) in CCl_4 and in the aliphatic hydrocarbons, cyclohexane and isooctane (2,2,4-trimethylpentane),[1] certain inconsistencies were encountered. Slope analysis of data from distribution studies indicated a step-wise change of the acid-TOPO complex coordination number from two to three at about 0.001 M TOPO in isooctane and 0.01 M in cyclohexane and CCl_4. A 3:1 TOPO:acid complex suggests the hydronium-ion core found in the extraction of these acids by tri-butylphosphate (TBP)[2] and other not too basic extractants such as Ketones, ethers, etc. However, loading curves indicated the stoichiometric limit, the saturation coordination number of TOPO, was only 2. This was true even for those ranges of TOPO concentration where an overwhelming amount of 3:1 complex would be expected from slope analysis. Similar studies with the same acids in TOPO-benzene, TOPO-$CHCl_3$ and TOPO-sym-triethylbenzene systems[3] had demonstrated the presence of only a two-TOPO, unhydrated proton complex. It was thought somewhat unreasonable that the acid complex structure could be changed so drastically from a proton to an hydronium ion by simply using a series of somewhat more poorly solvating diluents.

It is now believed the error lies in the slope analysis, and arises from an erroneous, though usually empirically valid, assumption that the organic-phase activity coefficient ratio of the acid complex to TOPO, y_{HX}/y^n_{TOPO}, remains reasonably constant in these dilute (< 0.1 M) solutions. Apparently, this assumption (made due to the lack of experimental values) breaks down for TOPO concentrations < 0.001 M in isooctane and < 0.01 M in both CCl_4 and cyclohexane.

To learn more about the nature of the possible TOPO-acid complexes, infrared spectra were taken of a number of $HAuCl_4$-TOPO solutions (Fig. 2) and for comparison with hydronium-ion-base complexes, of some acid-TBP solutions,[2] (Fig. 1). Curve 1 of Fig. 1 is the spectrum of 0.024 M $HAuCl_4$ in 0.367 M TBP against dry 0.367 M TBP. Those peaks labeled TBP·H_2O are associated with the water extracted by the non-acid bound TBP. Spectrum 2 of Fig. 1 shows the result of removing these TBP·H_2O bands by vapor phase drying

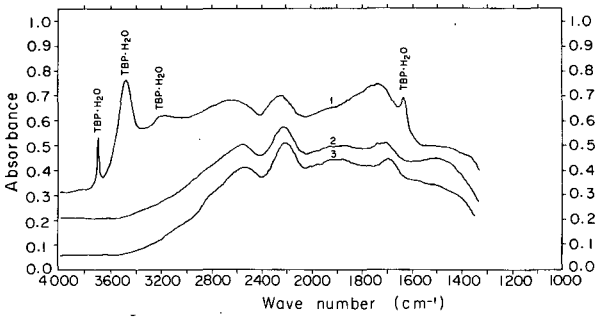

Fig. 1. The infrared spectrum in the region 1300 to 4000 cm^{-1} for 0.024 M $HAuCl_4$ in 0.367 M TBP in CCl_4 (curve 1); the same TBP solution dried over P_2O_5 via the vapor phase to remove TBP·H_2O bands (curve 2); and dried 0.037 M $HReO_4$ in 0.367 M TBP in CCl_4 (curve 3). (XBL 718-4018)

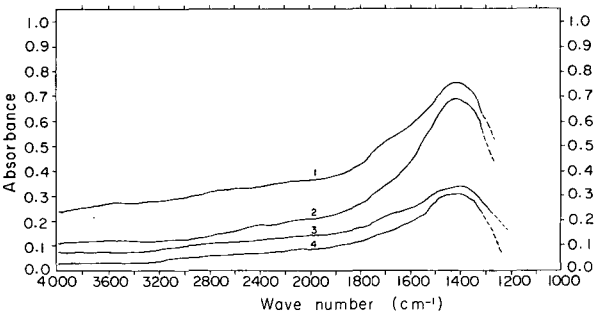

Fig. 2. The infrared spectrum in the region 1300 to 4000 cm^{-1} for 0.05 M $HAuCl_4$ in 0.10 M TOPO in benzene (curve 1); in CCl_4 (curve 2), in cyclohexane (curve 4), and for dried over P_2O_5 0.05 M $HAuCl_4$ and 0.20 M TOPO in isooctane (curve 3).
(XBL 718-4017)

over P_2O_5 the same solution as used in spectrum 1. Several broad but distinct peaks show in the range 3200 to 1600 cm^{-1}, and we believe them to be representative of the hydronium-based 3:1 TBP:acid complex formed by very strong acids extracted by TBP. Curve 3 shows the spectrum for dried 0.037 M $HReO_4$ in 0.367 M TBP-CCl_4. The TBP coordination number in this system is 2, instead of 3 as in spectrum 2; but this change seems to have little effect upon the spectral pattern, and presumably indicates little difference in the hydronium-ion based cationic complex.

Figure 2 shows spectra for the 0.05 M $HAuCl_4$ acid complex in 0.10 M TOPO-benzene (line 1); 0.10 M TOPO-CCl_4 (line 2), dried over P_2O_5; 0.2 M TOPO-isooctane (line 3); and 0.10 M TOPO-cyclohexane (line 4). The main feature of these spectra is the single broad peak centered at about 1450 cm^{-1}. Very noticeable is the absence of absorbance peaks similar to those found in the TBP systems. This result clearly indicates that the acid complex with TOPO is not based on a hydronium-ion core. It is difficult to conceive of a cationic structure, other than the hydronium-ion core, to which three TOPO molecules could be bound and thus, we believe, only the 2:1 TOPO:H^+ species is present in all these systems.

Probably the broad band centered at ~1450 cm^{-1} is the (asymmetric)stretching vibration of the $R_3PO\cdots H^+\cdots OPR_3$ ion. Confirmation that it is associated with hydrogen motion was obtained by replacing the protons with deuterons. This substitution causes the disappearance of the 1450 cm^{-1} peak, but unfortunately shifts it into a region of strong interference from the solvent and TOPO bands. Spectra have also been taken (not shown) of the 1:1 TOPO:acid complex in CCl_4 for $HAuCl_4$ and $HReO_4$; these show a peak at ~3200 and ~2750 cm^{-1}, respectively, resembling the trilaurylammonium salt spectra,[4] as expected. Dilution of these solutions of 1:1 complex with an equal amount of TOPO causes the disappearance of the absorbance around 3000 cm^{-1} and the appearance of the 1450-cm^{-1} band. The magnitude of the shift in going from 1:1 to a 2:1 complex ($\Delta\nu$ = 1750 to 1300 cm^{-1}) is similar to the large shifts found in going from HF to HF_2^- ($\Delta\nu$ = 2500 cm^{-1}),[5] and from HCl_2^- ($\Delta\nu$ = 1200 cm^{-1}).[5] This behavior, too, suggests to us a structure for the $H^+(TOPO)_2$ cation similar to that of the dihalide ions, namely $R_3PO\cdots H^+\cdots OPR_3$. From these and previous studies, however, it is not yet possible to decide whether this hydrogen-bonded system is symmetric as in HF_2^- or asymmetric as in certain crystalline salts of HCl_2^-.[5,6]

References

1. J. J. Bucher and R. M. Diamond, UCRL-19530, (1969), p. 293.

2. J. J. Bucher and R. M. Diamond, J. Phys. Chem. 73, 675 (1969); ibid., 73, 1494 (1969).

3. J. J. Bucher, M. Zirin, R. C. Laugen, and R. M. Diamond, J. Inorg. Nucl. Chem. 33, 3869 (1971).

4. W. E. Keder and A. S. Wilson, Nucl. Sci. Engr. 17, 287 (1963).

5. J. W. Nibler and G. C. Pimental, J. Chem. Phys. 47, 710 (1967).

6. S. Chang and E. F. Westrum, J. Chem. Phys. 36, 2571 (1962);
J. C. Evans and G. Y. -S. Lo, J. Phys. Chem. 70, 11 (1966).

THE VAPOR PRESSURE OF PROTACTINIUM METAL

R. L. Dod and T. C. Parsons

Two determinations of the vapor pressure of Pa metal have been reported,[1,2] but they differ from each other by orders of magnitude, and neither seems entirely reliable. We have recently completed a series of measurements of this vapor pressure and find a value different from and intermediate to the previously reported values.

Since the previous determinations had indicated that the vapor pressure of Pa metal was very low, in order to have reasonable hope of success an apparatus was developed capable of heating a tungsten Knudsen effusion crucible to temperatures of approximately 2700°K. The choice of tungsten for the crucible material is somewhat unfortunate as protactinium is known to alloy with tungsten, but the temperatures necessary severely restricted the choice of materials. The crucible was heated directly with an induction coil inside a water-jacketed Pyrex chamber which could be continuously pumped. A platinum collection foil was located 21 cm above the crucible behind a 1-cm-diameter collimator mask. The foil was exposed in five different locations during each sequence, following which the foil was changed and the individual exposures separated and α-counted.

Table I. Vapor pressure of Pa metal.

Crucible No.	Sequence No.	Temperature (°K)	Vapor pressure (atm)
1	2	2105	2.51×10^{-7}
		2224	2.08×10^{-7}
		2352	5.71×10^{-7}
		2466	4.07×10^{-6}
		2605	1.74×10^{-6}
	7	2165	2.38×10^{-7}
		2265	3.98×10^{-7}
		2358	6.77×10^{-7}
		2488	1.10×10^{-6}
		2625	1.69×10^{-6}
2	II	2118	1.18×10^{-7}
		2247	2.99×10^{-7}
		2363	3.28×10^{-7}
		2485	4.43×10^{-7}
		2593	2.46×10^{-6}
	VIII	2168	4.76×10^{-8}
		2288	2.98×10^{-7}
		2353	6.14×10^{-7}
		2470	2.14×10^{-6}
		2646	3.62×10^{-6}

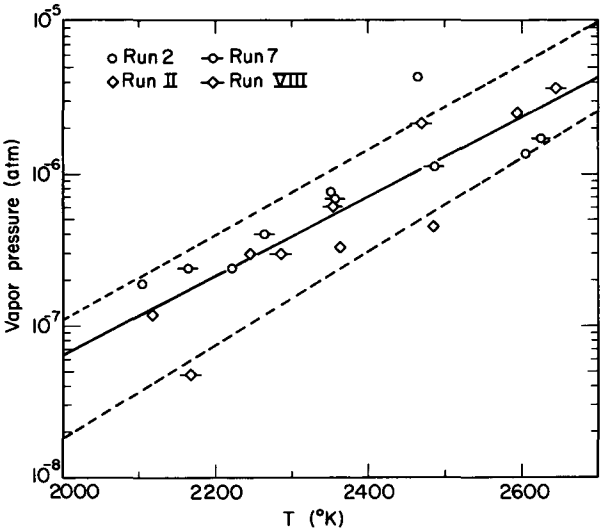

Fig. 1. Vapor pressure of protactinium metal. The solid line represents the linear least-squares fit of all data; the dashed lines include the extremes of linear least-squares fits of individual runs.

Two crucibles were manufactured from 1/2-inch tungsten rod and suitably cleaned and degassed to temperatures of ~2500°K. Each was loaded with a multimilligram piece of pure protactinium metal that had been scraped clean. In turn, each was loaded into the vacuum system and slowly heated, maintaining the pressure in the chamber below 5 μTorr to avoid reaction of the protactinium with the desorbed gases. The initial heating sequence on each crucible took it only slightly above the melting point of Pa metal (~1565°C) in order to release radioactive decay products trapped in the body of the metal and at the same time minimize alloying with the tungsten.

Following this procedure, a series of exposure sequences was made with each crucible. The measured vapor pressure increased with each exposure sequence until a limit seemed to be reached at about the sixth or seventh sequence, representing that many hours at temperatures at or above 2000 °K. This effect was determined to be due to protactinium metal diffusing through pores in the tungsten cap of the crucible, thus increasing the effective area of the effusion orifice. A mask was prepared for each crucible of 2-mil Ta foil which was held slightly above the top surface of the cap. A hole slightly larger than the effusion hole in the cap was drilled in the masks and located directly above the effusion hole. A single exposure sequence was made with each crucible with the masks in place, and the resulting data agreed well with those of the first sequence with each crucible.

The measured vapor pressures of Pa metal and the temperatures at which the measurements were made are listed in Table I for the first and last exposure sequence with each crucible. This data is also plotted in Fig. 1 with a line representing a linear least-squares fit of all data points. The dashed lines indicate the extremes of the linear least-squares fits for the individual exposure sequences.

This measured vapor pressure is consistent with the vapor pressures of others of the light actinides, and although the possibility of oxide vaporization cannot be excluded, the true pressure is probably quite close to that measured.

References

1. Murbach, NAA-SR-1988 (1957).

2. B. Cunningham, in Pa conference proceedings, Schloss Elmau, Germany, 1969.

THE CONCENTRATION OF HIGH BOILING IMPURITIES FROM LOW BOILING COMPOUNDS BY REVERSE FLOW GAS CHROMATOGRAPHY*

A. S. Newton

It has been suggested that one method of concentrating high boiling impurities in air or breath is the use of reverse-flow gas chromatography.[1] In this method the sample is introduced onto a suitable GLC column with characteristics such that the major components of the sample (O_2, N_2, Ar, H_2O, and CO_2 in the case of an air sample) are rapidly eluted from the column. The flow is then reversed and the impurities still on the column are eluted in a short time and can be collected for analysis by another method such as mass spectrometry or a more sensitive GLC column. The method is not limited to air but can be used on any system in which the bulk component can be rapidly eluted from a suitable column while the impurity components of interest are still held on the column.

While reverse-flow gas chromatography is widely used to rid columns of high boiling materials which are not of interest in the analysis under consideration, no detailed studies of the reverse GLC process were found. Therefore the process has been studied to evaluate its possibilities and limitations as a concentration method.

Most of this work was done with a 30-inch column of 0.25-inch-diameter stainless steel tubing packed with 80-100 mesh Porapak Q.[2] The column was enclosed in a laboratory oven, the temperature of which was controlled by a variable transformer. The helium flow through the column was controlled to operate in the forward or reverse direction with a six-port valve. The ports on this valve are se-

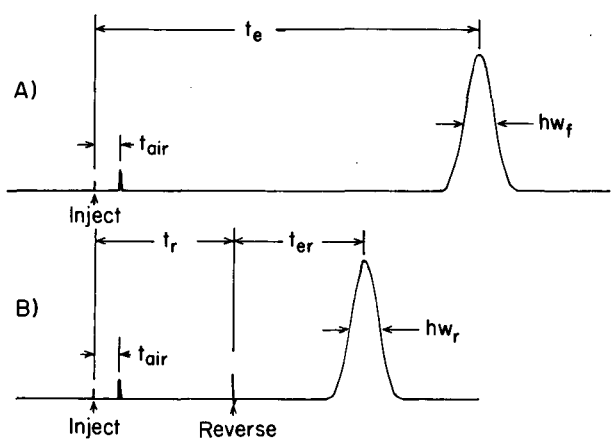

Fig. 1. Definitions of terms used in characterizing gas chromatographic peaks when: A) the chromatographic column is operated in the normal manner, and B) the helium flow through the column is reversed at a time t_r.
(XBL 7112-1796)

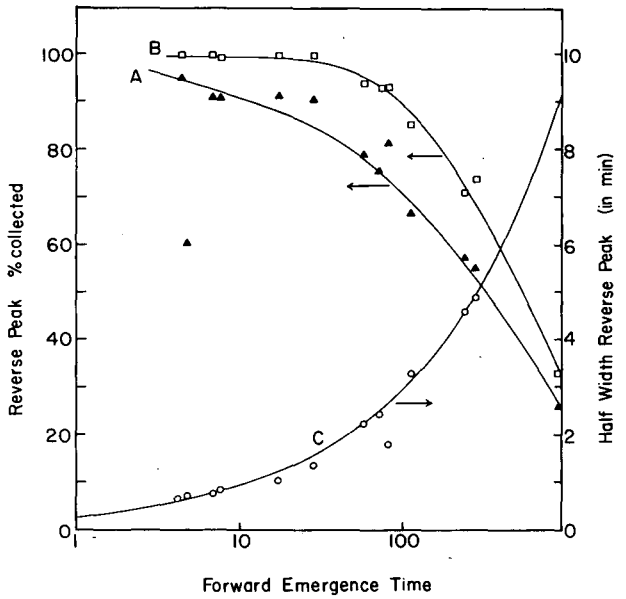

Fig. 2. Collection efficiency of various compounds when column flow is reversed after 4 min and the reverse peak collected for 4 min (curve A) and 5 min (curve B) as a function of the emergence time of the compound in the forward direction. Curve C is the half width of the reverse peak after reversal at 4 min. Points are experimental; line is calculated from Eq. (2). (XBL 7112-1799)

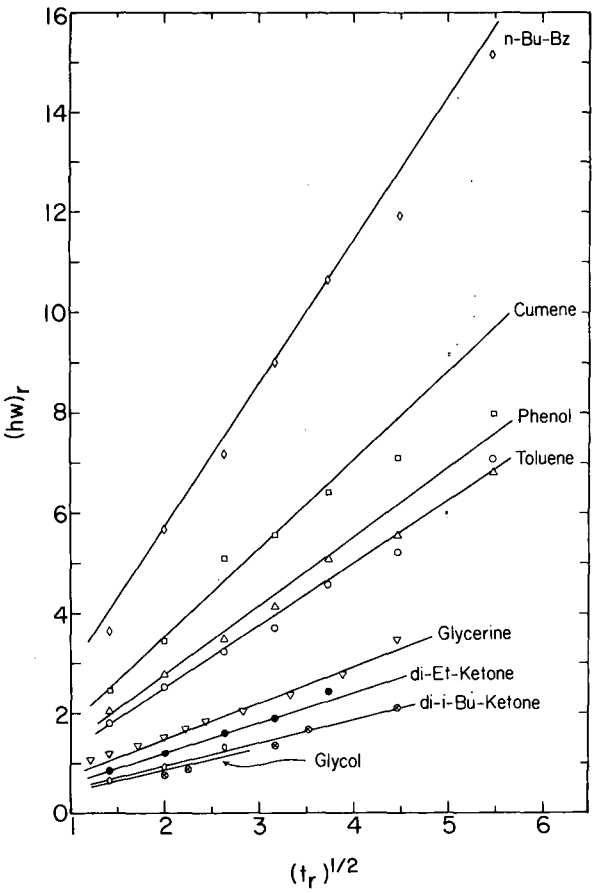

Fig. 3. Half width of reverse peaks of various compounds as a function of time of reversal of the helium flow rate. Lines are calculated from Eq. (3); points are experimental.

lected by a series of Viton-A O-rings on a push-pull shaft. The helium flow of 40 ml/min was controlled by a Miniflow controller. The detector was a thermal conductivity cell operated at 150°C.

Samples were dissolved in methanol, and 1 µl samples of a 5% solution in methanol were sufficient in most cases to give peaks suitable for characterization. On this column at 150°C, methanol is eluted in 2 min and the recorder is back at the baseline 4 min after injection. The peaks forward and reverse are characterized as shown in Fig. 1.

A series of samples with elution times in the forward direction, t_e, of from 4.2 to >1000 min were run with $t_r = 4$ min. The characteristics of these peaks are shown in Fig. 2. The half width of the forward peak follows the relation,

$$hw_f = k_1 t_e , \qquad (1)$$

while the half width of the reverse peak follows the relation

All except di-isobutyl ketone determined with Porapak Q column, 30-in. length, 150° C, 40 ml He/min, $k_1 = 0.100$. Di-isobutyl ketone determined with 6-ft column packed with 20% di-nonyl phthalate on 60-80 mesh Chromosorb, 120°, 120° C, 40 ml He/min, $k_1 = 0.054$. (XBL 7112-1797)

$$hw_r = k_2 t_e^{1/2} . \qquad (2)$$

In Eq. 2, k_2 must be a function of $t^{1/2}$.

The fractions of the respective reverse peaks collectable in 4 min after reversal and 5 min after reversal are also shown in Fig. 2. For t_e less than 100 min, the fraction collectable is > 75% for 4 min and > 90% for 5 min collection (except CH_3COOH, which has a poor collectability owing to severe tailing of the re-

verse peak). Beyond t_e = 100 min the fraction collected falls off, and at t_e = 1000 min is of the order of 25 to 30%.

Toluene was used to evaluate Eq. (2) as a function of the time of reversal, t_r. It was found that the half width of the reverse peak follows the equation:

$$hw_r = k_1 t_r^{1/2} t_e^{1/2}. \qquad (3)$$

The generality of this function is shown in Fig. 3 where a variety of compounds were investigated as a function of the time of reversal. The lines are calculated from Eq. (3). It is seen that the data fits Eq. (3) quite well, though with some compounds, e.g., isopropyl benzene and phenol, hw_r falls off at longer times of reversal of the flow.

The effect of large amounts of water was also investigated by injecting 40 μl of a 0.2% solution of ethylene glycol in water. At this level the column is overloaded and tailing of the water peak occurs. At t_r = 4 min, the concentration factor in a single pass with this amount of water is ~ 1500. It can be improved to $> 10^6$ by reinjecting and making a second separation of the water peak. Alternately, with two-column operation, the first column could be a preparatory column in which samples as large as 1 ml liquid could be injected. If this is followed by reinjection of the collected reverse flow material onto an analytical column, then a concentration factor of 10^6 can be achieved with adequate amounts of the impurities for determination and identification by various physical methods. A concentration of 1 part in 10^9 should be readily handled by two-column operation.

Footnote and References

*Condensed from LBL-283.

1. Private communication from Nabil Amer and Walter Perkins, Lawrence Berkeley Laboratory.

2. Porapak Q is the trade name of a proprietary copolymer of styrene and di-vinyl benzene.

SEARCH FOR SUPERCONDUCTIVITY IN LITHIUM AND MAGNESIUM*

T. L. Thorp, B. B. Triplett, W. D. Brewer, M. L. Cohen, N. E. Phillips, D. A. Shirley, J. E. Templeto. R. W. Stark,† and P. H. Schmidt‡

Recent advances in the theory of metals raise the possibility of reliably predicting the critical temperatures of superconductors from normal-state data. In particular, Allen and Cohen[1] have used a pseudopotential method to treat the electron–phonon interaction for a number of metals, and shown that Mg and Li might be superconducting at experimentally accessible temperatures. A verification of their calculation by the discovery of superconducting transitions in these metals would be of sufficient interest to justify a search for superconductivity, even though it is not possible to cover the whole of the temperature regions corresponding to the recognized uncertainty in the calculations. We have accordingly tested magnesium and lithium for superconductivity down to 4 m°K. The results were negative, but they serve to set limits for the parameters related to the critical temperature

The cryostat system used for this experiment was similar to that described by Brewer. Temperatures were measured by using a nuclear orientation thermometer. A single crystal of hexagonal cobalt was cut into needles with the axis of the needles parallel to the c axis. The needles were irradiated with neutrons to produce ^{60}Co in situ. For a good single crystal the large anisotropy field of 5 kOe and the small demagnetizing factor ensure that closure domains are small and most of the Co atoms are in domains magnetized along the c axis, subjecting all the nuclei to the same hyperfine interaction. The ^{60}Co nuclei are thermally distributed among the magnetic sublevels of the ground state split by the hyperfine interaction. Gamma rays emitted from states in ^{60}Ni fed from the ^{60}Co ground state have an anisotropic distribution; the anisotropy depends on the extent of the polarization of the ^{60}Co nuclei, the nature of the gamma transitions, and the depolarizing effects of intermediate transitions. We have checked for complete saturation of the magnetization of the single-crystal ^{60}Co thermometer. We compared the measured temperature with and without an external polarizing field and found that for the thermometer used in the experiments there was agreement to within the experimental error of 5%. The accuracy was limited by drifts in temperature due to applying field.

In order to check that the apparatus was working properly, the critical field curve of a sample of 99.999% tungsten was measured. The tungsten was attached to the copper stalk by plating copper onto a surface of gold partially diffused into the bulk material. The resistivity ratio (4–300°K) of the sample after diffusion bonding and plating was 17000. In addition to the transition near 15 m°K, a transition was also observed near 2°K. A sample which had not been subjected to the gold evaporation, heating, and bonding process did not show this high-temperature transition. We attribute this transition to the presence of small amounts of β tungsten formed during the bonding process which becomes superconducting in that region. The critical field curve measured in two experiments on tungsten to 5 m°K gave values of H_c about 10% different from those of Black et al.[3]

We were unable to find a superconducting transition in any of the magnesium or lithium samples. This does not completely rule out the possibility that T_c is greater than 4 m°K, because the samples may have supercooled. For pure, unstrained materials with a transition temperature in the m°K range, the coherence length ξ at T = 0 is very long, giving a small Ginsburg-Landau κ and type-I superconductivity. At a temperature at which the thermodynamic critical field is H_c the lowest field to which the sample can remain normal is $H_{c3} = 2.4\kappa H_c$ for surface nucleation, and $H_{c2} = \sqrt{2}\,\kappa H_c$ for bulk nucleation.

In summary, we have cooled lithium and magnesium to 4 m°K in magnetic fields of 10^{-2} Oe and to 5 m°K at 5×10^{-3} Oe without observing superconducting transitions. The possibility that the samples supercooled precludes setting a definite upper limit to T_c, but it seems probable that $T_c \lesssim 6$ m°K. At best, we have explored 60% of the temperature range predicted for T_c for magnesium; for lithium the theoretical estimates of T_c are so much in doubt that we may still be far from the region of the transition.

Footnotes and References

*Condensed version of a paper that appeared in J. Low Temp. Phys. 3, 589 (1970).

†Institute for the Study of Metals, University of Chicago, Chicago, Illinois.

‡Bell Telephone Laboratories, Murray Hill, New Jersey.

1. P. B. Allen and M. L. Cohen, Phys. Rev. 187, 525 (1969).

2. W. D. Brewer, Ph. D. thesis, University of California, Berkeley, 1970.

3. W. C. Black, R. T. Johnson, and J. C. Wheatley, J. Low Temp. Phys. 1, 641 (1969).

A PROPOSED ABSOLUTE TEMPERATURE SCALE FOR CERIUM MAGNESIUM NITRATE BELOW 0.003° K*

J. J. Huntzicker† and D. A. Shirley

Cerium magnesium nitrate, $Ce_2Mg_3(NO_3)_{12}\cdot 24H_2O$ (CMN), has long been recognized as a substance capable of being cooled by adiabatic demagnetization to extremely low temperatures. The pioneer investigation of the temperature scale for single-crystal CMN was reported by Daniels and Robinson[1] in 1953. Using calorimetric methods, they found that the minimum temperature reached was 3.08 m°K (millidegrees K) and was constant for all values of the magnetic entropy in the range $S/R \leq 0.45$. Above 6 m°K Curie's law was found to be obeyed, with T and S related by $\ln 2 - S/R = 3.2\times10^{-6}T^{-2}$. In a subsequent reanalysis of their data, de Klerk[2] asserted that the temperature did not become constant at S/R = 0.45 but continued to decrease to 2.25 m°K at S/R = 0.150.

In 1965 Frankel, Shirley, and Stone[3] demonstrated that nuclear orientation could be used to determine the temperature scale of CMN. They found that both of the above T-S relations were unable to explain the nuclear orientation results for ^{137m}Ce in CMN below 3 m°K. Using their data and the Daniels and Robinson results above 6 m°K, Frankel et al. derived a new T-S relation. They found that the temperature did not become constant at any value of entropy in the range available to them and at S/R = 0.303 (the lowest entropy which they reached), they reported T = 1.94 m°K.

In a recently reported investigation of single-crystal CMN, Hudson and Kaeser[4] studied both spherical and ellipsoidal samples by using the calorimetric γ-ray heating method. They found no shape dependence in the T-S correlation, and they confirmed that Curie's law was obeyed down to 6 m°K. However, they found that for the Curie law region $\ln 2 - S/R = 2.88\times10^{-6}T^{-2}$, in significant disagreement with the

value given by Daniels and Robinson. At temperatures greater than 15 m°K they observed a departure from the T^{-2} dependence. At the low-temperature end of the scale their results differed somewhat from those of Frankel et al., and below S/R = 0.296 they found the temperature to be essentially constant and equal to 1.53 ± 0.3 m°K.

Shortly after the present experimental work was completed, a calorimetric study of CMN was reported by the Leiden group (Mess et al.[5]). This work differed from the earlier calorimetric studies in two respects. First, the energy input was accomplished by Joule heating rather than by γ-ray heating. Secondly, lower entropies were obtained through a two-stage adiabatic demagnetization process. The results of this work can be summarized as follows: In the temperature range 8 m°K ≤ T ≤ 20 m°K, $\ln 2 - S/R = (2.4 \pm 0.1) \times 10^{-6} T^{-2}$, while for 20 m°K ≤ T ≤ 150 m°K the T^{-2} dependence is not obeyed. Above 150 m°K, $\ln 2 - S/R = 3.1 \times 10^{-6} T^{-2}$. The lowest temperature measured was 1.0 ± 0.3 m°K at S/R = 0.02. Finally, magnetic susceptibility measurements indicated that at T = 1.9 ± 0.1 m°K CMN undergoes a transition to a ferromagnetic state.

The work reported in this paper was undertaken to extend the entropy-temperature relation over a wide range via the nuclear orientation method. The absolute temperature scale for single-crystal cerium magnesium nitrate (CMN) has been extended to entropies as low a S/R = 0.002 by adiabatic demagnetization from values of H/T up to 68 kOe/°K. The temperature dependence of the highly anisotropic angular distribution of the 255-keV γ ray from oriented ^{137m}Ce in the CMN provided the thermometric parameter. The nuclear orientation results were interpreted with the spin Hamiltonian $\mathcal{H} = g_{\perp} \beta H_x S_x + B(S_x I_x + S_y I_y)$, where H_x is a calculated dipolar field. The hyperfine structure constant B was determined by normalizing the higher temperature nuclear orientation results to the calorimetric results of Hudson and Kaeser and of Mess et al. at high

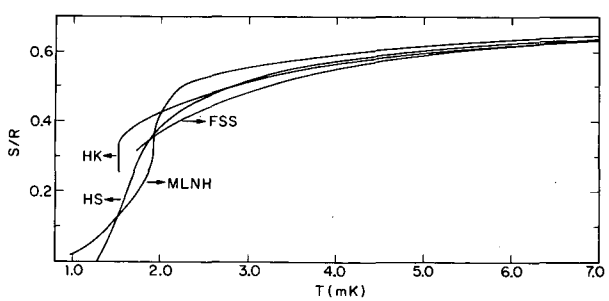

Fig. 1. S/R vs T. Hudson and Kaeser[4] (HK); Mess et al.[5] (MLNH); Frankel et al.[3] (FSS); this work (HS). (XBL 701-2278)

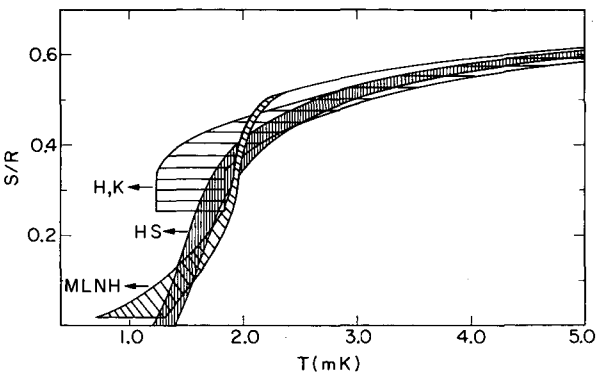

Fig. 2. Comparison of quoted experimental errors. Shaded area, this work; horizontal lines, Hudson and Kaeser; slanting lines, Mess et al. (XBL 701-2279)

entropies. A provisional temperature scale, based on both our nuclear orientation results and the calorimetric work, is proposed. This scale is compared in detail with the results from earlier studies of CMN.

The four most recent T-S scales are shown in Fig. 1. The two nuclear orientation scales (Frankel et al. and Huntzicker and Shirley) are in reasonable agreement although the Frankel et al. results yield systematically higher temperatures for a given entropy than do the present results. The results of Frankel et al. have been renormalized to the average of the Mess et al. and Hudson and Kaeser results at high temperatures.

There is a small systematic discrepancy between the two sets of orientation data. The explanation for this difference probably lies in the method of correction for the background under the γ-ray peak. This is a difficult correction to make, and the present work represents a somewhat more sophisticated approach to the problem than used by Frankel et al. Moreover, inspection of the data of Frankel et al. reveals that their experimental scatter is somewhat greater than in our work. We believe, therefore, that the present results are definitely to be preferred over those of Frankel et al.

The disagreement between our results and the calorimetric results appears to be more serious—especially for temperatures below 2 m°K. Furthermore there is a complete lack of agreement between the two calorimetric scales themselves. In Fig. 2 the quoted errors are depicted for our work and for the two calorimetric scales. This figure illustrates one of the most important advantages of the nuclear orientation method: namely, that it retains

Table I. Entropy-temperature relations for CMN, including proposed T_A scale.

S/R	T_{MLNH} (m °K)	T_{HK} (m °K)	T_A (m °K)
0.002			1.29(9)[b]
0.010			1.30(9)
0.020	1.0[a]		1.32(9)
0.040			1.36(9)
0.050	1.2		1.38(9)
0.070			1.41(9)
0.100	1.42		1.46(9)
0.130			1.51(9)
0.150	1.60		1.54(9)
0.170			1.57(9)
0.200	1.75	(1.53)[a]	1.62(9)
0.230	1.82	(1.53)	1.66(10)
0.250	1.86	(1.53)	1.69(10)
0.270	1.88	(1.53)	1.72(10)
0.300	1.92	1.53	1.77(10)
0.330	1.93	1.54	1.83(11)
0.350	1.94	1.56	1.88(12)
0.370	1.95	1.64	1.95(13)
0.400	1.97	1.81	2.07(13)
0.420	2.00	1.94	2.18(14)
0.450	2.07	2.24	2.37(15)
0.480	2.16	2.57	2.62(15)
0.500	2.25	2.84	2.81(17)
0.510	2.34	2.98	2.92(17)
0.520	2.45	3.06	3.04(18)
0.530	2.58	3.32	3.18(18)
0.540	2.75	3.50	3.35(19)
0.550	2.94	3.69	3.55(20)
0.560	3.20	3.92	3.79(22)
0.570	3.58	4.20	4.05(23)
0.580	3.75	4.48	4.34(25)
0.590	4.07	4.87	4.68(27)
0.600	4.40	5.30	5.06(29)[c]
0.610	4.80	5.75	5.47(30)
0.620	5.30	6.26	5.93(32)
0.630	6.00	6.76	6.46(35)

[a] We have made graphical interpolations, where necessary, using the values of T given in Table I of Ref. 4 and in Table I of Ref. 5. The precision of the interpolation is $2\text{–}3 \times 10^{-5}$ °K.

[b] Errors in last place are given parenthetically for the T_A scale. Errors in the other two scales are not indicated here. See Refs. 4 and 5.

[c] For $S/R < 0.590$, T_A depends on the other two scales through the normalization procedure discussed in text. For $S/R < 0.590$, T is derived directly from the (normalized) nuclear orientation data. Only in the entropy range $0.655 \leq S/R \leq 0.687$, is T_A equal to $1/2\,(T_{MLHN} + T_{HK})$.

considerable sensitivity even to the lowest temperatures where the calorimetric methods deteriorate. It should be noted that the error limits on our scale can be reduced by 50-70% when an accurate value of the hyperfine structure parameter B becomes available.

The most serious problem encountered in the calorimetric technique is that the temperature is obtained by a differentiation of th experimental S-Q curve. Thus the derived temperature is very sensitive to the curve fitting of the S-Q data. Moreover, any experimental scatter at the lowest entropies can cause large uncertainties in the slope (T) since there is no fixed point other than absolute zero to anchor the T-S curve. It should be noted that the heat function, Q, is determined in the calorimetric experiments by heating the specimen from various low temperatures to a given high temperature, T_0. It takes a given length of time, $\Delta t'$, to heat the specimen from a given low-temperature point, T'(S'), to T_0. Thus one must extract a heat function, Q', from a time interval $\Delta t'$, making appropriate corrections for heat leak, etc. While certain checks can be made on the various assumptions that go into determining Q' from $\Delta t'$, we feel that these checks are not totally convincing. Even if one accepts the Q-S curve as being free of systematic error, the data that have been presented by the two groups doing calorimetric work (Fig. 5 in Ref. 4 and Fig. 7 in Ref. 6) do not seem to us to be a quality that can be differentiated with confidence to give $T = dQ/dS$ with very high accuracy below 2 m°K.

The question of error estimates is also important. We note that the error estimates in the HK and MLNH studies are grossly different. At S/R = 0.50, for example, the HK estimate is ±0.3 m°K. Mess et al. give no error explicitly for this entropy, but their discussion implies that the error is much smaller than ±0.10 m°K. This difference is not supported by the apparent relative quality of the two sets of Q-S data (Ref. 4, Fig. 5, and Ref. 5, Fig. 7). We note, on closer study, that the Q values for a given entropy are in very bad disagreement in these two figures, differing by about a factor of 1.5 at the highest entropies. Apparently systematic errors in the calorimetric work should receive further study before firm conclusion about magnetic transitions can be drawn, especially since the Q-S curves must be differentiated to yield the absolute temperature. In the nuclear orientation technique the temperatures are derived directly from the γ-ray anisotropies: no differentiation is required.

As we have already pointed out, the two nuclear orientation scales are reasonably consistent while the two calorimetric scales are quite different. Moreover it should also be pointed out that although the two nuclear orientation scales originated from the same laboratory, the apparatus, the samples, and the methods of data analysis were different for the two scales. Thus any systematic errors peculiar to a particular apparatus can be ruled out. For this reason and those cited above, we feel that the low-temperature (T < 3 m°K) results of the present work more closely represent the thermal behavior of CMN than do the calorimetric scales. We therefore propose the T-S scale labeled as T_A in Table I.

Footnotes and References

*Condensed version of a paper published in Phys. Rev. (1971).

†Present address: I. Physikalisches Institut, Freie Universität, Berlin, Germany.

1. J. M. Daniels and F. N. H. Robinson, Phil. Mag. 44, 630 (1953).

2. D. DeKlerk, in Handbuch der Physik (Springer-Verlag, Berlin, 1956), Vol. 15, p. 38.

3. R. B. Frankel, D. A. Shirley, and N. J. Stone, Phys. Rev. 140, A 1020 (1965); ibid. 143, 334 (1966).

4. R. P. Hudson and R. S. Kaeser, Physics 3, 95 (1967).

5. K. W. Mess, J. Libbers, L. Niesen, and W. J. Huiskamp, Physica 41, 260 (1969).

DISTRIBUTION COEFFICIENTS OF SIXTEEN ELEMENTS ON THE ANION EXCHANGE RESIN DOWEX-I IN THE AZIDE FORM

U. Abed, R. D. Giauque, and E. H. Huffman

The ability of the azide ion, N_3^-, to form complexes of varying strengths with many metals is the basis for determining distribution coefficients which are useful when separation procedures are considered.

Adsorptions, expressed as K_d values, for V^{5+}, Mn^{2+}, Fe^{3+}, Co^{2+}, Ni^{2+}, Cu^{2+}, Zn^{2+},

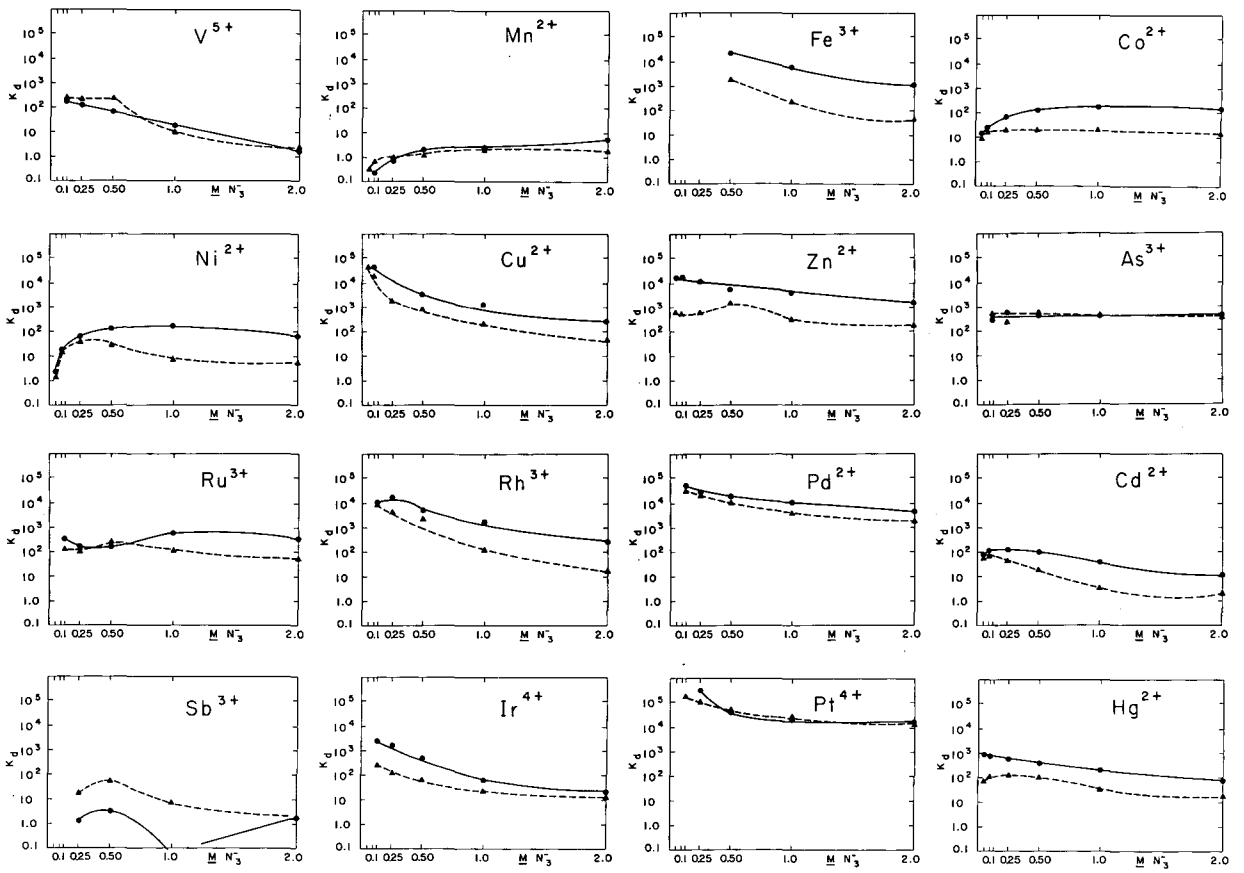

Fig. 1. Adsorption of the elements from sodium azide solutions.
Broken line = pH 5
Continuous line = pH 6.

(XBL 721-2024)

As^{3+}, As^{5+}, Ru^{3+}, Rh^{3+}, Pd^{2+}, Cd^{2+}, Sb^{3+}, Ir^{4+}, Pt^{4+}, and Hg^{2+} were determined at pH 5 and pH 6 for azide concentrations of 0.05, 0.10, 0.12(5), 0.25, 0.50, 1.0, and 2.0 M.

The affinity of these metals for the azide form of the resin was frequently found to differ from their respective adsorptions on the resin in the chloride form (Ref. 1).

Ti, Cr, Ga, Ge, In, Tl, Pb, and Bi precipitate under the experimental conditions of pH 5 and pH 6.

K_d values were normally measured after a 16-hour batch equilibration at 25° C in a constant-temperature water-bath, followed by colorimetric determinations of the metal remaining in the supernatant above the resin.

See the results in Fig. 1. As^{5+} showed zero adsorption for all azide concentrations, both at pH 5 and pH 6, and is therefore not represented graphically, while the K_d's for As^{3+} indicate a fairly level adsorption horizontal.

Phenomena of chemical and/or physical nature were observed with V^{5+}, Ru^{3+}, Rh^{3+}, and Sb^{3+} in the azide medium, the investigation of which could lead to the development of new colorimetric or electrochemical methods.

The study of other metals is in progress.

Reference

1. K. A. Kraus and F. Nelson, Anion Exchange Studies of the Fission Products, A/CONF/8/P/837, U.S.A., 23 June 1955.

RADIOLYSIS OF LIQUID N-ETHYLACETAMIDE*

H. A. Makada and W. M. Garrison

The radiation chemistry of simple organic amides is of considerable intrinsic interest and at the same time has potential application in the development of our understanding of the actions of ionizing radiations on more complex biochemical systems. Studies of the radiation chemistry of liquid formamide,[1,2] of liquid N, N-dimethyl formamide,[3] and of acetamide[4] in both liquid and solid states have recently been published. However, none of the simple amides studied contain the characteristic peptide function, $RCONHCHR_2$, which is of particular interest from the radiation biochemical viewpoint. In the present work we consider the radiation chemistry of one of the simplest peptide derivatives, N-ethylacetamide.

The 100-eV yields (G-values) of degradation products formed in the γ-radiolysis of liquid N-ethylacetamide are summarized in Table I. Yields are essentially independent of dose rate over the range 3.5×10^{16} eV/g min 1×10^{18} eV/g min and independent of total dose up to values of approximately 5×10^{19} eV/g.

The evidence is that heterolytic processes are of prime importance in the radiolytic degradation of the peptide bond to yield the aldehyde and amine functions. The scheme of reactions given in Eqs. (1) to (9) are consistent with the major experimental requirements of the present system.

$$RCONHCHR_2 \xrightarrow{\sim} RCONH\dot{C}R_2 + H^+ + e^-, \quad (1)$$

$$RCONHCHR_2 \xrightarrow{\sim} RCON=CR_2 + H_2, \quad (2)$$

$$e^- + RCONHCHR_2 \longrightarrow R\dot{C}(O^-)NHCHR_2, \quad (3)$$

$$H^+ + R\dot{C}(O^-)NHCHR_2 \longrightarrow R\dot{C}(OH)NHCHR_2, \quad (4)$$

$$R\dot{C}(OH)NHCHR_2 + RCONH\dot{C}R_2 \longrightarrow 2\ RCONHCHR_2, \quad (5)$$

$$R\dot{C}(OH)NHCHR_2 + RCONHCHR_2 \longrightarrow R\dot{C}(OH)\underset{\displaystyle RC(OH)NHCHR_2}{\underset{|}{N}}CHR_2, \quad (6)$$

$$R\dot{C}(OH)\underset{\displaystyle RC(OH)NHCHR_2}{\underset{|}{N}}CHR_2 + RCONH\dot{C}R_2 \longrightarrow RCONHCHR_2 + (RCO)_2NHCHR_2 + NH_2CHR_2, \quad (7)$$

$$2\ RCONH\dot{C}R_2 \longrightarrow RCONHCHR_2 + RCON=CR_2. \quad (8)$$

Table I. Product yields in the γ-radiolysis of N-ethylacetamide.

Product	G
Acetaldehyde	1.1
Ethylamine	1.2
Ammonia	< 0.1
Hydrogen	0.8
Carbon Monoxide	0.4
Methane, Ethane	< 0.3

The dehydropeptide, $RCON=CR_2$, formed in reaction (8) is labile and yields carbonyl through hydrolysis during the sequence of analytical manipulations

$$H_2O + RCON=CR_2 \longrightarrow RCONH_2 + R_2CO. \quad (9)$$

Electrons produced in the radiation-induced step (1) can be detected through use of electron scavengers such as organic chloro compounds, RCl, which species have been shown to be effective in trapping electrons produced in the radiolysis of polar media[5,6]

$$e^- + R'\ Cl \longrightarrow R' + Cl^-. \quad (10)$$

The production of chloride ion in the γ-radiolysis of liquid N-ethyl acetamide containing increasing concentrations of ethylene dichloride is shown in Fig. 1; a reciprocal yield plot is shown in the insert. These results provide a measurement of the yield of reaction 1, viz., $G_{e^-} \approx 3.2$.

The effect of ethylene dichloride on the yields of ethyl amine and acetaldehyde is summarized in Table IIA. In the presence of RCl, reaction (10) occurs in competition with

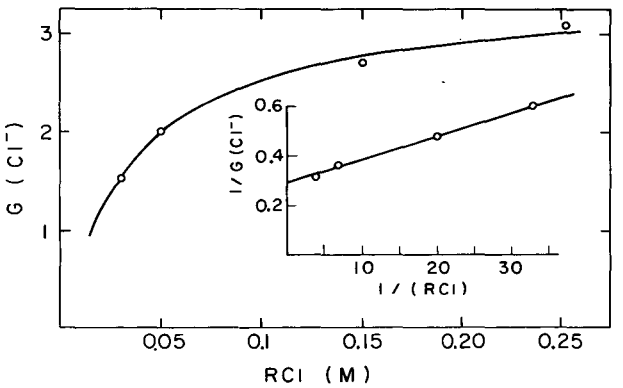

Fig. 1. Chloride ion yield in the γ-radiolysis of liquid N-ethylacetamide containing increasing concentrations of ethylene dichloride, R'Cl. Insert: reciprocal yield plot.
(XBL 709-3826)

Table II. Effect of added scavengers on acetaldehyde and ethylamine yields in the γ-radiolysis of N-ethylacetamide.

		G(RCHO)	G(RNH_2)
A. Ethylene dichloride (M)			
	None	1.10±0.05	1.21±0.1
	0.05	1.61	0.66
	0.16	1.82	0.76
	0.25	1.89	0.47
	0.32	2.03	----
	0.39	2.06	0.61
B. Ferric ion (mM)			
	None	1.10	1.21
	0.13	1.36	----
	1.32	2.79	----
	5.48	----	0.68
	13.2	3.92	----
	132	3.96	0.50

reaction (3), and this leads to a decrease in the amine yield since reactions (3), (4), and (7) are blocked. The fact that the amine yield levels off at a limiting value of $G(RNH_2) \approx 0.5$ at the higher R'Cl concentrations is interpreted as evidence that part of the amine production arises from a "high-energy" reaction, e.g.,

$$RCONHCHR_2 \xrightarrow{\sim} R + CO + \dot{N}HCHR_2, \qquad (11)$$

where the radical products of reaction (13) have excess energy and abstract H from $RCONHCHR_2$ to yield $RCONH\dot{C}R_2$. Such reaction also provides the source of the small amounts of methane and carbon monoxide reported in Table I. The acetaldehyde yield increases in the presence of ethylene dichloride as seen in Table IIA. At sufficiently high concentrations of R'Cl, reaction (1) is followed preferentially by reaction (10).

Oxidizing solutes such as Fe III scavenge both electrons and radicals. Effects of increasing Fe III concentrations on the yield of aldehyde and amine are shown in Table IIB. At sufficiently high concentrations of Fe III, the electrons produced in reaction (1) are preferentially scavenged via

$$e^- + Fe\,III \longrightarrow Fe\,II. \qquad (12)$$

Here again the scavenging of e^- prevents reaction (3), and as a result the amine yield decreases to the limiting value of $G(RNH_2) = 0.5$. The α-carbon radicals are scavenged by Fe III:

$$RCONHCR_2 + Fe\,III \rightarrow RCON{=}CR_2 + Fe\,II + H^+ \qquad (13)$$

$$RCONHCR_2 + Fe\,III \rightarrow Products. \qquad (13a)$$

We find at the higher Fe III concentrations that $G(RCHO) = 3.9$. The magnitude of this value indicates that a major fraction of the $RCONH\dot{C}R_2$ radicals is removed via step (13).

Footnote and References

*Condensed from Int. J. Radiat. Phys. Chem. 3, 179 (1971).

1. A. Matsumoto, N. Hayashi, and N. C. Lichtin, Radiation Res. 41, 299 (1970).

2. D. A. Head and D. C. Walker, Can. J. Chem. 48, 1657 (1970).

3. N. Colbourne, E. Collinson, and F. S. Dainton, Trans. Faraday Soc. 1963 59, 886 (1963).

4. E. Hayon and J. Weiss, Proc. 2nd Intern. Conf. Peaceful Uses Atomic Energy, Geneva, 1958, Vol. 29, pp. 80-85.

5. P. B. Ayscough, R. G. Collins, and F. S. Dainton, Nature 205, 965 (1965).

6. K. N. Rao and A. O. Allen, J. Phys. Chem. 72, 2181 (1968).

RADIOLYTIC OXIDATION OF PEPTIDE DERIVATIVES OF GLYCINE IN AQUEOUS SOLUTION*

H. A. Makada and W. M. Garrison

Radiolytic oxidation of peptide derivatives of the simpler α-amino acids in aqueous solution is initiated by OH attack at the C-H position of the peptide main-chain.[1] With peptide derivatives of alanine, for example, such attack in the presence of oxygen leads to formation of peroxy radicals of the type:

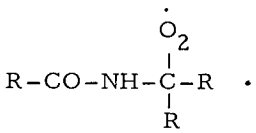

I

We have recently completed a study of the chemistry of such radicals as formed in the radiolytic oxidation of aqueous N-acetylanine and polyalanine.[2] In the present work we consider the nature of the intermediate processes involved in the radiolytic oxidation of peptide derivatives of glycine. In this case the degradation involves the radical species

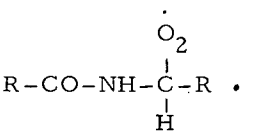

II

It was expected that the presence of the C-H linkage of radical II in place of the C-R linkage of radical I would lead to differences in the subsequent chemistry. We present here a detailed study of the γ-ray-induced oxidation of the simple peptide derivatives, N-acetylglycine and glycylglycine.

Radiolytic oxidation of the peptide main-chain in dilute oxygenated solution is characterized by the formation of labile amide-like degradation products.[1-3] A summary of the yields of inorganic and organic products observed in the radiolysis of 0.01 M N-acetylglycine and 0.01 M glycylglycine solutions under one atmosphere of oxygen is given in Tables I and II respectively.

The evidence from previous radiation-chemical studies[1] in which FeIII was used as a radical scavenger is that the OH radical formed in the radiation-induced step 1[4-6]

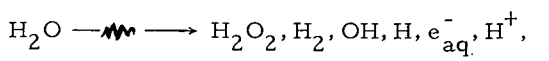

(1)

reacts with simple peptide derivatives such as N-acetylglycine and glycylglycine at the α-carbon position; i. e.,

Table I. Product yields in the γ radiolysis of N-acetylglycine (0.01 M) in oxygenated solution.

Product	Yield (g)
NH_3(total)[a]	2.9
NH_3(free)	< 0.2
CHOCOOH	0.3
CH_2O	0.1
HCOOH	2.9
$(COOH)_2$	< 0.1
H_2O_2	2.1
ROOH[b]	< 0.1

[a]Amide plus free ammonia.

[b]Total organic peroxide, unspecified.

Table II. Product yields in the γ radiolysis of glycylglycine (0.01 M) in oxygenated solution.

Product	Yield (g)
NH_3(total)[a]	4.8
NH_3(free)	~ 2
CHOCOOH	1.9
CH_2O	0.1
HCOOH	1.6
$(COOH)_2$	< 0.1
H_2O_2	2.1
ROOH[b]	< 0.1

[a]Amide plus free ammonia.

[b]Total organic peroxide, unspecified.

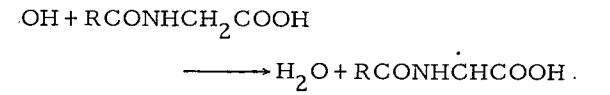

(2)

In the presence of oxygen, the peptide radicals, $RCONH\dot{C}HCOOH$, are scavenged via

$$O_2 + RCONH\dot{C}HCOOH \longrightarrow RCONHCH(\dot{O}_2)COOH. \quad (3)$$

In the case of N-acetylglycine the subsequent major steps include

$$2RCONHCH(\dot{O}_2)COOH \longrightarrow 2RCONHCH(\dot{O})COOH + O_2, \quad (4)$$

which reaction is followed by

$$O_2 + RCONHCH(\dot{O})COOH \longrightarrow RCONHCHO + CO_2 + HO_2, \quad (5)$$

where the diamide RCONHCHO is labile and yields amide and formic acid on mild hydrolysis:

$$H_2O + RCONHCHO \longrightarrow RCONH_2 + HCOOH. \quad (6)$$

In explaining the remarkably high yield of total ammonia, $G(NH_3) = 4.58$, from glycylglycine, we note that in the earlier study of the radiolytic oxidation of alanine peptides[2] there was some evidence that the alkoxy radical sites formed in reaction of the type given in Eq. (4) can react intramolecularly with other C–H linkages along the chain. In the case of the alkoxy radicals formed from glycylglycine via step 4, the subsequent chemistry would be of the form

$$NH_2CH_2CONHCH(\dot{O})COOH \longrightarrow NH_2\dot{C}HCONHCH(OH)COOH. \quad (7)$$

The radical product of reaction (7) reacts in turn with oxygen:

$$O_2 + NH_2\dot{C}HCONHCH(OH)COOH \longrightarrow NH = CHCONHCH(OH)COOH + HO_2 \quad (8)$$

$$H_2O + NH = CHCONHCH(OH)COOH \longrightarrow NH_3 + CHOCONH_2 + CHOCOOH. \quad (9)$$

The glyoxylamide, $CHOCONH_2$, then yields additional ammonia and glyoxylic acid on acid hydrolysis.

Footnote and References

*Condensed from LBL-242, October 1971; to appear in Radiation Res. 50, 48 (1972).

1. H. L. Atkins, W. Bennett-Corniea, and W. M. Garrison, J. Phys. Chem. 71 772-774 (1967).

2. W. M. Garrison, M. Kland-English, H. A. Sokol, and M. E. Jayko, J. Phys. Chem. 74 4506-4509 (1970).

3. W. M. Garrison, M. E. Jayko, and W. Bennett-Corniea, Radiation Res. 16, 483-502 (1962).

4. E. J. Hart and J. W. Boag, J. Am. Chem. Soc. 84, 4090 (1962).

5. A. O. Allen, Radiation Res. Suppl. 4, 54-73 (1964).

6. G. Czapski and H. J. Bielski, J. Phys. Chem. 67, 2180-2184 (1963).

SULFUR DIOXIDE AS A RADICAL SCAVENGER IN ALKENE SYSTEMS

D. C. Fee and S. S. Markowitz

A thermal distribution of the energies of reactive species is a barrier to the study of high-energy chemical reactions. The techniques of hot-atom chemistry have been developed to circumvent this carrier by introducing a highly energetic species, a "hot" atom, at the upper end of the chemically interesting energy region. Hot tritium atoms are produced by $^3He(n, p)T$ reactions with 192 000 eV of kinetic energy. They undergo successive energy-losing collisions with the molecules or atoms of the gas in which they are made, until they enter the energy range below 20 eV, where chemical reaction is thought to occur. Carbon-carbon and carbon-hydrogen bond energies are 3 to 4 eV, so

any reaction is energetically possible. The vast number of hydrocarbons in the environment has focused attention on the kind of information that can be obtained from recoil tritium chemistry. The typical experiment involves sealing known amounts of ^3He and a hydrocarbon in a 1720 Pyrex glass capsule which is irradiated with neutrons to form tritium. The products are separated by gas chromatography and measured in a flow proportional counter by monitoring the radioactive tritium. The general reaction pathways are[1]

abstraction $T\cdot + RH \longrightarrow R\cdot + HT$

addition $T\cdot + R-\underset{|}{C}=\underset{|}{C}-R \longrightarrow R-\underset{T}{\underset{|}{C}}-\underset{|}{C}-R$

substitution $T\cdot + RX \longrightarrow RT + X\cdot$

X=H, halogen, alkyl group.

The T-for-X substitution reaction may bring an excessive amount of energy into the RT species, causing it to undergo unimolecular decomposition.

Many recoil tritium experiments have used scavengers to remove thermalized tritium atoms and radical intermediates from the system before such species yield products that might be confused with high-energy tritium reactions.[1] Oxygen,[2] iodine,[3] bromine,[3] deuterated ethylene,[4] nitric oxide,[5] and iodine halides[6] have been used in gas phase experiments. All of these satisfy some of the criteria for a good scavenger proposed by Hawke and Wolfgang,[6] namely:

1) A scavenger must react avidly with the atoms and radicals to be removed, preferably with a collision efficiency near unity. It may then be used in sufficiently low concentrations so as not to interfere with the hot or other primary processes being studied. We are interested in recoil tritium reactions with alkenes, particularly cyclohexene and the methylcyclohexenes. Deuterated ethylene is thus eliminated by this criterion since its scavenging ability is of the same order of magnitude as other alkenes.[7]

2) A scavenger should be inert with respect to the bulk reagent. For alkene systems this eliminates iodine, bromine, and the iodine halides, since they would undergo rapid addition to the double bond. Oxygen may also be eliminated as a scavenger in cyclohexene systems since the rate of cyclohexene hydroperoxide formation is non-negligible at room temperature and increases with temperature. In addition a pyrex glass surface has a catalytic effect on the initial stages of the reaction.[8] This may rule out simultaneously raising the vapor pressure of cyclohexene by elevating the temperature and employing O_2 as a scavenger.

3) Products of the scavenging reaction should not react further, or if they do, such reaction should be controllable. In the recoil tritium-transbutene system, the presence of nitric oxide increased the 1-butene-t yield by 100%, presumably through a reversible reaction with sec-butyl-t radicals.[9] Thus nitric oxide is an unreliable scavenger for alkenes.

4) A gas phase scavenger must have an adequate vapor pressure at the temperature in question. Oxygen, the only reported scavenger left for alkene systems, readily satisfies this criterion.

5) Furthermore it is highly desirable, but not always essential, that the scavenged species be detectable. The peroxy radicals formed from

$$T + O_2 \rightarrow TO_2 \qquad (1)$$

are not readily assayed in the conventional radiogas chromatographic methods used for recoil tritium experiments. In addition, the peroxy radicals may react further with either the bulk reagent or other radicals in the system. As yet, there is no evidence that such further reaction results in products that might be mistaken for the yield of a hot reaction.

We report here a comparison between oxygen and sulfur dioxide as scavengers for recoil tritium-alkene systems. Sulfur dioxide was selected, since its reaction with radicals in other systems was known.[10]

The efficiency of a scavenger is determined by the dependence of various products on scavenger concentration. The yield of products formed solely by hot reactions will remain unchanged over a wide range of scavenger concentrations. The yield of products formed by both thermal and hot processes will decrease rapidly with the addition of scavenger until a plateau is reached where the yield is relatively insensitive to scavenger concentration. In this region, all thermal reactions, except with the scavenger, have presumably been suppressed and the yield is due entirely to hot reactions.[6]

In the T+cyclohexene system, the scavengeable thermal reaction product is cyclohexane-t, which results largely from thermal addition of T to the double bond to form a cyclohexyl-t radical. This radical then abstracts a hydrogen from the bulk system to form cyclohexane-t. Ethylene-t and butadiene-t are high-energy products from the unimolecular decomposition of excited cyclohexene-t formed by direct substitution.[11] The yields of these products for both O_2 and SO_2 scavenger are shown in Fig. 1. The sharp drop in cyclo-

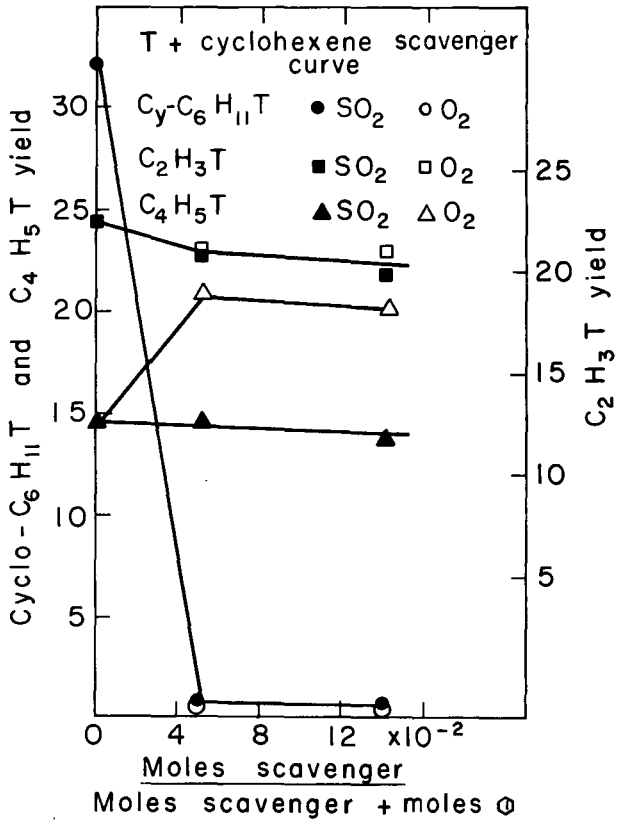

Fig. 1. Curves of T+cyclohexene system scavenged with SO_2 or O_2. Product yields are listed relative to cyclohexene-t yield as 100. The zero scavenger data point and the 5 mole % scavenger data point have been connected with a line for clarity. We do not mean to imply that the variation of yield with added scavenger is linear in this region.
(XBL 714-3238)

hexane-t yield is the same for both O_2 and SO_2. The small drop in the ethylene-t yield is the same for both O_2 and SO_2 and indicates a small thermal route in ethylene-t formation. The butadiene-t yield is constant with SO_2 scavenging but increases by 50% with O_2 scavenging! This anomalous increase in butadiene-t yield with O_2 scavenging is being investigated.

The comparison of O_2 and SO_2 was also made in the T + trans butene system. As shown in Fig. 2, the yield of butane-t, a product analogous to cyclohexane-t, was sharply reduced on the addition of both O_2 and SO_2. All other products exhibited the same yields for both O_2 and SO_2 scavenging, including a 50% decrease in the 1 butene-t yield. The anomalous increase in the 1 butene-t yield with NO as scavenger was duplicated in this laboratory.

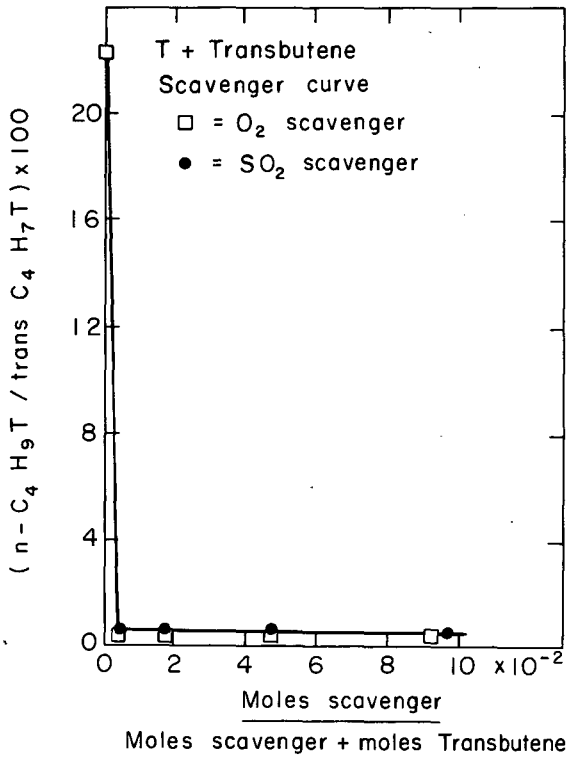

Fig. 2. Curves of T+trans-butene system scavenged with SO_2 or O_2. The ordinate gives the butane-t yield relative to the transbutene-t yield as 100. (XBL 714-3239)

Sulfur dioxide thus compares favorably with oxygen in some alkene systems and is superior in others. Sulfur dioxide has an adequate vapor pressure of over two atmospheres at room temperature.[12] Similar to oxygen scavenging, SO_2-scavenged species of the form R-SO_2 and HSO_2 are a) capable of further reaction (no problems of this sort are apparent in the SO_2 data to date), b) undetected in conventional analysis of gas phase products.

We have also compared the scavenging ability of SO_2 and O_2 in an alkane system where hydrogen abstraction to form HT is the low-energy reaction. The SO_2 data points show no scavenger plateau. In addition all of the thermal tritium atoms are not being removed by SO_2, since the HT yield is higher for the SO_2 than for the O_2-scavenged samples. The difference in scavenging efficiency observed here can be attributed to the large difference in collisional efficiency between O_2 and SO_2 for reaction with thermal tritium atoms:

$$T + SO_2 \rightarrow TSO_2 . \qquad (2)$$

The measured rate constants for reactions (1)[13] and (2)[14] for protium in place of tritium show a 10^5 preference for O_2 over SO_2.

We conclude that while SO_2 is not a good scavenger in alkanes it compares favorably with O_2 as a scavenger for alkenes. The use of SO_2 as a scavenger may be advantageous in alkenes since O_2, the only other scavenger available, shows some anomalous effects in cyclohexene.

References

1. R. L. Wolfgang, in Progress in Reaction Kinetics, III, edited by G. Porter (Pergamon, Oxford, 1965).

2. A. H. Rosenberg and R. L. Wolfgang, J. Chem. Phys. 41, 2159 (1964).

3. D. S. Urch and M. J. Welch, Trans. Faraday Soc. 62, 388 (1966).

4. R. T. K. Baker and R. L. Wolfgang, Trans. Far day Soc. 65, 1842 (1969).

5. J. K. Lee, B. Musgrave, and F. S. Rowland, Can. J. Chem. 38, 1756 (1960).

6. J. Hawke and R. Wolfgang, Radiochimica Acta. 14, 116 (1970).

7. K. R. Jennings and R. J. Cvetanovic, J. Chem. Phys. 35, 1233 (1961).

8. A. T. Touma and F. H. Verhoek, in Fifth Symposium on Combustion, Pittsburgh 1954, p. 741.

9. F. S. Rowland, J. K. Lee, B. Musgrave, and R. M. White, in Chemical Effects of Nuclear Transformations (IAEA, Vienna, 1961), Vol. 1, p. 67.

10. A. Henglein, H. Url, and W. Hoffmeister, Z. Physik. Chem. 18, 26 (1958).

11. R. W. Weeks and J. K. Garland, J. Chem. Phys. 73, 2508 (1969); R. W. Weeks and J. K. Garland, J. Am. Chem. Soc. 93, 2380 (1971).

12. Handbook of Chemistry and Physics, 49th ed. (Chemical Rubber Company, Cleveland, 1968).

13. R. W. Getzinger and G. L. Schott, J. Chem. Phys. 43, 3237, 1965.

14. R. W. Fair and B. A. Thrush, Trans. Faraday Soc. 65, 1550 (1969).

MUTUAL AFFINITY OF AMINO ACID SPECIES

J. M. Krochta,* C. Alesandrini,† and T. Vermeulen

Dimerization of amino acid molecules occurs appreciably in aqueous solution, and is important as a measure of the chromatographic-adsorption affinity between a free amino acid and one bound in a polymeric matrix. Dimerization is postulated to involve hydrogen bonding or electrostatic attraction between the zwitterionic NH_3^+ and COO^- groups:

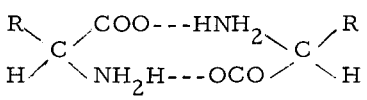

The tendency to dimerize can be measured by an equilibrium constant:

$$K_D = \frac{\text{dimer concentration}}{(\text{monomer concentration})^2} ,$$

where the monomer value is given by the total dissolved concentration, less the amount of monomer converted to dimer.

The activity of water, observed by a freezing-point lowering, measures the dimerization for an ideal solution but not otherwise. Glycine appears to form an ideal solution, and its freezing-point drop gives $K_D = 0.105 \pm 0.005$. Nonselective two-point interaction of zwitterion groups should be almost unaffected by the nature of R, the attached organic group, thus giving general predictive values of $K_D = 0.105$ in self-dimerization and $K_D = 0.21$ in inter-dimerization between dissimilar molecules.

Selectivity in dimerization arises when another part of each interacting molecule enhances or inhibits the two-point interaction. Three-point interaction has been shown to occur by Buss,[1] who found that the solubility of pure amino acid enantiomers shows unequal degrees of enhancement by a pure enantiomer of different amino acid. The corresponding inter-dimerization constants are always substantially greater than 0.2, usually between 0.5 and 2.0; and D- and L-values may differ as much as 30 to 40%. Additional values based on solubility have been provided by Su and Shafer,[2] and by Krochta and Vermeulen.[3]

The non-constancy of specific optical rotation for pure amino acid enantiomers has been measured accurately, and used to obtain self-dimerization K_D values (the same for either isomer of a pair). The workability of this new method suggests that various spectrometer measurements may also prove fruitful; such methods are needed, because for most amino acids the freezing-point data are obscured by nonideal-solution effects. From specific rotation measurements on a Bendix 143A Polarimeter, with a new data-analysis technique, the following self-dimer K_D values have been found: arginine, 0.68; arginine hydrochloride, 0.35; lysine hydrochloride, 1.30; histidine hydrochloride, 0.58. Four other amino acids showed inconclusively small changes in specific rotation, suggesting strongly that they undergo only the minimum two-point interaction. Such self-dimer constants must be known before fully dependable values of inter-dimer constants can be arrived at in the solubility studies.

Footnotes and References

*Present address: Western Regional Laboratory, U.S. Dept. of Agriculture, Albany, California.
†Present address: Norway Technical University, Trondheim, Norway.

1. D. R. Buss, Ph.D. Dissertation in Chemical Engineering, University of California, Berkeley, 1966.
2. S. C. K. Su and J. A. Shafer, J. Am. Chem. Soc. 90, 3961 (1968).
3. J. M. Krochta and T. Vermeulen, UCRL-20429, 1971.

THREE-COMPONENT ION EXCHANGE IN FIXED BEDS

A. G. Sassi, G. Klein, and T. Vermeulen

Local-equilibrium theory for multicomponent systems in packed columns predicts a complex effluent concentration profile, the number of transitions in it being one less than the number of exchangeable ionic species, and the number of intervening constant-composition plateaus being one less than the number of transitions.[1] These plateaus are approached, or even fully attained, in real systems; however, the rate-limited real transitions are always more sloping than those given by equilibrium theory.[2] This study has been

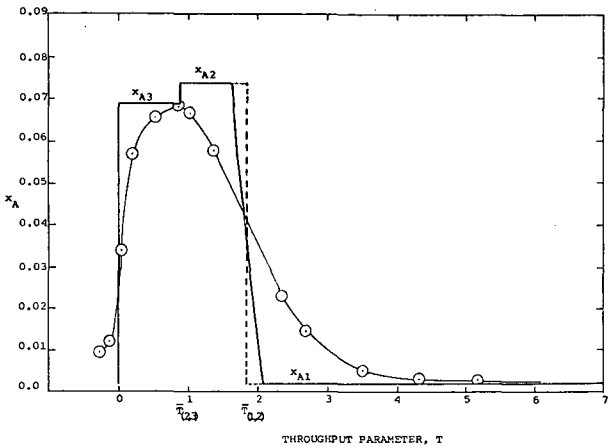

Fig. 1. Resin regeneration by four-times-concentrated brine in column uniformly presaturated with sea water. Plateaus and transitions from equilibrium theory (solid lines) compared to experimental calcium effluent-concentration history.

made to interpret theoretically a representative set of experimental three-component data, in terms of both equilibrium and nonequilibrium influences.

The data involve sea water, considered as a three-cation mixture (sodium, magnesium, and calcium), in which calcium removal is desired in order to avoid calcium-scale formation in an evaporator. Regeneration of the exhausted calcium-bearing resin can be carried out with a reject evaporator brine that is two to four times as concentrated as sea water, and thus gives a lower affinity of calcium for the resin. [3]

Equilibrium plateaus were fitted to the experimental curves by use of averaged binary mass-action constants: for Ca replacing Na, on Duolite C-24 resin, K = 0.97 (g/ml); for Mg replacing Na, K = 0.45 (g/ml); and for Ca replacing Mg, 2.15. Errors in the total numbers of equivalents of Ca or Mg leaving the column were attributed to small variations in column capacity, and were corrected for.

Because the primary process interest is in removing calcium rather than magnesium, the shapes of the transitional breakthrough curves for calcium were used to determine mass-transfer rates, treating the other ions present (principally Na, but also Mg) as a single component. In regeneration, the experimental curves for two consecutive transitions overlapped greatly; and only the last part of the curve lying wholly within the last transition, as shown in Fig. 1, was taken for fitting.

Standard breakthrough curves based on a reaction-kinetic model of mass transfer and on the applicable separation factor (analogous to relative volatility) were matched to the experimental curves to obtain the number of mass-transfer units N_R in each run. For a 4-ft column with 20-50 mesh resin, N_R ranged from 12 to 28 in calcium-removal runs and from 3 to 14 in regenerations with four-times-concentrated brine. The results showed that solid-phase diffusion controls in this operation, rather than pore diffusion or external mass transfer; they agreed within 2 to 20% with standard correlations, and indicated a diffusion coefficient of 3.0×10^{-7} cm^2/sec for the solid phase. [4]

References

1. G. Klein, D. Tondeur, and T. Vermeulen, Ind. & Eng. Chem. Fundamentals 6, 339 (1967).

2. R. N. Clazie, G. Klein, and T. Vermeulen, U. S. Off. Saline Water R & D Prog. Report 326 (1968).

3. G. Klein et al., Desalination 4, 158 (1968).

4. A. G Sassi, G. Klein, and T. Vermeulen, Report LBL-299, Jan. 1972.

MASS-TRANSFER COEFFICIENTS AND INTERFACIAL AREA FOR GAS ABSORPTION BY AGITATED AQUEOUS ELECTROLYTE SOLUTIONS

C. W. Robinson and C. R. Wilke

In order to design or optimize the operation of stirred-tank gas absorbers, such as are used for the submerged cultivation of aerobic microorganisms wherein oxygen is supplied by mass transfer from dispersed air bubbles, it is necessary to characterize the oxygen mass-transfer capabilities in terms of the physicochemical properties of the aqueous phase, the agitation power input, and the aeration rate. The oxygen mass-transfer capability of a completely mixed tank can be described in terms of the overall volumetric mass transfer

coefficient, $K_L a$, defined by the equation

$$R_A = K_L a V_L (C^* - C_B) \cdots, \qquad (1)$$

where: R_A = the total rate of absorption, lb mols/sec,
K_L = overall liquid phase mass-transfer coefficient, cm/sec,
a = gas-liquid interfacial area per unit volume of liquid, cm^3/cm^2,
V_L = volume of liquid in the tank, cm^3,
C^* = equilibrium solubility of the gas at the concentration in the gas leaving the tank, lb mols/cm^3,
C_B = concentration of the absorbed gas in the bulk liquid, lb mols/cm^3.

For a slightly soluble gas such as oxygen the overall mass-transfer coefficient is essentially equivalent to the liquid phase mass-transfer coefficient, so that $K_L a$ can be determined from physical absorption and desorption measurements. In more general cases, not involved in the study, it is necessary to account for the gas phase resistance to obtain $K_L a$.

$K_L a$ measurements for oxygen transfer were made in several aqueous electrolyte solutions of varying ionic strength over a wide range of agitation-aeration intensity in a 2.5-liter fully-baffled stirred tank having standard geometric ratios and equipped with a turbine-type impeller. Both steady-state and unsteady-state experimental methods were applied, utilizing a dissolved oxygen probe to measure the aqueous-phase oxygen tension or its rate of change. Mathematical analysis of and computer solutions for probe response in unsteady-state absorption or desorption are given in the original report. [1]

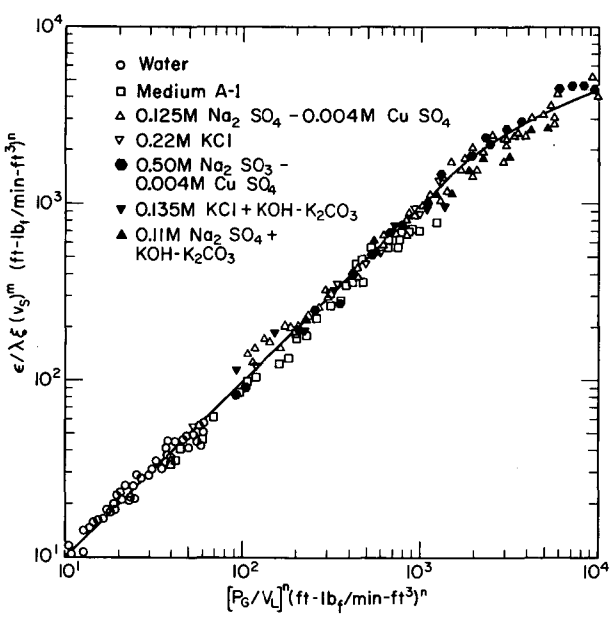

Fig. 1. Generalized correlation for oxygen mass transfer overall volumetric coefficients in aerated and agitated aqueous phases. (XBL 714-3207)

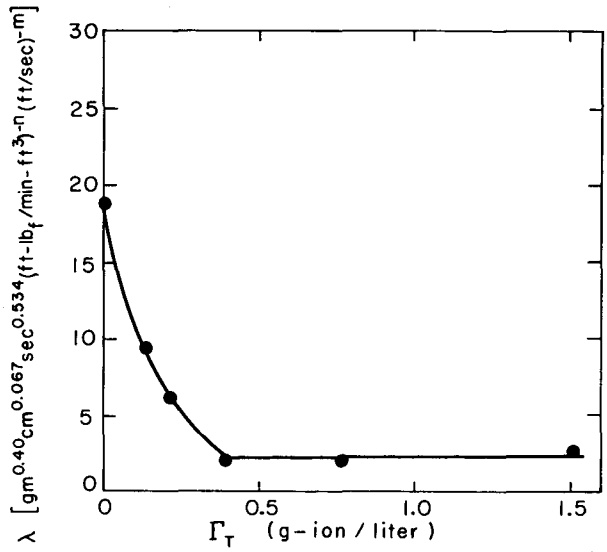

Fig. 2. Variation of λ with ionic strength. (XBL 714-3218)

$K_L a$ values were obtained as a function of the agitation power input per unit volume (P_G/V_L), superficial gas velocity (v_S), and

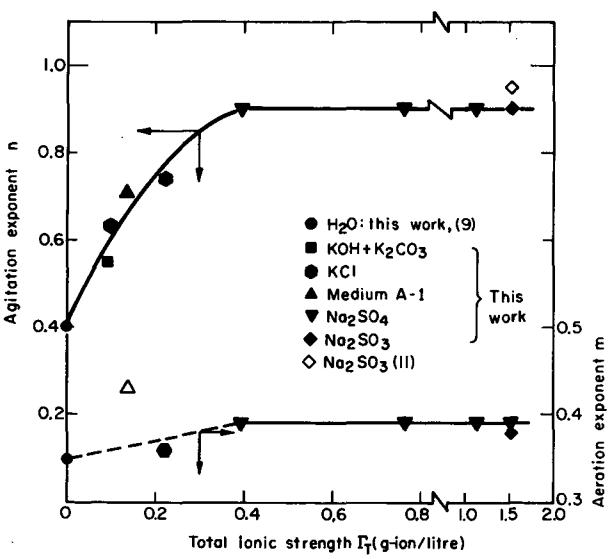

Fig. 3. Effect of ionic strength on agitation power per unit volume and superficial gas velocity exponents. (XBL 714-3208)

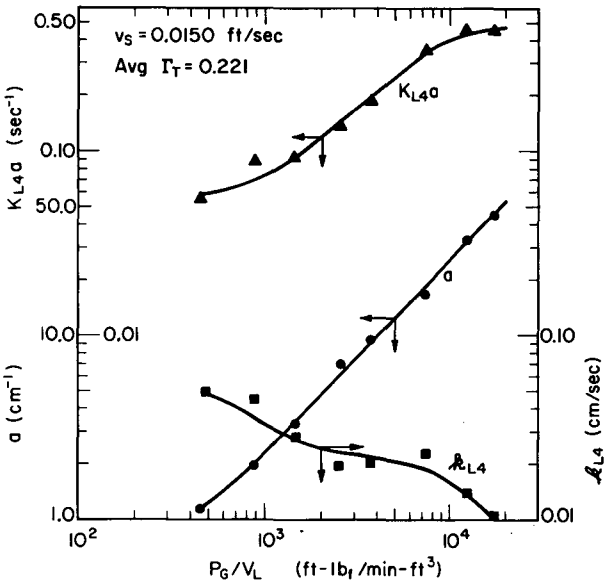

Fig. 4. Oxygen mass transfer coefficients and specific interfacial area in 0.135 M KCl + KOH - K_2CO_3 solution.
(XBL 711-2573)

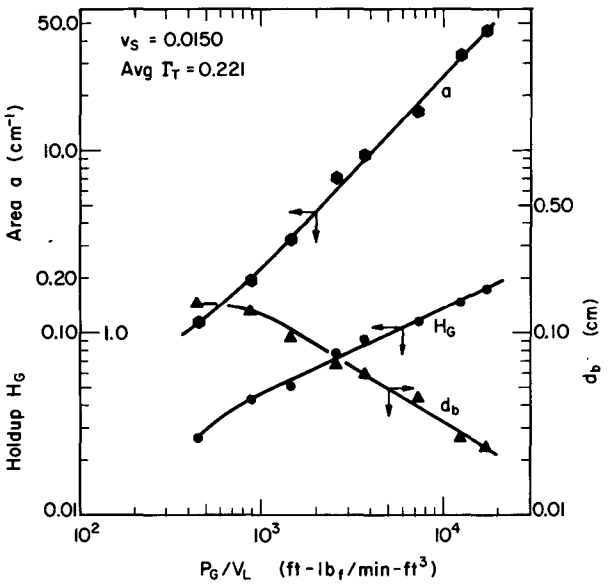

Fig. 5. Specific interfacial area, gas fractional holdup, and average bubble diameter in 0.135 M KCl + KOH - K_2CO_3 solution.
(XBL 711-2577)

solution ionic strength. The results indicate that the ionic strength has a pronounced effect on the value of K_La at constant P_G/V_L and v_S; the effect of ionic strength heretofore has not been explicitly described in the literature. A generalized dimensional correlation for the prediction of K_La for electrolyte solutions or for water was developed for the particular type of stirred tank used. The group $\epsilon/(\lambda\xi\, v_S^m)$ is expressed as a function of the power per unit volume as shown in Fig. 1 where

$\epsilon \approx K_La$ = volumetric liquid phase mass transfer coefficient, sec^{-1},
(P_G/V_L) = power per unit volume, ft lb/min ft^3
ξ = physical property factor,
$\xi = \rho_L^{0.533} D_L^{2/3}/(\sigma^{0.6}\, \mu_L^{1/3})$,
ρ_L = liquid density, g/cm^3,
D_L = liquid phase diffusion coefficient, cm^2/sec,
σ = liquid surface tension, dynes/cm,
μ_L = liquid viscosity, poises,
v_S = superficial gas velocity, ft/sec,
m = exponent on v_S,
n = exponent on (P_G/V_L),
λ = proportionality constant.

The exponents m and n and the proportionality constant λ were found to be functions of ionic strength of the liquid, as shown in Figs. 2 and 3.

A new simultaneous measuring technique involving concurrent chemical absorption of carbon dioxide and desorption of oxygen was developed for separately evaluating the liquid-phase oxygen mass transfer coefficient, k_L, and the specific interfacial area, a. Results from three different non-viscous electrolyte solutions showed that at high agitation power input levels, such that the average gas bubble diameter is between 0.02 and 0.25 cm, k_L decreases with increasing P_G/V_L. Figures 4 and 5 illustrate typical results. This behavior is in contrast with the results of others at lower agitation levels or in non-electrolytic liquids, but is in general agreement with previous results for the behavior of single bubbles or bubble swarms having the same range of average bubble diameter produced in viscous non-electrolytic aqueous solutions.

Reference

1. Based on UCRL-20472, April 1971.

MASS AND/OR HEAT TRANSFER BETWEEN FLUID PHASES: INFLUENCES OF INTERFACIAL INSTABILITY AND HIGH RATES OF MASS AND/OR HEAT TRANSFER

I. F. Davenport and C. J. King

It is becoming increasingly apparent that mass and heat transfer rates in liquid-liquid and gas-liquid contacting devices (e. g., extractors, absorbers) are often strongly influenced by interfacial instability arising from the mass and/or heat transfer itself. The instability may be caused by gradients in interfacial tension or density, which in turn are caused by developing gradients in composition and/or temperature. The goal of this project has been to gain a sufficient understanding of these phenomena to permit the development of rational design methods which take these effects into account. Gas-liquid and solid-liquid systems have been selected for the initial studies because it is possible to confine the influences of the instability to the liquid phase alone. With liquid-liquid systems the instability affects both liquid phases, and it becomes more difficult to isolate individual effects as is required to gain the fundamental understanding.

Experiments were carried out to measure and correlate the onset of convection when a liquid is heated from below through a horizontal solid-liquid interface, or cooled from above through a horizontal air-liquid interface. The experimental conditions were designed so that the temperature profile through the liquid was highly nonlinear (time dependent). This corresponds to situations most commonly found in practice.

Convection at the liquid-solid interface was shown to be density-driven for a number of liquids with a wide range of viscosity. The solid-liquid temperature was increased linearly with time. The results could be correlated by a time-dependent Rayleigh number (Ra_t) and the Prandtl number (Pr), when the temperature penetration depth was small compared with the fluid depth (see Fig. 1).

When the penetration depth, as expressed by $(\alpha t)^{1/2}$, was comparable to the fluid depth (H), the time-dependent Rayleigh number was observed to increase as shown in Fig. 2. In the "shallow pool" region, the results were independent of Prandtl number and approached a time-independent asymptote, expressed by a Rayleigh number based on height (Ra_H) having a constant value of about 1700. This plot helps to explain the transition mechanism in density-driven convection which is observed when the Rayleigh number (Ra_H) has a value of about 10^5. Our results show that for Ra_H greater than the transition value, the mechanism is time-dependent, fluid-depth-independent, whereas for lower values of Ra_H, the mechanism depends less on time and more on fluid depth.

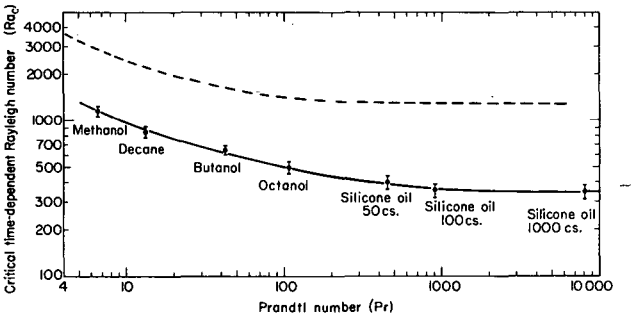

Fig. 1. Effect of Prandtl number on time-dependent, deep-pool convection initiation.
- - - Theoretical prediction of Foster for an amplification factor of 10^8. The experimental results could be identified with an amplification factor in the range 10^3 to 10^4.

(XBL 724-2769)

Experiments in which the fluid was vibrated sinusoidally showed that stability was decreased under various vibration conditions. There was no significant difference observed

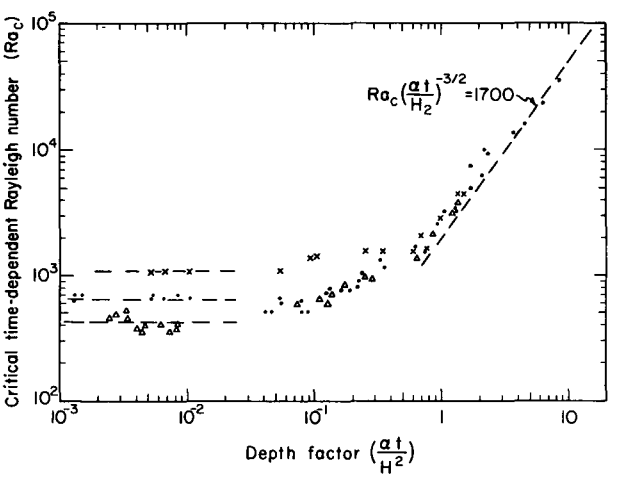

Fig. 2. Effect of fluid depth on time-dependent convection initiation.
x Methanol, Pr= 6.6
• Butanol, Pr= 43
△ Silicon oil 50cs., Pr= 450.

(XBL 724-2770)

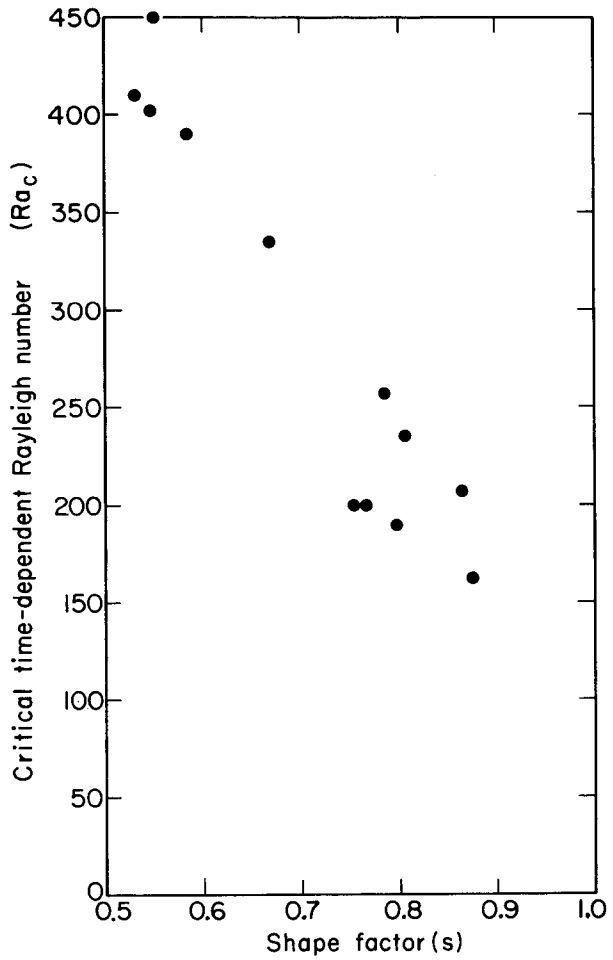

Fig. 3. Effect of shape factor on time-dependent, deep-pool convection initiation for octanol (Pr= 108). (XBL 724-2771)

between fluids that were contained by a solid surface at the upper edge of the liquid and those that were open to the air, provided the vibrating motion did not promote turbulence. Viscous heating was observed when the amplitude at any given frequency was high enough. Considering onset of viscous heating as an upper bound to the degree of vibration considered, the Rayleigh number (Ra_t) for methanol and octanol was found to have a maximum decrease of almost 40% from the value obtained on a "vibration-free" table, when oscillated to 60 Hz. The range of oscillation, 10 to 8000 Hz, was considered to be the range of common environmental vibration.

The wall spacing (D) was observed to have little effect on the results, provided the temperature penetration depth was much less than the wall spacing ($\alpha t/D^2 < 0.1$).

Convection at the horizontal air-liquid interface was produced by cooling through an air space (in contrast to cooling by evaporation). When thermal gradients along the air-liquid surface were eliminated, the convection was observed to be dominated by density forces.

The influence of the fluid depth when it was either much greater or comparable to the penetration depth was found, for n-butanol, to be similar to the results obtained for the solid-liquid surface convection. This implied that density effects continued to dominate over surface-tension forces even when the fluid depth was decreased to 2 mm and the temperature penetration was described by $\alpha t/H^2 = 8$.

The Rayleigh number for the air-liquid convection was observed to be similar to that obtained for the solid-liquid convection, over a range of Prandtl number values. This result is in contradistinction to results of various theoretical models which have been proposed.

Experiments showed that the Rayleigh number (Ra_t) for a linear decay in surface temperature with time was about 2.8 times as large as that produced by a step change in surface temperature. The trend observed by five liquids was similar to that shown for octanol in Fig. 3.

The effect of vibration (environmental "noise") on the air-liquid surface was observed to lower the Rayleigh number. This effect increased as the liquid viscosity decreased. In our apparatus there was no significant decrease for octanal (viscosity of 7.9 cm), but the decrease was almost 50% for decane (viscosity of 0.87 cp). The effect could be explained by the presence of surface waves and the action of surface-tension forces on a wavy surface to decrease stability.

A result of the study is a better understanding of the initiation, transient, and steady-state stages of interfacial instability. A new set of coordinates has been proposed to describe the heat or mass transfer coefficient during the transient and steady-state stages, with much more flexibility and accuracy than those currently existing in the literature.

A report describing this work is due for release during the coming year.[1]

Reference

1. I. F. Davenport and C. J. King, LBL-660 (1972).

PROTON MAGNETIC RESONANCE SHIFTS IN BIS (CYCLOOCTATETRAENYL) URANIUM (IV)†

N. Edelstein, G. N. Lamar,* F. Mares,‡ and A. Streitwieser, Jr.‡

The question of the extent of participation of the f orbitals in the metal-ligand covalency of organometallic actinide complexes has received renewed attention recently[1-4] with the emphasis on interpreting the Fermi contact contribution to the observed proton NMR shift of such paramagnetic complexes.[1] In complexes with magnetic anisotropy[2,3] both the contact and dipolar interactions[5,6] contribute to the isotropic shift, and before any interpretation of the contact shift can be put forth an estimate of the dipolar shift must be made. The lack of reliable structural or magnetic data has prevented detailed and unambiguous analyses for most systems. We wish to present here solution proton NMR data for bis(cyclooctatetraenyl)uranium(IV), $U(COT)_2$ (Ref. 7), also called "uranocene," for which both the structural[8] and magnetic[9] data are available, and interpret the shifts in terms of a crystalline field model.[9] From our analysis, we determine that part of the isotropic shift arises from the Fermi contact term, and reach some qualitative conclusions as to its electronic origin in relation to the metal-ligand bonding.

Samples of uranocene prepared according to the method of Streitwieser and Müller-Westerhoff[7] were dissolved in hot THF-d_8 or deuterated toluene and sealed under argon. The proton magnetic resonance shifts were measured on a Varian HR-100 spectrometer modified for variable frequency modulation. The temperature was controlled by a precalibrated Varian V-4343 unit. The shifts measured are plotted in Fig. 1 and tabulated in Table I. All shifts are referenced to the proton resonance in COT^{2-} which was taken as -5.9 ppm with respect to TMS. The actual data were measured with respect to the trace amounts of protons in the deuterated solvents and were later corrected to the proton resonance of COT^{2-}. The shifts in both solvents agreed within experimental error. The line widths appeared to be temperature independent and of the order of 10 Hz.

Table I. Contributions to the measured proton shifts at 302°K from the dipolar and Fermi contact terms for various values of the angle Ω.

R (Å)	$(3\cos^2\Omega - 1)$	$\langle \Delta H_D/H \rangle$ (ppm)	$\langle \Delta H_F/H \rangle$ (ppm)
3.481	-0.092	+ 8.6	+33.3
3.498	-0.152	+14.0	+27.9
3.515	-0.210	+19.2	+22.7

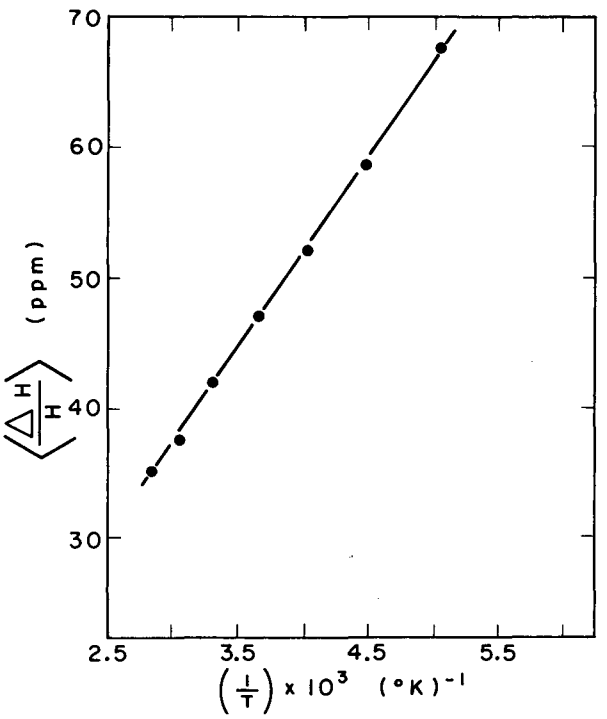

Fig. 1. Proton resonance shifts as a function of 1/T for $U(COT)_2$ (referenced with respect to COT^{2-}). (XBL 7012-4170)

The measured proton resonance shifts of $U(COT)_2$, Fig. 1, are analyzed on the basis of a crystalline field model and magnetic susceptibility data. In $U(COT)_2$ the orbital and spin angular momenta are coupled antiparallel for the ground state, so that a positive hyperfine coupling constant due to the Fermi contact term will result in an upfield proton resonance shift. The measured shifts are classified according to the mechanism of interaction in Table I. From this data the Fermi contact term A_F is found to be $A_F = (+0.90 \pm 25\%)$MHz.

If only pi bonding were present in this complex we would expect much smaller Fermi contact shifts and the opposite sign. Therefore, sigma bonding is certainly important if not dominant, although as yet we do not have enough information to be quantitative. Furthermore, even the sigma spin delocalization need

not be directly related to 5f covalency, since exchange polarization between the 5f and 6s or 6p electrons or other mechanisms cannot be ruled out.[10-12] Further investigations, some of which are currently in progress in our laboratories, are required to elucidate the bonding in this complex.

Footnotes and References

†Published in Chem. Phys. Letters 8, 399 (1971).

*Present address: Chemistry Dept., University of California, Davis, California.

‡Chemistry Department, University of California 94720.

1. R. von Ammon, B. Kanellakopulos and R. D. Fischer, Chem. Phys. Letters 2, 513 (1968).

2. R. von Ammon, B. Kanellakopulos, R. D. Fischer, and P. Lauberau, Inorg. Nucl. Chem. Letters 5, 219, 315 (1969).
R. von Ammon, B. Kanellakopulos, and R. D. Fischer, Radiochim. Acta 11, 162 (1969).

3. R. von Ammon, B. Kanellakopulos, and R. D. Fischer, Chem. Phys. Letters 4, 553 (1970).

4. N. Paladino, G. Lugli, U. Pedretti, M. Brunnell, and G. Giacometti, Chem. Phys. Letters 5, 15 (1970).

5. D. R. Eaton and W. D. Phillips, in Advances in Magnetic Resonance, Vol. 1, edited by J. S. Waugh (Academic Press, New York, 1965), p. 103.

6. R. J. Kurland and B. R. McGarvey, J. Magnetic Res. 2, 286 (1970).

7. A. Streitwieser, Jr. and V. Müller-Westerhoff, J. Am. Chem. Soc. 90, 7364 (1968).

8. A. Zalkin and K. N. Raymond, J. Am. Chem. Soc. 91, 5667 (1969).

9. D. G. Karraker, J. A. Stone, E. R. Jones, Jr., and N. Edelstein, J. Am. Chem. Soc. 92, (1970) 4841 (1970).

10. W. B. Lewis, J. A. Jackson, J. F. Lemons, and H. Taube, J. Chem. Phys. 36, 694 (1962).

11. R. E. Watson and A. J. Freeman, Phys. Rev. 156, 251 (1967).

12. R. E. Watson and A. J. Freeman, Phys. Rev. Letters 6, 277 (1961).

DIRECT NEAR-HARTREE-FOCK CALCULATIONS ON THE 1s HOLE STATES OF NO^+

P. S. Bagus* and H. F. Schaefer III†

For an open-shell molecule, ejection of an inner shell electron will give rise to several different electronic states of the resulting positive ion.[1] The separations between the above electronic states, arising from the same electron configuration, have been called[1] "exchange-induced splittings." This terminology is a result of the fact that, using single-configuration wave functions, the magnitude of the splitting is often given by a single exchange integral. Using photoelectron spectroscopy (also called ESCA[2]), such exchange splittings have been observed[2,3] in O_2 and NO and in a number of Mn and Fe compounds.[4,5]

The language used to describe the above phenomena implies clearly that single-configuration Hartree-Fock wave functions should render an accurate description of the observed splittings. The purpose of the present communication is to provide a test of this hypothesis. To do this we have performed direct Hartree-Fock calculations on the ionic states of interest. In addition, it is of considerable interest[6] to see if these splittings can be reproduced by using the simple exchange integral approach described above. Calculations of this type are carried out in terms of the neutral ground state molecular orbitals and are analogous to those for closed-shell molecules using Koopmans' theorem. We refer to this type of calculation as a frozen orbital approximation. Prior to the present calculations, we carried out a related study of the O_2 hole states. However, the existence of localized and delocalized hole states confused the interpretation. Therefore we turned to the conceptually simpler NO radical.

The calculations were carried out at 2.1747 bohrs separation, using a very large set of Slater functions (7s, 6p, 3d, and 2f on each atom), and the resulting molecular self-consistent-field energies are certainly no more than 0.0005 Hartree (0.01 eV) above the exact Hartree-Fock

Table I.

	State of NO^+	Frozen orbital approximation E(hartrees)	Frozen orbital approximation I. P. (eV)	Direct hole state calculation E(hartrees)	Direct hole state calculation I. P. (eV)	Experiment
Oxygen 1s	$^3\Pi$	-108.6097	562.93	-109.3771	542.05	543.3[a], x[b]
	$^1\Pi$	-108.5829	563.66	-109.3594	542.53	544.0[a], x+0.495±0.04[b]
Nitrogen 1s	$^3\Pi$	-113.5847	427.56	-114.1872	411.17	410.3[a], x[b]
	$^1\Pi$	-113.5396	428.79	-114.1375	412.52	411.8[a], x+1.415±0.02[b]

[a]Ref. 2.

[b]Ref. 9. Only the splittings are measured in this work.

energies. The NO ground state SCF energy is -129.29815 Hartrees. Two types of calculations are reported:

a) Frozen orbital approximation. These calculations are in terms of the $^2\Pi$ NO ground state orbitals and the splitting is given by a single exchange integral.

b) Direct hole state calculations.[7] These are near-Hartree-Fock calculations on the appropriate states of the NO^+ positive ion. The only previous molecular calculations of this type are those of Schwarz.[8]

The results are compared with experiment[2,9] in Table I. The first point to be made is that the ionization potentials predicted by the direct calculations are much closer (within 1.5 eV in all four cases) to experiment than are the frozen orbital results. This trend has been pointed out earlier.[7,8] The splittings have recently been determined experimentally with relatively high precision by Davis and Shirley.[9] For the oxygen 1s hole, the frozen orbital splitting is 0.73 eV, the direct calculation splitting 0.48 eV, and experiment 0.495±0.04 eV. For the nitrogen 1s hole the same three splittings are 1.23, 1.35, and 1.415±0.02 eV. We see that

a) the frozen orbital calculations are in qualitative agreement with experiment, and

b) the direct hole state calculations agree quantitatively with experiment.

Using a much smaller "double zeta" basis set and the frozen orbital approach, Schwarz[6] predicts splittings of 0.77 and 1.26 eV for the O and N hole states. The close agreement with our results implies that double zeta calculations may be quite reliable.

On the basis of the present NO results therefore, it appears that the single-configuration Hartree-Fock approximation is quite adequate for the description of exchange splittings of inner shell ionization energies.

The calculations reported here were carried out on the 360/91 computer at IBM Research Laboratory, San Jose.

Footnote and References

*Present address: IBM Research Laboratory, Monterey and Cottle Roads, San Jose, California 95114.

1. C. S. Fadley and D. A. Shirley, Phys. Rev. Letters 21, 980 (1968).

2. K. Siegbahn, C. Nordling, G. Johansson, J. Hedman, P. F. Heden, K, Hamrin, U. Gelius, T. Bergmark, L. O. Werme, R. Manne, and Y. Baer, ESCA Applied to Free Molecules (North Holland, Amsterdam, 1969).

3. J. Hedman, P. F. Hedman, C. Nordling, and K. Siegbahn, Phys. Letters 29A, 178 (1969).

4. C. S. Fadley, D. A. Shirley, A. J. Freeman, P. S. Bagus, and J. V. Mallow, Phys. Rev. Letters 23, 1397 (1969).

5. C. S. Fadley and D. A. Shirley, Phys. Rev. A2, 1109 (1970).

6. M. E. Schwarz, Theoretica Chimica Acta 19, 396 (1970).

7. P. S. Bagus, Phys. Rev. 139, A619 (1965).

8. M. E. Schwarz, Chem. Phys. Letters 5, 50 (1970).

9. D. W. Davis and D. A. Shirley, J. Chem. Phys. 56, 669 (1972).

LOCALIZED AND DELOCALIZED 1s HOLE STATES OF THE O_2^+ MOLECULAR ION

P. S. Bagus* and H. F. Schaefer III

The photoelectron spectrum of the oxygen molecule has been studied rather carefully by experimentalists[1-5] and its interpretation presents a significant challenge to theoreticians. For this reason we decided to carry out very accurate near-Hartree-Fock calculations on the hole states of O_2^+. The results are of particular interest because they show that the 1s hole states of O_2^+ are localized—that is, the ejected electron has been specifically removed from one of the two atoms.

The near-Hartree-Fock calculations were carried out in a manner similar to those reported recently[6] for the hole states of NO^+. The NO^+ calculations[6] were noteworthy in that the theoretical 1s ionization potentials were within 0.3% of experiment, and the 1s "exchange splittings"[7] were within a few hundredths of an electron volt of experiment. The present calculations were carried out at the experimental ground state internuclear separation for O_2, 2.282 bohrs. The direct

Table I. Ionization potentials, in eV, of the oxygen atom. Our self-consistent-field energy for the ^3P ground state of O is -74.80941 hartrees.

	State of O^+	Frozen orbital approximation	Direct hole state calculation	Experiment[a]
1s ejected	^4P	561.44	543.41	
orbital energy	^2P	564.31	548.09	
= 562.39 eV	^2D	564.59	547.81	
	^2S	567.88	551.97	
2s ejected	^4P	29.58	26.93	28.49
orbital energy	^2D	34.96	34.06	34.20
= 33.86 eV	^2S	39.34	37.72	37.88
	^2P	42.42	40.76	39.98
2p ejected	^4S	14.45	11.89	13.62
orbital energy	^2D	17.74	15.67	16.94
= 17.19 eV	^2P	19.94	18.16	18.63

[a] C. E. Moore, "Atomic Energy Levels," Nat. Bur. Std. (U. S.) Circ. No. 467 (1949).

Table II. Ionization potentials, in eV, of the oxygen molecule. The self-consistent-field energies for the $^3\Sigma_g^-$ state of O_2 are -149.66584 hartrees for the frozen orbital calculations and -149.66664 for the direct hole state calculations. Experimental values are in parentheses.

	State of O_2^+	g and u orbital symmetry required/frozen orbital approximation	g and u symmetry required/direct hole state calculations	No g and u orbital symmetry required/direct hole state calculations
$1\sigma_g$ ejected	$^4\Sigma_g^-$	563.52	554.44(543.1[a])	542.03
orbital energy	$^2\Sigma_g^-$	565.20	556.58(544.2[a])	542.64
= 564.07 eV	$^2\Delta_g$	565.38	556.63	
	$^2\Sigma_g^-$	566.67	558.07	
$1\sigma_u$ ejected	$^4\Sigma_u^-$	563.49	554.39	
orbital energy	$^2\Sigma_u^-$	565.19	556.57	
= 564.04 eV	$^2\Delta_u$	565.35	556.60	
	$^2\Sigma_u^+$	565.65	558.04	
$2\sigma_g$ ejected	$^4\Sigma_g^-$	43.38	40.99(39.6[a])	
orbital energy	$^2\Delta_g$	46.16	44.02	
= 44.88 eV	$^2\Sigma_g^+$	47.46	45.39	
	$^2\Sigma_g^-$	47.83	45.88(41.6[a])	
$2\sigma_u$ ejected	$^4\Sigma_u^-$	27.44	26.04(24.6[b])	
orbital energy	$^2\Delta_u$	31.19	29.97	
= 29.91 eV	$^2\Sigma_u^+$	32.49	31.32	
	$^2\Sigma_u^-$	34.81	33.45(27.9[a])	
$3\sigma_g$ ejected	$^4\Sigma_g^-$	19.10	19.10	
orbital energy	$^2\Delta_g$	21.32	21.32	
= 20.03	$^2\Sigma_g^-$	21.86	21.86	
	$^2\Sigma_g^+$	22.61	22.61	

Table II. (continued)

	State of O_2^+		g and u orbital symmetry required/frozen orbital approximation	g and u symmetry required/direct hole state calculations	No g and u orbital symmetry required/direct hole state calculations
$1\pi_u$ ejected	$^4\Pi_u$		16.02	14.28(16.10[b])	
orbital energy	$^2\Pi_u$	a)	17.26	15.63(17.05[b])	
= 19.20 eV		b)	20.25	18.80	
		c)	32.42	31.22	
	$^2\Phi_u$		18.34	16.78	
$1\pi_g$ ejected					
orbital energy	$^2\Pi_g$		14.47	13.09(12.1[b])	
= 14.49 eV					

[a]Ref. 2.
[b]Ref. 4.

hole state calculations were done using a very large basis set of Slater functions (7s, 6p, 3d, and 2f on each atom), and the resulting molecular self-consistent-field energies should lie no more than 0.01 eV above the exact Hartree-Fock energies.

In an attempt to gain some insight into the physical nature of the ionization processes, three types of calculations were carried out:

a) The frozen orbital approximation consists of evaluating the energy of O_2^+ wave functions constructed from the near-Hartree-Fock orbitals[8] for the ground state of neutral O_2. These calculations will be comparable to those obtained for closed-shell systems using orbital energies via Koopmans' theorem. From atomic calculations,[9] we know that the ionization potentials obtained in this way will usually be too large, since the positive ion wave function is not allowed to relax following the loss of an electron.

b) Direct hole state calculations were carried out for the pertinent states of O_2^+. As is normally the case, for homonuclear diatomic molecules each molecular orbital was required to have either g or u inversion symmetry.

c) Since the 1s ionization energies obtained in b) were not in satisfactory agreement with the experiment, direct hole state calculations were carried out without the restriction that each molecular orbital be of g or u symmetry.

Calculations on the oxygen atom ionization potentials are shown in Table I, and Table II contains our molecular results. There are three $^2\Pi_u$ states of O_2 arising from the $1\pi_u^3 1\pi_g^2$ electron configuration, and the values in Table II are the results of solving the 3×3 configuration interaction. For the direct hole state work, the three ionization potentials are the results of separate three-configuration MCSCF calculations. In general the frozen orbital ionization potentials are in fair-to-good agreement with experiment, and the direct hole state results are somewhat better. These re-

sults provide a clear indication of the kind of agreement with experiment that can be obtained by pushing to the very limit of the independent particle approximation.

The results for the 1s electrons in O_2 are of particular importance. The frozen orbital ionization potentials are about 20 eV too large. More surprisingly, the direct hole state calculations b) yield ionization potentials that are still more than 10 eV too large. Only after obtaining such poor 1s results from calculation b) did we decide to drop the orbital symmetry requirement and carry out calculation c). As Table II shows, the direct hole state calculations without g,u restriction yield ionization potentials within 1.5 eV of experiment, which is about as good as can be expected in light of inherent errors due to relativistic effects and electron correlation.[9]

If one removes a $1\sigma_g$ or $1\sigma_u$ orbital from a single-configuration wave function, in the resulting O_2^+ state a population of 7-1/2 electrons can be assigned to each oxygen atom. It is reasonable to designate such a state a delocalized hole state since the loss of electron is equally shared by the two atoms. Our calculations show that there is such a delocalized solution of the Hartree-Fock equations. However, by dropping the requirement that the ejected electron occupy either the $1\sigma_g$ or $1\sigma_u$ orbital, we have obtained a second solution of the Hartree-Fock equations. In fact there are two equivalent solutions of this type, one in which the electron is ejected from oxygen atom A and the second in which oxygen atom B loses an electron. Since these two localized Hartree-Fock wave functions result in energies more than 12 eV below the delocalized solutions, we must conclude that the localized solutions correspond to physical reality. A properly symmetrized total wave function (Σ_g or Σ_u) can be formed by mixing these two equivalent solutions.

The extent of the localization of the valence shell orbitals which results as a consequence of localizing the core is surprisingly large. In Table III, we list the gross atomic populations[10] for the $^4\Sigma^-$ localized 1s-hole state. The σ valence shell orbitals are still nearly symmetry-adapted, but the π orbitals are quite localized. Thus, the electronic structure in the valence shells appears to be that appropriate for FO^+. Recently, Snyder[11] has suggested that core holes should be localized on one of a number of equivalent centers based on arguments about the increase of atomic relaxation energy. Our calculations show that the localization is favored because of the large charge transfer between the two O atoms which gives rise to a molecular relaxation energy of ~ 12 eV.

Table III. Cross atomic populations for the localized orbital 1s-hole $^4\Sigma^-$ state of O_2^+. The valence shell orbitals are labeled to indicate the O_2 symmetry orbital which they most nearly resemble.

	Population	
Shell	Center A	Center B
$1s_A$	1.00	0.00
$1s_B$	0.00	2.00
$\sim 2\sigma_g$	1.13	0.87
$\sim 2\sigma_u$	0.92	1.08
$\sim 3\sigma_g$	1.03	0.97
$\sim 1\pi_u$	3.44	0.56
$\sim 1\pi_g$	0.26	1.74
Total	7.78	7.22

Footnote and References

*Present address: IBM Research Laboratory, Monterey and Cottle Roads, San Jose, California 95114.

1. D. W. Turner, C. Baker, A. D. Baker, and C. R. Brundle, Molecular Photoelectron Spectroscopy (Wiley-Interscience, 1970).

2. K. Siegbahn, C. Nordling, G. Johansson, J. Hedman, P. F. Heder, K. Jamrin, U. Gelius, T. Bergmark, L. O. Werme, R. Manne, and Y. Baer, ESCA Applied to Free Molecules (North Holland, Amsterdam, 1969).

3. R. N. Dixon and S. E. Hull, Chem. Phys. Letters 3, 367 (1969).

4. O. Edquvist, E. Lindholm, L. E. Selin, and L. Asbrink, Physica Scripta 1, 25 (1970).

5. D. W. Davis and D. A. Shirley, J. Chem. Phys. 56, 669 (1972).

6. P. S. Bagus and H. F. Schaefer, J. Chem. Phys. 55, 1474 (1971).

7. C. S. Fadley and D. A. Shirley, Phys. Rev. Letters 21, 980 (1968).

8. P. E. Cade, to be published.

9. P. S. Bagus, Phys. Rev. 139, A619 (1965).

10. R. S. Mulliken, J. Chem. Phys. 23, 1833 (1955).

11. L. C. Snyder, J. Chem. Phys. 55, 95 (1971).

ELECTRONIC STRUCTURE OF DIATOMIC MOLECULES

P. K. Pearson, S. V. O'Neil, and H. F. Schaefer III

The purpose of this article is to summarize theoretical work carried out at Berkeley during the past year[1-9] on the electronic structure of diatomic molecules. Some[10-12] of the work along these lines discussed in the Nuclear Chemistry Annual Report for 1970 (see page 190) did not appear in print until this year. Our theoretical calculations are ab initio, that is they result from the rigorous application of the variational principal to Schrödinger's equation within the Born-Oppenheimer approximation.

Collisional Quenching of Metastable Hydrogen Atoms[1]

Quenching of metastable hydrogen atoms by low-energy collisions with atoms and molecules is considered, the actual process being $H(2s) + X \rightarrow H(2p) + X$. The Born approximation, with long-range multipole-multipole interactions, is used to describe collisions of H(2s) with molecules, and simple formulas for the cross section result. Collisions with spherically symmetric species (i.e., rare gas atoms) are treated in the adiabatic approximation, and the process is seen to be formally identical to symmetric charge transfer. Numerical results for collisional quenching by helium, based on accurately computed potential curves, are presented. Shortly after the appearance of our $H(2s) + He \rightarrow H(2p) + He$ results,[1] an experimental paper[13] appeared in Physical Review Letters verifying in detail our predictions.

Krypton Nonofluoride and Its Positive Ion[2]

Nonempirical quantum mechanical calculations have been carried out on KrF and KrF^+. A large basis set of Slater functions was used, and the self-consistent-field (SCF) total energies for both diatomics are estimated to lie no more than 0.005 hartrees above the exact nonrelativistic Hartree-Fock energies. The KrF SCF potential curve is repulsive and dissociates smoothly to Kr+F atoms. The KrF^+ potential curve displays a minimum at 1.68 Å and spectroscopic constants $D_e = -0.02$ eV, and $\omega_e = 810$ cm^{-1}. The importance of polarization functions (d and f orbitals) in the single-configuration wave functions is discussed. Electron correlation in both molecules has been investigated by using first-order wave functions,[12] which have yielded dissociation energies in excellent agreement with experiment for several smaller diatomic molecules. A 158 configuration correlated wave function predicts a flatter but nevertheless repulsive potential curve for KrF. We conclude that, except for the van der Waals interaction, KrF is unlikely to exist in the gas phase. The relation between this work and the observation of the KrF ESR in crystals of KrF_2 is discussed. First-order wave functions containing 210 configurations for KrF^+ yield the following predictions: $r_e = 1.75$ Å, $D_0 = 1.90$ eV, $\omega_e = 621$ cm^{-1}. Chupka and Berkowitz report the experimental value $D_0 \geq 1.58$ eV for KrF^+. Several molecular properties are predicted for KrF^+.

Role of Electron Correlation in a Priori Predictions of the Electronic Ground State of BeO[3,7]

Ab initio wave functions including electron correlation have been calculated for the $^1\Sigma^+$, $^3\Sigma^+$, $^3\Sigma^-$, and $^3\Pi$ states of BeO. A (4s 2p 1d) basis set of Slater functions was centered on each atom. The iterative natural orbital method was used to optimize the set of molecular orbitals employed in each multiconfiguration first-order wave function. The $^3\Pi$ energy calculated here is 0.73 eV above the $^1\Sigma^+$ energy obtained in a comparable calculation. Since near Hartree-Fock calculations result in a $^3\Pi$ energy below the $^1\Sigma^+$ energy, it seems clear that electron correlation plays a crucial role in the ordering of these states. Predicted spectroscopic constants for the different states are seen in Table I. Natural orbital occupation numbers and coefficients of important configurations in the CI wave functions are presented to describe the electronic structure of BeO.

Theoretical Description of Molecular Rydberg States: $B^1\Sigma^+$ and Lowest $^3\Sigma^+$ States of BH[4]

Ab initio calculations, including electron correlation, have been carried out on the $X^1\Sigma^+$, $B^1\Sigma^+$, and lowest $^3\Sigma^+$ states on BH.

Table I. Summary of predicted spectroscopic constants for low-lying states of BeO. (Experimental values in parentheses.)

State	T_e(eV)	R_e(Å)	ω_e(cm^{-1})	B_e(cm^{-1})
$^1\Sigma^+$	0	1.313(1.331)	1629(1487)	1.699(1.651)
$^3\Pi$	0.734	1.463	1270	1.365
$^1\Pi$	(1.166)	(1.463)	(1144)	(1.366)
$^3\Sigma^+$	1.93	1.384	1234	1.527
$^3\Sigma^-$	Repulsive			

The last two states can be thought of as arising from the $1\sigma^2 2\sigma^2 3\sigma 4\sigma$ electron configuration. A double-zeta-plus-polarization and Rydberg function basis of Slater functions is used and electron correlation is considered through the use of approximate "first-order" wave functions. Optimum wave functions for the $B^1\Sigma^+$ state are obtained by repeated diagonalization of the density matrix arising from the second eigenvalue of the $^1\Sigma^+$ secular equation. For the ground state the ab initio dissociation energy is 3.27 eV, compared to Gaydon's experimental value 3.54±0.04 eV. Other spectroscopic constants for the $X^1\Sigma^+$ and $B^1\Sigma^+$ states are also in good agreement with experiment. The X-B separation is calculated to be 51 770 cm^{-1}, compared to the experimental value 52 347 cm^{-1}. The $B^1\Sigma^+$ calculations confirm the double minimum predicted by Browne and Greenawalt. The lowest $^3\Sigma^+$ state is predicted by the present treatment to be Rydberg-like (with a minimum at 1.173 Å) for short internuclear separations and valence-like (repulsive) for large separations. A maximum occurs in the $^3\Sigma^+$ potential curve at 1.45 Å. Natural-orbital analyses and electron density plots are used to describe the valence to Rydberg "transition."

Curve Crossing of the $B\ ^3\Sigma_u^-$ and $^3\Pi_u$ States of O_2 and Its Relation to Predissociation in Schumann-Runge Bands[5]

Nonempirical quantum mechanical calculations including electron correlation have been carried out for the lowest $^3\Sigma_u^-$ and $^3\Pi_u$ states of O_2. A relatively large basis set is used and 257 $^3\Sigma_u^-$ and 345 $^3\Pi_u$ symmetry-adapted configurations are included in the first-order wave functions. For the $B\ ^3\Sigma_u^-$ state the theoretical spectroscopic constants (with experimental values in parentheses) are T_e 6.16 eV (6.17), D_e 0.76 eV(1.01), r_e 1.64 Å (1.60), ω_e 679 cm^{-1} (709), and B_e 0.783 cm^{-1} (0.819). Neither state is well described by a single electron configuration and the $B\ ^3\Sigma_u^-$ state is seen to have a normal (non-Rydberg) electron distribution. The calculated potential curves indicate that the repulsive $^3\Pi_u$ curve crosses the inner limb of the $B\ ^3\Sigma_u^-$ curve. Analogous calculations on the repulsive $^1\Pi_u$ state yield a crossing of the outer limb of the $B\ ^3\Sigma_u^-$. Figure 1 shows the predicted potential energy curves. Since previous interpretations of the predissociation of $B\ ^3\Sigma_u^-$ have suggested that $^3\Pi_u$ crosses the outer limb, this predissociation is discussed in some detail. It is concluded that spin-orbit coupling is the principal interaction responsible for the predissociation, so that all four repulsive states that dissociate to ground state atoms are expected to predissociate $B\ ^3\Sigma_u^-$ to roughly the same degree.

Molecular Autoionization Lifetimes and Cross Sections for Penning Ionization: Numerical Results for $He^*(1s2s\ ^3S) + H(1s\ ^2S)$[6]

The width Γ (or lifetime $\hbar/\Gamma$) for autoionization of $He^*(1s2s\ ^3S) + H(1s\ ^2S)$ has been calculated as a function of internuclear distance, and cross sections for Penning and associative ionization ($He^*+H \rightarrow He+H^+ + e^-$, $HeH^+ + e^-$) have been determined for low collision energies. Associative ionization is 22% of the total ionization cross section in the limit of zero collision energy; this fraction decreases with increasing energy, being

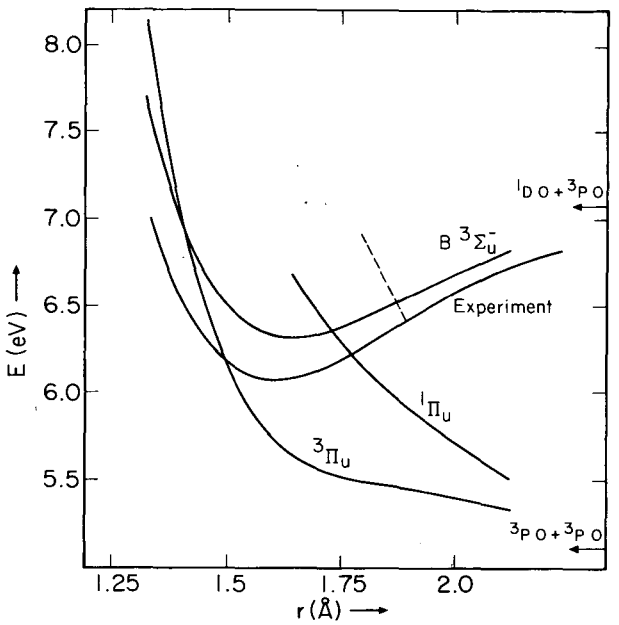

Fig. 1. Theoretical potential curves for the $^3\Pi_u$, $^1\Pi_u$, and B $^3\Sigma_u^-$ states of O_2. The experimental B state curve is that of Albritton, Schmeltekopf, and Zare. The dashed line is the repulsive curve inferred by Murrell and Taylor. The energy scale is relative to the v = 0 level of the X $^3\Sigma_g^-$ ground state.

~ 18% at a collision energy corresponding to 300°K. The distribution in energy of the ionized electron is also calculated, and it is seen that measurement of this quantity should lead to a good estimate of the well-depth of the He^*-H potential. Comparison of these results to those obtained by an orbiting model shows that the model (suitably scaled) is adequate in predicting the total ionization cross section, but is less accurate for the more detailed collision properties.

Interatomic Correlation Energy and the van der Waals Attraction Between Two Helium Atoms[8]

A priori calculations have been carried out on He-He for 26 internuclear separations between 3.0 and 10.0 bohrs. The interatomic correlation energy is added to the Hartree-Fock energy to predict a potential energy curve. The calculated potential parameters are ϵ = 12.02°K, σ = 2.608 Å, R_e = 2.944 Å. Predicted values of the coefficients C_6 and C_8 are within 7% and 3% of the accepted values. The interatomic correlation energy is divided into contributions from atomic and molecular orbitals of different symmetry types.

Excited Bound States of Neon Hydride[9]

A theoretical study of the ground states of OH, HF^+, HF, HF^-, NeH^+, and NeH has been carried out. Extended basis sets were used and electron correlation was included by way of first-order wave functions. Dissociation energies and other spectroscopic constants are in good agreement with available experimental data except for the bond distance of HF^+. Electron detachment in collisions between H and F^- is discussed on the basis of the calculated potential curves. Potential curves were also obtained ab initio for the three lowest excited states of NeH. These curves are qualitatively similar to those reported earlier by Slocomb, Miller, and Schaefer[1] for HeH. The $C^2\Sigma^+$ state of NeH is predicted to have a potential maximum of 0.87 eV at internuclear separation ~ 4 bohrs.

Acknowledgments

We wish to thank Charles A. Slocomb, William H. Miller, Bowen Liu, Charles F. Bender, Donald R. McLaughlin, and Vladimir Bondybey for their contributions to the work reviewed herein.

References

1. C. A. Slocomb, W. H. Miller, and H. F. Schaefer, J. Chem. Phys. 55, 926 (1971); also UCRL-20527.

2. B. Liu and H. F. Schaefer, J. Chem. Phys. 55, 2369 (1971).

3. S. V. O'Neil, P. K. Pearson, and H. F. Schaefer, Chem. Phys. Letters 10, 404 (1971).

4. P. K. Pearson, C. F. Bender, and H. F. Schaefer, J. Chem. Phys. 55, 5235 (1971).

5. H. F. Schaefer and W. H. Miller, J. Chem. Phys. 55, 4107 (1971); also UCRL-20598.

6. W. H. Miller, C. A. Slocomb, and H. F. Schaefer, J. Chem. Phys. 56, 1347 (1972); also UCRL-20709.

7. P. K. Pearson, S. V. O'Neil, and H. F. Schaefer, J. Chem. Phys. 56, 3938 (1972).

8. D. R. McLaughlin and H. F. Schaefer, Chem. Phys. Letters 12, 244 (1971).

9. V. Bondybey, P. K. Pearson, and H. F. Schaefer, J. Chem. Phys., submitted; also LBL-258.

10. H. F. Schaefer and T. G. Heil, J. Chem. Phys. 54, 2573 (1971); also UCRL-19983.

11. S. V. O'Neil and H. F. Schaefer, J. Chem. Phys. 55, 394 (1971); also UCRL-20401.

12. H. F. Schaefer, J. Chem. Phys. 55, 176 (1971); also UCRL-20417.

13. R. S. Kass and W. L. Williams, Phys. Rev. Letters 27, 473 (1971).

A PRIORI POTENTIAL ENERGY SURFACES FOR SIMPLE POLYATOMIC SYSTEMS

D. H. Liskow, S. V. O'Neil, C. F. Bender,* and H. F. Schaefer III

One of the most exciting developments in theoretical chemistry over the past few years has been the emergence of theoretical and computational methods for the reliable a priori prediction of the electronic structure of polyatomic molecules.[1] The purpose of the present discussion is to review work[2-7] carried out along these lines at Berkeley during the past year. Some[8-11] of our work on polyatomic molecules discussed in the 1970 Nuclear Chemistry Annual Report (UCRL-20426, pp. 190 and 223) did not appear in print until this year.

Geometry and Electronic Structure of the Hydroperoxyl Radical[2]

Self-consistent-field (SCF) and configuration-interaction (CI) calculations have been carried out, to investigate the geometry and electronic structure of the $^2A''$ ground state of the HO_2 radical. A slightly better than double-zeta-basis set of contracted gaussian functions was used. First-order wave functions including 500 configurations were used to describe electron correlation in HO_2. The iterative natural orbital procedure was used to generate an optimum set of molecular orbitals. The SCF predicted geometry is r(H-O) = 0.968 Å, r(O-O) = 1.384 Å, and bond angle 106.8°. The first-order geometry is r(O-H) = 0.973 Å, r(O-O) = 1.458 Å, and bond angle 104.6°. Our bond angle is consistent with Walsh's prediction, and the overall geometry is in essential accord with that suggested by Paukert and Johnston. However, several earlier theoretical predictions are not consistent with our results. Force constants are predicted which suggest that the O-H is similar to that in water, but the O-O bond is much weaker than that in the O_2 molecule. The H-O_2 dissociation energy is predicted to 2.36 eV in the SCF approximation and 2.82 eV from CI, compared with an experimental value of 2 eV. The electronic structure of HO_2 is discussed in terms of the natural orbital occupation numbers and the most important configurations.

Electronic Splitting Between the $^2B_1$ and $^2A_1$ States of the NH_2 Radical[3]

Theoretical calculations are reported for the ground and first-excited states of NH_2. A contracted gaussian basis of four s, two p, and one d functions is centered on the nitrogen atom, while for hydrogen, two s and one p functions are used. Both self-consistent-field (SCF) and multiconfiguration first-order wave functions have been computed, the latter using the iterative natural orbital method. Two new theoretical ideas were tested and found useful: (a) Bunge's partitioning of degenerate spaces and (b) a procedure for generating uniform sets of starting orbitals for multiconfiguration calculations. For the $^2B_1$ state the SCF, CI, and experimental geometries are θ = 105.4°, r = 1.019 Å; θ = 102.7°, r = 1.055 Å; θ = 103.3±0.5Å, r = 1.024±0.005 Å. The analogous results for the $^2A_1$ state are θ = 141.9°, r = 0.997 Å; θ = 144.7°, r = 1.010 Å;

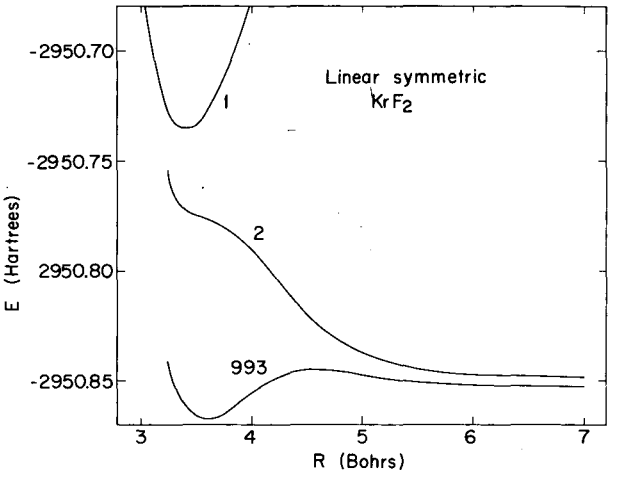

Fig. 1. Potential curves for the symmetric dissociation of KrF_2. 1 refers to the conventional SCF calculation, 2 to the two-configuration SCF, and 993 to the approximate first-order wave function. (XBL 719-4325)

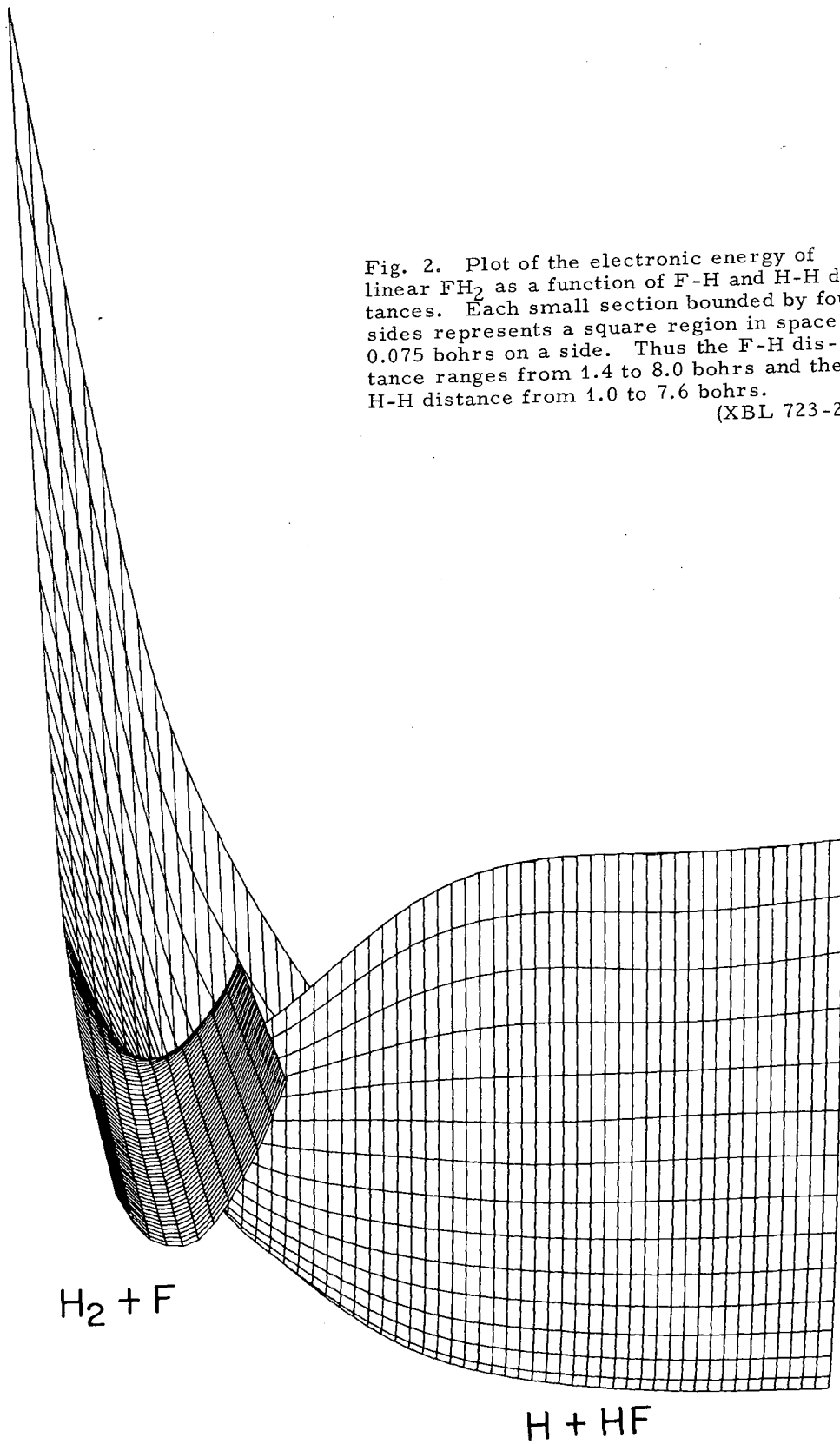

Fig. 2. Plot of the electronic energy of linear FH_2 as a function of F-H and H-H distances. Each small section bounded by four sides represents a square region in space 0.075 bohrs on a side. Thus the F-H distance ranges from 1.4 to 8.0 bohrs and the H-H distance from 1.0 to 7.6 bohrs.
(XBL 723-2655)

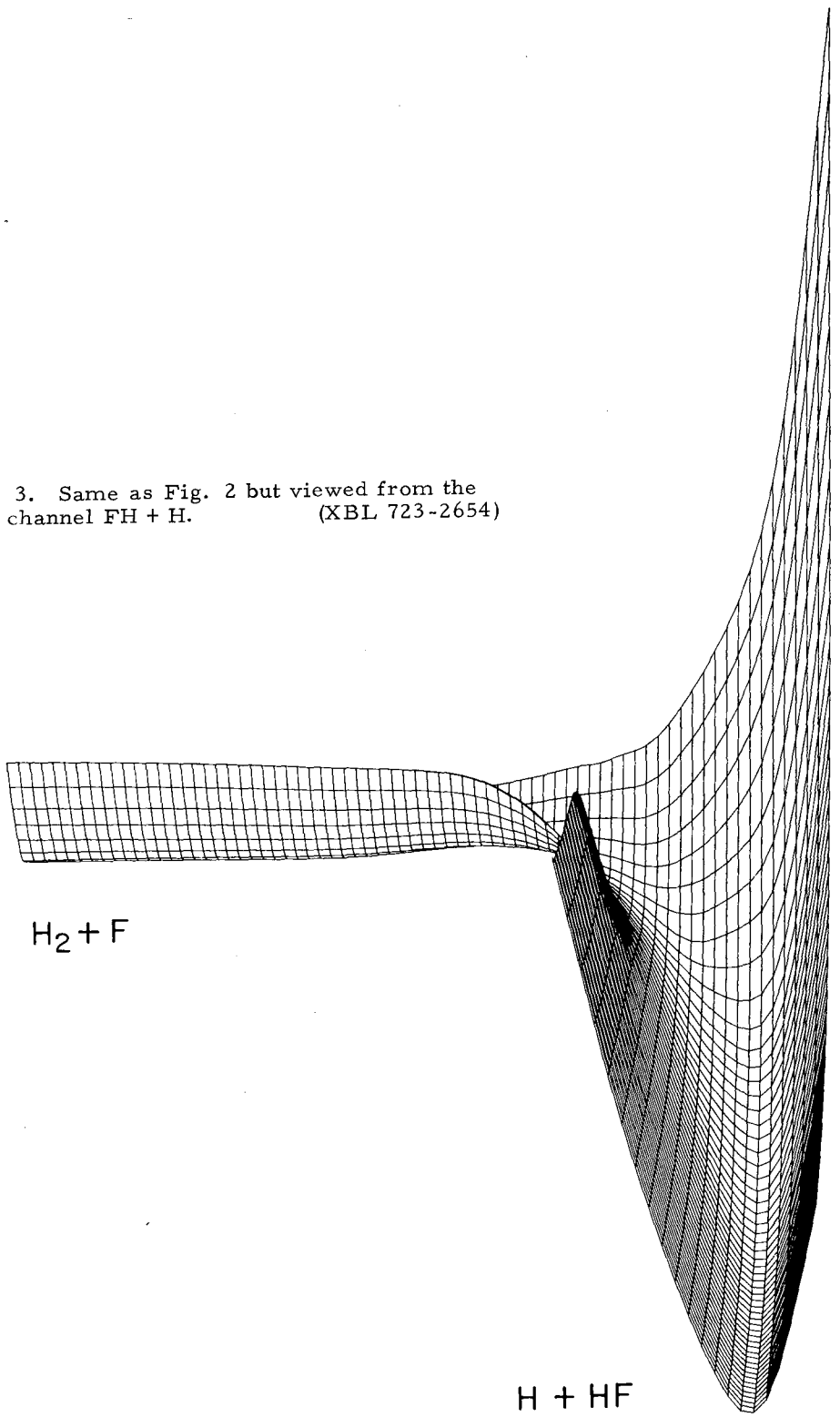

Fig. 3. Same as Fig. 2 but viewed from the exit channel FH + H. (XBL 723-2654)

θ = 144±5°, r = 0.97-1.00 Å. For the upper $^2A_1$ state the barrier to linearity is 1370 cm^{-1} in the SCF approximation, 1030 cm^{-1} from the correlated wave functions, and 770±100 cm^{-1} experimentally. The $^2B_1$-$^2A_1$ splitting T_e is predicted to be 12 800 cm^{-1} (SCF) and 14 500 cm^{-1} (CI), whereas the experimental value is thought to be ~ 11 000 cm^{-1}. Potential curves are shown and electronic structure considerations discussed.

Self-Consistent-Field Potential Energy Surface in Three Dimensions for the Cl + H_2 → ClH + H Chemical Reaction[4]

Nonempirical self-consistent-field calculations have been carried out for 38 points on the potential surface for the Cl+H_2 → ClH+H chemical reaction. A basis set of seven s, five p, and one d functions on chlorine and three s and one p on each hydrogen atom was used. The least-energy path occurs for the linear Cl-H-H arrangement. A much higher barrier is found for the approach of Cl along the H-H perpendicular bisector. The linear barrier height is predicted to be 26.2 kcal/mol and the saddle point occurs for R(Cl-H ≈ 1.46 Å, R(H-H) ≈ 0.94 Å. The experimental activation energy is 5.5 kcal/mol. It seems likely that a general feature of the Hartree-Fock approximation is an over-estimation of barrier heights. The exothermicity is calculated to be -6.7 kcal/mol, compared with the near-Hartree-Fock result -2.3 kcal/mol and experiment -3.0 kcal/mol.

Geometry and Force Constant Determination from Correlated Wave Functions for Polyatomic Molecules: Ground States of H_2O and CH_2[5]

Ab initio calculations including electron correlation are reported for the water and methylene molecules as a function of geometry. A large contracted gaussian basis set is used and the multiconfiguration wave functions, optimized by the iterative natural orbital procedure, include 277 and 617 configurations for H_2O and CH_2 respectively. The method of selecting configurations, yielding "first-order" wave functions, is discussed in some detail. For H_2O, the SCF geometry is r = 0.942 Å, θ = 105.8°; the correlated result is r = 0.968 Å, θ = 103.2°; and the experimental r = 0.957 Å, θ = 104.5°. The water stretching force constants, in millidynes/Å, are 8.72 (SCF), 8.75 (CI), and 8.4 (experiment). Bending force constants are 0.88 (SCF), 0.83 (CI), and 0.76 (experiment). For methylene the SCF geometry is r = 1.072 Å, θ = 129.5°, while the result from first-order wave functions is r = 1.088 Å, θ = 134°. The predicted CH_2 force constants are 6.16 (SCF) and 6.13 (CI) for stretching and 0.44 (SCF) and 0.33 (CI) for bending.

Electronic Structure of Krypton Difluoride[6]

Nonempirical quantum mechanical calculations have been carried out on KrF_2, using a basis set of Slater functions, Kr (8s 6p 5d 2f) and F (4s 3p 2d 1f). Self-consistent-field (SCF) calculations imply that 4d functions centered on Kr are much less important than suggested by minimum-basis-set calculations. In the SCF approximation, KrF_2 is predicted to be unbound by 2.98 eV with respect to three ground state atoms. Two-configuration SCF calculations were carried out to allow proper dissociation to three atomic SCF wave functions. Although the two-configuration potential energy curve for symmetric dissociation displays an inflection point, KrF_2 is again predicted to be unbound. Use of 993 configuration first-order wave functions does predict a bound KrF_2 molecule, with Kr-F bond distance 1.907 Å, as opposed to experiment 1.889±0.01 Å. An interesting feature of the predicted KrF_2 $^1\Sigma_g^+$ potential curve is a potential maximum, occurring at 2.42 Å and lying 0.22 eV above the dissociation limit. Figure 1 shows the calculated potential energy curves. Coulson's ionic-covalent picture of bonding in KrF_2 gives a qualitative explanation of this potential maximum. Additional support for Coulson's model is given by the abrupt change in the electric field gradient at Kr near the potential maximum. Finally, Koopmans'

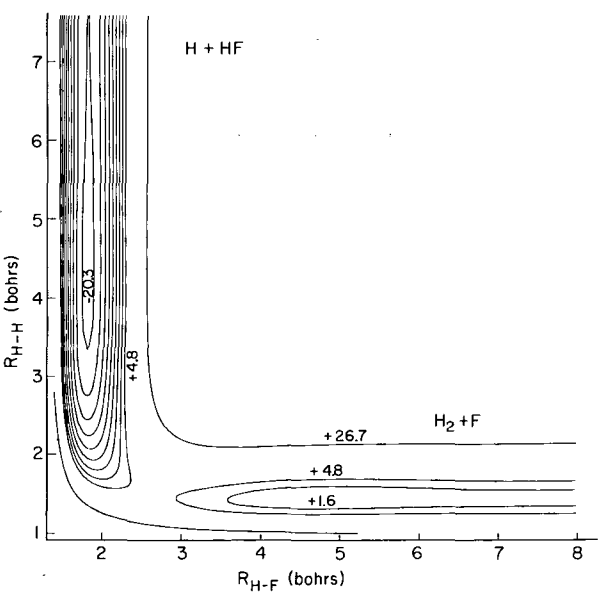

Fig. 4. Traditional contour map of the FH_2 surface. As in the three-dimensional plots, the F-H distance goes from 1.4 to 8.0 bohrs and the H-H distance from 1.0 to 7.6 bohrs.
(XBL 718-4140)

theorem ionization potentials are compared with the experimental photoelectron spectrum.

Potential Energy Surface Including Electron Correlation for the $F + H_2 \rightarrow FH + H$ Reaction[7]

Rigorous quantum mechanical calculations have been carried out for about 150 linear and 200 nonlinear geometries for the FH_2 system. The contracted gaussian-basis set used consisted of four s and two p functions on fluorine and two s functions on hydrogen. The barrier height and exothermicity are poorly predicted by single-configuration self-consistent-field calculations. However, the 214 configuration-correlated results are in qualitative agreement with experiment (low barrier height and substantial exothermicity). The reaction coordinate is discussed, and pictures of the potential surface are presented in Figs. 2, 3, and 4. A second series of calculations is being carried out with a larger basis set. These latter calculations yield nearly quantitative agreement with experiment for both the barrier height and exothermicity.

Acknowledgments

We thank Stephen Rothenberg, Donald R. McLaughlin, Bowen Liu, Paul S. Bagus, and Peter K. Pearson for their contributions to the work reported herein.

Footnote and References

*Present address: Lawrence Livermore Laboratory, Livermore, California.

1. H. F. Schaefer, The Electronic Structure of Atoms and Molecules: A Survey of Rigorous Quantum Mechanical Results (Addison-Wesley, Reading, Massachusetts, 1972).

2. D. H. Liskow, C. F. Bender, and H. F. Schaefer, J. Am. Chem. Soc. 93, 6734 (1971).

3. C. F. Bender and H. F. Schaefer, J. Chem. Phys. 55, 4798 (1971); also UCRL-73267.

4. S. Rothenberg and H. F. Schaefer, Chem. Phys. Letters 10, 565 (1971).

5. D. R. McLaughlin, C. F. Bender, and H. F. Schaefer, Theoretica Chimica Acta, submitted; also UCRL-73318.

6. B. Liu, P. S. Bagus, and H. F. Schaefer, J. Am. Chem. Soc., submitted.

7. C. F. Bender, P. K. Pearson, S. V. O'Neil, and H. F. Schaefer, J. Chem. Phys. 56, 4626 (1972).

8. C. F. Bender and H. F. Schaefer, J. Mol. Spectroscopy 37, 423 (1971).

9. S. V. O'Neil, H. F. Schaefer, and C. F. Bender, J. Chem. Phys. 55, 162 (1971).

10. S. Rothenberg and H. F. Schaefer, Mol. Phys. 21, 317 (1971); J. Chem. Phys. 54, 2764 (1971).

11. O. R. Platas and H. F. Schaefer, Phys. Rev. A4, 33 (1971).

EVIDENCE FOR MAGMATIC MIXING IN BORAX LAKE OBSIDIAN AND DACITE[1]

H. R. Bowman, F. Asaro, and I. Perlman

In a previous study, the chemical compositions of obsidian from Borax Lake (in Lake County, California) was measured by using neutron activation analysis where some 40 elements were tested for. Many of the elemental abundances appeared to be nearly constant, but about a dozen varied extensively. The variable elements were found to be linear with respect to each other and equations were developed to express each of the compositions as a function of that of Fe.

It was found that the composition given for a dacite flow[1] which is under the obsidian flow at Borax Lake could be roughly expressed by these same equations for a few elements. Because the composition data on the dacite rock was very meager, a detailed comparison could not be made.

In the present work, eight samples of Borax Lake dacite were obtained from the site and analyzed along with two samples from the University of California Geological Museum. The samples were subjected to the same type of neutron activation analysis as the obsidian samples. The dacite results fell into five different chemical composition groups. The abundances for 26 of the elements are plotted against iron content in Figs. 1, 2, 3, and 4. The obsidian data are those data to the left of 2% Fe, and the dacite data are shown to the right of 2% Fe, although it should be noted that the "dacite" with the lowest iron content virtually coincides with the highest Fe value of "obsidian."

The points represent the ten obsidian and five dacite groups, all on the same graph. It is seen that all of the functional relations are linear, that the slopes vary considerably, and both positive and negative slopes are represented. The linear relationships strongly suggest simple mixing of two phases in various proportions, and that both the obsidians and dacites belong to the same system. We now propose to examine the nature of these two phases.

One of the phases (Phase A) is obviously a rhyolite, so it will be referred to as such. The second will only be termed "Phase B" for the present. Some of the lines with positive slope extrapolate to zero concentration of the elements while the iron value is still positive. We shall first examine these. One of them, Co, becomes zero at a higher Fe value than any of the other elements with lines of positive

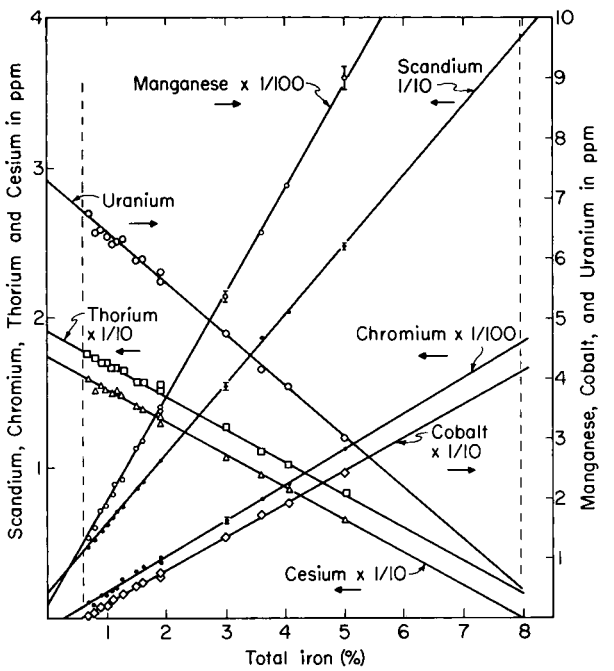

Fig. 1. The chemical variation of Th, U, Mn, Sc, Cr, Co, and Cs plotted against total iron content for Borax Lake obsidian and dacite. (XBL 7110-4480)

slope. The significance of this point of intersection is that it establishes one of the limits in the composition of the rhyolitic phase, because its content of Co cannot be less than zero. The content of each of the other elements in this limiting composition is given by the intercept of each line with the iron content representing zero-Co. The other limit to the composition of the rhyolitic phase is given by that obsidian group with lowest Co value. It is seen that the limits of composition are so close to each other that the rhyolitic phase is quite sharply defined. In other words, those obsidian specimens of lowest Fe content represent this phase quite well.

In this type of reasoning, it is seen that one limit of a phase composition is given precisely by an extrapolation to zero concentration of a single element and the other limit by an actual sample with the lowest concentration noted for that element. If these almost coincide, the possible range is small. Turning to Phase B, we shall see that it is not possible to obtain a narrow range because the lowest concentration

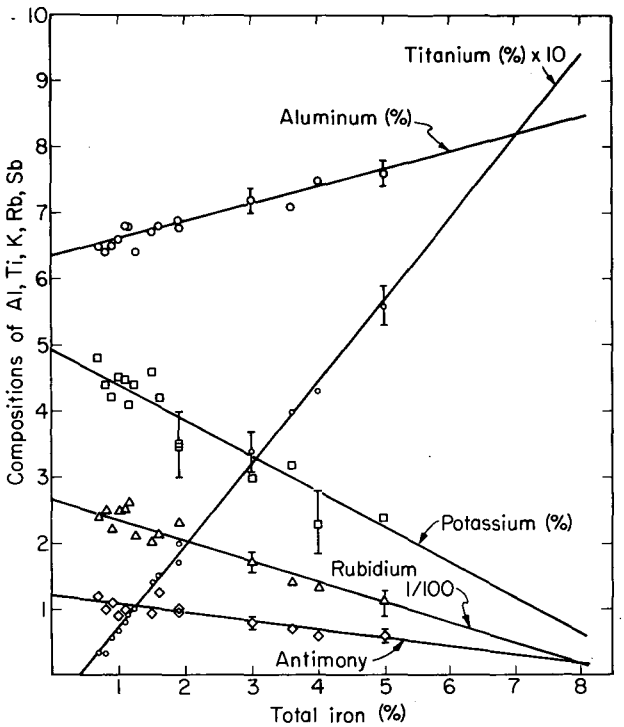

Fig. 2. The chemical variation of Ti, Al, K, Rb, Sb plotted against total Fe content for Borax Lake obsidian and dacite.
(XBL 721-2037)

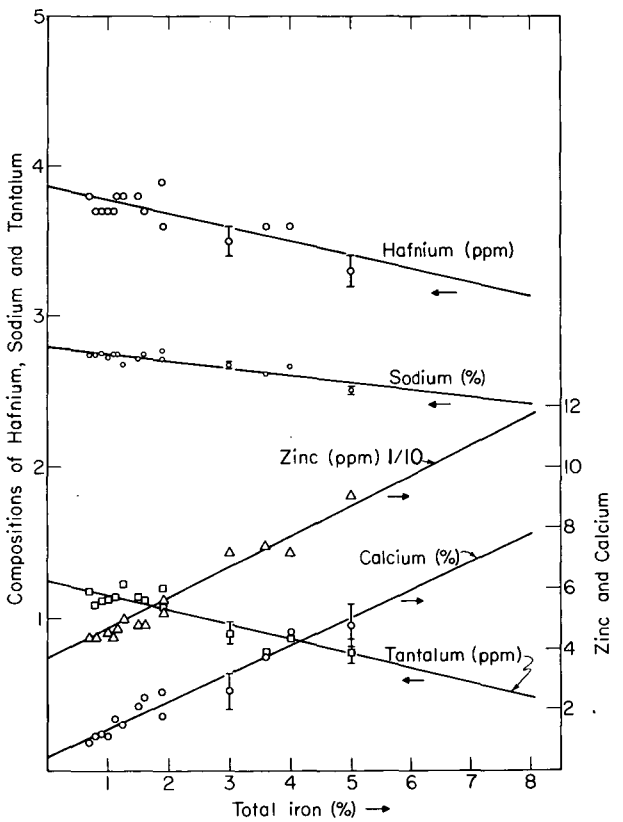

Fig. 3. The chemical variations of Hf, Na, Zn, Ca, Ta plotted with total Fe.
(XBL 7110-4481)

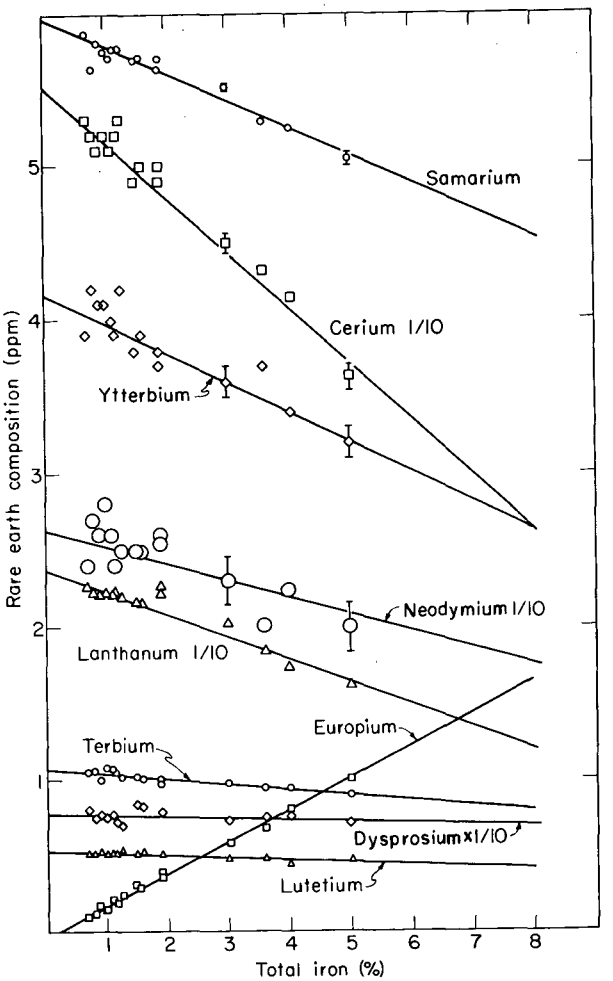

Fig. 4. The rare earth chemical variations plotted against total iron.
(XBL 7110-4478)

Table I. BASA II abundances calculated from Borax Lake obsidian and dacite samples. (in ppm or %)

	Calculated abundances	Measured abundance
Fe%	7.7	7.74±0.10
Sc	37.5	39.2 ±0.1
Ti%	0.90	0.93±0.02
Co	39.6	40.7 ±0.5
Cr	178	194±3
Th	2.5	2.2 ±0.1
Cs	0.51	0.8 ±0.3
Hf	3.2	3.0 ±0.1
Al%	8.4	8.2 ±0.2
Ca%	7.5	7.5 ±0.6
Mn	1370	1300±20
K%	0.8	0.9 ±0.5
U	0.72	0.81±0.02
Ta	0.52	0.45±0.09
Sb	0.3	0.4 ±0.1
Rb	27	40±15
Zn	115	100±10
Na%	2.43	2.00±0.03
Sm	4.60	3.72±0.01
Dy	7.1	5.7 ±0.2
La	12.5	8.3 ±0.5
Lu	0.43	0.34±0.02
Nd	18	11±2
Ce	28	20±1
Yb	2.7	2.4 ±0.2
Eu	1.6	1.3 ±0.1
Tb	0.81	0.81±0.04

in available samples is not close to the zero concentration. The element selected for extrapolation is Cs, which has a negative slope and extrapolates to zero concentration at an Fe content of 7.93%. The highest iron content in the dacites analyzed is 4.98%, so the range of permissible compositions for all elements corresponds with the band between these limits.

Despite this large uncertainty as to the exact composition of Phase B, it seems certain that it is basaltic. Anywhere in the allowed range, the characteristics of certain basalts appear: high values for Fe, Co, Sc, and low values for Cs, Th, U and rare earth elements. Unfortunately, there are no basalt outcroppings at Borax Lake itself. Several samples from the general vicinity were analyzed, but these are not likely candidates. The analyses showed them to be unacceptable as the actual Phase B, although one specimen was unmistakably similar and will now be compared.

The particular basalt sample was obtained from Anderson[1] who collected it about 2 miles east of the Borax Lake flow and described the site as a member of the Cache Formation. The composition of Phase B was taken as that corresponding with 0.5% Cs, which is close to one of the limiting compositions. This calculated composition for Phase B is compared with the reference basalt (BASA2) in Table I. The error limits shown for each element in BASA2 is simply the precision of measurement.

It is seen from Table I that for many elements the agreement between the calculations for Phase B and reference basalt (BASA2) is remarkably close. However, the values for Na and most of the rare earth elements are distinctly different. Despite the similarities, this means that BASA2 cannot represent the basaltic material which we call Phase B and which is responsible for the dispersion in compositions of the obsidians and dacites of Borax Lake. The similarities do show that Phase B is a basalt and its composition is not grossly unlike a specimen found in the general area. Finally the juxtaposition of the values for Phase B and Phase A point up the large differences in a number of the trace elements between a rhyolite and a basalt.

It will be noted that Figs. 1-4 are familiar "variation diagrams," but there are features not common to most geochemical studies. The elements included are only those which can be determined by gamma-ray spectroscopy after neutron irradiation, and without resorting to chemical separations. Employing this system of analysis, one automatically stresses an array of trace elements and sacrifices information obtainable from some of the major constituents. Some of these are not measured at all and others only with poor accuracy. The other feature pertains to this particular problem. Here, we are dealing with a postulated mixing of two phases in which certain trace elements which are very low in one phase are reciprocally high in the other. The happenstance permits calculation of the compositions of the phases within more or less narrow limits.

A rapidly growing body of information is appearing on trace element behavior as well as thoughtful discussion as to what these data imply. In the present report we have considered it prudent to avoid discussion of the prehistory of the magmas because we feel that a more comprehensive body of accurate information on trace elements in various media will permit one to make deductions with greater certainty.

Reference

1. C. A. Anderson, Bull. Geol. Soc. Am. 47, 629 (1936).

PROVENIENCE OF TWO MYCENAEAN PICTORIAL SHERDS FROM KOUKLIA (PALAEPAPHOS), CYPRUS*

V. Karageorghis,† F. Asaro,‡ and I. Perlman‡

Mycenaean pottery of the pictorial style is rather scarce on the west coast of Cyprus as compared with the large quantities found on the south and east coasts. In the pictorially decorated category, we know of two fragments which have been published: one from a 14th century chariot crater and another, again from a crater, decorated with what appears to be a "Minoan Lady."[1] This second fragment was found at site "Evreti," east of Kouklia[2] village.

The same site, "Evreti," produced another fragment from an open bell crater, decorated with the forepart of a bull in front of a tree motif; it was first published by one of the present writers (V. K.) and ascribed to the early part of the Rude Style period, dating chronologically to the last quarter of the 13th century.[3] There are up to now seven such vases of the early Rude Style, all decorated with bulls; five vases were found in Cyprus and two at Ras Shamra.[4]

When the Evreti Mycenaean III A fragment with "Minoan Lady" (referred to later also by its laboratory serial number PPAP120) was exhibited at the site museum at Kouklia side by side with the Rude Style fragment with the bull and tree motifs (PPAP119), one of the present authors (V. K.) was struck by the similarity of their fabric, slip, and paint; in fact, had it not been for the two centuries which separate the two fragments stylistically, one might prima facie suggest that the two fragments belonged to the same vase. Consequently small chips of these two sherds were taken for laboratory analysis in Berkeley to find out if the similarity which was striking to the naked eye existed also in the chemical composition of the clay. Any close affinity found would be of crucial importance. Although the two fragments came from the same site, they belong stylistically to two distinct classes of pottery, one (PPAP120) thought by several scholars to have been imported from the Greek mainland[5] and the other (PPAP119) universally accepted as of Cypriote manufacture. An exploration of the possible scope of application of laboratory analysis for deducing pottery provenience as an adjunct to expert stylistic examination is, of course, a central objective of such interdisciplinary studies at the moment.

The chemical compositions of the two Mycenaean sherds, will be compared with each other and with reference materials in order to obtain evidence concerning provenience. The tabulated data designate these two fragments as PPAP119, and PPAP120, which numbers pertain to the "Rude Style" and "Minoan Lady" sherds respectively.

The first comparison of compositions will be made between these sherds and a group of MycIIIC:1 sherds from Kouklia. The reference group consists of 19 pieces, all from the excavation of Maier at the Evreti site.[2] In Fig. 1 the values for each element in PPAP119 and 120 are shown as the two thin bars at the left in each box. The next thicker bar is the mean value for the 19 sherds in the reference group, and the hatched zone indicates the spread in composition expressed as the standard deviation, σ. The numerical data upon which these bar-graphs are based are tabulated in Table I for those interested in the actual numbers. Before providing more detailed discussion, the conclusion will be stated: namely, that both PPAP119 and PPAP120 likely have the same provenience as the reference group and therefore the same as each other. We shall first examine the basis for this provenience and then the question of whether the locality is Kouklia.

The supposition is made that the 18 elements used for diagnostics may be treated as independent variables and that the variation of each el-

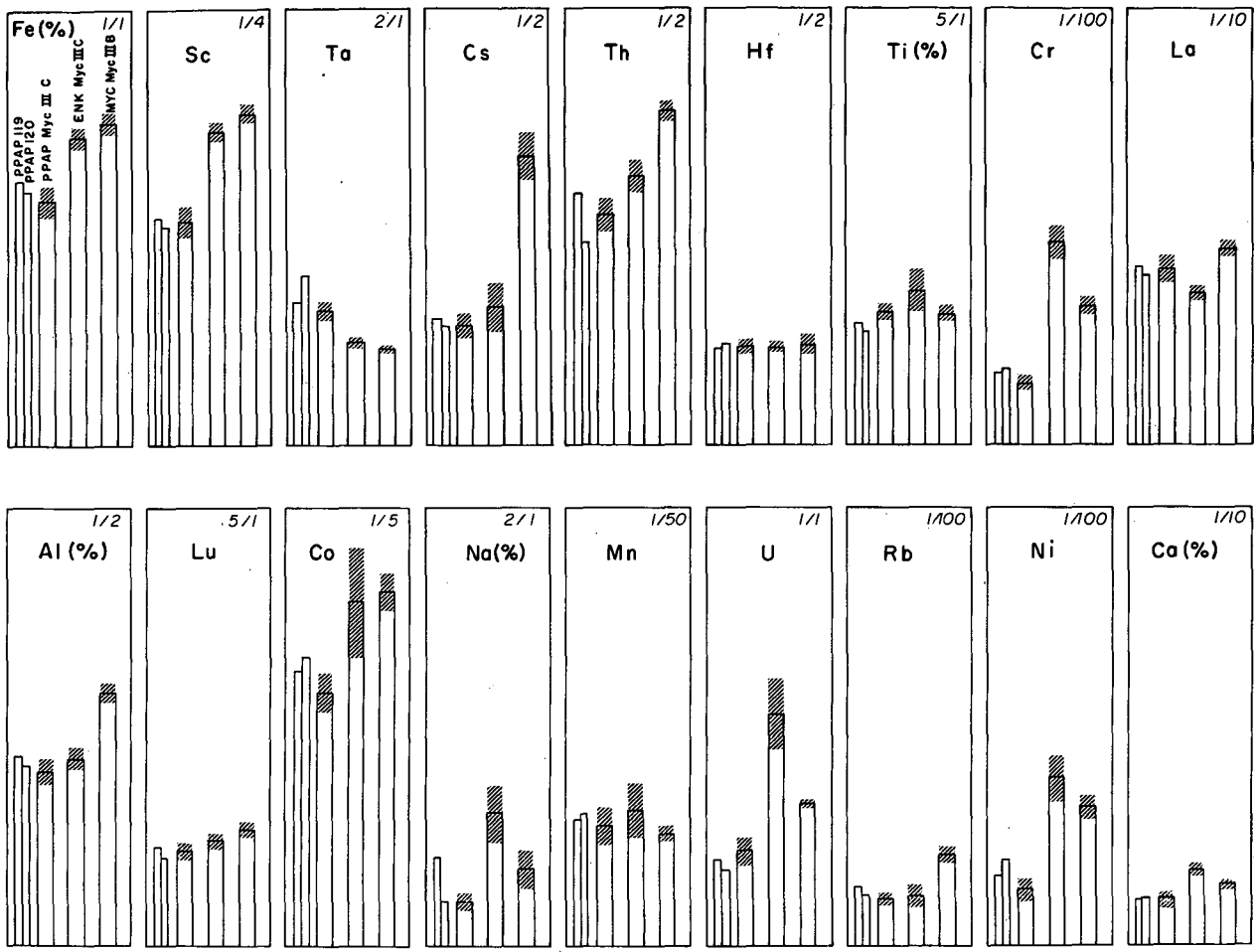

Fig. 1. The two narrow bars at the left in each box represent the values for the indicated element in the two sherds, PPAP119 (Rude Style, bull motif) and PPAP120 (Minoan Lady). The three wider bars represent mean values for the indicated pottery groups; the hatched zone on each is ± the standard deviation for the group. PPAP MycIIIC is a group of 19 sherds of MycIIIC:1 ware excavated at Kouklia; ENK MycIIIC is for 11 sherds of similar wares from Enkomi; MYC MycIIIB is for 16 sherds of MycIIIB wares excavated at Mycenae. For convenience, the scale used is different for the different elements. The actual numbers are given in Table I. (XBL 7112-4948)

Table I.[a]

	(1)[b] PPAP119 Rude Style X ± ϵ	(2)[b] PPAP120 Minoan Lady X ± ϵ	(3)[c] PPAP MycIIIC:1 (19 pieces) M ± σ	(4)[c] ENK MycIIIC:1 (11 pieces) M ± σ	(5)[c] MYC MycIIIB (16 pieces) M ± σ
Fe(%)	4.24 ±0.06	4.07 ±0.06	3.92 ±0.25	4.95 ±0.16	5.16 ±0.18
Sc	14.45 ±0.06	13.45 ±0.05	14.16 ±1.00	20.04 ±0.58	21.11 ±0.61
Ta	1.131 ±0.008	1.342 ±0.008	1.071 ±0.077	0.765 ±0.033	0.822 ±0.039
Cs	3.98 ±0.23	3.76 ±0.20	3.79 ±0.40	4.40 ±0.82	9.19 ±0.76
Ti(%)	0.384 ±0.020	0.356 ±0.019	0.424 ±0.024	0.490 ±0.069	4.18 ±0.23
Cr	113 ±3	118 ±3	97 ±11	325 ±26	221 ±14
Th	8.03 ±0.13	6.48 ±0.11	7.35 ±0.53	8.59 ±0.47	10.70 ±0.29
Hf	3.08 ±0.10	3.21 ±0.09	3.13 ±0.22	3.11 ±0.16	3.21 ±0.31
La	28.6 ±0.8	27.0 ±0.7	27.6 ±2.3	23.2 ±3.0	34.1 ±1.2
Al(%)	6.07 ±0.13	5.78 ±0.14	5.58 ±0.42	6.02 ±0.36	8.09 ±0.30
Lu	0.319 ±0.019	0.282 ±0.016	0.303 ±0.020	0.337 ±0.018	0.374 ±0.016
Co	22.07 ±0.34	23.20 ±0.32	20.21 ±1.65	27.39 ±4.35	28.24 ±1.42
Na(%)	0.720 ±0.011	0.355 ±0.009	0.354 ±0.085	1.065 ±0.223	0.615 ±0.139
Mn	1014 ±15	1057 ±16	962 ±156	1092 ±220	901 ±66
U	1.37 ±0.03	1.21 ±0.03	1.52 ±0.22	3.70 ±0.57	2.28 ±0.09
Rb	95 ±15	18 ±13	74 ±10	78 ±18	145 ±14
Ni	113 ±17	135 ±15	92 ±17	269 ±38	223 ±19
Ca(%)	7.3 ±0.5	7.6 ±0.4	7.3 ±1.6	12.1 ±0.8	9.8 ±0.8

[a] All numbers entered are in parts-per-million unless the element bears the % sign.

[b] Columns (1) and (2): Measured values (X) in the respective sherds and their errors of measurement (ϵ). The error, ϵ, gives the precision of each value according to the statistics of radioactive counting.

[c] Columns (3), (4), and (5): Mean values (M) and standard deviations (σ) for the indicated pottery groups. These groups were excavated at Kouklia (Palaepophos), Enkomi, and Mycenae respectively.

ement follows a normal distribution curve. On the basis of much work done to date we are convinced that any shortcomings in terms of strict validity are not serious. A sherd may then be compared with a reference group as follows: It fits the group if only about six elements of 18 fall outside of 1σ and of these, only one element should depart by as much as 2σ. It should be realized that we are dealing with the statistics of small numbers and there are other hazards involving systematic errors, so the criterion just outlined cannot be applied blindly.

When PPAP120 is compared with the group of 19 MycIIIC:1 sherds we find that seven elements lie outside of 1σ and one of these, Ta, if off by 3.5σ. If it were not for the single element Ta this would be as good a fit as can be expected.

The same comparison can be made between PPAP119 and the group of MycIIIC:1 ware from Kouklia. The results are much the same as for PPAP120. The fit is as good as can be expected, with one "wild" element: in this case, Na. This single descrepancy is not considered serious because Na is very pervasive as a contaminant and wild values are not uncommon in otherwise well-behaved materials.

The evidence seems to us very strong that both PPAP119 and PPAP120 were made at the

Table II.[a]

	(1)[b] PPAP MycIIIC:1 (19 pieces) M ± σ	(2)[c] PPAP MycIIIC:1 (6 pieces) M ± σ	(3)[d] ENK MycIIIC:1 (11 pieces) M ± σ	ENK MycIIIC:1 (10 pieces) M ± σ
Fe(%)	3.92 ±0.25	4.32 ±0.18	4.95 ±0.16	5.67 ±0.18
Sc	14.16 ±1.00	17.38 ±0.69	20.04 ±0.58	23.19 ±1.01
Ta	1.071±0.077	0.878±0.117	0.765±0.033	0.706±0.036
Cs	3.79 ±0.040	3.41 ±0.41	4.40 ±0.82	4.18 ±0.53
Ti(%)	0.424±0.024	0.420±0.027	0.490±0.069	0.455±0.025
Cr	97±11	118±9	325±26	452±86
Th	7.35 ±0.53	5.99 ±0.26	8.59 ±0.47	7.13 ±0.32
Hf	3.13 ±0.22	2.90 ±0.09	3.11 ±0.16	3.17 ±0.21
La	27.6 ±2.3	23.1 ±1.1	23.2 ±3.0	22.3 ±2.1
Al(%)	5.58 ±0.42	5.89 ±0.24	6.02 ±0.36	6.83 ±0.43
La	0.303±0.020	0.291±0.022	0.337±0.018	0.346±0.013
Co	20.21 ±1.65	19.87 ±1.90	27.39 ±4.35	28.77 ±2.28
Na(%)	0.354±0.085	0.611±0.062	1.065±0.233	1.316±0.237
Mn	962±156	780±108	1092±220	1068±90
U	1.52 ±0.22	1.46 ±0.17	3.70 ±0.57	1.95 ±0.35
Rb	74±10	61±15	78±18	75±14
Ni	92±17	77±21	269±38	198±30
Ca(%)	7.3 ±1.6	7.3 ±1.2	12.1 ±0.8	9.8 ±0.9

[a] All numbers entered are in parts-per-million unless the element bears the % sign.

[b] Column (1): Group of MycIIIC:1 ware from Kouklia reproduced from Table I.

[c] Column (2): Another group of 6 sherds of similar ware from Kouklia.

[d] Column (3): Group of MycIIIC:1 ware from Enkomi reproduced from Table I.

[e] Column (4): Another group of 10 sherds of similar ware from Enkomi.

same place as the group of MycIIIC:1 wares also excavated at Kouklia.

One of the questions to be answered in this study is whether the "Minoan Lady" sherd has a chemical composition that conforms with that of the fine MycIII A and B wares thought to be unique to the Greek mainland. A large number of specimens of these wares excavated at a number of sites in Greece are currently being analyzed, and the results on one such group from Mycenae are presented in Fig. 1 and Table I. Although this study is not yet completed we know that these wares are distinctly similar to each other,[6] at least when drawn from a number of sites in the Argolid. The group from Mycenae (Fig. 1) is quite representative of much of the material that has been analyzed so far. It is seen that the materials from Kouklia are grossly different: for example, the "Minoan Lady" (PPAP120) as compared with the group from Mycenae falls within 1σ for only 1 element; it falls outside of 2σ for 16 elements, and of these, 9 elements are beyond 5σ and 4 elements beyond 10σ. This gross difference lends some perspective to the fine distinctions discussed above in trying to decide whether PPAP120 belonged to the group of MycIIIC:1 wares from Kouklia. Figure 1 also shows a group of MycIIIC:1 ware from Enkomi near the east coast, and again it is seen that there are great differences.

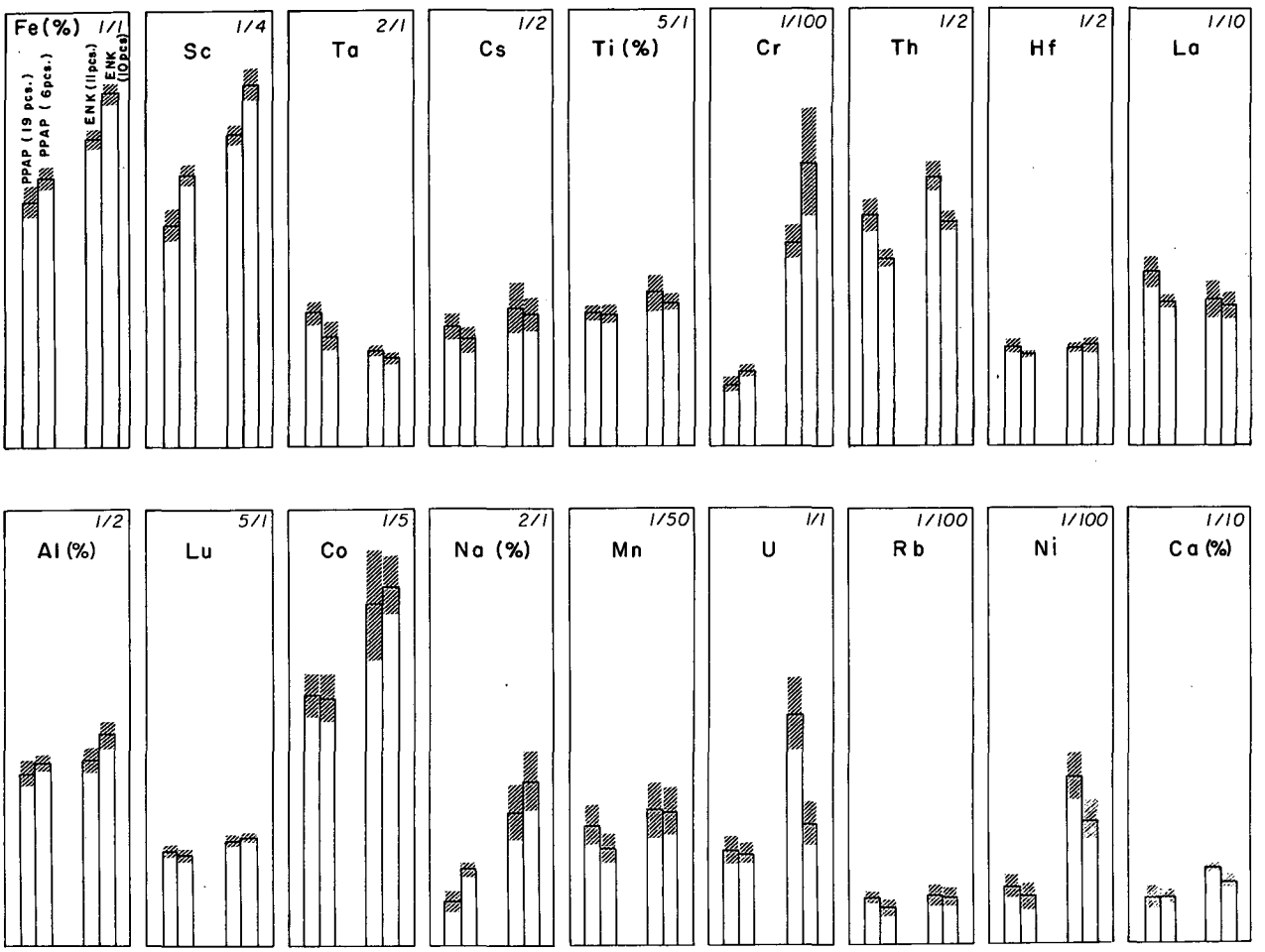

Fig. 2. The bars and hatching have the same meaning as in Fig. 1. All wares shown are of MycIIIC:1 style. PPAP (19 pieces) is the same group from Kouklia shown in Fig. 1 and labeled PPAP MycIIIC; PPAP (6 pieces) represents another chemical group also excavated at Kouklia. ENK (11 pieces) is the same group from Enkomi shown in Fig. 1 and labeled ENKIIIC; ENK (10 pieces) represents another chemical group also excavated at Enkomi. For convenience, the scale used is different for the different elements. The actual numbers are given in Table II. (XBL 7112-4949)

The answer to the question of whether the "Minoan Lady" and its reference group (MycIIIC:1 ware from Kouklia) are indeed local to Kouklia is more complex. If all of the sherds analyzed from Kouklia made up a single compact chemical group one might reasonably assume that this composition is representative of local clays. However, all of the wares excavated at Kouklia were not the same in composition. In addition to the reference group of 19 sherds, there were 18 others which did not fit this group. These, in turn, were not homogeneous and could be separated into five other groups, one with six members and one with only two members. These groups were not grossly different from each other or from the group of 19 sherds. It is possible that all of these merely reflect a diversity of clay sources used in that single area. In order to illustrate how one of these small groups re-

lates to the group of 19 sherds, the latter group has been entered on Fig. 2 alongside of the group of six sherds just mentioned. It is seen that for the majority of the elements these two groups are indistinguishable, but for some there are substantial differences: for example, Sc, Th, and Na. The general similarity of all these wares does not prove that they are all local, but this would seem a reasonable hypothesis to entertain pending the accumulation of further evidence.

Also entered in Fig. 2 is the group of 11 sherds from Enkomi previously shown in Fig. 1. Here again, not all the MycIIIC:1 wares analyzed belong to this group and another group of 10 sherds from Enkomi is entered. In the case of Enkomi, we can be more sure that both of these groups are local, because we have analyzed a much larger collection of wares embracing many styles and the two groups shown in Fig. 2 have chemical parallels among these diverse ceramics. Furthermore, samples of grey clay from the Enkomi Village area[7] were analyzed and agreed quite well with the ancient potteries shown in Fig. 2.

The point being made by these comparisons concerns the mounting evidence that potters from a single site employed different clay sources, which are readily distinguishable by a sensitive method of analysis. If this is so, the rather similar wares from the Kouklia area may well be local to that site. None of these arguments are entirely convincing at this stage, but it should also be recognized that even such complex situations can likely be resolved by sufficient sampling and analysis.

Conclusions

The evidence outlined above is quite convincing that PPAP119 (Rude Style) and 120 (Minoan Lady) have the same provenience and that they were made from the same clay source as were the preponderance of MycIIIC:1 wares also excavated at Kouklia. It is not rash to assume that these were all made at Kouklia, particularly in view of the evidence that this was probably the most important Late Bronze Age site in Western Cyprus. Even taken by itself, the "Minoan Lady" vessel very definitely does not come from the same clay sources responsible for the fine Mycenaean ware of the IIIA and IIIB periods found in Greece and as imports in other places.

As we now consider in addition the stylistic differences between PPAP119 and PPAP120, we are led to two divergent interpretations, the resolution of which is of some importance in the general problem of Mycenaean pottery in the Levant, particularly in Cyprus.

1) If these two vessels are indeed 200 years apart as the stylistic criteria demand, this would simply mean that Mycenaean wares encompassing this particular time span were made at Kouklia. To support this view, one should search for other examples of locally made Mycenaean pottery of the 14th century.

2) If, on the other hand, careful search should reveal no other evidence for local manufacture of Mycenaean ware during the 14th century, one might conclude that the "Minoan Lady" is of a later date. If this should prove correct, this vessel becomes an unusual example of "14th century artistry" practiced at a later date.

Footnotes and References

*The present report was written in Berkeley while one of the authors (V. K.) was there in the autumn of 1971 as Regents' Lecturer.

†Department of Antiquities, Republic of Cyprus.

‡Lawrence Berkeley Laboratory and Department of Chemistry, University of California, Berkeley.

1. Cf. recently H. W. Catling, "A Mycenaean pictorial fragment from Palaepaphoas," Archaeol. Anzeiger 85, 1970, 24ff.; for previous literature see V. Karageorghis, Nouveaux Documents pour l'Etude du Bronze Récent à Chypre (Paris, 1965), p. 231ff.

2. For a general account on Late Bronze Age Kouklia see F. G. Maier, "Excavations at Kouklia (Palaepaphos), Third Preliminary Report: Season 1968," RDAC 1969, p. 33ff., where references to previous literature are given; see also idem "The cemeteries of Old Paphos," Archaeologia Viva 3, 116ff (1969).

3. V. Karageorghis, Nouveaux Documents... 236, pl. XXIII, 5.

4. Ibid., pp. 232-239.

5. E.g., Catling in BSA 60, 219ff. (1965).

6. H. W. Catling, E. E. Richards, and A. E. Blin-Stoyle [BSA 58, 94-115 (1963)] came to this same conclusion earlier on the basis of chemical analysis employing another technique.

7. These clays were obtained from a present-day potter in Famagusta who told us that they were drawn from the vicinity of Enkomi village.

TWO CHEMICAL GROUPS OF DICHROIC GLASS BEADS FROM WEST AFRICA*

C. C. Davison, R. D. Giauque, and J. D. Clark†

Certain blue glass beads from West African archaeological sites were found by x-ray fluorescence analysis to fall into two chemical groups. Each group includes beads that exhibit blue/yellow dichroism and/or cords. In incident daylight the dichroic beads appear blue, but transmitted daylight causes them to appear yellow-green. The non-dichroic corded beads appear blue in both incident and transmitted daylight. Some beads show both cords and dichroism. All dichroic and/or corded beads analyzed fell into one or the other of the two groups.

The archaeological implications of the findings are discussed. These beads had been problematic, but the present results form a basis for resolution of some of the problems.

There are five typewritten pages of references of a historical nature in the UCRL report. The UCRL report number is 20474. A slightly revised version is in press in Man.

Footnotes

*Condensed from UCRL-20474.

†Department of Anthropology, University of California, Berkeley.

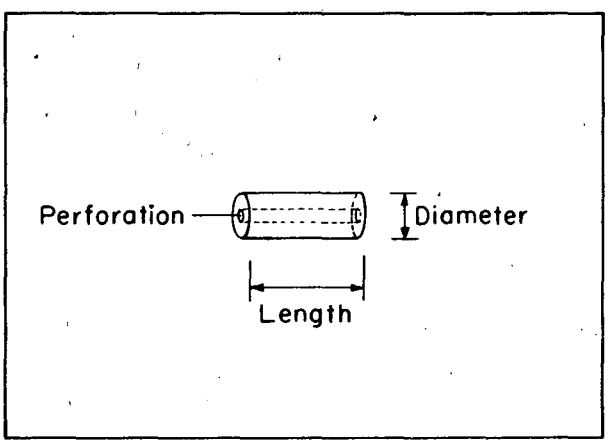

Fig. 1. Diagram of bead. The length measured is that of the perforation.
(XBL 714-3286)

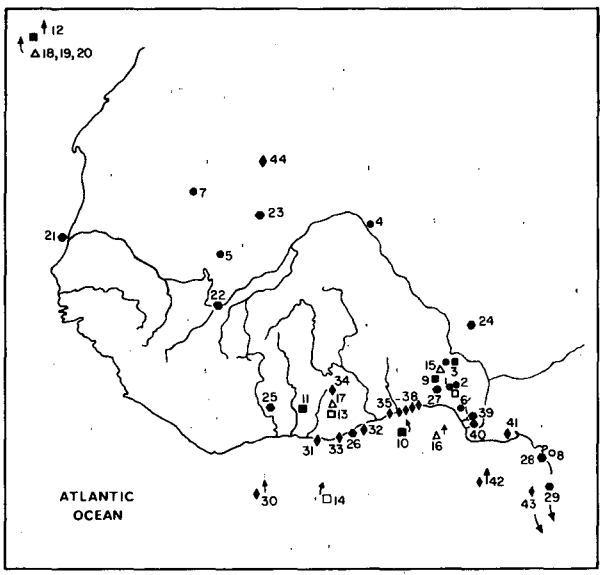

Fig. 2. Distribution of blue dichroic and corded beads in West Africa.
(XBL 714-3287)

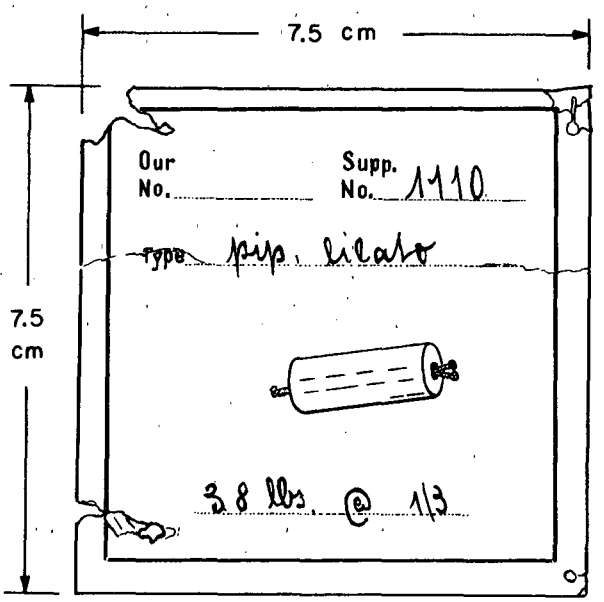

Fig. 3. Bead specimen "Cambridge, #1" on bead card. The print is in black ink and the handwriting in red ink. (XBL 714-3285)

DETERMINATION OF ATMOSPHERIC LEAD, BROMINE, AND IRON BY NON-DISPERSIVE X-RAY FLUORESCENCE*

J. G. Conway, H. R. Bowman, F. Asaro, and L. Y. Goda

A series of filter papers was collected weekly over the past eight years in downtown Berkeley, California by the Safety Services department of the Lawrence Berkeley Laboratory as part of an environmental survey system.[1] The downtown sampling station is located on a busy street (Shattuck Avenue between Hearst and Berkeley Way), and the air intake to the system is located about 8 ft from the curb and about 7 ft above the street level, facing the street. The air was filtered through HV 70 filter paper at an average flowrate of 4 ± 0.5 cfm, and the aerosols were collected on an open area of ~196 cm^2.

Each of the over 400 filter papers was analyzed for 2 min on the x-ray fluorescence spectrometer. The filter papers were folded twice (to increase by a factor of 4 the effective lead and bromine seen by the x-ray detector) and placed in a holder that compressed the papers and held them at a fixed geometry with respect to the x-ray fluorescence system. Eight hundred channels of pulse-height information were taken on each two-minute run and stored on magnetic tape in digital form at the end of each run. The lead and bromine concentrations were obtained by summing a number of channels over the Pb Lα and Br Kα peaks, subtracting the nearly negligible background and comparing the results to standards treated in the same manner. A number of techniques were used to calibrate the filter papers for lead and bromine. These included: analyses of weighed amounts of lead metal and of KBr which had been vaporized onto Al foils, wet chemical analyses of foils and some filters, and independent x-ray fluorescence analyses of some of the filters by R. D. Giauque. The lead and bromine results agreed within standard deviations of 7 and 13%, respectively.

The atmospheric lead and bromine concentrations for the years 1963 to 1970 are plotted in Fig. 1. An average bromine-to-lead weight ratio of 1:60 has been reported for six cities of the United States. Our study indicates a ratio of 1:3.2, which is closer to the ratio found for automobile exhaust gases. We have no explantion for this difference.

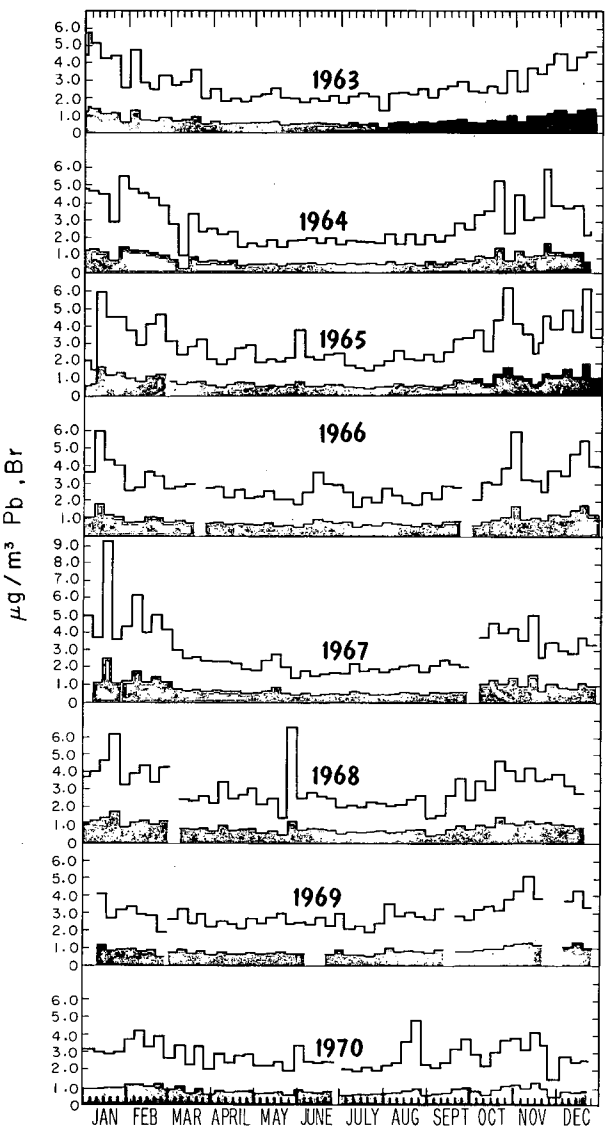

Fig. 1. Atmospheric lead (upper solid line) and bromine (shaded area) concentrations in downtown Berkeley (1963-1970).
(XBL 714-3234)

The seasonal variations are similar to those reported for San Diego by Chow and Earl for lead,[1] and correlate very well with climatological data for wind direction and speed. In the summer the San Francisco Bay Area has winds of average speed of 9 to 10 miles per hour and these winds are from the Pacific Ocean. The winter winds average 5 to 7 miles per hour and have no predominant direction. The higher-speed winds from the cleaner areas of the ocean result in the cleansing of the Bay Area, and as a result the lead and bromine concentrations are lower in the summer. There seems to be no correlation with rainfall. Filter paper samples collected at other sites in the area are being analyzed in a similar manner.

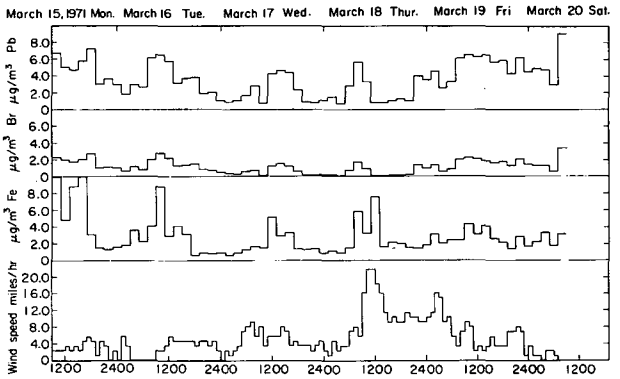

Fig. 2. Atmospheric iron, lead, and bromine concentrations near a freeway, and the wind speed at LBL. (XBL 721-2088)

In another series, samples were taken for two-hour intervals over a one-week period in March, 1971, at a location 500 yards from U. S. route 80 in Emeryville, California. The sample was collected on Whatmann #41 paper which is low in iron, so iron as well as lead and bromine were determined. The results are plotted in Fig. 2. The wind velocity information is from data collected by John Peck of the Safety Services department at a location on the grounds of the Lawrence Berkeley Laboratory. That wind velocity and traffic pattern are not the only important factors can be illustrated by the data from 1500 hours on March 18th and 0900 on the 19th. The velocity was high but the contaminants built up. In this case the wind direction was variable so that the wind, while high in velocity, was not cleaning out the area. After this period the wind stopped and the concentration of iron, lead, and bromine remained high.

Footnote and References

*Portions of this report have been accepted for publication in Environment Science and Technology.

1. H. P. Cantelow, J. S. Peck, A. E. Salo, and P. W. Howe, UCRL-10255.

2. T. S. Chow and J. L. Earl, Science Vol. 169, August 1970.

IV. Instrumentation and Systems Development

Solid State Detectors

Nuclear and Accelerator Systems

Chemical and Environmental Instrumentation

General Instrumentation

HIGH-PURITY GERMANIUM: CRYSTAL GROWING*

W. L. Hansen

We have been growing germanium crystals of high structural perfection for some time for use in making lithium-drifted detectors.[1] Stimulated by the recent work of Hall,[2] we thought it would be useful to investigate the possibilities and limitations of our techniques when applied to growing very pure germanium. We orginally thought that the lack of facilities to control airborne contamination (by laminar flow work stations, etc.) might make our chances of success very small, but the results indicate that this prejudice was unjustified and that our previously developed crystal-growing techniques were applicable to this work.

The selection of starting material for growing high-purity germanium crystals presents a dilemma. Polycrystalline ingots can be zone-refined to high purity by using a large number of zone passes, but measuring the purity of the resulting material is impossible with existing techniques. Refined polycrystalline ingots can be seeded on the final zone pass to give a single crystal whose purity can be measured, but the seeding process almost certainly introduces contamination. Commercially available high-purity germanium includes polycrystalline material that is not measurable, and single crystal material that has a higher impurity concentration (10^{11} to $10^{12}/cm^3$) than is desirable. While some of our earlier crystals were grown from commercial starting material, we now zone-refine our own polycrystalline starting material under conditions thought to be much cleaner than those of the crystal puller, then grow a crystal from this material in a vertical crystal puller.

The starting material for our zone-refining consists of ingots of 10-cm^2 cross section and 62 cm long. The trapezoidal quartz boat is lined with carbon smoke made by burning propane. A 2-cm wide melted zone is formed by direct coupling to the germanium charge with a single-turn 450-kHz rf coil that travels along the charge at 11 cm/h. About 20 zone passes are made. We find that only about the last cubic centimeter of charge to freeze shows extrinsic conductivity at 25° C.

A standard procedure has been used throughout for cleaning all quartz and germanium. The piece is hand-held with a polyethylene outer glove over an inner rubber glove, and is rotated under a stream of 5:1 HNO_3:HF, then deionized water, then 6:1:1 H_2O:HCl:H_2O_2,[3] and finally, a stream of deionized water. The work and glove are immediately blown dry with nitrogen, and with the same glove the work is placed in the crystal grower.

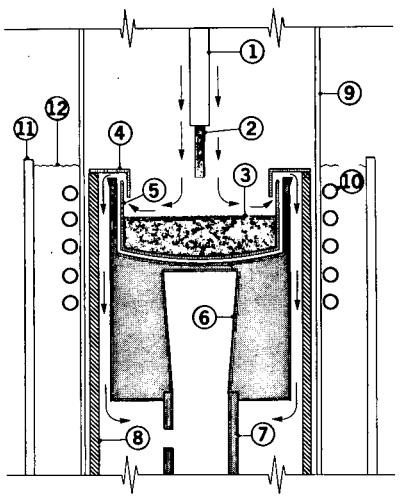

1. MOLYBDENUM SEED ROD
2. SEED
3. GERMANIUM MELT
4. QUARTZ GAS DEFLECTOR
5. QUARTZ CRUCIBLE
6. CARBON SUSCEPTOR
7. CARBON SUSCEPTOR PEDESTAL
8. SAND QUARTZ HEAT SHIELD
9. QUARTZ OUTER ENVELOPE
10. R.F.COIL
11. PYREX FISHBOWL
12. DEIONIZED WATER

Fig. 1. Crystal puller. (XBL 711-73)

With the exception of the heat shielding, the crystal grower is identical with that previously reported[1] and is shown in Fig. 1. The ambient gas is pure hydrogen at 8 liters/min and the flow path is as indicated by the arrows in Fig. 1. The 1,0,0 oriented seed is rotated at 40 rpm, the susceptor at 2 rpm and the pull rate is about 12 cm/h. Typical charges used up to the present time are about 800 g, and the pulled crystals have diameters between 24 and 36 mm. Most crystals have been held to almost constant diameter by varying the temperature of the melt, and have almost circular cross section for the entire length. The melt was grown to depletion during the pulling operation to avoid breakage of the quartz crucible.

The net ionized charge concentration in the pulled crystals is determined by measuring the resistivity at 77° K since the mobility is not limited by impurity scattering. The resistivity is found by passing 10 to 100 μA of current through the crystal, and recording the voltage measured by probes placed on filled notches at 1-cm intervals. Typical impurity profiles are shown in Fig. 2.

The two low-purity crystals in Fig. 2 (150

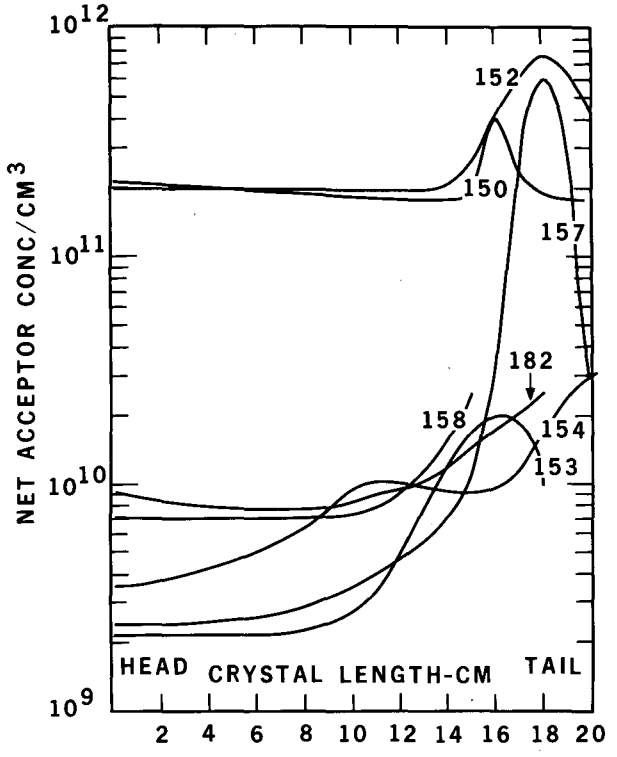

Fig. 2. Acceptor profiles of dislocated and dislocation-free crystals. The two upper curves are for dislocation-free crystals while the lower five are for crystals dislocated throughout their cross section. (XBL 7110-1546)

and 152) are dislocation free, while the others all contain dislocations–this is the only known difference between these crystals. High-quality, 1-cm-thick detectors, which are free of charge trapping, were made from most of the high-purity crystals while the dislocation-free crystals made thin detectors that showed considerable charge trapping.

High-purity germanium detectors have shown undetectable charge trapping for the extreme cases of high total ionization and for low temperature. Symmetrical peaks of 19 keV FWHM were observed for 40-MeV protons and no trapping could be found with natural α particles at 1°K.

Footnote and References

*Condensed from Nucl. Instr. Methods 94, 377-380 (1971); LBL-503.

1. W. Hansen, R. Pehl, E. Rivet, and F. Goulding, Nucl. Instr. Methods 80, 181 (1970).

2. R. N. Hall, IEEE Trans. Nucl. Sci. NS-18, No. 1 (1971).

3. W. Kern and D. Puotinen, RCA Rev. 31, No. 2, 187 (1970).

HIGH-PURITY GERMANIUM: CRYSTAL EVALUATION*

W. L. Hansen and E. E. Haller†

When attempting to grow high-purity crystals, it is natural to attribute variations in impurity concentration to uncontrolled chemical contaminations. We found, however, that the impurity concentration in our crystals seemed not to be affected by our cleaning procedures, and the impurity variation along the length of a crystal could not be represented by any reasonable distribution coefficient. In fact, the impurity variations seemed incompatible with any melt-solid distribution law. Furthermore, it was found that minute changes in the crystal growing conditions (pull-rate, diameter, etc.) led to large changes in acceptor concentration. Evidently we were seeing an effect due to the mechanical structure of the crystals, and not due to chemical impurities. An appreciation of these effects has allowed us to grow p-type germanium crystals, with high yield, with a net acceptor concentration of less than $10^{10}/cm^3$ over most of their length.

Crystal Acceptor-Concentration Profiles

All the crystals reported here were grown in pure hydrogen; they were about 3 cm in diameter, 20 cm long and 800 g in weight.[1] They had acceptor concentrations in the range 10^9 to $5\times10^{11}/cm^3$. [All crystals grown in hydrogen have been p-type. Crystals grown in environments containing residual oxygen (forming gas, water vapor, nitrogen, and vacuum) have been p-type at the head end and n-type at the tail.] The crystal acceptor-concentration profiles can be naturally classed according to the distribution of dislocations in the crystals: a) dislocation free, b) uniformly dislocated, and c) crystals containing significant regions of each type. Crystals typical of the first two classes are shown in Fig. 2 of report "High-Purity Germanium: Crystal Growing" (the preceding report). The two upper profiles (150 and 152) are for dislocation-free crystals,

while the higher-purity profiles (153, 154, 157, 158, and 182) show crystals whose cross sections exhibit almost uniform dislocation densities. The dislocations in the tail end of the higher purity crystals show tension-compression ring structure to various degrees, due to the thermal strain introduced as the melts were depleted.

A noteworthy feature of these profiles is the long regions of almost constant acceptor concentration. Since the rate of pull from the melt is constant, this result is incompatible with the distribution of an impurity from a melt. We note also that the detectors made from these crystals show no detectable radial impurity gradient.

Figure 1 shows the impurity distribution of a crystal that was examined in detail. This crystal was sectioned in 5-mm-thick slices and the etch-pit distribution observed throughout the entire crystal. The head slice had a total of only four dislocations, and an impurity concentration of $2\times10^{11}/cm^3$. The dislocation density multiplied down the length of the crystal, leaving islands of dislocation-free material which became progressively smaller until,

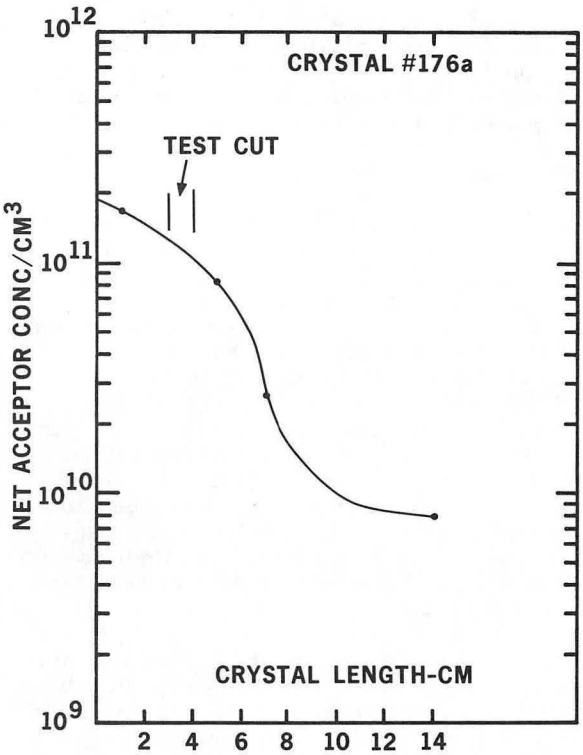

Fig. 1. Acceptor profile of a crystal that was cut into 5-mm sections. The crystal contains only four dislocations at the head end, but by 10 cm its cross section is completely dislocated. (XBL 7110-1548)

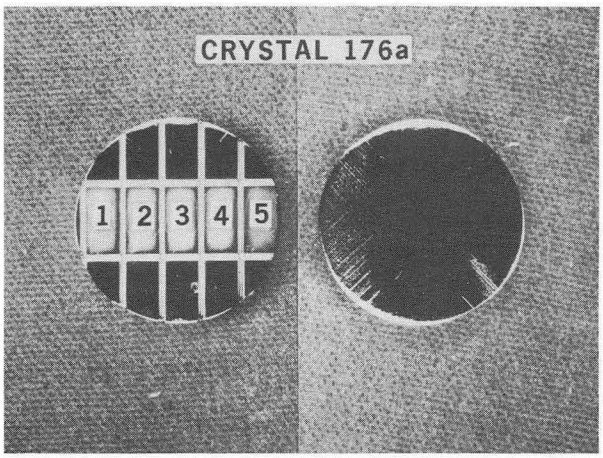

Fig. 2. The dislocation distribution, and the configuration of the diode array made from a slice of the crystal shown in Fig. 4 cut at 3.5 cm. The cut between the diodes 1 and 2 has been aligned with the boundary of the dislocated region. (XBB 7110-5091)

by 10 cm, the whole area was dislocated and the impurity concentration was less than $10^{10}/cm^3$. The etch-pit distribution of the slice at 3 cm from the head is shown in Fig. 2. Five diodes (detectors) of 10×5 mm area were made as shown in this figure. Figure 3 shows the C-V characteristics of these five diodes. It is seen that the "impurity" concentration as measured by capacitance is strongly correlated with the absence of nondislocated areas. Diode #1 is uniformly dislocated and has an "impurity" concentration of $6\times10^{10}/cm^3$, while #4 and #5, that have an impurity concentration of 4×10^{11}, are almost dislocation free. Diodes 2 and 3 have intermediate purity and have a few dislocations.

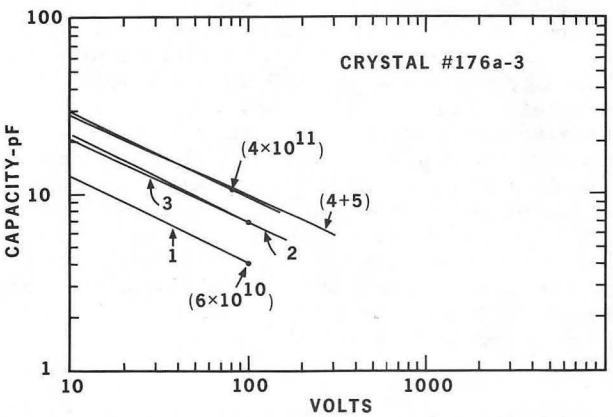

Fig. 3. Capacity-voltage characteristic of the five diodes shown in Fig. 5. Diode No. 1 is almost uniformly dislocated while 4 and 6 are almost dislocation free. (XBL 7110-1547)

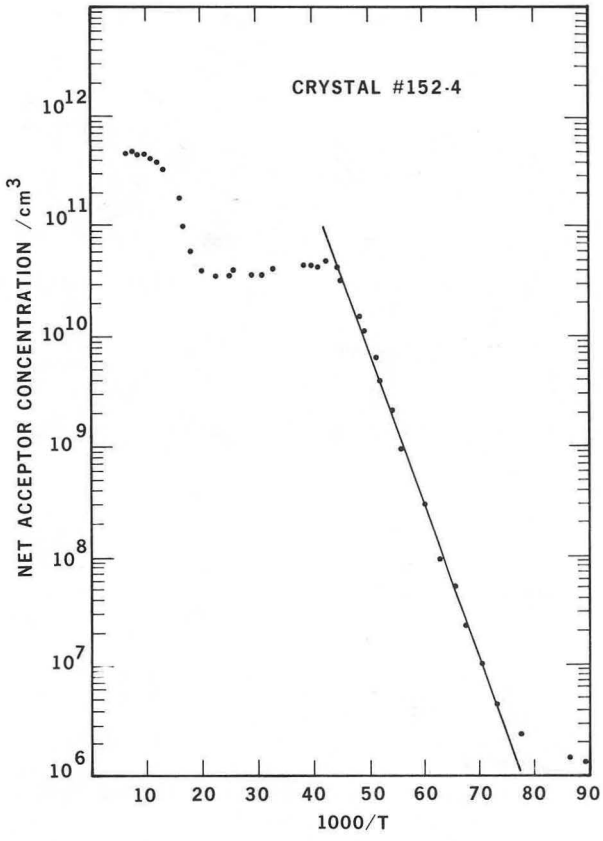

Fig. 4. Acceptor concentration vs temperature determined from conductivity measurements on a full-area slice of a dislocation-free crystal. The rapid fall in acceptor concentration near 70°K is attributed to a sudden change in the nature of vacancy clusters.
(XBL 7110-1562)

The temperature dependence of the acceptor concentration, as derived from conductivity measurements, is shown for a dislocation-free crystal in Fig. 4, and for a dislocated crystal in Fig. 5. Also shown in Fig. 5 is the carrier concentration derived from a measurement of the resistivity of the undepleted material in a detector made from another section of the same crystal. In this very low-temperature region the two types of material appear similar. The acceptor concentration begins to decrease at about 20°K at too fast a rate to be characterized by a simple acceptor level such as would be produced by a chemical impurity.

For the dislocation-free material, another more populous level exists which deionizes between 100 and 50°K.

It is tempting to try to explain away the absence of any observable effect of impurities as being due to some constant and secondary phenomenon such as compensation by levels near the middle of the band-gap or by precipitation of impurity atoms at dislocations.

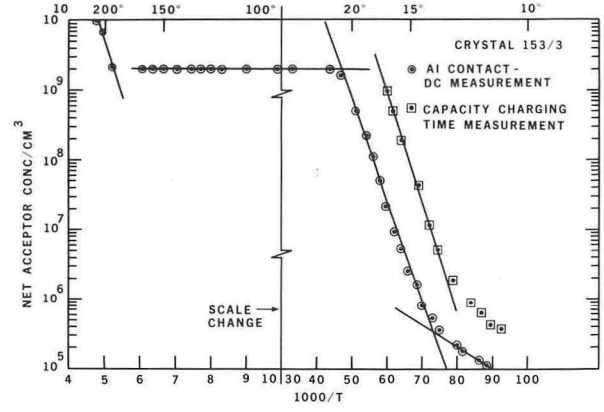

Fig. 5. Acceptor concentration vs temperature determined from conductivity measurements on a full-area slice of a uniformly dislocated crystal. The rate of deionization of the acceptor centers in this crystal below 20°K, and also of the crystal in Fig. 4, is too rapid to be characteristic of a simple acceptor impurity. It is believed to be associated with a sudden change in the acceptor energy level at this temperature. (XBL 7110-1550)

The degree of compensation by deep levels may be studied by measuring the capacitance-voltage characteristic, and the charge collection in detectors made from these crystals at 77°K. If deep levels were present, they would show up as a higher impurity concentration derived from the capacity-voltage measurement over that from conductivity, as the former measures the net fixed charge in the lattice, while the latter measures the equilibrium free-carrier concentration. In our high-purity crystals, the acceptor concentrations derived from capacity and from conductivity agree within experimental error in the temperature range above 20°K. This applies even to crystals in the low $10^9/cm^3$ range of impurity concentration, so that concentration of deep levels must be very low.

The long regions of constant acceptor concentration make it unlikely that these acceptors result from chemical impurities. Czochralski growth is incompatible with constant impurity concentration along the length of a crystal, except for the unique case of unity segregation coefficient. (No such impurities are known to exist in germanium.) Furthermore, the temperature behavior of the acceptor-concentration data indicates that the acceptor levels are

more complex than simple impurity deionization.

Thermodynamic considerations require that the dislocation-free material be saturated with vacancies. A possible explanation of the level which disappears below 100°K in dislocation-free material is that a change in the nature of vacancy clusters takes place, so as to change the activation energy at this temperature. It is also possible that the level that begins to freeze out at 20°K in both dislocation-free and dislocated material is simply another configuration of vacancies that changes its activation energy at this temperature. The rapid change of hole concentration with temperature that occurs below 20°K is not consistent with simple deionization of an acceptor.

Footnotes and Reference

*Condensed from IEEE Trans. Nucl. Sci., NS-19, No. 1 (1972); presented at the IEEE Nuclear Science Symposium, Nov. 3-5, 1971.

†Presently working with grants from Janggen-Poehn Stiftung and the Kanton Basel-Stadt, Switzerland.

1. W. L. Hansen, Nucl. Instr. Methods 94, 377 (1971).

HIGH-PURITY GERMANIUM: DETECTOR FABRICATION AND PERFORMANCE

R. H. Pehl, R. C. Cordi, and F. S. Goulding

During the past year we have seen high-purity germanium detectors advance from being an interesting plaything to the point where they are on the verge of competing directly, and successfully, against lithium-drifted germanium detectors.

Since lithium drifting is not necessary, these high-purity germanium detectors have the fundamental advantages of being simpler and quicker to fabricate, and they can be stored at room temperature without deterioration. These factors facilitate the construction of large-area mosaics of detectors, or thick stacks suitable for measurements on high-energy particles.

Over the past year we have made a total of almost 100 detectors from 15 of the germanium crystals grown by W. L. Hansen at Lawrence Berkeley Laboratory.[1] Nearly all the crystals have been p-type. Consequently, almost all our detector development work has been devoted to working with p-type material. P-type material appears to be easier to work with because n^+ contacts that will support high fields are more readily made than p^+ contacts.

Initially the same techniques used for making contacts on lithium-drifted germanium detectors were used for high-purity germanium.[2,3] The n^+ contact was formed by lithium evaporation onto a lapped surface followed by a six-minute diffusion at 400°C, and the metal barrier contact consisted of a gold evaporation onto an etched surface.

Although a number of good detectors were made using the Au contact, it would not consistenly sustain a large overvoltage. Since development of a contact that would consistently allow the application of a significant overvoltage was imperative if high-purity germanium detectors were to become practical, we then tried a Cr evaporation. This proved to be an improvement, and most of our detectors have a Cr back. We later tried a few Pt evaporations; these detectors all withstood very high overvoltage (> 1000 V), and additional Pt backs will be tried when electron-gun evaporating facilities are available. Recently we have also worked with a Pd-Ge back that appears to be very promising, especially in regard to producing an extremely thin entrance window. An Al diffused p^+ contact has also shown promise.

The lithium-diffusion temperature has now been reduced to 330°C because of an apparent anomalously deep lithium-diffusion tail that extends the n^+-p junction far into the germanium. When lithium is diffused at > 350°C, the effect of the diffusion tail is large in germanium having $\approx 10^{10}$ acceptors/cm^3 or less.

We have yet to see any deterioration of the lithium contact due to lithium precipitation in detectors that have been stored at room temperature for a year. Other laboratories have reported the same experience.[4]

After the contacts have been made, the contact surfaces are protected with etch-resistant tape, and the exposed surfaces are etched for two minutes in 3:1 HNO_3:HF mixture. The etch is quenched in methanol, which is blown off with nitrogen. After removing the tape, the device is mounted in the cryostat. A thin film of indium-gallium eutectic is spread on the n^+ surface to provide a good electrical con-

tact.

Contrary to Llacer,[5] we have found surface-state problems to be far less troublesome than for lithium-drifted germanium detectors. In fact nearly every case of high leakage current has been caused by electron injection at the metal barrier contact. Furthermore, the surfaces are surprisingly stable. Apart from examples where the p^+ contact is damaged during handling, we have found no cases of detector degradation.

Figure 1 presents the ^{55}Fe spectrum obtained with a 5-mm thick, 1-cm diameter detector that depleted at about 375 V. Even without overvoltage the entrance window was extremely thin; there were no more counts below the 5.9-keV line without overvoltage than the negligible number observed at higher voltages. This apparently is due to a built-in field that is characteristic of the Pd back. If a Au or Cr back had been used on this detector, an overvoltage of at least 100 V, probably 200 V, would be necessary before the effective window thickness would have decreased to a minimum, and even then the background would probably be significantly higher than shown in Fig. 1.

This detector, mounted in the guard-ring configuration, has an effective capacity of about 4.4 pF. The 180-eV resolution for the 5.9-keV Mn x-ray, obtained with an amplifier peaking time of 17 μsec, is nearly equal to the best resolution obtained with a Si(Li) detector of equivalent area. Since the pulser resolution was 150 eV, the effective Fano factor was 0.10.

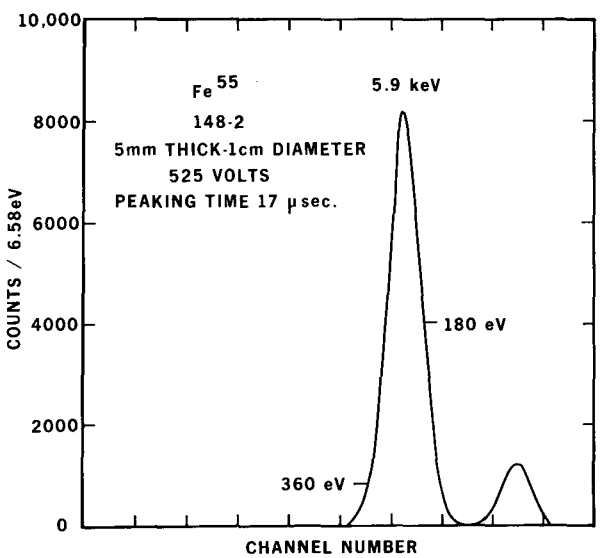

Fig. 1. X-ray energy spectrum from a ^{55}Fe source. There were a negligible number of counts down to about 1 keV, where the spectrum was electronically cut off.
(XBL 7110-1566)

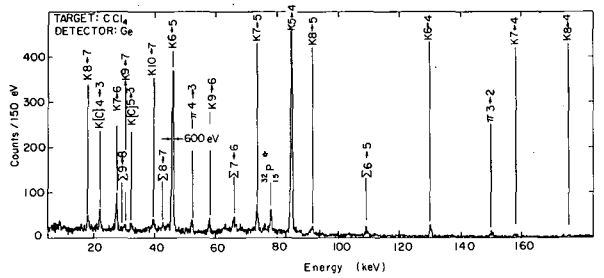

Fig. 2. Kaonic x-ray spectrum of Cl. X rays from pionic and sigma-hyperonic atoms, and a kaonic-induced nuclear γ-ray, were also detected. (XBL 7110-4529)

The same Fano factor is determined from the 470-keV resolution obtained with this detector for the 122-keV γ ray of ^{57}Co.

Figure 2 shows a spectrum from the first significant physics experiment to use a high-purity germanium detector. A 4-mm-thick 18-mm-diameter detector was used to obtain this kaonic x ray spectrum of Cl. X rays from hydrogen-like atoms in which the electrons have been replaced by a kaon, a pion, or a sigma are observed. This spectrum has a considerably lower background than any previous mesic x-ray spectrum. It is also the first and only spectrum to show a kaonic induced nuclear γ ray, in addition to x-ray transitions from the three different types of exotic atoms.

We have made a number of approximately 7-cm^3 detectors (≈ 3 cm diameter, 1 cm thick). The performance of these devices was essentially equivalent to a good Ge(Li) detector of the same size. As expected, there has been no indication that the best high-purity germanium will provide better or worse resolution than the best lithium-drifted detectors.

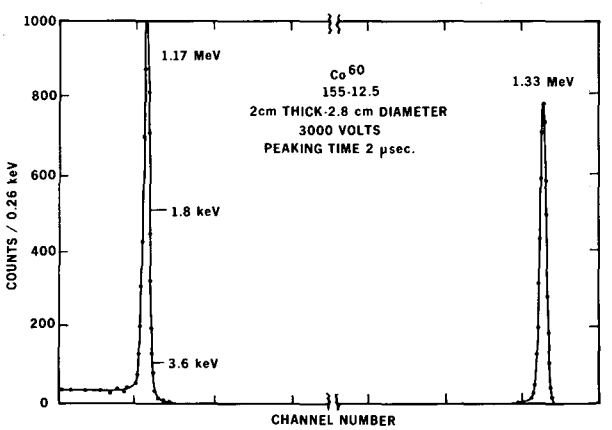

Fig. 3. ^{60}Co energy spectrum.
(XBL 7110-1567)

The availability of germanium crystals having less than 10^{10} acceptors/cm^3 makes the fabrication of very-large-volume planar detectors feasible. Figure 3 shows the ^{60}Co spectrum from a 2-cm-thick 2.8-cm-diameter detector. The capacity of this 12-cm^3 detector is only 4.2 pF. Since depletion is reached at 1000 V the acceptor concentration is only 5×10^9/cm^3.

The charge collection across such a long distance is excellent in this device. With no overvoltage (1000-V bias) the resolution for the 1173-keV ^{60}Co γ ray is 2.6 keV, at 1500 V it is 2.0 keV, and at 3500 V it is 1.9 keV—slightly worse than the resolution presented in Fig. 4 at 3000 V because of additional noise.

The largest planar detector we have yet made is 25 cm^3 (2 cm thick, 4.0 cm diameter), from another crystal that had an acceptor concentration of only 5×10^9/cm^3.

In December 1970, a brief test of stopping 40-MeV protons from the 88-inch cyclotron was made. A proton spectrum obtained by placing a 6-mm-thick 1-cm^2-area detector directly in the magnetically analyzed beam (protons were not scattered off a target) is presented in Fig. 4. The device was operated in the scattering-chamber vacuum; thus the protons did not pass through a window prior to impinging on the detector. Collimation of the incident protons limited the exposed area to about the center 4×6 mm of the detector. The energy spread in the beam itself supposedly was 10 keV. Since the electronic noise was about 7 keV, the observed resolution for the entire system of 19 keV is only slightly worse than predicted.[6]

Significant charge trapping has not been observed in any detectors made from crystals grown in pure hydrogen, except in a few cases where fabrication techniques were proven to be

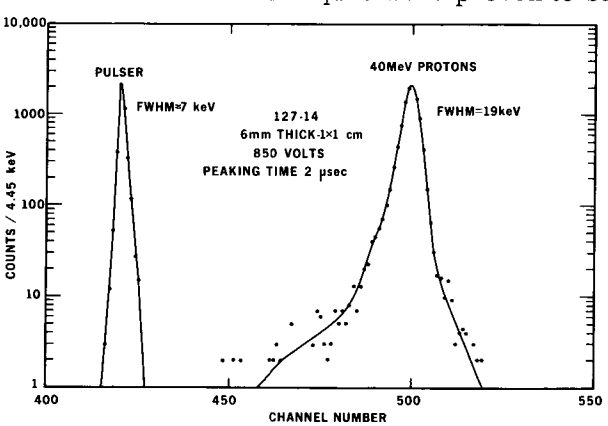

Fig. 4. Energy spectrum of 40-MeV protons. (XBL 7110-1565)

at fault. However, detectors made from crystals grown in nitrogen invariably exhibited very severe trapping, and detectors made from a crystal grown in vacuum had significant trapping, while detectors made from crystals grown in forming gas showed slight trapping. Residual oxygen in the crystal-growing environment apparently creates charge trapping centers in the germanium.

Radial scans of several good detectors have been made by directing a collimated beam of conversion electrons from ^{207}Bi onto the p^+ side at different bias voltages. Since we found no variation of the electron peaks along the diameter there can be no significant radial change in the acceptor concentration. This observation is contrary to that reported by Sakai, McMath, and Fowler[7] on detectors made from high-purity germanium crystals grown by R. N. Hall at General Electric.[8] Whether this discrepancy is due to different fabrication techniques or to the different germanium-growing techniques is not known.

References

1. W. L. Hansen, Nucl. Instr. Methods 94, 94, 377 (1971). W. L. Hansen and E. E. Haller, "High-Purity Germanium-Observations on the Nature of Acceptors," 1971 Nuclear Science Symposium, to be published in IEEE Trans. Nucl. Sci. NS-19, No. 1 (1972).

2. F. S. Goulding, Nucl. Instr. Methods 43, 1 (1966).

3. R. H. Pehl, D. A. Landis, and F. S. Goulding, IEEE Trans. Nucl. Sci. NS-13, No. 3, 274 (1966).

4. I. L. Fowler and T. A. McMath, "Germanium Detectors—Current State of the Art," AECL-3991, presented at Strasbourg-Cronenbourg, France, June 29-30th, 1971.

5. J. Llacer, "Planar and Coaxial High-Purity Germanium Radiation Detectors," Brookhaven National Laboratory Report BNL-15910, to be published in Nucl. Instr. Methods.

6. F. S. Goulding, D. A. Landis, and R. H. Pehl, "The Energy Resolution Capabilities of Semiconductor Detectors for Particles in the 10- to 100-MeV Range," Semiconductor Nuclear-Particle Detectors and Circuits, National Academy of Sciences Publication #1593 (1969), p. 744.

7. E. Sakai, T. A. McMath, and I. L. Fowler, IEEE Trans. Nucl. Sci. NS-18, No. 1, 228 (1971).

8. R. N. Hall and T. J. Soltys, IEEE Trans. Nucl. Sci. NS-18, No. 1, 160 (1971).

A SURVEY OF RADIATION DAMAGE IN SEMICONDUCTOR DETECTORS*

F. S. Goulding and R. H. Pehl

The history of an 11-mm-thick, 3-cm-diameter, lithium-drifted germanium planar detector that is representative of many examples seen in our laboratory is outlined in Table I. The history is typical, and conclusions drawn from the data can be regarded as generally valid for lithium-drifted germanium detectors.

The shape of the 1.17-MeV ^{60}Co line at various times is given in Fig. 1, and capacity vs voltage data are presented in Fig. 2. The following notes relate to various stages in this history.

Stages #1 and 2. These represent the situation before damage. The levelling operation performed between #1 and #2 flattened the capacity voltage curve, but produced no significant effect on resolution.

Stage #3. Following accidental neutron damage (dose unknown) in pionic x-ray experiments, the ^{60}Co peak exhibited severe tailing characteristic of charge-trapping. The capacity–voltage relationship was not significantly changed from stage #2, so no ionized donors

TABLE I : DETECTOR # 40A HISTORY

DATA SET #	DATE	NOTES
1	4-24-68	FIRST TEST (DRIFT 9.5mm)
		STORED THEN LEVELLED
2	5-1-68	TEST PRIOR TO USE
		NEUTRON DAMAGE IN MESIC
		X-RAY EXPERIMENTS
3	5-28-68	TESTED WHILE AT 77°K
4	5-28-68	SCAN TESTS AT 77°K
5	5-28-68	AFTER BRIEF WARM-UP TO 25°C
6	5-29-68	AFTER FURTHER BRIEF
		WARM-UP
7	5-29-68	AFTER FURTHER BRIEF WARM-UP
8	5-29-68	AFTER FURTHER 5 MIN. WARM-UP
9	5-31-68	AFTER FURTHER 5 MIN WARM-UP
10	5-31-68	AFTER FURTHER 8 MIN WARM-UP
11	5-31-68	AFTER FURTHER 12 MIN WARM-UP
12	5-31-68	AFTER FURTHER 15 MIN WARM-UP
		REHEAT TO 400°C
		AND REDRIFT 3 DAYS
13	6-7-68	RETEST-THEN
		TO HILAC FOR EXPT'S.
14	5-25-69	TESTED AFTER NEUTRON DAMAGE
15	5-26-69	AFTER 4 HOURS DRIFT
		AND LEVELLING
		IN USE AT HILAC UNTIL NOW

N.B: ALL TESTS CARRIED OUT WITH DETECTOR AT 77°K

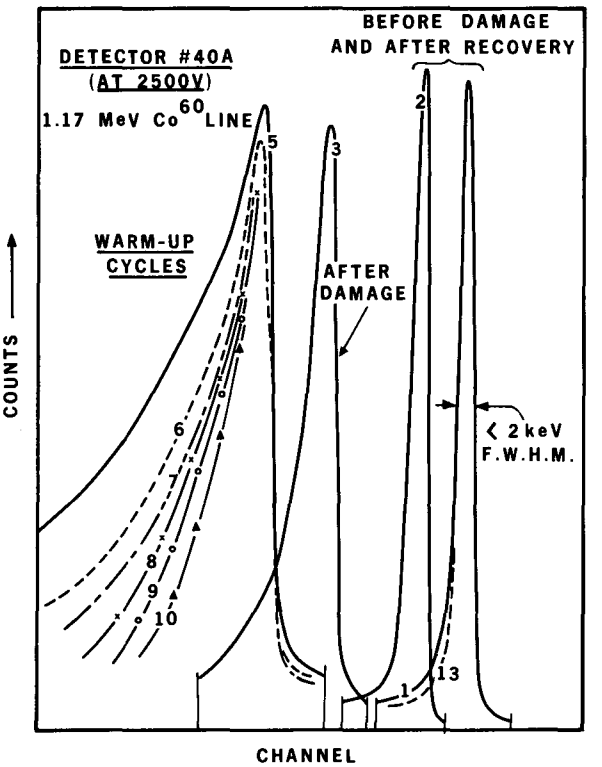

Fig. 1. Detector #40A; showing the shape of 1.17 MeV ^{60}Co peak at various stages (see Table I). No relevance should be attached to the peak position. (XBL 7110-1526)

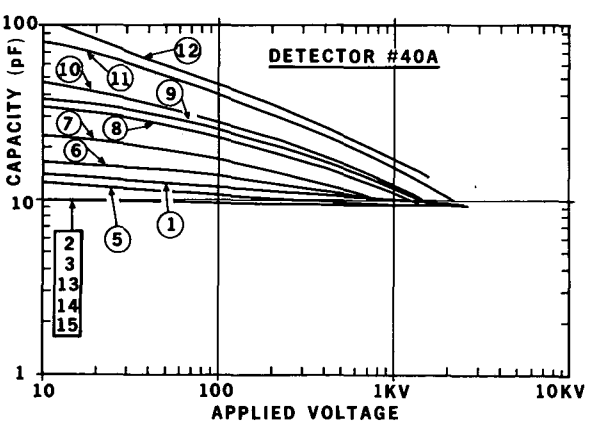

Fig. 2. Detector #40A; capacity-voltage relationship at various stages (see Table I). (XBL 7110-1522)

or acceptors (or perhaps equal numbers of each) were produced. Both capacity and spectral data were taken while the detector was still at 77°K.

Stage #4. With the detector still at 77°K, it was scanned from electrode to electrode by collimated γ rays from a ^{137}Cs source. This scan revealed severe hole trapping. (i.e., performance was best when the γ-ray beam impinged near the p-type side.) This behavior contrasts with that of undamaged detectors made with this material where very slight electron trapping is observed.

Stage #5. Following a brief warm-up to 25° C (while still mounted in its holder), the detector was again cooled to 77°K, and tested with ^{60}Co. The trapping now appears to be much worse than in #4, and the capacity-voltage relationship indicates the appearance of either donors or acceptors.

Stage #6. The steps of #5 are repeated. Surprisingly, trapping is reduced although the concentration of active acceptors or donors has increased. We know from other evidence that acceptors are becoming dominant at this and later stages.

Stage #7. After an additional repeat of the steps of #5 and 6, the trends of stage #6 continued.

Stages #8 through 12. Longer warm-up cycles continued the trends of stages #6 and 7. No data for stages #11 and 12 are given in Fig. 1, as the detector would no longer sustain the 2500 V necessary for direct comparison with earlier stages. Re-etching was not carried out at any stage. After stage #12, the net acceptor concentration in the material corresponded to 10^{11} acceptors/cm^3. This compares with an initial net concentration below $10^9/cm^3$, and with total lithium and gallium concentrations of $3 \times 10^{14}/cm^3$.

Stage #13. Following a reheat to 400° C and three days drifting under normal drift conditions, the detector was again tested. Its γ-ray performance and capacity-voltage curve were virtually identical to those seen at Stage #2. This represents complete recovery from the effects of damage.

Stages #14 and 15. After additional neutron damage, the detector was recovered again—this time by a four-hour drift followed by levelling overnight at -20° C. Due to improved procedures and better electronics developed during the period of this history, the final detector resolution after stage #14 is slightly better than after stage #12.

The detector is still in use in experiments, and has not suffered significant additional neutron damage.

We will now try to relate these experimental results to the work of others. Kraner, et al.[1] irradiated a series of lithium-drifted germanium detectors to levels ranging from about 10^7 to 10^{11} n/cm^2.

Severe spectral deterioration occurs for neutron exposure greater than about $10^{10}/cm^2$ and, as in our case, the primary effect at 77°K is the introduction of neutral hole traps. Very low production of acceptors or donors is observed in both sets of detectors when kept at 77°K. We further agree that complete recovery of detectors by lithium-drifting occurs—this implies that precipitation of lithium at damage sites reduces the cross section of the traps to essentially zero.

The prompt effect of heating to room temperature after exposure at 77°K is the production of donors, but precipitation of lithium becomes dominant quickly, and the loss of lithium ions results in p-type material. The improvement in resolution after prolonged periods at 25° C supports the contention that the hole traps produced by radiation are annihilated by lithium precipitation.

The nature of the neutral traps produced by radiation at 77°K is unknown. The primary damage sites may be responsible, but combinations of gallium plus vacancies or lithium plus vacancies may be involved. These latter mechanisms demand migration of vacancies at 77°K. It is of interest to examine high-purity germanium detectors where the acceptor and/or donor levels are less by a factor of 10^4 than in lithium-drifted material, and where the possibility of acceptor/donor-defect interactions is negligible.

Two tentative suggestions can be made, based on comparing high-purity germanium results with those for lithium-drifted detectors:

a) The threshold dose for severe damage effects is similar in the two cases. This strongly suggests that production of neutral hole-traps will be the initial mechanism observed in spectroscopy experiments with either type of detector. If this is true, it indicates that vacancy plus lithium or vacancy plus gallium pairs are not a factor in the degradation process in lithium-drifted detectors when maintained at 77°K.

b) Raising the detector temperature to 25° C for a significant length of time results in generation of acceptors in both cases. While lithium precipitation must be a major factor

in this process in lithium-drifted detectors, the pure-germanium work suggests that a damage process basic to the germanium also contributes acceptors.

The mechanisms used to repair damage in the two cases are quite different. In lithium-drifted detectors, we assume that lithium ions precipitate at damage sites, annihilating the traps, and that each site can probably accept only one lithium atom. The redrift-repair process presumably replaces the lithium lost by precipitation. On the other hand, the high-temperature anneal process used to repair pure-germanium detectors (which is not applicable to lithium-drifted detectors) must involve reassociation of vacancy-interstitial pairs produced by the radiation damage. It is surprising that the reassociation is so complete; perhaps it would not be if the damage were uniformly distributed. In both cases studied here, the damage produced by individual collisions of neutrons or protons is locally intense, and the high-density damage clusters may be easier to anneal than the distributed isolated damage sites characteristic of γ-ray damage.

Footnote and Reference

*Presented at the IEEE Nuclear Science Symposium, San Francisco, CA, Nov. 3-5, 1971; also to be published in IEEE Trans. Nucl. Sci. NS-19, No. 1 (1972).

1. H. W. Kraner, C. Chasman, and K. W. Jones, Nucl. Instr. Methods 62, 173 (1968).

THE "BEVALAC" – A VERSATILE ACCELERATOR CONCEPT*

A. Ghiorso

For many years the biomedical groups of the Lawrence Radiation Laboratory have been interested in a high-energy medium-heavy-ion accelerator which could be used for extremely important extensions of the field of nuclear medicine. Unfortunately, new high-energy machines with the necessary capability are, of necessity, very costly, so that there has been a natural reluctance in the past to fund the projects that have been proposed for this purpose. The latest of these studies is for a synchrotron ring to accept particles from the SuperHILAC and accelerate them up to energies of several hundred MeV per nucleon. This project is feasible but suffers from the difficulties of cost (about 6 million dollars) and marginal utility. We have just recently come to the realization that the inexorable advance of accelerator technology now makes it possible to use the existing facilities at Berkeley in a novel manner to furnish the biomedical groups with ample beams of fast heavy particles at a very moderate cost without disturbing the normal operation of these facilities.

By combining the new SuperHILAC, which will be operating early in 1972, with the pioneering high-energy proton accelerator, the Bevatron, we obtain at minimal cost a very powerful team that can undertake a number of important tasks. The missing ingredient for the combination to be successful is a booster to raise the velocity of the SuperHILAC ions to the point where they will match the velocity of the protons that are normally injected into the Bevatron. The other requirement, because of the relatively "poor" vacuum in the Bevatron, is that the ions be completely stripped of electrons; the booster makes this possible for the heavier atoms that we desire to inject into the Bevatron. It turns out that such a booster, another linear accelerator, can be very valuable in its own right for both biomedical purposes and nuclear chemistry–physics. The booster would be able to accelerate all of the ions emitted from the SuperHILAC to energies in the region of 50 MeV/nucleon, depending on the atomic number. Its duty cycle would be comparable to that of the SuperHILAC and it would have its own modest target area for those experiments requiring the intermediate energies.

The most logical site for the booster is adjacent to the SuperHILAC exit but at an elevation about 30 ft lower. The linac would point toward the south to take advantage of the terrain and to get its exit beam closer to the Bevatron. A beam line for inflection of fully stripped 13-MeV/nucleon heavy ions into the Bevatron would be about 400 ft long; such a length is easily handled by about 20 quadrupole magnets similar to those used in the SuperHILAC itself.

The "BevaLac" will be able to accelerate heavy ions to energies as high as 2700 MeV/nucleon. The upper limit in Z that can be accelerated depends upon the ion velocity out of the booster. Detailed information as to the velocity for complete stripping is not yet known for atoms beyond argon, but it is expected that an appreciable current of 180-BeV Kr ions can be obtained. The beam current of ions such as neon could be as high as 10^{11} ions per second. With further modifications of the Bevatron and the booster it should be possible to accelerate U ions to 460 BeV.

The Bevatron can readily be adapted at modest cost to a time-share mode of operation so that the therapeutic use of the machine can be performed constantly. The SuperHILAC, by the addition of a third 800-kV injector, is already designed with this time-sharing capability. Since the time required to fill the Bevatron accelerating ring is only a few hundred microseconds there will be no problem in furnishing a beam pulse whenever desired by the medical facility. After exploratory "tuning" work has been accomplished with the "BevaLac" it should be a routine procedure that can be handled by computers.

The tremendous range of capabilities of the proposed combination uncovers possibilities far beyond its use for cancer research and therapy and has thus aroused the excitement of many in the nuclear chemistry-physics community. Clearly a whole new field of theoretical and experimental science would open up rather quickly at minimal cost. The collective effects of the nucleons in a complex ion traveling at high velocity should be a rather interesting phenomenon; many scientists feel that these effects will not be simply those of individual nucleons traveling separately at the same speed. For the first time an exploratory effort will be possible.

The availability of high-energy complex ions in the laboratory is very important for biomedical studies of the hazards that they may present in long spacecraft flights, and this is planned as a part of the biomedical research program. This facility would also be very valuable to the research workers in the space sciences, since for the first time they would be able to use a versatile machine for calibra-

tion purposes. The exciting discovery of high-energy uranium ions in the cosmic flux opens a new window looking out into the universe.

The concept that has been outlined briefly can be accomplished with great rapidity and at modest cost. It will not interfere with either the construction or operation of the SuperHILAC - in fact, by judicious design we believe it may be possible to incorporate certain qualities in the proposed booster that will enable future changes in the present post-stripper so that even more efficient acceleration of the heaviest ions will become possible.

The joint additional operating costs of the new concept will be comparable to that expected for the originally-proposed synchrotron.

Footnote

*This memorandum was sent by Albert Ghiorso to Edwin McMillan on 22 March 1971 to outline an inexpensive concept of combining the SuperHILAC with the Bevatron to enable the acceleration of heavy ions to high energies and thus achieve one of the important goals of the ill-fated Omnitron project. As it turned out, the Bevatron is able to accept ions from the SuperHILAC even without the booster that was suggested in the memo, and thus it will be possible to make the BevaLac operational late in 1973 if the funds for the transfer line between the two facilities become available as expected. To prove that the Bevatron could accelerate heavy ions efficiently, a crash program was undertaken in the summer of 1971 and was, indeed, successful in accelerating to very high energies a small beam of nitrogen ions from its own injector.

88-INCH CYCLOTRON OPERATION AND DEVELOPMENT

J. Bowen, D. J. Clark, J. P. Meulders,* and J. Steyaert*

During 1971 the cyclotron was operated 20 8-hour shifts per week for experiments on light and heavy ions. One shift per week was a shutdown day for maintenance. The time distribution for operation and maintenance is shown in Table I. The distribution of beam particles is shown in Table II. Ions heavier than helium occupied over 25% of operating time, and in the last quarter of the year increased to 40%.

The main emphasis in development was on producing high-intensity heavy-ion beams for use in nucleon transfer reaction experiments in the recently constructed spectrometer magnet. A new heavy-ion source of the Penning type was built and put into successful operation by October. This source uses a 5/16-in. diameter arc in a copper anode, and tantalum cathodes at each end. An arc power of 3 to 4 kW provides much greater output of high-charge-state heavy ions than the 1/8-in.-diameter, 500-W arc of the conventional filament-type source. External beam currents of 10 to 20 μA of 60- to 100-MeV O^{4+}, and several μA of 160-MeV N^{4+} and 250-MeV N^{5+} have been run. Cathode life is about 3 to 5 h. This source is described in a separate article in the Annual

Table I. 1971 Time Distribution

Tune-up	7%		
Beam Optics	5%		
Experiments	44%		
Beam Development	8%		
Operating Time		64%	(5331 hours)
Planned Shutdowns		25%	
Unplanned Maintenance		11%	
TOTAL WORK TIME		100%	(8368 hours)

Table II. 1971 Particle Distribution

Internal Ion Source:		
Protons	20%	
Deuterons	3%	
Helium 3	10%	
Helium 4	27%	
Nitrogen	5%	
Oxygen	17%	
Other	6%	
Total		88%
External Polarized Source		12%
TOTAL OPERATING TIME		100% (5331 hours)

Report. A new ion-source elevator was put into operation in the pit. It will pull the source without turning off the main magnet, making more rapid on-source changes possible. The roof and wall shielding was completed for the new north experimental area containing both the spectrometer and two other beam lines from the analyzing magnets.

Our development projects during the year included testing of a new master oscillator-power amplifier system for the main dee radio-frequency voltage, by the electronic engineering group. This will replace the present self-excited oscillator, to give better dee voltage and frequency stability. The design of a modification of the third section of the new deflector was completed and sent to the shop. This will provide radial quadrupole electrostatic focusing to the extracted beam. Since the internal heavy-ion source was working very well, the external heavy-ion source mounted on the axial injection system is not yet able to provide similar intensities. A lithium oven was built for it, to develop lithium beams for the cyclotron, since lithium in the center of the cyclotron would cause dee voltage-sparking problems. This work is described in other papers in this Annual Report.

There was a shutdown in January and part of February for general maintenance, and for repair of a blockage in one of the dee water circuits. The blockage caused unsymmetrical heating of the dee and vertical bending, which caused variations in the center region alignment. A piece of solder was removed to clear the cooling line. Also during this shutdown the loose inconel dee lips were replaced by copper lips. Puller east-west motion was reinstalled, and a new half-turn collimator was built to operate independently of the center region inserts.

In July another 1-1/2-week shutdown was required to repair cracks in the skin of the dee stem near the trimmer capacitor. This crack was causing an erratic vertical dee motion of 0.040 to 0.080 in. Late in the year a poor contact in the dee stem short area developed, causing heating of the rear tank wall at high frequencies. It was repaired and a new clamp bar was designed and built, to be installed in early January 1972. A hole was cut in the south dee tank wall, during the Christmas shutdown, for later installation of a sublimation pump.

Footnote

*On leave of absence from the University of Louvain, Ottignies, Belgium.

AN EXTERNAL HEAVY-ION SOURCE FOR THE BERKELEY 88-INCH CYCLOTRON*

D. J. Clark, J. Steyaert,† A. Carneiro, D. Elo, P. Frazier, D. Morris, and M. Renkas

A heavy ion source of the PIG (Penning Ion Gauge) type has been installed on the axial injection line at the 88-inch cyclotron. It is now in the testing phase. Arc powers up to 4 kW have been run, and hydrogen and nitrogen beams have been injected and accelerated in the cyclotron.

Design of the Source

For the production of highly charged heavy ions, the best source appears to be the PIG type.[1] For the present source, the present version of the source originally developed for the Berkeley Hilac[2] was chosen as a starting point.

The PIG source and injection area are shown in Fig. 1. The source anode is biased to +10 kV, so the beam is accelerated to 10 kV/charge by the puller at ground potential. The cathode is biased 1 to 3 kV negative with respect to the anode by the arc supply. The source magnet with a field of 2 to 5 kG bends the beam through 120 deg and selects the charge state to be transmitted. The exit edge of the magnet is cut back 25 deg to give axial focusing to the beam. An iron shield, cut to the same angle, gives a sharp field cutoff and defines the magnetic edge.

In Fig. 2 is seen a detailed view of the anode and puller. The anode is of water-cooled copper. The puller blades are replaceable tantalum sheets. The puller is remotely movable parallel to the anode face. The cathodes are tantalum cylinders mounted with setscrews into water-cooled copper plates. Boron nitride insulators separate cathode and anode. They are mounted eccentrically to catch the tantalum cathode flakes falling from the ends of the horizontally oriented arc column.

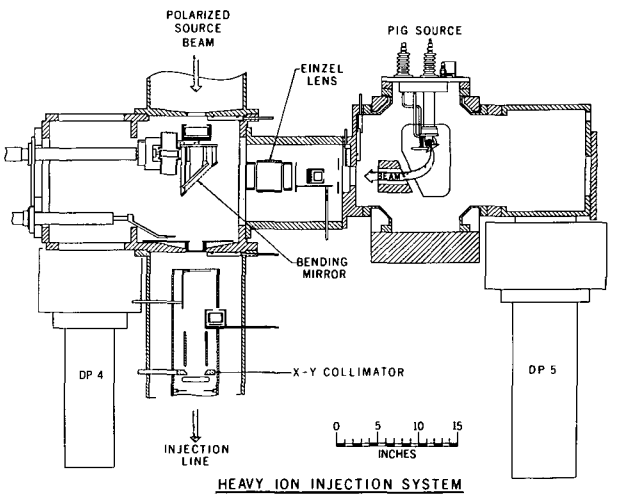

Fig. 1. PIG source injection system showing source, focusing lens, bending mirror, Faraday cups, and scanning wires for beam monitoring. (XBL 712-294)

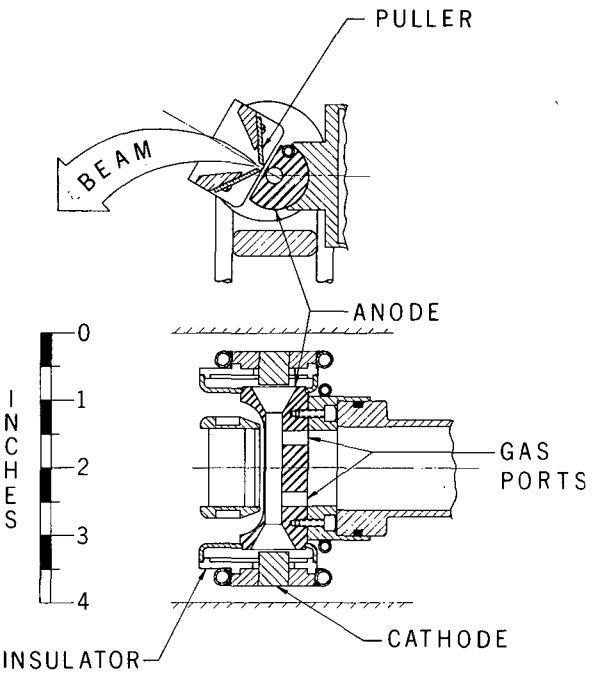

Fig. 2. Cross sections of anode-puller region. (XBL 712-308)

In the following sections of the system (Fig. 1), the beam is transported through a 90-deg bend to the entrance to the quadrupole injection line. Just beyond the source, a plate with a cross pattern of holes is used with a motor-driven scanning wire to measure source emittance. An einzel lens and electrostatic mirror bring the beam to the injection line entrance.

Initial Performance

The testing of the source began in late 1970. The first operation was with an uncooled inconel anode. It was found that the output of N^{4+} beams was poor and that the anode melted near a cathode. Also a great quantity of flakes was produced. An improvement was obtained when water cooling was added along the side of the anode. A further improvement came by using water-cooled copper, instead of inconel. This gave both better arc stability of 3 to 4 kW, and better high charge state production. At present the arc runs stably up to 1 kV × 4A = 4 kW.

The charge distribution at optimum gas pressure of a nitrogen beam of 10 kV was measured on the Faraday cup after the source (Fig. 1). It is shown in Table I. Total beam current was about 10 mA.

Table I. Nitrogen-beam charge-state distribution.

	N^{1+}	N^{2+}	N^{3+}	N^{4+}	N^{5+}	V_{arc}	I_{arc}
Beam(%)	32	40	23	4.1	0.36	1 kV	3.1A

An initial measurement of the emittance of the source with the cross-plate and scanning wires just beyond the source was made. The values are 900 mm-mr vertically, and 500 mm-mr horizontally, for about 80% of the beam in each plane. The vertical plane is the bending plane, so that emittance includes source energy spread.

Some initial transmission measurements into the cyclotron were also made. For protons, the overall transmission from the source to the external cyclotron beam is about 0.5% without a buncher. By more careful matching of source emittance to the line, and by use of the buncher this should approach the 5% obtained with the polarized source. Beams of N^{3+} and N^{4+} were injected and accelerated in the cyclotron. These tests indicate that the overall transmission from source to external beam would be about 0.05%. The reduced transmission is due to gas charge exchange in the injection line and the cyclotron. By improving the injection line pressure, the optics, and using the buncher this transmission should approach 1%.

Some Operating Procedures

Two powerful modes of operation of the arc are possible: a positive resistance (+R) mode (1A of arc and 2 kV) and a negative resistance (-R) mode (3A or more at 1 kV or less). In this last mode the cathodes are hot enough to emit thermionic electrons, the highest charge state is produced, and some "filaments" are seen between both lips of the anode slit. In the +R mode the beam is not seen when looking axially at it, while in the -R mode the beam is clearly visible, due to a high proportion of excited ions. A less powerful arc (0.1 to 0.3 A at 3 kV) exists when starting the arc. It was most used when running the PIG source as a proton source.

Footnotes and References

*Condensed from UCRL-20406; IEEE Trans. Nucl. Sci., NS-18, No. 3, (1971).

†On leave of absence from University of Louvain and IISN, Belgium-NATO Fellowship.

1. R. S. Livingston, The Acceleration of Heavy Ions, Part. Accel. 1, 51 (1970).

2. C. F. Anderson, K. W. Ehlers, Ion Source for the Production of Multiply Charged Heavy Ions, Rev. Sci. Instr. 27, 809 (1956).

HEAVY-ION DEVELOPMENT AT THE BERKELEY 88-INCH CYCLOTRON

D. J. Clark, J. Steyaert,* A. Carneiro, and D. Morris

Introduction

Interest in heavy-ion experiments has been increasing during the past year at the 88-inch cyclotron. The beams required are lithium, carbon, nitrogen, and oxygen in the 50- to 80-MeV region for studies of nuclear structure and reaction mechanisms. Also nitrogen beams of the highest available energy are used for biomedical studies of radiation damage. The original internal ion source[1] has been used to produce these beams, but has limited arc power and filament life. To get more arc power, a Penning Ion Gauge or "PIG"-type source was built, and is now being tested. The external PIG source reported in March 1971[2] is being developed for lithium beam production by the addition of an oven.

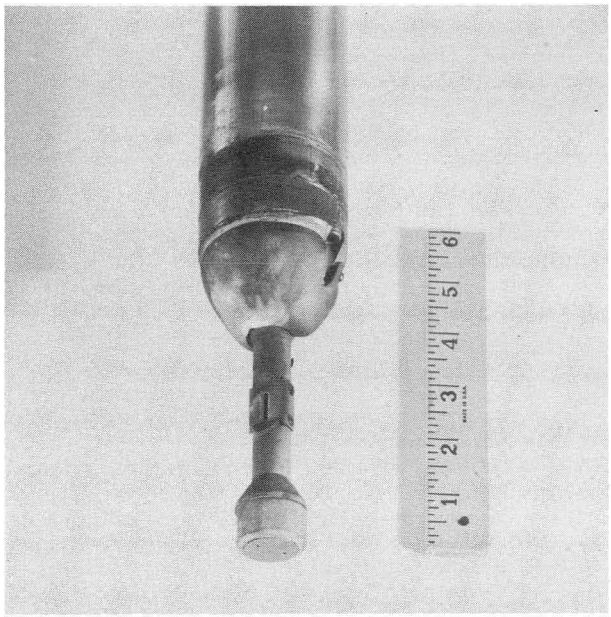

Fig. 1. Standard 88-inch cyclotron internal ion source mounted on shaft which goes through lower pole of cyclotron. Scale in inches.
(CBB 7110-4842)

Operation with Heavy Ions

The 88-inch cyclotron can accelerate ions heavier than α particles to an energy of $E = 140\ Q^2/A$ MeV, where Q and A are, respectively, ion charge and mass in proton units. The cyclotron settings of center region, trim coils, and deflector for heavy ions are based upon the best operating beams of light ions. Center region source and puller positions are set to be the same as a light-ion beam having the same number of revolutions during acceleration. The computer code CYDE is used to calculate a set of trim-coil currents that gives the same magnetic field center bump and edge fall-off as a light-particle beam having the same number of revolutions. If no reference light-particle beam exists, or if a new third- or fifth-harmonic beam is required, we start from the best estimated settings and optimize them with beam on the cyclotron. The deflector position settings are obtained from a light-ion beam, scaling the deflector voltage proportional to energy/charge of the ion.

There is charge exchange during acceleration owing to the tank pressure of about 4×10^{-6} mm. The resulting loss in beam is a factor of 2 to 4. Two diffusion pumps have been added to the dee tank to reduce this pressure, but it would be best to have a larger pump on the dee tank, rather than on the rf panel tank as at present.

Standard Internal Ion Source

The internal ion source used since the cyclotron first operated in 1961 was developed by Ehlers.[1] A photo of it is shown in Fig. 1. It is quite reliable in producing beams of protons, deuterons, ^{3}He, and α particles. The available currents of these ions are generally more than the deflector can handle—internal beams of up to 5 mA of protons and deuterons, and 100 to 500 μA of ^{3}He and α particles. The filament life is about a week on ^{3}He and α particles, and much longer on protons and deuterons.

This source has been used also for heavier ions for the past several years. But the usable arc power was limited to about 500 W because of limited anode cooling, and the filament life was reduced to a few hours owing to heavy ion sputtering. We improved the cooling by extending the water cooling from the bottom up around the top of the anode. This increased the useful arc power from 500 to about 800 W. Thicker filaments were made, giving lifetimes of 4 to 12 h on heavy ions. The best results for beam currents of heavy ions are shown in the upper section of Table I. The source is usually run at lower output to conserve filament life.

Internal PIG Source

After the above improvements in the standard filament-type source, the beam currents of the most useful heavy ions of N^{4+}, N^{5+}, and O^{3+} were much less than those reported by workers at cyclotrons using PIG sources. Some of these are the Dubna group,[3] Bennett at Harwell,[4] the IPCR Tokyo group,[5] and the Oak Ridge ORIC group.[6] The high beam currents apparently come from the higher arc

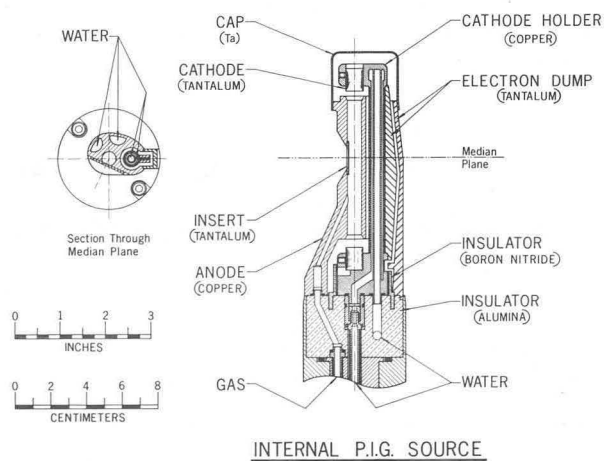

Fig. 2. Drawing of new internal PIG ion source showing various parts in two sections.
(XBL-7110-1536)

Table I. Best performance of 88-inch cyclotron ion sources on heavy ions.

Ion source	Ion	Energy (MeV)	Harm. no.	Anode slit (in.)	External (μA)
Standard filament type	N^{3+}	60	3	0.080×0.440	4
	N^{4+}	160	1		3
	N^{5+}	250	1		0.03
	O^{3+}	52	3		16
	Kr^{5+}	36	5		0.02
PIG type	N^{4+}	160	1	0.090×0.120	10
	N^{5+}	250	1		7

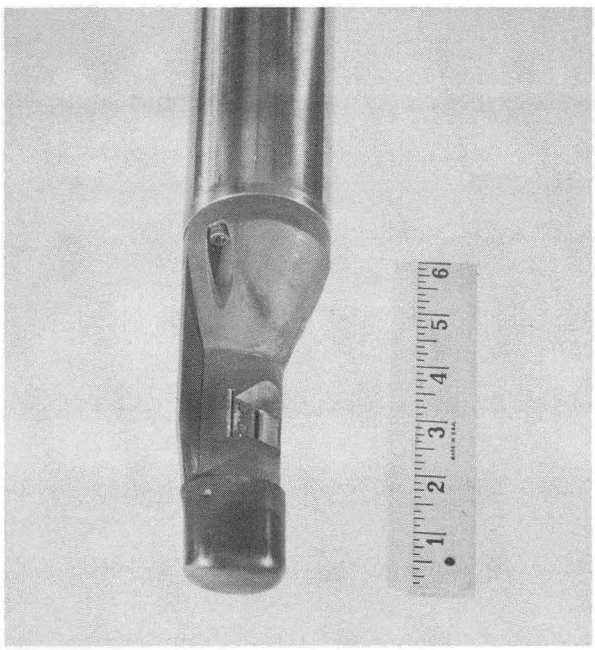

Fig. 3. New internal PIG ion source mounted on shaft. (CBB 7110-4844)

power which is available from the larger area of the cathodes used, compared with the small area of emitting filament in our standard source. The high arc power provides a higher flux (current) or higher energy (voltage) for electrons to produce the high charge states.

The design of our PIG source is shown in the schematic drawing, Fig. 2, and in the photo of Fig. 3. The cathodes are connected by a copper water-cooling tube which fits inside the anode. Each cathode is held in a copper water-cooled holder with a setscrew. When the source was first operated, the copper tube connecting the cathodes showed signs of wear by sputtering from the E×B discharge around it. A tapered tantalum bar was attached to it to dump the discharge along the magnetic field. Since the sputtering was still present, the copper tube was wrapped with tantalum foil, which shows no

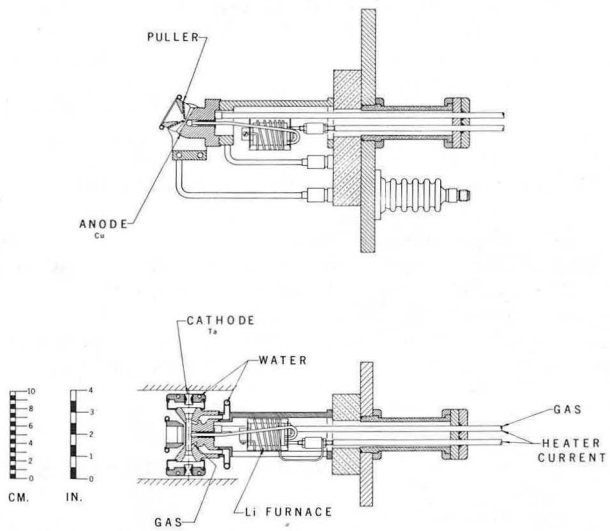

Fig. 4. Drawing of external PIG source in two sections, showing source and new lithium furnace. Source is installed vertically with the arc chamber at the bottom.
(XBL 7110-1535)

signs of sputtering wear. A boron nitride insulator is dropped into a groove in the base alumina. It can be easily removed for cleaning or replacement and avoids chemical reaction between alumina and condensed tantalum.

The source produced beam in September 1971 and has been in the testing and debugging phase since then. It has been run mostly on nitrogen, and the lower part of Table I shows the best beam results obtained. For N^{4+} and N^{5+} the beam currents are about 10 to 100 times larger than with the standard filament source, per unit slit area. Beam current is nearly proportional to slit area. The N^{5+} beam is much cleaner in the internal beam region owing to less spurious N^{1+}, making it much easier to tune up with the PIG source. The main problem remaining is to improve the cathode life. At present the cathodes have to be replaced every 2 to 3 hours, because the arc is extinguished by the deep craters in the cathodes.

One disadvantage of internal sources is the gas load produced in the center region. For the PIG source, however, there is a self-pumping effect from the high-arc current, which converts 80 to 95% of the gas into ions.

External Lithium Source Development

Since the last reports on the external source in March 1971,[2] the decision was made to develop an internal PIG source for most heavy-ion beams, because the transport problems down the axial injection line for the external source can be eliminated. The external source would be developed for ions which would be difficult to run internally. The first requirement was for lithium, which would cause sparking and cleaning problems in the center of the cyclotron if used in an internal source.

A stainless steel furnace was built to produce lithium vapor for the arc. Basic requirements in the design of the furnace were: high enough temperature to vaporize the lithium ($\approx 600°$ C), temperature gradient to prevent the molten lithium from flowing outside, and corrosion-resistant materials like austenitic stainless steel and tantalum.[7] The electric current flows through the 0.06-in.-diameter tantalum wire coil used as a heater, and through the pipe (0.125 in., 0.016 in. wall) transporting the lithium vapor to the arc chamber. The stainless steel pipe is warmer than the oven to prevent condensing. The top plug closing the oven is sealed with a tantalum gasket. A hollow in that plug contains the thermocouple head.

Thus far beams of 200 μA of Li^{+} and 40 μA of Li^{2+} have been obtained from the source running at 2 kV and 0.7 A. A small beam of a few nanoamps of Li^{2+} has been injected and accelerated in the cyclotron up to 80 MeV, but not extracted.

Footnote and References

†Condensed from LBL-223; JEEE Trans. Nucl. Sci. NS-19, No. 2 (1972).

*On leave of absence from University of Louvain and IISN, Belgium-NATO Fellowship.

1. K. W. Ehlers, Nucl. Instr. Methods 18, 571 (1962).

2. D. J. Clark et al., IEEE Trans. Nucl. Sci. NS-18, 102 (1971).

3. P. M. Morozov et al., Atomnaya Energiya 2, 272 (1957).

4. J. R. J. Bennett, in Fifth International Cyclotron Conf., 1969 (Butterworths, London, 1971) p. 499.

5. Y. Miyazawa et al., Japan. J. Appl. Phys. 9, 532 (1970).

6. E. D. Hudson et al., IEEE Trans. Nucl. Sci. NS-18, 113 (1971).

7. P. I. Vasiliev et al., Nucl. Instr. Methods 71, 201 (1969).

A PARTICLE-IDENTIFYING SPECTROMETER FOCAL-PLANE DETECTOR*

B. G. Harvey, R. F. Burton, S. W. Cosper,† J-C. Faivre,‡ F. S. Goulding, D. L. Hendrie, D. G. Kovar, D. A. Landis, J. Mahoney, J. R. Meriwether,† F. Pühlhofer,§ and M. S. Zisman

The magnetic spectrometer at the 88-inch cyclotron has many advantages for the study of heavy-ion transfer reactions. Its solid angle—1msr—is 10 to 20 times greater than

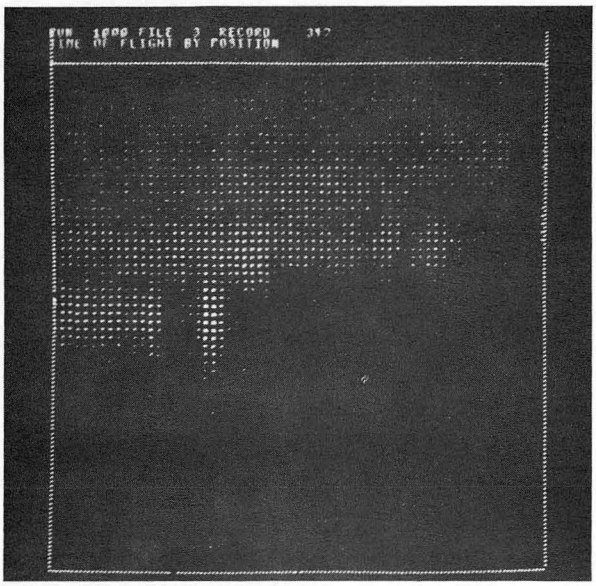

Fig. 1. Two-dimensional display of time of flight vs position for 104-MeV ^{16}O on ^{208}Pb, 60^{o} (lab). Dot intensity is proportional to log (number of events). (XBB 721-424)

the solid angles commonly used in ΔE-E solid-state counter systems. The movable focal plane permits compensation for the reaction kinematics so that the large solid angle can be exploited while retaining good energy resolution. The dispersion compensation allows the use of a dispersed rather than an energy-analyzed beam on the target with a resultant large gain in beam intensity.

The spectrometer was therefore equipped with a heavy-ion detection system capable of adequate position resolution (≈ 0.5 mm). Particles are identified by measurement of their time of flight (velocity, v), energy loss dE/dx ($dE/dx \propto \sqrt{m}Z^2/\sqrt{E}$ for heavy ions of mass number m, atomic number Z and kinetic energy E), and position. The focal-plane position signal measures magnetic rigidity $B\rho \propto mv/q$ where q is the charge state of the particle ($q \leq Z$).

Position and dE/dx are measured in a resistive-wire proportional counter[1] 45 cm long and 1 cm deep. This length covers an energy range of 24%. To obtain sufficient vertical sensitive aperture, six wires are used with a vertical spacing of 1 cm. At a pressure of 0.2 atm of Ar + 7% CH_4, heavy ions typically lose about 1 MeV in the counter gas.

In order to reduce the capacity at the input of the 12 preamplifiers (one for each end of each wire), the twelve FET's are placed inside the counter as close as possible to the ends of the wires. The remaining parts of the preamplifiers are in air outside the spectrometer vacuum system. After generation of logic pulses to identify the wire, all sig-

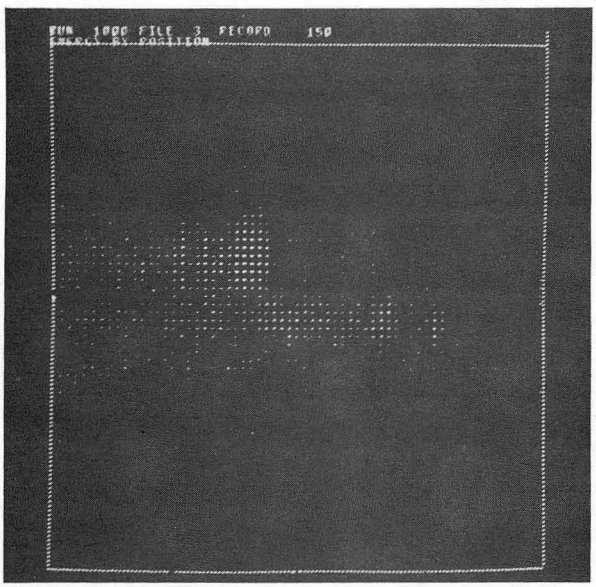

Fig. 2. Two-dimensional display dE/dx vs position for particles of m/q = 2.1 from ^{16}O (104 MeV) on ^{208}Pb. Dot intensity is proportional to log (number of events). (XBB 721-428)

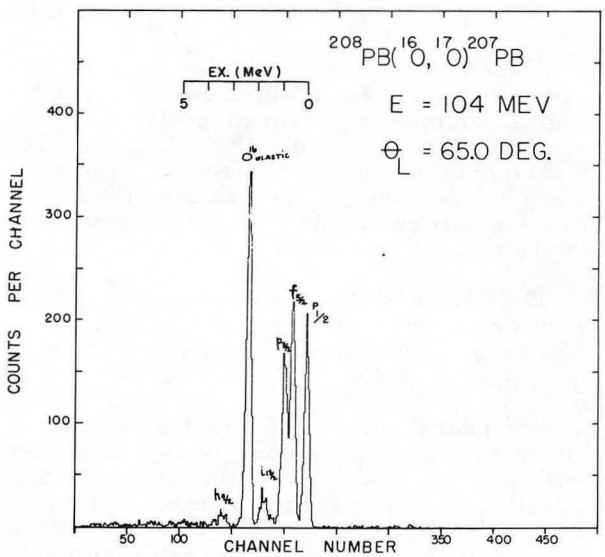

Fig. 3. Spectrum of ^{17}O from the reaction $^{208}Pb(^{16}O, ^{17}O)^{207}Pb$, E_{16_O} = 104 MeV. Particle identification has eliminated most of the ^{16}O elastic peak and all of the ^{15}N peaks that are very prominent in the raw position spectrum. (XBL 721-89)

nals from each end are mixed. Position is determined by comparing the rise times of coincident pulses from the two ends of a wire. Energy loss dE/dx is measured by adding the outputs of all twelve preamplifiers. For 60-MeV ^{16}O ions, dE/dx resolution is 10%.

Time of flight with respect to the cyclotron oscillator is measured with a Pilot F plastic scintillator-light pipe-photomultiplier system behind the proportional counter. The intrinsic time resolution of the counter is < 2 nsec, but in practice the width of a peak is limited to 5 to 7 nsec by the time width of the beam pulses given by the cyclotron.

Figure 1 shows a two-dimensional display of time of flight and position (v vs mv/q). The separate horizontal lines correspond to different values of the quantity m/q. Computer gates select a chosen value of m/q. Particles with the chosen m/q are separated by their Z value by setting gates on their value of dE/dx vs position. Figure 2 shows a two-dimensional display of dE/dx vs position for particles of m/q = 2.1 coming from ^{16}O (104 MeV) on a target of ^{208}Pb. Figure 3 shows an energy spectrum of ^{17}O ions from the reaction $^{208}Pb(^{16}O, ^{17}O)^{207}Pb$.

An energy resolution of 0.1% has been obtained from the scattering of 60-MeV ^{16}O ions from targets of ^{62}Ni and ^{197}Au, but in realistic experiments the results are usually 2 to 3 times worse because of practical limitations on target thickness and kinematic effects. Nevertheless, the resolution is substantially better than can be obtained with silicon counters.

Footnotes and References

*Bull. Am. Phys. Soc. 17, No. 1, Abstract JE 14 (1972).

†Permanent address: Physics Dept., University of Southwestern Louisiana, Lafayette, Louisiana.

‡Permanent address: CEN Saclay, France.

§Permanent address: Universität Marburg, Marburg, Germany.

1. C. J. Borkowski and M. K. Kopp, IEEE Trans. Nucl. Sci. NS-17, No. 3, 340 (1970).

PDP 8/E COMPUTER SYSTEM USED IN THE NUCLEAR CHEMISTRY PROGRAM AT THE BEVATRON

R. E. Eppley and E. K. Hyde

A computer system has been installed recently at the Bevatron which consists of a Digital Equipment Corporation PDP 8/E minicomputer with 8K of core in conjunction with a variety of peripheral equipment. The primary use for this system has been the on-line acquisition of data in conjunction with the helium jet experiments. [1]

The PDP 8/E is a machine having 12-bit words and a 1.2-μsec memory cycle time. The core can be expanded in 4K steps to a maximum of 32K.

Peripheral equipment includes two bulk-storage devices: a removable cartridge disk and magnetic tape. In addition, there is a 165-character per second matrix printer, Model 33 teletype with paper tape I/0, 4096 channel analog-to-digital converter, an eight-parameter analog stretcher - multiplexer, scalers, real-time clock, storage scope, and remote control console interfaced to the computer.

The disk system is a System Industries Model 3500 removable cartridge system [2] having a capacity of 1.66 million 12-bit words with transfer rate of 130 K words/sec. The system includes a Model 3010 Controller and Model 3090 power supply built around a Diablo Model 31 disk drive. The disk is presently being used as the system device, including the storage of all system and user programs.

The magnetic tape transport is used primarily to store raw data for later sorting and reduction at the CDC 6600. It is also used as the back-up device for the disk, [3] the entire disk image being dumped to magnetic tape at periodic intervals.

The high-speed matrix printer is a Centronics Model 101. [4] It has a printing rate of 165 characters per second or 60 lines per minute (132 characters line), which is approximately 16 times as fast as the Model 33 Teletype. The print head is composed of seven solenoid-activated print wires. Printing is accomplished by selectively pulsing these wires against an inked ribbon as the print head travels across the page. This printer makes it practical to output long lists such as program listings or spectra printout (e. g., a

2048-channel spectrum takes approximately 1-1/2 minutes). The ADC is a 12-bit successive binary approximation type[4] which has been described previously. Its constant encoding time of 25 μsec is faster than can be used at present since all transfers proceed through the computer accumulator. The computer requires about 75 μsec to process each event, thus placing an upper limit of 10K to 12K events per second on the data rate. In conjunction with the ADC is an analog multiplexer[5] that allows the acquisition of up to 8-parameter coincidence events with a single ADC. The heart of the software is the Digital Equipment Corporation PS/8 Monitor System. It is presently being used for program editing, assembling, compiling, loading, copying, etc. Included in this system is an 8K version of Fortran II.

Three stand-alone, data-acquisition programs have been written—PHA2, HAFLIF, and PROTON—each of which can be loaded from the disk, as a user program under PS/8 control.

PHA2 is a single-parameter program which stores information from the ADC in a 2048-channel, double-precision histogram. Functions are available for displaying this histogram, or expanded segments, on the storage scope. Other functions include integration between markers, and output of the histogram on the matrix printer or teletype. Magnetic tape is used to store the histogram, together with identification, as a single record. At any later time the tape record can be read back into the computer and displayed.

HAFLIF is a two-parameter program written primarily for the acquisition of half-life information. Each coded event is stored together with its time of arrival relative to the beginning of the counting period. These event-pairs are stored in a raw data buffer, and when full, the buffer is read out to magnetic tape. Later the tape can be sorted by time to arrive at a series of spectra representing successive counting intervals. The net peak area can be derived, for a peak of interest, in each spectrum of the series and the results analyzed in the usual way to arrive at a value for the half-life. Other program functions are similar to those of PHA2, described above.

PROTON accepts six-parameter coincidence data (5 detector parameters and time) on an event-by-event basis and stores buffers of these data for later read-out to magnetic tape. This program utilizes the analog-multiplexer in conjunction with a single ADC. Display facilities include scope display of four of the input parameters as well as three gated spectra which can be defined at the beginning of each run. Other functions are similar to those of PHA2.

References

1. See "On-Line Study of α-Emitting Products of Interaction of Heavy Nuclei with 5-GeV protons," in this report.

2. System Industries, 535 Del Rey Avenue, Sunnyvale, California 94086.

3. L. B. Robinson, F. Gin, and F. S. Goulding, A High-Speed 4096-Channel Analogue-Digital Converter for Pulse Height Analysis, UCRL-17419, January 1968.

4. Centronics, c/o Electronic Marketing Specialists, 999 Commercial Street, Palo Alto, California 94303.

5. L. B. Robinson, F. Gin, and H. Cingolani, An Analog Store and Multiplexer for Pulse Height Analysis, UCRL-18867, April 1969.

EQUIPMENT USED IN THE HELIUM-JET EXPERIMENTS AT THE BEVATRON

R. E. Eppley, J. D. Bowman, and E. K. Hyde

On-line nuclear spectroscopy is becoming increasingly popular as new experimental methods are developed. One method, which has been used successfully for several years at the Hilac,[1,2] is the study of α-emitters that occur as recoil products from the reaction of these targets with accelerated ions. These recoil nuclei are thermalized in a helium atmosphere, transported via capillary tubing, and deposited on a catcher where their decay can be observed by various detectors.

A modification of the Hilac system has been successfully built and operated at the Bevatron,[1] and a short description of this system is given here. The experimental results from using this system are described elsewhere in this Annual Report.

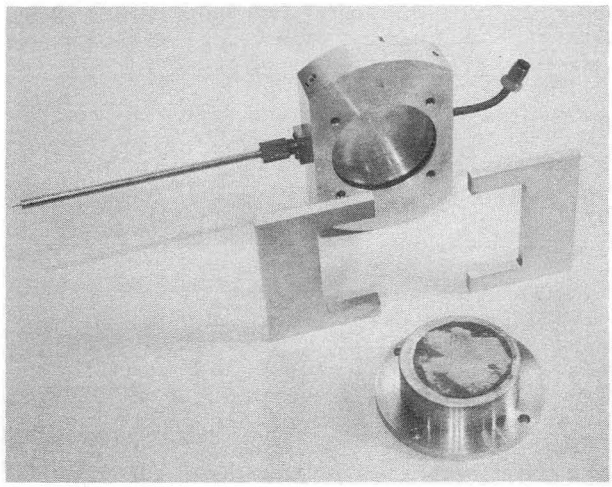

Fig. 1. Reaction cell used in the helium jet experiments. Helium enters from the right and exits through the stainless steel capillary on the left. Shims of various thickness are used to define the cell volume. Target foils are fastened to the inside of a window face. (XBB 716-2469)

The main differences between the Bevatron and Hilac helium-jet systems are the size and shape of the reaction cells and the distance over which the activity must be transported. Many of the problems associated with obtaining a high α yield at the catcher can be minimized by using short ($\approx$ 1 ft) capillaries, as used at the Hilac. However, at the Bevatron large radiation fields in the vicinity of the reaction cell rapidly caused radiation damage to the detector and contributed to a large background on the spectrum of interest. This necessitated the placement of the detector outside the shielding, an arrangement which required transportation of the activity a distance of approximately 20 ft.

The reaction cell pictured in Fig. 1, was fashioned from an aluminum block. The cell itself is a circular cylinder having a 3-in. diameter. The height of the cylinder is adjustable, by the use of shims, between 4 mm and 20 mm. Metal target foils are held to an inside face of the cell with epoxy. Helium is drawn through the cell, parallel to the target surface, and exits through a metal capillary. Stainless steel capillaries have been used in the range of 0.016 in. i.d. $\times$ 8 in. to 0.035 in. i.d. $\times$ 18 in.

Tygon, Teflon, and polyethylene tubing have each been tried for the connection between the short metal capillary and the vacuum chamber. Most of the successful runs this past summer were obtained while using a 0.033-in. i.d. $\times$ 24-in. SST capillary in conjunction with a 0.041-in. i.d. $\times$ 18-ft Teflon capillary. Several other combinations have been tested successfully including one in which a short SST capillary was placed ahead of a 50-ft length of 1/8-in. i.d. tygon tubing.

The vacuum chamber, used to house the surface barrier detector and catcher plate for the transported activity, was situated outside the shielding at a location as near the cell as the shielding would permit. This meant a minimum capillary path length of 18 ft. The present chamber is a 15- $\times$ 15- $\times$ 12-in. aluminum tank having a plexiglass cover plate. These dimensions allow the use of a tape transport, described below, inside the chamber.

A stationary catcher foil is adequate for studying single-parameter spectra over short periods of time. However, the yield of α activity in recent experiments was such that 12 to 24 hours was necessary to obtain spectra possessing high statistical accuracy. This situation caused the spectra to be distorted since the long-lived activities build up on the catcher and obscure some of the short-half-life, low-intensity peaks. Also, there appeared to be a broadening of the long-half-life peaks during long runs. This phenomenon was attributed to impurities (i.e., oil, etc.) in the supply being deposited on the catcher along with the α activity. Thus, the long-half-live α transitions were observed through several layers of material and the energy resolution was degraded by energy loss in this material.

These problems are avoided by providing clean catcher surfaces at short intervals. Magnetic tape provided us with this capability.

A TEAC Model A-1230 tape deck was modified for incremental motion and for operation in a vacuum. It was necessary to move all electronic components outside the vacuum chamber for proper operation. The transport motors, and capstan and brake solenoids remained in the vacuum and were cooled by water-cooled copper heat sinks.

The heart of the transport apparatus is the vacuum pump system. Experience at the Hilac indicated that successful runs required a relatively large helium flow rate. Thus, a Leybold-Heraeus pump system was obtained, consisting of an E-250 single-stage, rotary-piston mechanical pump (147 cfm displacement) and a WA-1000 Roots-type Blower (685 cfm displacement). This system was connected to the vacuum chamber through a 6-foot stainless steel bellows. The pump system typically pumps helium at the rate of

10 cfh while maintaining a vacuum-chamber pressure in the range of 500 μ, an operating pressure which has proved to be satisfactory for the operation of surface-barrier detectors. Generally, Ortec gold-plated, silicon surface-barrier detectors have been used, having a surface area of 50 mm and a thickness of 100 μ.

Presently, an Ortec electronics system is being used, consisting of a Model 109A preamplifier, Model 451 main amplifier, and a Model 444 biased amplifier. The biased amplifier furnishes the signal to the ADC, which in turn transmits a digitized signal to the computer. The computer-ADC system is described separately in this Annual Report.

The yield at the catcher is a complex function of several parameters, including the mass flow rate through the capillary, the material and shape of the catcher, and the distance between the catcher and the end of the capillary tubing. Assuming viscous flow through the capillary, the mass flow rate, Q, is proportional to $\Delta P D^4/L$, where ΔP is the pressure differential across the capillary, D is the tubing diameter, and L is the tubing length. The length generally has been kept as short as possible with ΔP and D being varied to obtain the desired flow rate of 8 to 10 cfh.

There does seem to be a measurable difference in yield, depending on whether the capillary resistance is distributed equally along the length of tubing (single tube of constant diameter) or defined by a short length of small-diameter tubing near the reaction cell. For this second case, a large-diameter tubing (e. g., 1/8-in. i. d.) with a very low resistance carries the activity the remaining distance to the catcher. This arrangement has produced noticeable increase in the α-activity yield. For a given configuration the yield is maximized when the distance between the end of the capillary and the catcher surface is 3 to 4 mm. A shorter distance causes a precipitous decrease in yield, while a larger distance produces a more gradual drop in the yield.

References

1. K. Valli and E. Hyde, Phys. Rev. 176, 1377 (1968).

2. J. Borggreen, K. Valli, and E. K. Hyde, Phys. Rev. C2, 1841 (1970).

A HIGH-RESOLUTION DETECTION SYSTEM FOR SHORT-LIVED GASEOUS ACTIVITIES*

J. E. Esterl,† R. G. Sextro, J. C. Hardy,‡ G. J. Ehrhardt,§ and J. Cerny

The usual method[1] of observing light β-delayed proton emitters ($\tau_{1/2} \approx 10$ to 200 msec) has been to detect the protons in a silicon detector or telescope that directly views the target in which the activity is produced. However, the necessarily high beam currents, thick targets, and consequent β-pile-up problems combine to limit the energy resolution (full width at half maximum, FWHM) obtainable using standard techniques to about 100 keV. Thus in order to study nuclei of interest to us—^{9}C, ^{13}O, ^{17}Ne, and ^{33}Ar—a fast gas-sweeping system similar to that used[2] in the characterization of the decay properties of ^{8}He was developed.

Figure 1 shows the apparatus used in the study of ^{33}Ar($\tau_{1/2}$ = 173 msec) produced by the ^{32}S(^{3}He, 2n) reaction.[3] No solid target capable of withstanding prolonged high-current bombardment was available, so CS_2 vapor was used. An external beam from the 88-inch cyclotron passed continuously through a target chamber which consisted of a 20-cm^3, 10-cm-long cylinder fitted with 2.5-μm-thick Havar windows. When valve 1' operated, CS_2 vapor from the CS_2 reservoir filled the target chamber. The 1.5-liter reservoir was heated to about 30°C. At the same time as the target chamber filled, a 10-cm^3 ballast chamber filled with 1.5 atm of helium that had been passed through a liquid nitrogen trap to remove any condensable impurities.

After a predetermined bombardment time, valves 2, 2', and 4 opened and the high-pressure helium expanded, sweeping the CS_2 vapor and the various beam-induced activities (including ^{33}Ar) through the dry ice-trichloroethylene trap, whose total volume was about 60 cm^3. This trap condensed approximately 80% of the CS_2 from the gas stream. The helium gas and gaseous activities then passed through a small glass-wool trap which removed the particulate sulfur formed by radiation decomposition of the CS_2. Finally the gas passed through 5 meters of 6.4-mm (i. d.) Teflon tubing and into a well-shielded counting chamber located above the experimental area, valve 4 closed, and the counting period began.

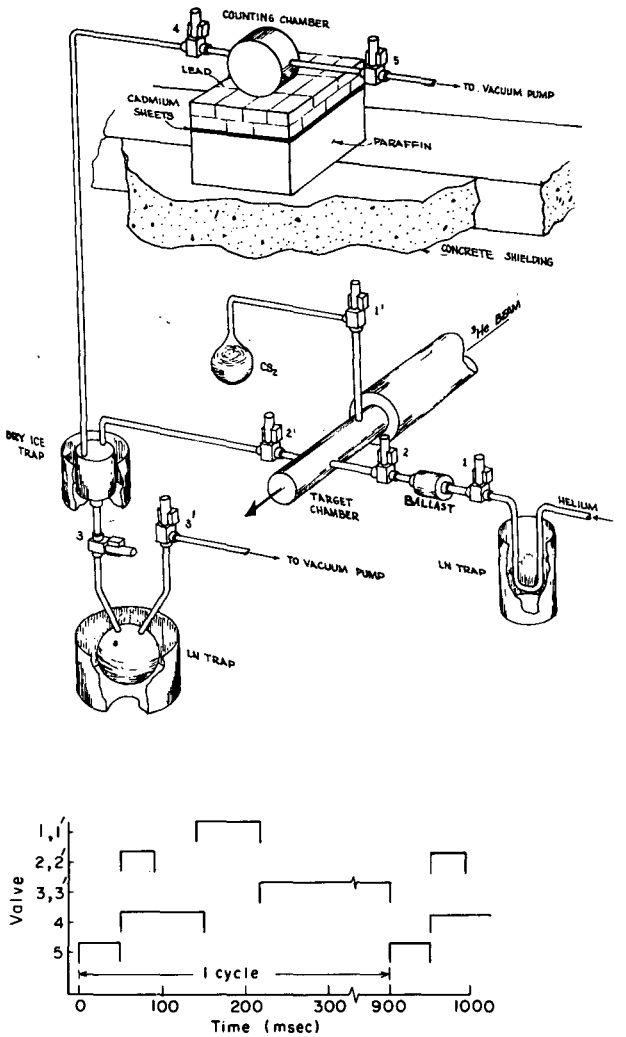

Fig. 1. A schematic diagram of the apparatus used for the production of ^{33}Ar from the reaction $^{32}S(^3He, 2n)^{33}Ar$. The sequence of valve operation is shown at the bottom; valve open times are indicated. (XBL 708-3569)

The transit time was typically less than 100 msec. During the counting period, valves 3 and 3' opened, draining the dry-ice trap into a liquid nitrogen trap used to solidify the CS_2. The residual gas remaining in the line between the target and counting chambers was also pumped out to improve the efficiency of the system. Finally, at the end of the counting period, valve 5 opened and the counting chamber was evacuated. The diagram at the base of Fig. 1 shows the order in which the operations described above were performed and typical times allotted for each procedure. The entire sequence was repeated every second.

Figure 2 shows a cross-sectional view of the counting chamber. The chamber was constructed of aluminum with a stainless steel standoff for the copper cold-finger. Liquid nitrogen was used to cool the detectors because the high rate of gas flow through the chamber necessitated a high-capacity cooling system. A resistive-bridge pressure-transducer was located near the base of the conical counting chamber, providing continuous monitoring of the time behavior of the gas flow. The end wall at the base of the counting volume was kept to a thickness of 0.8 mm to reduce attenuation of γ rays. A 2-in. $\times$ 2-in. NaI(Tl) detector was used for p-γ coincidence work while singles γ-ray data were generally taken with a Ge(Li) detector.

The counter telescope consisted of a phosphorous-diffused silicon ΔE counter whose thickness ranged from 14 to 50μm and a 1.0-mm lithium-drifted E counter. They were cooled to -30°C and operated satisfactorily in an atmosphere whose pressure fluctuated from about 35 Torr (counting) to 0.5 Torr (evacuated). The signals from the two detectors were required to be in fast coincidence ($2\tau \approx 15$ nsec) before being fed into a Goulding-Landis particle identifier.

Counting was begun well after the signal to close the valve to the counting chamber had been sent, allowing time for the valve to close. The valve control unit started a time router that permitted storage of separate energy spectra for up to eight time intervals. For example, in the study of ^{33}Ar all eight channels were set at 100 msec. In addition, it started a multiscaler which allowed half-life measurements of a selected proton peak. Inhibit signals from either the valve control unit or time router ensured that only data taken during desired counting periods were stored.

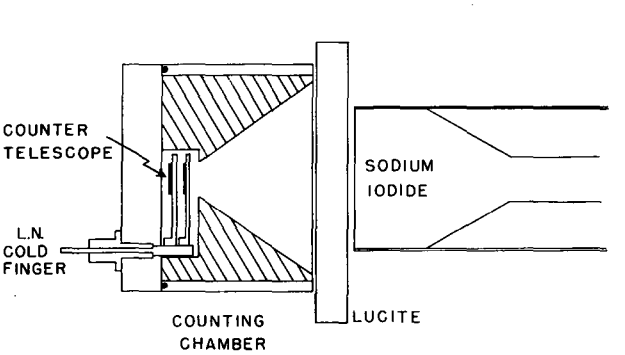

Fig. 2. A schematic drawing of the counting chamber used for both delayed-proton and γ-ray studies. The spacer used to confine the gas to the region viewed by the counter telescope is shown cross-hatched. The active volume is about 65 cm^3. (XBL 711-74)

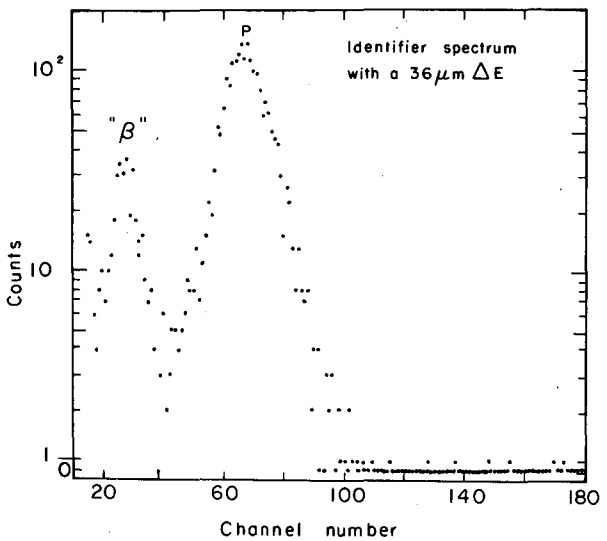

Fig. 3. The particle-identification spectrum following ^{17}Ne decay obtained by using a 36-μm ΔE counter. The structure labeled "β" is discussed in the text. (XBL 711-2539)

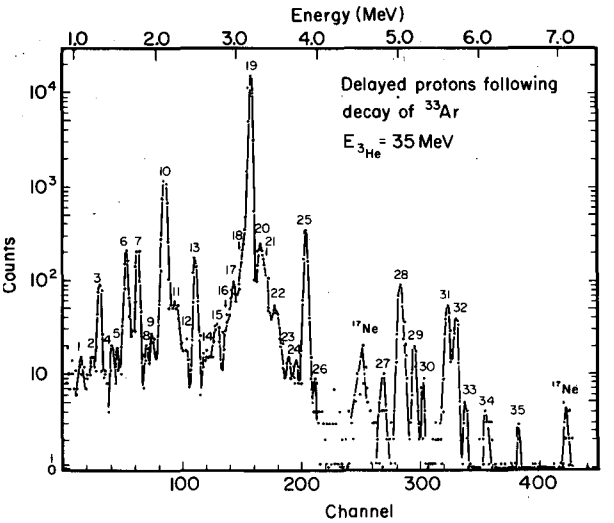

Fig. 4. Spectrum of delayed protons observed following 35-MeV ^{3}He bombardment of CS_2. The use of a 14-μm ΔE detector in the counter telescope permitted identification of protons having energies as low as 1.3 MeV. (XBL 707-3451)

Figure 3 shows an ungated particle identifier spectrum. The structure labeled "β" is believed to be due to multiply-scattered β particles since its relative magnitude decreases with decreasing ΔE-counter thickness. Low-energy electronic cutoffs probably convert the expected exponential shape into something resembling a peak. Gates set around the identified-proton peak help to further reduce the background by eliminating these unwanted events.

A sample delayed-proton spectrum from ^{33}Ar is shown in Fig. 4. Note the extremely low background level even at the lowest proton energies. The pulser resolution (FWHM) in this case was 35 keV while the observed peak-widths of narrow states were 45 keV. This greater width for observed states is due principally to an energy spread in this sequential decay caused by the momentum transfer effects from the preceding β decay. The study of ^{17}Ne and ^{33}Ar required γ-ray measurements. Details of singles γ-ray studies and p-γ coincidence studies are given in Ref. 3.

The efficiency of the system was such that we were able to observe about one proton per μC of integrated beam current for several different target-activity combinations. Rough calculations indicate that on the order of 10% of the activity that is produced arrives in the counting chamber. The proton-detection efficiency of the counting chamber illustrated in Fig. 2 was calculated[3] to be $(1.26 \pm 0.13) \times 10^{-3}$.

In the course of studying nuclei besides ^{33}Ar, both solid and gaseous targets were used. These targets are discussed in the original paper.* The variety of target materials, along with the capability for γ-ray measurements, gives the system considerable flexibility. This system should prove useful not only in investigations of light nuclei but also in studies of many gaseous activities with half-lives ranging from minutes to milliseconds.

Footnotes and References

*Condensed from Nucl. Instr. Methods 97, 229 (1971).

†Present address: USS HOLLAND (AS-32), FPO N. Y., N. Y. 09501.

‡Present address: Chalk River Nuclear Laboratories, Chalk River, Ontario, Canada.

§Present address: Chemistry Department, Washington University, St. Louis, Missouri.

1. A. M. Poskanzer, R. McPherson, R. A. Esterlund, and P. L. Reeder, Phys. Rev. 152, 995 (1966); J. C. Hardy and R. I. Verrall, Can. J. Phys. 43, 418 (1965); see also J. Cerny, Ann. Rev. Nucl. Sci. 18, 27 (1968).

2. A. M. Poskanzer, R. A. Esterlund, and R. McPherson, Phys. Rev. Letters 15, 1030 (1965).

3. J. C. Hardy, J. E. Esterl, R. G. Sextro, and J. Cerny, Phys. Rev. C3, 700 (1971).

ENVIRONMENTAL INSTRUMENTATION SURVEY

D. A. Mack, N. Amer, R. Budnitz, G. Gabor, R. Graven,
C. Hollowell, R. McLaughlin, G. Welch, G. Y. Gee,
R. M. Johnson, and P. Finn

In July of 1971 a proposal to conduct an environmental instrumentation survey received funding from the National Science Foundation. The proposal divided the areas of concern into four broad classes: air, water, radiation, and biomedical. In each of these areas, present monitoring instruments were to be described and compared, new instrumentation and techniques were to be recommended and proper usage and maintenance procedures would be discussed. Instrument descriptions would be accomplished by writing "instrument notes" for each monitor, and a comparison note would be written for each pollutant considered.

During the first six months of this contract some 70 instrument notes for SO_2 monitors and an SO_2 comparison note were written. These notes are now being reviewed by members of the California State Public Health Service, Bay Area Air Pollution Control District, and Environmental Protection Agency. Work on the draft stage of the radiation section is nearing completion. The emphasis in this area is on a discussion of the type of problems present in radiation monitoring and methods of solving these problems; about 200 instrument notes are also included. In addition a general survey of the air, water, and biomedical monitoring problems has been completed. Initial reaction has demonstrated that this survey will be extremely valuable to workers in the environmental monitoring field.

ZEEMAN-EFFECT ATOMIC ABSORPTION SPECTROMETER

R. D. McLaughlin

Recently a new method of correcting for interferences in atomic absorption spectroscopy was described and applied to the detection of Hg in foodstuffs.[1] Instead of monitoring the presence of Hg by the change in the intensity of the 253.6 resonant line, this technique utilizes the Zeeman split components of this line. The change in intensity of those components that are shifted outside the region of main absorption of Hg from the sample are used to sense the presence of substances which absorb or scatter 253.6 radiation. By electronically taking the difference between the radiation that is absorbed by the Hg atoms and the radiation that interacts with interferences it is possible to monitor Hg in foodstuffs by simply volatilizing the sample with a furnace in such a manner that the gases pass through an absorption cell. The Hg concentration is immediately displayed on a meter which registers the difference in intensity caused by the vapors from the sample.

Since the feasibility of this approach was demonstrated, effort has been expended to build instrumentation that will allow for the routine running of samples and that will have improved operating characteristics compared with the prototype. The improved instrument is diagrammed in Fig. 1 of the next article.

The use of a ^{198}Hg lamp in a 7-kG parallel magnetic field provides greater difference between I_S and I_R than was formerly achieved with a perpendicular field and ^{199}Hg lamp for the same amount of Hg in the detection cell. This use of a single photomultiplier has lessened the zero drift that resulted from the use of separate photomultipliers to monitor I_R and I_S. Larger quantities of potentially interfering substances can be tolerated because of improvements in furnace design and correcting electronics. Under present running conditions the furnace has a useful lifetime of a few hours. After this time reproducible results are no longer obtained. Efforts to design better furnaces are still under way.

The immediate goal of this effort is to use the instrument to verify results obtained by other methods of analysis. Thanks to cooperation from other laboratories, we now have a collection of samples including orchard leaves, various kinds of fish, minerals, gelatin, and horse liver; the Hg content of each has been determined by a variety of methods. These samples will be run as soon as the next stage of optimization has been achieved.

Reference

1. T. Hadeishi and R. D. McLaughlin, Science 174, 404 (1971).

MERCURY DETECTOR FOR TUNA FISH

T. Hadeishi and M. Nakamura

A prototype instrument has been developed and constructed for the detection of traces of mercury in tuna fish. The instrument uses the hyperfine- and isotope-shift Zeeman effect.

Advantages in the use of this instrument for the detection of mercury in tuna fish are:

1) Sensitivity of 1 nanogram or less
2) No need of chemical separation of the trace element from the host material
3) Results measured in ppm in about a minute
4) Such operational simplicity that a semi-skilled person can operate it
5) Moderate cost.

To our knowledge, no other analytical device possesses the capability of this prototype instrument for the detection of mercury in tuna fish. Theory, operational characteristics, and performance of this instrument are published elsewhere.[1] This prototype unit based on the hyperfine- and isotope-shift Zeeman effect has a detection sensitivity of 40 ppb, which is already adequate to monitor the 0.5 ppm limit on mercury in food set by the F. D. A.

Figure 1 shows the block diagram of the ^{198}Hg isotope-shift Zeeman-effect Hg detector. A lamp containing ^{198}Hg, excited by a 100-MHz oscillator and in a 7-kG magnetic field, passes its light through a pyrolysis furnace containing the sample of tuna fish. The light alternator chops the two optical light paths, I_S and I_R, which are then recombined onto a single 1P28 photomultiplier tube with a 2537-Å filter in front of its entrance window. I_R must pass through a filter cell of Hg in 1 atmosphere of N_2. A light-emitting diode (LED) and a photodiode combine to give

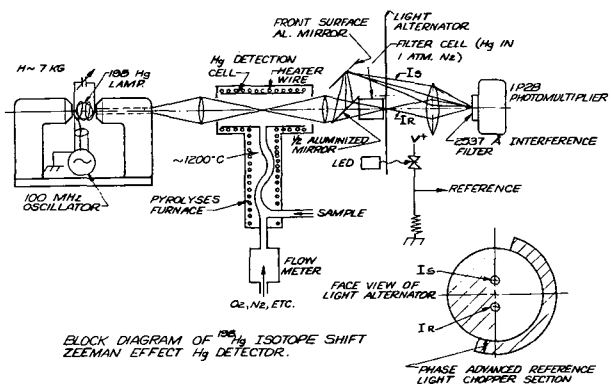

Fig. 1. Diagram of ^{198}Hg isotope-shift Zeeman-effect Hg detector. (XBL 7111-1698)

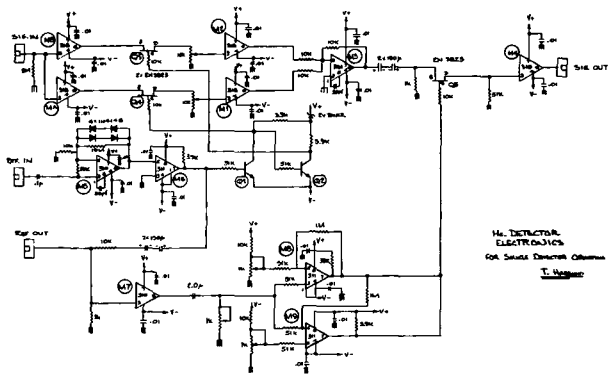

Fig. 2. Electronic circuit for obtaining $V_S V_R$. (XBL 7110-1502)

a reference signal used in the signal processing chain.

The electronics for extracting the information contained in the optical paths I_S and I_R are shown in Fig. 2. The reference signal is amplified via a logarithmic amplifier and squared via M6. This signal is applied to FETs Q3 and Q4 which separate the photomultiplier tube signal into V_S and V_R, which are proportional to I_S and I_R respectively. The two 10-K potentiometers following the FETs are adjusted so that the output of M3 is zero with no mercury present in the absorption cell furnace. With mercury in the furnace the output of M3 is no longer zero: it contains an ac voltage proportional to $V_S - V_R$ which is then detected by means of a phase-sensitive lock-in amplifier. The reference signal is also differentiated so that a portion of the ac signal which corresponds to the noisy transition periods of the alternator can be masked out via series FET Q5. With the output voltage of the lock-in amplifier fed into a voltage-to-frequency converter followed by a pulse counter, one can easily integrate the voltage to obtain a number proportional to the total amount of mercury liberated from the sample of tuna fish during the run. If the sample were carefully measured before the run, the number could be interpreted directly in ppm.

Reference

1. T. Hadeishi and R. D. McLaughlin, Hyperfine-Zeeman-Effect Atomic Absorption Spectrometer for Mercury, UCRL-20643 (preprint); Science 174, 404 (1971).

TRACE-ELEMENT ANALYSIS BY X-RAY FLUORESCENCE*

F. S. Goulding and J. M. Jaklevic

Recent months have been marked by a new public awareness of the adverse effects of trace elements in the air we breathe, in the water we drink, and in the food we eat. Since many trace elements are known to be essential to life in its wide variety of forms, a better definition of the roles of trace elements, both adverse and desirable, in biological systems seems essential. These factors all point to the need for a measurement technique capable of rapid assessment of a broad range of trace elements present at very low levels (0.1 to 100 ppm) in all types of organic material. We hope to show that x-ray fluorescence analysis using semiconductor detectors provides this tool.

The analytical technique of x-ray emission spectroscopy depends upon the detection of x rays whose energies are characteristic of the individual elements in the sample being observed and requires the measurement of both x-ray energy and intensity. Both functions are performed conveniently and well by semiconductor detectors—hence the power of these devices as analytical tools.

The simple design of a semiconductor x-ray fluorescence spectrometer is shown in Fig. 1; the physical mechanisms involved in the fluorescence process are also illustrated. The orbital diagram of Fig. 1 is sufficient to discuss the qualitative features of the atomic shell transitions generating the x rays of interest in this paper. In the energy range of interest here, the energy resolution of semiconductor-detector spectrometers is such that energy separations of levels within a major shell are not resolved, thus designated Kα and corresponding to a transition from the L to K shells. Similarly, Kβ refers to the M (and N, ···) transitions to the K shell. The intensity of the Kβ peak is always much smaller than that of the Kα line.

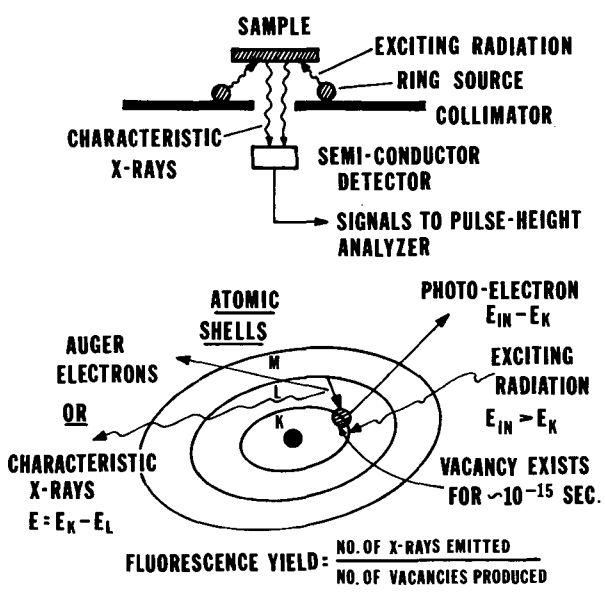

Fig. 1. Basic x-ray fluorescence spectrometer and the atomic processes. (XBL 713-393)

Energies of primary interest lie below 30 keV, where the K x rays of elements with $Z < 55$ are observed, and the L x rays of the heavy elements also appear. The principal L x rays of interest are the Lα, and Lβ, transitions and are both of approximately equal intensities. Figure 2 shows the energies of these x rays. The L x-ray energy of a heavy element may be the same as the K x-ray energy of a light element, causing confusion in analysis; but heavy elements are relatively rare in biological material, so the resulting problem is of less importance in practice

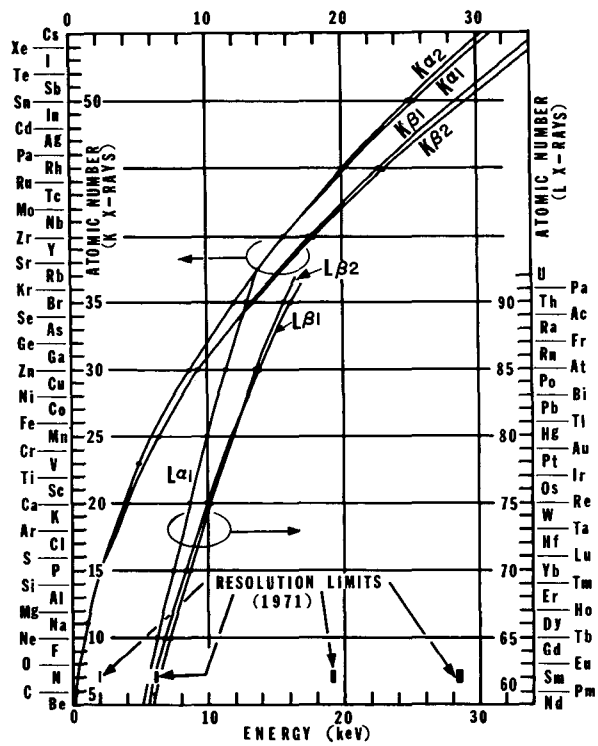

Fig. 2. Energies of K and L x rays up to 30 keV. (XBL 713-381)

than perhaps might be expected. Often, the presence of two strong L lines is useful—for example, Pb Lα coincides with the common As Kβ, but Pb Lβ only clashes with Kr, an uncommon contaminant. This fact permits determination of lead even when arsenic is present.

Two efficiency factors are important in the design of an x-ray spectrometer. The efficiency of any detector falls at high energies, causing a loss of counts. Lithium-drifted silicon detectors 5 mm thick were used in these studies, so their efficiency is essentially unity in the energy range of interest here. Choosing the energy of the exciting radiation is a major step in the design of x-ray fluorescence experiment; the probability of creating a vacancy is a maximum when the energy of the exciting radiation just exceeds the binding energy of the atomic shell involved. For this reason it may be necessary to use more than one exciting energy to cover a broad range of elements with maximum sensitivity.

We have so far considered only the fluorescent x rays produced in the sample, their excitation and transmission to the detector, and their absorption in the detector. The main mechanism for absorption in the detector in this energy range is the photoelectric process; even where Compton scattering occurs in the detector, the scattered photon will nearly always be absorbed photoelectrically to produce a total charge in the detector proportional to the total energy of the original incoming x ray. This situation is a pleasant contrast to the dominance of the Compton effect in spectra observed when detecting higher-energy γ rays. However, scattering processes are still a major factor in x-ray fluorescence spectroscopy—this time, due to the effect of scattered radiation from the sample into the detector. Both coherent (elastic) and incoherent (Compton) scattering from the sample matrix, the organic base containing the trace elements, are present, the relative proportions depending on the ratio of light to heavy nuclei present. However, the photon energy loss involved in Compton collision is very small at these energies. For example, 180° scattering of 20-keV photons involves an energy loss of only 1.5 keV.

We are now in a position to appreciate the general form of the spectrum (Fig. 3) observed by an x-ray fluorescence spectrometer. The dominant feature of the spectrum is the large scatter peaks that may constitute 99% of the total counts observed. At the very-low-energy end of the spectrum we see the effect of scattered photons from the sample which happen to Compton-scatter from electrons in the detector and escape, leaving only the knock-on electron energy in the detector. The central region of the spectrum contains the interesting information on fluorescent x rays emitted by the sample—unfortunately superimposed on a background that, in an ideal case, is due only to photoelectrons from the detector escaping from its surface. Since the photons producing these electrons are primarily those scattered from the sample, and only part of the photon energy is converted into ionization in the detector, a continuum of pulse heights below the scatter peaks is generated by this process.

The validity of this general picture is illustrated in an x-ray fluorescence spectrum obtained recently using Mo Kα x rays for excitation. The data of Fig. 4 were obtained on a freeze-dried sample of swordfish and illustrate the well-known case of Hg pollution in certain species of fish. The large incoherent

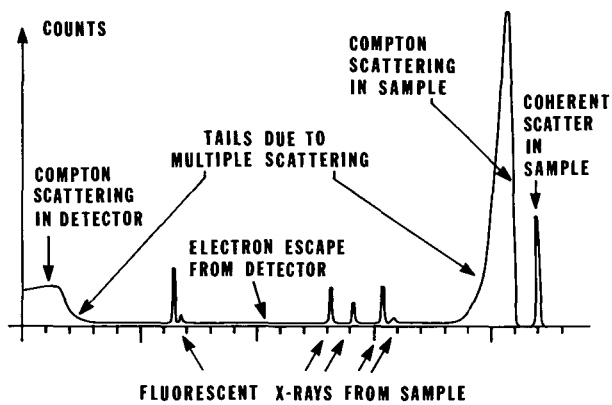

Fig. 3. Idealized spectrum observed by an x-ray fluorescence spectrometer.
(XBL 713-396)

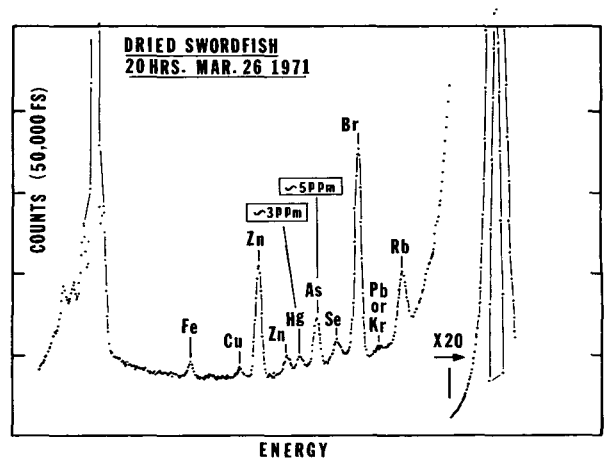

Fig. 4. Dried-swordfish spectrum.
(XBL 713-566)

scatter peak is shown in the figure; the coherent peak is just beyond the right margin of the plot. Figure 5 is a spectrum obtained with a similar sample of tuna fish, again showing Hg in concentrations of 0.5 ppm in the freeze-dried sample; this represents a level of 0.1 ppm referred to the original sample.

The outstanding quality of these data and the corresponding improvement in analytical sensitivity have been made possible by recent advances involving several aspects of semiconductor x-ray spectrometer performance. Included in these are electronic noise performance and high-counting-rate capabilities together with improved background characteristics of the Si(Li) detectors. A related development in high-rate excitation sources (x-ray tubes) has also contributed. Summaries of these improvements together with data obtained with other samples are contained in succeeding papers in the Annual Report.

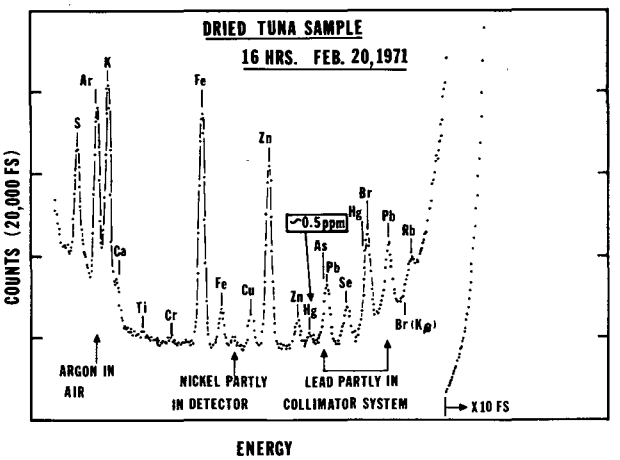

Fig. 5. Dried-tuna spectrum. Features due to the collimator system and other extraneous materials are indicated. (XBL 713-392)

Footnote

*Condensed from UCRL-20625.

DETECTOR BACKGROUND AND SENSITIVITY OF X-RAY FLUORESCENCE SPECTROMETERS*

F. S. Goulding, J. M. Jaklevic, B. V. Jarrett, and D. A. Landis

Introduction

Semiconductor-detector x-ray fluorescence spectrometers are now commonly used for analysis of materials for constituents present at levels over 10 ppm. Slightly lower limits of detection can be achieved in favorable circumstances, and if long counting times are employed. However, the sensitivity range below 1 ppm, which is of great interest in biological and environmental studies, is not easily accessible using existing x-ray spectrometers; the purpose of the work described here is to lower detection levels down to about 0.1 ppm.

Figure 1 shows the x-ray spectrum produced by a conventional spectrometer using molybdenum fluorescer excited by an ^{125}I ring source. In a system of this type, no low-energy radiation is produced by the exciting source, and the semiconductor detector should observe only fluorescent x-rays from the sample together with the exciting radiation backscattered by the sample. In practice, well over 90% of the counts should occur in the backscatter peak at the high-energy end of the spectrum, but, if degraded in any way, they constitute a general background hiding the peaks characteristic of trace elements in the specimen. In the case shown in Fig. 1, about 20% of the backscatter

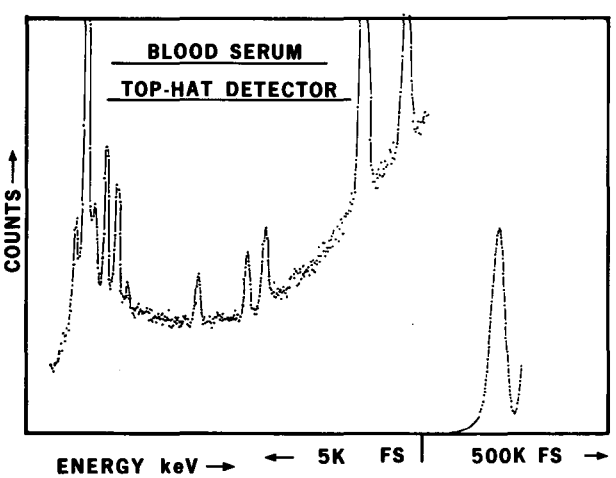

Fig. 1. Fluorescence x-ray spectrum of a blood serum specimen using a conventional silicon detector spectrometer. (XBL 717-1177)

events are degraded to produce background.

We shall show that these degraded background pulses are the result of imperfect charge collection in detectors, and that they can be virtually eliminated by new detector techniques.

Detectors in X-ray Spectrometers

Figure 2 shows three silicon detector configurations used in x-ray spectrometers. The first type is referred to as the "top-hat" geometry, and is characterized by low-leakage current and excellent high-voltage behavior. The second type, the "grooved" detector, possesses the same advantages as the "top-hat" geometry. The third geometry, generally referred to as "planar," exhibits higher leakage current and capacity than the other two types, and is therefore rarely used in x-ray spectrometers. However, its background properties probably deserve investigation. The presence of n-type surface layers distorts the internal electric field pattern in the detector in such a way that collection of charge produced by x rays interacting in some parts (shown by horizontal-line shading in Fig. 2) is via the surface layers. This causes a loss of charge, so that signals that should appear in the backscatter peaks appear in the general background in spectra. The tests presented in this paper show that this is the predominant source of background in existing spectrometers.

Guard rings have been employed for many years to overcome fringing field effects in standard capacitors, and have also found application[1] in semiconductor detectors as a device to reduce edge leakage. It therefore seems an obvious step to use a guard ring to define the boundary of the sensitive volume of a detector by internal electric field lines rather than by a physical surface with its unknown charge-trapping characteristics. This can be considered as an electronic collimation technique. Figure 3a shows the simple implementation of the idea; note that the output signal is derived only from the central region, while the guard ring and the central region are maintained at the some dc potential (ground).

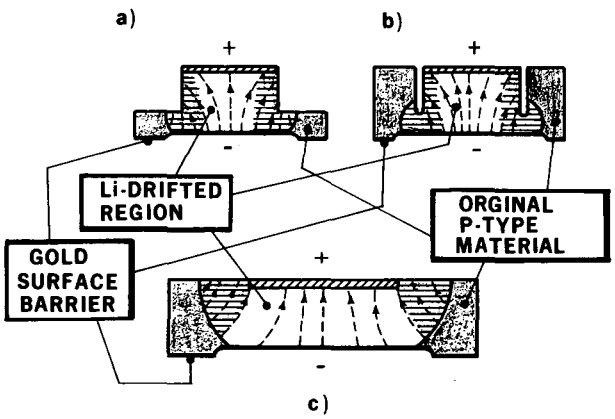

Fig. 2. Types of detector configuration used in x-ray spectrometers:
a) Top-hat detector
b) Grooved detector
c) Planar detector. (XBL 717-1179)

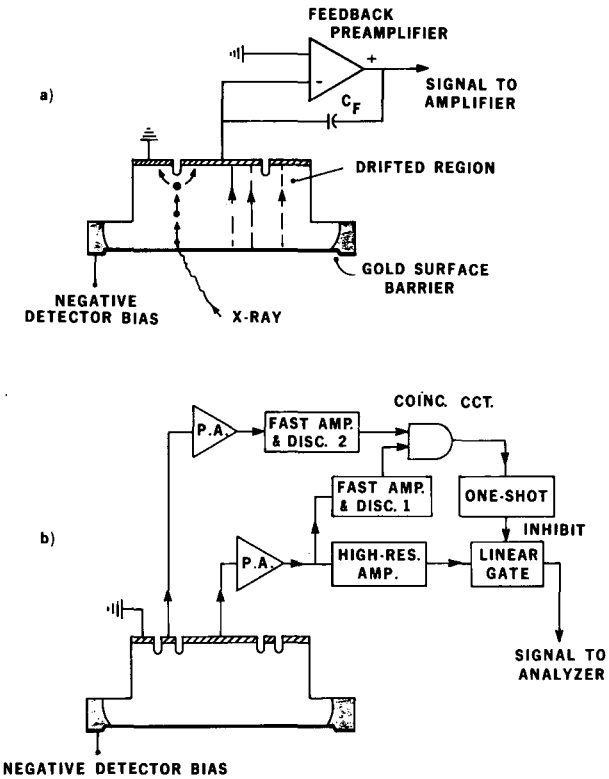

Fig. 3. Guard-ring detectors.
a) Simple guard-ring approach showing the mechanism for degraded pulses.
b) Double guard-ring detector with pulse-reject circuitry to remove degraded pulses.
(XBL 717-1181)

Even this configuration suffers from a signal degradation problem at the edge of the central region. The initial x-ray interaction in this peripheral region produces a dense cloud of charge ~ 5 microns in diameter; in the electric field, holes and electrons are separated, drifting toward their appropriate electrode. The internal repulsive fields existing within the hole and electron clouds are very large compared with the drift field in the detector—therefore, the cloud dimensions rapidly increase until the internal repulsive field approaches the same value as the drift field. This means that the cloud dimensions reach about 100 μ during the charge collection process. Consequently, a peripheral region of 100 μ thickness exists around the sensitive region from which only part of the charge due to an event is collected

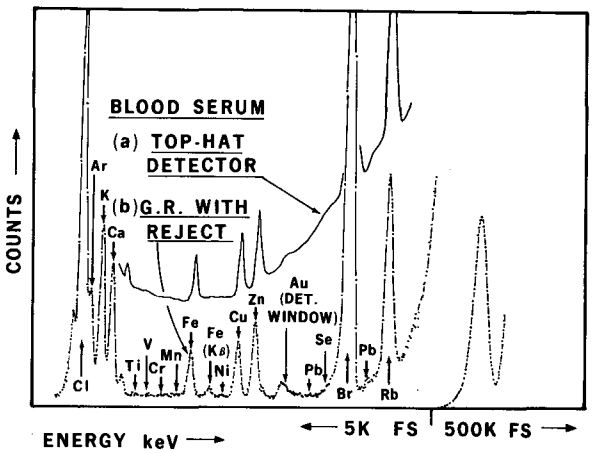

Fig. 4. Fluorescence x-ray spectrum obtained on a blood serum specimen using a spectrometer equipped with guard-ring detector and reject circuitry (b). For comparison, the spectrum obtained on the same sample with the same geometry, and the same total counts in the scatter peak, but with a simple top-hat detector, is so shown (a). This is a smooth curve drawn through the points of Fig. 1.
(XBL 717-1180)

in the central region–this means that many of the backscattered events appear in general background. Our measurements show that the background present with a simple guard-ring detector is from 2 to 10 times smaller than that with a top-hat detector, the exact factor depending on the energy of the backscatter peak.

A further reduction in background is achieved by sensing coincident signals between the guard-ring and central regions, and rejecting the central region signal when such a coincidence is registered. This "guard-ring reject" system effectively eliminates the partial collection from the peripheral region of the sensitive volume of the detector. With such an arrangement, we approach the background level expected due to electron escape from the detector surface. In our actual detector, shown in Fig. 3b, a double guard-ring is used, the outer ring serving to reduce edge leakage in the inner ring, and thereby improving its noise properties so that the inner guard-ring signal discriminator can be set low to detect very small signals.

Figure 4 illustrates the improvement achieved by using this technique on a typical sample. The same blood serum sample used for Fig. 1 was examined, and the same total number of counts was accumulated in the molybdenum x-ray backscatter peak. The reduction in background seen in this spectrum, averaged over the full energy range, is about a factor of 15. Much larger factors, ranging up to about 60, have been observed for higher-energy excitation. Comparison of Fig. 4 with Fig. 1 shows the improvement in ability to see small traces of elements, such as nickel, present in the specimen at a level near 0.1 ppm. Better statistics realized by a longer count, or with more intense excitation, would further reduce the detection limit.

Footnote and References

*Condensed from LBL-9. Presented at the 20th Annual Denver X-Ray Conference, Aug. 11-13, 1971.

1. W. Hansen and F. S. Goulding, Leakage, Noise, Guard Rings and Resolution in Detectors, in Proceedings of Asheville Conference, NAS-NRC Report No. 32, 202 (1961).

SOME ASPECTS OF X-RAY FLUORESCENCE SPECTROMETERS FOR TRACE-ELEMENT ANALYSIS*

D. A. Landis, F. S. Goulding, and B. V. Jarrett

The ability to perform x-ray fluorescence analysis with Si(Li) detectors is due in large part to the continuing improvement in the energy resolution capabilities of the spectrometer system. The first major step toward improving energy resolution below 2 keV full width at half maximum (FWHM) resolution, the level common in 1964, came with the development of low-noise field-effect transistors by a number of transistor manufacturers. Earlier field-effect transistors exhibited considerable surface noise, and their performance was not superior to the vacuum tubes commonly used in earlier preamplifiers. Following the development of a new generation of FET's (notably the 2N3823, then the 2N4416), low-temperature operation of these devices to reduce noise was introduced by a number of groups. Work at the Lawrence Berkeley Laboratory in mid-1965[1] achieved an energy resolution of 700 eV(FWHM), and stimulated the first suggestion[2] that a semiconductor detector spectrometer could provide a useful x-ray fluorescence analyzer. This resolution permits separation of elements above

zinc in the periodic table.

A long slow period of development followed this initial jump in performance. Small improvements resulted from use of the 2N4416 to replace the 2N3823, from rigorous selection of these transistors, and from optimization of the operating temperature of the field-effect transistor. Changes in manufacturing techniques led to some improvement, but also some setbacks. By early 1969, a few outstanding spectrometers were capable of achieving energy resolutions as low as 250 eV (FWHM) at low energies, making separation of elements above calcium practicable.

A series of advances made at LBL over the past two years and illustrated in Fig. 1 have reduced the energy resolution of x-ray spectrometers to 100 eV or less, making possible the separation of all elements above carbon in the periodic table. The resistor, traditionally used to provide low-frequency feedback to a low-noise preamplifier as shown in Fig. 1A, was replaced by light coupling, from a light-emitting diode (LED) to the photosensitive drain-gate FET junction (Fig. 1B).[3] This step eliminated the feedback resistor, a noisy and unreliable component; it also entailed remounting the small FET silicon chip in a new package, thereby eliminating noise produced by the FET header. The elimination of these noise sources permits use of longer pulse-shaping times in the main amplifier, thereby achieving energy resolution below 100 eV at low counting rates. In this simple light feedback system, nonlinearity of the LED current-light relationship degraded performance at higher counting rates. This led to the pulsed-light feedback scheme shown in Fig. 1c.[4] Here the LED is pulsed when necessary to maintain the preamplifier output in its normal range. When pulsing occurs, a reject waveform is fed to the main amplifier, and all signal are rejected until the system resumes normal operation. Apart from the use of the FET as a photodiode, this scheme is quite similar to that first used by Kandiah.[5]

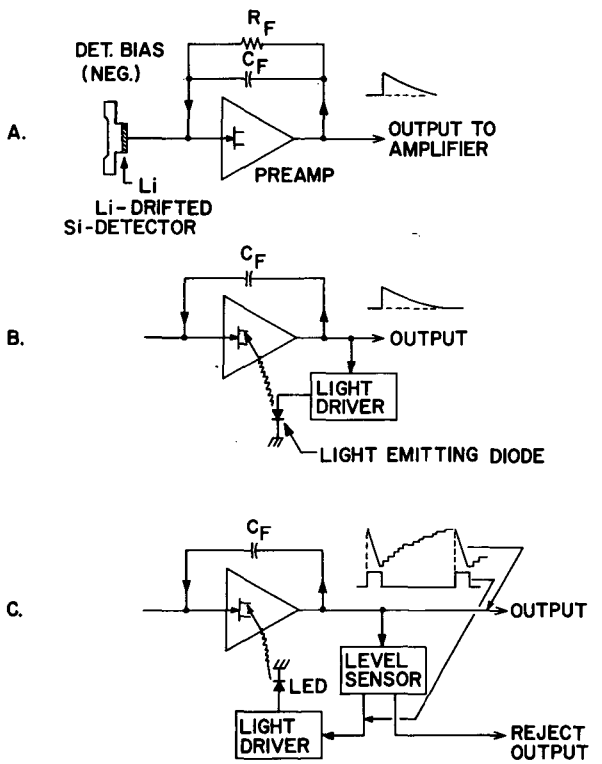

Fig. 1. Development of pulsed-light feedback preamplifier from a resistor feedback configuration. (XBL 713-563)

The simplified diagram of the amplifier system used in the pulsed-light feedback unit, shown in Fig. 2, gives some idea of the complex processing performed on signals before they are allowed to proceed to a pulse-height analyzer. Signals from the preamplifier are differentiated, shaped, and amplified in a linear amplifier, then fed to a circuit that accurately fixes the baseline of the signals at zero. The action of this restorer is inhibited during the reset action in the preamplifier. A fast channel also processes the signals, looking for cases where pile-up occurs in the slow channel—in which case the events are rejected. If no pile-up occurs, the signal in the slow channel is examined; and if its level exceeds a selected bias level, the signal peak is stretched. Shortly after the signal peak, the stretched output is sampled by a linear gate, and a 2-μsec-wide output signal, proportional in amplitude to the difference between the signal and the selected bias, is produced. It is an impressive demonstration of the power of modern integrated circuits that these functions—amplification, shaping, pile-up rejection, dc restoration, gating, signal stretching, and

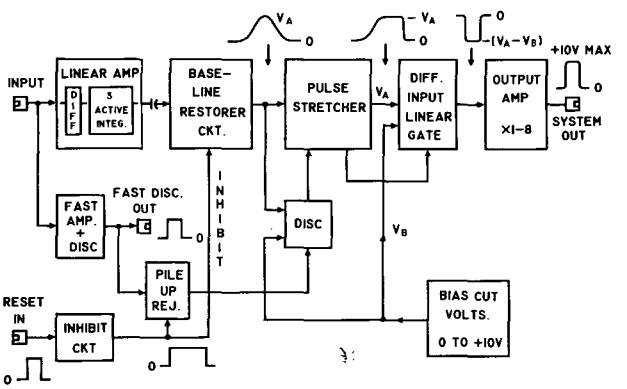

Fig. 2. Block diagram of the amplifier unit used with a pulsed-light feedback system. (XBL 711-75)

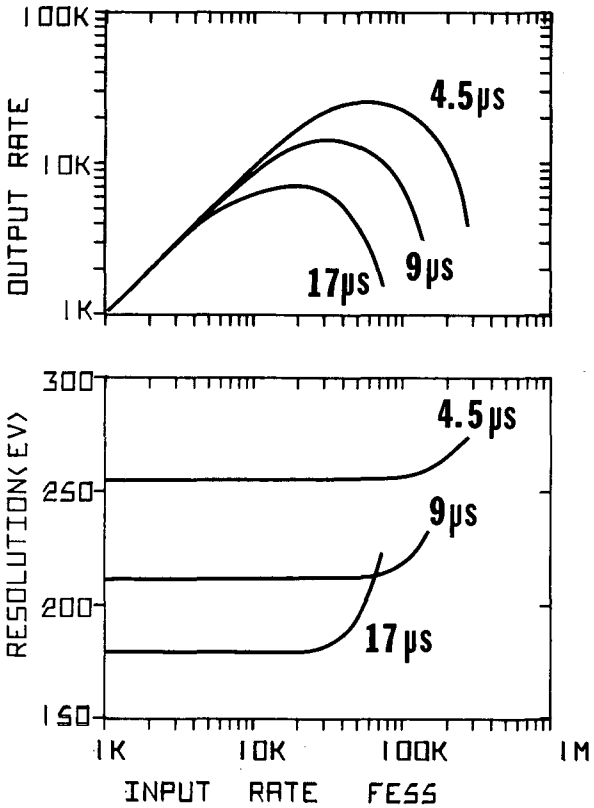

Fig. 3. Showing the effect of counting rate on resolution on Mn x rays for different Gaussian peaking times. The output counting rate is al' shown. (XBL 7010-6806)

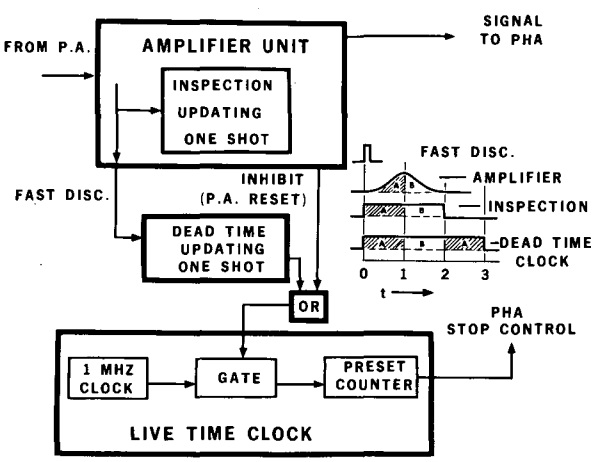

Fig. 4. Method of correcting for dead-time. (XBL 718-1233)

biased amplification–are performed in a single module (NIM-2 width).

Figure 3 shows the variation of energy resolution with counting rate measured on manganese x rays produced by an ^{55}Fe source, Gaussian pulse shaping was used with various peaking times as indicated on the curves. Figure 3 also shows the output pulse-rate variation; the difference between it and the input counting rate represents those pulses rejected by the pile-up rejector.

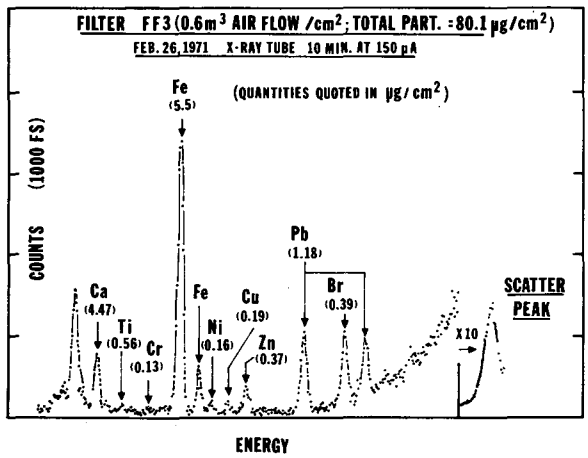

Fig. 5. Air-filter spectrum. (XBL 713-398)

The most efficient input rate for the peaking time used can be determined from these curves. The dead time can be corrected by gating a live-time clock using the dead time generated by the circuit shown in Fig. 4. The number of pulses rejected is more than one might initially expect from the value of the inspection time. This is because both pulses are rejected if the second pulse comes before the peak of the first pulse, and only the second pulse is rejected if it comes after the peak of the first pulse. Consequently, we use a dead time in the clock channel approximately 1.5 times the signal inspection time, thereby giving double weight to losses in the first half of the inspection period.

An example of the performance of x-ray spectrometers in analytical application is shown in Fig. 5. The spectrum of an air pollution filter was obtained using a guard ring reject detector and pulsed light-feedback electronics. The data were obtained in 10 min using a transmission x-ray tube for fluorescence excitation. Elemental concentrations are obtained by appropriate calibration procedures after making corrections for amplifier dead time as described above.

Footnote and References

*Condensed from LBL-320. Presented at the Second Symposium on Semiconductor Detectors for Nuclear Radiation, Munich, Germany, September 6-10, 1971.

1. E. Elad, Nucl. Instr. Methods 37, 327 (1965).

2. H. R. Bowman, E. K. Hyde, S. G. Thompson, and R. C. Jared, Science 151, 562 (1966).

3. F. S. Goulding, J. Walton, D. Malone, Nucl. Instr. Methods 71, 273 (1969).

4. D. A. Landis, F. S. Goulding, R. H. Pehl, and J. T. Walton, IEEE Trans. Nucl. Sci., NS-18, No. 1, 115-124 (1971).

5. K. Kandiah and A. Stirling, Semiconductor Nuclear-Particle Detectors and Circuits, National Academy of Sciences Publication 15943, 495 (1969).

SMALL X-RAY TUBES FOR ENERGY DISPERSIVE ANALYSIS USING SEMICONDUCTOR SPECTROMETERS*

J. M. Jaklevic, R. D. Giauque, D. F. Malone, and W. L. Searles

Introduction

We have explored the use of small x-ray tubes as an alternative means of fluorescence excitation with particular emphasis on applications to analysis of trace quantities (down to less than 1 ppm). Their principle advantage is the large characteristic x-ray flux which can be generated with a relatively small expenditure of power input to the tube. However, analytical sensitivity, using fluorescence excitation with normal x-ray tubes, is limited by the continuous Bremstrahlung background generated by the deceleration of the electrons in the anode. Scattering of this spectrum from the sample to detector is unavoidable and is a particularly serious limitation when using low-background semiconductor spectrometers. In the present work we describe techniques for generating nearly monoenergetic x-ray tube outputs with minimal background interference.

The simplest method for reducing continuum background is to use suitable x-ray filters to transmit as much of the characteristic radiation as possible while attenuating all other energies. Since any given element is a good transmission filter for its own characteristic x-rays, the anode of the x-ray tube can be made of an appropriate thickness to effectively filter the transmitted x-ray spectrum. Although filtering the spectrum produced at backward angles to the target would achieve the desired result, it proves convenient to employ the transmission geometry since more efficient anode-to-sample spacings are possible and the use of multiple targets is facilitated. Further filtering can be included to selectively reduce the Kβ intensity and more closely approach a monoenergetic x-ray beam.

A scale drawing of the x-ray tube is shown in Fig. 1. The electron beam is obtained from a tungsten filament and the current can be controlled either by the filament power or with the intermediate electrode voltage. The beam is focused on the target anode which is held at the high positive voltage and supported by the ceramic insulator. (Operation of the anode at positive voltage instead of ground potential is dictated mostly by convenience of design. There are possible advantages to operation at ground potential since the exit window may then also be the transmission target filter, thus effecting higher geometric efficiency.) Optimum filter thickness is determined empirically but 3 to 5 half-thicknesses of the target material are nearly optimum. A portion of the total filter thickness is mounted external to the tube to eliminate unwanted characteristic x-rays from the stainless steel vacuum enclosure.

Most of the present data were obtained with

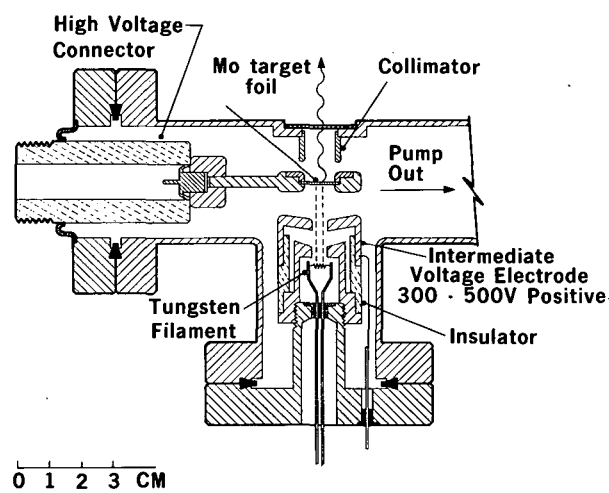

Fig 1. Schematic of transmission x-ray tube. (XBL 716-1154)

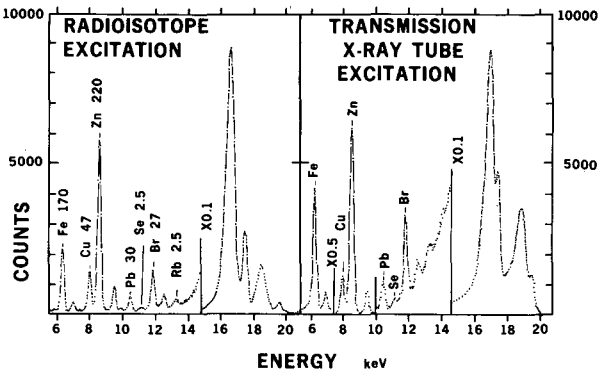

Fig. 2. Comparison of excitation modes showing spectra obtained from biological specimen (lyophilized horse liver). Numbers on peaks indicate concentrations in ppm for the sample pellet. (XBL 716-1155)

molybdenum target and total filter thickness of 0.012 cm. The tube was operated at 42 keV with variable currents up to 500 μA. The maximum beam power of 25 watts was dissipated mostly by radiation from the anode structure. Although increasing the beam voltage would result in improved characteristic x-ray yield relative to Bremsstrahlung, a practical limit is set by the transmission of the high-energy continuum Bremsstrahlung x-ray through the filter. Stable emission is achieved via feedback to the filament supply.

Figure 2 is a comparison of fluorescence spectra obtained using radioisotope excitation and transmission x-ray tube excitation for the case of a biological sample. The spectra were obtained using a low-background guard-ring reject system[1] and pulsed-light feedback electronics;[2] only the high-energy portions are shown since there is no significant difference in background at lower energies. The radioisotope source-target assembly employed a 125-mCi ^{125}I source separated by 1 cm from the molybdenum target, which in turn was 1 cm from the sample. The x-ray tube anode filter was 0.012 cm molybdenum and gave a ratio of 30:1 for the Kα x-ray peak height-to-background height just below the Kα peak in the tube output spectrum. With the x-ray tube operating at 100 μA and 42 keV the spectrum was acquired in approximately 15 min at a total counting rate of 4000 cts/sec Trace-elements concentrations for the 0.3 mm-thick sample were obtained by the method described in Ref. 3. With a 500-μA beam current and the anode to sample distance of 8 cm as used in these measurements, the counting rate was 50 times that obtained with the radioisotope source.

An interesting feature of the data is the difference in the ratio of backscatter peak height to fluorescence x-ray intensity between the two spectra. Although a part of this difference can be accounted for by the lower peak-to-background in the x-ray tube output spectrum, most of the difference is due to the difference in source-sample-detector geometry. In the source-target assembly the average scattering angle for the molybdenum x-rays is near 180° whereas the x-ray tube is mounted horizontally with a total scattering angle of approximately 90°. These angles are the respective maximum and minimum in the incoherent scattering differential cross section. These conclusions are supported by data obtained with the secondary fluorescence tube operated in a similar geometric configuration.

A substantial further reduction in continuum background can be realized by using a secondary excitation mode analogous to the source-target arrangement The x rays generated in the anode by the electron beam are made to strike a secondary target--the characteristic x rays from this target then are used to excite x rays from the sample. Although this conversion process results in a reduction in x-ray output for a given electron-beam power, it virtually eliminates the continuous background in the output spectrum. Since the secondary target need not be an electrical conductor or dissipate large amounts of power, it is possible to generate characteristic x-rays from elements not available as metallic foils.

We have constructed such a tube with a rhodium anode and molybdenum secondary target.

Direct measurement of the output spectrum shows a ratio of peak-to-background height of greater than 300:1 however the x-ray production efficiency was much less than with the transmission-type anode.

Footnote and References

*Condensed from LBL-10. Presented at the 20th Annual Denver x-Ray Conference, Aug. 11-13, 1971.

1. F. S. Goulding, J. M. Jaklevic, B. V. Jarrett, and D. A. Landis, Detector Background and Sensitivity of X-ray Fluorescence Spectrometers, presented at the 20th Annual Denver X-ray Conference, August 11-13, 1971; Lawrence Berkeley Laboratory Report LBL-9.

2. D. A. Landis, F S Goulding, and R. H. Pehl, IEEE Trans. Nucl. Sci. NS-18, 115 (1971).

3. R. D. Giauque and J. M. Jaklevic, Rapid Quantitative Analysis by X-ray Spectrometry,

presented at the 20th Annual Denver X-ray Conference, August 11-13, 1971.

RAPID QUANTITATIVE ANALYSIS BY X-RAY SPECTROMETRY

R. D. Giauque and J. M. Jaklevic

An x-ray fluorescence analysis method applicable to the case of fluorescent spectra excited with monoenergetic x-rays has been developed. The technique employs one calibration, uses a single-element thin-film standard, and depends upon theoretical cross sections and fluorescence-yield data to interpolate from element to element. The samples are treated as thin films and corrections for absorption effects are easily determined. Enhancement effects, if not negligible, are miniminzed by sample dilution techniques.

The intensity of a K or L x-ray line from an element j in a thin specimen for which the critical thickness has not been reached and for which enhancement effects are negligible can be written as follows:

$$I = I_0 \, G \csc \phi_1 m_j \tau_j \, [1 - (1/J_{K,L})]$$

$$\times \omega_{K,L} \, f \, A_b \epsilon [1 - \exp(-am)] / am \qquad (1)$$

Using data available in the literature Eq. (1) may be reduced as shown:

$$I = C \, K_j m_j \, [1 - \exp(-am)] / am \qquad (2)$$

At constant primary radiation intensity and at constant geometry, the value of C may be determined from a single-element thin-film standard for which absorption effects are negligible. The value of K_j is constant for the element j and is calculated. The quantity m_j is the concentration (g/cm^2) of the element j to be determined. The quantity exp(-am) is the product of the total absorptions of the primary and characteristic radiations in the total sample thickness. The value of this quantity can be determined by measuring the relative intensity with and without the specimen of the K or L x-ray line of interest from a target of element j located at a position adjacent to the back of the thin specimen. The expression may be written as follows:

$$[I_{(\text{target} + \text{sample})} - I_{\text{sample}}] \div I_{\text{target}} = \exp(-am) \qquad (3)$$

Using the described procedure several specimens were analyzed. The data were obtained using a low-background guard-ring detector with pulsed light feedback electronics. Excitation was provided by a molybdenum transmission x-ray tube. A single thin-film standard, copper of mass 101 $\mu g/cm^2$, was used to standardize for analysis.

Table I. Analysis of pottery

	X-ray fluorescence	Neutron activation
Ti	0.76% ± 0.02	0.78% ± 0.03
Cr	114 ppm ± 6	115 ppm ± 4
Mn	47 ppm ± 5	40.9 ppm ± 0.5
Fe	1.05% ± 0.01	1.017% ± 0.012
Ni	301 ppm ± 6	279 ppm ± 20
Cu	55 ppm ± 2	60 ppm ± 8
Zn	60 ppm ± 2	59 ppm ± 8
Ga	40 ppm ± 2	44 ppm ± 5
As	29 ppm ± 2	30.8 ppm ± 2.2
Rb	58 ppm ± 2	70.0 ppm ± 6.3
Sr	123 ppm ± 3	145 ppm ± 22
Pb	31 ppm ± 2	———

Table II. Analysis of plant specimen

	X-ray fluorescence	Neutron activation
Ti	121 ppm ± 5	< 0.01%
Cr	26 ppm ± 1	23.8 ppm ± 0.9
Mn	60 ppm ± 2	49.3 ppm ± 1.4
Fe	0.186% ± 0.002	0.201% ± 0.006
Ni	8 ppm ± 1	13.8 ppm ± 3.0
Cu	21 ppm ± 1	———
Zn	80 ppm ± 1	84 ppm ± 8
Br	48 ppm ± 1	42 ppm ± 1
Rb	7 ppm ± 1	7.0 ppm ± 1.4
Sr	97 ppm ± 2	236 ppm ± 66
Pb	206 ppm ± 3	———

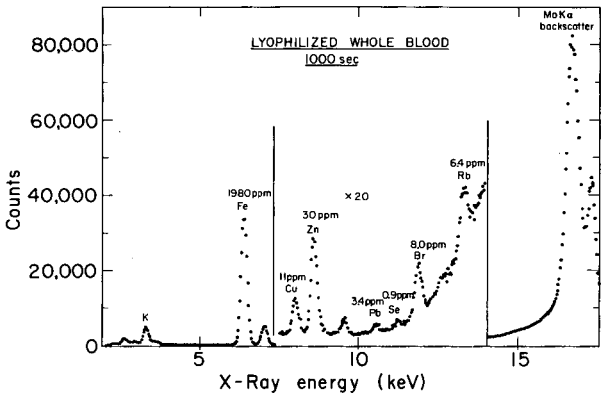

Fig. 1. Spectrum from lyophilized whole blood specimen. Concentrations listed are for the lyophilized specimen. This preparation gave a concentration factor of five.
(XBL 717-3813)

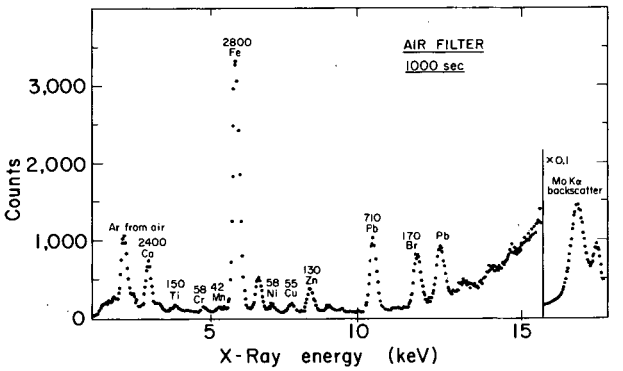

Fig. 2. Spectrum from air filter of mass 3 mg/cm^2. Concentrations listed in nanograms/cm^2. (XBL 717-3814)

Table I shows a comparison of the results obtained by x-ray fluorescence and neutron activation analysis on a pottery specimen. Total analysis time was one hour. The precisions listed are for one standard deviation.

Table II shows a comparison of the results obtained on a dried plant specimen. Analysis time was one-half hour.

Figure 1 shows the spectrum and results obtained on a human whole blood specimen which had been freeze dried. Since the concentration factor obtained by freeze drying the specimen was a factor of five, the concentrations of the elements in the original specimen are one-fifth the reported values. The content of lead in this specimen is several times the normal value.

Figure 2 shows the spectrum and results obtained on an air pollution filter of mass 3 mg/cm^2. The results are reported in nonograms/cm^2.

The calibration method used has been successfully applied to trace element analyses in light element matrices. When used in conjunction with low-background detector systems and x-ray tube excitation, it can provide rapid and accurate multielement analyses down to concentrations of less than 1.0 ppm.

A BIPOLAR DIGIPOTENTIOGRATOR*

W. W. Goldsworthy and R. G. Clem

The bipolar "digipotentiograter" is a direct outgrowth of the previously developed digital integrator which served as a voltage-to-frequency converter in our first electroanalytical effort.[1] The same principle was later applied to the digitizing of charge liberated in a nuclear-event detector and resulted in the development of a digital nuclear spectrometer.[2] Both of these initial instruments served passively to neutralize incoming charge to a preset null through digital feedback of charge of opposite polarity. Neither was designed to perform a control function on the external system, although in some systems it seemed reasonable that they could be made to do so. The validation of this reasoning took the form of the monopolar digipotentiograter described in a recent correspondence.[3] The present bipolar device is a more sophisticated instrument and is more generally applicable to electroanalytical problems. It is presented as the heart of a new system which includes a digital wait-gate, a pulse-height analyzer for data storage, an analyzer interface, an incremental digital differentiator, a voltage-step ramp generator, and a program timer.

The system shown in Fig. 1 is a complete divergence from previous electroanalytical systems. The familiar train of instruments, a potentiostat, a current-to-voltage converter, and an analog-to-digital converter are absent. In their place, one finds a single device, the bipolar digipotentiograter, which functions as a potentiostat through pulsed injection or extraction of charge to maintain a desired cell

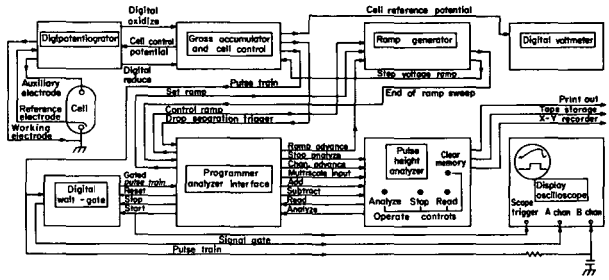

Fig. 1. Block diagram of the system. (XBL 7111-4638)

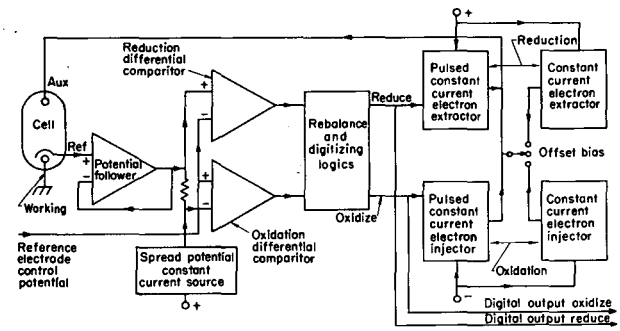

Fig. 2. Block diagram of the bipolar digipotentiogrator. (XBL 7111-4642)

control potential and consequently serves as a current-to-digital converter. If the current pulses are counted and summed in time, the device subsequently functions as an integrator.

Figure 2 is a block diagram of the bipolar digipotentiogrator. The reference electrode is connected through a unity-gain, impedance-coupling amplifier to the inputs of the two differential comparators. The logic circuitry in turn senses the need for rebalance current and controls the rate of pulsed current required to satisfy the cell current demands at the control potential selected.

Cell potential control is effected either through a local potential source or an external source applied to the other input terminals of the differential comparator pair. A resistor connected between the signal inputs of the comparators, and driven with a constant current source, generates a potential separation between the two comparators to prevent "chattering".

In addition to the digipotentiogrator, several other pieces of equipment are required. They are: a voltage-step ramp generator used to drive the cell when scanning, a dual time-base generator which can serve as a wait-gate, an analyzer interface unit which also includes the necessary logic to permit incremental differentiation. Much of the equipment termed "miscellaneous" in the previous paper is re-employed here.[1]

This system also includes a Cipher Model 70 magnetic tape recorder and a Northern Model 406M tape controller. The latter unit permits communication between the analyzer and the tape in either a READ or a WRITE mode.

Footnote and References

*Accepted by Anal. Chem. (In press)

1. R. G. Clem and W. W. Goldsworthy, Anal. Chem. 43, 418 (1971).

2. W. W. Goldsworthy, Nucl. Instr. Methods 94, 221 (1971).

3. W. W. Goldsworthy and R. G. Clem, Anal. Chem. 43, 1718 (1971).

A DIGITAL POTENTIOSTAT*

W. W. Goldsworthy and R. G. Clem

Reported for the first time is an instrument for potentiostatic control of an electrochemical cell that employs a new technique--digital current feedback. Digital current pulses, which can be scaled to read out directly on a scaler the weight of sample oxidized or reduced, pass through the auxiliary electrode of the cell and are used to maintain control potential. Since the instrument operates simultaneously as a potentiostat, a current-to-frequency converter, and subsequently as a digital integrator, a new term "digipotentiogrator" (DPI) has been coined to identify it.

This new device is simple, inexpensive to construct, and has very low power requirements. The arrangement shown in Fig. 1 is used to digitally maintain a control-potential and to digitally measure the charge transfer which occurs in an electrochemical reaction. Two charge sources are connected to the auxiliary electrode. One source injects charge digitally, while the other source,

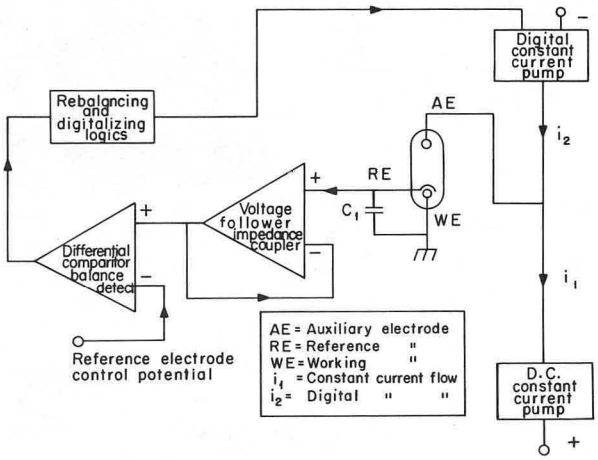

Fig. 1. Digipotentiograter (DPI) Block Diagram. (XBL 715-3531)

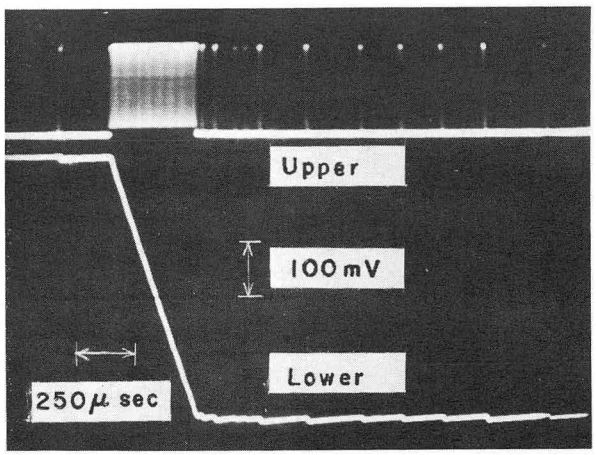

Fig. 2. DPI transient response for a dummy cell.
upper trace: Current pulses
lower trace: Control-potential response
time base: 250 μsec/division
(XBB 715-2225)

which is a constant current driver, extracts charge on a continuous basis. Both drivers are designed to deliver up to 10 mA of average current and to perform independently of the potential of the auxiliary electrode.

The cell reference electrode is connected to the positive terminal of a differential comparator through a unity-gain impedance-coupling amplifier and the desired control-potential is applied to the negative terminal. Any positive output from the differential comparator-balance detector initiates operation of the digital charge pump for fixed time periods and at rates determined by the charge demands of the cell. A local 500-kHz crystal clock furnishes digital injector drive intervals up to the clock frequency and therefore provides very good digital resolution. Since the charge demand of sampling is made only between possible injector drive intervals, the occurrence of partial current drive intervals is prevented.

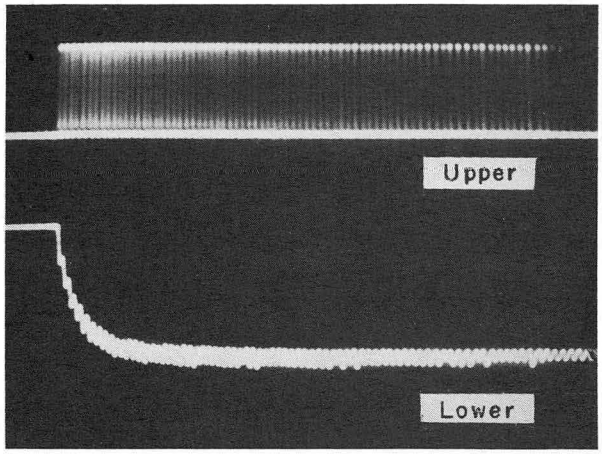

Fig. 3. DPI transient response for an electrochemical cell (1). Parameters the same as for Fig. 2.
(XBB 715-2227)

The small value capacitor C_1 is attached from the reference electrode to the grounded working electrode to maintain potential control when the cell is driven through its electrocapillary maximum potential.

Figure 2 illustrates the current and voltage response in time to a -500 mV-to-ground square-wave applied to the control input of the DPI when employing a capacitive-resistive simulated cell load. Note that in this system, the descent time is limited only by the current capability of the digital charge source and by the dead time between pulses.

Figure 3 shows a repeat of the above experiment using an anodic stripping cell employing 0.01M KCl as the supporting electrolyte.

The current drift of this device amounts to only 0.04% over a period of 1.4 h. The internal potential control is better than 1 mV.

Footnote

*Taken from Anal. Chem. 43, 1718 (1971).

A ROTATED PLATINUM CELL FOR CONTROLLED-POTENTIAL COULOMETRY*

R. G. Clem

The novel, rotated platinum cell is a conceptual departure from the widely used stationary, platinum gauze, stirred-solution designs and is the result of an extension of previous work which led to the development of the rotated mercury cell.[1]

The cell, which is made entirely of platinum, is a gauze-lined cylinder, closed at the bottom, and partially opened at the top. It is held inside a plastic cylinder, with a partially opened, plastic, screw-cap top. (See Fig. 1.) The plastic cylinder is attached to a copper turntable, and the cell-turntable combination is mounted in the previously described 1800-rpm motor-driven apparatus.[1] The sample solution, upon rotating the cell wall with centrifugal force is contacted and efficiently stirred with a coaxial, combination, reference-auxiliary electrode probe. This efficient stirring combined with a favorable working electrode surface-area to solution-volume ratio results in the attainment of what quite possibly are the highest electrolysis rate constants ever achieved with a platinum electrode. Rate constants of 0.13, 0.82, and 0.064 sec^{-1} are calculated for Au(III), Fe(III), and NO_2^-, respectively. In contrast, constants of only 0.014 and 0.005 sec^{-1} are found for Au(III) and NO_2^- in a conventional cell.[2, 3, 4]

The rate constants are sensitive to sample volume changes. (See Fig. 2.) The electrolysis constant for a 5-ml sample is no larger than that obtained with a conventional cell. A 2-ml sample volume was selected for this cell because the rate constants are high, and this volume is convenient. Attempts to contact a much smaller volume of sample can result in the scraping of the platinum gauze against the counter electrode-reference probe.

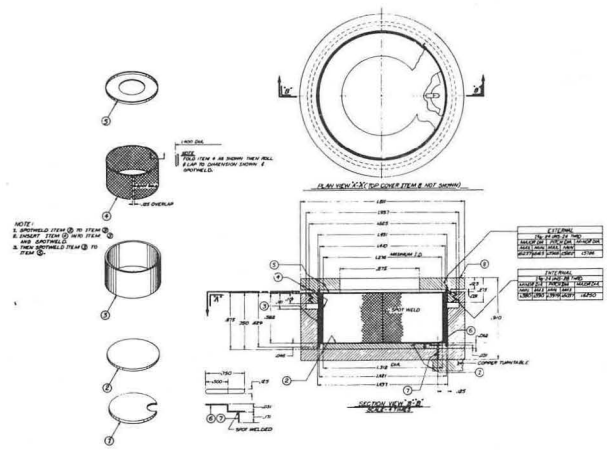

Fig. 1. Exploded, top, and cross sectional views of the platinum cell and plastic holder. (XBL 714-671)

The results for Au(III), Fe(III), and NO_2^- are shown in Table I.

Table I. Reproducibility*

Au^{3+} (μg)				Fe^{3+} (μg)				NO_2^- (μg)			
Added	Found	Av. Dev.	n	Added	Found	Av. Dev.	n	Added	Found	Av. Dev.	n
1032	1029.8	0.4	5	761	759.0	0.3	5	3882	3104	7	n
516	514.8	0.2	6	380	379.0	0.4	6	1294	1283.6	1.3	5
258	257.5	0.2	5	76	77.2	0.2	5	647	648.2	0.8	6
								517	514.9	0.5	4
								326	323.7	0.3	5
								129	128.8	0.2	4
								65	66.7	0.1	5

*All results obtained by normalization.

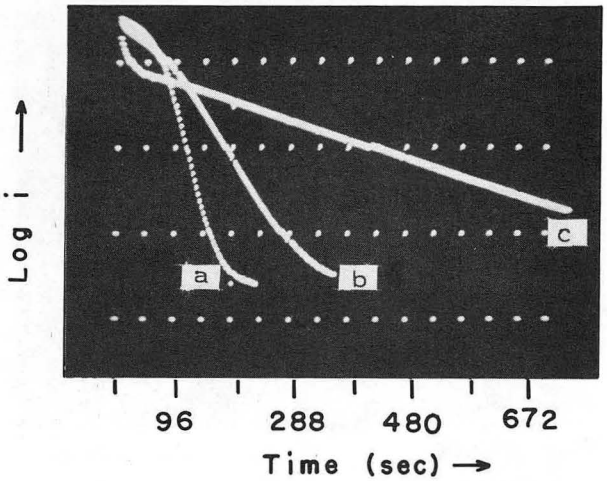

Fig. 2. Effect of volume on the electrolysis rate
647 μg nitrite in: A. 2, B. 3, and C. 5 ml of 1M acetate buffer, pH 4.7. Rate constants for curves A, B, and C are 0.064, 0.023, and 0.005 sec^{-1}, respectively.
(XBB 714-1528)

Footnote and References

*Condensed from UCRL-20473 Rev., April 1971. Published Anal. Chem. 43, 1853 (1971).

1. R. G. Clem, F. Jakob, D. H. Anderberg, and L. D. Ornelas, Anal. Chem. 43, 1398 (1971).

2. J. E. Harrar, Ibid. p. 143.

3. J. E. Harrar, "Manual of Controlled-Potential Coulometric Methods," University of California, Lawrence Radiation Laboratory Report UCID-15528, (1970).

4. J. E. Harrar, AEC Report, UCRL-50417, Livermore, California, March 1968.

A ROTATED CELL FOR ANODIC STRIPPING ANALYSIS: COMPUTER RESOLUTION OF PEAK(S) AND BACKGROUND DATA

R. G. Clem, G. Litton, and L. D. Ornelas

The determination of several trace elements of environmental importance, with anodic stripping voltammetry, is now made possible on a routine and rapid basis through recent improvements in cell design and methodology. The kinds of samples to which this approach is amenable are: water, water extracts of air, aqueous soil leachings, and possibly to the direct analysis of trace metals in biological fluids.

This improved cell, shown in Fig. 1, features very rapid sparging characteristics like its predecessors;[1,2] thus the time required for purging the sample of electroreducible oxygen is reduced, from 10-20 min in a conventional cell, to ~1 min in the presented cell. This large time reduction is effected by initially rotating the cell (sample container), which is partially closed at the top, at 1800 rpm. The sample solution containing an added, known amount of a mercury salt is thrown against the container wall and forced into a thin film about 1-mm thick with centrifugal force and the film sparged with nitrogen at a rate of ≥5 liters/min. After the sample is sparged, the cell is stopped; the sample solution returns to the bottom of the container.

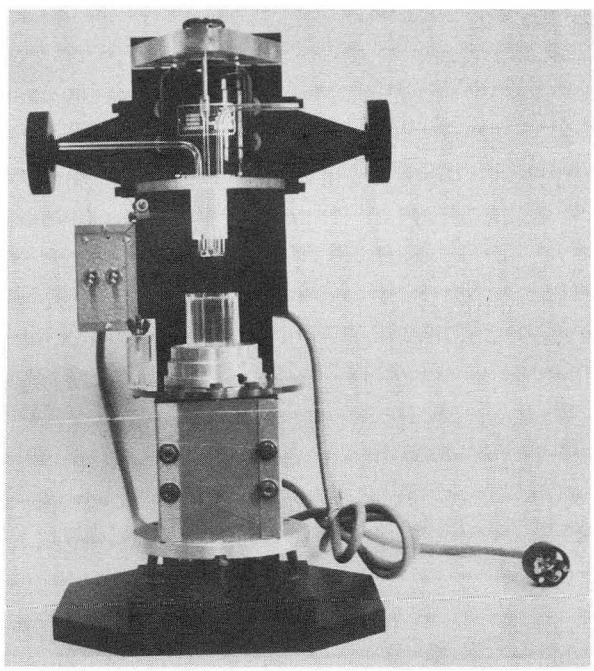

Fig. 1. The rotated cell for anodic stripping analysis. (XBB 7112-6111)

The stirring motor is started, and the trace metals and mercury are reduced simultaneously, employing a potential of -1.0 to -1.4 V for seven min. The paraffin-impregnated, graphite electrode employed is oriented 90° to the vertical. This prevents the clinging of hydrogen bubbles which initially form on the active surface. Bare graphite has poor hydrogen overvoltage characteristics; however, hydrogen overvoltage characteristics on the mercury-plated graphite are virtually the same as for mercury alone.

At the end of the accumulation period, the control potential is scanned in a step- and-hold manner to a potential sufficiently positive to cause stripping of the mercury film. The resulting current-potential information is temporarily stored in a pulse-height analyzer, then transferred onto magnetic tape in permanent storage for computer analysis. The total analysis time is about 8 min. This time is compared with $\geq$ 30 min required using conventional cells. A typical stripping polarogram is shown in Fig. 2. Upon concluding the analysis, the probes (reference electrode, auxiliary electrode, and stirrer) are racked up and out of the cell compartment and the spent sample solution is removed with a vacuum spitzer. After rinsing the cell, the next sample is added.

Digital signal recording is almost essential for anodic stripping analysis. The relative peak heights can vary over two to three orders of magnitude in a single run. If analog recording is employed, one must first estimate by a trial run the magnitude of the peak; then, after adjusting the recorder parameters accordingly, a second run is made to obtain the peak required. Digital recording, on the other hand, allows one to first obtain the whole voltammogram on the first run, then electronically expand or compress the data at will after the fact to observe all the peaks of interest.

In addition, several programs have been developed to store and analyze the raw data obtained from anodic stripping experiments. The raw experimental data from each sample is initially stored on magnetic tape prior to its processing to obtain a clean spectrum followed by its storage in a library which has been established on the Laboratory Mass Storage System. This library has been constructed so that the data for any given sample may be easily obtained for analysis.

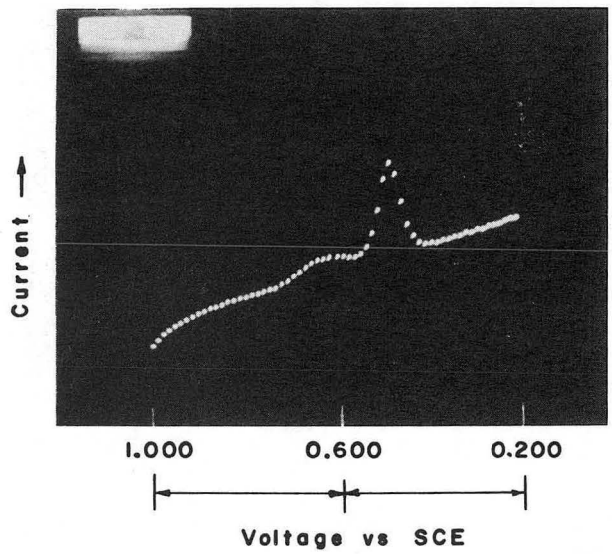

Fig. 2. A typical stripping polarogram. (XBB 715-2224)

The basic analysis package consists of a set of routines which first decomposes each spectrum into separate peaks, followed by a calculation of the areas associated with each peak. For a single, well-defined peak, the area is obtained by fitting the background under the peak to a high-order polynomial, subtracting the background, then finally integrating the residual spectrum numerically.

For composite peaks, the area of each component is obtained by first fitting the composite to a sum of gaussians, then finding the area under each gaussian by numerical integration.

Further work is under way to extend the basic analysis package to incorporate a set of interactive routines, which will allow the user to monitor and control the analysis of complex spectra.

References

1. R. G. Clem, F. Jakob, D. H. Anderberg, and L. D. Ornelas, Anal. Chem. 43, 1398 (1971).

R. G. Clem, ibid., p. 1853.

A SCANNING DIGITAL COULOMETER

R. G. Clem and W. W. Goldsworthy

Classical controlled-potential coulometry is insensitive to qualitative measurements. The electroactive ion(s) of interest as well as the electroinactive, supporting electrolyte, ions must be known prior to the analysis. If, however, a step and hold potential sweep is employed in conjunction with an exhaustive coulometric measurement at each step, useful qualitative information can be obtained. Only those potential regions near the half-wave potentials of the materials in the sample will contain useful information, so some sort of an arrangement which favors these regions is desirable if a coulometric scan is to be made within a reasonable time period.

One such scheme allowing this type of selective favoring is that shown in Fig, 1. This arrangement is readily applicable to any system in which the analog of the cell current is converted into a digital form--e.g. Ref. 1. In this approach a pulse-rate threshold is set which allows all faradic data exceeding this rate to be examined in detail while background data are passed over at a predetermined rate. A step-potential ramp generator supplies the desired potential scan. A pulse-height analyzer operated in the multichannel scaling mode is used to accumulate data in consecutive addresses whose number is equal to that of the steps in the entire potential scan. A timer supplies the signal to advance the analyzer and simultaneously to step the ramp generator. A threshold-sensing count rate meter is used to sense the current level of the incoming data and to block the ramp and channel advance signal when the current level (pulse rate) is above the threshold level.

Figure 2 indicates the operation of the count rate meter in more detail. The first three blocks: a one-shot, a charge injector, and an integrator, develop an output voltage at point A proportional to the input pulse rate. This potential is sensed with a differential comparator whose sensing level can be adjusted by potentiometer R_1. Whenever the potential at A is lower than the threshold set by R_1, the output of the comparator is low. This allows signals to be developed from the output of the NAND-gate whenever timing signals occur, thus providing rapid advancement of the ramp potential and memory address. If, however, the potential at A is higher than the threshold, the output from the NAND-gate is blocked. The potential ramp and memory address can be advanced only after the cell current drops below the set threshold level.

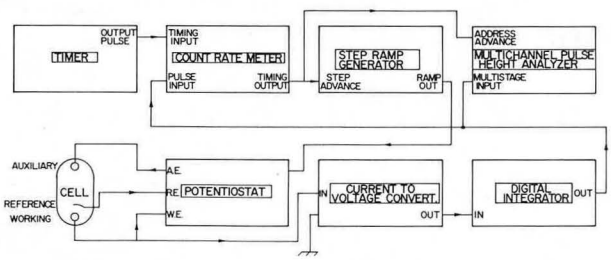

Fig. 1. Block diagram of the scanning digital coulometer. (XBL 7112-1836)

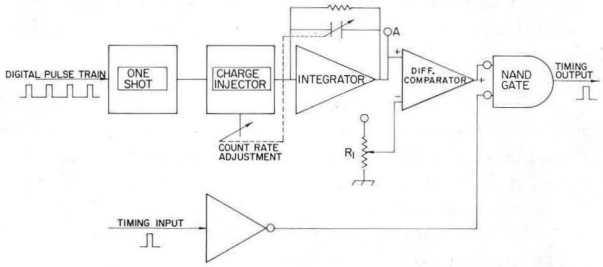

Fig. 2. Block diagram of the threshold sensing count rate meter. (XBL 7112-1835)

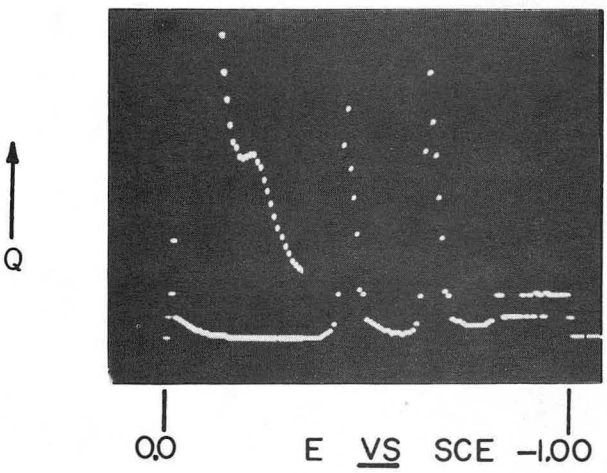

Fig. 3. A coulometric scan of Pb and Cd in a 1M KC1 supporting electrolyte. Solution: 52.5 μg Pb, 33.3 μg Cd. Scanned from 0.00 to -1.00 V vs SCE. Expanded portion of the scan (upper left) shows the reduction of 0.05 μg Cu. (XBB 7112-6112)

In this way, potential regions containing only background current are passed over rapidly at a rate predetermined by the timer setting while those regions containing the faradic current of interest are titrated to virtually the background current level. Near-equilibrium conditions are therefore maintained throughout the sweep.

Scanning coulometry is capable of sensitivity two orders of magnitude as great as that of the classical controlled-potential method and is also capable of much higher resolution. Figure 3 shows a coulometric scan for Pb and Cd in a 1M KCl supporting electrolyte solution. Determination of these two couples in the selected supporting electrolyte would be difficult by the classical method.

It appears that computer programs developed for the automation of anodic stripping analysis can be applied directly to these coulometric data.

Future, further reduction of the Nernst diffusion layer in the rotated mercury cell[1] should permit even more sensitive determination of electroactive species, provided the cell noise is not increased.

Reference

1. R. G. Clem, F. Jakob, D. H. Anderberg, and L. D. Ornelas, Anal. Chem. 43, 1398 (1971).

PLUG-IN ION SOURCE

M. C. Michel and E. C. Miner

Although samples can be introduced into the Cascade Isotope Separator without breaking vacuum, many operations require removal of the entire ion source after venting the large vacuum chamber to air. This operation becomes a potential hazard to the operator and the local environment as the level of residual radioactivity builds up from a variety of samples. Reducing the physical manipulation of the ion-source assembly to a minimum thus becomes a reasonable safety goal and allows for easy adaptation to a very simple, completely enclosed, transfer system at a later time if the level of radioactivity requires it. This argument is a particularly compelling one if the primary residual activities are alpha emitters (as is the case for the Isotope Separator), which can be controlled very effectively by a simple enclosure.

For this reason, and to reduce installation errors, we felt that a universal ion-source mount, plug, and alignment system would be a great advantage. The design that resulted from our work is sketched in Fig. 1. The aluminum oxide insulator to the right of the figure mounts on a vertical 19.5-in. vacuum flange (not shown) which in turn is moved to the left to contact its mating flange by operation of a standard machine tool slide, thus carrying the ion-source assembly into operating position. At the same time all twelve possible electrical connections are automatically made by means of the contact mounting ring and a corresponding set of plugs mounted permanently in the vacuum chamber. Six of these connectors are rated at 50 A and six at 5 A each. These features were already in existence and the plug-in ion source had to adapt to this system.

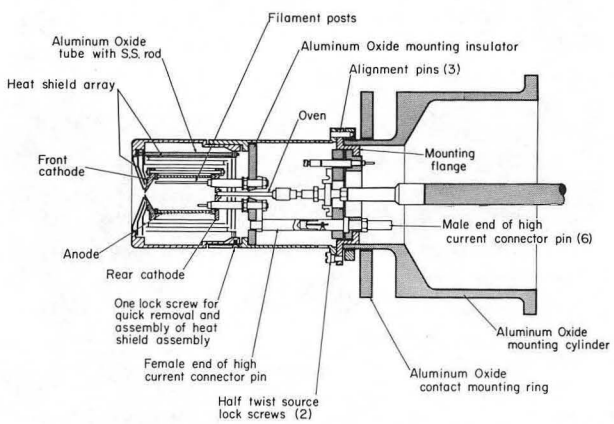

Fig. 1. Plug-in ion-source assembly. (XBL 719-4297)

Alignment of the source assembly, which is critical for operation of the isotope separator, is accomplished by the mounting flange, rigidly attached to the end of the main insulator and accurately aligned to be perpendicular to the beam axis. The flanged ion-source can is accurately pinned in position by three nonsymmetrically arranged alignment pins to guarantee reproducibility of the source position and prevent improper insertion. The aluminum oxide mounting insulator in the ion-source can is thus properly positioned, the twelve connectors mount from the right side and the ion source itself is built up on supports at the left side. All high-current connections from the connectors to the ion-source electrodes are made by machined copper bus-bars that serve as part of the mounting system hardware.

The heat-shield assembly is a slip fit into the main source-can structure and the inner front heat shield engages a step in the ion-source front cathode to complete the alignment of the ion exit hole at the beam axis. The heat shielding is sufficiently efficient to allow operation of the source at a temperature limited by volatilization of the aluminum oxide insulators with a power input of less than 300 W.

Provision is made for two different directly heated tube sample ovens, one of which can be inserted from outside the vacuum chamber through a bellows, valve, and vacuum lock combination. The other oven is mounted off the center axis and can be loaded only when the source is removed from the socket.

In operation, only two half-twist locking

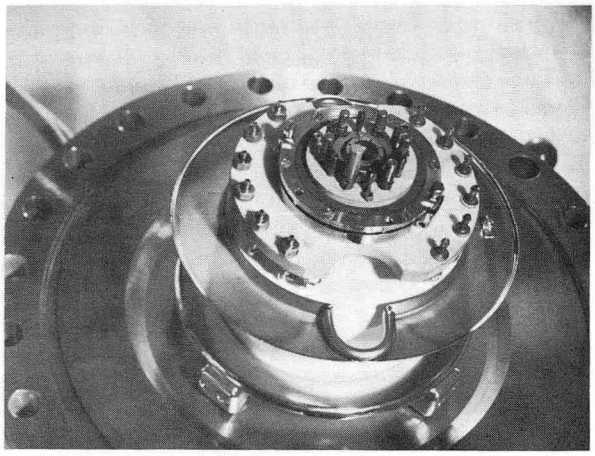

Fig. 2. Main insulator and source mounting flange. (XBB 719-4257)

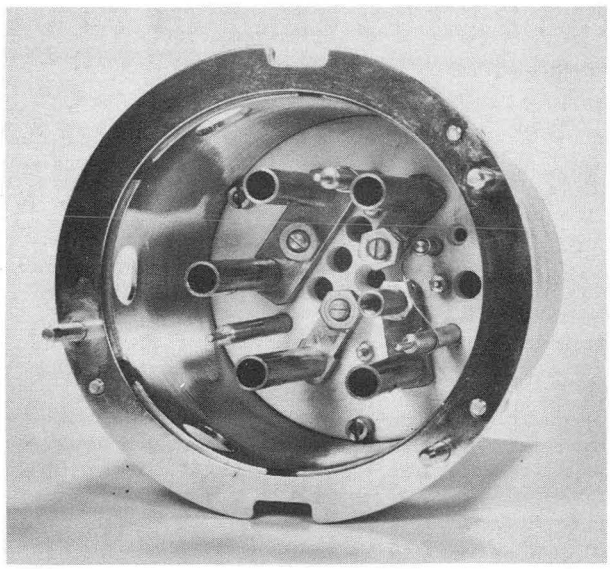

Fig. 3. Rear view of source.
(XBB 719-4254)

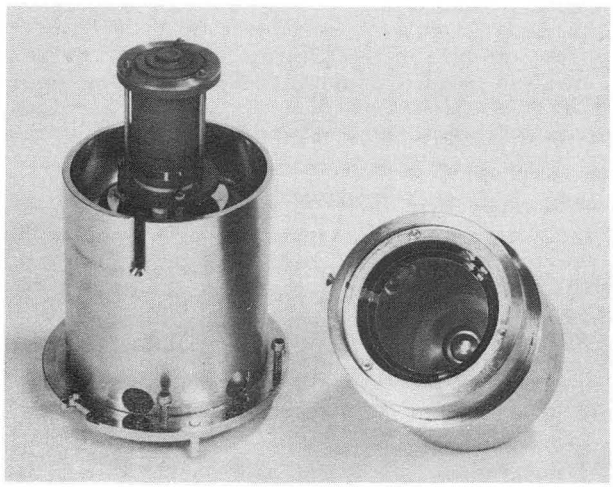

Fig. 4. Ion source without heat shields.
(XBB 719-4252)

screws need be loosened in order to remove the entire source from the socket. Another prepared source can be installed in a few seconds and pumpdown initiated as soon as the flange can be closed. Repeated use of several sources at high temperatures for hundreds of hours has yet to result in a failure of the basic plug or alignment system. All surfaces which must move relative to others are lubricated with molybdenum disulfide, tungsten diselenide or niobium diselenide, depending on the nature of the materials and their function. Even the copper-to-copper high-current plug contacts have remained free of any indication of sticking or wear.

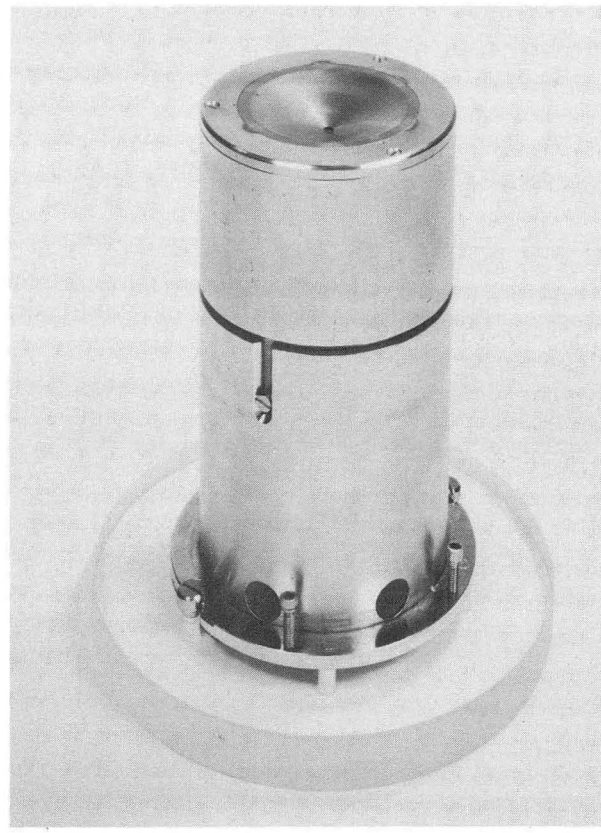

Fig. 5. Complete ion-source assembly.
(XBB 719-4255)

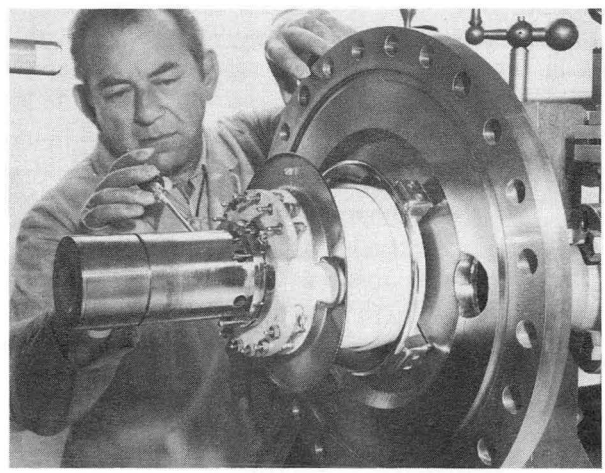

Fig. 6. Source in place in separator.
(XBB 719-4253)

Figure 2 shows the main insulator, contact mounting ring and the source mounting flange with the male socket pins in the center.

Figure 3 shows the rear of the main source

can with its aligning flange and pins as well as the female high-current plugs extending forward from the mounting insulator base.

Figure 4 is a view of the front of the ion source can, with a graphite oscillating electron-type plasma ion source in place. The heat shield assembly which covers the ion source when assembled is to the right.

Figure 5 shows a complete source assembly ready to plug in to the base plate and Fig. 6 is an overall view of the entire source region including the main vacuum flange.

A MOLECULAR BEAM ELECTRIC DEFLECTION APPARATUS*

P. Yarnell, A. J. Hebert, and K. Street, Jr.

The gas phase geometry of the metal dihalides, MX_2, poses an interesting problem in bonding theory, in that experimental results indicate that some of these molecules are bent and others are linear. A particularly interesting case is that of the alkaline earth dihalides, where whether a molecule is "bent" or "linear" depends in some cases on the nature of the halide ligand rather than on the central metal atom.[1]

Two different experimental methods have been the principle sources of information on the geometry of these molecules. Infrared absorption measurements on rare gas matrix isolated molecules are interpreted to indicate that the molecule is "bent" if a frequency is observed that can be assigned to the ν_1 vibration.[2] In experiments in which a molecular beam is deflected in an inhomogeneous electric field, "bent" molecules have states with positive Stark energies; these states can be refocused along the axis of a quadrupole electric field. In these experiments failure to observe a refocused beam is interpreted to indicate a "linear" molecule.[1] In some cases the two experimental methods do not agree-i.e., MgF_2 is reported "bent" by the matrix method[2] and "linear" by the deflection method.[1] The validity of the deflection results depends, critically, on the sensitivity for detecting a small refocused beam, while the effects of the matrix itself may influence the absorption results.

We have constructed a high-sensitivity electric deflection apparatus by modification of an existing molecular beam mass spectrometer.[3] The spectrometer consists of three sections: an oven chamber, a buffer chamber, and a detection chamber. It is used for determining the composition of molecular beams, and detection is by means of electron bombardment ionization and mass analysis with an Electronic Associates, Inc. quadrupole mass filter assembly. This apparatus was converted for deflection experiments by inserting an electric quadrupole assembly in the oven chamber. High sensitivity is achieved by placing the quadrupole deflecting field close to the oven source to give a large acceptance aperture. In addition, the high voltage to the quadrupole is repeatedly pulsed so that the output of the detector can be fed to a multichannel analyzer with a synchronous time base for signal averaging.

The performance of the apparatus was checked by studying molecules on which all previous experimental evidence agreed. BaF_2 is bent and ZnF_2 is linear as determined by both the matrix isolation method[4,5] and the electric deflection method.[1,6] Our experiments give the same results.

We have also run $SrCl_2$ and $SrBr_2$. Previous deflection experiments[7] indicate that $SrCl_2$ is bent and $SrBr_2$ linear. However, a polarizable ion model[8] predicts very similar bending potential curves for the two compounds, hence very similar structures. Our experiments give refocused beams for <u>both</u> molecules, indicating they are both <u>bent</u>.

Further experiments are planned for other metal di- and trihalides.

Footnote and References

*Abstract of LBL-600.

1. A. Büchler, J. L. Stauffer, and W. Klemperer, J. Am. Chem. Soc. 86, 4544 (1964).

2. D. E. Mann, G. V. Calder, K. E. Seshadri, D. White, and M. J. Linevsky, J. Chem. Phys. 46, 1138 (1967).

3. C. Melendres, UCRL-18344.

4. V. Calder, D. E. Mann, K. E. Seshadri, M. Allavena, and D. White, J. Chem. Phys. 51, 2093 (1967).

5. A. Loewenschuss, A. Ron, and O. Schnepp, J. Chem. Phys. 49, 272 (1968).

6. A. Büchler, J. L. Stauffer, and W.

Klemperer, J. Chem. Phys. 40, 3471 (1964).

7. L. Wharton, R. A. Berg, and W. Klemperer, J. Chem. Phys. 39, 2023 (1963).

8. P. Yarnell and K. Street, Jr., Polarizable Ion Model, unpublished results.

ELECTRON CYCLOTRON RESONANCE IN A PENNING ION SOURCE*

G. Fuchs,† J. Steyaert,‡ and D. J. Clark

Introduction

Calculations of charge state distributions[1] show that the output of highly charged ions from Penning sources is limited mainly by the low electron temperature (50 · · · 300 eV) if the source is run in the negative resistance mode (mode 2). For mode 1 we will show in this paper that the electron temperature can be increased considerably if the source is operated under cyclotron resonance conditions.

Recently electrons with higher energies than the corresponding applied arc voltage were detected in a Penning source by measuring the emitted Bremsstrahlung x-ray spectrum.[2] It was not clear from the measurements whether the highly energetic electrons were produced by energy spread due to collision of the primary electrons with the background plasma,[3] by heating due to two-stream instability, or by heating due to an interaction between two-stream instability and electron cyclotron resonance modes.[4,5] As will be shown in this paper, electron cyclotron modes can be excited if the cathodes are flat.

Experimental Device

The experimental setup, similar to that of Ref. 2, is shown in Fig. 1. The Penning source was the external heavy-ion source from the Berkeley 88-in. cyclotron,[6] run on nitrogen gas. The x-ray spectra were detected with a 3-mm thick Li-drifed silicon counter cooled with liquid nitrogen (resolution 150 eV at 6 keV). The pulses were amplified with a high resolution preamplifier and amplifier,[7] analyzed by a 400-channel analyzer (MCA) and read out on an x-y plotter. The experiment was arranged so that only the x rays emitted from the plasma (and not those produced by electrons striking the anode) were seen by the detector. The counting rate was so low that pile-up in the detector could be neglected. The background was negligible for energies E > 1 keV. A correction was made for the absorption of low-energy x rays in the 0.0125-mm-thick Be window. Because of the uncertainty in the window thickness, only x rays with energies E > 1 keV were taken for the evaluation.

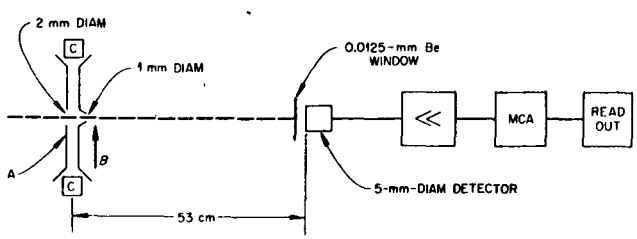

Fig. 1. Experimental setup.

(XBL 723-495)

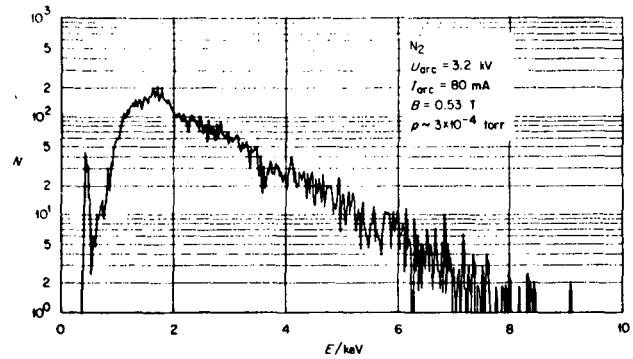

Fig. 2. Measured spectrum using flat cathodes (N = counts/min).

(XBL 723-493)

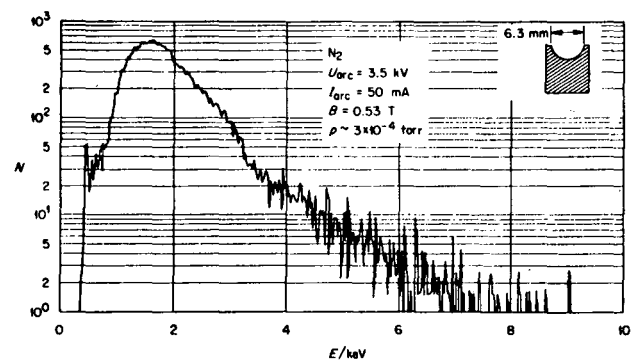

Fig. 3. Measured spectrum using cathodes with hemi-spherical holes.

(XBL 723-492)

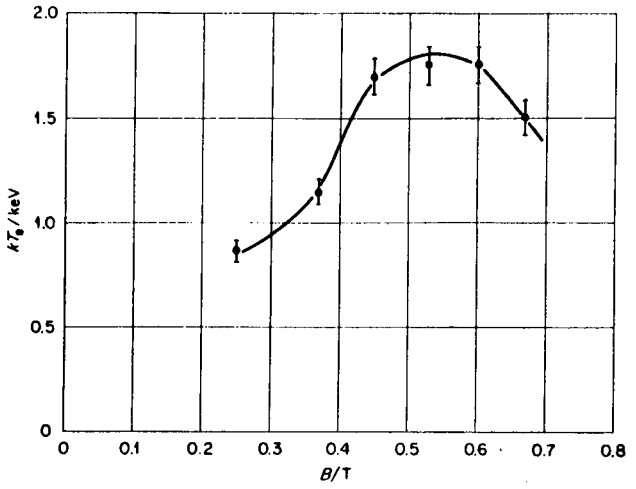

Fig. 4. Measured electron temperature versus magnetic field.

(XBL 723-494)

Measured Spectra

In Fig. 2 and 3, two typical x-ray spectra for two different cathode shapes are given. Figure 2 shows a spectrum for a flat cathode. This spectrum was taken at B = 0.53 T at the observed resonance (Fig. 4). The electron distribution function is in the observed part close to a Maxwellian one [compare Ref. 4]. In Fig. 3 a spectrum for cathodes with hemispherical holes is shown. The shape of the spectrum is different here in the ranges below and above the applied voltage (3.5 kV).

Electron Cyclotron Resonance

It is known from the experiments in ELMO[8] and BURNOUT[9] that plasma electrons can be heated to high temperatures by electron cyclotron resonance. To see if the conditions for electron cyclotron resonance can be met in a Penning source, we plotted the electron temperature versus magnetic field for a low value of gas flow and arc current. The electron temperature and electron density were obtained from the measured x-ray spectra multiplied by $h\nu$, using the equation:[10, 11, 12]

$$\frac{dj_E}{d\nu} = \sum_Z C\, n_e\, n_i^{Z+}\, Z^2\, (R/kT_e)^{1/2} \times \bar{G} \exp(-h\nu/kT_e). \qquad (1)$$

(This formula holds for a Maxwellian distribution of the electrons.) j_E is the x-ray energy flux emitted per unit volume, $h\nu$ is energy, $C = 1.7\times10^{-40}$ erg/cm^3, n_e and n_i^{Z+} are the densities of the electrons and the Z times charged ions respectively, R is the Rydberg energy, T_e the electron temperature, and $\bar{G}$ the free-free Gaunt factor which in our case is close to unity.[12,13] We take $\bar{G} \equiv 1$.

The electron temperature as obtained from the measured spectra and Eq. (1) is plotted in Fig. 4 versus magnetic field. T_e shows a maximum at B ≈ 0.53 T.

For a resonance between the two-stream instability and electron cyclotron modes, the cyclotron and the plasma frequencies have to be approximately equal:[4]

$$\omega_p = \left(\frac{e^2 n_e}{m_e \epsilon_0}\right)^{1/2} = \omega_c = \frac{Be}{m_e}, \qquad (2)$$

At the maximum of the electron temperature we find from Fig. 4 $\omega_c = 9\times10^{10}$ Hz. $\omega_p \approx 9\times10^{10}$ Hz was calculated from the measured density $n_e \approx 2.5\times10^{12}$ cm^{-3}. This good agreement suggests that we have indeed a resonance between two-stream instability and cyclotron modes.

Discussion and Conclusions

The plasma conditions we had in our experiment are not the same as those typically used for the Penning discharge as an ion source. The degree of ionization $n_e/n_0 \approx 1$ is too low so that no high ion currents, especially in high charge states,[1] can be expected.

In order to improve the output of the highly charged ions it would be necessary to increase the degree of ionization, which requires an increase in n_e. The source has then to be operated in the negative resistance mode.[6] An increase of n_e by a factor of 100 requires, because of Eq. (2), an increase of the applied magnetic field by a factor of 10, which is still feasible.

Footnotes and References

*In IEEE Trans. Nucl. Sci. April 1972, NS-19, No. 2.

†Visiting scientist at Oak Ridge National Laboratory, from University of Marburg, Germany; sponsored by the Bundesforschungsministerium and GSI Darmstadt.

‡On leave of absence from University of Louvain, Belgium and IISN, Belgium-NATO Fellowship.

1. G. Fuchs, IEEE Trans. Nucl. Sci. NS-19, No. 2 (1972).

2. M. L. Mallory, E. D. Hudson, and G. Fuchs, IEEE Trans. Nucl. Sci. NS-19, No. 2 (1972).

3. W. M. MacDonald, M. N. Rosenbluth, and W. Chuck, Phys. Rev. 107, 350 (1957).

4. I. Alexeff et al., Phys. Rev. Letters 10, 273 (1963).

5. T. H. Stix, Phys. of Fluids 7, 1960 (1964).

6. D. J. Clark, J. Steyaert, et al., IEEE Trans. Nucl. Sci. NS-18, 102 (1971).

7. D. A. Landis et al., IEEE Trans. Nucl. Sci. NS-18, 115 (1971).

8. R. A. Dandl et al., Nuclear Fusion 4, 344 (1964).

9. I. Alexeff, R V Neidigh, and W. F. Peed, Phys. Rev. 136A, 689 (1964).

10. G. Elwert, Z. Naturforschung 7A, 432 (1959).

11. T. F Stratton in Plasma Diagnostic Techniques, edited by Huddelstone and Leonhard (Academic Press, New York, 1965).

12. I. P. Shkarofsky, T. W. Johnston, and M. P. Bachynsky, The Particle Kinetics of Plasmas, Chap. 6 (Addison-Wesley, 1966).

13. W. J. Karzas and R Latter, Astrophys. J. Suppl. Series 6, 187 (1961).

14. B. L. Schram et al., Physica 32, 185 and 197 (1966).

15. M. J. van der Wiel et al., Physica 42, 411 (1969).

IMPROVEMENTS ON VAPOR PRESSURE OSMOMETER

M. Nakamura

A commercial vapor pressure osmometer has been available for several years. The osmometer has a special thermostated chamber in which two carefully matched heat-sensing thermistors are placed. The thermistors are part of a resistive bridge network, and molecular weight determinations as osmatic coefficients can be made indirectly by measuring the variation of resistance in one of the thermistors by changing a "Dekastat" to keep the bridge in balance. The drawback of this commercial unit was that its usable sensitivity was good only to ~0.01M. In addition the "Dekastat" had to be manipulated by hand which meant that constant attention was required and it was difficult to get information on time-dependent phenomena.

It was decided that we should automate the "Dekastat" control function and get the resistance variation information directly onto a chart recorder. This we have done by modifying most of the electronics which originally came with the instrument. Figure 1 shows a simplified diagram of the electronics system which evolved. We replaced the battery source for the bridge with a 1-kHz square wave generator to minimize problems of 60 Hz pickup. We also reduced the voltage supplied to the bridge to minimize self-heating in the thermistors. A switch was added to the bridge so that we could select either the original "Dekastat" or the relay-driven resistor chain for maintaining balance in the bridge. We replaced the original vacuum tube amplifier system since it was too slow and insensitive. The differential amplifier detects very small resistance variations (0.01Ω) in the sample thermistor. The lock-in amplifier further amplifies the difference signal and demodulates the signal with the synchronizing signal from the 1-kHz square wave generator. The voltage comparator signal is sampled 150 times a second and its output delivers either an add or subtract command to the reversible scaler. The scaler simultaneously drives relays which add or subtract resistance to the bridge thermistor leg and

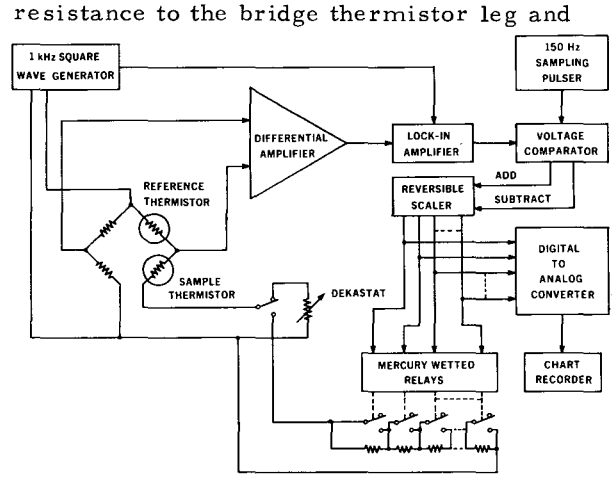

Fig. 1. Simplified diagram of electronics for Vapor Pressure Osmometer.

(XBL 715-3459)

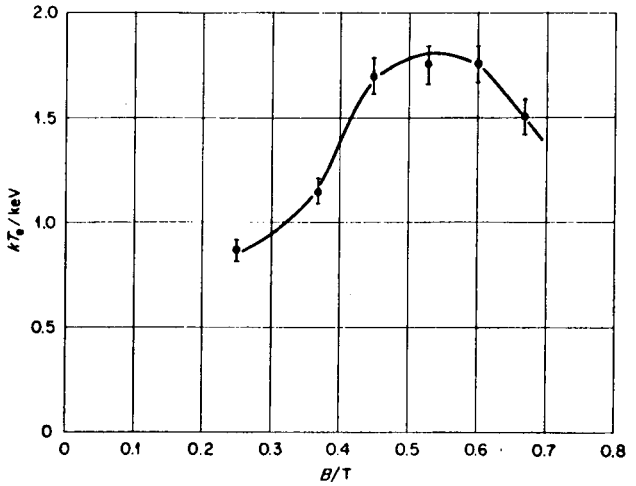

Fig. 4. Measured electron temperature versus magnetic field.

(XBL 723-494)

Measured Spectra

In Fig. 2 and 3, two typical x-ray spectra for two different cathode shapes are given. Figure 2 shows a spectrum for a flat cathode. This spectrum was taken at B = 0.53 T at the observed resonance (Fig. 4). The electron distribution function is in the observed part close to a Maxwellian one [compare Ref. 4]. In Fig. 3 a spectrum for cathodes with hemispherical holes is shown. The shape of the spectrum is different here in the ranges below and above the applied voltage (3.5 kV).

Electron Cyclotron Resonance

It is known from the experiments in ELMO[8] and BURNOUT[9] that plasma electrons can be heated to high temperatures by electron cyclotron resonance. To see if the conditions for electron cyclotron resonance can be met in a Penning source, we plotted the electron temperature versus magnetic field for a low value of gas flow and arc current. The electron temperature and electron density were obtained from the measured x-ray spectra multiplied by $h\nu$, using the equation:[10, 11, 12]

$$\frac{dj_E}{d\nu} = \sum_Z C\, n_e\, n_i^{Z+}\, Z^2\, (R/kT_e)^{1/2} \times \bar{G} \exp(-h\nu/kT_e). \qquad (1)$$

(This formula holds for a Maxwellian distribution of the electrons.) j_E is the x-ray energy flux emitted per unit volume, $h\nu$ is energy, $C = 1.7\times10^{-40}$ erg/cm^3, n_e and n_i^{Z+} are the densities of the electrons and the Z times charged ions respectively, R is the Rydberg energy, T_e the electron temperature, and $\bar{G}$ the free-free Gaunt factor which in our case is close to unity.[12,13] We take $\bar{G} \equiv 1$.

The electron temperature as obtained from the measured spectra and Eq. (1) is plotted in Fig. 4 versus magnetic field. T_e shows a maximum at B ≈ 0.53 T.

For a resonance between the two-stream instability and electron cyclotron modes, the cyclotron and the plasma frequencies have to be approximately equal:[4]

$$\omega_p = \left(\frac{e^2 n_e}{m_e \epsilon_0}\right)^{1/2} = \omega_c = \frac{Be}{m_e}, \qquad (2)$$

At the maximum of the electron temperature we find from Fig. 4 $\omega_c = 9\times10^{10}$ Hz. $\omega_p \approx 9\times10^{10}$ Hz was calculated from the measured density $n_e \approx 2.5\times10^{12}$ cm^{-3}. This good agreement suggests that we have indeed a resonance between two-stream instability and cyclotron modes.

Discussion and Conclusions

The plasma conditions we had in our experiment are not the same as those typically used for the Penning discharge as an ion source. The degree of ionization $n_e/n_0 \approx 1$ is too low so that no high ion currents, especially in high charge states,[1] can be expected.

In order to improve the output of the highly charged ions it would be necessary to increase the degree of ionization, which requires an increase in n_e. The source has then to be operated in the negative resistance mode.[6] An increase of n_e by a factor of 100 requires, because of Eq. (2), an increase of the applied magnetic field by a factor of 10, which is still feasible.

Footnotes and References

*In IEEE Trans. Nucl. Sci. April 1972, NS-19, No. 2.

†Visiting scientist at Oak Ridge National Laboratory, from University of Marburg, Germany; sponsored by the Bundesforschungsministerium and GSI Darmstadt.

‡On leave of absence from University of Louvain, Belgium and IISN, Belgium-NATO Fellowship.

1. G. Fuchs, IEEE Trans. Nucl. Sci. NS-19, No. 2 (1972).

2. M. L. Mallory, E. D. Hudson, and G. Fuchs, IEEE Trans. Nucl. Sci. NS-19, No. 2 (1972).

3. W. M. MacDonald, M. N. Rosenbluth, and W. Chuck, Phys. Rev. 107, 350 (1957).

4. I. Alexeff et al., Phys. Rev. Letters 10, 273 (1963).

5. T. H. Stix, Phys. of Fluids 7, 1960 (1964).

6. D. J. Clark, J. Steyaert, et al., IEEE Trans. Nucl. Sci. NS-18, 102 (1971).

7. D. A. Landis et al., IEEE Trans. Nucl. Sci. NS-18, 115 (1971).

8. R. A. Dandl et al., Nuclear Fusion 4, 344 (1964).

9. I. Alexeff, R V Neidigh, and W. F. Peed, Phys. Rev. 136A, 689 (1964).

10. G. Elwert, Z. Naturforschung 7A, 432 (1959).

11. T. F Stratton in Plasma Diagnostic Techniques, edited by Huddelstone and Leonhard (Academic Press, New York, 1965).

12. I. P. Shkarofsky, T. W. Johnston, and M. P. Bachynsky, The Particle Kinetics of Plasmas, Chap. 6 (Addison-Wesley, 1966).

13. W. J. Karzas and R Latter, Astrophys. J. Suppl. Series 6, 187 (1961).

14. B. L. Schram et al., Physica 32, 185 and 197 (1966).

15. M. J. van der Wiel et al., Physica 42, 411 (1969).

IMPROVEMENTS ON VAPOR PRESSURE OSMOMETER

M. Nakamura

A commercial vapor pressure osmometer has been available for several years. The osmometer has a special thermostated chamber in which two carefully matched heat-sensing thermistors are placed. The thermistors are part of a resistive bridge network, and molecular weight determinations as osmatic coefficients can be made indirectly by measuring the variation of resistance in one of the thermistors by changing a "Dekastat" to keep the bridge in balance. The drawback of this commercial unit was that its usable sensitivity was good only to ~0.01M. In addition the "Dekastat" had to be manipulated by hand which meant that constant attention was required and it was difficult to get information on time-dependent phenomena.

It was decided that we should automate the "Dekastat" control function and get the resistance variation information directly onto a chart recorder. This we have done by modifying most of the electronics which originally came with the instrument. Figure 1 shows a simplified diagram of the electronics system which evolved. We replaced the battery source for the bridge with a 1-kHz square wave generator to minimize problems of 60 Hz pickup. We also reduced the voltage supplied to the bridge to minimize self-heating in the thermistors. A switch was added to the bridge so that we could select either the original "Dekastat" or the relay-driven resistor chain for maintaining balance in the bridge. We replaced the original vacuum tube amplifier system since it was too slow and insensitive. The differential amplifier detects very small resistance variations (0.01Ω) in the sample thermistor. The lock-in amplifier further amplifies the difference signal and demodulates the signal with the synchronizing signal from the 1-kHz square wave generator. The voltage comparator signal is sampled 150 times a second and its output delivers either an add or subtract command to the reversible scaler. The scaler simultaneously drives relays which add or subtract resistance to the bridge thermistor leg and

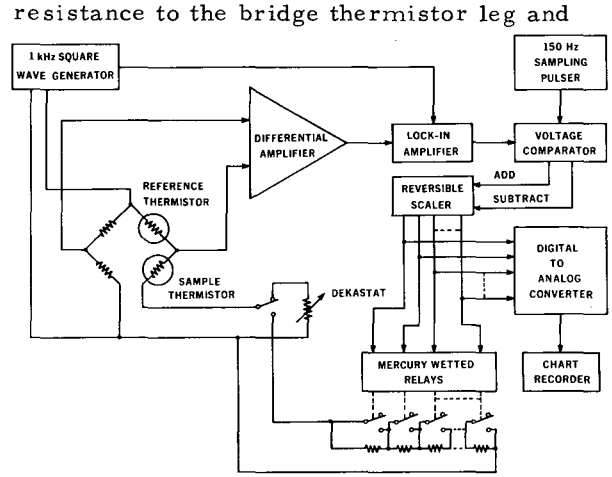

Fig. 1. Simplified diagram of electronics for Vapor Pressure Osmometer.

(XBL 715-3459)

drives a digital-to-analog converter whose output is fed to a chart recorder.

Osmometric determinations upon as low as 0.001 M organic solutions (at 25° C) can now be made. With the higher sensitivity and the continuous record kept by the chart recorder, we are able to observe phenomena which may have good and bad effects on the outcome of an experiment. Osmometer-chamber temperature variations due to the chamber heater turning on and off can be distinctly observed as well as room temperature and room and building pressure changes. The optimum voltage across the bridge was calculated and experimentally verified to have minimal self-heating effects and yet have sufficient error signal available to detect 0.01-Ω differences in the sample thermistor. Experimental procedures and techniques have been worked on and improved to minimize experimental errors.

A VOLTAGE-CONTROLLED MOTOR SPEED CONTROL

M. Nakamura

A motor-speed control was required for velocity selection in experiments to determine the chemical composition (monomer, dimer, etc.) of NaCN by recording the velocity distributions of NaCN on a multichannel analyzer. The experiment is described in detail elsewhere in this annual report.

The range of motor speeds is controllable from a few revolutions per second to 400 revolutions per second--the top speed of the two-phase hysteresis motor used in the experiment. The motor speed is controlled by using an analog signal which corresponds to the channel number of a multichannel analyzer. By using this technique, the motor speed and its corresponding channel number can be calibrated and reproduced to a few parts in ten thousand.

The motor-speed control is made up of a voltage-to-frequency converter, a flip-flop, a 90° phase shift, and an external power amplifier for driving the motor. The 90° phase shift is necessary for producing the proper signal for the second winding of the two-phase hysteresis motor. See Fig. 1. The motor-speed control is capable of controlling speeds far in excess of 400 revolutions per second, but we designed the upper limit to meet the top speed of the motor used in the experiment.

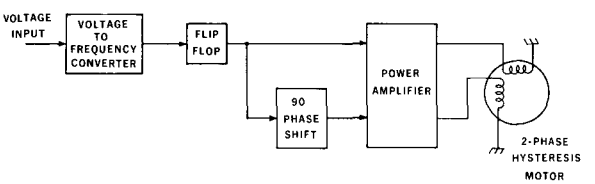

Fig. 1. Simplified block diagram of voltage-controlled motor speed control.
(XBL 723-491)

RELATIVE INTENSITY CALIBRATION OF A Ge(Li) GAMMA-RAY SPECTROMETER*

L. J. Jardine

The relative gamma-ray intensities of the eleven most intense transitions of ^{182}Ta in the energy range of 100-1300 keV were remeasured on a 10-cm^3 Ge(Li) detector. These results, together with other measurements),[1,2,3] are shown in Table I. The relative intensities are believed accurate to ±3% over the entire energy range and to ±1.5-2% over the smaller energy range of 1000-1300 keV.

^{182}Ta, in addition to ^{180m}Hf and ^{24}Na, were suggested as supplements to the IAEA standard intensity source set which is commonly used in the determination of the relative gamma-ray photopeak efficiency of Ge(Li) spectrometers. Relative and absolute gamma-ray intensities for ^{182}Ta, ^{180m}Hf, ^{24}Na, and the IAEA isotopes were included in tables in order to collect the best sets of data necessary to calibrate spectrometers over the energy range of 100-2750 keV to ±4%. As an example, these intensities were used to define the relative efficiency curve to ±4% of the Ge(Li) detector shown in Fig. 1.

It is of interest to note here that a recent compilation[5] (which is being currently updated) of the best energy values for many common gamma-ray energy standards in the range

Table I. Energies and relative intensities of ^{182}Ta in energy range 100-1300 keV.

E_γ [a]	Edwards et al. [1] I_γ [b]	White et al. [2] I_γ [c]	Sapyta et al. [3] I_γ [c]	Present work I_γ [c]
100.104 ± 0.002	40.2		40.7 ± 4.1	40.2 ± 1.0
152.435 ± 0.003	20.5 ± 0.8	21.3 ± 1.0	19.5 ± 2.0	20.5 ± 0.5
156.387 ± 0.003	8.04 ± 0.4	8.07 ± 0.4	7.5 ± 0.75	7.6 ± 0.2
179.393 ± 0.004	9.2 ± 0.4	9.57 ± 0.5	8.7 ± 0.9	8.8 ± 0.3
222.109 ± 0.005	22.5 ± 0.9	22.6 ± 1.2	21.2 ± 2.1	21.3 ± 0.55
229.322 ± 0.005	11.1 ± 0.5	10.9 ± 0.5	10.5 ± 1.1	10.3 ± 0.3
264.072 ± 0.009	10.8 ± 0.5	10.6 ± 0.4	10.3 ± 1.0	10.1 ± 0.3
E_γ [d]				
1121.298 ± 0.013		100.	100.	100.
1189.046 ± 0.013		47.4 ± 0.7	46.3 ± 3.2	46.5 ± 0.7
1221.399 ± 0.013		79.3 ± 1.2	77.3 ± 5.4	77.3 ± 1.2
1231.010 ± 0.013		33.4 ± 0.5	32.7 ± 2.3	32.8 ± 0.5

[a] Energies listed in keV are those reported by Edwards et al. [1]

[b] Intensities [1] are renormalized to the 100-keV transition of present work.

[c] Intensities are normalized to 1121-keV transition.

[d] The energies listed in keV are those reported by White and Birkett. [4]

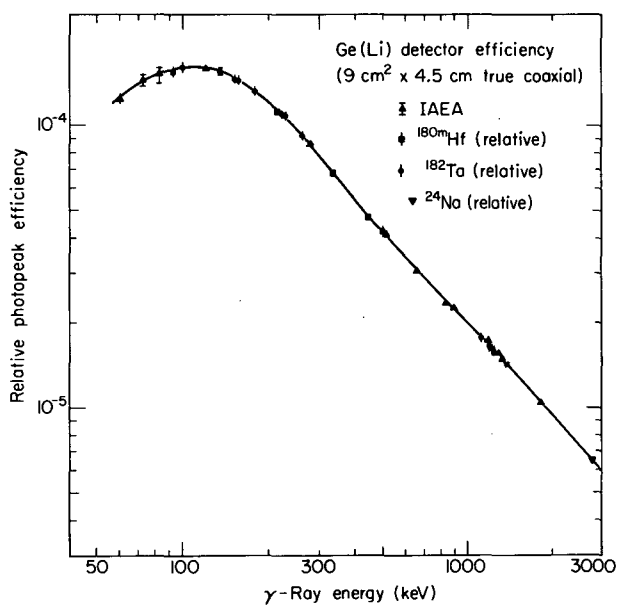

Fig. 1. The relative photopeak efficiency curve as a function of energy obtained using the isotopes and intensities reported.
(XBL 715-3459)

of 25-3452 keV was given in UCRL-20476. [6]

Footnote and References

*Condensed from Nucl. Instr. Methods 96, 259 (1971), and UCRL-20435 (May 1971).

1. W. F. Edwards, F. Boehm, J. Rogers, and E. J. Seppi, Nucl. Phys. A63, 97 (1965).

2. D. H. White, R. E. Birkett, and T. Thomson, Nucl. Instr. Methods 77, 261 (1970).

3. J. J. Sapyta, E. G. Funk, and J. W. Mihelich, Nucl. Phys. 139, 161 (1969).

4. D. H. White and R. E. Birkett, Nucl. Phys. A136, 657 (1969).

5. International Atomic Energy Agency, Vienna [Set of calibrated (to ≤ 1%) absolute intensity sources].

6. L. J. Jardine, Lawrence Radiation Laboratory Report UCRL-20476 (1971).

V. Thesis Abstracts

CYCLING ZONE ADSORPTION: SEPARATION OF GAS MIXTURES

Dwain E. Blum

(LBL-247)

A theoretical explanation is presented for cycling zone adsorption, a wave-propagating separation process utilized to effect separations of gaseous mixtures. Experimental results confirming the theoretical predictions are also included. The minor effect of finite mass transfer rates on the separative power was also investigated.

The addition of an isothermal adsorbent bed to a cycling zone adsorption process being fed a dilute mixture of adsorbing components is suggested to enhance the separation further. Elimination of the carrier gas was found not to alter the separative power of the process significantly.

A frequency response method was used for determination of equilibrium distribution coefficients for the fluid-solid adsorbing systems investigated.

ABSORPTION OF N_2O_3 INTO WATER

Clarence E. Corriveau, Jr.

(UCRL-20479)

The rates of the simultaneous absorption of NO_2 and NO into water were measured experimentally, using a five-sphere, laminar film, laboratory absorber. The data indicate that the two compounds enter the liquid film as N_2O_4 and N_2O_3 respectively, the rates of solution per unit interfacial area in each instance being governed by the solubility of the unreacted oxide and by its chemical rate of reaction with water. The data indicate that the half-lives of dissolved N_2O_4 and N_2O_3 are approximately 34 and 0.59×10^{-4} sec, respectively, and that N_2O_4 is much more soluble than is N_2O_3. The result is that the rate of absorption per unit interfacial partial pressure is about the same for the two oxides.

Industrial applications of the new data are discussed.

CALORIMETRIC DETERMINATION OF THE TRANSITION ENERGY OF URANIUM – 235m

Barbara Ellen Bailey Culler

(LBL-221)

The isomeric state of uranium-235 decays by internal conversion, emitting electrons of extremely low energy. Hence, the transition energy is difficult to measure by conventional means. A microcalorimeter was designed and constructed to measure directly the heat produced by the decay. The value obtained for the transition energy was 572 ± 33 eV.

The half life for alpha decay of the isomer was calculated to be 5.9×10^8 years. In addition the probability of Coulomb excitation of the isomeric state by interstellar protons was estimated and found to be negligible. These two results eliminate a possible uranium-235 removal mechanism in space, and substantiate the use of the ratio $^{235}U/^{238}U$ to determine the age of the galaxy.

ISOSPIN PURITY AND VIOLATIONS OF MIRROR SYMMETRY: THE BETA-DELAYED PROTON DECAY OF ^{9}C, ^{13}O, ^{17}Ne, AND ^{33}Ar

John Edward Esterl

(UCRL-20480)

Beta-delayed proton studies of some light $A = 4n+1$, $T_z = -3/2$ nuclei have been made. Supplementary γ-ray measurements were made where necessary. A fast gas-transport system and particle-identification techniques combined to produce proton spectra in which the resolution was limited by the momentum spread of the preceding beta-ray. The half-lives measured are: ^{9}C, 126.5 ± 1.0 ms; ^{13}O, 8.95 ± 0.20 ms; ^{17}Ne, 109.0 ± 1.0 ms; and ^{33}Ar, 173.0 ± 2.0 ms. Precise level energies in ^{17}F and ^{33}Cl have been measured and a discrepancy concerning levels in ^{17}F has been resolved. Absolute log ft-values for the β-decay branches of ^{13}O, ^{17}Ne, and ^{33}Ar have been obtained; these measurements indicate violations of mirror symmetry in beta-decay. They also indicate that the lowest $T = 3/2$ state in ^{17}F has an isospin purity of $\geq 95\%$, in contrast to the lowest $T = 3/2$ state in ^{33}Cl, for which an impurity of $\sim 10\%$ is suggested. Circumstantial evidence indicates that four $T = 1/2$ states within 350 keV of the analogue state cause the impurity observed in ^{33}Cl.

DECAY OF THE $^{50}Cr^{*}$ COMPOUND NUCLEUS FORMED BY THE NUCLEAR REACTIONS $^{3}He + ^{47}Ti$, $^{4}He + ^{46}Ti$ $^{16}O + ^{34}S$, $^{18}O + ^{32}S$, AND $^{22}Ne + ^{28}Si$

Man K. Go

(UCRL-20483)

Experimental excitation functions have been measured for nuclear reactions $^{3}He + ^{47}Ti$, $\alpha + ^{46}Ti$, $^{16}O + ^{34}S$, $^{18}O + ^{32}S$, and $^{22}Ne + ^{28}Si$. The observed products are ^{48}Cr and ^{48}V, and for the ^{3}He- and α-induced reactions, the ^{49}Cr production cross sections are also measured. The excitation function $^{46}Ti(\alpha, p)^{49}V$ is also obtained. Simple theoretical calculation based on the compound-statistical model is performed to calculate the excitation functions from ^{3}He and α reactions and found to agree reasonably with experiment.

The observed cross sections from the ^{18}O- and ^{22}Ne-induced reactions have been strongly suppressed by the Coulomb barrier. The $^{47}Ti(^{3}He, n)^{49}Cr$ excitation function is similarly found to be an order of magnitude smaller than that for the corresponding α-induced reaction.

A displacement of the experimental excitation functions relative to one another along the excitation energy axis is observed and explained by the effect of angular momentum upon the de-excitation of the compound nucleus. The shapes and magnitudes of the ratios of the various experimental excitation functions indicate the compound-nucleus model can be applied to these reactions. Bohr's independence postulate is valid, if corrections are made for the difference in angular momentum of the different entrance channels.

Recoil ranges for ^{49}Cr and ^{48}Cr from $\alpha + ^{46}Ti$ reaction are obtained by measuring the recoil distribution of these nuclei from a thick target. These recoil ranges are found to be consistent with the calculation based on the theory of Lindhard, Scharff, and Schiøtt for a compound-nucleus reaction.

THE DECAY OF T = 2 STATES IN T_z = 0 NUCLEI

George William Goth

(LBL-224)

The particle decays of the lowest T = 2 states of ^{20}Ne, ^{24}Mg, ^{28}Si, ^{32}S, ^{40}Ca and ^{56}Ni have been measured. The states were populated through the (p,t) reaction on T = 1 targets and their isospin forbidden particle decays were measured by observing coincidences between tritons and protons [E_p(max) = 2.6 - 3.7 MeV] and/or alpha-particles [E_α(max) = 1.8 - 12.0 MeV]. These experiments established that particle decay accounts for almost all of the total widths of the states ($\Gamma_{particle}/\Gamma = 0.99 \pm 0.11$). The major decay modes of the states were found to be: ^{20}Ne($\alpha_1+\alpha_2$, $\alpha_3+\alpha_4$); ^{24}Mg(p_0); ^{28}Si(α_0); ^{32}S(p_0); ^{40}Ca(α_0); ^{56}Ni(p_0). Comparison of these experiments with results from resonance reaction studies shows qualitative agreement. Simple Coulomb calculations were performed for the decay of the T = 2 state in ^{40}Ca; these assumed pure shell model configurations and considered isospin mixing in only the (1d, 1f) shells. They failed to predict the relatively large T = 2 isospin admixtures necessary to explain the observed alpha-decay of this state.

KINETICS OF THE REACTION OF CARBON DIOXIDE WITH HYDROXYL ION

Shirley Hsu

(UCRL-20461)

The kinetics of the combination of carbon dioxide and hydroxyl ion is of considerable industrial interest. The reaction is second-order in the forward direction

$$CO_2 + OH^- \xrightarrow{K} HCO_3^-$$

and the rate is given by:

$$\text{Rate (g mole}/\ell\text{ s)} = -\frac{d(CO_2)}{dt} = K(CO_2)(OH^-)$$

where K is the second-order rate constant for OH^-, (ℓ/g mole s), (CO_2) and (OH^-) are the concentrations of CO_2 and OH^- at any stage of the reaction respectively, g mole/ℓ.

The data of the kinetic constant K in various temperatures and salt solutions are very useful in the calculations for designing the process of using hydroxide solutions to remove carbon dioxide from gas mixtures. The calculation of the actual rate of the reaction between carbon dioxide and hydroxyl ion in salt solutions is very complicated because of the effect of ionic strength and the nature of salts. A discussion on the theoretical approach to the calculation will be given in the next section.

The value of K has been measured by some workers. Except the data reported by Pinsent and Nijsing, few data are useful for industrial applications. The kinetic constant K is strongly affected by the ionic strength and the nature of the ions present and, therefore, its value cannot be accurately predicted for the salt solutions in which it has not been measured. A review of the methods which have been used for measuring the kinetic constant will be given in a later section. The results obtained by various methods will be compared and the best method for measuring K in the salt solutions will be discussed.

EXPERIMENTAL INVESTIGATION OF THE ELECTRON CAPTURE DECAY OF ^{210}At AND ^{209}At: THE LEVEL SCHEMES OF ^{210}Po AND ^{209}Po

Leslie James Jardine

(LBL-246)

The nuclear levels of ^{210}Po and ^{209}Po populated by the electron-capture decay of ^{210}At and ^{209}At have been studied. Experimental level schemes have been constructed by using data obtained from gamma-ray singles, internal conversion electron, and gamma-gamma coincidence measurements with high resolution Ge(Li) and Si(Li) spectrometers.

For the case of ^{210}Po, present data have been used to define twenty-three levels. The multipolarity of thirty-six transitions in ^{210}Po have been determined and combined with data from recent reaction studies to assign spins and parities to the levels. All levels arising from the two-proton configuration $(h_{9/2})^2$ and from the multiplets due to the configurations $(h_{9/2}\, f_{7/2})$ and $(h_{9/2}\, i_{13/2})$, except for the lowest spin members, have been identified. The level structure is compared with two-proton shell model calculations and experimental transition probabilities for gamma decay of the $(h_{9/2}\, f_{7/2})$ and $(h_{9/2})^2$ proton multiplets are compared with predictions using several sets of shell model wave-functions. Evidence is presented which locates the 3^- collective level in ^{210}Po at 2400 keV above the ground state. The electron-capture transition rates to odd parity levels above 2.9 MeV are discussed in terms of neutron-neutron and proton-proton particle-hole excitations of the ^{208}Pb core. A weak-coupling calculation using experimental data of neighboring isotopes in the lead region is made for the energies of the 3^- and 5^- core states of ^{210}Po.

For the case of ^{209}Po, twenty-levels have been defined by the present data. Multipolarities of thirty-one transitions in ^{209}Po have been determined and used to assign spins and parities to the levels. Five states arising from the odd neutron in ^{209}Po have been assigned by a comparison of the experimental level spectrum and the decay characteristics of levels with a shell model calculation and the levels in ^{207}Pb. A weak coupling calculation using experimental data from isotopes in the lead region to approximate residual interactions was found to explain the level structure of ^{209}Po below 2 MeV.

ASYMMETRIC INTERACTIONS AND THE SEPARATION OF OPTICAL ISOMERS BY OPTICALLY ACTIVE SORBENTS

John M. Krochta

(UCRL-20471)

The stereospecific molecular structure of living things has important consequences in the synthesis of biochemicals for food supplementation, pharmaceutical purposes and other biological uses. The optical isomers obtained must usually be separated, because man and other organisms can most often utilize only one of them. In this work, stereospecific sorption has been studied as an alternate method to better known procedures for separating optical isomers.

In an exploratory study, pure optical isomers of aspartic acid were found to dissolve in measurably different amounts into aqueous solutions of other amino acids, used as optically active solvents. The largest observed effect was a 1.1% difference for the aspartic acid isomers in 0.05M glutamic acid. Such differences in optical-isomer solubilities are explained by differences in binary association between solute and solvent, caused by structural effects which alter the bonding strength at the third of three points of intermolecular contact. Analysis of solubility and activity data yields a value close to 0.20 $(\text{moles/liter})^{-1}$ for the dimerization constant describing quadrupole formation between two different amino acids. Minimum-value equilibrium constants (neglecting self-dimerization) calculated for several other cases of inter-dimer formation are significantly greater.

The solubility results indicated that amino acids attached to a polymer matrix would be

effective in resolving other amino acid optical isomers. The synthesis of such a material consisted of three steps: imine formation by reacting previously formulated polystyrene beads with an amino acid ester, reduction of the imine with $NaBH_4$, and hydrolysis of the attached ester. In separate chromatographic experiments using short columns containing L-tyrosine, L-glutamic acid and L-aspartic acid resins, respectively, the optical isomers of DL-mandelic acid have been partially separated in methanol. Samples with isomer ratios up to 1.10 have been obtained with the L-tyrosine resin. All attempts to separate amino acid optical isomers on the amino acid resins, in both methanol and water, have failed. The bound amino acid appears less accessible for complex formation, and shows effectively zero retention of most dissolved amino acids.

A second type of asymmetric sorbent was synthesized by hydrolyzing chitin, poly(N-acetyl-D-glucoseamine) to chitosan, poly(D-glucoseamine), a weak base. This was followed by crosslinking with epichlorohydrin to preserve the structure of chitosan in acidic solutions. Chitosan has been used successfully to obtain partial separations of the optical isomers of DL-mandelic acid; samples with isomer ratios up to 1.98 have been achieved in methanol. Of the amino acids, only aspartic acid and glutamic acid show a tendency to sorb onto chitosan, but no optical isomer separation was detected in these cases. However, chitosan displays a striking ability to separate the optical isomers of N-acylated amino acids. Samples with isomer ratios up to 2.9 were obtained in a partial separation of the optical isomers of N-acetyl-DL-phenylalanine in methanol. The conditions under which a complete separation should occur have been predicted, and are quite accessible.

SYSTEMATICS OF THE DIRECT (p, α) REACTION

Creve Cowen Maples, Jr.

(LBL-253)

The (p, α) reaction was investigated on ^{16}O, ^{15}N, ^{14}N, ^{13}C, and ^{12}C targets at proton energies between 43.7 and 54.1 MeV. Levels were examined in the residual nuclei up to a maximum of from 15 to 22 MeV in excitation and angular distributions were obtained to approximately 90° c.m. The reaction was found to proceed predominantly via a direct pickup mechanism and to strongly populate only levels consistent with this mechanism. The angular distributions exhibited a strong dependence on the value(s) of J, the total angular momentum transfer. For a given J, the shapes of the distributions were relatively uniform and reasonably independent of kinematic effects. The (p, α) reaction was also observed to preferentially populate higher spin levels. As a consequence of these properties a number of p-shell levels were identified, some of which were previously unreported, and spin and parity assignments were made.

The experimental results were found to be in excellent agreement with the general expectations of theory. The DWBA calculations, assuming a triton transfer, were able to predict a pronounced J-dependence in the (p, α) reaction which, at forward angles ($\theta_{c.m.} < 70°$) was both consistent and uniform. The results of these calculations reproduced the qualitative features of the angular distributions although, in general, the predictions displayed a more rapid decrease in the cross section with angle than was observed. The effect of non-local and finite-range corrections to the calculations were examined but were found to be unimportant.

UTILIZATION OF ALGAE FOR WATER PURIFICATION AND PROTEIN PRODUCTION

Steven Frank Miller

(LBL-289)

This thesis contains a broad ecological sketch as well as specific design information for solving problems of water purification and food production. A plant is designed

utilizing algae as living ion exchange beads for removal of Sr from low level radioactive waste streams. Preference of Sr over Ca by Pandorina morum Borey is found to be 1.2 to 1 with a higher than expected value of 1.4 milliequivalents of cation exchange sites available per gram dry weight of algae. Plant economics based on utilization of conventional separators are found to be unpromising.

A "Phototactic" separation device is designed and data presented for this novel means of harvesting algae at a possible reduced cost. Cheap algal harvesting also has implications for algal agriculture. Pandorina was analyzed for protein content and found promising. Methods of Pandorina culture are discussed briefly.

A novel laboratory algal growth reactor with an externally falling cooling film is also presented.

MASS TRANSFER COEFFICIENTS AND INTERFACIAL AREA FOR GAS ABSORPTION BY AGITATED AQUEOUS ELECTROLYTE SOLUTIONS

Campbell W. Robinson

(UCRL-20472)

In order to design or optimize the operation of stirred-tank gas absorbers, such as are used for the submerged cultivation of aerobic microorganisms wherein oxygen is supplied by mass transfer from dispersed air bubbles, it is necessary to be able to characterize the oxygen mass transfer capabilities in terms of the physicochemical properties of the aqueous phase, the agitation power input, and the aeration rate. The oxygen mass transfer capability of a particular tank can be described in terms of the overall volumetric mass transfer coefficient, $K_{L4}a$.

$K_{L4}a$ measurements were made in several aqueous electrolyte solutions of varying ionic strength over a wide range of agitation-aeration intensity in a 2.5 litre fully-baffled stirred tank having standard geometric ratios and equipped with a turbine-type impeller. Both steady-state and unsteady-state experimental methods were applied, utilizing a dissolved oxygen probe to measure the aqueous-phase oxygen tension or its rate of change. Unsteady-state oxygen probe response methods are described which permit measurement of $K_{L4}a$ with a minimum of experimental complexity. Mathematical analysis of and computer solutions for probe response are given.

$K_{L4}a$ values are reported as a function of the agitation power input per unit volume (P_G/V_L), superficial gas velocity (v_S), and solution ionic strength. The results indicate that the ionic strength has a pronounced effect on the value of $K_{L4}a$ at constant P_G/V_L and v_S; the effect of ionic strength heretofore has not been explicitly described in the literature. A generalized correlation for the prediction of $K_{L4}a$ for electrolyte solutions or for water is given for the particular type of stirred tank used. Physical absorption results are compared to oxygen absorption-with-reaction results obtained from the copper-catalysed sulphite oxidation method.

A new simultaneous measuring technique involving concurrent chemical absorption of carbon dioxide and desorption of oxygen is developed for separately evaluating the liquid-phase oxygen mass transfer coefficient, k_{L4}, and the specific interfacial area, a. Results from three different non-viscous aqueous electrolyte solutions show that at high agitation power input levels, such that the average gas bubble diameter is between 0.02 and 0.25 cm, k_{L4} decreases with increasing P_G/V_L. This behavior is in contrast with the results of others at lower agitation levels or in non-electrolytic liquids, but is in general agreement with previous results for the behavior of single bubbles or bubble swarms having the same range of average bubble diameter produced in viscous, non-electrolytic aqueous solutions.

THREE-COMPONENT ION-EXCHANGE IN FIXED BEDS APPLICATION TO PRE-TREATMENT OF SALINE-WATER EVAPORATOR FEED

Angelo G. Sassi

(LBL-299)

The existing column-performance theory for multicomponent ion exchange utilizes the local-equilibrium conditions to determine the limiting concentration profiles inside the column, and in the effluent. These profiles contain a series of constant-composition plateaus with intervening transitions; the total number of transitions between feed and presaturant is one less than the total number of components. The actual shapes of transitions can then be calculated from nonequilibrium theory.

Sea-water softening by ion-exchange as a pretreatment before distillation removes scale-forming calcium compounds. Regeneration of the exhausted ion-exchange resin can be carried out using reject evaporation-brine, two or four times as concentrated as sea water. In this report, sea-water softening is examined as a three-component system involving calcium, magnesium, and sodium ions.

Equilibrium theory is applied to this system for a number of experimental saturation and regeneration runs at different operating conditions. Reported effluent-concentration-histories, involving stoichiometric values of throughput parameter for each transition and limiting concentration levels of each plateau, are compared with the predicted plateaus and transitions.

The nonequilibrium or dynamic behavior is approximated by a binary system in which a sodium-magnesium gross-ion counterdiffuses against calcium. The experimental calcium-concentration histories are matched to the theoretical binary master curves within the plateau-zone limits identified by equilibrium theory. The resulting numbers of reaction units (or values of mass-transfer coefficients) are used to identify internal diffusion as the mechanism controlling the rate of mass-transfer. The contribution of fluid-phase pore diffusion to the mechanism of internal transport is found to be negligible compared to solid-phase diffusion. The results obtained for regeneration steps are found consistent with those for softening steps.

OPTICAL STUDIES OF LANTHANIDE AND ACTINIDE IONS IN CALCIUM FLUORIDE

James Joseph Stacy

(LBL-281)

Optical absorption and thermoluminescence measurements were used to study the effects of γ-irradiation on trivalent actinide ions in CaF_2. Thermoluminescent glow curves for Np, Pu, Am and Cm (and, for comparison, the lanthanides Er, Ho and Tm) were measured between 100° and 300°K. These were found to be remarkably similar, with glow peaks occuring at nearly the same temperatures for each of the ions. The activation energies for each of the glow peaks were estimated. High resolution measurements of the spectra of the thermoluminescence showed that the emission is identical to the fluorescence of the trivalent ions, and determines the site symmetry of the emitting ion. Evidence was presented that the glow emission below 300°K originates from trivalent actinide ions in cubic sites. In the model proposed to explain these data, irradiation at 77°K produces hole traps and electrons which are localized near cubic Ac^{3+} ions. Heating allows a hole to diffuse to the site of a localized electron. The hole and extra electron recombine, leaving an excited trivalent actinide ion. Decay of this ion to its ground state results in the observed thermoluminescence.

When the Ac^{3+}-CaF_2 crystals were irradiated at 300°K, the actinide ion was oxidized to the tetravalent state. In the model proposed, heating allows electrons which had become trapped in the lattice to recombine with the Ac^{4+} ions. The decay of the newly formed Ac^{3+} ion to its ground state results in the observed thermoluminescence.

The optical Zeeman rotation spectra were taken of some selected transitions in Am^{3+}, Cm^{3+}, and Nd^{3+} embedded in CaF_2. Only

symmetry sites arising from tetragonal compensation could be positively identified, although there was evidence for the existence of lower symmetries. This technique is of general applicability to problems of non-equivalent sites and provides a more positive identification than Zeeman studies restricted to a few crystallographic directions.

VI. 1971 Publications

1971 Publications

Papers Published and UCRL Reports Issued, 1971

ALBURGER, D. E., (See Cerny, J., LBL-240)

ALEXANDER, E. C., Jr., R. S. Lewis, J. H. Reynolds, and M. C. Michel
Plutonium-244: Confirmation as an extinct radioactivity
UCRL-20482, May 1971
Science 172, 837 (1971)

ALLRED, D., (See Esterl, J. E., UCRL-20400)

ANDERBERG, D. H., (See Clem, R. G., UCRL-20457)

ANDERBERG, D. H., (See Clem, R. G., UCRL-20457-Rev.)

ASARO, F., I. Perlman, and M. Dothan
An introductory study of mycenaean IIIC1 ware from Tel Ashdod
LBL-231, August 1971
Archaeometry 13, 169 (1971)

ASARO, F., (See Bowman, H. R., UCRL-20403)

ASARO, Frank, (See Bowman, Harry, UCRL-20490 Abstract)

ASCUITTO, R. J., N. K. Glendenning, and B. Sørensen
Twice double-transfer in inelastic proton scattering process involving collective pairing states, studied in a coupled channels formalism
UCRL-20496, June 1971
Nucl. Phys. A170, 65 (1971)

ASCUITTO, R. J., and N. K. Glendenning
Quantum mechanical treatment of particle transfer between heavy ions near the Coulomb barrier in the presence of Coulomb excitation
LBL-233, September 1971
Nucl. Phys.

ASCUITTO, R. J., N. K. Glendenning, and B. Sørensen
The importance of indirect transition on (p, t) reactions on deformed nuclei
LBL-248, October 1971
Nucl. Phys.

BACHER, A. D., (See de Swiniarski, R., LBL-201)

BACHER, A. D., (See Plattner, G. R., LBL-269)

BACHER, A. D., G. R. Plattner, H. E. Conzett, D. J. Clark, H. Grunder, and W. F. Tivol
Polarization and cross-section measurements for p-^{4}He elastic scattering between 20 and 45 MeV
LBL-280, November 1971
Phys. Rev. C 5, 1147 (1972)

BACHER, A. D., E. A. McClatchie, M. S. Zisman, T. A. Weaver and T. A. Tombrello
Observation of the 14 MeV resonance in ^{12}c(p, p)^{12}C with molecular ion beams
UCRL-20903, June 1971
Nucl. Phys. A181, 453 (1972)

BACON, F., J. A. Barclay, W. D. Brewer, D. A. Shirley, and J. E. Templeton
A temperature-independent spin-lattice relaxation time in metals at low temperatures
UCRL-20465, March 1971
Phys. Rev. B 5, 2397 (1972)

BACON, F., G. Kaindl, H. -E. Mahnke, and D. A. Shirley
Magnetic moment of the 12^- isomer of ^{196}Au
LBL-239, September 1971
Phys. Letters 37B, 181 (1971)

BACON, F., G. Kaindl, and H. -E. Mahnke
Magnetic moment of the $13/2^+$ isomer of ^{195}Pt
LBL-264 Abstract, November 1971
Meeting of the American Physical Society, San Francisco, California, January 31 - February 3, 1972

BACON, F., H. Haas, G. Kaindl, and H. -E. Mahnke
Magnetic hyperfine fields at bismuth in iron and nickel
LBL-603, December 1971
Physics Letters - A

BARCLAY, J. A. and H. Gabriel
Nuclear Spin Relaxation Rates by NMR on Oriented Nuclei; $Co^{60}Co$
UCRL-20433, January 1971
J. Low Temp. Phys. 4, 459 (1971)

BARCLAY, J. A., (See Bacon, F., UCRL-20465)

BENDER, C. F., P. K. Pearson, S. V. O'Neil, and H. F. Schaefer III
Potential energy surface including electron correlation for the chemical reaction $F + H_2 \rightarrow FH + H$. I. Preliminary surface
LBL-250, October 1971
J. Chem. Phys.

BENDER, C. F., (See Liskow, D. H., LBL-290)

BENDER, C. F., (See Liskow, D. H., LBL-291)

BLUM, D. E.
Cycling Zone Adsorption
Separation of gas mixtures
LBL-247, September 1971
Ph. D. Thesis

BONDYBEY, V., P. K. Pearson, and H. F. Schaefer III
Ground and excited electronic states of neon hydride
LBL-258, November 1971
J. Chem. Phys.

BORSIG, M. V., and M. Weigel
Effect of nonlocal forces on the integrated cross section of photonuclear reactions
LBL-244, October 1971
Phys. Rev. Letters

BOWMAN, H. R., J. G. Conway, and F. Asaro
Atmospheric lead and bromine concentration in Berkeley, Calif.
UCRL-20403, April 1971
Environmental Sci. and Tech.

BOWMAN, H. F. Asaro, and I. Perlman
Chemical variations in lava flows
UCRL-20490 Abstract, May 1971
Pacific Conference on Chemistry and Spectroscopy, Anaheim, Calif., 18-20 October 1971

BOWMAN, H. R., (See Wilhelmy, J. B., LBL-256)

BOWMAN, T. D., (See Eppley, Richard E., LBL-272 Abstract)

BREWER, W. D., (See Bacon, F., UCRL-20465)

BROWN, S., (See Kenjo, T., LBL-249)

DAVIS, D. W., and D. A. Shirley
Splitting in nitrogen and oxygen 1s photoelectron peaks in two paramagnetic molecules: Spin density implications
UCRL-20485, May 1971
J. Chem. Phys. 56, 669 (1972)

DAVIS, D. W., D. A. Shirley, and T. D. Thomas
K-electron binding energy shifts in fluorinated methanes and benzenes: comparison of a CNDO potential model with experiment
LBL-216, August 1971
J. Chem. Phys. 56, 671 (1972)

DAVIS, D. W., D. A. Shirley, and T. D. Thomas
X-ray photoelectron spectroscopy of fluorinated benzenes
LBL-270, November 1971
J. Am. Chem. Soc.

DAVISON, C. C., R. D. Giauque, and J. D. Clark
Two chemical groups of dichroic glass beads from West Africa
UCRL-20474, April 1971
Man

de BOER, J., (See Stephens, F. S., UCRL-20477)

de SWINIARSKI, R., A. D. Bacher, F. G. Resmini, G. R. Plattner, D. L. Hendrie, and J. Raynal
Determination of deformation parameters of ^{20}Ne and ^{22}Ne by inelastic scattering of polarized protons
LBL-201, July 1971
Phys. Rev. Letters

DIAMOND, R. M., (See Maier, K. H., UCRL-19593)

DIAMOND, R. M., (See Leigh, J. R., UCRL-20448 Abstract)

DIAMOND, R. M., G. D. Symons, J. L. Quebert, K. H. Maier, J. R. Leigh, and F. S. Stephens
Lifetimes of ground-band states in ^{154}Sm
UCRL-20463, March 1971
Nucl. Phys.

DIAMOND, R. M., (See Stephens, F. S., UCRL-20477)

DIAMOND, R. M., (See Maier, K. H., UCRL-20481)

DIAMOND, R. M., (See Maier, K. H., LBL-202)

DIAMOND, R. M., (See Jensen, C. H., LBL-225)

DIAMOND, R. M., (See Pühlhofer, F., LBL-229 Abstract)

DIAMOND, R. M., (See Maier, K. H., LBL-243)

DIAMOND, R. M., (See Kenjo, T., LBL-249)

DIAMOND, R. M., (See Maier, K. H., LBL-276)

DOEBLER, R. E., (See Guile, Jean, LBL-257 Abstract)

DOTHAN, M., (See Asaro, F., LBL-231)

DROŻDŻYŃSKI, J., and J. G. Conway
Low temperature absorption spectrum of uranium(+3) formate energy level scheme of uranium(+3)
LBL-218, August 1971
J. Chem. Phys. 56, 883 (1972)

FAIVRE, J.-C., (See Harvey, B. G., UCRL-20454)

FAIVRE, J.-C., (See Harvey, B. G., LBL-266 Abstract)

FEE, D., and S. S. Markowitz
Sulfur dioxide as a radical scavenger in alkene systems
UCRL-20470, April 1971
Akademische Verlagsgesellischaft, Frankfurt/M., Cronstettenstrasse 6a, Academic Press Inc., 111 Fifth Avenue, New York 3

FRAZIER, P., (See Clark, D. J., UCRL-20406)

GABRIEL, H., (See Barclay, J. A., UCRL-20433)

GARRISON, W. M.
Radiation-induced reactions of amino acids and peptides
UCRL-20440, March 1971
Advances in Chemistry Series

GARRISON, W. M., (See Makada, H. A., UCRL-20437 A)

GARRISON, W. M., (See Makada, H. A., LBL-242)

GATTI, R. C., (See Gilbert, A., LBL-207)

GARSIDE, ., (See Weigel, M., UCRL-20439 Abstract)

GAVIN, B. F., (See Spence, D. A., UCRL-20452)

GHIORSO, A.
A history of the transplutonic elements
LBL-213, July 1971
Handbook of Experimental Pharmacology

GHIORSO, A., M. Nurmia, K. Eskola, and P Eskola
Two new alpha-particle emitting isotopes of element 105, ^{261}Ha and ^{262}Ha
UCRL-20487, May 1971
Phys. Rev. C 4, 1850 (1971)

GHIORSO, A., M. Nurmia, K. Eskola, and P. Eskola
Comments on "Chemical separation of Kurchatovium"
LBL-230, September 1971
Inorg. Nucl. Chem. Letters 7, 1117 (1971)

GHIORSO, A., (See Eskola, K., UCRL-20442)

GIAUQUE, R. D., and J. Jaklevic
Rapid quantitative analysis by X-ray spectrometry
LBL-204, July 1971
Advances in X-ray Analysis

GIAUQUE, R. D., (See Davison, C. C., UCRL-20474)

GILBERT, A., R. C. Gatti, G. L. Struble, and S. G. Thompson
Basic formulation of nuclear level density calculations
LBL-207, July 1971
NFP

GIORNI, A., (See Sherman, J. D., LBL-265 Abstract)

GLENDENNING, N. K., (See Ascuitto, R. J., UCRL-20496)

GLENDENNING, N. K., (See Ascuitto, R. J., LBL-233)

GLENDENNING, N. K., (See Ascuitto, R. J., LBL-248)

GO, M. K.
Decay of the $^{50}Cr^{*}$ compound nucleus formed by the nuclear reactions $^{3}He + ^{47}Ti$, $^{4}He + ^{46}Ti$, $^{16}O + ^{34}S$, $^{18}O + ^{32}S$, and $^{22}Ne + ^{28}Si$
UCRL-20483, May 1971
Ph. D. Thesis

GOLDSWORTHY, W. W.
Digital nuclear spectrometer
UCRL-20434, January 1971
Nucl. Instr. Methods

GOLDSWORTHY, W. W. and R. G. Clem
A digital potentiostat
UCRL-20486, May 1971
Anal. Chem. 43, 1718 (1971)

GOLDSWORTHY, W. W., and R. G. Clem
A bipolar digipotentiograter for electronanalytical uses
LBL-282, December 1971
Anal. Chem.

GOOSMAN, D. R., (See Cerny, J., LBL-240)

GOTH, G. W.
The decay of T = 2 states in T_z = 0 nuclei
LBL-224, August 1971
Ph.D. Thesis

GOUGH, R. A., J. Cerny, R. G. Sextro, and J. E. Esterl
Beta-delayed protons from ^{23}Al
UCRL-20436, February 1971
International Conference on Heavy Ion Physics, Dubna, February 1971)

GOUGH, R. A., J. Cerny, R. G. Sextro and J. E. Esterl
Beta-delayed protons from ^{23}Al
UCRL-20436 Abstract, February 1971
Meeting of the American Physical Society, Washington, D. C., 26-29 April 1971

GOUGH, R. A., and R. D. Macfarlane
Energy loss and straggling of ^{12}C, ^{14}N, and ^{16}O ions in Ni foil
LBL-267 Abstract, November 1971
Meeting of the American Physical Society, San Francisco, California, January 31-February 3, 1972

GOULDING, F. S., (See Harvey, B. G., LBL-266 Abstract)

GRENNBERG, B., A. Rytz, and F. Asaro
Corpuscular physics--absolute measurement of the α energy of ^{253}Einsteinium
LBL-236, September 1971
C. R. Acad. Sc. Paris 272, 283 (1971)

GRUNDER, H., (See Bacher, A. D., LBL-280)

GUILE, J. R. E. Doebler, Wm. C. McHarris, and W. H. Kelly
Decay of ^{202m}Pb
LBL-257 Abstract, October 1971
Meeting of the American Physical Society, San Francisco, California, January 31-February 3, 1972

HAAS, H., (See Bacon, F., LBL-603)

HADEISHI, T., and R. D. McLaughlin
Hyperfine-Zeeman-effect atomic absorption spectrometer for mercury
LBL-20643, May 1971
Science

HYDE, E. K., G. W. Butler, and A. M. Poskanzer
Characteristics of fragments produced in the interaction of 5.5 GeV protons with silver
UCRL-19991, October 1970
Phys. Rev. C 4, 1759 (1971)

HYDE, E. K., (See Eppley, R. E., LBL-272 Abstract)

IMMELE, J. D., and G. L. Struble
Gamma and octupole vibrations in deformed nuclei
LBL-238, September 1971
Nucl. Phys.

IMMELE, J. D. and G. L. Struble
Gamma and octupole vibrations in deformed nuclei
LBL-238 Abstract, November 1971
Meeting of the American Physical Society, San Francisco, California, January 31-February 3, 1972

JAKLEVIC, J. M., (See Lederer, C. M., UCRL-19987)

JAKLEVIC, J., (See Giauque, R. D., LBL-204)

JAKOB, F., (See Clem, R. G., UCRL-20457)

JAKOB, F., (See Clem, R. G., UCRL-20457-Rev.)

JARDINE, L. J.
Relative intensity calibration of a Ge(Li) gamma-ray spectrometer
UCRL-20435, May 1971
Nucl. Instr. Methods 96, 259 (1971)

JARDINE, L. J.
Gamma-ray calibration standards
UCRL-20476, April 1971
NFP

JARDINE, L. J.
Experimental investigation of the electron capture decay of ^{210}At and ^{209}At: The level schemes of ^{210}Po and ^{209}Po
LBL-246, December 1971
Ph. D. Thesis

JARDINE, L. J., S. G. Prussin, and J. M. Hollander
Decay of ^{210}At to levels in ^{210}Po
LBL-278, November 1971
Nucl. Phys.

JARED, R. C., (See Cheifetz, E., UCRL-20450 Abstract)

JARED, R. C., (See Wilhelmy, J. B., UCRL-20489 A)

JARED, R. C., (See Cheifetz, E., UCRL-20498)

JARED, R. C., (See Wilhelmy, J. B., LBL-255)

JARED, R. C., (See Wilhelmy, J. B., LBL-256)

JENSEN, C. H., A. Partridge, T. Kenjo, J. Bucher, and R. M. Diamond
Anion exchange in aqueous-organic solvent mixtures, II
LBL-225, August 1971
J. Phys. Chem. 76, 1040 (1972)

KAINDL, G., D. Salomon and G. Wortmann
Quadrupole splitting of the 6.2 keV gamma rays of ^{181}Ta in rhenium metal
LBL-279, November 1971
Phys. Rev. Letters

KAINDL, G., and D. Salomon
Mössbauer-NMR on ^{181}Ta
UCRL-20449 Abstract, February 1971
Meeting of the American Physical Society, Washington, D. C., 26-29 April 1971

KAINDL, G., D. Salomon, and D. A. Shirley
Isomer shift study with the 6.25 keV γ rays of ^{181}Ta
LBL-217 Abstract, November 1971
Meeting of the American Physical Society, San Francisco, California, January 31-February 3, 1972

KAINDL, G., (See Salomon, D., LBL-217)

KAINDL, G., (See Bacon, F., LBL-239)

KAINDL, G., (See Salomon, D., LBL-259 Abstract)

KAINDL, G., (See Bacon, F., LBL-603)

KAINDL, G., (See Bacon, F., LBL-264 Abstract)

KELLY, W. H., (See Guile, J., LBL-257 Abstract)

KENJO, T., S. Brown, E. Held, and R. M. Diamond
Coordination of fluoride and chloride anions with alcohol and phenol
LBL-249, October 1971
J. Phys. Chem.

KENJO, T., (See Jensen, C. H., LBL-225)

KOLBE, W. and N. Edelstein
Endor of Pu^{3+} in CaF_2
UCRL-20414, January 1971
Phys. Rev. B 4, 2869 (1971)

KOVAR, D. G., (See Harvey, B. G., LBL-266 Abstract)

KROCHTA, J. M., D. R. Buss, and T. Vermeulen
Asymmetric interactions and the separation of optical isomers by optically active sorbents
UCRL-20471, April 1971
Ph. D. Thesis

LANDIS, D. A., (See Harvey, B. G., LBL-266 Abstract)

LANG, S. B. and C. R. Wilke
A hydrodynamic mechanism for the coalescence of liquid drops. I. Theory of coalescence at a planar interface
UCRL-20900, June 1971
Ind. Eng. Chem., Fundamentals 10, 329 (1971)

LANG, S. B. and C. R. Wilke
A hydrodynamic mechanism for the coalescence of liquid drops. II. Experimental studies
UCRL-20901, June 1971
Ind. Eng. Chem., Fundamentals 10, 341 (1971)

LEDERER, C. M., J. M. Jaklevic, and J. M. Hollander
In-beam gamma-ray spectroscopy of odd-neutron Mo and Ru isotopes
UCRL-19987, January 1971
Nucl. Phys. A169, 489 (1971)

LEIGH, J. R., K. H. Maier, R. M. Diamond and F. Pühlhofer
A high-energy and high-spin isomer in ^{211}At
UCRL-20448 Abstract, February 1971
Meeting of the American Physical Society, Washington, D. C., 26-29 April 1971

LEIGH, J. R., J. O. Newton, L. A. Ellis, M. C. Evans, and M. J. Emmott
A study of the odd-A rhenium isotopes: ^{179}Re and ^{177}Re
UCRL-20494, June 1971
Nucl. Phys.

LEIGH, J. R., (See Maier, K. H., UCRL-19593)

LEIGH, J. R., (See Diamond, R. M., UCRL-20463)

LEIGH, J. R., (See Maier, K. H., UCRL-20481)

LEIGH, J. R., (See Maier, K. H., LBL-202)

LEIGH, J. R., (See Maier, K. H., LBL-243)

LEIGH, J. R., (See Maier, K. H., LBL-276)

LEWIS, R. S., (See Alexander, E. C., Jr., UCRL-20482)

LISKOW, D. H., C. F. Bender, and H. F. Schaefer III
Theoretical reaction coordinate for the methyl isocyanide isomerization
LBL-290, December 1971
J. Am. Chem. Soc.

LISKOW, D. H., C. F. Bender, and H. F. Schaefer III
Bending frequency of the C_3 molecule
LBL-291, December 1971
J. Chem. Phys.

MACFARLANE, R. D., (See Gough, R. A., LBL-267 Abstract)

MAHNKE, H.-E., (See Bacon, F., LBL-239)

MAHNKE, H.-E., (See Bacon, F., LBL-264 Abstract)

MAHNKE, H.-E., (See Bacon, F., LBL-603)

MAHONEY, J., (See Harvey, B. G., UCRL-20454)

MAHONEY, J., (See Harvey, B. G., LBL-266 Abstract)

MAIER, K. H., K. Nakai, J. R. Leigh, R. M. Diamond, and F. S. Stephens
Effective single-particle magnetic moments around ^{208}Pb
UCRL-19593, October 1970
Nucl. Phys.

MAIER, K. H., (See Leigh, J. R., UCRL-20448 Abstract)

MAIER, K. H., J. R. Leigh, F. Pühlhofer, and R. M. Diamond
A high-spin isomer in ^{211}At
UCRL-20481, May 1971
Phys. Letters 35B, 401 (1971)

MAIER, K. H., J. R. Leigh, and R. M. Diamond
Measurement of the magnetic moment and lifetime of the $13/2^+$ level in ^{205}Pb
LBL-202, July 1971
Nucl. Phys. A176, 497 (1971)

MAIER, K. H., K. Nakai, J. R. Leigh, R. M. Diamond, and F. S. Stephens
Stroboscopic measurement of the g-factors of the 7^- isomer in ^{206}Pb and the $21/2^+$ isomer in ^{207}Bi
LBL-243, October 1971
Nucl. Phys.

MAIER, K. H., J. R. Leigh, F. Pühlhofer, and R. M. Diamond
Excited levels in N = 126 isotones studied by (HI, xnγ)-reactions
LBL-276, November 1971
Journal de Physique

MAIER, K. H., (See Diamond, R. M., UCRL-20463)

MAIN, R. M.
Review of linear accelerator for heavy ions
UCRL-20453, March 1971
Particle Accelerator Conference, Chicago, Illinois, 1-3 March 1971

MAKADA, H. A., W. M. Garrison
Radiolysis of liquid N-ethylacetamide
UCRL-20437 Abstract, January 1971
Meeting of the Radiation Research Society, Boston, Massachusetts, 9-13 May 1971

MAKADA, H. A., and W. M. Garrison
Radiolytic oxidation of peptide derivatives of glycine in aqueous solution
LBL-242, October 1971
Radiation Research

MAPLES, C. C., Jr.
Systematics of the direct (p,α) reaction
LBL-253, October 1971
Ph. D. Thesis

MAPLES, C., and J. Cerny
High-spin assignments in the 1p-shell utilizing the J-dependent (p,α) reaction
LBL-288, December 1971
Phys. Rev. Letters

MAREI, S. A., and B. B. Cunningham
Magnetic measurements of curium metal, CmF_3, and CmOCl
LBL-200, July 1971
J. Inorg. Nucl. Chem.

MARGARITIS, A., and C. R. Wilke
Engineering analysis of the rotorfermentor
LBL-222, August 1971
Annual Meeting of the Society for Industrial Microbiology, Aug. 29-Sept. 4, 1971, Colorado State University, Fort Collins, Colorado

MARKOWITZ, S. S., (See Fee, D., UCRL-20470)

MARRUS, R., R. W. Schmieder
Lifetime of the 2^1S_0 state of heliumlike argon
UCRL-20458, March 1971
NFP

MARRUS, R., and R. W. Schmieder
Forbidden decays of hydrogenlike and heliumlike argon
UCRL-20823, June 1971
Phys. Rev. A 5, 1160 (1972)

MARRUS, R., (See Schmieder, R. W., UCRL-20902 A)

MATTHIAS, E., B. Olsen, D. A. Shirley, R. M. Steffen, and J. E. Templeton
The theory of nuclear magnetic resonance detected by nuclear radiations
UCRL-18413, January 1971
Phys. Rev. A 4, 1626 (1971)

Mc CLATCHIE, E. A., (See Bacher, A. D., UCRL-20903)

McHARRIS, Wm. C., (See Guile, J., LBL-257 Abstract)

McLAUGHLIN, R. D., (See Hadeishi, T., UCRL-20643)

MERIWETHER, J. R., (See Harvey, B. G., UCRL-20454)

MERIWETHER, J. R., (See Harvey, B. G., LBL-266 Abstract)

MICHEL, M. C., (See Alexander, E. C., Jr., UCRL-20482)

MILLER, S. F.
Utilization of algae for water purification and protein production
LBL-289, December 1971, M. S. Thesis

MILLS, B. E., (See Hashmall, J. A., LBL-211)

MINER, C. E., (See Fadley, C. S., UCRL-20478)

MORETTO, L. G.
Shell model calculations of fission decay widths and probabilities in superheavy nuclei
LBL-206, July 1971
Nucl. Phys. A180, 337 (1972)

MORETTO, L. G.
Statistical description of a paired nucleus with the inclusion of angular momentum
LBL-219, August 1971
Nucl. Phys.

MORETTO, L. G.
Statistical description of deformation in excited nuclei and disappearance of shell effects with excitation energy
LBL-228, August 1971
Nucl. Phys. A182, 641 (1972)

MORETTO, L. G.
Stability towards fission of excited super-heavy nuclei
LBL-261 Abstract, November 1971
Meeting of the American Physical Society, San Francisco, California, January 31-February 3, 1972

MORETTO, L. G.
Level densities and deformation of excited nuclei from realistic shell models
LBL-262 Abstract, November 1971
Meeting of the American Physical Society, San Francisco, California, January 31-February 3, 1972

MORETTO, L. G.
Angular momentum and pairing correlation in nuclear level densities
LBL-263 Abstract, November 1971
Meeting of the American Physical Society, San Francisco, California, January 31-February 3, 1972

MORETTO, L. G.
Note on the shell effects disappearance with excitation energy and its relation with the Strutinski smoothing procedure
LBL-287, December 1971
Phys. Letters

MORRIS, D., (See Clark, D. J., UCRL-20406)

MORRIS, D., (See Clark, D. J., LBL-223)

MYERS, W. D.
The droplet model
LBL-209, Abstract, July 1971
Proceedings of the Mont Tremblant International Summer School on "The Dynamic Structure of Nuclear States", Mont Tremblant, Canada, August 1-14, 1971

NAKAI, K., (See Maier, K. H., UCRL-19593)

NAKAI, K., (See Maier, K. H., LBL-243)

NEWTON, A. S. and G. E. Thomas
Electron impact excitation functions of radiating and metastable states of carbon monoxide
UCRL-20905, June 1971
Chem. Phys. Letters 11, 171 (1971)

NEWTON, A. S.
The concentration of high boiling impurities from low boiling compounds by reverse flow gas chromatography
LBL-283, December 1971

NEWTON, J. O., (See Leigh, J. R., UCRL-20494)

NURMIA, M., (See Eskola, K., UCRL-20442)

NURMIA, M., (See Ghiorso, A., UCRL-20487)

NURMIA, M., (See Ghiorso, A., LBL-230)

OLSEN, B., (See Matthias, E., UCRL-18413)

O'NEIL, S. V., (See Pearson, P. K., LBL-214)

O'NEIL, S. V., (See Bender, C. F., LBL-250)

ORNELAS, L. D., (See Clem, R. G., UCRL-20457)

ORNELAS, L. D., (See Clem, R. G., UCRL-20457-Rev.)

PARSONS, T. C., (See Cummingham, B. B., LBL-212 A)

PARTRIDGE, A., (See Jensen, C. H., LBL-225)

PEARSON, P. K., S. V. O'Neil, and H. F. Schaefer III
Role of electron correlation in a priori predictions of the electronic ground state of BeO
LBL-214, August 1971
J. Chem. Phys.

PEARSON, P. K., (See Bender, C. F., LBL-250)

PEARSON, P. K., (See Bondybey, V., LBL-258)

PERLMAN, I., (See Bowman, H., UCRL-20490 Abstract)

PERLMAN, I., (See Asaro, F., LBL-231)

PETERS, R., (See Spence, D. A., UCRL-20452)

PETROVICH, F. L., (See Schaeffer, R., UCRL-20432)

PIGFORD, R. L., (See Corriveau, C. E., Jr., UCRL-20479)

PLATTNER, G. R., A. D. Bacher, and H. E. Conzett
Phase shifts for p-^{4}He elastic scattering between 20 and 40 MeV
LBL-269, December 1971
Phys. Rev.

PLATTNER, G. R., (See de Swiniarski, R., LBL-201)

PLATTNER, G. R., (See Bacher, A. D., LBL-280)

POSKANZER, A. M., (See Hyde, E. K., UCRL-19991)

POTTER, E., (See Robinson, H. P., UCRL-20418)

PRUSSIN, S. G., (See Jardine, L. J., LBL-278)

PÜHLHOFER, F., (See Leigh, J. R., UCRL-20448 Abstract)

PÜHLHOFER, F., (See Maier, K. H., UCRL-20481)

PÜHLHOFER, F. and R. M. Diamond
Excitation functions for direct heavy-ion reactions on ^{27}Al at energies between 4 and 10 MeV/nucleon
LBL-229 Abstract, August 1971
Meeting of the American Physical Society, Tucson, Arizona, 4-6 November 1971

PÜHLHOFER, F., (See Harvey, B. G., LBL-266 Abstract)

PÜHLHOFER, F., (See Maier, K. H., LBL-276)

QUEBERT, J. L., (See Diamond, R. M., UCRL-20463)

RASMUSSEN, J. O., (See Wilhelmy, J. B., LBL-256)

RAY, S., (See Templeton, D. H., UCRL-20438 A)

RAYNAL, J., (See de Swiniarski, R., LBL-201)

REGINATO, L. L., (See Spence, D. A., UCRL-20452)

RENKAS, M., (See Clark, D. J., UCRL-20406)

RESMINI, R. G., (See de Swiniarski, R., LBL-201)

REYNOLDS, J. H., (See Alexander, E. C., Jr., UCRL-20482)

ROBINSON, C. W. and C. R. Wilke
Mass transfer coefficients and interfacial area for gas absorption by agitated aqueous electrolyte solutions
UCRL-20472, April 1971
Ph. D. Thesis

ROBINSON, H. P. and E. Potter
Mathematical constants
UCRL-20418, March 1971
NFP

ROTHSTEIN, E. V.
Two-center integrals involving correlated orbitals.
I. Inclusion of James-Coolidge or Hylleraas r_{tj}^n terms
UCRL-20459, April 1971
Phys. Rev. A 3, 1581 (1971)

RUBEN, H., (See Zalkin, A., UCRL-20493 A)

SALOMON, D., (See Kaindl, G., UCRL-20449 Abstract)

SALOMON, D., G. Kaindl, and D. A. Shirley
Isomer shifts of the 6.25 keV γ rays of ^{181}Ta
LBL-217, August 1971
Phys. Letters

SALOMON, D., (See Kaindl, G., LBL-217 Abstract)

SALOMON, D., (See Kaindl, G., LBL-279)

SALOMON, D., G. Kaindl, and G. Wortmann
Quadrupole interaction of ^{181}Ta in rhenium metal
LBL-259 Abstract, November 1971
Meeting of the American Physical Society, San Francisco, California, January 31-February 3, 1972

SASSI, A. G.
Three-component ion-exchange in fixed beds application to pre-treatment of saline-water evaporator feed
LBL-299, December 1971
NFP

SCHAEFER, H. F., III, (See Pearson, P. K., LBL-214)

SCHAEFER, H. F., III, (See Bender, C. F., LBL-250)

SCHAEFER, H. F., III, (See Bondybey, V., LBL-258)

SCHAEFER, H. F., III, (See Liskow, D. H., LBL-290)

SCHAEFER, H. F., III, (See Liskow, D. H., LBL-291)

SCHAEFER, R. and F. L. Petrovich
A suggestion for choosing the single-particle energies in double closed shell nuclei
UCRL-20432, January 1971
Phys. Rev. Letters 26, 1380 (1971)

SCHMIEDER, R. W., and R. Marrus
Lifetime of the $2^2S_{1/2}$ state of hydrogenlike sulphur
UCRL-20902 Abstract, June 1971
Meeting of the American Physical Society, Seattle, Wash., 25-27 August 1971

SCHMIEDER, R. W.
Proposed electron/laser interferometer: applications
UCRL-20906 Abstract, June 1971
Meeting of the American Physical Society, Seattle, Wash., 25-27 August 1971

SCHMIEDER, R. W.
Proposed electron/laser interferometers: theory
UCRL-20907 Abstract, June 1971
Meeting of the American Physical Society, Seattle, Wash., 25-27 August 1971

SCHMIEDER, R. W.
Proposed laser-modulated electron interferometer
LBL-220, August 1971
Applied Physics Letters

SCHMIEDER, R. W.
A proposal for observation and study of coherent electron/laser interactions in solids
LBL-252, September 1971

SCHMIEDER, R. W.
Proposed electron/laser interferometer: applications
LBL-271 Abstract, November 1971
Meeting of the American Physical Society, San Francisco, California, January 31-February 3, 1972

SPENCE, D. A., B. F. Gavin, R. Peters, L. L. Reginato, B. H. Smith, and R. C. Wolgast
A 3-MeV injector for the SuperHilac
UCRL-20452, June 1971
NFP

STACY, J. J.
Optical studies of lanthanide and actinide ions in calcium fluoride
LBL-281, October 1971
Ph. D. Thesis

STEFFEN, R. M. (See Matthias, E., UCRL-18413)

STEPHENS, F. S., R. M. Diamond, and J. de Boer
E4 moments in ^{152}Sm and ^{154}Sm
UCRL-20477, April 1971
Phys. Rev. Letters 27, 1151 (1971)

STEPHENS, F. S., and R. S. Simon
Coriolis effects in the yrast states
LBL-273, November 1971
Nucl. Phys.

STEPHENS, F. S., (See Maier, K. H., UCRL-19593)

STEPHENS, F. S., (See Diamond, R. M., UCRL-20463)

STEPHENS, F. S., (See Maier, K. H., LBL-243)

STEYAERT, J., (See Clark, D. J., UCRL-20406)

STEYAERT, J., (See Clark, D. J., LBL-223 Abstract)

STEYAERT, J., (See Clark, D. J., LBL-223)

STREITWIESER, A., JR. (See Hashmall, J. A., LBL-211)

STRUBLE, G. L., (See Gilbert, A., LBL-207)

STRUBLE, G. L., (See Immele, J. D., LBL-238 Abstract)

STRUBLE, G. L., (See Immele, J. D., LBL-238)

STRUBLE, G., (See Wong, J., LBL-285 Abstract)

SYMONS, G. D., (See Diamond, R. M., UCRL-20463)

TEMPLETON, L. K. and D. H. Templeton
The crystal structure of $POBr_3$: Space group and refinement by least squares
UCRL-20430, January 1971
Acta Cryst. B 27, 1678 (1971)

TEMPLETON, D. H., S. Ray, and A. Zalkin
Diverse structures of the isomorphous hexahydrated fluosilicates
UCRL-20438 Abstract, January 1971
Meeting of the American Crystallographic Association, 1-4 February 1971, Columbia, South Carolina

TEMPLETON, J. E., (See Matthias, E., UCRL-18413)

TEMPLETON, J. E., (See Bacon, F., UCRL-20465)

TEMPLETON, D. H., (See Templeton, L. K., UCRL-20430)

TEMPLETON, D. H., (See Zalkin, A., UCRL-20493 A)

THOMAS, G. E., (See Newton, A. S., UCRL-20905)

THOMAS, T. D., (See Davis, D. W., LBL-216)

THOMAS, T. D., (See Davis, D. W., LBL-270)

THOMPSON, S. G., (See Cheifetz, E., UCRL-20450 Abstract)

THOMPSON, S. G., (See Wilhelmy, J. B., UCRL-20489 A)

THOMPSON, S. G., (See Cheifetz, E., UCRL-20498)

THOMPSON, S. G., (See Gilbert, A., LBL-207)

THOMPSON, S. G., (See Wilhelmy, J. B., LBL-255)

THOMPSON, S. G., (See Wilhelmy, J. B., LBL-256)

TIVOL, W. F., (See Bacher, A. D., LBL-280)

TOMBRELLO, T. A., (See Bacher, A. D., UCRL-20903)

TSANG, C. F., and J. B. Wilhelmy
Interpretation of mass asymmetry in fission based on deformation energy surfaces
UCRL-20488 Abstract, May 1971
National American Chemical Society Meeting, Washington, D. C., 12-17 September 1971

TSANG, C. F., and J. B. Wilhelmy
Interpretation of mass asymmetry in fission based on deformation energy surfaces
LBL-254, November 1971
Nucl. Phys.

VERMEULEN, T., (See Krochta, J. M., UCRL-20471)

WEAVER, T. A., (See Bacher, A. D., UCRL-20903)

WEIGEL, M., L. Garside, and P. K. Haug
Renormalization constants for the particle-hole force
UCRL-20439 Abstract, February 1971
Meeting of the American Physical Society, Washington, D. C., 26-29 April 1971

WEIGEL, M.
Some approximations in the theory of moments and transitions for even-odd nuclei
UCRL-20495, June 1971
Annals of Physics

WEIGEL, M., (See Borsig, M. V., LBL-244)

WILCOX, K. H., (See Harney, H. L., LBL-268 Abstract)

WILHELMY, J. B., E. Cheifetz, R. C. Jared, and S. G. Thompson
Prompt gamma ray spectra from products formed in the spontaneous fission of ^{252}Cf
LBL-255, November 1971
NFP

WILHELMY, J. B., E. Cheifetz, R. C. Jared, S. G. Thompson, H. R. Bowman, and J. O. Rasmussen
Angular momentum of primary products formed in the spontaneous fission of ^{252}Cf
LBL-256, November 1971
Phys. Rev.

WILHELMY, J. B., (See Cheifetz, E., UCRL-20450 Abstract)

WILHELMY, J. B., (See Tsang, C. F., UCRL-20488 A)

WILHELMY, J. B., E. Cheifetz, R. C. Jared, and S. G. Thompson
Detailed spectroscopy on prompt fission products
UCRL-20489 Abstract, May 1971
National American Chemical Society Meeting, Washington, D. C., 12-17 September 1971

WILHELMY, J. B., (See Cheifetz, E., UCRL-20498)

WILHELMY, J. B., (See Tsang, C. F., LBL-254)

WILKE, C. R., (See Robinson, C. W., UCRL-20472)

WILKE, C. R., (See Lang, S. B., UCRL-20900)

WILKE, C. R., (See Lang, S. B., UCRL-20901)

WILKE, C. R., (See Margaritis, A., LBL-222)

WOLGAST, R. C., (See Spence, D. A., UCRL-20452)

WORDEN, E. F., (See Conway, J. G., LBL-210 Abstract)

WORTMANN, G., (See Kaindl, G., LBL-279)

WORTMANN, G., (See Salomon, D., LBL-259 Abstract)

WONG, J., and G. Struble
The effect of ground state correlations associated with generalized nuclear vibration
LBL-285 Abstract, December 1971
Meeting of the American Chemical Society, Boston, Massachusetts, 9-14 April 1972

WOZNIAK, G. J., (See Harney, H. L., LBL-268 Abstract)

ZALKIN, A., (See Templeton, D. H., UCRL-20438 A)

ZALKIN, A, H. Ruben, and D. H. Templeton
The crystal and molecular structure of 7,8,15,16-tetrathiadispiro [5.2.5.2] hexadecane, $C_{12}H_{20}S_4$
UCRL-20493 Abstract, June 1971
Meeting of the American Crystallographic Association, Ames, Iowa, 15-20 August 1971

ZISMAN, M. S. and B. G. Harvey
High-spin proton states observed in the $^{90}Zr(\alpha,t)^{91}Nb$ and $^{92}Mo(\alpha,t)^{93}Tc$ reactions at 50 MeV
UCRL-20466, March 1971
Phys. Rev. C 4, 1809 (1971)

ZISMAN, M. S., and B. G. Harvey
High-spin levels of $^{92,93,94,95,96}Nb$ and ^{94}Tc populated with (α,d) and (α,t) reactions at 50 MeV
LBL-226, August 1971
Phys. Rev. C 5, 1031 (1972)

ZISMAN, M. S., (See Bacher, A. D., UCRL-20903)

ZISMAN, M. S., (See Sherman, J. D., LBL-227)

ZISMAN, M. S., (See Harvey, B. G., LBL-266 Abstract)

VII. Author Index

Author Index

Contributors to This Report